

MODELLING OF MIXED LUBRICATION IN PLAIN  
BEARINGS BASED ON THE THEORY OF FLOW  
FACTORS AND INCORPORATING A DRY CONTACT  
ANALYSIS

by

Anton Manoylov

Thesis submitted in candidature for the degree of  
Doctor of Philosophy at Cardiff University

Tribology and Contact Mechanics Research Group  
Institute of Mechanics and Advanced Materials  
School of Engineering  
Cardiff University

*December 2013*

(Intentionally blank)

## Declaration

This work has not been submitted in substance for any other degree or award at this or any other university or place of learning, nor is being submitted concurrently in candidature for any degree or other award..

Signed ..... (Anton V. Manoylov) Date .....

### *Statement 1*

This thesis is being submitted in partial fulfilment of the requirements for the degree of Philosophy Doctor.

Signed ..... (Anton V. Manoylov) Date .....

### *Statement 2*

This thesis is the result of my own independent work/investigation, except where otherwise stated. Other sources are acknowledged by explicit references. The views expressed are my own.

Signed ..... (Anton V. Manoylov) Date .....

### *Statement 3*

I hereby give consent for my thesis, if accepted, to be available for photocopying and for inter-library loan, and for the title and summary to be made available to outside organisations.

Signed ..... (Anton V. Manoylov) Date .....

### *Statement 4*

I hereby give consent for my thesis, if accepted, to be available for photocopying and for inter-library loans after expiry of a bar on access previously approved by the Academic Standards & Quality Committee.

Signed ..... (Anton V. Manoylov) Date .....

(Intentionally blank)

## Summary

Three topics are considered in this thesis. The first is evaluation of the effective elastic moduli of porous materials and considers materials such as porous glass, sandstone, sintered bronze and iron materials, porous ceramics. Models with spherical pores were first considered showing good agreement for some materials but not for materials prepared by powder sintering. A number of modifications of increasing complexity were introduced accounting for non-spherical pores and their interaction. The models then compare well with experimental data for sintered materials.

The other topics of the thesis can be used to model mixed lubrication in plain bearings where part of the load is carried by contacting asperities and part by the lubricant film. The roughness features affect the ability of the lubricant to flow in the gap between the surfaces and surface deflection is caused by asperity contact pressures only.

A method is presented to solve dry contact problems for nominally plane surfaces using a simple elastic-plastic model at asperity contacts and a differential formulation for the elastic deflection. Periodic roughness defined over a representative area is incorporated using Fourier transforms to calculate the convolutions. The method is validated by comparison with the results of an elastic-plastic rough surface contact analysis obtained using a finite element method.

A method is then developed to model the mixed lubrication problem based on the homogenised Reynolds equation where the effect of the roughness features is isolated from that of the global geometry of the bearing. Local rough problems are solved and the average effect of the roughness on lubricant flow expressed in terms of flow factors, which are functions of global film thickness. When direct asperity contact occurs the deflected shape is obtained from dry contact analysis of the representative roughness area. The global problem is then solved using the Reynolds equation modified with appropriate flow factors taking the mean contact pressure obtained from the local problem into account in load determination.

The homogenised method is validated against the series of deterministic solutions and cases of surfaces with measured roughness are presented

## Acknowledgements

This work was funded by the European Commission within the MINILUBES project (FP7 Marie Curie ITN network 216011-2) and by the Austrian Research Promotion Agency (FFG) within the framework of the COMET K2 Excellence Centre of Tribology (X-Tribology). Part of the work done for this thesis was funded by UK Engineering and Physical Sciences Research Council grant EP/G06024X/1, The British Gearing Association, and Rolls-Royce Goodrich Engine Control Systems Ltd. The financial support is very much appreciated.

This work would never be possible without supervision and guidance from Prof. F.M. Borodich and Prof. H. P. Evans. I am thankful for their time and efforts invested in me, for sharing their ideas and providing feedback when necessary.

I also appreciate the valuable discussions with colleagues in Cardiff and AC<sup>2</sup>T, fellow MINILUBers, Dr. W. Pahl from GKN and Prof. R.L. Salganik from Ishlinsky Institute for Problems in Mechanics, Moscow.

I am grateful to Dr M. J. Bryant for sharing the results he obtained for elastic-plastic contact analysis using ABAQUS. It was very encouraging to find his results being not so different from mine.

Finally I would like to thank my parents, friends and colleagues for moral support, and especially my future wife Ksenia for being supportive, patient and a very good listener.

# Contents

Declaration .....	III
Statement 1 .....	III
Statement 2 .....	III
Statement 3 .....	III
Statement 4 .....	III
Summary .....	V
Acknowledgements .....	VI
Contents .....	VII
Nomenclature .....	XI
List of acronyms .....	XVI
1. Introduction .....	1
1.1. Ionic liquids as potential lubricants .....	1
1.2. The MINILUBES project .....	3
1.3. Porous bearings .....	5
1.4. Structure of the thesis .....	6
1.5. Evolution of the contact mechanics methods .....	8
1.6. Mixed lubrication in plain bearings .....	11
2. The effective elastic properties of porous materials .....	15
2.1. Introduction .....	15
2.2. Vavakin-Salganik (VS) model .....	18
2.3. The extended VS approach .....	21
2.4. Comparison of the extended VS model with experiments .....	24
2.5. Merged pores model (MPM) .....	29
2.6. Comparison of the MPM model with experiments .....	32
2.7. Open pores model (OPM) .....	33
2.8. Combined model (OPMPM) .....	39
2.9. Conclusions .....	40
3. Dry contact analysis of rough nominally flat surfaces .....	43
3.1. Introduction .....	43
3.2. Theoretical background .....	45
3.2.1. Formulation .....	45
3.2.2. Elastic deflection .....	47
3.2.3. Differential deflection formulation .....	48
3.2.4. Convolution theorem .....	49
3.2.5. Harmonic roughness and periodic boundary .....	53
3.3. Numerical implementation .....	55

3.3.1	Flowchart of the differential deflection method.....	58
3.4	Results and discussion .....	59
3.4.1	Westergaard solution .....	59
3.4.2	Two-dimensional roughness .....	61
3.4.3	Extruded roughness profile .....	65
3.4.4	Full 3D FEA comparison.....	72
3.5	Conclusions .....	76
4	Theory of flow factors .....	79
4.1	Introduction .....	79
4.2	Classical Reynolds' equation .....	80
4.3	Periodic roughness and two-scale expansion .....	82
4.4	Flow factors.....	91
4.5	Flow factors for oblique roughness.....	92
5	Evaluation of the flow factors.....	97
5.1	Solving the local problems.....	97
5.1.1	Numerical solution.....	97
Discretisation .....	97	
Gauss-Seidel iterative method.....	99	
Boundary conditions .....	100	
5.1.2	Analytical solution for $\chi_1$ .....	101
Evaluating the integral .....	101	
Boundary conditions .....	103	
Summary.....	103	
Comparison of the analytical and numerical solutions .....	104	
5.1.3	Analytical solution for $\chi_3$ .....	110
Indefinite integrals .....	111	
Boundary conditions .....	112	
Summary.....	113	
Comparison of the analytical and numerical solutions .....	113	
5.2	Calculating of the flow factors .....	119
5.2.1	Numerical evaluation of the flow factors .....	120
5.2.2	Analytical calculation of flow factors .....	120
Calculating the flow factor $a_{11}$ .....	121	
Calculating the flow factor $a_{22}$ .....	121	
Calculating the flow factor $b_{11}$ .....	124	
Calculating the flow factor $b_{22}$ .....	124	
5.2.3	Comparison of the analytical and numerical flow factors .....	125
5.2.4	The effect of the roughness orientation .....	130

5.2.5	Double cosine roughness .....	134
5.2.6	The effect of the local cell dimensions on the flow factors.....	140
5.2.7	Flow factors for measured surfaces .....	144
	Axially ground disc.....	145
	Super finished surface .....	148
	Surface prepared by electrical discharge machining.....	151
6	Mixed lubrication in plain bearings .....	157
6.1	Introduction.....	157
6.2	Formulation of a tilted pad problem .....	158
6.3	Solving the Reynolds equation using the Gauss-Seidel method .....	161
6.3.1	Discretisation .....	161
6.3.2	Boundary conditions .....	166
6.3.3	Convergence .....	166
	Effect of the asperity wavelength on the convergence speed.....	166
	Convergence of a tilted pad bearing problem using the Gauss-Seidel iterative method .....	167
6.4	The multigrid method .....	168
6.4.1	Introduction.....	168
6.4.2	Fine and coarse grids.....	169
6.4.3	Intergrid transfers .....	171
	Restriction operator .....	171
	Interpolation operator.....	173
6.4.4	Correction scheme .....	176
6.4.5	Multi level coarse grid correction scheme .....	178
6.4.6	Full multigrid.....	181
6.4.7	Multigrid boundary conditions .....	182
6.5	Solving the tilted pad bearing problem using the multigrid method .....	182
6.5.1	The convergence speed.....	183
6.5.2	Coarse grid roughness problem.....	187
6.5.3	Extruded cosine roughness.....	190
6.5.4	Extruded cosine roughness: contact case .....	199
6.5.5	The oblique roughness effect .....	201
6.5.6	The two dimensional roughness problems .....	206
6.5.7	Measured roughness cases .....	216
	Ground surface.....	217
	Super finished surface .....	224
	EDM surface .....	231
6.6	Practical guidelines on using the flow factors approach .....	237

6.7	Discussion .....	239
7.	Conclusions and potential developments .....	243
7.1.	Elastic properties of the porous materials.....	243
7.2.	Dry contact analysis.....	244
7.3.	Evaluation of the flow factors .....	246
7.4.	Mixed lubrication analysis based on the theory of flow factors .....	248
	Appendices.....	251
	Appendix A Evaluating the integral of $(a+\cos t)^{-3}$ .....	251
A.1	The integration by substitution .....	251
A.2	Integral of the rational functions .....	253
A.3	Calculating the definite integral on the interval $[0,x]$ .....	255
	Appendix B Evaluating the integral of $(a+\cos t)^{-2}$ .....	256
B.1	The integration by substitution .....	256
B.2	Integral of the rational functions .....	256
B.3	Calculating the definite integral on the interval $[0,x]$ .....	258
	References.....	259

## Nomenclature

Note that due to the diversity of the problems covered in the thesis the same notations may have different meanings in different chapters

Chapter 2 Effective elastic properties of porous materials	
$E, \nu$	Elastic modulus, Poisson's ratio of the material
$K, \mu$	Bulk modulus, shear modulus
$E_0, \nu_0, K_0, \mu_0$	Elastic properties of the host material, i.e. with no pores
$\rho$	Porosity
$r_i$	Pore radius with index $i$
$N_i$	Number of pores of radius $r_i$
$n$	Number of different pore radii
$i$	Dummy index
$\rho$	Concentration of pores
$E_b, \nu_b$	Elastic properties of the material with pores of radii $r < r_i$
$f(r)$	Probability density function of pore radius
$d$	Distance between pore centres
$\phi(d)$	Probability function for the distance between 2 random points
$P_{merge}(r_i, r_j)$	Probability of spherical pores of radii $r_i$ and $r_j$ to merge
$N$	Total number of spherical pores
$N_{ii}$	Number of pair combinations of pores of the same radius $r_i$
$N_{ij}$	Number of pair combinations of pores of different radii $r_i$ and $r_j$
$p_{ii}^{merged}$	Volume fraction of elliptical pores created by merging of spherical pores of the same radius $r_i$
$p_{ij}^{merged}$	Volume fraction of elliptical pores created by merging of spherical pores of different radii $r_i$ and $r_j$
$\omega, \phi$	Damage/integrity parameters of the material. $\omega + \phi = 1$
$A$	Area of the cross section of the porous sample
$A_{open}$	Area of the cross section of the sample occupied by open pores

**Chapter 3 Dry contact analysis**

<i>Continuous</i>	<i>Discrete</i>	
$r(x,y)$	$R_{i,j}$	Undeformed rough surface height from datum
$R_{min}, R_{max}$	$R_{min}, R_{max}$	The $R$ values of the deepest valley and of the highest
$h(x,y)$	$H_{i,j}$	Gap between the surfaces
$\bar{h}$		Mean line of the rough surface in an undeformed condition
$p(x,y)$	$P_{i,j}$	Contact pressure distribution
$S$		Rigid body movement (elastic approach)
$P_{max}$	$P_{max}$	Maximum contact pressure possible, hardness.
$d^{elast}(x,y)$	$D_{i,j}^{elast}$	Elastic displacement
$d^{plast}(x,y)$	$D_{i,j}^{plast}$	Plastic displacement
$\mathbf{Z}$		Space of all integer numbers
$\mathbf{R}$		Space of all real numbers
	$\mathbf{\Omega} \subset \mathbf{Z}$	Finite discrete domain that is the solution space.
$L, W$	$N_x, N_y$	Dimensions of the solution space; periods of the periodic functions
	$\Delta x, \Delta y$	Size of the mesh cell
$x, y \in \mathbf{R}$	$i, j \in \mathbf{\Omega}$	Lateral dimensions, number of mesh points
$E'$		Reduced elastic modulus, $E' = 2\{(1-\nu_1^2)/E_1 + (1-\nu_2^2)/E_2\}^{-1}$
$s, t$	$k, l$	Dummy variables for convolution
$g(s,t)$	$G_{k,l}$	Pressure influence coefficients for deflection
$\nabla^2$		Laplace operator
$f(s,t)$	$F_{k,l}$	Pressure influence coefficients for differential deflection
$\phi$	$\Phi$	Fourier transform
$\bullet$		Point wise product
$\otimes$		Convolution operator
	$N_x^*, N_y^*$	Dummy number of elements in definition of the Fourier transform

$a, b \in \mathbf{Z}$		Dummy integers indicating infinite periodic repetition
$i$		$\sqrt{-1}$
$G_{i,j}^{Periodic}$	Infinite periodic summation	$\sum_{a=-\infty}^{\infty} \sum_{b=-\infty}^{\infty} G_{i-aN_x^*, j-bN_y^*}$
$F_{i,j}^{Periodic}$	Infinite periodic summation	$\sum_{a=-\infty}^{\infty} \sum_{b=-\infty}^{\infty} F_{i-aN_x^*, j-bN_y^*}$
$\gamma(x,y)$	$\Gamma_{ij}$	Right hand side of Poisson equation for $h$ .
$h_{max}$	$H_{max}$	The H value at the point $(x_0, y_0)$ , the deepest valley of the surface
$x_0, y_0$	$i_0, j_0$	Position of deepest valley feature
	$\lambda$	Index for point $i, j$ and 8 <i>near</i> neighbours in equations (3.20-3.22)
	$B_\lambda$	Summation coefficient for neighbouring points in $\nabla^2 H$

#### Chapter 4,5: Flow factors, theory and evaluation

$\rho$		Density of the fluid
$h(x,y)$	$H_{ij}$	Gap between the surfaces
$p(x,y)$	$P_{ij}$	Hydrodynamic pressure distribution
$\eta$		Dynamic viscosity [Pa·s]
$\bar{u}$		Mean velocity of the surfaces
$\lambda$	$= 12\eta\bar{u}$	Coefficient in the isoviscous incompressible Reynolds equation
$x, y \in \mathbf{R}$		The system of coordinates associated with the global problem
$\Omega \subset \mathbf{R}$		Solution domain for the local problem
$\xi, \psi \in \Omega$		The system of coordinates associated with the local problem
$\varepsilon$		Global to local scaling factor
$p_s(x, y, \xi, \psi)$		Asymptotic solution for pressure
$p_0, h_0$		Global pressure, film thickness
$p_1, h_1$		Local pressure, film thickness
$A_1$		$\frac{\partial}{\partial \xi} \left( h^3 \frac{\partial [\cdot]}{\partial \xi} \right) + \frac{\partial}{\partial \psi} \left( h^3 \frac{\partial [\cdot]}{\partial \psi} \right)$
$A_2$		$\frac{\partial}{\partial \xi} \left( h^3 \frac{\partial [\cdot]}{\partial x} \right) + \frac{\partial}{\partial \psi} \left( h^3 \frac{\partial [\cdot]}{\partial y} \right) + \frac{\partial}{\partial x} \left( h^3 \frac{\partial [\cdot]}{\partial \xi} \right) + \frac{\partial}{\partial y} \left( h^3 \frac{\partial [\cdot]}{\partial \psi} \right)$

$A_3$	$\frac{\partial}{\partial x} \left( h^3 \frac{\partial [\cdot]}{\partial x} \right) + \frac{\partial}{\partial y} \left( h^3 \frac{\partial [\cdot]}{\partial y} \right)$
$B^\xi, B^\psi$	$\lambda \frac{\partial [(\cdot)h]}{\partial \xi} ; \lambda \frac{\partial [(\cdot)h]}{\partial \psi}$
$B^x, B^y$	$\lambda \frac{\partial [(\cdot)h]}{\partial x} ; \lambda \frac{\partial [(\cdot)h]}{\partial y}$
$\theta$	Angle of rotation of the local coordinate system; oblique direction
$\chi_1, \chi_2, \chi_3, \chi_4$	Solutions of the local problems
$a_{11}, a_{22}$	Poiseuille flow factors calculated in the axes of periodicity
$a_{12}, a_{21}$	Cross (diagonal) Poiseuille flow factors in the axes of periodicity
$b_{11}, b_{22}$	Couette flow factors calculated in the axes of periodicity
$b_{12}, b_{21}$	Cross (diagonal) Couette flow factors in the axes of periodicity
$A_{11}, A_{22}, A_{12}, A_{21}$	Poiseuille flow factors (oblique) calculated in the axes coinciding with the entrainment and transverse to entrainment directions
$B_1, B_2$	Couette flow factors (oblique) calculated in the axes coinciding with the entrainment and transverse to entrainment directions
$h_r$	Amplitude of the sine/cosine roughness function
$\tau$	$=h_0/h_r$ Ratio of the mean gap value and amplitude of the waviness
$k$	Number of sine/cosine waves in the roughness profile
$F$	Function used for the analytical evaluation of the integral
$F_1, F_2, F_3$	Constants involved in F, see Appendix A
$n$	Number of full periods of sine function in the interval from 0 to the current point
$\lfloor \rfloor$	Rounding down to the nearest integer value
$G$	Function used for the analytical evaluation of the integral
$G_1, G_2$	Constants involved in G, see Appendix B
$\kappa$	Stretching coefficient in section 5.2.6

## Chapter 6 Mixed lubrication

$L, W$  Physical dimensions of the solution space

$x, y \in \mathbf{R}$  Coordinates associated with the global problem

$h_{min}$	The lowest value of the film thickness (at the exit of the bearing)
$\alpha$	Tilting angle of the inclined pad
$\gamma$	Tilting ratio of the pad ( $=\tan \alpha$ )
$h(x,y)$	Total film thickness
$h_0(x,y)$	Global film thickness, defined by the geometry of the problem
$R(x,y)$	Roughness function with zero mean line
$p(x,y)$	Hydrodynamic pressure distribution
$A_{11}, A_{12}, A_{21}, A_{22}$	Poiseuille flow factors (in the axis coinciding with the entrainment and transverse to entrainment directions)
$B_1, B_2$	Couette flow factors (in the axis coinciding with the entrainment and transverse to entrainment directions)
$N_x, N_y$	Number of nodes on the mesh grid
$\Phi_{ij}^k$	$k=1-4$ ; Volume component of the Poiseuille flow reduced due to the presence of roughness by means of the flow factors (6.4)
$\Phi_{ij}^k$	$k=5,6$ ; Gap component of the Couette flow reduced due to the presence of roughness by means of the flow factors (6.4)
$C_k$	$k=0-8$ ; influence coefficients of the neighbouring pressure values in discretised Reynolds equation (6.13, 6.14)
$E_{i,j}$	Right hand side of the discretised Reynolds equation (6.13, 6.14)
$C$	Matrix of coefficients in linearised Reynolds system of equations
$C^k$	Matrix of coefficient of the level $k$ linearised problem
$\Delta x, \Delta y$	Rectangular grid cell size (target grid, level 0)
$m$	Total number of grid levels
$N_x^k, N_y^k$	$k=0..m$ ; number of nodes on the grid of level $k$
$\Delta_k x, \Delta_k y$	Rectangular grid cell size (target grid, level $k$ )
$I_k^{k+1}$	Restriction operator from the finer level $k$ onto coarser level $k+1$
$r^k$	The vector of residuals; also used in (6.18), (6.22) as a dummy function defined on the level $k$ grid
$I_{k+1}^k$	Interpolation operator from coarser level $k+1$ onto the finer level $k$

$l_i$	Coefficients of the Lagrange polynomial in cubic interpolation
$\tilde{p}^k$	Approximate solution for pressure of the level k problem
$v^k$	Error vector for the level k approximated solution
$T_k$	Total number of relaxation sweeps on level k level during the full multigrid routine
$v_0$	Number of relaxations on the coarsest level
$v_1$	Number of pre-relaxations
$v_2$	Number of post-relaxations
$v_3$	Number of target grid relaxations after the full multigrid routine
$\omega$	Type of the multi-level relaxation cycle
$n_c$	Number of correction cycles
$A$	$= (h_{min} + h_{max}) / (2S_q)$

## List of acronyms

IL(s)	Ionic liquid(s)
AC <sup>2</sup> T	Austrian Centre of Competence in Tribology
JKR	Johnson, Kendall , Roberts
DMT	Derjaguin, Muller, Toporov
RUC	Representative Unit Cell
AFA	Average Field Approximation
EMA	Effective Medium Approximation
VS	Vavakin and Salganik
MPM	Merged Pores Model
OPM	Open Pores Model
OPMPM	Open and Merged Pores Model (combination of both)
FEA/FEM	Finite Element Analysis/Method
DFT/FFT	Discrete/Fast Fourier Transform
DDM	Method developed in the thesis based on the Differential Deflection Method
EDM	Electrical Discharge Machining

## 1. Introduction

The work discussed in this thesis was carried out within the framework of the multidisciplinary project MINILUBES ([Mechanisms of interactions in nano-scale of novel ionic lubricants with functional surfaces](#)). This was a 12 partner Marie Curie Initial Training Network aimed at thorough investigation of ionic liquids as potential lubricants. The role of the author in this network was to develop mixed lubrication analysis methods for plain bearings with surface roughness taken into account with a view to modelling applications in the field of porous bearings. Porous bearings are a potential application for ionic liquid lubricants because of their low rates of evaporation. In this chapter ionic liquids are discussed, as well as the particular role of the author in the project and the work that has been carried out by the author. The structure of the thesis and a general literature review are given.

### 1.1. Ionic liquids as potential lubricants

In most of the applications the term Ionic liquids (ILs) refers to organic salts with a melting point of below 100°C. As indicated in the review of Freemantle (1998) they were first discovered in 1970s and were used as electrolytes in batteries. ILs were also proposed as a new class of green solvents by e.g. Appleby and Seddon (1986). The chemical properties, synthesis and applications of ILs are reviewed by Welton (1999) and Earle and Seddon (2000) who are quite well-known scientists in the field of ILs. According to the paper of Minami (2009), where application of ILs in the field of tribology is reviewed, the first record of using ionic liquids as lubricants is by Smith (1961) in application to high temperature bearings for a nuclear power plant. A mixture of lithium fluoride, beryllium di-fluoride and uranium tetra-fluoride was used as a lubricant operating in the temperature range of 650-815°C.

Forty years later the use of room temperature organic liquids as lubricants was first suggested by Ye et al (2001). ILs are attractive in lubrication for their non-flammability, high thermal stability and low volatility as indicated by e.g. Earle and Seddon (2000) and Liu et al (2002). For this reason ILs are considered as potentially advantageous lubricants in high temperature and/or low ambient pressure (vacuum) conditions (Minami, 2009).

Ionic liquids consist of an anion ionically bound to a cation. Typical anions for ionic lubricants are tetra-fluoroborate  $[\text{BF}_4]^-$ , hexa-fluorophosphate  $[\text{PF}_6]^-$ ,

## Section 1.1 Ionic liquids as potential lubricants

bis(trifluoromethylsulphonyl)imide [Tf<sub>2</sub>N]<sup>-</sup>, sulphates [mSO<sub>4</sub>]<sup>-</sup> and sulphonates [mSO<sub>3</sub>]<sup>-</sup>, although there are many other possibilities. The cation moieties typical for ionic lubricants are based on imidazolium, ammonium or phosphonium with alkyl chains of various lengths as mentioned by e.g. Minami (2009).

Varying the chemical structure of either anion or cation (or both) as well as extending the length of the alkyl chain changes the chemical and tribological properties of ILs. Indeed, it was shown by e.g. Pagano et al (2012) that the higher carbon numbers (longer alkyl chains) in hexa-ethyleneglycol and oligo-ethyleneglycol cations led to improved tribological behaviour. The effect of longer alkyl chains of IL components is the same as that of fatty acids in conventional lubricants described by Bowden and Tabor (1945). They explained that longer alkyl chains help to form a protective tribofilm covering the working surfaces. However, Pagano et al (2012) as well as other researchers e.g. Liu et al (2006) indicated strong corrosive effects of ILs. Therefore it was suggested to use ILs as additives to conventional oils so that the corrosive effect is minimised. It was shown by Pagano et al that even a small amount of dicationic ILs in the lubricant significantly reduced friction and wear in steel/steel contacts.

In other research papers the effect of the anion on the tribological properties has also been investigated. In the work of Kronberger et al (2012) it was shown that the tribological behaviour of the ILs based on sulphates and sulfonates as anions was superior to those based on bis(trifluoromethylsulfonyl)imide anion, which were less soluble in the base oil. Efficiently reducing friction, sulphates and particularly sulphonates however caused higher wear rate supposedly due to tribo-corrosion. Pejakovic et al (2012) showed similar results for different cations. It was confirmed that tribofilm formed by ILs creates efficient protection against friction and abrasive wear and the main wear mechanism when using ILs is a result of corrosion.

The important point of the three works mentioned is that friction can be significantly reduced even when using ILs as additives and the effect of corrosion can be minimised by choosing the optimal concentration of ILs in the mixture. Also, it was shown that the advantages of ILs become more pronounced for elevated temperatures (100-150°C). The variety of cation and anion combinations, as well as the adjustable length of the side alkyl chains allows the properties of the ILs to be tailored for the required conditions.

## 1.2. The MINILUBES project

The acronym MINILUBES stands for Mechanisms of Interaction of Novel Ionic Lubricants with Functional Surfaces. As mentioned, the overall aim of the project was to investigate various aspects of using the ionic liquids as lubricants. The parties involved include 7 Universities in UK, France, Germany, Spain, Slovenia, Poland and Romania, 2 non-academic research organisations in Austria and Spain, and 3 industrial partners from Germany, Italy and Austria. The research was divided into four major topics: synthesis of ILs, analysis, tribology, and numerical simulations.

Synthesis was done mainly at the University of Vigo, Spain, the University of Halle-Wittenberg, Germany and the University of PetruPoni, Romania. As mentioned previously, the choice of the anion-cation couples and the configuration of the side chains affect the chemical, rheological and tribological properties of ILs. This part of the team was responsible for developing and improving methods of obtaining the required chemical structure as well as for the characterisation of prepared substances by means of mass-spectrometry, chromatography and x-ray crystallography. See e.g. Mahrova et al (2012) for more information on synthesis and characterization of alkane sulphate and sulphonate based ILs, Zare et al (2012) for poly-ethylene glycol based ILs and Ranetcaia et al (2013) for modified poly(dimethylsiloxane–alkylene oxide) graft copolymers.

The analysis group specialised in studying the degradation of ILs in the presence of air, toxicity and ecological impact and was primarily carried out in AC<sup>2</sup>T Research GmbH, Austria, University of Gdansk, Poland, and non academic research and development organisation IK4 Tekniker, Spain. For example it was shown by Pisarova et al (2012) that ILs based on (2-methoxyethyl)- and (2-hydroxyethyl) trimethyl-ammonium cation and products of their degradation can be classified as harmful or even toxic to aquatic organisms and therefore they are not recommended for general use in IL-based lubricants. On the other hand pyrrolidinium and butyl-trimethyl-ammonium cations have been shown to be harmless to aquatic organisms as indicated by Stolte et al (2012) and therefore applicable for use as potential lubricants. As for anions, according to Stolte et al (2012) sulphates and sulphonates are a preferable choice over bis(trifluoromethylsulphonyl)imide and other fluorine containing anions.

The tribological aspects of ionic liquids included the measurements of friction and wear as well as corrosion associated with the use of ILs as lubricants. The institutions

### **Section 1.3 Porous bearings**

responsible for these aspects were the University of Ljubljana, Slovenia, IK4 Foundation Tekniker, Spain and AC<sup>2</sup>T Research, Austria. The research carried out by these partners included the works of Kronberger et al (2012), Pejakovic et al (2012) and Pagano et al (2012). All studies confirmed that the tendency to reduce friction and wear remains even if ILs are added to the reference oil (glycerol) in concentration of 2.5wt% (Kronberger et al, 2012, Pagano et al, 2012) and 0.625wt% (Pejakovic et al, 2012). It was also shown that the improved tribological behaviour of ILs is more pronounced for higher temperatures of 100-150°C. However, despite of the apparent improvement in tribological behaviour of neat ILs in comparison to reference oil, corrosion caused by using ILs remains the major concern. Therefore using ILs as additives appears to be more promising (Pagano et al, 2012). For this purpose the optimal concentration of ILs has to be established as well as the optimal choice of anion and cation moieties.

The simulation group included researchers based in Cardiff University, UK, University of Blaise Pascal, France and AC<sup>2</sup>T Research, Austria. One of the responsibilities of the simulation group was to perform the molecular dynamics simulations aimed at connecting the chemical structure to the global physical and rheological properties of ILs. The pressure-viscosity dependence of ILs was presented in e.g. the work of Pensado et al (2008a) mainly consisting of the experimental data, however the experimental techniques have limited pressure and temperature ranges. Mendonca et al (2012) applied a method based on molecular dynamics simulations to calculations of the viscosity of ILs at high pressure and temperature values using the known viscosity at ambient conditions. This method is similar to the one developed by Pensado et al (2008b) Other aspects of the project covered by the simulations group were the modelling of hydrodynamic lubrication in porous journal bearings at AC<sup>2</sup>T and modelling of the mixed lubrication in plain bearings by the author at Cardiff University. These models were developed in terms of a general formulation with the possibility of incorporating the properties of the ILs.

#### **1.3.Porous bearings**

One of the industrial partners of the project was GKN SinterMetals, Bruneck, Italy, which is a manufacturer of sintered porous bearings. These bearings are produced from metal powders. The metals used can be copper, tin, iron and others. During the manufacturing process the powders are mixed, pressed in the required form of the

component (bearing, bushing, thrust washer etc). After that the parts are placed in an oven and baked (sintered) at a temperature that is below the melting point of each of the metals used. For example the high temperature sintering of the iron, nickel, chromium, silicon and molybdenum mixture requires the temperature of 1200°C with the melting points of the components being from 1200°C for iron and 2600°C for molybdenum as specified in the manufacturer's brochure. The iron bearings are typically sintered at a temperature of 800°C. This process creates sufficiently strong bonds between the grains of the metals for the material to support the bearing loads. However it results in the material containing pores, which are spaces between the grains. These pores are then impregnated with the lubricant oil. This technology allows the bearings to be self-lubricated and as a result they can be long lasting with low maintenance requirements. The use of ILs instead of conventional oils is of high interest for the manufacturers of porous bearings. Having low volatility, ILs evaporate very slowly and may persist within the porous bearing structure for longer time than conventional lubricants.

In spite of these advantages of using porous bearings they do have a serious disadvantage. The porous structure of the material significantly reduces the load carrying capacity. This limits the range of applicability to moderate load conditions, with bearing radial load of up to 20MN/m<sup>2</sup> at surface velocities of up to 0.2m/s and load of up to 0.2MN/m<sup>2</sup> at velocities of up to 20m/s according to the manufacturer's recommendations. The limits on the load conditions are due to the load carrying capacity of the bearing, whereas velocity limits are typically imposed due to lubrication failure and scuffing damage associated with frictional heating, which increases at higher velocities. Specifications of the porous bearings can also be found in the handbook edited by Neale (1995). The type of the material used is prescribed by the specific needs.

In this thesis Chapter 2 is dedicated to a model developed for predicting the effective elastic properties, such as Young's modulus and Poisson's ratio in the porous materials in terms of the properties of the metal and the nature of the material porosity.

Two main types of pores can be distinguished in porous materials prepared by the powder sintering: first are the materials which contain isolated pores and second are materials with so called *open pores*, which can be described as a complex network of channels connected to the surface of the bearing. The total volume of pores can be

## Section 1.4 Structure of the thesis

measured by comparing the volume of the raw material used to prepare the product and the total volume of the product. The fraction of each type of pore can be distinguished by weighing the product placed in a vessel filled with fluid. The data obtained by the author by means of personal communication with Pahl (2010) indicates that materials used by the manufacturer of porous bearings with the total porosity value greater than 18-20% have all the pores connected.

### 1.4. Structure of the thesis

This thesis is mainly based on research carried out by the author within the framework of the MINILUBES project. The particular role of the author involved the evaluation of the effective elastic properties of sintered porous bearings as well as the investigation of the effect of roughness on the lubrication of plain bearings.

The first part of the work is presented in Chapter 2, where a semi-analytical model is developed for predicting the effective elastic properties of the porous materials as a function of porosity. The chapter starts with a review of existing models used to evaluate the effective elastic properties of porous materials. The majority of the models examined are based on the mechanics of composites. A series of assumptions on the porous microstructure are made and the associated models are developed. Experimental data for a number of porous materials are compared to the predictions of the various models presented, and their combinations. It is shown that the porous microstructure and the associated elastic behaviour depend on the manufacturing process of the porous material significantly. The models developed can be applied to porous materials in general as well as to sintered materials. However, in the case of sintered bearings, a dry porous material is considered. It is expected, that pores filled with the liquid lubricant will behave differently to the dry ones. A paper has been published by the author based on the methods and results discussed in this chapter (Manoylov et al, 2013a).

The second major part of the thesis is concerned with the dry contact analysis of rough surfaces which is presented in Chapter 3. This chapter starts with the literature review relevant to the subject, continues with the theoretical background and formulation of the problem and finishes with the implementation and validation of the model. The model is designed to evaluate the deflected shape of the rough surface and the contact pressure distribution corresponding to the given displacement. In the case of the elastic pressure exceeding the given maximum value (nominally equal to the

hardness value of the material) at a contact area, the further deflection is assumed to be plastic and the resulting residual deflection of the surface is established. The results of the model are compared with those obtained by means of finite element analysis. The method discussed in this chapter and the corresponding results were published by the author (Manoylov et al, 2013b).

The third part of the thesis presents the mixed lubrication model applicable to the plain bearings. This model is based on the theory of flow factors, which are the measure of the average effect of roughness on the flow of liquid lubricant. In the case of the film thickness not being sufficient to prevent direct contact of the asperities, the deflected shape and the associated contact load are evaluated by means of the dry contact analysis. This model is presented in Chapters 4 to 6. Chapter 4 gives a review of mixed lubrication models based on the theory of flow factors and proceeds to present the general concept of homogenisation in application to the Reynolds' equation and the theoretical derivation of the flow factors. In Chapter 5 the method of evaluating the flow factors numerically is described and the flow factors obtained are compared to those calculated analytically. Flow factors are evaluated for various surface roughness functions, including surface roughness examples measured by a Taylor-Hobson profilometer. Various shapes of the flow factor functions are illustrated and their physical interpretation discussed.

Finally, the application of the mixed lubrication model based on the theory of flow factors to inclined pad bearings is considered. In Chapter 6 first the description of inclined pad bearings is given and the geometry of the problem is formulated. The mixed lubrication of the inclined pad bearing can be modelled using the homogenised Reynolds equation. The numerical methods of solving the homogenised Reynolds equation are discussed and it is suggested that the multigrid method is suitable and beneficial. The multigrid method is quite a complex technique which is therefore described in detail in Chapter 6, Section 6.4. After that solutions of the homogenised Reynolds equation are presented which includes a series of cases for which the deterministic solution is available as well as the cases of measured surface roughness. Various properties of the roughness, such as wavelength, orientation of surface lay to the entrainment direction, and the proximity of the rough surface to the counterface are illustrated as well as how these effects are captured by the homogenised solution.

## Section 1.5 Evolution of the contact mechanics methods

Finally, the conclusions to the thesis are given as well as suggestions for future development.

### 1.5. Evolution of the contact mechanics methods

The third chapter of the thesis is concerned with modelling of the dry contact of rough surfaces. In this thesis the model developed is used as a part of the mixed lubrication analysis; however it has a meaningful standalone application in the field of contact mechanics. The review of the literature relevant to the dry contact of rough surfaces is provided in Chapter 3, whereas in this section the more general review of the evolution of the contact mechanics methods is given.

The foundation of the classical contact mechanics is associated with Hertz and his early work of 1881 *Ueber die Beruehrung elastischer Koerper* (On Contact Between Elastic Bodies). Hertz described the contact of two elastic bodies with curved surfaces. Hertzian theory is used nowadays where the non-adhesive contact of curved surfaces is considered.

Bradley (1932) was the first who considered attractive forces between two contacting absolutely rigid spheres. He calculated point wise the attraction between the spheres. Derjaguin (1934) pointed out that elastic deformations of the spheres need to be accounted as well as the adhesive interactions. He presented the first attempt to consider the problem of adhesion between elastic spheres: calculating the deformed shape of the spheres using Hertzian contact theory, he evaluated the work of adhesion assuming only the pair wise interactions of the closest surface elements. The interaction energy per unit area between small elements of curved surfaces was assumed the same as for parallel planes. Almost all common models of adhesive contact do not use the point-wise calculations of the adhesive force and are based (sometimes implicitly) on the Derjaguin approximation.

On the other hand, Johnson (1958) made an attempt to solve the adhesive contact problem by combining the Hertzian spherical contact problem and the problem of a rigid flat-ended punch. According to Kendall (2001, pages 185-186), Johnson et al. (1971) applied Derjaguin's idea to equate the work done by the surface attractions against the work of deformation in the elastic spheres to Johnson's combined stress superposition. This resulted in the creation of the famous JKR (Johnson, Kendall, and Roberts) theory of adhesive contact.

Nowadays there are several well-established classic models of adhesive contact that include the JKR model, the DMT (Derjaguin-Muller-Toporov) model, and the Maugis transition solution between the JKR and DMT models. A detailed description of the theories is given by Maugis (2000). These models propose methodologies to predict the adhesion force between contacting spherical surfaces (Johnson et al. 1971, Derjaguin et al. 1975, Maugis 1992). These classic models are very helpful for studying various phenomena that involve molecular adhesion. For example, a method has been introduced by Borodich and Galanov (2008) for the determination of the work of adhesion and of the elastic contact modulus of the materials from the indentation experiments. This method is based on the Maugis theory and it was shown to be fast and robust (Borodich et al. 2012).

Although the phenomenon of adhesion plays an important role in some problems of contact mechanics, it is however not considered in this thesis. Numerous studies of adhesive contact showed a rapid decay of adhesive force when the real contact area decreases (see e.g. Kendall, 2001). As discussed later, the real contact area in the presence of roughness is significantly smaller than the nominal contact area obtained considering the geometrical shape of the surfaces. Moreover, in the mixed lubrication analysis considered in the thesis only occasional contacts occur which makes the effect of adhesion negligible in comparison to other forces.

As for the contact of rough surfaces, its importance in contact mechanics was first emphasized by Bowden and Tabor (1939). They were measuring the electrical conductivity between contacting bodies and found that the real area where the surfaces touch is significantly smaller than the apparent area. This discovery had a drastic effect on the understanding of friction, which was known to be due to adhesive forces and therefore proportional to the area of contact. According to the Hertz theory for point contact, the area of contact is proportional to the normal load in the power  $2/3$ , therefore in case of elastic deformation the classical Amontons' law of friction being proportional to the normal load did not hold. Zhuravlev (1940) built a theoretical justification of the Amontons' law in the case of rough surface contact. He assumed surface asperities having hemispheric shape and behaving as individual elastic Hertzian contacts. Using the same main assumptions as in Zhuravlev (1940, 2007) model, Greenwood and Williamson (1966) considered the contact of two nominally flat surfaces whose height distributions of asperity caps are Gaussian. According to Greenwood and Williamson (1966), although the distribution of the asperity height

## Section 1.5 Evolution of the contact mechanics methods

tends to be Gaussian rather than exponential, the exponential distribution is a good approximation to the highest 25% of the asperities of most surfaces. Moreover, using the exponential distribution allowed the exact formulae to be derived for load, contact area and conductance. Using this approach they showed that the contact area is directly proportional to the external compressing load. They have also extended the model to the case of contact between elastic-plastic asperities (see also discussion by Borodich, 2007).

Several models of contact between the rough surfaces incorporating the effect of adhesion were developed, see e.g. Maugis (2000), Galanov et al (2010). They are based on the Derjaguin (1934b) model of friction. A contribution of Archard (1957) should also be mentioned here, who has shown experimentally that the Amonton's law is obeyed for the surfaces with a large number of contacts.

Treating the surface asperities as individual spherical contacts allows the Hertzian theory to be used for establishing the contact pressure values. However, as shown by Bush et al (1975), theories based on this assumption fail once the interaction of adjoining asperities becomes too significant for them to be treated independently. This leads to the need for a method that allows the elastic contact problem to be solved for the general shape of the surface roughness, i.e. the solution of the equation with an unknown complicated boundary. The solution for bi-sinusoidal surface roughness was presented by Johnson et al (1984). They gave a numerical solution for the whole range of loads based on Kalker's (1977) procedure of minimising the total complementary energy. They also gave asymptotic closed form solutions for the cases of very light and very heavy loads, when the surface had either isolated circular contact zones, or all of the asperities were significantly flattened leaving isolated circular trapped volumes. They stated that an analytical solution might not be possible due to the shape of the contact areas being circular for light loads and approximately square for higher loads.

The development of computers and numerical analysis allowed the elastic contact problem with unknown boundary to be solved numerically. The theoretical foundation for the numerical methods, such as that given by Kalker (1977) is the solution of the deflection of the linearly elastic half space caused by the concentrated normal or tangential load obtained by Boussinesq and Cerutti respectively (see Love, 1952). The superposition of contact pressures at different points leads to the Boussinesq-Cerutti integral used for calculating the deflection at a given point on the half space. The

method developed in Chapter 3 of this thesis is also based on Kalker's numerical solution. Further review of the methods of solving the dry contact of the rough surfaces problem is provided in Chapter 3.

### 1.6. Mixed lubrication in plain bearings

Mixed lubrication is a condition where the working surfaces are mostly separated by the fluid film, although direct mechanical contact occasionally occurs at surface asperity features. In this thesis only the lubrication of the plain bearings is considered, which consist of two conformal working surfaces in relative motion separated by a lubricant film. Typical types of the plain bearings are journal bearings, slider or linear motion bearings, inclined pad bearings or tilting pad bearings. Although the methods developed in this thesis are applied to study the effect of roughness on the lubrication of the inclined pad bearing, they can be easily adapted to consider different bearing geometries or to study the effect of lubricant viscosity in mixed lubrication, for example. In the thesis the inclined pad bearings are commonly referred to as tilted pad bearings, although this definition is correct only as far as the tilting angle is fixed.

The hydrodynamic lubrication was first studied by Beauchamp Tower in 1883, who conducted experiments of the journal bearing dipped in the oil bath. He pointed out the importance of the bearing being fully lubricated (Reynolds, 1886, Rayleigh, 1918). The first mathematical theory of the lubrication was developed by Reynolds (1886) that explained all these experiments perfectly well. The main observation made by Tower and theoretically justified by Reynolds was that the film "wedge" forms underneath or around the shaft which creates the hydrodynamic pressure that carries the load. The improvements of the Reynolds theory allowed the hydrodynamic pressure distribution to be predicted for the tilting pad bearing, designed by Michell (1905), or step bearing designed by Rayleigh (1918).

The majority of models in the field of lubrication are based on solving the well known Reynolds equation. Closed form solutions of the Reynolds' equation are available for some simple geometries and boundary conditions. Cameron and Wood (1958) for example gave an analytical solution of the isoviscous Reynolds equation for the (finite) parallel surface thrust bearing based on the Bessel functions. This and other solutions however considered bearings with smooth surfaces only.

## Section 1.6 Mixed lubrication in plain bearings

According to Tzeng and Saibel (1967) a number of researchers pointed out the significance of the roughness on the pressure distribution during hydrodynamic lubrication. For the general case of surface roughness the analytical solution of the Reynolds equation is not possible. The general cases of the rough surfaces could not be solved numerically at that time due to the lack of computational power.

A number of research papers were published based on the probabilistic approach, i.e. by introducing the probability density function of the surface asperity heights. Tzeng and Saibel (1967) gave the closed form solution for the load and friction force in the case of one dimensional Beta distribution of the surface asperity heights. Christensen and Tonder (1971, 1972) developed the stochastic Reynolds equation for the longitudinal and transverse roughness in application to journal and slider bearings.

All the stochastic models showed the increased effect of roughness as the distance between the surfaces decreases. Johnson et al (1972) considered the mixed lubrication case based on a stochastic representation of the roughness. They assumed that part of the load is carried by the pressurised lubricant whereas another part is due to the direct contact of the asperities. The contact part of the load was calculated using the Greenwood and Williamson's (1966) contact theory which considered Gaussian distribution of the asperity heights. Christensen (1972) noted that in case of the mixed lubrication the friction between the working surfaces is governed by the contacting asperities whereas the load is mainly controlled by the hydrodynamic properties of the bearings. This is why it is extremely important to understand the effect of roughness in the mixed lubrication regime.

Patir and Cheng (1978) noted that the existing methods of the mixed lubrication analysis based on stochastic approach do not consider real rough surfaces. Indeed, the stochastic analysis of the two dimensional surface roughness function is rather sophisticated. They introduced a method to study the effects of an arbitrary surface roughness through flow simulation. For this purpose they compared the average flow of the lubricant through an area of the rough surface bearing and corresponding flow in the smooth bearing. The ratio between these two flows gave a quantitative measure of the effect of roughness on the flow of lubricant. In 1979 they extended their theory to account for the rough surface Couette flow.

The first of the new class of methods based on the homogenised Reynolds equation was the one introduced by Bayada (1988, 1989). These methods consider a two scale

approach to the rough surface bearing: the global scale being the shape of the smooth bearing, and the local one being the roughness. The effects of the local roughness and the global shape are treated separately. The local roughness is assumed to be periodic, so that the solution can be sought for a small representative area. The averaged solution of the local problem summarises the effect of the roughness on the flow in a set of so called flow factors, which are then incorporated into the smooth surface Reynolds equation. The homogenisation theory has been subsequently developed by Jai (1995), Kane and Bou-Said (2004), Almqvist and Dasht (2006) and others. Bou-Said noted that as opposed to stochastic methods the theory of homogenisation gives accurate results in the case of the arbitrary orientation of the characteristic roughness features. For the cases of isotropic, longitudinal or trasverse roughness the homogenised solution was shown to agree well with the Patir and Cheng theory (Sahlin et al, 2010a). It was however noted that in the case of anisotropic roughness the Patir and Cheng theory does not take into account the diversion of the flow of lubricant caused by the asperities (Almqvist et al, 2011). This was accounted for in the homogenised Reynolds equation by introduction of cross derivative terms.

Patir and Cheng theory allowed direct contact of the asperities to be considered, however the elastic deflection of the surface roughness features was not considered. Sahlin et al (2010a, 2010b) developed a mixed lubrication analysis method based on the homgenisation theory and incorporated the elastic and plastic deflection of the surface asperities evaluated by means of dry contact analysis.

This thesis presents a method similar to the one developed by Sahlin et al (2010a, 2010b) in the sense that it incorporates the dry contact analysis described in Chapter 3. The homogenisation theory in this thesis applies the formulae developed by Bayada (2005) for the oblique sinusoidal roughness to real roughness. The procedure for evaluating the flow factors is validated where possible and the method developed is applied to study various effects of roughness on the mixed lubrication in the pad bearings. Note that the EHL effects are not considered in this thesis, which makes the method developed inapplicable to the cases of concentrated contacts.

## Section 1.6 Mixed lubrication in plain bearings

(Intentionally blank)

## 2. The effective elastic properties of porous materials

### 2.1. Introduction

Porous materials are heterogeneous media that contain a number of voids. The main material that is used in the manufacturing process is called the host material or matrix. For example, the host material can be a metal, ceramic or polymer. The voids or pores may have a rather different nature: in sintered materials they are the spaces between the grains of host material that occurred during the manufacturing process, whereas in foamed materials such as porous glass or titanium foam they are gas bubbles.

Assuming that the porous material is a linear elastic isotropic solid, the elastic behaviour can be defined by any two constants selected from such material characteristics as elastic modulus ( $E$ ), Poissons ratio ( $\nu$ ), bulk modulus ( $K$ ), shear modulus ( $\mu$ ) and Lamé parameter ( $\lambda$ ). These elastic characteristics are connected by the following relations (see e.g. Timoshenko, 1970):

$$K = \frac{E}{3(1 - 2\nu)}, \quad \mu = \frac{E}{2(1 + \nu)}, \quad \lambda = \frac{E\nu}{(1 + \nu)(1 - 2\nu)}. \quad (2.1)$$

If the pores are filled with gases, their elastic stiffness may be assumed negligible. Therefore the effective elastic properties of the porous material are different to those of the host material. The effective elastic properties of porous materials are the object of interest of this chapter. In a wide class of approaches to estimation of the elastic characteristics of a porous material it is assumed that the porous structure of the medium repeats a certain periodic pattern. The elastic fields are calculated over the representative unit cell (RUC) and homogenisation theory is applied to evaluate the global stress-strain behaviour (see, e.g. Bakhvalov, 1974). The periodic structures representing the porous medium can be chosen in various ways. For example, Chapman and Higdon (1994) considered the porous medium as a packed set of spheres; Poutet et al (1996) considered three types of unit cells: deterministic, fractal and random; Garboczi and Berryman (2001) and Roberts and Garboczi (2002) used the finite element method to calculate the elastic properties of periodic porous media with quasi-random RUCs. The methods based on the concept of an RUC are easy to implement, however, real materials have a rather random micro-structure, and it is difficult to justify the periodic structure assumption (see Figure 2. in Section 2.4).

## Section 2.1 Introduction

A number of empirical relations of elastic characteristics of a porous medium with its porosity have also been published such as the classical Ryshkewitch-Duckworth and Spriggs equations (see e.g. Wang, 1984a, 1984b):

$$S = S_0 e^{-\alpha p}, \quad E = E_0 e^{-\beta p}, \quad (2.2)$$

where  $p$  is the value of porosity, i.e. the volume fraction of pores per unit volume of the material,  $E$  and  $S$  are the elastic modulus and the strength of the porous material respectively, and  $\alpha, \beta$  are empiric parameters related to the host material. Here and henceforth, the subscript 0 means that the elastic characteristic is attributed to the host material. These and other similar methods require a set of experimental measurements and are not based on the micro-mechanical behaviour of pores in the material.

Many approaches to calculate the effective elastic properties are based on physics of composite materials. These approaches consider a material with inclusions subjected to a uniform field, that can have an electrical, elastic or other nature. A statistically homogeneous material is considered and the individual disturbance of the field caused by a particular inclusion is assumed to vanish far from the disturbance. This leads to a system of equations for the effective properties of the material. The classical models of physics of composites include the effective medium approximation (EMA) introduced by Bruggeman (1935) for various physical properties of a composite, and average field approximation (AFA), presented by Polder and Vansanten (1946). These models were intensively studied and further developed by e.g. Avellaneda (1987), Milton (1981, 1984) and others. The homogenization methods developed can be applied to calculate both the effective dielectric and elastic properties of the composite; however, the interest of the current paper is in its mechanical properties.

The EMA and AFA methods are limited to cases of inclusions of the same shapes and sizes. Therefore a class of differential schemes for calculating the effective properties of composite materials was developed by e.g. Berryman (1980, 2006). In these methods, first a solution for a single inclusion is considered. If the inclusion has a shape of elliptical origin (sphere, disk, cylinder, prolate or oblate spheroid, arbitrary ellipsoid) then the general procedure for calculating the elastic field outside an ellipsoidal inclusion obtained by Eshelby (1957, 1959) can be applied. The differential methods assume constructing a composite by adding a group of inclusions incrementally to the

material. The effective properties are calculated at each step and are used as properties of the host matrix for the next iteration. The increment of inclusion phase is then considered to be continuous which leads to ordinary differential equations for the effective characteristics of the material. Salganik (1973) and Vavakin and Salganik (1975, 1978) considered media with pores and rigid inclusions for both two- and three-dimensional cases. Pores were either randomly oriented cracks or isolated spheres of different radii. Based on these works the effective characteristics of layered media with flattened pores were obtained by Borodich (1984, 1987). Norris (1985a) and Norris et al (1985b) generalized the differential scheme and assumed a fictitious media where inclusions of two or more phases were added incrementally until the point is reached where the volume fraction of the matrix vanishes. A review of methods based both on periodic and homogenized boundaries is given by e.g. Pindera (2009).

Sevostianov and Kachanov (2012) stated that a common drawback of any differential scheme is adopting the assumption of dilute concentration of the newly added group of inclusions in the matrix. The differential schemes therefore neglect the interaction between the individual inclusions within the same group. The interactions between inclusions from different groups are taken into account only in the homogenised sense, i.e. the homogenised contribution of the latest group on the effective properties of the material with inclusions of all the previous groups.

The purpose of the present work is to give a general procedure for evaluation of the effective elastic properties of porous materials with particular interest in properties of sintered materials. These properties can then be used in modelling engineering applications. The approach developed may be considered as a combination of a differential scheme similar to the Vavakin-Salganik (VS) method and a self consistent embedding scheme (see e.g. Willis (1977) and Talbot and Willis (1987)). Because the classic form of the VS approach is restricted to spherical pores and does not consider the specific statistical distribution of pore radii, the VS approach has been modified so that it can take various distributions of pore radii into account. In an attempt to account for the interaction of the spherical inclusions of the same or different groups the probability that the spherical pores overlap and form doublets was calculated. The effect of overlapped pores is then treated as one of ellipsoidal inclusions with each having the same volume as the overlapping pores that it replaces. This modification

## Section 2.2 Vavakin-Salganik (VS) model

helps to overcome the dilute concentration limitation of differential schemes mentioned above. It is shown that introducing the elliptical pores into the model improves the predictions of the elastic properties of porous materials with merged pores. However, the micrographic analysis of sintered materials shows (see Figures 2.5 and 2.9) a much more complex structure of pores, which cannot be approximated by isolated and overlapped spheres only. An additional modification has been developed that treats complex agglomerates of pores, which cannot be approximated as spherical or elliptical ones, as damaged material. It is assumed that the damaged material does not transfer any load. This approach is similar to the one described by Rabotnov (1979) and Kachanov (1974) for materials with a large number of cracks. The comparison of the predictions given by models presented to the available experimental data shows that a good fit can be achieved with an appropriate choice of the model according to the complexity of the porous micro-structure. The predictions of the model are limited to determining the homogenized material properties which is the objective of the study.

### 2.2.Vavakin-Salganik (VS) model

Using results obtained by Eshelby (1957, 1959) and assuming a dilute concentration of spherical pores such that their interaction can be neglected, the following formulae were derived by Krivoglaz and Cherevko (1959) for elastic modulus and Poisson's ratio of a material with pores of equal size:

$$E = E_0 \left( 1 - p \frac{3(1-\nu_0)(9+5\nu_0)}{2(7-5\nu_0)} \right), \quad \nu = \nu_0 + p \frac{3(1-\nu_0^2)(1-5\nu_0)}{2(7-5\nu_0)} \quad (2.3)$$

In Equations (2.3)  $E$  and  $\nu$  are the effective elastic modulus and Poisson's ratio of the medium with pores,  $E_0$  and  $\nu_0$  are the characteristics of the host matrix, and  $p$  is the volume fraction of pores in the unit volume of the host material.

Vavakin and Salganik (1975, 1978) considered the porous medium with spherical pores of  $n$  different radii  $r_1, \dots, r_n$  arranged in increasing order, so that

$$r_{i+1} > r_i, \text{ for } i = 1 \text{ to } n, \quad r_1 = r_{min}, \quad r_n = r_{max} \quad (2.4)$$

where  $r_{min}, r_{max}$  are the minimal and maximal radii respectively. Using the above assumptions Equations (2.3) were written in terms of the concentration parameter  $\rho$ :

$$E = E_0 \left( 1 - 2\pi\rho \frac{(1 - \nu_0)(9 + 5\nu_0)}{(7 - 5\nu_0)} \right), \quad \nu = \nu_0 + 2\pi\rho \frac{(1 - \nu_0^2)(1 - 5\nu_0)}{2(7 - 5\nu_0)}, \quad (2.5)$$

For the case of single size spherical pores  $\rho$  is defined as

$$\rho = Nr^3 \quad (2.6)$$

where  $N$  is the number of pores of radius  $r$  per unit volume of the material.

In order to calculate the effective elastic moduli for the material with pores of different sizes the differential scheme was used, where formulae (2.5) were applied at each step to the medium where only pores of smaller radii are present, starting from the host material as shown schematically on the flowchart of

Figure 2.1. For this purpose the concentration term  $\rho$  in (2.5) was replaced by  $d\rho_i$  which is the concentration of pores of radius  $r_i$  per unit volume of the space between pores of greater radii  $r > r_i$ :

$$d\rho_i = \frac{N_i r_i^3}{1 - \frac{4}{3}\pi \sum_{j>i} N_j r_j^3}, \quad i = 1, \dots, n. \quad (2.7)$$

In other words,  $d\rho_i$  is the increment of the concentration parameter  $\rho$  due to adding a set of pores of radius  $r = r_i$ . The increment  $d\rho_i$  is then assumed to be continuous.

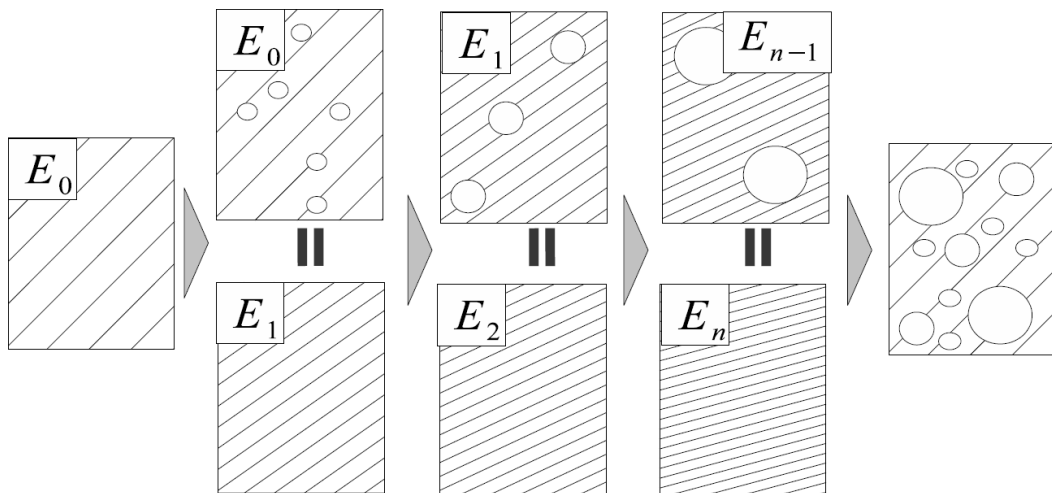


Figure 2.1 The bottom-up iterative approach: starting from the host material pores of a particular radius are added into the specimen. Their contribution to the effective elastic properties is calculated and used as the properties of the host material for the set of pores of the next radius

The change in porosity  $dp$  corresponding to taking into consideration pores of radius  $r_i$  is connected to  $d\rho_i$  by the following relation:

## Section 2.2 Vavakin-Salganik (VS) model

$$dp = \frac{4}{3}\pi d\rho_i(1-p), \quad \rho = -\frac{3}{4\pi}\ln(1-p), \quad (2.8)$$

where the loss of volume due to presence of smaller pores is accounted for by the multiplier  $(1-p)$ .

To calculate the elastic properties  $E_i$  and  $\nu_i$  of the medium with pores of radii  $r_1, \dots, r_i$  the formulae (2.5) were modified using  $d\omega_i$ :

$$E_i - E = -2\pi d\rho_i \frac{(1-\nu)(9+5\nu)}{(7-5\nu)}, \quad \nu_i - \nu = 2\pi d\rho_i \frac{(1-\nu^2)(1-5\nu)}{(7-5\nu)}, \quad (2.9)$$

where  $E = E_{i-1}$  and  $\nu = \nu_{i-1}$  are the elastic moduli of the material with pores of radius  $r < r_i$  obtained from the previous step. The moduli of the host material  $E_0$  and  $\nu_0$  are used as initial values.

In a similar way to the definition (2.7) of the change in the concentration value  $d\omega_i$  due to adding pores of the next group, the increments  $dE_i$  and  $d\nu_i$  were introduced as corresponding changes in the  $E_i$  and  $\nu_i$  values:

$$dE_i = E_i - E_{i-1}, \quad d\nu_i = \nu_i - \nu_{i-1} \quad (2.10)$$

In the limit this leads to the following system of ordinary differential equations:

$$\frac{dE}{d\rho} = -2\pi E \frac{(1-\nu)(9+5\nu)}{(7-5\nu)}, \quad \frac{d\nu}{d\rho} = 2\pi \frac{(1-\nu^2)(1-5\nu)}{(7-5\nu)}, \quad (2.11)$$

with initial conditions  $E = E_0$ ,  $\nu = \nu_0$  when  $\rho = 0$ . Vavakin and Salganik showed that the Poisson's ratio  $\nu \rightarrow 0.2$  when porosity  $p \rightarrow 1$ . The influence of  $\nu$  on the value of  $E$  is neglected in the VS model for simplicity, therefore  $\nu(\rho)$  is assumed to be constant. For  $\nu_0 = 0.2$  and  $\nu(\rho) = \text{const}$  the former Equations (2.11) can be integrated as

$$E = E_0 e^{-2\rho}, \quad \nu = 0.2. \quad (2.12)$$

Substituting (2.8) to (2.12) results in

$$E = E_0(1-p)^2, \quad \nu = 0.2, \quad (2.13)$$

and this solution is referred to as the VS model.

In the original VS approach the general case of a distribution of pores by size is approximated by an asymptotic solution. No specific distribution of pores by size is

considered and therefore it does not allow the influence of pores of a particular radius  $r_i$  on the elastic properties of the material to be considered. In addition, the change in the Poisson's ratio due to increasing porosity is neglected. For the 2-dimensional case Vavakin and Salganik (1975, 1978) showed an excellent agreement of their model with experiments carried out by stretching a plate with a number of circular holes of different sizes drilled in it. For the 3-dimensional case the comparison is presented in the Section 2.4. The current work is based on the VS model described above.

### 2.3.The extended VS approach

In the current work the VS approach is extended to take particular distributions of pores by size into account.

Let the distribution of pores by size be defined as a discrete probability density function  $f(r_i)$ :

$$f(r_i) = \frac{N_i}{\sum_{i=1}^n N_i}, \quad \sum_{i=1}^n f(r_i) = 1. \quad (2.14)$$

The extension of the VS model is implemented by step by step application of formulae (2.9) to the porous material with pores of radius  $r_i$ , where the elastic moduli  $E_{i-1}$  and  $\nu_{i-1}$  are the effective properties of the material where pores of radii  $r_1, \dots, r_{i-1}$  only are present. The use of (2.9) is not reduced to the differential Equations (2.11) as in VS model and therefore more sophisticated numerical experiments can be implemented including various statistical distribution of pore sizes. This extended model is referred to as the *extended VS model*.

Various distributions of pores by size with the same value of total porosity have been examined. A group of continuous distribution functions  $f(r)$  with  $r \in [r_{min}, r_{max}]$  based on the Gaussian distribution is given below. These distributions

- Normal:  $f(r) = \frac{1}{\sqrt{2\pi\sigma^2}} e^{-\frac{(\mu-r)^2}{2\sigma^2}}$ ,  $\mu = \frac{r_{max} + r_{min}}{2}$ ,  $\sigma = \frac{r_{max} - r_{min}}{6}$
- Left normal:  $f(r) = \frac{1}{\sqrt{2\pi\sigma_1^2}} e^{-\frac{(\mu_1-r)^2}{2\sigma_1^2}}$ ,  $\mu_1 = \frac{r_{max} + 2r_{min}}{3}$ ,  $\sigma = \frac{r_{max} - r_{min}}{6}$

## Section 2.3 The extended VS approach

- Right normal:  $f(r) = \frac{1}{\sqrt{2\pi\sigma_1^2}} e^{-\frac{(\mu_3-r)^2}{2\sigma_1^2}}$ ,  $\mu_3 = \frac{2(r_{max} + r_{min})}{3}$ ,  $\sigma = \frac{r_{max} - r_{min}}{6}$

- Double normal:  $f(r) = \frac{1}{\sqrt{2\pi\sigma_2^2}} e^{-\frac{(\mu_2-r)^2}{2\sigma_2^2}} + \frac{1}{\sqrt{2\pi\sigma_2^2}} e^{-\frac{(r_{max} - \mu_2 - r)^2}{2\sigma_2^2}}$ ;   
  $\mu_2 = \frac{r_{max} + 2r_{min}}{3}$ ,  $\sigma = \frac{r_{max} - r_{min}}{12}$

- Uniform:  $f(r) = \frac{1}{r_{max} - r_{min}}$

are shown in Figure 2.2 together with the uniform distribution, which provides the same number of pores of each radius.

Skewed distributions such as

- Linear descending:  $f(r) = A\left(\frac{r_{max} - r_{min}}{2} - r\right) + \frac{1}{r_{max} - r_{min}}$    
  $A = \frac{8}{3(r_{max} - r_{min})^2}$

- Linear ascending:  $f(r) = A\left(r - \frac{r_{max} - r_{min}}{2}\right) + \frac{1}{r_{max} - r_{min}}$ ,   
  $A = \frac{8}{3(r_{max} - r_{min})^2}$

- $1/R^3$  distribution:  $f(r) = \frac{1}{r^3}$

- Gamma left:  $f(r) = \frac{r^{\kappa-1} e^{-\frac{r}{\theta}}}{\theta^{\kappa} \Gamma(\kappa)}$ ,  $\kappa = 5$ ,  $\theta = \frac{3(r_{max} - r_{min})}{20}$

- Gamma right:  $f(r) = \frac{(r_{max} - r)^{\kappa-1} e^{-\frac{r_{max} - r}{\theta}}}{\theta^{\kappa} \Gamma(\kappa)}$ ,  $\kappa = 5$ ,  $\theta = \frac{3(r_{max} - r_{min})}{20}$

are illustrated in Figure 2.3. The  $1/R^3$  distribution provides the same volume fraction of groups of pores of each radius.

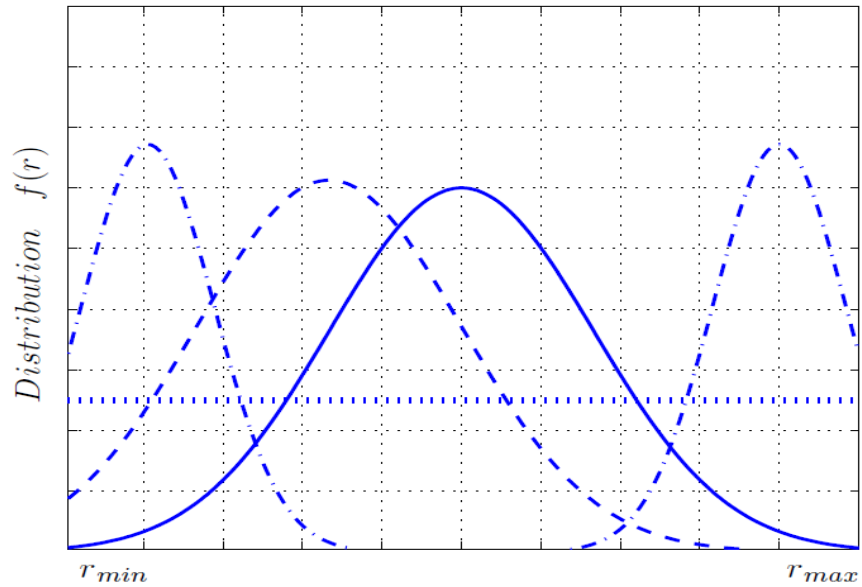


Figure 2.2 Distributions of pores by size. Normal (solid), Left normal (dashed), Uniform(dotted), Double normal(dashed and dotted);

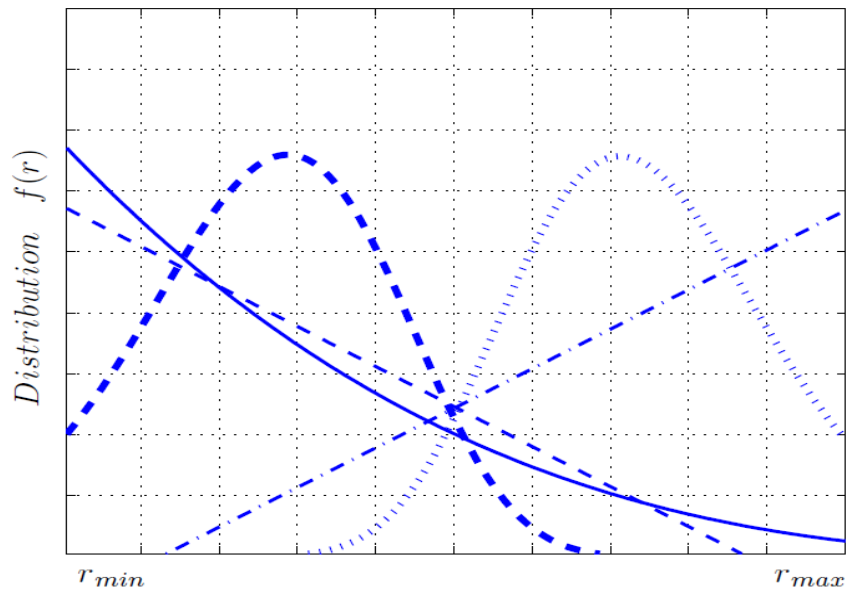


Figure 2.3 Distributions of pores by size.  $1/R^3$  distribution (solid), Linear descending (dashed thin), Linear ascending (dashed and dotted thin), Gamma right (dashed and dotted thick), Gamma left (dashed thick)

Note that for modelling purposes the discrete distribution functions  $f(r_i)$  are used where the set of radii  $r_i$  is discretized as:

$$r_i = r_{min} + \Delta r(i - 1), \quad \Delta r = \frac{r_{max} - r_{min}}{n-1}, \quad i = 1 \text{ to } n. \quad (2.15)$$

The effect of different distribution of pores by size on the elastic properties of the material was examined. This effect is summarized in Figure 2.4, which shows the variation in elastic modulus with volume fraction of pores for all the distributions considered. It is clear that the maximum difference does not exceed 1% for porosity of  $p \leq 0.7$ . Hence, the difference between the various statistical distributions of pore

## Section 2.4 Comparison of the extended VS model with experiments

sizes is considered as negligible for  $p \leq 0.7$ , and the extended VS model with various statistical distributions of pore sizes has an excellent agreement with the classical VS model. Higher values of porosity ( $>0.7$ ) where small differences in  $E/E_0$  do occur are not considered as they are not practical materials for the engineering applications that are of interest in this thesis. Thus, it can be concluded that the governing parameter of the models for materials with isolated spherical pores is the total porosity  $p$  and the VS model can be applied to describe the elastic characteristics of the materials. The uniform distribution of pores by size is thus considered in this study.

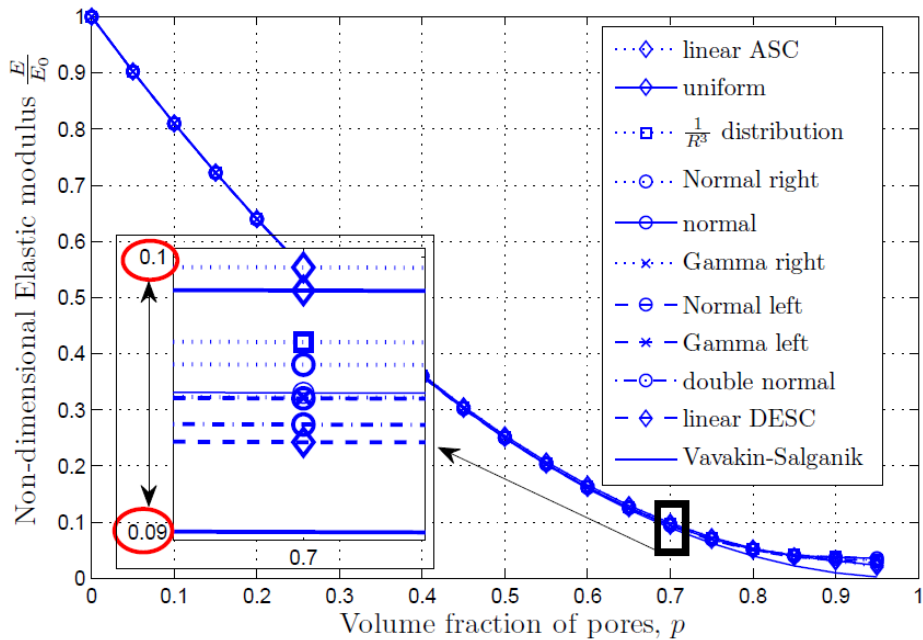


Figure 2.4 Variation of calculated elastic modulus for the VS model and the extended VS models corresponding to the different distributions considered.

### 2.4. Comparison of the extended VS model with experiments

A literature survey was carried out to find published experimental data on the influence of the porosity on the elastic moduli of porous materials. The data used in the present paper include experimental values of elastic characteristics for natural materials, foams and sintered materials. If the bulk modulus  $K$  values are examined in the paper then substituting  $E$  and  $\nu$  obtained from the extended VS model into (2.1) allows the predictions of bulk modulus  $K$  to be calculated and compared with given experimental values.

The experimental data are available for (i) natural materials and foams with isolated pores such as: glass foams (Walsh et al, 1965), synthetic sandstone (Berge et al, 1995), sandstone and clay (Mukerji et al, 1995), sandstone and shale (Mukerji et al, 1995, Ji et al, 2006), titanium foam (Shen et al, 2006) as well as for (ii) sintered materials such as silicon carbide (Reynaud et al, 2005), sintered alumina oxides (Wang, 1984b) and

## Chapter 2 The effective elastic properties of porous materials

synthetic sandstone (Berge et al, 1995); and (iii) other sintered materials including titanium aluminide compacts (Matikas, 1997), sintered titanium (Oh et al, 2003), alumina oxides (Spriggs, 1961, Knudsen, 1962), magnesium oxides (Spriggs, 1962) , magnesium and alumina oxide aggregates (Porter, 1977).. For comparison purposes the experimental data are divided into three groups ((i), (ii) and (iii)) as specified in the tables below.

**Table 2.1 Sources of experimental data on elastic properties of natural porous materials and synthetic foams (group (i))**

Porous material	Reference
Glass foams $p$ from 0 to 70%	Walsh et al, (1965)
Synthetic analogue of sandstone prepared from glass beads $p$ from 0 to 43%	Berge et al, 1995),
Natural sandstone	Mukerji et al (1995)
Natural sandstone and shales	Mukerji et al (1995), Ji et al(2006),
Titanium foam	Shen et al (2006)

The natural porous materials considered are clean and clay-bearing sandstones and shale. The laboratory data consists of normalized bulk moduli  $K/K_0$  for dry sandstones under  $40MPa$  confining pressure as given in Mukerji et al (1995).

Experimental data for both clean and clay-bearing sandstones (with up to 10% of clay) was obtained from Mukerji et al (1995). For the clean sandstones, the elastic moduli of the host matrix ( $E_0, \nu_0$ ) or ( $K_0, \mu_0$ ) were those of quartz; while for the clay-bearing ones, they were obtained from the zero porosity interception of linear regression for shaly sandstones ( $K_0 = 31GPa$  and  $\mu_0 = 34GPa$ ).

**Table 2.2 Sources of experimental data on elastic properties of sintered materials (group (ii))**

Porous material	Reference
Porous polycrystalline $SiC$ aggregates $p < 42\%$	Reynaud et al (2005)
Porous alumina	Wang (1984b)
Synthetic analogue of sandstone prepared from glass beads $p$ from 0 to 43%	Berge et al (1995)

**Table 2.3 Sources of experimental data on elastic properties of sintered materials (group (iii))**

Porous material	Reference
Porous titanium aluminide compacts	Matikas (1997)

## Section 2.4 Comparison of the extended VS model with experiments

Sintered titanium compacts	Oh et al (2003)
porous $Al_2O_3$ $p < 40\%$	Spriggs (1961)
porous $Al_2O_3$ polycrystalline aggregates $p < 30\%$	Knudsen (1962),
porous $MgO$ aggregates $p < 40\%$	Spriggs (1962)
Polycrystalline spinel $MgAl_2O_4$ aggregates prepared by hot pressing	Porter (1977)..

The group of materials also includes foamed titanium, porous glass and synthetic sandstone. The properties of a porous titanium foam have been investigated by Shen et al (2006). Results of a number of experiments on the bulk moduli  $K$  of glass foams of different porosities are published by Walsh et al (1995) and Ji et al (2006). The pores in the samples were nearly spherical and non-interconnecting (see e.g. Figure 2.5). The elasticity of synthetic sandstone was obtained in Berge et al (1995). The samples were prepared using sintered glass beads and were in essence porous glass specimens with porosities ranging from 0 to 0.43. The glass characteristics are  $E_0 = 72.3GPa$  and  $\mu_0 = 29.2GPa$ .

The experimental data of the natural materials and foams in group (i) are summarized and compared with the predictions given by the extended VS model in Figure 2.6 where the influence of the porosity value on the normalized bulk modulus  $K/K_0$  is shown.

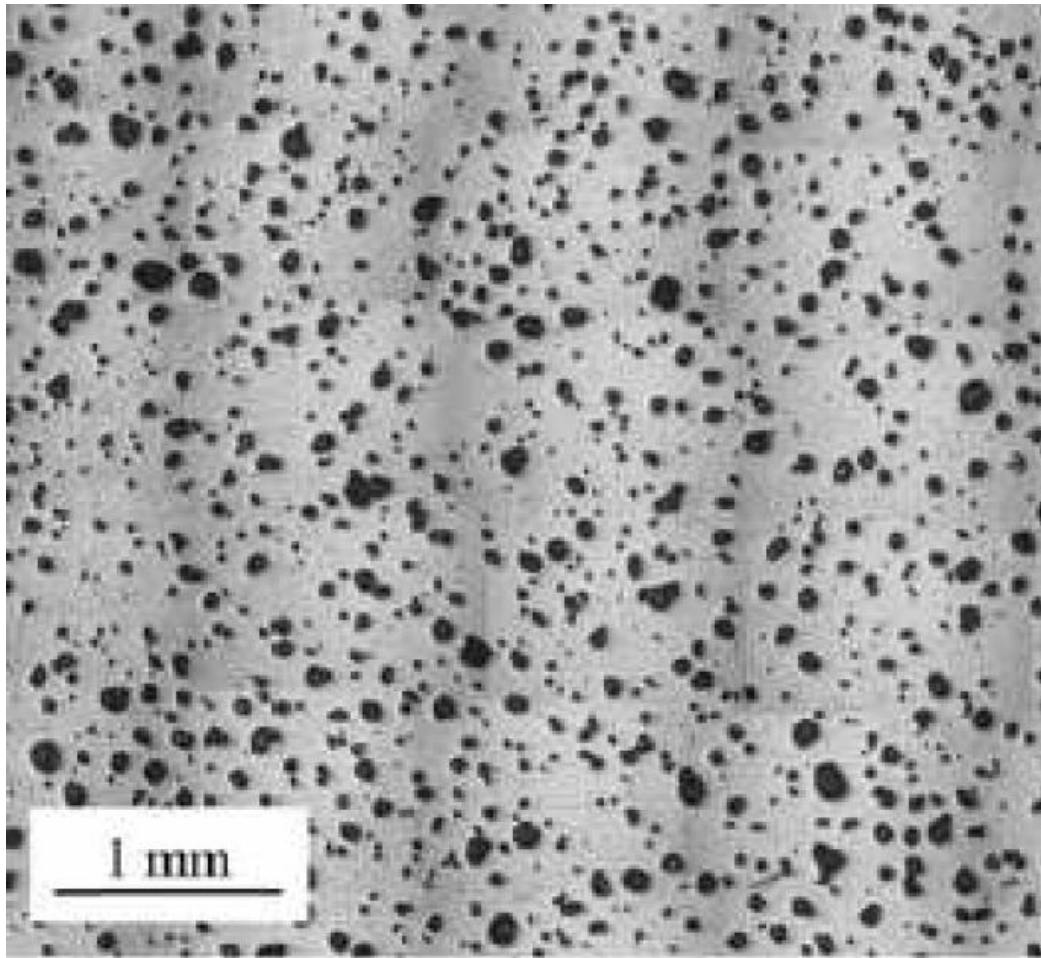


Figure 2.5 The metallographic cross-sections of titanium foam with porosity of 0.15, showing that pores are roughly spherical and isolated. Figure taken from Shen et al (2006).

The remaining experimental data considers the materials prepared from different powders by compressing and sintering. The powders used include alumina, titanium, silicon-carbide, alumina and magnesium oxides and others.

The comparison of experimental data on elastic modulus of porous materials in group (ii) with the predictions given by the extended VS model is given in Figure 2.7, and the comparisons for the materials in group (iii) are given in Figure 2.8. In these figures the non-dimensional elastic modulus  $E/E_0$  is plotted against the value of porosity.

Experimental data for both clean and clay-bearing sandstones (with up to 10% of clay) were obtained from Mukerji et al (1995). For the clean sandstones, the elastic moduli of the host matrix ( $E_0, \nu_0$ ) or ( $K_0, \mu_0$ ) were those of quartz; while for the clay-bearing ones, they were obtained from the zero porosity interception of linear regression for shaly sandstones ( $K_0 = 31GPa$  and  $\mu_0 = 34GPa$ ).

## Section 2.4 Comparison of the extended VS model with experiments

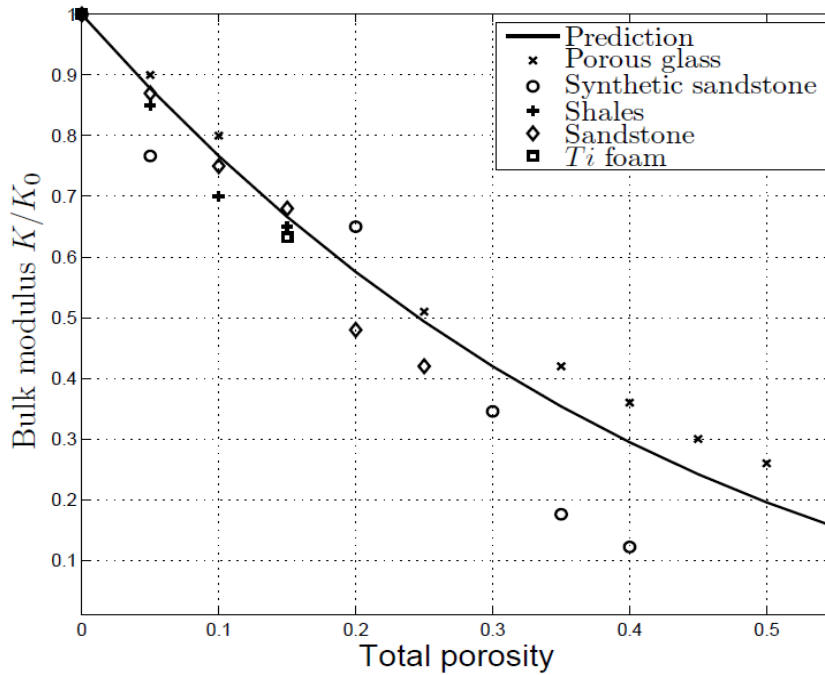


**Figure 2.6** The influence of the total porosity on the bulk modulus of the materials of group (i) with isolated spherical pores: predictions given by the extended VS model (solid line), the experimental data for the materials given in Table 2.1

Two main observations can be made from data plotted in Figure 2.6-Figure 2.8. First, the data on bulk modulus of natural materials and foams is in good agreement with the predictions of the extended VS model. This can be explained by the fact that pores are roughly spherical and isolated as is observed in the optical micrograph of metallographic cross-section for a titanium foam with porosity of 0.15 (Figure 2.5). In section 2.3 the extended VS model was shown to be equal to the classical VS model, therefore all the statements about the extended VS model can be assumed to be true for the classical VS model.

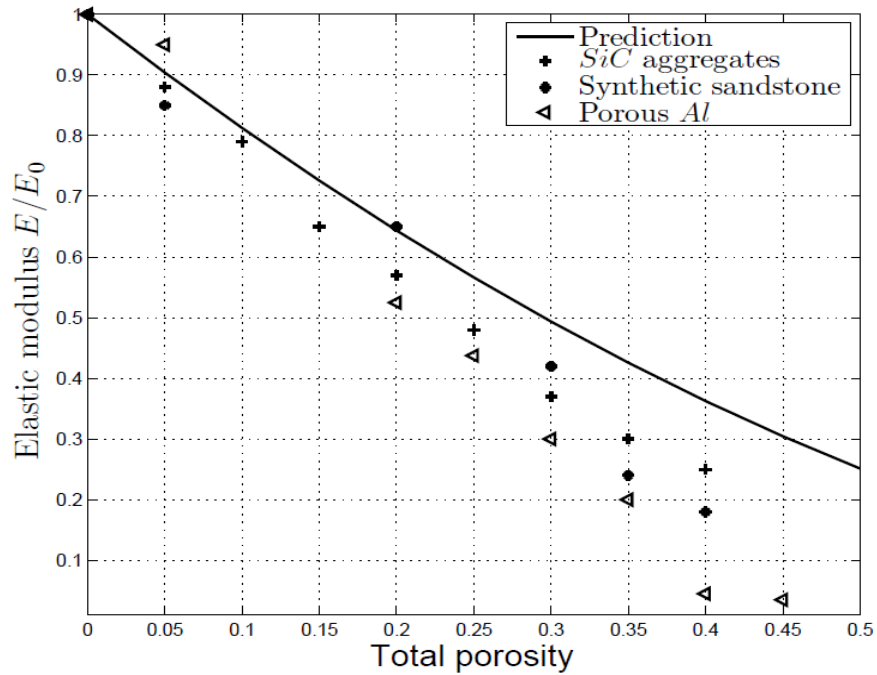


Figure 2.7 The influence of the total porosity on the elastic modulus of the sintered materials of group (ii): the predictions given by the extended VS model (solid line) compared with experimental data for various materials. Experimental data for materials given in Table 2.2.

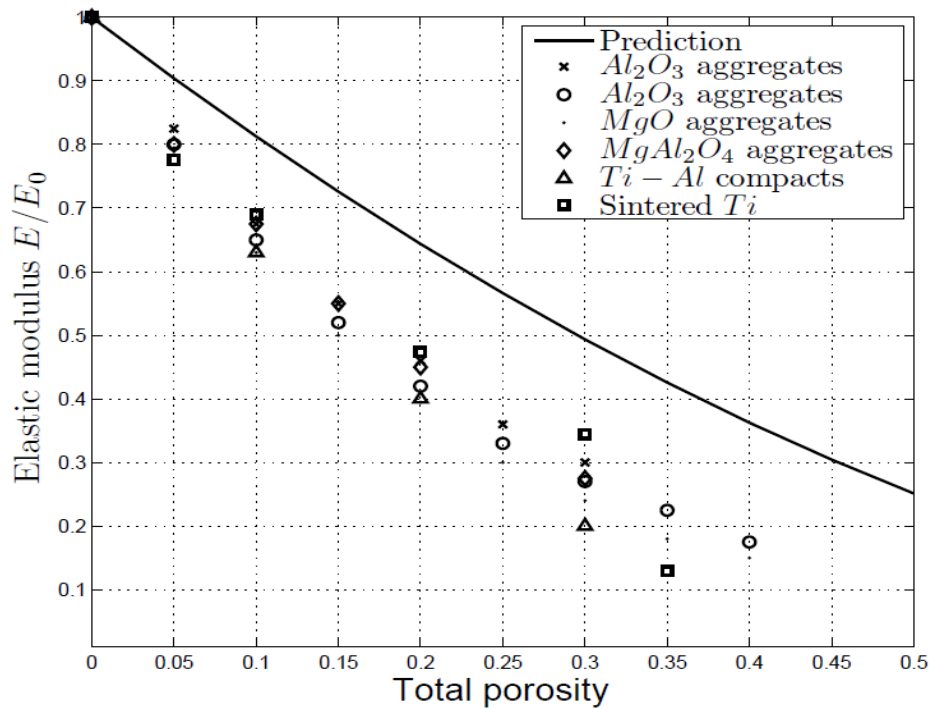


Figure 2.8 The influence of the total porosity on the elastic modulus of the sintered materials of group (iii): the predictions given by the extended VS model (solid line) compared with experimental data for various materials. Experimental data for materials given in Table 2.3

Second, the data on elastic modulus of materials prepared by sintering does not fit to the predicted values. This can be explained by the different type of porous structure present in the sintered materials. Indeed, the metallographic picture of the sintered bearing (Figure 2.) shows that pores merge to form complex agglomerates and can interconnect to form an open pore structure.

## Section 2.5 Merged pores model (MPM)

It can be concluded that for materials whose pores can be approximated as isolated spheres (Figure 2.5) the extended VS model gives good predictions, while for materials with merged pores (Figure 2.) further development of the physical model is required.

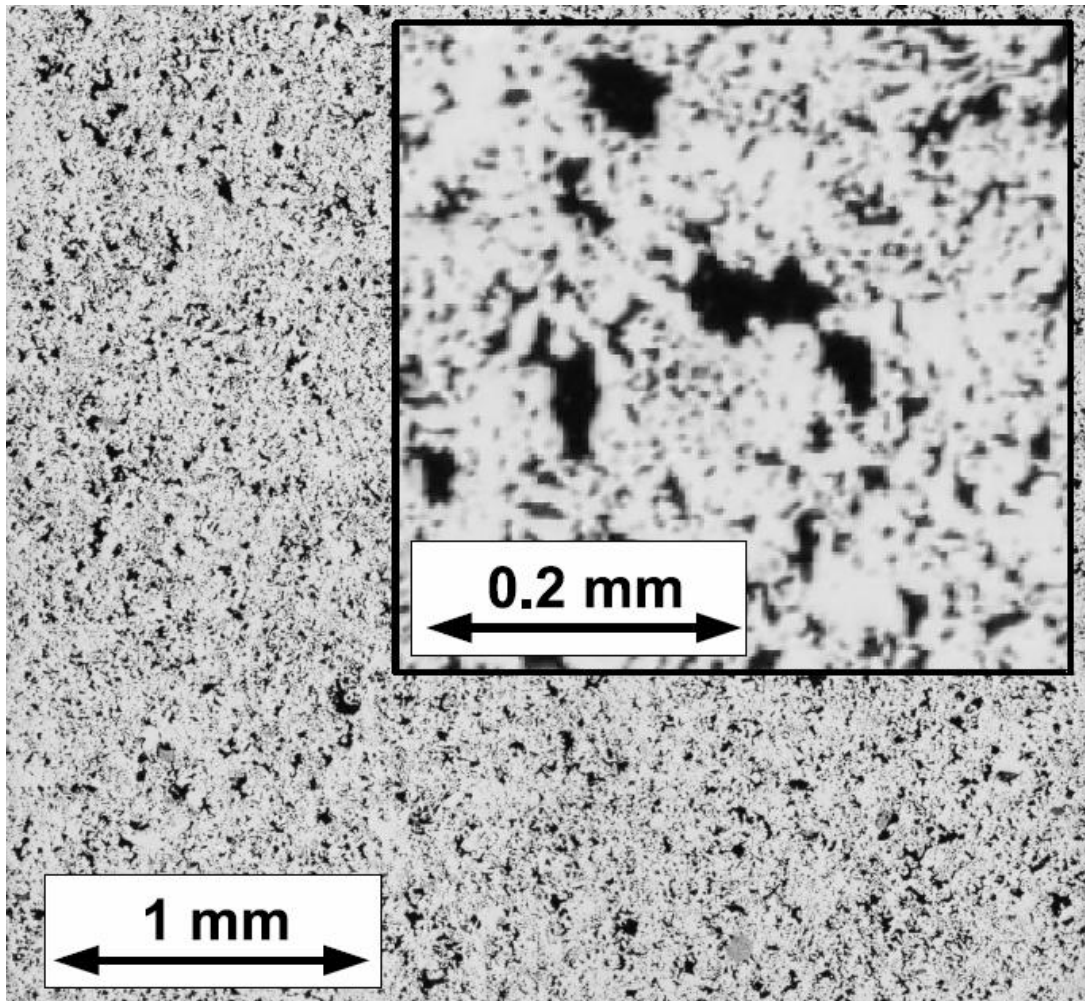


Figure 2.9 The metallographic cross-sections of sintered iron bearing with porosity of 0.2 (GKN Sinter Metals Bruneck, Italy)

### 2.5.Merged pores model (MPM)

Both the analysis of the micro structure of the porous materials (Figure 2.) and comparison of the existing differential scheme with the experimental results shown in Figures 2.5 to 2.7 suggest that the assumption of a dilute concentration is applicable for the class of porous materials given in Table 2.1 but not for materials given in Tables 2.2 and 2.3. To improve the physical model of the materials with merged pores a new differential scheme is presented in this section. In this scheme isolated spherical pores are treated according to the extended VS model, while each merged pore occurrence is approximated by an ellipsoid having the same volume as the merged pores. The effect of merged pores on the elastic properties of the porous material is more significant than the effect of isolated pores of the same volume, consequently the model has been extended to account for the interaction between individual pores. In

order to estimate the number of merged pores the theory of geometrical probabilities has been exploited.

Geometrical probabilities have been intensively studied, see e.g. Kendall and Moran (1963) and Elias and Hyde (1980). In particular, Armitage (1949) studied a problem of overlapping particles in an application concerned with the counting of cells in biological experiments. In the paper a number of particles were considered randomly distributed on a plate and then the probability of the circular particles being isolated, forming doublets, and forming triplets was calculated. In the present paper the approach of Armitage to overlapping particles was generalized to a 3-dimensional case of spherical pores that may overlap. For this problem the probability density function for the distance  $d$  between two points placed randomly inside the volume  $V$  is

$$\phi(d) = \frac{4\pi d^2}{V}. \quad (2.16)$$

The spatial distribution of the point in the volume is assumed to be homogeneous. The merging distance  $d$  for the two spherical pores of radii  $r_i$  and  $r_j$  is defined as the distance between their centres that allows the pores to overlap, i.e.  $r_i < d < r_i + r_j$ . The probability  $P_{merge}(r_i, r_j)$  for a pore of radius  $r_i$  to overlap a pore of the radius  $r_j$  is then calculated as the volume of points that are within merging distance from the center of the  $r_i$ -pore per total volume  $V$ . This leads to the following formula for  $P_{merge}(r_i, r_j)$ :

$$P_{merge}(r_i, r_j) = \int_{r_i}^{r_i+r_j} \phi(d) dd \quad (2.17)$$

Substituting (2.16) into (2.17) gives

$$P_{merge}(r_i, r_j) = \int_{r_i}^{r_i+r_j} \frac{4\pi s^2}{V} ds = \frac{4\pi((r_i + r_j)^3 - r_i^3)}{3V} \quad (2.18)$$

If the distribution of pores by size is given by the probability density function  $f(r)$  for the pore of radius  $r$ , and the total number of pores is  $N$  then the number of pores of a particular radius  $r_i$  is  $Nf(r_i)$  and therefore the number  $N_{ii}$  of pairs of pores of the same radius  $r_i$  is

$$N_{ii} = \frac{Nf(r_i)}{2}. \quad (2.19)$$

## Section 2.5 Merged pores model (MPM)

Similarly,

$$N_{ij} = \min(Nf(r_i), Nf(r_j)) \quad (2.20)$$

is the total number of pairs of pores of different radii  $r_i$  and  $r_j$ ,  $r_i > r_j$ . The concentration of merged pores in the representative volume is then

$$p_{ii}^{merged} = \frac{28\pi r_i^3 Nf(r_i)}{3V} N_{ii}, \quad (2.21)$$

for merged pores of the same radius  $r_i$ , and, similarly,

$$p_{ij}^{merged} = \frac{4\pi((r_1 + r_2)^3 - r_1^3)Nf(r_i)}{3V} N_{ij}, \quad (2.22)$$

for the merged spherical pores of different radii  $r_i > r_j$ .

The contribution of the merged pores of radii  $r_i$  and  $r_j$  to the mechanical properties of the porous material has been calculated using the results obtained by Luo and Stevens (1996) for the material with randomly oriented elliptic inclusions. Merged spherical pores are approximated by ellipsoids (prolate spheroids, see sketch of Figure 2.10) of the same volume.

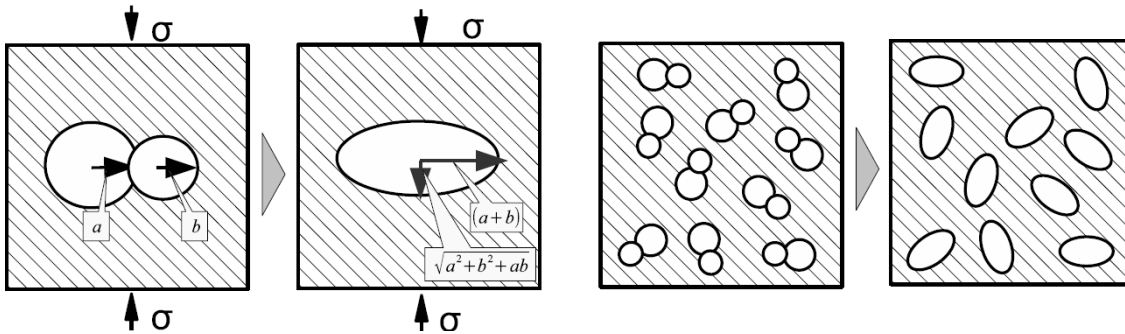


**Figure 2.10** The influence of two merged spherical pores on the elastic properties of the porous material is approximated by that of the prolate spheroid of the same volume.

In order to account for the merged pores of different sizes the iterative method similar to the extended VS model described in Section 2.3 was developed as follows:

- Introduce spherical pores of radius  $r_1$  into the host material with elastic modulus  $E_0$ .
- At each  $i - th$  step calculate the probabilities  $P_{merge}(r_i, r_j)$  of spheres with radii  $r_i$  to merge with spheres of radii  $r_j$  for any  $r_j \geq r_i$ .

- Obtain the number of merged pores for each  $j \geq i$ .
- Update the number of isolated spherical pores of radius  $r_i$  subtracting number of pores involved in merged pairs.
- Calculate the effective modulus  $E_{i,0}$  of the host material with isolated spherical pores as in extended VS model (Section 2.3).
- Calculate the effective modulus  $E_{i,i}$  of the material with merged pores of same radius  $r_i$ . Use  $E_{i,0}$  as the property of the host material.
- Calculate the effective modulus  $E_{i,j}$  of the material with merged pores of radii  $r_i$  and  $r_j$  for all  $j = i + 1, i + 2, \dots, n$ . Use  $E_{i,j-1}$  as the property of the host material.
- The procedure is repeated for all  $i = 1, \dots, n$ .

The algorithm is schematically illustrated on the flowchart of Figure 2.11.

In this work the above model is referred to as *merged pores model (MPM)*.

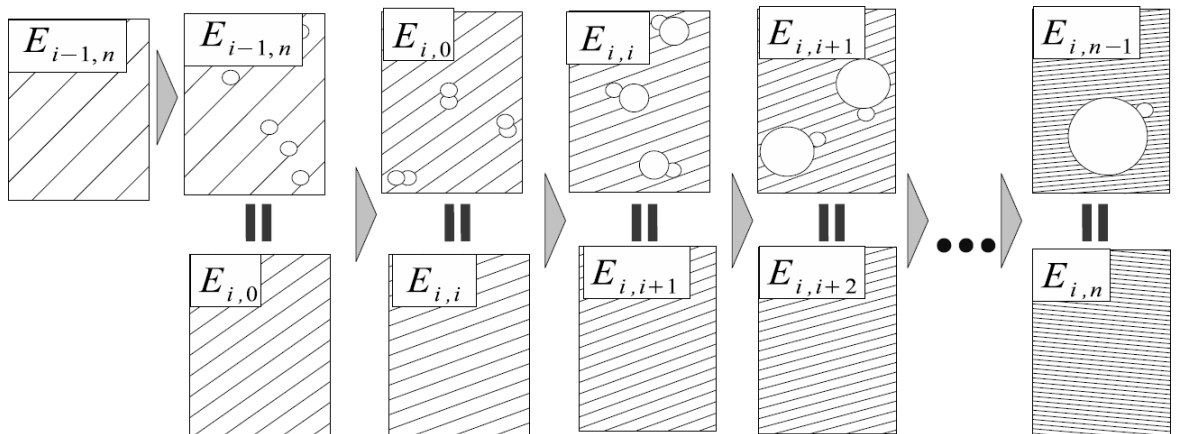


Figure 2.11 The bottom-up iterative approach for merged pores;  $E_{i,0}$  is the effective modulus of the media, where isolated spherical pores of radius  $r_i$  are placed into medium with effective modulus  $E_{i-1,n}$ ; then the contribution of merged pores of same radius  $r_i$  is taken into account which leads to the effective modulus  $E_{i,i}$ ; merged pores of radii  $r_i$  and  $r_j$  are then added into the material consequently which results in the effective moduli  $E_{i,j}$ ,  $j = i + 1, i + 2, \dots, n$ .

## 2.6. Comparison of the MPM model with experiments

In this section the predictions given by the MPM model are compared with the experimental data which is described in detail in Section 2.4. Since the elastic field outside the ellipsoidal inclusion is different to that of two isolated spherical pores of the same total volume, the current extension allows the interaction between pores to be taken into account. The difference can be summarized by the graphs shown in

## Section 2.7 Open pores model (OPM)

Figures 2.12 and 2.13 for the materials in group (iii). In these figures the predictions given by both the extended VS model and the MPM are compared to the experimental data. The results obtained by approximation of merged pores as ellipsoids give an improved fit to the data for the sintered materials in group (ii) (Figure 2.). For the sintered materials in group (iii), although the MPM model gives an improved fit to the data in comparison with the extended VS model (Figure 2.13), it is not a good fit to the data. The difference in behaviour between these two groups of materials is proposed to be due to the group (iii) materials containing a number of complex structures of interconnected pores which are in essence gaps between the grains of the raw material (see Figure 2.9). These structures are commonly referred to as open pores and cannot be approximated by either spheres or ellipsoids. The presence of open pores reduces the elastic moduli more significantly than predicted by the merged pores model. Hence, the influence of open pores has to be incorporated into the model.

### 2.7.Open pores model (OPM)

The model presented in this section considers the material with open pores to be a damaged material with reduced load carrying capacity. In the 1960s Rabotnov and Kachanov (see books by Rabotnov, 1979 and Kachanov 1974) investigated the creeping behaviour of material with a large number of micro-cracks , and introduced two parameters: a damage parameter of the material,  $\omega$  (Rabotnov), and an integrity parameter  $\phi = 1 - \omega$  (Kachanov). The damage parameter is a scalar associated with the area fraction of cracks or the area fraction of undamaged material in an arbitrary section of a sample.

In an axially loaded bar with a large number of cracks the real stress  $\sigma_{real}$  is calculated as load  $W$  over the effective cross-section area:

$$\sigma_{real} = \frac{W}{A_{eff}}, \quad A_{eff} = A(1 - \omega), \quad (2.23)$$

where  $A$  is the nominal cross-section area of the loaded sample,  $\omega$  is the damage parameter of the material, and  $A_{eff}$  is the effective undamaged area that carries all the load.

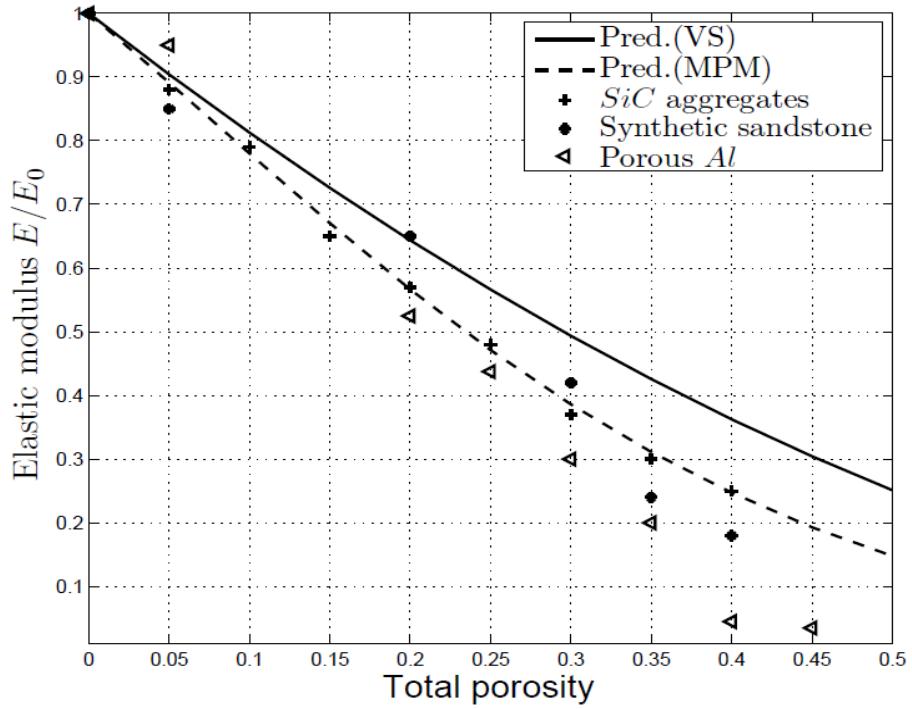


Figure 2.12 The influence of the total porosity on the elastic modulus of the sintered materials of group (ii): predictions given by the extended VS model (solid line), MPM (dashed line) compared with the experimental data for various materials. Experimental data for the materials given in Table 2.2

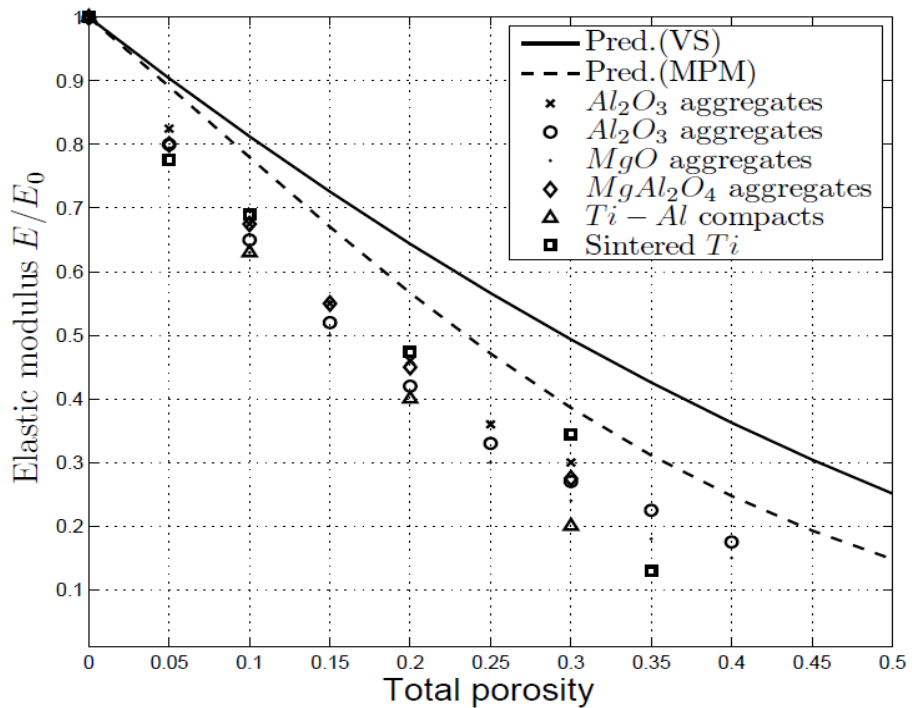


Figure 2.13 The influence of the total porosity on the elastic modulus of the sintered materials of group (iii): predictions given by the extended VS model (solid line), MPM (dashed line) compared with the experimental data for various materials. Experimental data for the materials given in Table 2.3

This makes the nominal uniaxial stress  $\sigma_{nom}$  to be equal to

$$\sigma_{nom} = \frac{W}{A} = \sigma_{real} (1 - \omega). \tag{2.24}$$

The effective elastic modulus  $E_{eff}$  is defined from Hooke's law for the nominal stress:

## Section 2.7 Open pores model (OPM)

$$\begin{aligned}\sigma_{nom} &= E_{eff} \varepsilon = \sigma_{real} (1 - \omega), \\ \sigma_{real} &= E_c \varepsilon,\end{aligned}\tag{2.25}$$

where  $\varepsilon$  is the elastic strain and  $E_c$  is the elastic modulus of the host undamaged material. It follows from (2.25) that the effective elastic modulus  $E_{eff}$  of the damaged material can be obtained as

$$E_{eff} = E_c (1 - \omega).\tag{2.26}$$

The validity of the Rabotnov-Kachanov approach in application to fracture mechanics was discussed by Salganik and Gotlib (2000) and indicated as questionable. Recently, Kusoglu et al (2008, 2009) applied the Rabotnov-Kachanov idea to porous polymer membranes. They considered materials with open porosity and assumed that the load is transferred only through the non-porous volume as in the Rabotnov-Kachanov approach for damaged bars. Here this approach is used as one of the simplest ways of describing the strong effect of the open pores on the effective moduli of the materials, namely that the stiffness of the material around the open pores is very low.

In the present study this idea is generalized and applied to porous materials with both open and isolated pores. The proposed approach can be interpreted as assuming that the entire load is being carried by the parts of the material with isolated pores only and the mechanical model is illustrated schematically in Figure 2.14. Hence, the value of elastic modulus obtained by MPM for the material with isolated and merged spherical pores is used to define  $E_c$ , while the damage parameter  $\omega$  can be connected to the amount of open pores:

$$\omega = \frac{A_{open}}{A},\tag{2.27}$$

where  $A_{open}$  is the area of the cross-section of the material that is occupied by open pores. Then for the case of open pores, one obtains

$$A_{eff} = A - A_{open} = A \left(1 - \frac{A_{open}}{A}\right) = A(1 - \omega),\tag{2.28}$$

To use this approach the effective area  $A_{eff}$  that carries all the load has to be established for the known value of open porosity. If the value of open porosity of the sample is  $p_{open}$  then the volume of open pores can be calculated as following:

$$V_{open} = p_{open} V_{total}\tag{2.29}$$

where  $V_{total}$  is the total volume of the sample.

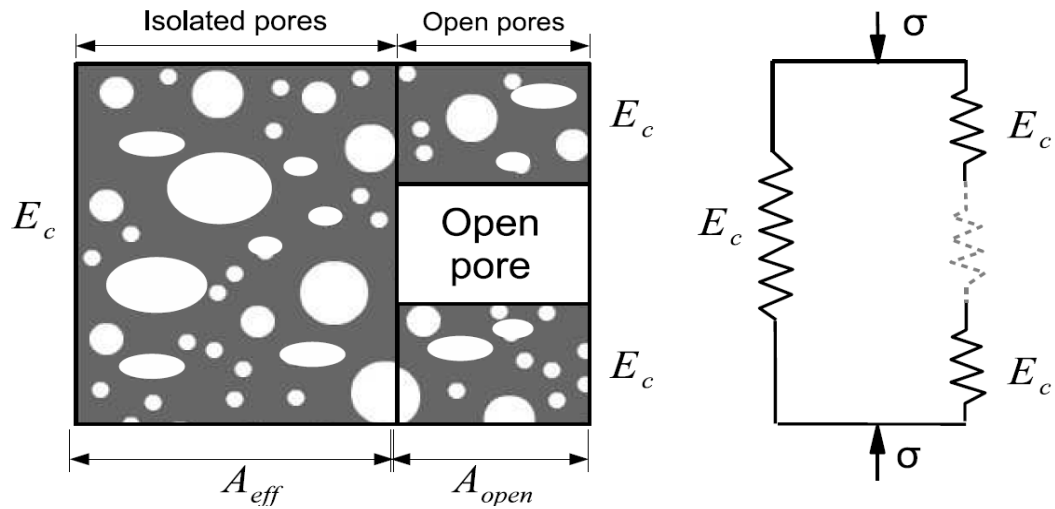


Figure 2.14 The mechanical model of the medium with developed open porosity, where all the load is carried by part of the material where no open pores are present

Let the representative volume of the material be a cube with a side  $h$  and let the Cartesian coordinate system be defined so that its origin is on the bottom side of the cube. The  $Z$  axis is defined perpendicular to the bottom side of the cube. In order to study the three-dimensional porous structure of the material, it is convenient to adopt the methods of stereology. Stereology is largely concerned with the three-dimensional interpretation of planar sections of materials or tissues. It provides practical techniques for extracting quantitative information about a three-dimensional material from measurements made on two-dimensional planar sections of the material.

It follows from the approach of stereology (see Elias and Hyde, 1980) that the volume of a three dimensional body can be approximated using the sequence of cross-sections with measured area. The same approach was applied to approximate the volume of open pores as the integration of the cross-sectional area occupied by open pores over the height of the sample:

$$V_{open} = \int_0^h A_{open}(z) dz \quad (2.30)$$

where  $A_{open}(z)$  is the area occupied by open pores in the cross-section of the representative volume parallel to the bottom side of the cubic representative volume, and  $z \in [0, h]$  is the position of the cross-section on the  $Z$  axis.

Since a uniform spatial distribution of pores is considered then  $A_{open}(z)$  is assumed to be constant. Let  $A_{open}(z) = A_{open}$ . Then (2.30) can be presented as  $V_{open} = hA_{open}$  which together with Equations **Error! Reference source not found.** leads to

$$A_{open} = p_{open} \frac{V_{total}}{h} = p_{open} A \quad (2.31)$$

## Section 2.7 Open pores model (OPM)

Therefore, the damage parameter  $\omega$  in the Equations (2.26) is equal to the value of open porosity  $p_{open}$  :

$$\omega = \frac{A_{open}}{A} = p_{open} . \quad (2.32)$$

Thus, the effective elastic modulus for the material with developed open porosity can be derived from Equations (2.26) as:

$$E_{eff} = E_c(1 - p_{open}) \quad (2.33)$$

where  $E_c$  is calculated according to the MPM with isolated spherical and elliptical pores, and  $p_{open}$  is the volume of the open pores within the representative volume of the sample. In this work the above model is referred to as the *open pores model (OPM)*.

For the OPM the volume fraction of open pores needs to be established. Laboratory data on open porosity of porous material was obtained from the literature. In the work of Altman et al (1966) the relationship between the total and open porosity of sintered Cu-Sn-C materials has been investigated. Other experimental data for open porosity of the sintered titanium compacts was taken from results obtained by Oh et al (2003). Data on total and open porosity of porous bearings sintered from Fe-Cu-Sn powders has been provided by the manufacturer of porous bearings (GKN Sinter Metals Bruneck, Italy) by means of personal communication.

In the present study the relationship between the total and open porosity of the materials has been approximated by an analytical function, which is a curve fit to the available experimental data:

$$p_{open} = \frac{p_{total}}{1 + Ap^{-\alpha}} \quad (2.34)$$

where the coefficients  $A, \alpha$  were selected to fit the available experimental data. Values  $A = 10^{-6}, \alpha = 5$  were used in further calculations as they provide a reasonably good fit to the experimental data on sintered materials obtained by Oh et al (2003). Values  $A = 2.5 * 10^{-5}, \alpha = 5$  were used to fit the experimental data on sintered Cu-Sn-C materials presented by Altman et al (1966), however, no data on elastic characteristics for was available for these materials.

The relation is summarized on the Figure 2.15 where the fraction of open pores within the total porous structure is plotted against the total porosity. The OPM model provides a better agreement with experimental data than the previous model. The

comparison of the predictions given for the sintered materials by both MPM and OPM models with the experimental data is plotted in Figure 2.16 for the group (ii) materials and Figure 2.17 for the group (iii) materials.

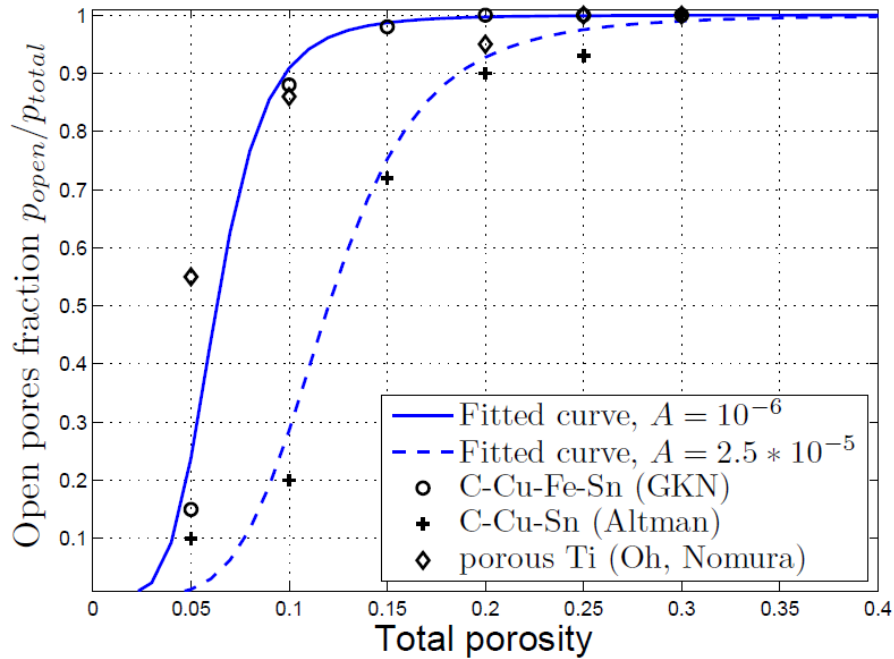


Figure 2.15 Fraction of open pores within the total porous structure plotted against the total porosity value. The approximate curve is compared with available experimental data. Solid line ( $A = 10^{-5}, \alpha = 5$ ) shows good agreement with data for Fe-Cu-Sn sintered bearings (GKN Sinter Metals Bruneck, Italy) and titanium compacts(Oh et al, 2003). Dashed line ( $A = 10^{-6}, \alpha = 5$ ) shows a better fit for Cu-Sn-C sintered materials (Altman, 1966).

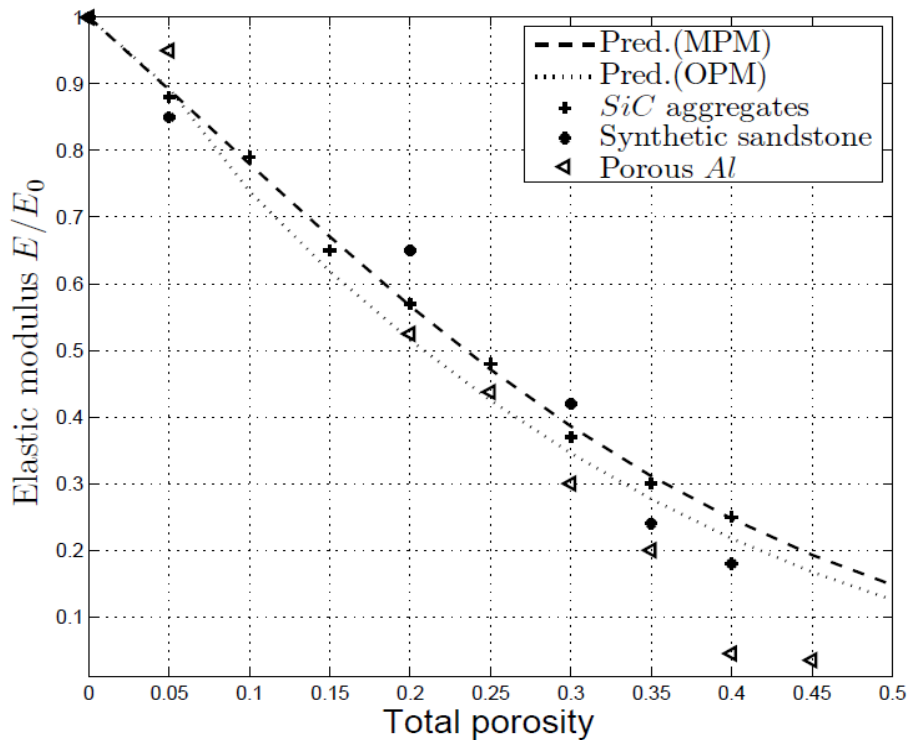


Figure 2.16 The influence of the total porosity on the elastic modulus of the sintered materials of group (ii): predictions given by the MPM (dashed line), OPM (dotted line) compared with the experimental data for various sintered materials. Experimental data for the materials given in Table 2.2

## Section 2.8 Combined model (OPMPM)

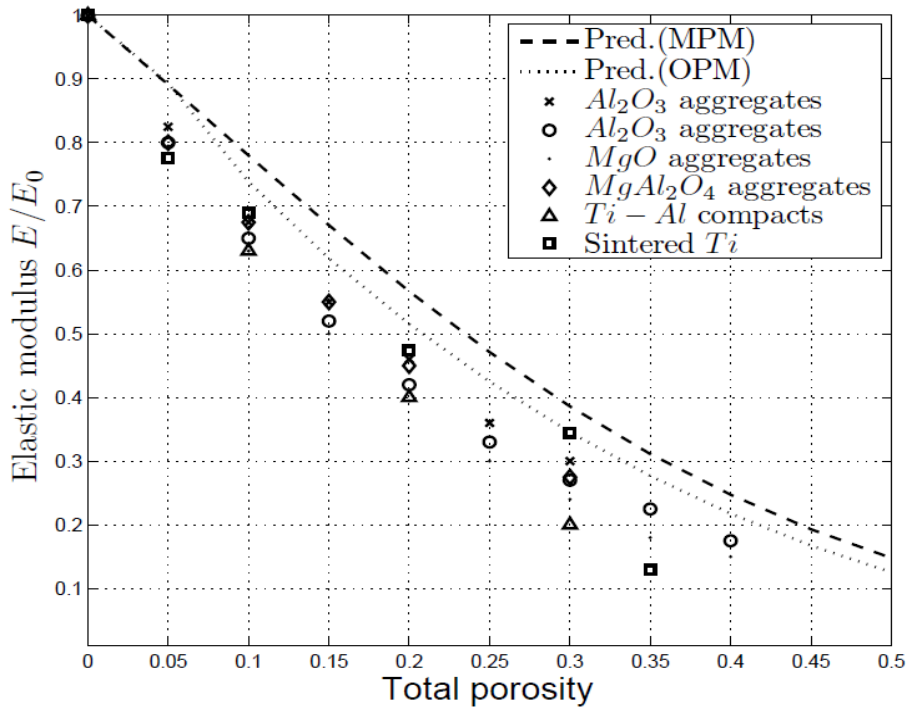


Figure 2.17 The influence of the total porosity on the elastic modulus of the sintered materials of group (iii): predictions given by the MPM (dashed line), OPM (dotted line) compared with the experimental data for various sintered materials. Experimental data for the materials given in Table 2.3

### 2.8. Combined model (OPMPM)

The combined model (OPMPM) of the present paper is a combination of the MPM and OPM and incorporates all the extensions described in the previous sections.

- Initially the calculation is performed according to the extended VS model for isolated spherical pores as described in Section 2.3.
- The influence of merged pores is calculated as by Luo and Stevens (1996) and incorporated in the model in a step by step manner as described in Section 2.5.
- The volume occupied by open pores is evaluated by the relation (2.34) with appropriate coefficients  $A, \alpha$  selected for a particular material. Then the elastic modulus of the porous medium with developed open porosity is calculated as given by Equations (2.33) in Section 2.7.

The comparison of the predictions given by the combined model with experimental data is shown in Figures 2.18 and 2.19 for the group (ii) and (iii) materials, respectively. A good agreement is apparent between the proposed combined model and the materials given by Table 2.3. This can be explained by the choice of the function (2.34) approximating the amount of open pores: it is selected to fit the data for sintered titanium and sintered porous bearings (see Figure 2.). To allow a better agreement

with properties of other materials, their open porosity to total porosity ratio has to be evaluated.

### 2.9. Conclusions

The analysis presented has shown that the elastic characteristics of a porous material are highly dependent on the porous micro-structure of the samples. Hence, the manufacturing process used to prepare the material is an important factor for choosing a proper model for prediction of the elastic characteristics of the material. Both the classic Vavakin-Salganik model and its extended modification with an arbitrary statistical distribution of pore radii (e.g. the uniform distribution function) show good results for materials with isolated spherical pores.

It is proposed that the theory of geometric probabilities is used to estimate the number of overlapping pores.

Overlapping spherical pores are treated as merged and approximated by ellipsoids which allows a better fit to the experimental results. This approach has been shown to be effective and it can be used in various applications related to the properties of multi-phase materials. A further modification of geometrical probabilities approach, not implemented in the current study, considers calculating the probability that three or more spherical pores merge.

For materials with developed porous micro-structure (open porosity), the volume fraction of open pores to the total volume of pores has to be established. The elastic properties of sintered materials may be affected not only by pores but also by cracks that could appear during the manufacturing process (see a discussion by Salganik and Fedotov, 2012). However the consideration of isolated cracks is outside the scope of the present paper. It is assumed that the load is transferred by the material containing closed pores that are either spherical or elliptical. The parts of the material containing open pores have very low stiffness and, therefore, do not carry any load. The function used to approximate the amount of open pores was selected to fit the experimental data for sintered titanium and sintered porous bearings. This results in a good agreement between the proposed combined elastic properties model for both merged and open pores with experimental results for these materials and other similar materials (see e.g. Table 2.3, Figure 2.19).

## Section 2.9 Conclusions

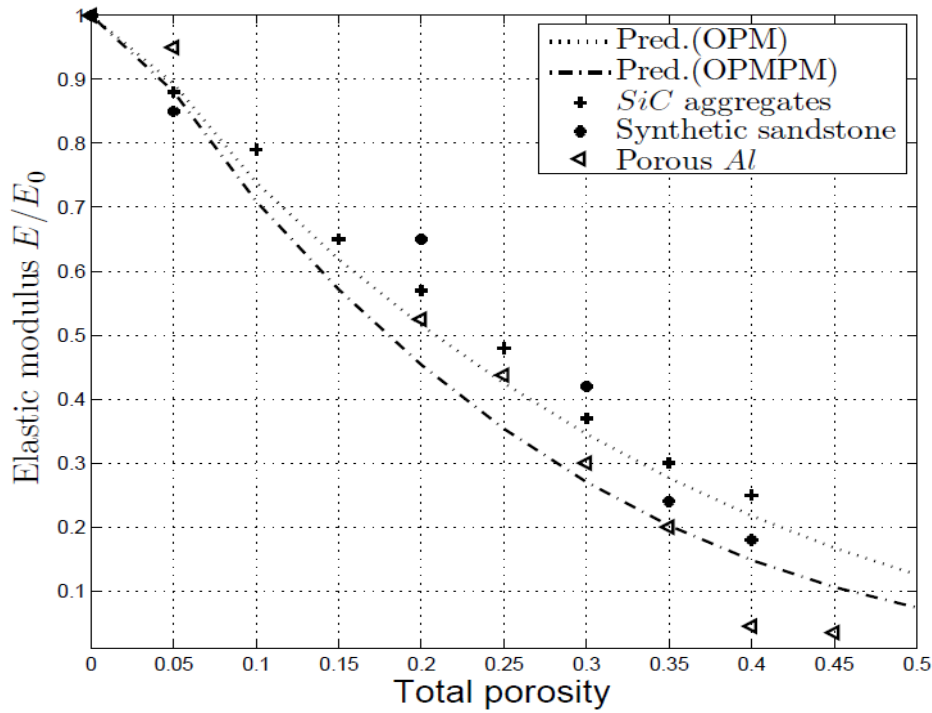


Figure 2.18 The influence of the total porosity on the modulus of the sintered materials of group (ii): predictions given by the OPM model (dotted line) and OPMPM model (dashed and dotted line) compared with the experimental data for various sintered materials. Experimental data for the materials given in Table 2.2.

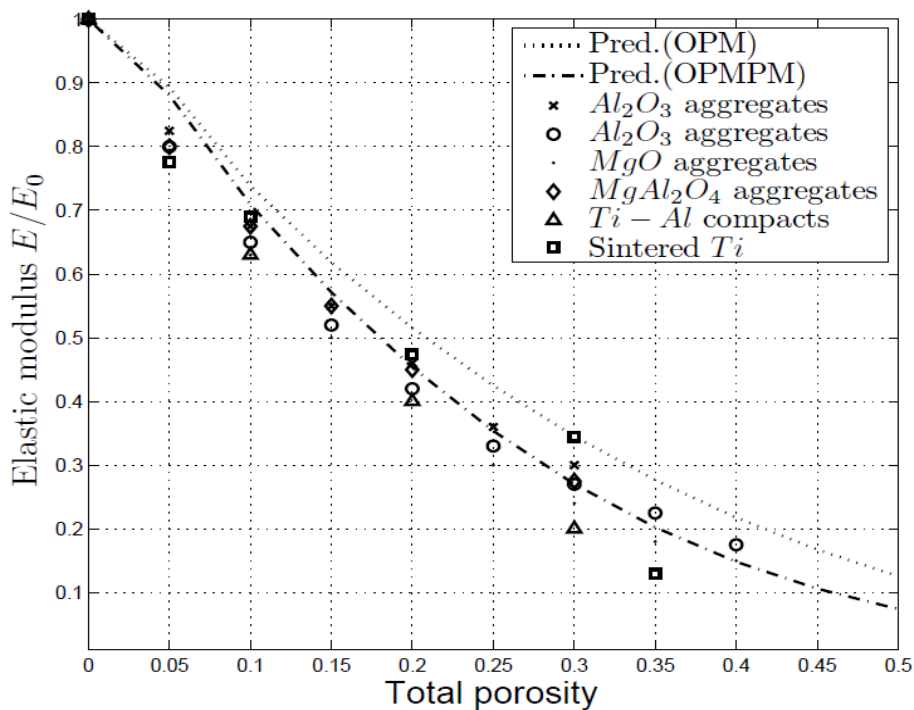


Figure 2.19 The influence of the total porosity on the elastic modulus of the sintered materials of group (iii): predictions given by the OPM model (dotted line) and OPMPM model (dashed and dotted line) compared with the experimental data for various sintered materials. Experimental data for the materials given in Table 2.3.

### 3 Dry contact analysis of rough nominally flat surfaces

#### 3.1 Introduction

Plain bearing problems are usually treated as having perfectly conforming smooth surfaces. In principle, waviness features can be incorporated in their analysis at the global scale. However, roughness features will obstruct the flow when the film becomes thin and will make contact when mixed lubrication occurs. To consider roughness effects a dry contact analysis of plane parallel surfaces is required, and in this thesis this is achieved using a repeated representative roughness area. As discussed later, the repeated roughness is a requirement for using the Fourier convolution theorem and is convenient for defining periodic boundary conditions in both dry contact analysis in this chapter and local scale flow analysis considered in Chapters 4 and 5.

This chapter is concerned with developing a method to model the elastic-plastic contact of nominally plane parallel surfaces where their local separation is significantly influenced by surface roughness. In this chapter the dry contact of rough surfaces is considered, however the method developed can be applied to the mixed lubrication analysis of plane bearings based on the theory of flow factors. The lubrication analysis based on the theory of flow factors is described in detail in Chapters 5 and 6.

The solution for the dry contact of rough surfaces has evolved considerably as a standalone method. The majority of methods developed in this area are based on calculating the elastic deflection of the surfaces using the classical Boussinesq-Cerutti integral of the contact pressures with a convolution kernel. The two main challenges for these methods are the following:

- A time consuming procedure of calculating the convolution integral which needs to be recalculated every time the pressure distribution has changed;
- A slow decay of the convolution kernel which makes even quite distant contact pressures highly influential on the deflection at the point of interest. This can result in a slow convergence of the numerical methods aimed to obtain the solution for contact pressures.

### Section 3.1 Introduction

Techniques based on multi-level multi-summation and the conjugate gradient method were developed by Polonsky and Keer (1999). Ju and Farris (1996), Stanley and Kato (1997) and Liu et al (2000) used Fourier transform (FT) methods to obtain the deflection as a convolution integral. All these works assumed purely elastic deformation of the materials. Subsequently, Keer and Wang (2005) adopted FT for evaluating stress and strain fields in a three dimensional elastic-plastic contact problem. Introducing a third dimension into the model allowed them to calculate von Mises subsurface stresses and, therefore, predict the plastic deformation of the body. A similar solution to the elastic-plastic contact problem was presented by Nelias et al (2007). Both linear and Swift's hardening laws were applied. These and other semi-analytical techniques were shown to be much faster than solutions based on finite element analysis (FEA) as indicated by Nelias et al (2007).

These semi-analytical methods use *fast Fourier transform* (FFT) with zero padding surrounding the pressure distribution in order to overcome the border aliasing error otherwise occurring (see e.g. Keer and Wang, 2005). Chen et al. (2008) used FFT methods without zero padding so that the resulting deflection convolution included the effect of periodic repeats of the pressure distribution in a semi-analytical method for elastic-plastic contacts similar to Nelias et al (2007) and Keer and Wang (2005). Sahlin and colleagues (2010a, 2010b) used FFT methods in the same way to obtain the deflection of the surface caused by the contact pressures. These methods thus solve for contact between surfaces with periodic repetition of a two dimensional representative roughness pattern which can be measured on real components using surface metrology techniques. Another difference of Sahlin's model was to include an evaluation of plastic deformation assuming limiting the elastic pressure value.

The current chapter presents a simple iterative approach to solving the harmonic contact problem based on a differential equation for the elastic and plastic deformations that is able to incorporate contact occurring at points on the boundary of the representative roughness and needs no special properties of the roughness on these boundaries. It is an extension of the differential deflection technique developed by Evans and Hughes (2000) to solve the mixed lubrication problem in concentrated contacts. The plastic deflection is accounted for in the same way as in Sahlin et al (2010a, 2010b) i.e. by limiting the maximum pressure to a hardness value of the material and determining the corresponding plastic deflection that limits the pressure

being developed at contacting points to this maximum value. Neglecting the hardening behaviour allows the deformations of the surface to be calculated as a function of contact pressures without introducing a third dimension. A comparison of the results obtained by the method presented and by an elastic-plastic FE analysis is provided in Section 3.4. The method benefits in time requirements and the resulting loaded shape can be used in a flow factor approach to mixed lubrication problems. It may also be possible to extend the method to the mixed lubrication problem which is currently being successfully approached by colleagues at Cardiff using the same differential formulation for the elastic deflection.

### 3.2 Theoretical background

#### 3.2.1 Formulation

The formulation of the problem considers two semi-infinite bodies in dry contact at their nominally plane contact surface. The lower body is elastic and has a rough nominally plane surface. The upper body is a plane, smooth semi-infinite body. The bodies are illustrated in (i) unloaded, and (ii) loaded configuration in Figure 3.1. The upper body is regarded as rigid as far as formulating the contact problem is concerned. The configuration can represent contact between two elastic bodies by a suitable choice of contact modulus,  $E'$ , and both surfaces can be rough if the lower surface is given a roughness that is the sum of the surface roughness of the two surfaces. In the loaded configuration of Figure 3.1 (ii) the unloaded position of the rough surface is shown as a broken curve.

Figure 3.1 shows a normal section through the contact and illustrates the notation adopted:  $h(x,y)$  is the gap between the surfaces,  $r(x,y)$  is the (composite) roughness which defines the surface heights with respect to an arbitrary datum. The maximum and minimum roughness heights for the rough surface(s) are  $R_{max}$  and  $R_{min}$ . The bodies are brought into dry contact by moving the upper surface towards the lower surface until contact occurs at zero load at the highest asperity tip. Further displacement of the upper body causes a contact load to be developed at that asperity and this additional displacement is called the approach distance and denoted  $S$ . The value of  $S$  thus controls the load developed at the asperity contacts. As  $S$  increases the number of asperities in contact increases, and the maximum contact pressure at each asperity contact, calculated based on elastic deflection, also increases.

## Section 3.2 Theoretical background

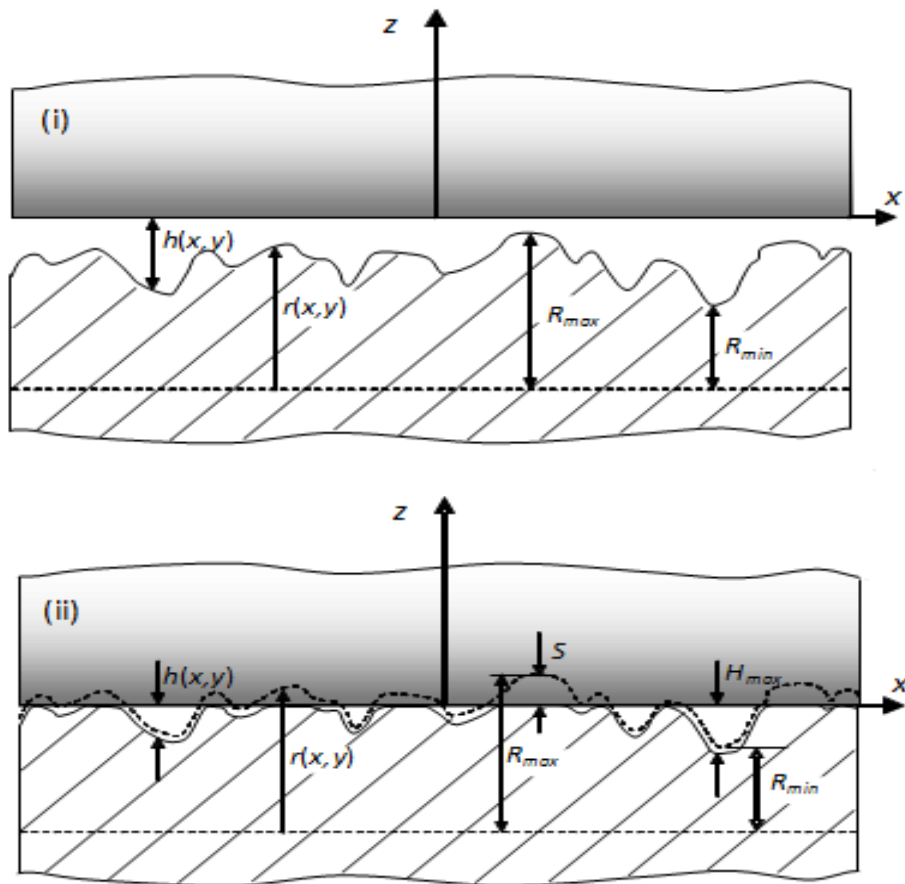


**Figure 3.1.** Section through contacting surfaces (i) showing undeformed non-contacting surfaces, and (ii) deformed contact under load for a specified value of approach distance,  $S$ , with the undeformed position of the hatched elastic body shown as a broken curve.

The obstruction of flow caused by the presence of elastically deformed asperities differs from that caused by the undeformed shape of the surfaces. Flow factors based on elastic contact analysis allows mixed lubrication to be considered in an approximate way. If plastic deformation occurs in the area adjacent to the contacting asperities then the elastic contact model overestimates the contact load and does not calculate the deformation of the shape correctly. An approximate plasticity model is introduced based on limiting the contact pressure by the value of  $P_{max}$  which is selected equal to the hardness value of the material. This model does not provide an accurate solution for the plastic deformation however it aims to improve the evaluation of the deflected shape of the surface and contact load in comparison to the pure elastic analysis. The model has shown a promising level of agreement with FEA as presented in Section 3.4

In the proposed model the contact is assumed to be elastic whilst the maximum pressure remains below the maximum value  $P_{max}$ , but when the elastic contact pressure exceeds  $P_{max}$  a plastic deflection is assumed to occur. This results in a change in the undeformed shape of the rough surface(s) that allows the contact load to be

### Chapter 3. Dry contact analysis of rough nominally flat surfaces

carried elastically with a contact pressure less than or equal to  $P_{max}$  as a result of asperity shape changes that have occurred due to plastic deformation. This change of shape is referred to as the plastic deflection,  $d^{plast}(x,y)$ .

The aim of the work is to determine the values of contact pressure  $p(x,y)$  and surface gap  $h(x,y)$  for a given composite roughness  $r(x,y)$  and  $S$  value and so to determine the load compliance behaviour based on this simple 'elastic-plastic' model of surface deflection. The solution is obtained by numerical means on the finite computational domain  $\Omega = [0, N_x - 1] \times [0, N_y - 1]$

The gap between the surfaces when  $S=0$  is  $h(x,y) = R_{max} - r(x,y)$  and the gap between the surfaces when  $S>0$  and the contact is under load is given by

$$h(x,y) = R_{max} - r(x,y) + d^{elast}(x,y) + d^{plast}(x,y) - S \quad (3.1)$$

Here  $d^{elast}(x,y)$  is the normal surface displacement caused by elastic deflection of the surface(s) and  $d^{plast}(x,y)$  is the reduction in asperity height due to plastic deflection.

#### 3.2.2 Elastic deflection

The elastic deflection at the point  $(x,y)$  is given by Boussinesq Cerutti integral (see e.g. Love, 1952 and Timoshenko and Goodier, 1970):

$$d^{elast}(x,y) = -\frac{2}{\pi E'} \iint_{p>0} \frac{p(s,t)}{\sqrt{(s-x)^2 + (t-y)^2}} dsdt \quad (3.2)$$

which can be written as

$$d^{elast}(x,y) = -\frac{2}{\pi E'} \iint_{p>0} g(x-s, y-t) p(s,t) dsdt \quad (3.3)$$

where  $s,t$  are the dummy variables, and the weighting function  $g(x,y)$  is defined as

$$g(x,y) = \frac{2}{\pi E' \sqrt{x^2 + y^2}} \quad (3.4)$$

For numerical evaluation of Equation (3.3) on an  $N_x$  by  $N_y$  rectangular mesh with spacing  $\Delta_x$  and  $\Delta_y$  in the  $x$  and  $y$  directions quadrature can be used to obtain the discrete weighting function  $G_{i,j}$  that gives the deflection at the mesh points as the discrete summation

$$D_{i,j}^{elast} = \sum_{k=0}^{N_x-1} \sum_{l=0}^{N_y-1} G_{i-k, j-l} P_{k,l}$$

## Section 3.2 Theoretical background

(3.5)

This study uses lower case symbols for continuous variables and upper case symbols for discrete variables. Note that  $G_{k,l}$  is defined for  $k, l \in [-N_x + 1, N_x - 1] \times [-N_y + 1, N_y - 1]$  to account for the influence of all pressures in the area of interest.

### 3.2.3 Differential deflection formulation

The differential deflection method casts Equation (3.1) in a differential form as originally proposed by Evans and Hughes (2000) for elastic deflection:

$$\nabla^2 h(x, y) = -\nabla^2 r(x, y) + \nabla^2 d^{elast}(x, y) + \nabla^2 d^{plast}(x, y) \quad (3.6)$$

This equation is solved numerically to obtain the gap  $h(x, y)$ , the pressure distribution  $p(x, y)$ , and the residual plastic deflection  $d^{plast}(x, y)$ . These variables must also satisfy one of the contact conditions:

$$h(x, y) > 0, \quad p(x, y) = 0, \quad d^{plast}(x, y) = 0 \quad (a)$$

$$h(x, y) = 0, \quad 0 < p(x, y) < P_{max}, \quad d^{plast}(x, y) = 0 \quad (b)$$

$$h(x, y) = 0, \quad p(x, y) = P_{max}, \quad d^{plast}(x, y) > 0 \quad (c) \quad (3.7)$$

which represent positions with (a) no contact, (b) elastic contact and (c) elastic-plastic contact.

It is clear from (3.7) that plastic deflection occurs only at the points where the pressure value is equal to the hardness of the material, which represents a perfectly plastic behaviour. The subsurface plasticity and hardening are therefore neglected.

Discrete numerical evaluation of  $\nabla^2 d^{elast}(x, y)$  on the rectangular mesh can be obtained in the form

$$\nabla^2 D_{i,j}^{elast} = \sum_{k=0}^{N_x-1} \sum_{l=0}^{N_y-1} F_{i-k,j-l} P_{k,l} \quad (3.8)$$

The matrix of  $F_{i,j}$  coefficients can be calculated by analytical means using quadrature (Evans and Hughes, 2000) or as a linear combination of the  $G_{i,j}$  obtained by differencing Equation (3.5) as in Elsharkawy et al (2006). As with  $G_{k,l}$ , the discrete function  $F_{k,l}$  is defined for  $k, l \in [-N_x + 1, N_x - 1] \times [-N_y + 1, N_y - 1]$ .

The benefits of the differential approach are that the effect of pressure values  $P_{k,l}$  on the Laplacian  $\nabla^2 D^{elast}(x, y)$  is much more localised as shown in Figure 3.2 where

normalised  $F_{0,l}$  and  $G_{0,l}$  coefficients are plotted against the distance in number of mesh points. This localisation allows the elastic-plastic contact problem to be solved with a simple iterative procedure, which is described in detail in Section 3.3. This approach has considerable advantages in the mixed EHL problem as it allows both the elastic and hydrodynamic differential equations to be solved simultaneously, see e.g. Holmes et al (2005) and Elsharkawy et al (2006).

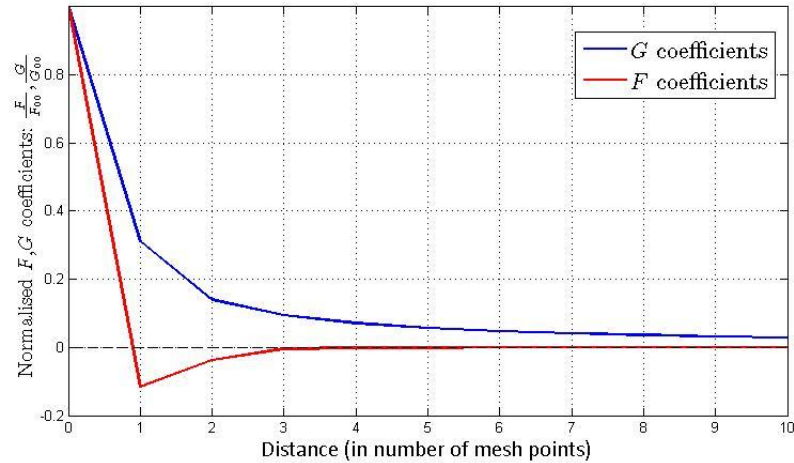


Figure 3.2 Normalised absolute values of  $F$  and  $G$  coefficients along the main symmetry axis

### 3.2.4 Convolution theorem

The deflection  $d^{elast}(x,y)$  and its Laplacian  $\nabla^2 d^{elast}(x,y)$  are convolution integrals of the pressure distribution  $p(x,y)$  with appropriate influence coefficients  $g(s,t)$  and  $f(s,t)$ . The convolution theorem for the continuous Fourier transform states that a convolution of two functions can be obtained as the inverse transform of the product of the individual transforms, i.e.

$$\phi\{g \otimes p\} = \phi\{g\} \cdot \phi\{p\} \Rightarrow g \otimes p = \phi^{-1}\{\phi\{g\} \cdot \phi\{p\}\} \quad (3.9)$$

where  $\phi$  denotes Fourier transform and  $\bullet$  is the point-wise product of two functions.

In the numerical implementation the continuous convolution for  $x,y,s,t \in \mathbb{R}$  is replaced by discrete summation over the finite computational domain for  $i,j,k,l \in [0, N_x^* - 1] \times [0, N_y^* - 1]$ . The continuous Fourier transform is replaced by the discrete Fourier transform operator (DFT)  $\Phi$  for the finite domain:

$$\Phi\{P\}_{i,j} = \sum_{k=0}^{N_x^*-1} \exp\left(-2\pi i \frac{ki}{N_x^*}\right) \sum_{l=0}^{N_y^*-1} \exp\left(-2\pi i \frac{lj}{N_y^*}\right) P_{kl}, \quad \text{where } i = \sqrt{-1}$$

for all  $i,j \in [0, N_x^* - 1] \times [0, N_y^* - 1]$

### Section 3.2 Theoretical background

(3.10)

For discrete sequences of finite length, the convolution theorem takes the form of the ‘circular convolution theorem’ also called linear convolution with aliasing (see e.g. Oppenheim et al, 1999, p. 577) and Equation (3.5) can be evaluated as:

$$D_{i,j}^{elast} = \Phi^{-1}\{\Phi\{G\} \cdot \Phi\{P\}\} = \sum_{k=0}^{N_x^*-1} \sum_{l=0}^{N_y^*-1} G_{i-k,j-l}^{Periodic} P_{k,l} \quad (3.11)$$

where

$$G_{i,j}^{Periodic} = \sum_{a=-\infty}^{\infty} \sum_{b=-\infty}^{\infty} G_{i-aN_x^*, j-bN_y^*}$$

$a$  and  $b$  are integers, and  $G^{Periodic}$  is a periodic summation term caused by aliasing. The comparison of (3.12) with (3.5) makes it clear, that calculating the elastic deflection as the inverse Fourier image results in including the pressure repeats into the consideration.

Similarly the differential deflection  $\nabla^2 D^{elast}(x,y)$  can be calculated as

$$\nabla^2 D_{i,j}^{elast} = \Phi^{-1}\{\Phi\{F\} \cdot \Phi\{P\}\} = \sum_{k=0}^{N_x^*-1} \sum_{l=0}^{N_y^*-1} F_{i-k,j-l}^{Periodic} P_{k,l} \quad (3.12)$$

Equations (3.11) and (3.12) represent the deflection and differential deflection caused not by pressure distribution  $P_{i,j}$  but by the periodic extension, such that:

$$P_{i+aN_x, j+bN_y} = P_{i,j}, \quad \forall a, b \in \mathbb{Z}, \quad i, j \in [0, N_x^* - 1] \times [0, N_y^* - 1] \quad (3.13)$$

The physical meaning of this periodic extension is that the elastic deflection is caused by contact of a rough surface which has a spatially periodic profile.

In a number of papers e.g. Ju and Farris (1996), Stanley and Kato (1997) and Liu et al (2000) the DFT is used to speed up the calculation of the convolution. The effect of periodic extension is suppressed by zero-padding which separates the unique pressure distribution from its periodic repeats so that the influence of the repeats becomes negligible. In the current work, however, the effect of periodic extension is exploited to calculate the deflection caused by the contact of the infinitely large surface with periodic roughness profile, as developed in Sahlin et al (2010a, 2010b).

### Chapter 3. Dry contact analysis of rough nominally flat surfaces

In order to calculate the circular convolution of Equations (3.11) and (3.12) by DFT  $P_{k,l}$ ,  $G_{i,j}$  and  $F_{i,j}$  must have the same dimensions, and  $G_{i,j}$  and  $F_{i,j}$  are written in wrap-around order, so that:

$$\begin{aligned} G_{-i,-j} &= G_{2N_x-i, 2N_y-j} \\ F_{-i,-j} &= F_{2N_x-i, 2N_y-j} \end{aligned}, \quad \forall i, j \in [0, N_x - 1] \times [0, N_y - 1] \quad (3.14)$$

Figure 3.3 and Figure 3.4 give illustrated sketches of this process where weighting function  $G_{i,j}$  is shown in both symmetric and wrap-around forms.

In addition  $P_{i,j}$  is defined on  $i, j \in [0, N_x - 1] \times [0, N_y - 1]$ , whereas after wrap-around modification  $G_{i,j}$  and  $F_{i,j}$  are defined on  $i, j \in [0, 2N_x - 1] \times [0, 2N_y - 1]$ . Consequently,  $P_{i,j}$  is repeated so that it is defined on  $i, j \in [0, 2N_x - 1] \times [0, 2N_y - 1]$ .

The discrete Fourier transform (3.11) or (3.12) is therefore performed on a  $2N_x \times 2N_y$  grid, so that  $N_x^* = 2N_x$  and  $N_y^* = 2N_y$ . Figure 3.5(a) shows schematically the unique pressure distribution defined on  $i, j \in [0, N_x - 1] \times [0, N_y - 1]$  which is then repeated to fill the twice larger domain. Figure 3.5(b) illustrates implementation of the convolution algorithm with zero padding which allows the aliasing effect of repeated pressure to be neglected.

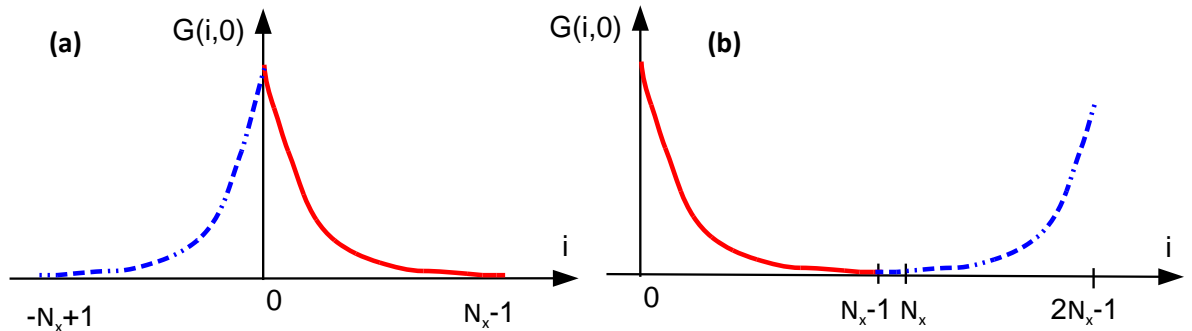


**Figure 3.3. (a) Example of symmetric response function; (b) Corresponding function in wrap around order**

Note that the periodic summation term  $G^{Periodic}$  in Equation (3.12) contains components  $G_{i-aN_x^*, j-bN_y^*}$ , whereas  $G_{k,l}$  is defined on  $k, l \in [-N_x + 1, N_x - 1] \times [-N_y + 1, N_y - 1]$  before the wrap-around modification. The values of  $G_{k,l}$  outside of the definition domain are then assumed to be zero. The same applies to the periodic summation term  $F^{Periodic}$  and Equation (3.12). The physical meaning of this is that the

## Section 3.2 Theoretical background

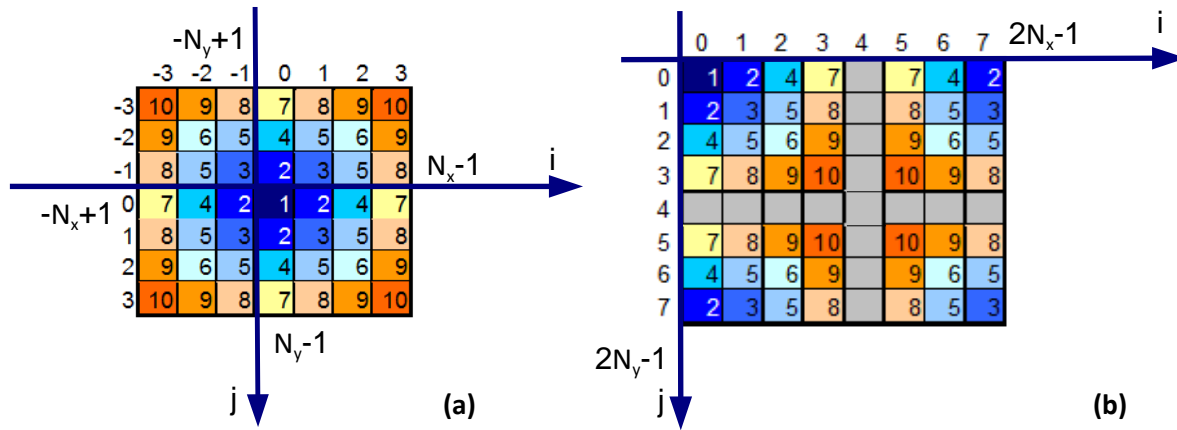


Figure 3.4. (a) Example of axisymmetric discrete response function (2D); (b) Corresponding function in wrap around order

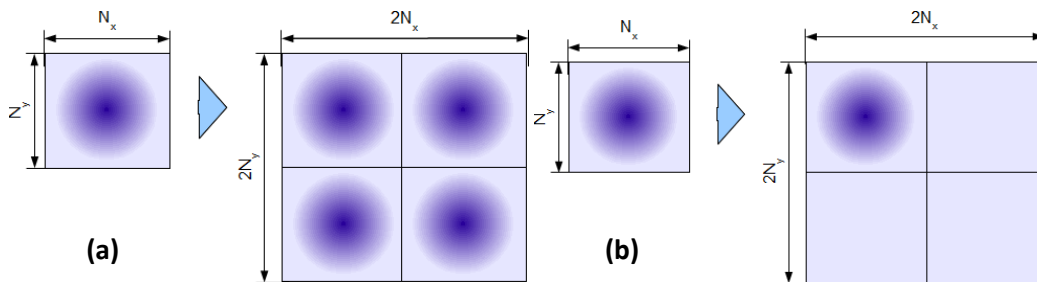


Figure 3.5 Example of a unique pressure distribution on a computational domain (a) doubled in both directions as a necessity for the discrete Fourier convolution; (b) surrounded by zero-padding in both directions

influence of the pressures which are more than one period ( $N_x$  or  $N_y$  mesh grid distances) further away from the point of interest is assumed negligible. Therefore, the periodic pressure distribution (3.13) includes not the infinite number of repeats but only eight adjacent repeats, as illustrated in Figure 3.6 by the dark grey area.

The equality in dimensions of the signal function (pressure) and response function ( $G_{i,j}$  and  $F_{i,j}$  coefficients) is a necessary requirement for the discrete convolution procedure. This requirement can be satisfied without doubling the pressure distribution function by reducing the domain of  $G_{i,j}$  and  $F_{i,j}$  coefficients down to  $i, j \in \left[1 - \frac{N_x}{2}, \frac{N_x}{2} - 1\right] \times \left[1 - \frac{N_y}{2}, \frac{N_y}{2} - 1\right]$  as schematically shown in Figure 3.7.

The reduced function  $G_{i,j}$  was used in many papers including Sahlin et al (2010a, 2010b). This modification of  $G_{i,j}$  allows the computational area to be of the same size as the area of interest and therefore saves computational time and memory. However, by reducing  $G_{i,j}$  down to  $\left[1 - \frac{N_x}{2}, \frac{N_x}{2} - 1\right] \times \left[1 - \frac{N_y}{2}, \frac{N_y}{2} - 1\right]$  the effect of the pressures at the points further than half the size of the original domain from the point of interest is neglected. The zone outside of the original computational domain where

the repeated pressures are taken into account when using the reduced function of influence coefficients is marked by the dashed rectangle in Figure 3.6.

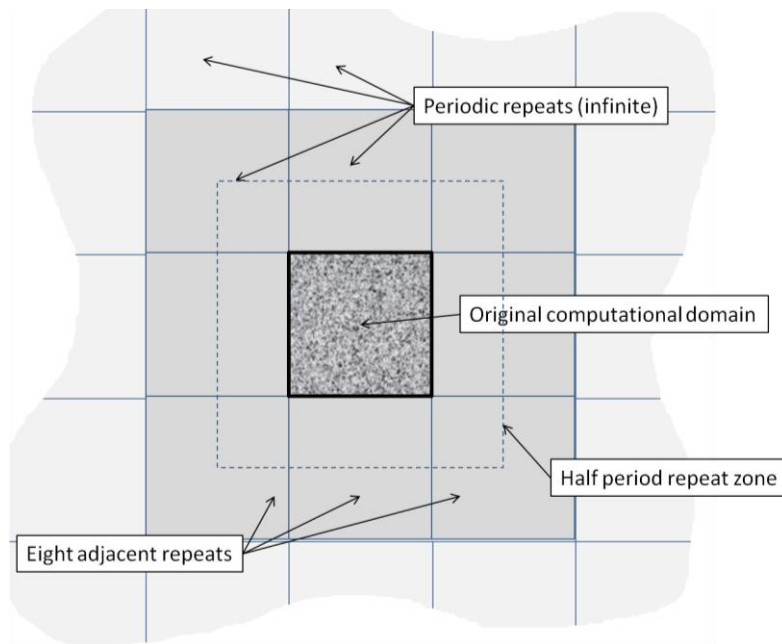


Figure 3.6 The original computational domain (textured), eight adjacent periodic repeats (dark grey), infinite set of periodic repeats (light grey);

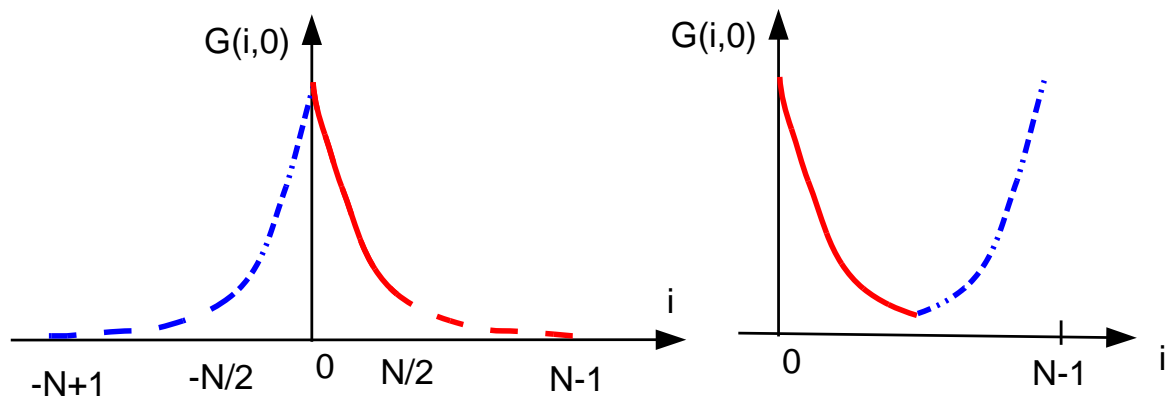


Figure 3.7. Reduced function of G coefficients and its wrap around order modification

### 3.2.5 Harmonic roughness and periodic boundary

All the functions of interest defined on  $i, j \in [0, N_x - 1] \times [0, N_y - 1]$  are assumed to be doubly periodic so that Equation (3.13) also holds for  $H, R, D^{elast}$  and  $D^{plast}$ , and for their Laplacians.

The differential deflection Equation (3.6) is therefore a Poisson equation with right hand side  $\gamma(x, y)$  that is periodic with periods  $L=N_x\Delta x, W=N_y\Delta x$  in the axis directions:

$$\nabla^2 h(x, y) = \gamma(x, y) \quad [= -\nabla^2 r(x, y) + \nabla^2 d^{elast}(x, y) + \nabla^2 d^{plast}(x, y)] \quad (3.15)$$

### Section 3.2 Theoretical background

Mason (1905) has considered the conditions necessary for a Poisson equation to have a periodic solution, and for a periodic solution  $h(x,y)$  with periods  $L, W$  to exist for Equation (3.15) the conditions

$$\int_0^L \int_0^W \gamma(x,y) dx dy = 0 \quad \text{and} \quad \gamma(x + aL, y + bW) = \gamma(x,y), \quad \forall a, b \in \mathbb{Z} \quad (3.16)$$

are necessary and sufficient, provided that  $h(x,y)$  has continuous derivatives everywhere.

This solution will however not be unique. Indeed, if  $h_1(x,y)$  and  $h_2(x,y)$  are both periodic solutions of Equation (3.15) then

$$\nabla^2 h_1(x,y) = \gamma(x,y) \quad \text{and} \quad \nabla^2 h_2(x,y) = \gamma(x,y)$$

so that  $\nabla^2 [h_1(x,y) - h_2(x,y)] = 0$  which is the Laplace equation.

The only periodic solution of the Laplace equation is a constant (see Mason, 1905) therefore

$$h_1(x,y) - h_2(x,y) = \text{constant} \quad (3.17)$$

Hence, the discretised version of Equation (3.6)

$$\nabla^2 H_{i,j} = -\nabla^2 R_{i,j} + \nabla^2 D_{i,j}^{elast} + \nabla^2 D_{i,j}^{plast} = F_{i,j} \quad (3.18)$$

has the unique periodic solution  $H_{i,j}$  if:

- $H_{i,j}$  is defined for at least one point, and
- the right hand side  $F_{i,j}$  satisfies the conditions of Equation (3.16).

In order to satisfy the first of these conditions the value of  $H_{i,j}$  is specified at a selected point  $i_0, j_0$  to be  $H_{max}$ . The point  $i_0, j_0$  is selected as the deepest valley of the surface, to ensure that no contact occurs at that point and, therefore, both  $P_{i_0, j_0} = 0$  and  $D_{i_0, j_0}^{plast} = 0$ . The rigid body movement  $S$  can then be calculated from Equation (3.1) with the given value  $H_{max}$ :

$$S = R_{max} - R_{min} + D_{i_0, j_0}^{elast} - H_{max}$$

The discretised form of the integral in Equation (3.16) is the double summation:

$$\int_0^L \int_0^W \gamma(x, y) dx dy \Rightarrow \sum_{i=0}^{N_x-1} \sum_{j=0}^{N_y-1} \Gamma_{i,j} = \sum_{i=0}^{N_x-1} \sum_{j=0}^{N_y-1} \left( -\nabla^2 R_{i,j} + \nabla^2 D_{i,j}^{elast} + \nabla^2 D_{i,j}^{plast} \right)$$

Consider  $\sum_{i=0}^{N_x-1} \sum_{j=0}^{N_y-1} \nabla^2 R_{i,j} = \sum_{i=0}^{N_x-1} \sum_{j=0}^{N_y-1} \frac{\partial^2 R_{i,j}}{\partial x^2} + \sum_{i=0}^{N_x-1} \sum_{j=0}^{N_y-1} \frac{\partial^2 R_{i,j}}{\partial y^2}$

$$\sum_{i=0}^{N_x-1} \frac{\partial^2 R_{i,j}}{\partial x^2} = \sum_{i=0}^{N_x-1} \left( \frac{R_{i+1,j} + R_{i-1,j} - 2R_{i,j}}{\Delta_x^2} \right) = \frac{1}{\Delta_x^2} \sum_{i=0}^{N_x-1} R_{i+1,j} + \frac{1}{\Delta_x^2} \sum_{i=0}^{N_x-1} R_{i-1,j} - \frac{2}{\Delta_x^2} \sum_{i=0}^{N_x-1} R_{i,j} = \frac{1}{\Delta_x^2} \sum_{i=1}^{N_x} R_{i,j} + \frac{1}{\Delta_x^2} \sum_{i=-1}^{N_x-2} R_{i,j} - \frac{2}{\Delta_x^2} \sum_{i=0}^{N_x-1} R_{i,j}$$

which due to the periodicity of  $R_{ij}$  gives

$$\sum_{i=0}^{N_x-1} \frac{\partial^2 R_{i,j}}{\partial x^2} = \frac{1}{\Delta_x^2} \sum_{i=0}^{N_x-1} R_{i,j} + \frac{1}{\Delta_x^2} \sum_{i=0}^{N_x-1} R_{i,j} - \frac{2}{\Delta_x^2} \sum_{i=0}^{N_x-1} R_{i,j} \equiv 0$$

Similarly,

$$\sum_{j=0}^{N_y-1} \frac{\partial^2 R_{i,j}}{\partial y^2} \equiv 0 \quad \text{and consequently} \quad \sum_{i=0}^{N_x-1} \sum_{j=0}^{N_y-1} \nabla^2 R_{i,j} \equiv 0$$

The periodicity of  $D_{i,j}^{elast}$  and  $D_{i,j}^{plast}$  means that

$$\sum_{i=0}^{N_x-1} \sum_{j=0}^{N_y-1} \nabla^2 D_{i,j}^{elast} \equiv 0 \quad \text{and} \quad \sum_{i=0}^{N_x-1} \sum_{j=0}^{N_y-1} \nabla^2 D_{i,j}^{plast} \equiv 0$$

so that  $\int_0^L \int_0^W \gamma(x, y) dx dy \Rightarrow \sum_{i=0}^{N_x-1} \sum_{j=0}^{N_y-1} \Gamma_{i,j} \equiv 0$  as required.

### 3.3 Numerical implementation

In this section the iterative procedure for solving Equation (3.18) with the contact conditions of Equations (3.7) is explained in detail. Equation (3.18) is

$$\nabla^2 H_{i,j} = -\nabla^2 R_{i,j} + \nabla^2 D_{i,j}^{elast} + \nabla^2 D_{i,j}^{plast}$$

The pressure enters into the equation via the term  $\nabla^2 D_{i,j}^{elast}$  given by Equation (3.8)

$$\nabla^2 D_{i,j}^{elast} = \sum_{k=0}^{N_x-1} \sum_{l=0}^{N_y-1} F_{i-k,j-l} P_{k,l}$$

The summation is considered to be made up of three terms as follows

$$\nabla^2 D_{i,j}^{elast} = F_{0,0} P_{i,j} + \sum_{k,l \in near} F_{i-k,j-l} P_{k,l} + \sum_{k,l \in far} F_{i-k,j-l} P_{k,l}$$

### Section 3.3 Numerical implementation

The *near* region consists of the eight points with indices  $k = i-1, i, i+1$  and  $l = j-1, j, j+1$  excluding point  $i, j$ . The *far* region consists of the remaining points in the total summation, and pressures in this region have less influence on  $\nabla^2 D_{i,j}^{elast}$  as can be appreciated from Figure 3.2.

The remaining terms in Equation (3.18) are discretised using central differences as

$$\nabla^2 H_{i,j} = \frac{H_{i+1,j} + H_{i-1,j} - 2H_{i,j}}{\Delta_x^2} + \frac{H_{i,j+1} + H_{i,j-1} - 2H_{i,j}}{\Delta_y^2}$$

and

$$\nabla^2 D_{i,j}^{plast} = \frac{D_{i+1,j}^{plast} + D_{i-1,j}^{plast} - 2D_{i,j}^{plast}}{\Delta_x^2} + \frac{D_{i,j+1}^{plast} + D_{i,j-1}^{plast} - 2D_{i,j}^{plast}}{\Delta_y^2}$$

This involves the values of these variables at the point of interest and the *near* region and the discretised equation can be written as:

$$\sum_{\lambda=0}^8 [B_{\lambda}(H_{i,j}^{\lambda} - D_{i,j}^{plast,\lambda}) - F_{\lambda}P_{i,j}^{\lambda}] = \sum_{k,l \in far} F_{i-k,j-l}P_{k,l} - \nabla^2 R_{i,j} \quad (3.19)$$

where the auxiliary index  $\lambda = 0, 1, \dots, 8$  denotes the point  $i, j$  and its near neighbours as illustrated in Figure 3.8. The coefficients  $B_{\lambda}$  and  $F_{\lambda}$  are then as follows:

$$\begin{aligned} B_2 = B_6 = 1/\Delta_x^2, \quad B_4 = B_8 = 1/\Delta_y^2, \quad B_0 = -2/\Delta_x^2 - 2/\Delta_y^2 \\ B_1 = B_3 = B_5 = B_7 = 0, \\ F_0 = F_{0,0} \quad F_1 = F_{-1,-1} \quad F_2 = F_{0,-1} \quad F_3 = F_{1,-1} \quad F_4 = F_{1,0} \\ F_5 = F_{1,1} \quad F_6 = F_{0,1} \quad F_7 = F_{-1,1} \quad F_8 = F_{-1,0} \end{aligned}$$

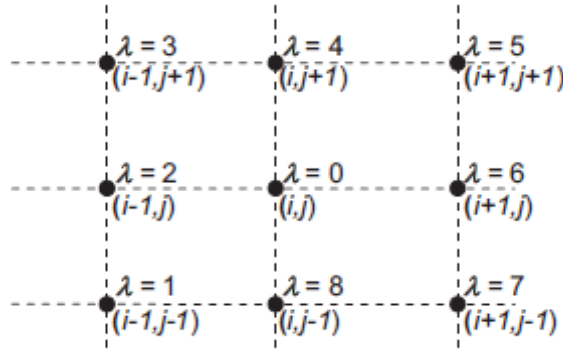


Figure 3.8 Grid point  $i, j$  and the near region points as denoted by auxiliary index  $\lambda$ .

Equation (3.19) consists of  $N_x \times N_y$  equations in the  $3 N_x \times N_y$  unknowns  $P_{i,j}$ ,  $H_{i,j}$  and  $D_{i,j}^{plast}$ . Additional constraints must be applied in the form of compatibility Equations (3.7). One of these equations will apply at each point in the mesh, and each of these equations prescribes values for two of the unknowns so that there are in fact  $3N_x \times N_y$  equations in the  $3N_x \times N_y$  unknowns. The solution is obtained by iteration using

### Chapter 3. Dry contact analysis of rough nominally flat surfaces

Equation (3.19) and one of Equations (3.7) at each point in the mesh. Equation (3.19) is rearranged as follows

$$B_0(H_{i,j} - D_{i,j}^{plast}) - F_0 P_{i,j} = A_{i,j} \quad (3.20)$$

Where

$$\begin{aligned} A_{i,j} &= RHS_{i,j} - \sum_{\lambda=1}^8 [B_{\lambda}(H_{i,j}^{\lambda} - D_{i,j}^{plast,\lambda}) - F_{\lambda} P_{i,j}^{\lambda}] \\ \text{and } RHS_{i,j} &= \sum_{k,l \in far} F_{i-k,j-l} P_{k,l} - \nabla^2 R_{i,j} \end{aligned} \quad (3.21)$$

The term  $RHS_{i,j}$  remains fixed during each stage of the iterative procedure and the *far* pressure summation is obtained for the trial pressure in the outer loop. For each point in the mesh  $A_{i,j}$  is evaluated using the current values of  $P_{i,j}$ ,  $H_{i,j}$  and  $D_{i,j}^{plast}$ . Equation (3.20) is then solved with the appropriate compatibility conditions from Equations (3.7) to give new values for  $P$ ,  $H$  and  $D^{plast}$  at the point according to the value of  $A_{i,j}$  as follows, noting that  $B_0$  and  $F_0$  are negative.

$$\begin{aligned} \text{if } A_{i,j} < 0 &\Rightarrow P_{i,j} = 0, \quad D_{i,j}^{plast} = 0, \quad H_{i,j} = A_{i,j}/B_0 \\ \text{if } 0 < A_{i,j} < -F_0 P_{max} &\Rightarrow H_{i,j} = 0, \quad D_{i,j}^{plast} = 0, \quad P_{i,j} = -A_{i,j}/F_0 \\ \text{if } -F_0 P_{max} < A_{i,j} &\Rightarrow H_{i,j} = 0, \quad P_{i,j} = P_{max}, \quad D_{i,j}^{plast} = -(A_{i,j} + F_0 P_{max})/B_0 \end{aligned} \quad (3.22)$$

The new values of  $P_{i,j}$ ,  $H_{i,j}$  and  $D_{i,j}^{plast}$  are used to calculate  $A_{i,j}$  from Equation (3.21) as soon as they are available. The iterative changes are applied to each point in the mesh to form a single sweep through the mesh, and convergence is assessed in terms of the changes made to  $P_{i,j}$ ,  $H_{i,j}$  and  $D_{i,j}^{plast}$  during a sweep. No iterative changes are applied at the point  $i_0, j_0$  where the variables take the values

$$H_{i_0, j_0} = H_{max}, \quad P_{i_0, j_0} = 0, \quad D_{i_0, j_0}^{plast} = 0 \quad (3.23)$$

When the changes occurring during an iterative sweep have become small the trial pressure is replaced by the new pressure distribution in the outer loop. Also in the outer loop an adjustment is made to ensure that the elastic deflection at point  $i_0, j_0$  is consistent with the imposed value of  $H_{i_0, j_0} = H_{max}$ . The discretised form of Equation (3.1) at point  $i_0, j_0$  is

$$H_{i_0, j_0} = R_{max} - R_{min} + D_{i_0, j_0}^{elast} - S \quad (3.24)$$

If the problem is solved for a specified value of  $H_{max}$  then the value of  $S$  is modified in the outer loop according to

### Section 3.3 Numerical implementation

$$S = R_{\max} - R_{\min} + D_{i_0 j_0}^{elast} - H_{\max} \quad (3.25)$$

If the problem is solved for a specified approach distance  $S$  then  $H_{\max}$  is updated in the outer loop using Equation (3.24).

#### 3.3.1 Flowchart of the differential deflection method

1. Set up roughness function  $R_{i,j}$
2. Calculate  $\nabla^2 R_{i,j}$
3. Calculate  $G_{k,l}$  for  $k, l \in [-N_x + 1, N_x - 1] \times [-N_y + 1, N_y - 1]$  according to (3.4)
4. Calculate  $F_{k,l}$  for  $k, l \in [-N_x + 1, N_x - 1] \times [-N_y + 1, N_y - 1]$
5. Calculate Fourier images  $\Phi\{G\}, \Phi\{F\}$
6. Calculate  $D_{i,j}^{elast} = \Phi^{-1}\{\Phi\{F\} \cdot \Phi\{P\}\}$
7. Calculate  $\nabla^2 D_{i,j}^{elast} = \Phi^{-1}\{\Phi\{F\} \cdot \Phi\{P^{old}\}\}$
8. Update  $H_{i,j}^{old} = H_{\max} + R_{\min} - R_{i,j} + D_{i,j}^{elast} - D_{i_0 j_0}^{elast} + D_{i,j}^{plast,old}$  according to (3.1) and (3.24) or (3.25).
9. Calculate *far* contributions  $\sum_{k,l \in far} F_{i-k,j-l} P_{k,l}^{old} = \nabla^2 D_{i,j}^{elast} - F_{0,0} P_{i,j}^{old} - \sum_{k,l \in near} F_{i-k,j-l} P_{k,l}^{old}$
10. Calculate  $A_{i,j} = \sum_{k,l \in far} F_{i-k,j-l} P_{k,l}^{old} - \sum_{\lambda=1}^8 [B_{\lambda}(H_{i,j}^{\lambda,new} - D_{i,j}^{plast,\lambda,new}) - F_{\lambda} P_{i,j}^{\lambda,new}]$  where  $P_{i,j}^{\lambda,new}$  are the most recent neighbouring  $P$  values
11. Apply contact condition system (3.22) to obtain new values  $P_{i,j}^{new}, H_{i,j}^{new}, D_{i,j}^{plast,new}$  from  $A_{i,j}$
12. Repeat 10-12 for all  $i, j \in [0, N_x - 1] \times [0, N_y - 1]$  until converged for fixed value of *far* contributions term  $\sum_{k,l \in far} F_{i-k,j-l} P_{k,l}^{old}$
13.  $P_{i,j}^{new} \Rightarrow P_{i,j}^{old}, H_{i,j}^{new} \Rightarrow H_{i,j}^{old}, D_{i,j}^{plast,new} \Rightarrow D_{i,j}^{plast,old}$
14. Repeat steps 6-13 until converged.

### 3.4 Results and discussion

The method described in the preceding sections has been applied to contact between two plane rough surfaces. A series of simulations was carried out for different types of surface roughness. The surface roughness is defined over a representative rectangular area  $L \times W$  and is doubly periodic with periodic lengths  $L$  and  $W$ . The different types of roughness considered were:

- analytic surfaces such as one- and two- dimensional sinusoidal waves
- stochastic, where  $R_{ij}$  is obtained as a quasi-random set of heights, and
- measured surface roughness obtained by profilometer.

For each of the rough surfaces considered a sequence of simulations was carried out for different  $H_{max}$  values in the range  $0 < H_{max} < R_{max} - R_{min}$  where  $H_{max} = R_{max} - R_{min}$  corresponds to  $S = 0$  where contact occurs at the highest asperity under zero load, and  $H_{max} = 0$  means that all the asperities have been flattened. Note that according to the asperity persistence concept introduced by Williamson and Hunt (1972) the asperities in real surface contacts are never completely flattened, therefore the case of  $H_{max} = R_{max} - R_{min}$  is not realistic. The load on the doubly periodic surfaces analysed is expressed as the mean contact pressure over the surface.

The case of pure elastic contact of a surface with sinusoidal waviness was validated via the comparison with the closed form solution obtained by Westergaard (1939). This comparison is given in Section 3.4.1. The results obtained for a 2D stochastic surface are presented in Section 3.4.2. The case of an extruded roughness problem with measured profile given by profilometer is provided in Section 3.4.3. These results are compared with 2D FEA solution for the same measured profile. Section 3.4.4 gives a comparison of the results obtained by the method developed with those obtained by 3D FEA which became recently available to the author (Yastrebov et al, 2011).

#### 3.4.1 Westergaard solution

Westergaard (1939) studied elastic contact of nominally flat surfaces with extruded sinusoidal waviness of wavelength  $L$ . A sequence of loading conditions were considered starting from the case where surfaces have periodic contact spots of width  $2a_0$  up to the case where the waviness has been completely flattened. Based on the Hertzian formulae for cylindrical contact, Westergaard (1939) derived a closed form solution for the contact pressure distribution  $P(x)$ :

### Section 3.4 Results and discussion

$$P(x) = -\frac{2P_{mean} \cos\left(\frac{\pi x}{L}\right)}{\sin^2\left(\frac{\pi a}{L}\right)} \sqrt{\sin^2\left(\frac{\pi a}{L}\right) - \sin^2\left(\frac{\pi x}{L}\right)} \quad (3.26)$$

where  $P_{mean}$  is the load expressed by means of homogeneous pressure distribution applied to one of the surfaces,  $a$  is a half-width of each contact spot,  $L$  is the period of the waviness. Note that Equation 3.26 defines the pressure distribution function which takes real and non zero values at the periodic contact spots of width  $2a$ . In order to validate the method developed in the thesis for the pure elastic case, an extruded sinusoidal surface of period  $L$  has been considered and the contact pressure distribution was calculated for a sequence of penetrations ( $S$ ). For each case the mean pressure  $P_{mean}$  and half width of the contact area  $a$  were calculated and substituted into Equation 3.26 to evaluate the corresponding Westergaard solution. The comparison of the DDM method and the Westergaard solution is given in Figures 3.9 and 3.10 where pressure and gap distributions are shown for the half of the sinusoidal feature. Note that the  $x$  coordinate is normalised with respect to  $L$ , i.e. the interval  $-0.5 < x < 0.5$  denotes the whole period of the waviness.

The comparison of the solutions given in Figure 3.9 shows a perfect agreement of the DDM method and the Westergaard solution with minor deviations of the DDM method at the boundaries of the contact zones caused most probably by the numerical approximation error. Note that the Westergaard solution plotted depends on the  $P_{mean}$  and  $a$  values calculated from the corresponding DDM solution, therefore the comparison is independent of the dimensions of the problem, material properties and amplitude of the waviness. For this comparison the material properties were selected as those of hardened steel (Elastic modulus 200 GPa, Poisson's ratio 0.3), whereas each waviness feature is 100  $\mu\text{m}$  wide and has 1  $\mu\text{m}$  amplitude with respect to the mean line. Analysis using DDM has been carried out assuming that the deformed gap at the lowest points of the surface has the value of  $H_{max}$  and there is no deformation at this point. The sequence of penetration values  $S$  used were then calculated according to Equation (3.25) from  $H_{max}$  values.

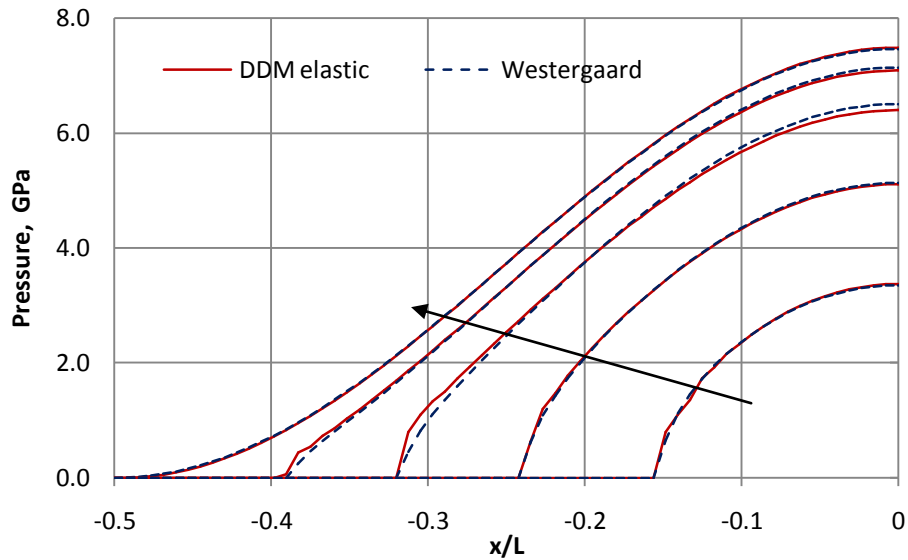


Figure 3.9. Sequence of pressure distributions obtained by DDM elastic (solid lines) and Westergaard solution (dashed lines) plotted against normalised  $x$  coordinate. Arrow indicates the sense of increasing the load until the wavy features are completely flattened.

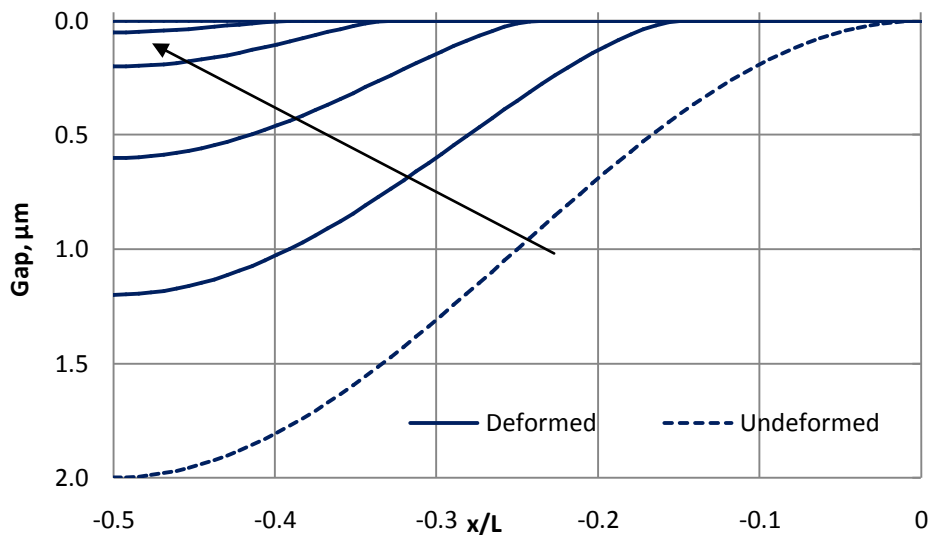


Figure 3.10 Undeformed gap (dashed line) and sequence of gap distributions obtained by DDM elastic (solid lines) plotted against normalised  $x$  coordinate. Arrow indicates the sense of increasing the load until the wavy features are completely flattened.

### 3.4.2 Two-dimensional roughness

In this section the results are presented for a rough surface with 2-dimensional profile obtained by the method developed by Chilamakuri and Bhushan (1998). A quasi-random surface with non-Gaussian distribution of heights is generated which has specified roughness parameters standard deviation,  $\sigma$ , skewness,  $S_{sk}$ , and kurtosis,  $S_{ku}$ . For the current paper the values specified were  $\sigma = 1.47 \mu\text{m}$ ,  $S_{sk} = -1.34$ , and  $S_{ku} = 8.45$  and the rough surface generated is illustrated in Figure 3.11. The material properties used are those of steel and the maximum pressure value of  $P_{max} = 4.37 \text{ GPa}$  is specified. The variation of contact load with approach distance for this surface is shown in Figure 3.12 which is obtained by numerical solution of the harmonic contact

### Section 3.4 Results and discussion

problem at different values of  $H_{max}$ . When contact first occurs it is at a single asperity and the load behaviour with increasing  $S$  represents the load compliance behaviour of that particular asperity. As  $S$  is increased, further asperities make contact and existing asperity contacts develop higher elastic pressures before becoming plastic.

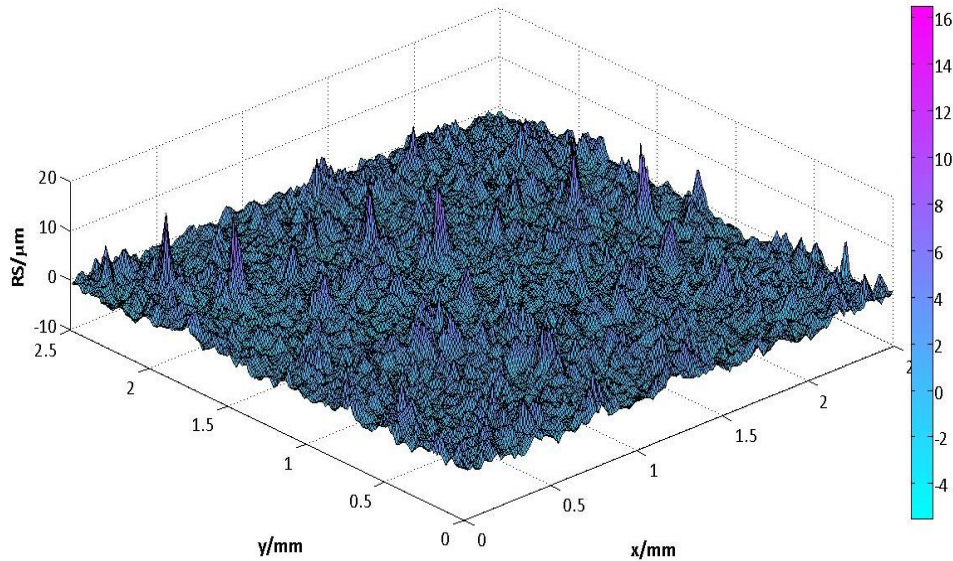


Figure 3.11 2D visualisation of the representative 2D random surface

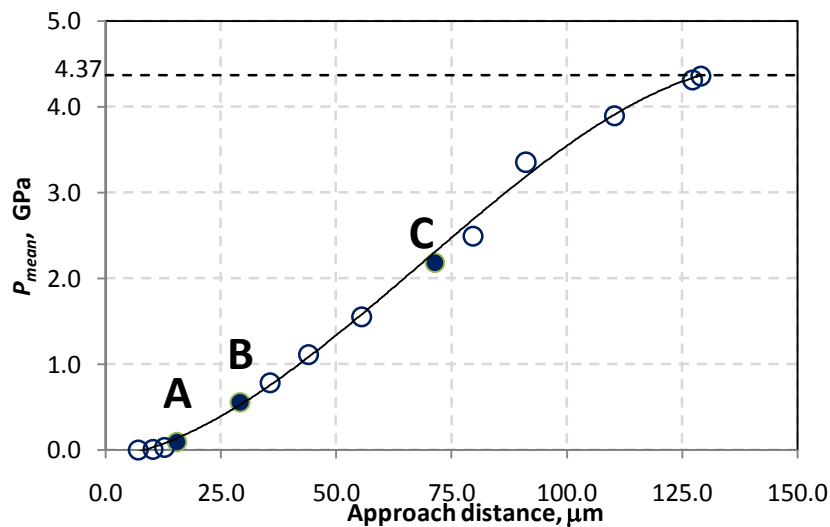


Figure 3.12 Variation of load with approach distance,  $S$ , for the 2D stochastic surface (empty circles), load cases selected for comparison (solid circles), corresponding to (A)  $S = 15 \mu\text{m}$ , (B)  $S = 30 \mu\text{m}$ , (C)  $S = 70 \mu\text{m}$ ; trend line (solid curve),  $P_{max}$  (broken curve).

The total dimensions of the rough surface are 2.5 mm by 2.5 mm and this is resolved using 256 by 256 mesh points. For the sake of clarity a 1 mm by 1 mm part is selected for illustration. Contact areas of the selected part are illustrated in Figure 3.13 for mean pressures of 90, 550 and 2200 MPa in this sequence with approach distances of 15, 30 and 70  $\mu\text{m}$ . In these figures the analysis area is represented by neighbouring pixels in a rectangular grid with each pixel coloured with the colour representing no-contact, elastic contact, or elastic-plastic contact.

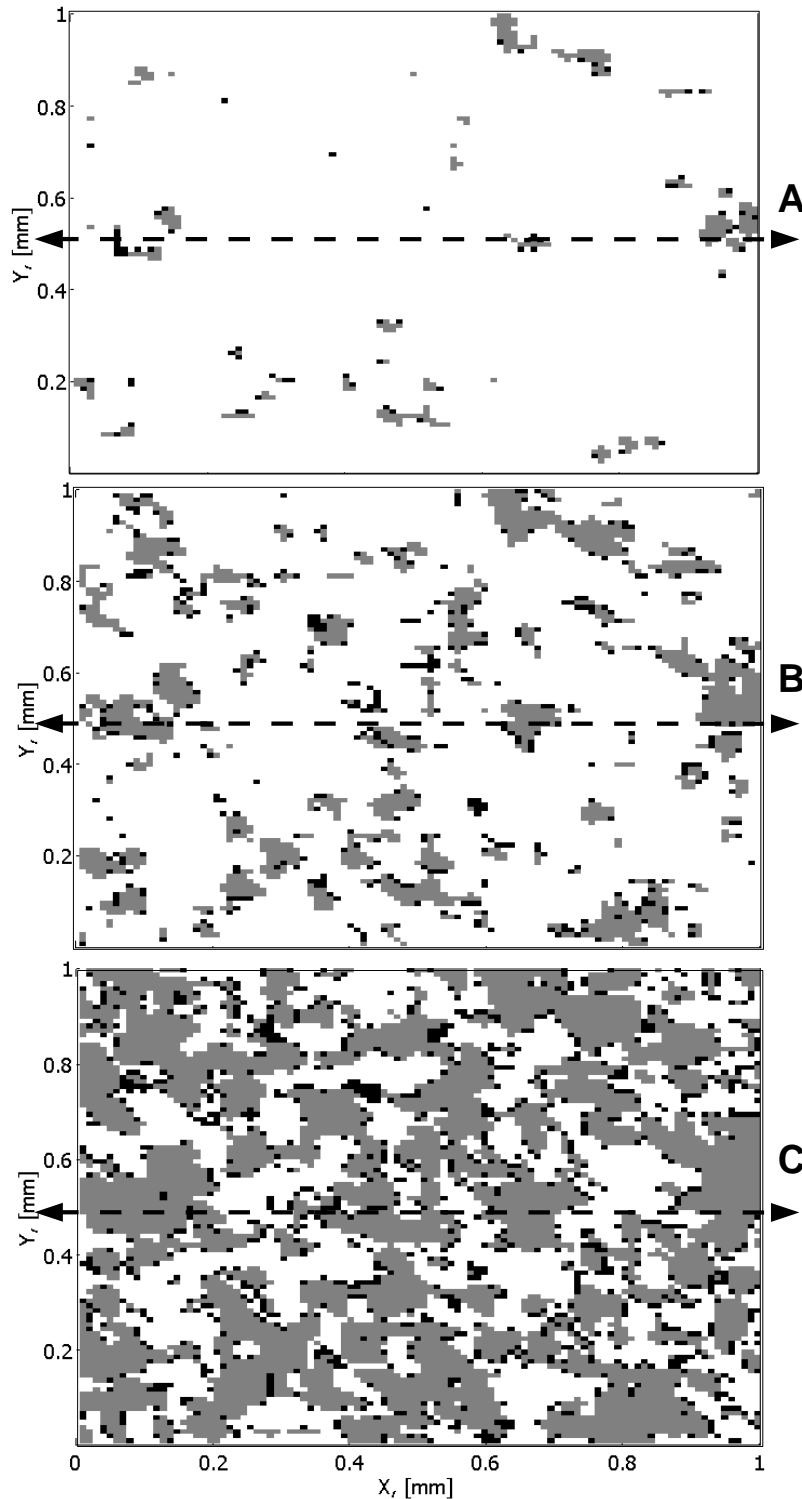


Figure 3.13 Illustration of contact condition over the representative contact area,  $\square$  - no contact,  $\square$  - elastic contact,  $\blacksquare$  - plastic contact; Broken line denotes sections selected for comparison; (A)  $S = 15 \mu\text{m}$ , (B)  $S = 30 \mu\text{m}$ , (C)  $S = 70 \mu\text{m}$ .

Comparison shows how contact load increases through an increased number of contacts and through existing and new contacts graduating from fully elastic to elastic-plastic conditions. Most of the asperity contacts are in the elastic-plastic condition, particularly at the higher of the three loads considered. This is because the asperities have low radii of relative curvature at the contact points and that these rapidly become plastic as the contact load increases.

### Section 3.4 Results and discussion

Figures Figure 3.14, Figure 3.15 and Figure 3.16 show contact conditions on central horizontal sections of Figure 3.13(A, B, C) at the three loads considered. In Figure 3.14 the roughness profiles are illustrated above the rigid counterface (i.e. in the sense of Figure 3.1 inverted). The sections are 1 mm long and are made up of 103 mesh points. The comparison of these sections shows how the individual asperity contacts develop.

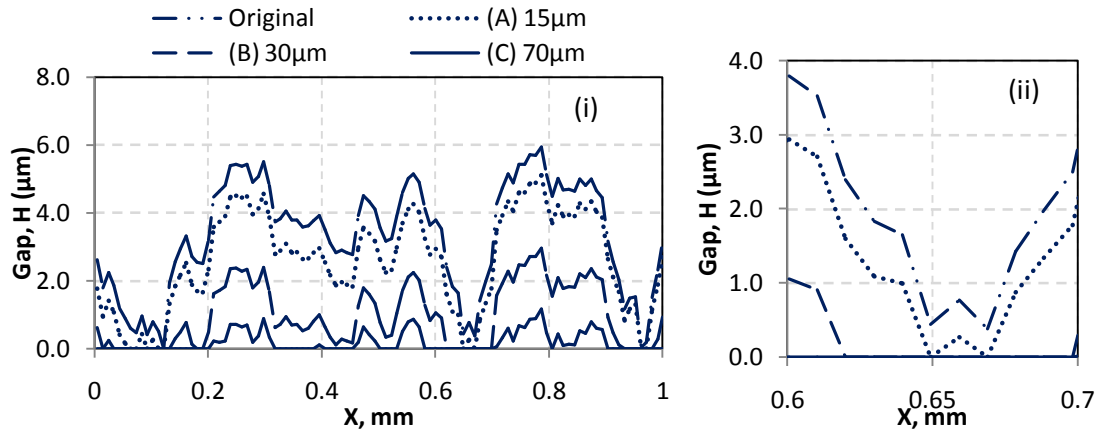


Figure 3.14 (i) Gap between surfaces on selected sections of Figure 8 A, B and C at the three loads considered (ii) subsection corresponding to  $x \in [0.6, 0.7]$

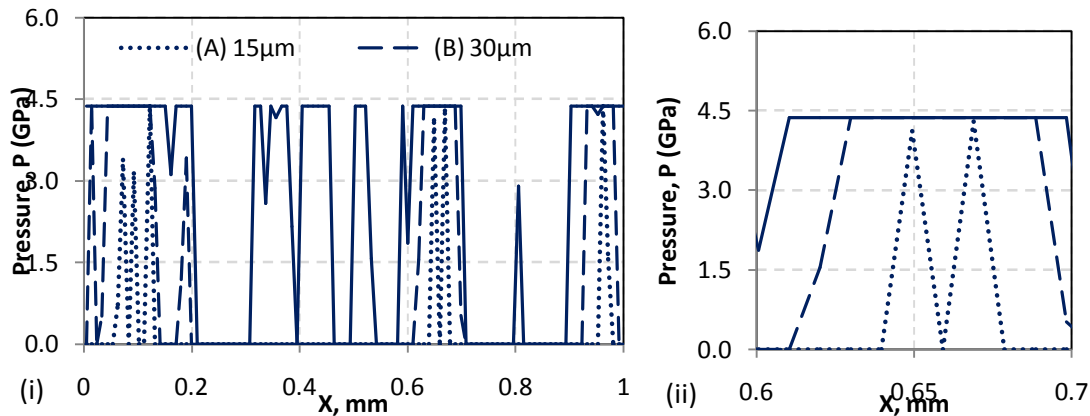


Figure 3.15 (i) Pressure distribution on selected sections of Figure 8 A, B and C at the three loads considered (ii) subsection corresponding to  $x \in [0.6, 0.7]$

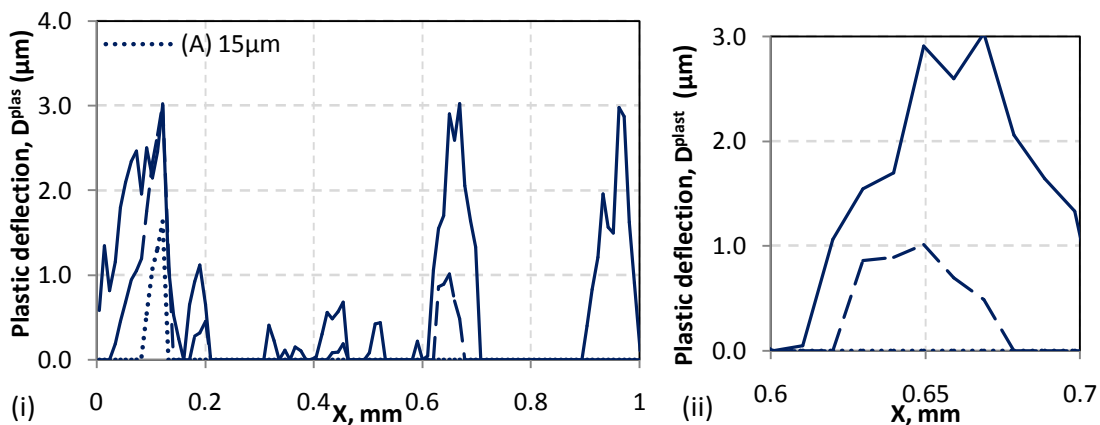


Figure 3.16. (i) Residual deflection on selected sections of Figure 8 A, B and C at the three loads considered, (ii) subsection corresponding to  $x \in [0.6, 0.7]$

### Chapter 3. Dry contact analysis of rough nominally flat surfaces

First, consider the asperity contact that occurs at 2 elastic contact points at  $x = 0.65$  mm and  $x=0.67$  mm for the lowest load (see subsections of Figures Figure 3.14, Figure 3.15 and Figure 3.16, corresponding to  $x$  from 0.6 to 0.7 mm). At the intermediate load the contact has extended to comprise neighbouring points, and is mostly plastic. The plastic deflection can be observed in Figure 3.16. At the highest load the contact area spreads beyond the subsection with all contact points plastic except that at the left boundary of the subsection zone. The pattern of new elastic contact points becoming plastic as the load is increased happens in both  $x$  and  $y$  directions as can be seen in Figure 3.13.

#### 3.4.3 Extruded roughness profile

In order to validate the results of the simple elastic-plastic contact model of harmonic roughness a comparison was made with the same problem subjected to a finite element contact analysis (FEA) which takes subsurface stresses and plastic behaviour into account in an elastic-plastic material model. The von Mises criterion of plasticity is used in the FEA analysis and the hardening behaviour is neglected. The problem chosen for this comparison is of one rough surface contacting a smooth plane surface. The FEA was for plane strain conditions to simulate the line contact analysis of a ground surface, i.e. in terms of Figure 3.1 the roughness profile is extruded perpendicular to the  $x$ - $z$  plane. To specify the harmonic roughness problem a 0.1 mm length of profile taken from a test gear surface was mirrored repeatedly to form a rough nominally flat surface which was loaded against a rigid smooth surface using the ABAQUS FEA software system by Bryant (2013). The transverse deflection of the plane strain FEA model was restrained at its (mirror image) transverse boundaries so that analysis of the single 0.1 mm length gives the solution to the full periodic problem. The dimension of the model in a direction measured normal to the contacting surfaces was sufficient to ensure effective semi-infinite deflection behaviour and the load was applied with a uniformly distributed force at this boundary. Simulation of repeated loading at the same load shows that the residual plastic deformation at an asperity occurs almost entirely in the first loading event (Evans et al, 2012).

In order to specify the symmetry boundary conditions for the differential deflection method (DDM) the 0.1 mm long profile was reflected to give the surface roughness and then extruded to form the representative roughness area that is repeated periodically in the harmonic analysis. This is illustrated in Figure 3.17 which shows the

### Section 3.4 Results and discussion

0.1 mm roughness profile schematically on AB. This is reflected at B to give profile BC, and the whole profile AC is extruded to form the representative 2D roughness area ACA'C'. The representative area ACA'C' is a rectangular computational domain of 2048x128 points which is naturally repeated in both directions as a consequence of using circular Fourier convolution theorem. Although the model performs a 2D point contact analysis, the 2D solution for the current problem should have no variation in the y direction and this was found to be the case. The value of  $P_{max}$  was taken to be 2.7 times the yield strength of 1.61 GPa specified in the FEA model, i.e.  $P_{max}=4.37$  GPa.

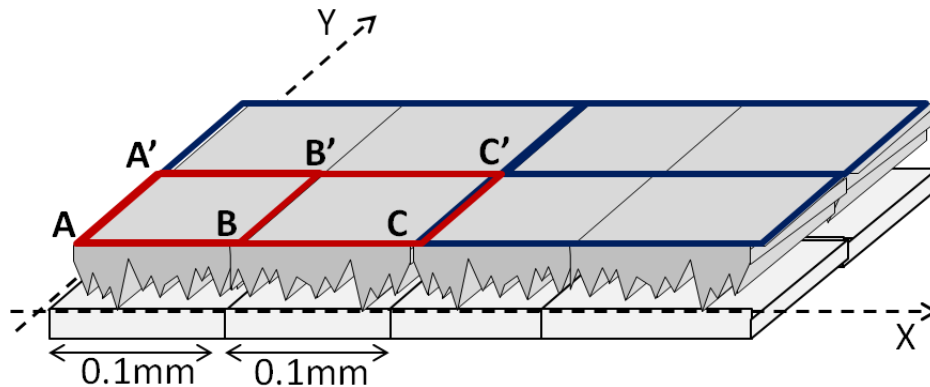


**Figure 3.17** Schematic showing how the 2D periodic roughness analysis is created from the single profile AB by reflection to form profile AC and extrusion to form the representative area ACA'C'.

In the DDM the load is imposed by specifying the  $H_{max}$  value, which is the depth of the deepest valley after the deformation occurs; load is then calculated as the sum of the pressures, generated at the points which are in contact. In order to compare the DDM results with available FEM results for the same surface profile, a number of problems were solved by the DDM for a sequence of  $H_{max}$  values. The results were then compared with those from the FEA model for the same mean pressure or for the same contact area.

The FE model used a roughness profile that consisted of 1001 points in AB section (see Figure 3.17). For use in the DDM this profile was adapted to a 1024 nodes grid, using a linear interpolation. The reflected profile AC has therefore 2048 nodes. The execution time of the FE contact analysis on Intel i3 32bit processor for a single load case varies from 1 h 45 min to 3 hours 45 min increasing for higher loads. The execution time of the DDM varies from 1 to 5 minutes, depending on the number of asperities which are in the transition range of the contact/no-contact or pure elastic/elastic-plastic conditions, i.e. very low pressure or gap values or pressure close to  $P_{max}$  value. The stated times are based on simple point iteration and have the potential for significant

reduction. This possibility is not covered by the present work. The relative error is  $10^{-7}$  for each node value for both methods.

Figure 3.18 shows the variation of mean contact pressure with contact length for the DDM model and includes the results for five load cases with  $P_{mean}$  varying from 220 MPa to 1025 MPa evaluated using the FEA method. The results given by DDM were compared to those obtained by FEA with the same contact length. The difference in  $P_{mean}$  at the lowest load is about 5% and at the highest load is about 10%. The reason for this discrepancy is discussed below.

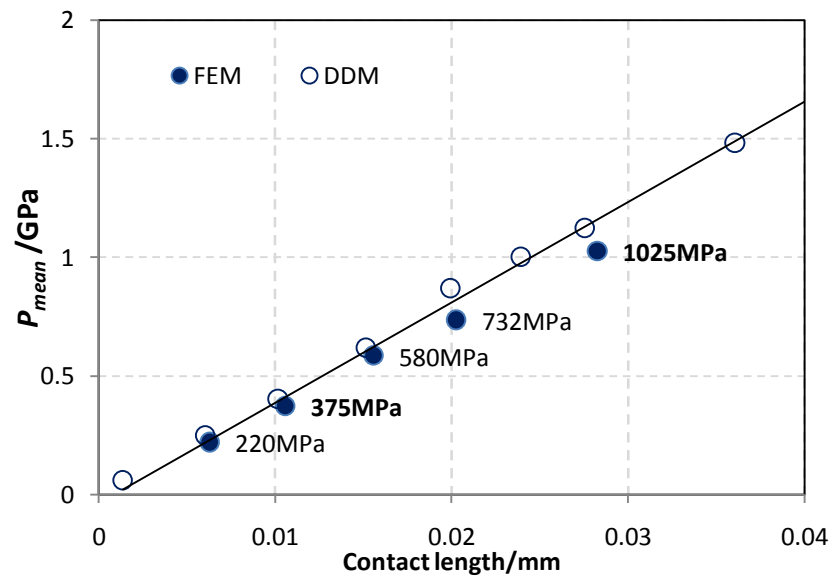


Figure 3.18 Comparison of mean contact pressure with profile contact length for differential deflection (empty circles) and FEA (solid circles) contact solutions; trend line for DDM solutions (solid line)

Figure 3.19 gives the load compliance behaviour for the DDM over the full range of loading possible. The highest approach distance used of  $1.65 \mu\text{m}$  corresponds to almost complete surface contact, and at that stage the mean contact pressure is very close to  $P_{max}$  which has the value 4.37 GPa for this analysis.

### Section 3.4 Results and discussion

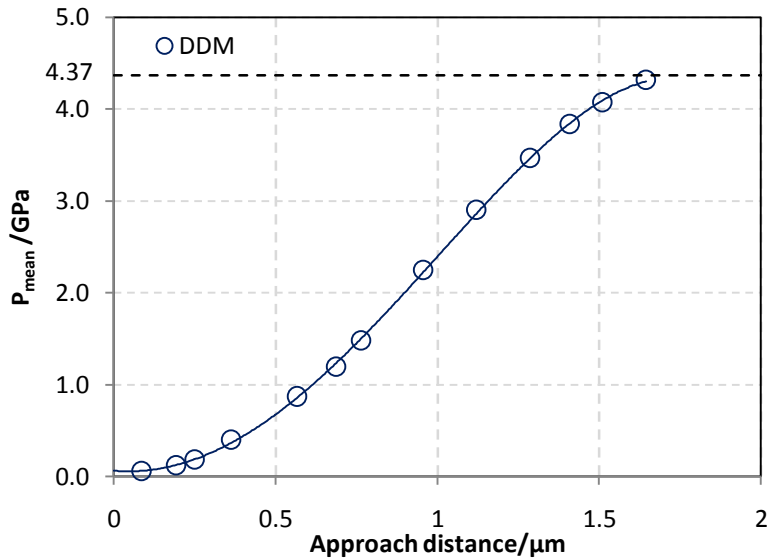
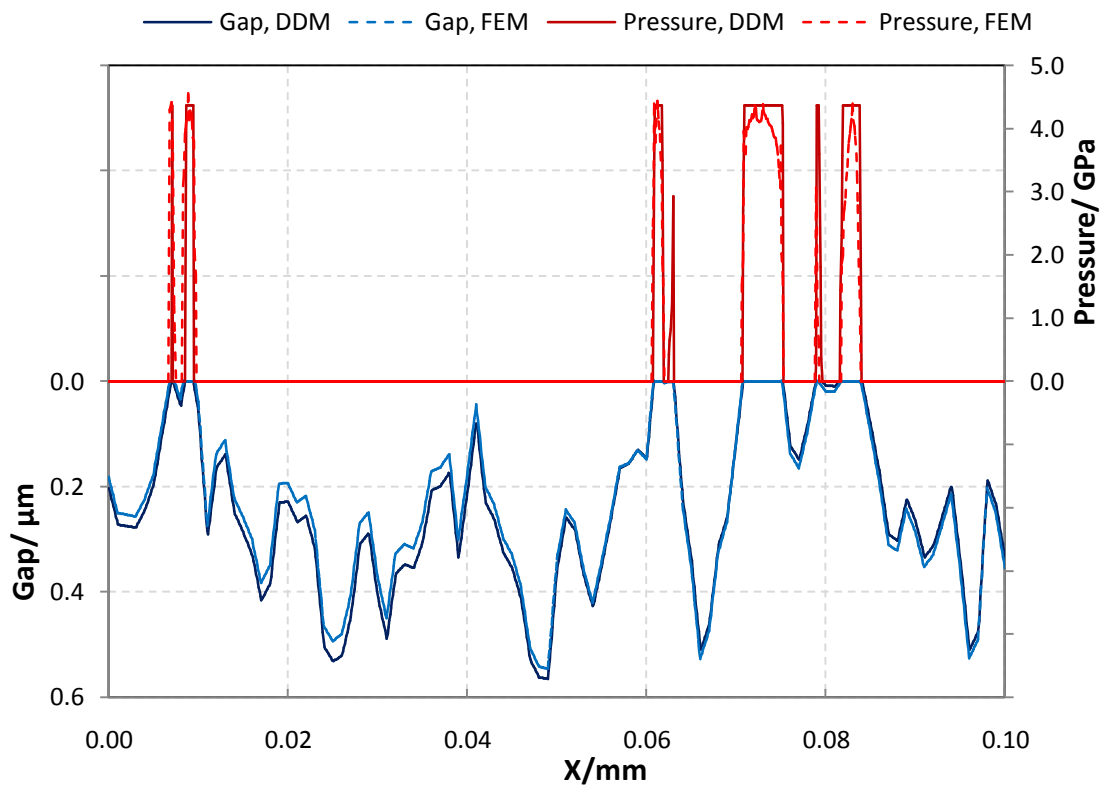


Figure 3.19 Variation of mean contact pressure with approach distance for differential deflection contact solution (empty circles), trend line (solid curve),  $P_{\text{max}}$  (broken blue curve).

Figure 3.20 and Figure 3.21 make a detailed comparison of the contact results obtained for the two FEA analysis load cases. The comparison is made on the basis of equal contact areas.

Figure 3.20 compares the results for the lower FEA load case which has  $P_{\text{mean}} = 375$  MPa. The figure shows the results from the two methods superimposed and shows the contact pressure and the contact gap for the two analyses. The contact gap is plotted in the positive downward sense so that the figure reflects the contact geometry in Figure 3.1. This also aids clarity as it has the advantage of preventing the pressure and film gap curves overlapping. The agreement between the contact gap between the two analyses is very good and since this is the key calculation as far as providing information for determining the influence of roughness on lubricant flow it is an encouraging level of agreement between the full FEA model and the simplified DDM model.



**Figure 3.20** Comparison of contact pressure and surface gap for differential deflection and FEA contact solutions at FEA contact load of 375 MPa.

The comparison of pressure distributions indicates differences in pressure detail but a good general agreement. The difference apparent in the contact pressures is that the DDM tends to calculate asperity contacts with greater areas experiencing the hardness pressure  $P_{max}$  than is the case with the FEA model. This is because of the simplified treatment of plastic effects and explains the observation that the DDM model tends to overestimate contact load.

Figure 3.21 makes the corresponding comparison for the FEA load case with  $P_{mean} = 1025$  MPa. Note that the DDM solution was selected from the sequence of solutions as the closest fit to the FEA analysis in terms of contact length value. The contact gap agreement is not as good in this case as that of Figure 3.20 and the load is overestimated by a greater factor. The higher load brings more asperities into contact, where part of the contact is plastic and in these cases the effect of plastic flow is more significant, which is reflected in the level of agreement in the gap for the higher load. For application of dry contact to predict elastic-plastic load compliance behaviour as part of a mixed lubrication analysis the most appropriate comparison is that on the basis of the approach distance,  $S$ , but that information is not available for the current FEA analysis which is loaded by application of the mean pressure. The distance of

### Section 3.4 Results and discussion

common approach then reflects the strain in the contacting bodies which are not semi-infinite.

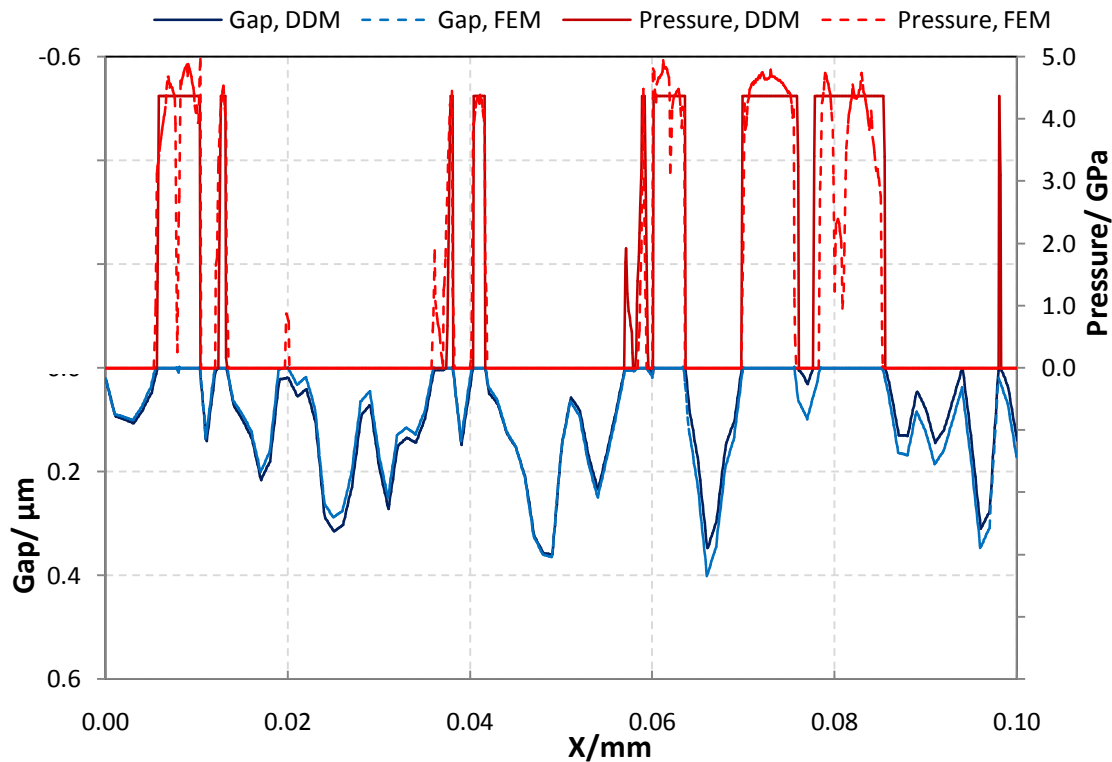


**Figure 3.21 Comparison of contact pressure and surface gap for differential deflection and FEA contact solutions at FEA contact load of 1025 MPa.**

Another comparison made between the models is that of the residual deflection obtained by both the FEM and DDM analyses. For the FEM solution this is the difference between the residual shape of the unloaded surface and the original surface. For the DDM the residual deflection is  $D^{plast}(x,y)$  value. Figure 3.22 gives the comparison for the lower of the two loads. This shows that for the FEA analysis the residual surface deflection may be negative in the areas adjacent to the contact area and this is a consequence of subsurface flow causing an upwelling of the material around the asperity contacts.

This effect is not obtained with the DDM analysis where the effect of plastic deformation is currently restricted to the contact points experiencing  $P_{max}$  pressures. To improve this aspect of the DDM model the effect of the subsurface plastic flow would need to be incorporated in some way. For example a concept of asperity persistence introduced by Williamson and Hunt (1972) could be adopted locally in the areas adjacent to the high pressure points.

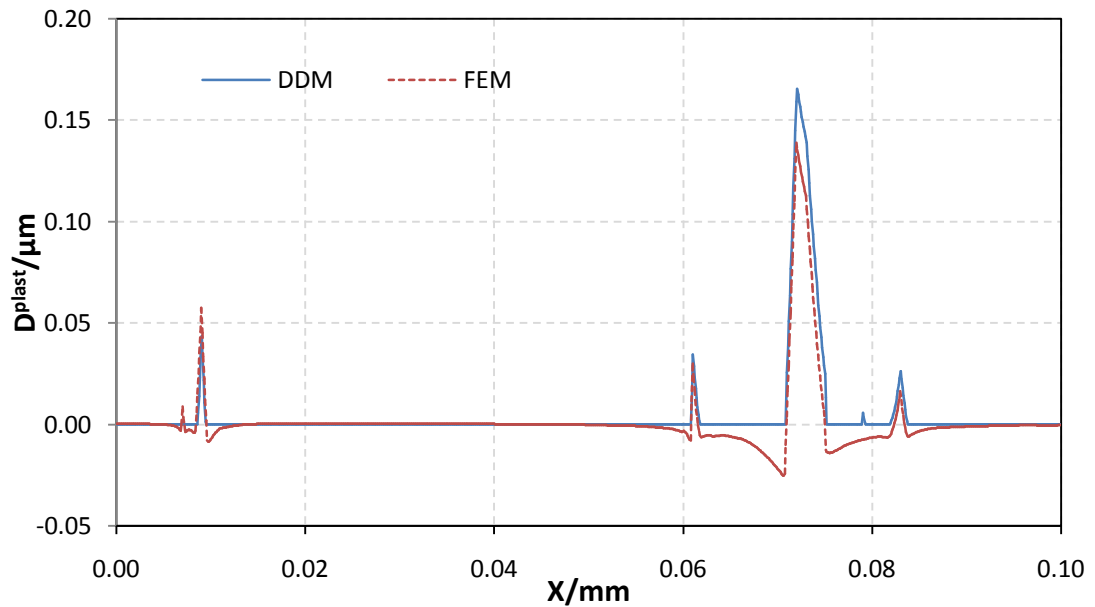


Figure 3.22 Comparison of residual deflection for differential deflection and FEA contact solutions at FEA contact load of 375 MPa.

However, the relative residual deflection between the contact points and the neighbouring non contact points is captured quite well. Figure 3.23 makes the corresponding comparison for the higher load case and has a different ordinate scale. Here there is a greater degree of residual deflection, and the upwelling of the surface areas surrounding the asperity contacts is greater. Here again it is apparent that in spite of its inability to predict the upwelling, the DDM predicts the relative residual deflection well.

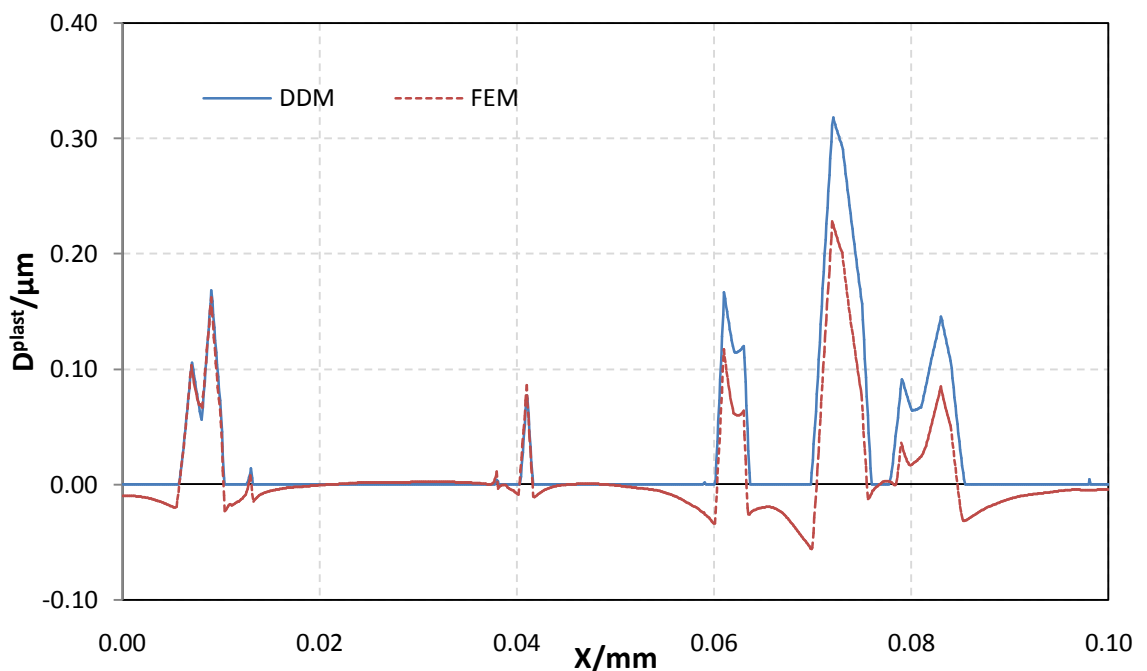


Figure 3.23 Comparison of residual deflection for differential deflection and FEA contact solutions at FEA contact load of 1025 MPa.

### Section 3.4 Results and discussion

The final comparison made between the results obtained by FEA and DDM for extruded rough surfaces is that of the free volume between the deformed surface and its rigid counterface. This comparison is considered to be relevant in application to the mixed lubrication as it demonstrates the capability of the load in plain bearing to be supported hydrodynamically despite the occasional contacting asperities. Figure 3.24 presents the free volume values (i.e. the volume between the surfaces) relative to the undeformed surface case plotted against the contact length of the profile. It can be observed that the results obtained via FEM are in a good agreement with corresponding solutions obtained via DDM with simple elastic-plastic model.

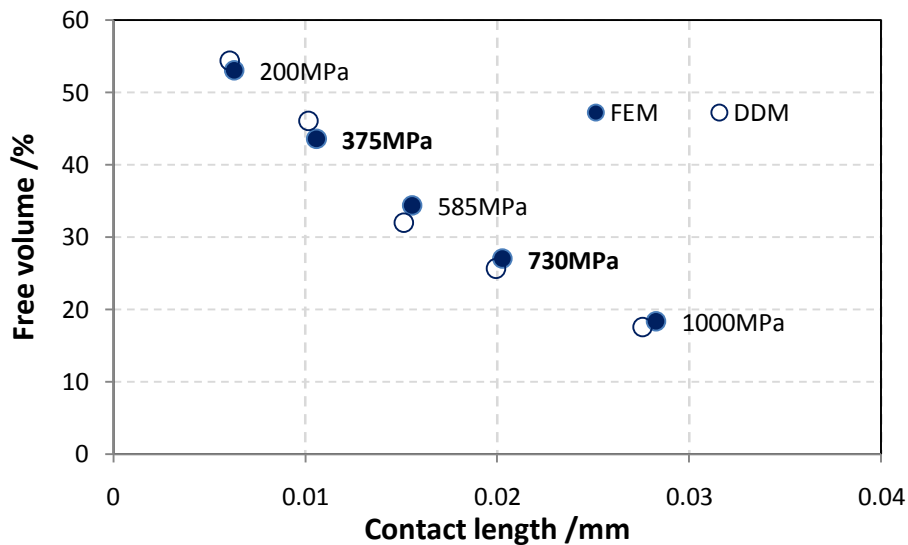


Figure 3.24 Comparison of relative free volume between the deformed rough surface and its rigid counterpart obtained via DDM (empty circles) and FEA (solid circles) .

#### 3.4.4 Full 3D FEA comparison

Comparison of the dry contact analysis using DDM and that obtained by means of FEM using ABAQUS has shown good agreement of the pressure distribution, contact zone and free volume for the one dimensional case with measured roughness profile. The difference between the deflected shapes obtained by the two methods was explained by the DDM being incapable of accounting for the subsurface plastic flow. The DDM method however is developed for solving a point contact problem, therefore a comparison of the method with full 3D FEA is considered beneficial.

Yastrebov et al (2011) developed a simplified dry contact analysis method based on the constitutive behaviour of the material calibrated using a FEA solution of a single asperity problem. For validation purposes they have also conducted a full 3D FEA of a dry contact of a rough surface with a rigid counterpart. The profile of a sand blasted surface was measured by Vallet et al (2009) and contained 66x66 measured heights. As

### Chapter 3. Dry contact analysis of rough nominally flat surfaces

indicated by Yastrebov et al (2011), the resolution of the asperity peaks plays an important role in creating a discrete mesh for the FEA study. For this purpose Yastrebov et al (2011) enriched the measured surface using a bi-cubic Bezier smoothing step which resulted in a surface representation using 330x330 nodes. Each asperity was then represented by 460 nodes on average. This surface containing 330x330 nodes was made available to the current author and interpolated onto a grid of 512x512 nodes, optimised for the FFT algorithm. The rough surface used is shown in Figure 3.25 in isometric view, and cross sections parallel to X and Y axis are given in Figures 3.26 and 3.27 respectively.

The FE analysis conducted by Yastrebov et al (2011) considered a representative volume element (RVE) with lateral dimensions 54x63  $\mu\text{m}$  and depth of 72  $\mu\text{m}$ . The top face of the RVE was rough and touching a rigid counterface. The loaded state was induced by specifying the vertical displacement at the bottom face of the RVE and by restraining the vertical displacement of the rigid counterface. Symmetry boundary conditions were imposed on the side faces of the RVE, i.e. no lateral displacements were allowed at these faces.

The material properties were those of NOREM alloy, which is a hardfacing alloy developed by Electric Power Research Institute for nuclear energy industry and its chemical composition is mostly iron with additions of chromium (25%), magnesium (4.5%), nickel (4%), molybdenum (2%) and other metals (<2%).

The material properties used were elastic modulus  $E=1.75$  GPa and Poisson's ratio 0.3. In the work of Yastrebov et al (2011) an isotropic hardening law was considered with the yield stress defined as follows:

$$\sigma_Y = R_0 + Q(1 - e^{-bp})$$

where the values  $R_0=442.7$  MPa,  $Q=493.5$  MPa and  $b=242.2$  Pa<sup>-1</sup>.

In the case of elastic perfectly plastic FE contact analysis considered in previous section the limiting pressure value  $P_{max}$  of the simple plasticity model of the DDM method was selected as approximately 2.7 times the yield stress of the material, which is the contact pressure observed over the contact zone after it is completely surrounded by the plastically deformed material. For comparison with a case that includes hardening it is not clear which value should be given for  $P_{max}$ . For this reason a sequence of analyses were performed for a range of  $P_{max}=2.6-4.3$  GPa. The case of 2.6 GPa is approximately 2.7 times ( $R_0+Q$ ).

### Section 3.4 Results and discussion

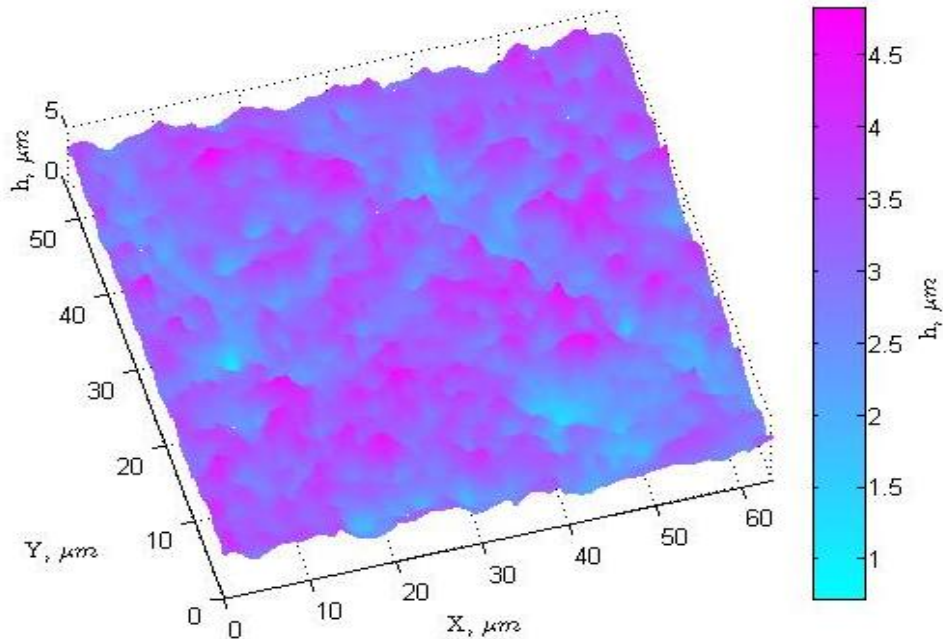


Figure 3.25 Sandblasted surface used in full 3D FEA, isometric view

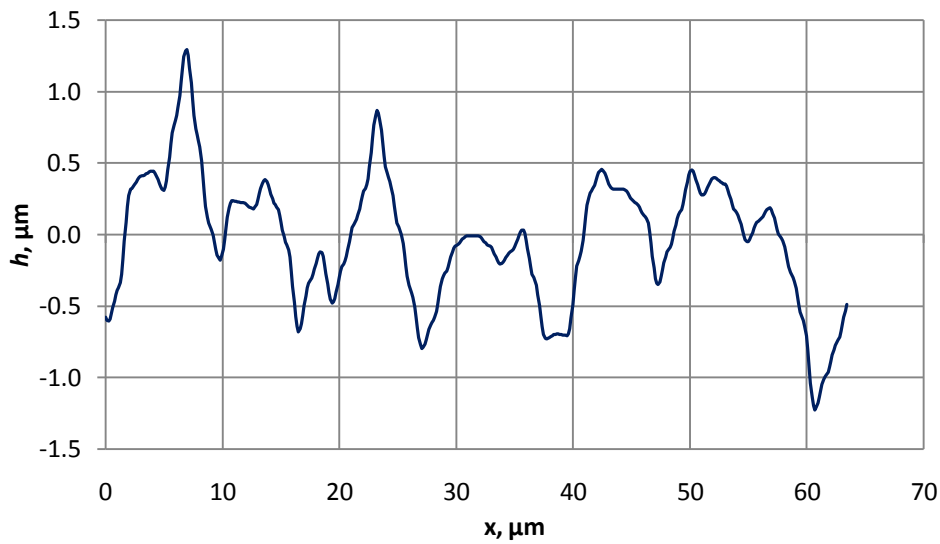


Figure 3.26 Sandblasted surface used in full 3D FEA, cross section parallel to the X axis,  $Y=13.6 \mu\text{m}$

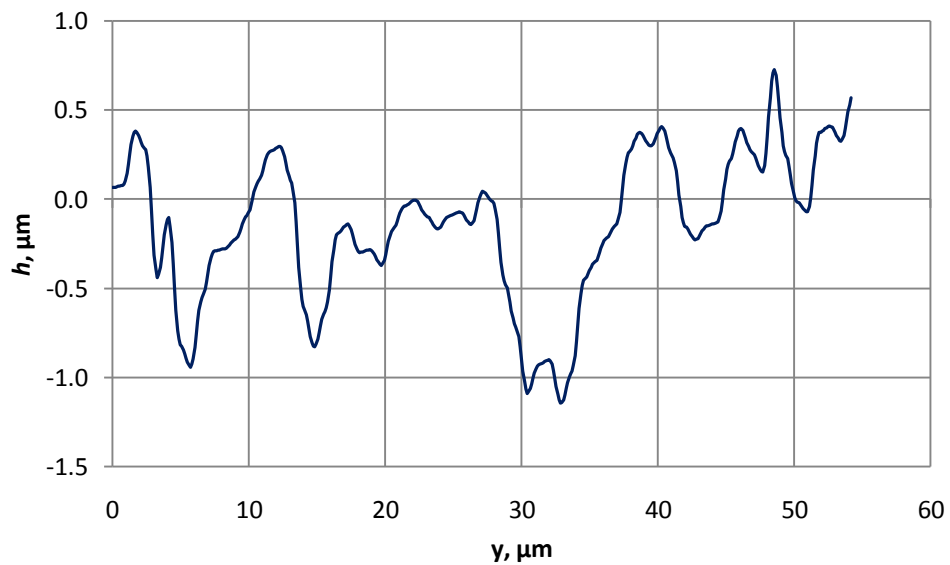


Figure 3.27 Sandblasted surface used in full 3D FEA, cross section parallel to the Y axis,  $X=15.8 \mu\text{m}$

### Chapter 3. Dry contact analysis of rough nominally flat surfaces

The comparison of the full 3D FEA with the DDM method using a simple plasticity model is summarised in Figures 3.28 and 3.29, where the force values are plotted against the contact area and relative free volume between the deformed surface and rigid counterface are plotted against force. Note that the contact area is displayed as a fraction of the total nominal area, the force is acting on the representative element and free volume values are relative to those corresponding to the undeformed surface.

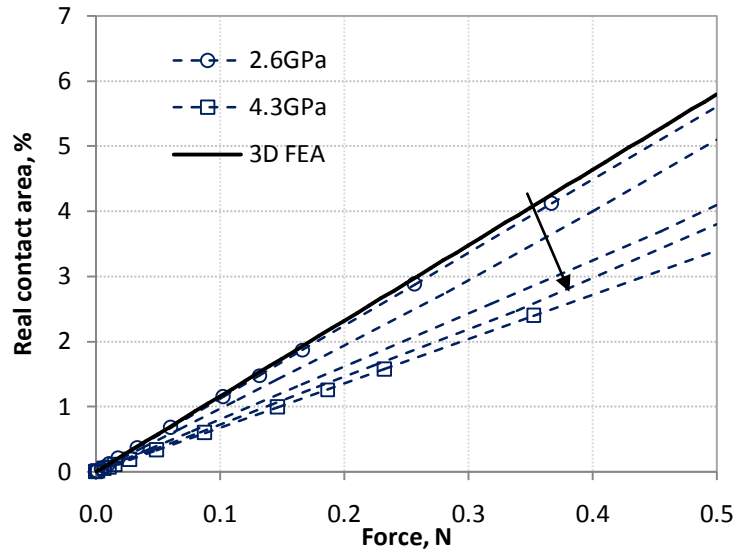


Figure 3.28 Contact area plotted against force obtained using full 3D FEA and DDM method for a sequence of  $P_{max}$  values. Arrow indicates the sense of increasing  $P_{max}$  value from 2.6 GPa to 4.3 GPa.

Figure 3.28 shows a progressively better agreement of the area-force curves obtained via 3D FEA and DDM methods as the  $P_{max}$  value down is decreased from 4.3 GPa to 2.6 GPa, which is equal to approximately  $2.7*(R_0+Q)$ .

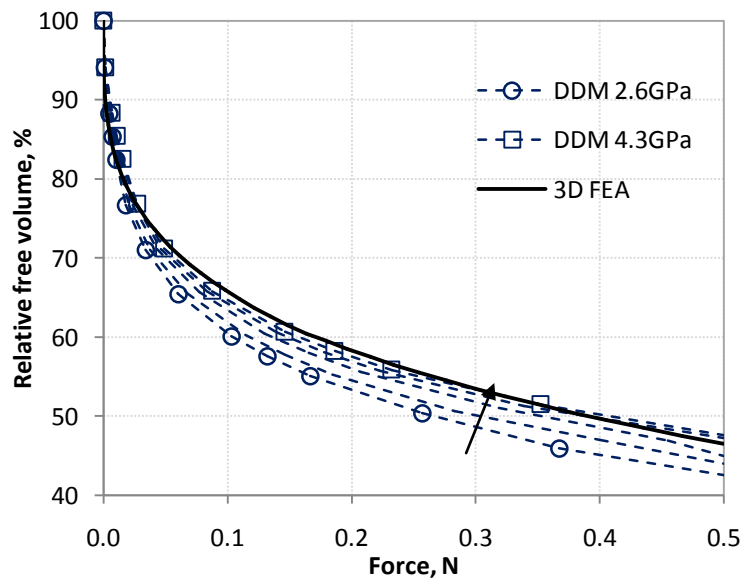


Figure 3.29 Free volume plotted against force obtained using full 3D FEA and DDM method for a sequence of  $P_{max}$  values. Arrow indicates sense of increasing  $P_{max}$  value from 2.6 GPa to 4.3 GPa.

## Section 3.5 Conclusions

On the other hand the free volume values obtained via DDM using  $P_{max}=2.6$  GPa show the worst agreement with those from 3D FEA, see Figure 3.29. The relative difference however does not exceed 10% for this case. This discrepancy can be explained by the fact that high pressure values generated at the most prominent surface asperities result in subsurface plasticity which forces the material adjacent to the plastic deformation zone to upwell, carry part of the load and thus prevent further reduction of the valley depth. In case of DDM if pressure exceeds  $P_{max}$  at the asperity tips the material is effectively removed allowing the depth of all the valleys to be decreased. The level of agreement is however very good considering that DDM requires significantly less computational resources. The full 3D FE analysis for the whole range of loads requires several days on a high performance computer (8 bi-core processors Intel Xeon X5550 2.67 GHz, 160 Gb RAM). The analysis of a single load case for the same problem using DDM takes approximately 8 mins on Intel I3 32 bit processor with 2 Gb RAM. Total of 15 load cases were evaluated for comparison in approximately two hours.

Final comparison of the contact analysis using DDM and full 3D FEA is made based on the contact zones obtained for the same elastic approach  $S=1$   $\mu\text{m}$ . The results are shown for  $P_{max}=2.6$  GPa and 4.3 GPa in Figures 3.30 and 3.31 respectively. In both cases of  $P_{max}$  value all the contact zones were captured by the DDM method correctly with better agreement in the case of  $P_{max}=2.6$  GPa. Contact zones obtained via DDM (dark red) are embedded in the larger contact areas predicted by the FE analysis. The larger area corresponds the upwelling of the material caused by subsurface plastic flow.

## 3.5 Conclusions

A simple iterative method to solve the rough surface contact problem for plane surfaces with periodic 2D roughness has been presented. The method is based on formulating the elastic deflection as a second order differential equation of the Poisson type that can be solved with periodic boundary conditions. The method requires no special properties of the specified roughness at the periodic boundaries. In case of elastic deformations only the solution obtained using DDM was validated via comparison with closed form solution obtained by Westergaard (1939). Results are also presented for a surface with 2D roughness showing the development of plastic contact zones. A detailed comparison with a 2 dimensional Finite Element

### Chapter 3. Dry contact analysis of rough nominally flat surfaces

elastic-plastic contact analysis is included as well as a comparison with full 3D FEA obtained from literature.

The method has been shown to give very good prediction of the deflected shape of the surface under moderate loads. Under high loads the method is less accurate due to simple model of plastic behaviour. However the DDM is 60-80 times faster than 2D FEA for the problem of the same resolution of the roughness profile. The DDM method is also significantly less computationally demanding than full 3D FE analysis. These considerations show that the DDM method is applicable in solving plane bearing mixed lubrication problems as a preliminary dry contact analysis to prepare for a homogenised Reynolds equation approach.

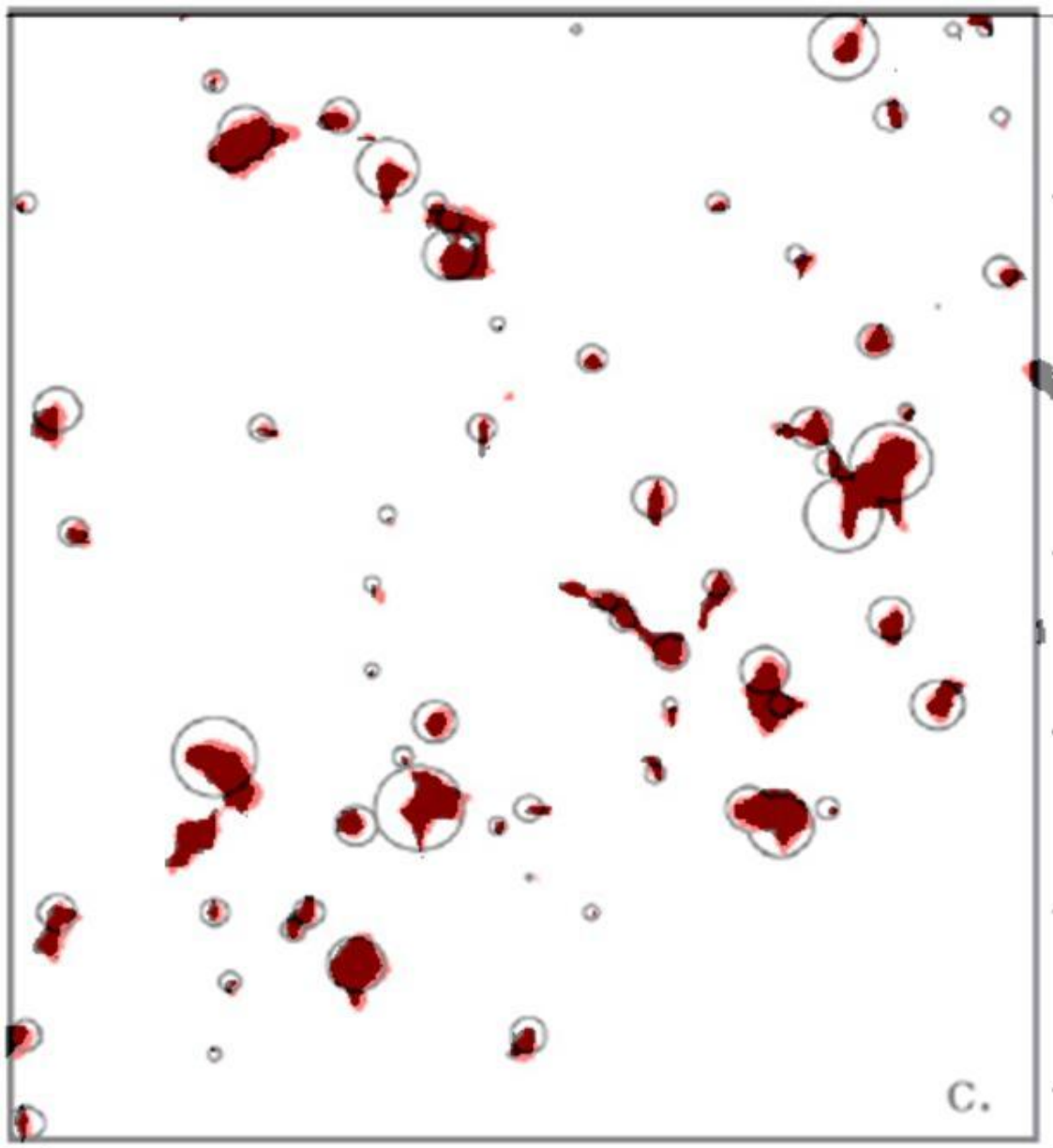


Figure 3.30 Overlapping contours of the contact zones obtained via full DDM (dark red, top layer) and full 3D FEA (light red, bottom layer).  $P_{max} = 2.6$  GPa. Circles denote contacts captured by the simplified analysis developed by Yastrebov et al (2011).

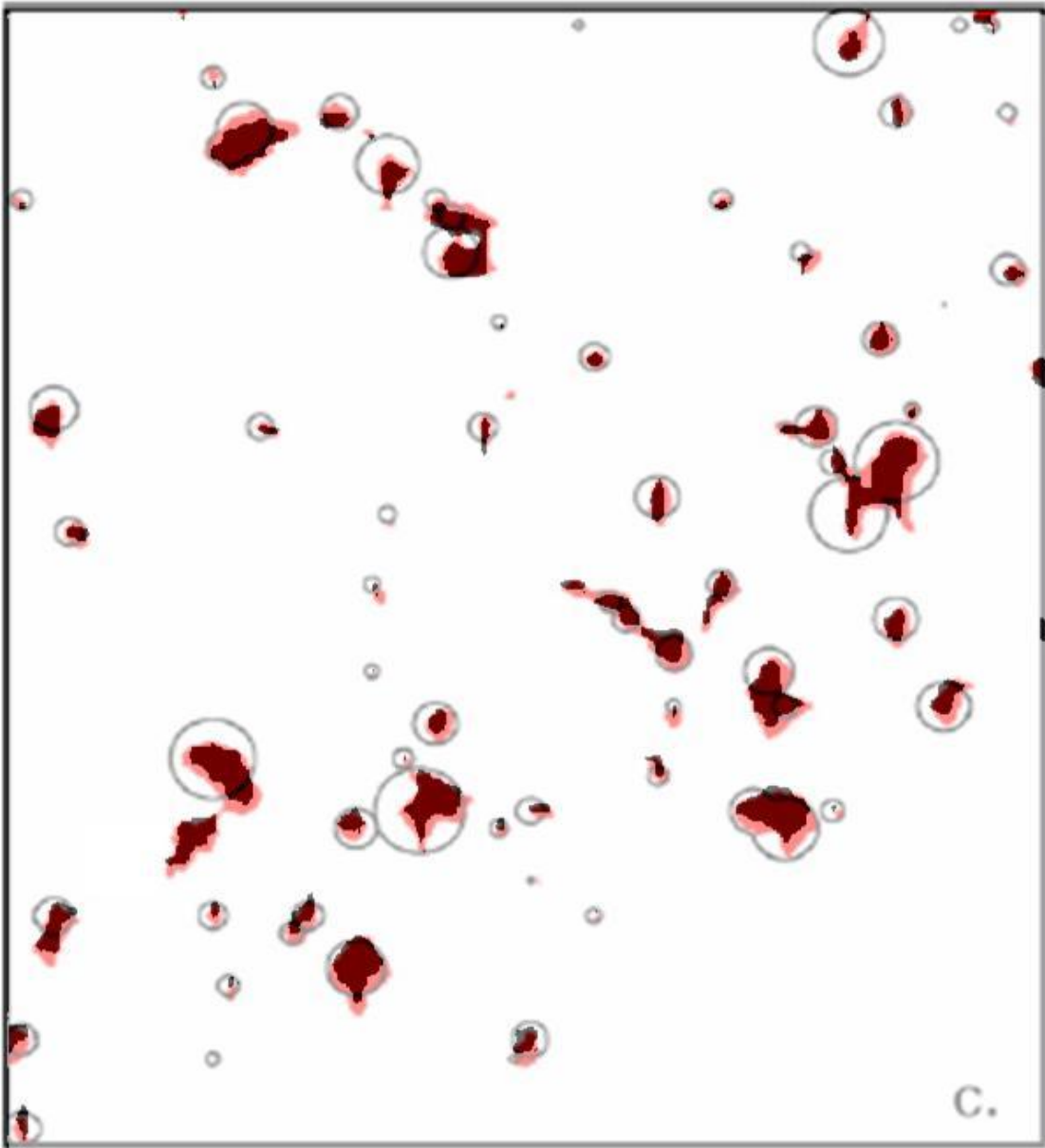


Figure 3.31 Overlapping contours of the contact zones obtained via full DDM (dark red, top layer) and full 3D FEA (light red, bottom layer).  $P_{max} = 4.3$  GPa. Circles denote contacts captured by the simplified analysis developed by Yastrebov et al (2011).

## 4 Theory of flow factors

### 4.1 Introduction

In a lubrication analysis the type of geometry considered is one where the gap between the working surfaces is significantly smaller than the characteristic dimensions of the system. This makes the Reynolds' equation applicable for describing the flow of liquid lubricant. The flow is then governed by the motion of the surfaces, the pressure gradients and local variations of the geometry. Real surfaces are never smooth, and the roughness features can play a significant role in the lubrication analysis because the separation of the working surfaces is small enough in comparison to the dimensions of the roughness features. A treatment of the problem based on an assumption of smooth surfaces will then be inaccurate. Large pressures are generated in the interaction regions of the most prominent surface asperities. Numerical treatment of lubrication problems of the rough surfaces requires a very fine resolution and large computational resources. Before those resources were available a number of efforts were made to analyse the effect of roughness on the flow of lubricant without taking into account the contribution of each individual asperity.

The first significant contribution was that of Patir and Cheng (1978, 1979) who introduced flow factors to modify the Reynolds equation so as to take roughness effects into account in an averaged way. The elastic deflection of the surface asperities was not taken into account in their work which limits the accuracy of the method in the case of mixed lubrication. The Greenwood and Tripp (1971) stochastic model for contact between two rough surfaces has been used extensively to model this aspect of the problem. The approach has been generalised (Tripp, 1983) and extended in many ways by a number of researchers, including incorporation of inter-asperity cavitation as in the work of Harp and Salant (2001). The flow factor approach has been subsequently generalised by Bayada and Chambat (1988), Bayada and Faure (1989) for example, leading to a homogenised Reynolds Equation which has also been developed by Kane and Bou-Said (2004) and Almqvist and Dasht (2006). In these approaches the surface is assumed to have a periodic roughness function which is superimposed on the global geometry of the problem. The flow factors are evaluated as functions of the surface roughness and separation of the mean lines of the surfaces, and the contact of the surfaces is not considered.

## Section 4.2 Classical Reynolds' equation

Sahlin et al (2010a, 2010b) incorporated the direct interaction of prominent surface asperities through a dry contact elastic analysis and the associated load-compliance behaviour. Flow factors are then calculated for the loaded surface shape obtained. Another route to incorporate the mechanical contact of the asperities into the flow factors approach was presented by Scaraggi et al (2011). They used a stochastic method for evaluating the average deformed shape of the surface developed by Persson (2001), which was heavily criticised by Borodich (2002) and Manners and Greenwood (2006).

The interest in the current work is in developing a mixed lubrication analysis method based on the homogenised Reynolds equation using the approach initially proposed by Bayada and Chambat (1988), Bayada and Faure (1989) and later used by Kane and Bou-Said (2004), Almqvist et al (2006) and others. In the case of low clearance values between the surfaces, the dry contact analysis method discussed in Chapter 3 is incorporated in order to calculate the effect of the deflected surface on the lubrication.

## 4.2 Classical Reynolds' equation

The classical Reynolds equation was first derived by Osborne Reynolds in 1886 in order to describe the flow of viscous liquids and create a first theory of lubrication in journal bearings. It is based on the Navier-Stokes equations for the motion of a viscous fluid and the conservation of mass in the fluid. The use of Reynolds equation in lubrication theory is justified under the following assumptions:

1. The film thickness is much smaller than the relative radius of curvature of the contact.
2. The film thickness is much smaller than the dimensions of the lubricated contact.
3. Reynolds number is small, flow is laminar and inertia terms are negligible.
4. No slip at the solid/lubricant boundaries.
5. Fluid is Newtonian; shear stress is proportional to shear strain rate.
6. Pressure, density and viscosity do not vary across the lubricant film, i.e. they only vary in the plane of the film.

Modifications of the Reynolds equation are possible where the last 4 of these conditions are relaxed. In the case of rough surface lubrication care should be taken that the radius of curvature of the asperities is big enough in comparison to the film thickness.

The Reynolds' equation consists of two main parts: the variation of flow of lubricant due to the pressure gradients and variation of flow caused by motion of the surfaces. If the origin of coordinates is fixed at the point of lowest film thickness such that the gap between the surfaces does not change with time then the time dependant terms can be omitted. If in addition one of the axes coincides with the motion direction of the surfaces, then the Reynolds' equation takes the commonly used form:

$$\frac{\partial}{\partial x} \left( \frac{\rho h^3}{12\eta} \frac{\partial p}{\partial x} \right) + \frac{\partial}{\partial y} \left( \frac{\rho h^3}{12\eta} \frac{\partial p}{\partial y} \right) = \frac{\partial(\rho \bar{u} h)}{\partial x} \quad (4.1)$$

where

$$\begin{cases} x - \text{coordinate coinciding with the motion direction} \\ y - \text{coordinate in the transverse direction} \\ p(x, y) - \text{pressure distribution} \\ h(x, y) - \text{gap between the surfaces} \\ \rho - \text{density} \\ \eta - \text{dynamic viscosity} \\ \bar{u} - \text{mean velocity of the surfaces} \end{cases}$$

If the system operates within a low pressure range then the lubricant can be assumed incompressible and isoviscous, i.e.  $\rho = \rho_0$  and  $\eta = \eta_0$ . The viscosity dependence on pressure for a liquid lubricant is found to be approximately

$$\eta(p) = \eta_0 e^{\alpha p}$$

where coefficient  $\alpha$  is called the pressure viscosity coefficient which has values in the range 10-40 GPa<sup>-1</sup> (van Leeuwen, 2009). When the pressure exceeds 1/ $\alpha$  the viscosity becomes high and very sensitive to pressure. Lubrication becomes elasto-hydrodynamic. For low pressures in comparison to 1/ $\alpha$  the variation of viscosity is not significant. Plain bearings are usually analysed by considering the lubricant to be isoviscous. In the method based on the flow factors this restriction can be relaxed at the global scale, i.e. non-isoviscous lubricant can be considered, however the viscosity variation within the local representative cells is assumed negligible and local problems are isoviscous.

### Section 4.3 Periodic roughness and two-scale expansion

Under the assumption of an isoviscous fluid the Reynolds' equation can be modified as follows:

$$\frac{\partial}{\partial x} \left( h^3 \frac{\partial p}{\partial x} \right) + \frac{\partial}{\partial y} \left( h^3 \frac{\partial p}{\partial y} \right) = \lambda \frac{\partial h}{\partial x} \quad (4.2)$$

where  $\lambda = 12\eta\bar{u}$ . The left hand side of Equation (4.2) is the variation of flow in both  $x$  and  $y$  directions caused by pressure gradients. This flow is commonly referred to as Poiseuille flow. The right hand side is the variation of flow caused by entrainment in the  $x$  direction. This flow is referred to as Couette flow. The variation of the Poiseuille flow is then equated with the variation of the Couette flow.

### 4.3 Periodic roughness and two-scale expansion

As mentioned in Section 4.1, the numerical solution for the rough surface lubrication problem requires very high resolution so that it is fine enough to represent each asperity with a sufficient number of mesh points. This results in a vast number of degrees of freedom and significantly increases the computational costs of the analysis. The main idea of the lubrication models based on the flow factors is to separate the effect of roughness on the flow of lubricant from the effect of the global shape.

For this purpose in addition to the system of global Cartesian coordinates  $(x,y)$  a system of local coordinates  $(\xi,\psi)$  is introduced as follows:

$$\begin{aligned} \xi &= \frac{x}{\varepsilon}; & \psi &= \frac{y}{\varepsilon}; \\ \xi, \psi &\in \Omega \end{aligned} \quad (4.3)$$

where  $\varepsilon$  is a scaling parameter and  $\Omega$  is the domain of the local coordinates. The global and local coordinate systems are illustrated in Figure 4.1.

Following the perturbation approach (Nayfeh, 2004) the pressure distribution for the rough surface lubrication problem can be approximated as a power series (known as perturbation series) of a small parameter,  $\varepsilon$ . The accuracy of the perturbation approach is good provided the local scale problem defined by the parameter  $\varepsilon$  is small compared to the global scale of the problem. For rough surfaces it is convenient to take  $\varepsilon$  as the size of the measured representative roughness area which needs to be small in comparison to the global geometry. If there are only few asperities in the representative area then it must be ensured that their lateral dimensions are at least

100 times smaller than the dimensions of the global problem. In the case of sinusoidal waviness considered in Chapter 6 the representative area consists of a single sinusoidal wave. It is shown that the homogenised solution is in a better agreement with the deterministic one if 128 or 64 waves are considered, rather than 32 or 16 waves, i.e.  $\varepsilon=1/128$ ,  $1/64$  showed better results than  $\varepsilon=1/16$  and  $1/16$  as expected.

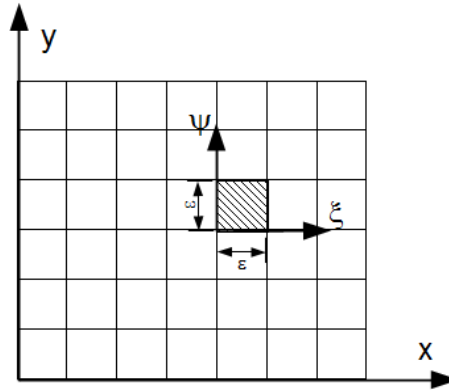


Figure 4.1 Global and local systems of coordinates

The first term in the series corresponds to the solution of the global (smooth) problem, whereas further terms represent the perturbation of the solution due to the deviations in the problem, i.e. the superimposed roughness:

$$p_\varepsilon(x, y, \xi, \psi) = p_0(x, y, \xi, \psi) + \varepsilon p_1(x, y, \xi, \psi) + \varepsilon^2 p_2(x, y, \xi, \psi) + \dots \quad (4.4)$$

According to the perturbation theory the limit of the approximated solution (4.4) tends to the exact solution for the rough problem when  $\varepsilon$  approaches to zero:

$$p_\varepsilon \xrightarrow{\varepsilon \rightarrow 0} p_0$$

which is the homogenised limit. Note that only  $p_0$  and  $p_1$  are preserved while the higher order terms are truncated.

The gap between the surfaces,  $h(x, y, \xi, \psi)$ , or the film thickness, is then presented as a combination of the globally defined function of  $(x, y)$  and a local function of  $(x, y, \xi, \psi)$ :

$$h_{total}(x, y, \xi, \psi) = h_0(x, y) + h_1(x, y, \xi, \psi) \quad (4.5)$$

where  $h_0(x, y)$  is the global shape of the system and  $h_1(x, y, \xi, \psi)$  is roughness function. The roughness function  $h_1(x, y, \xi, \psi)$  is assumed to be periodic, therefore it is independent of the global coordinates  $(x, y)$ :

$$h_1(x, y, \xi, \psi) = h_1(\xi, \psi).$$

### Section 4.3 Periodic roughness and two-scale expansion

The separation of the gap function into the global geometry and local roughness is schematically illustrated in Figures Figure 4.2 and Figure 4.3. Figure 4.2 shows the global shape (smooth surface) problem which in this illustration is a cylindrical roller contacting a plane surface. Figure 4.3 shows the periodic roughness function, and Figure 4.4 shows the total gap distribution of Equation (4.5).

Introducing the local coordinates modifies the derivatives so as to take into account the variation of the function with respect to  $(\xi, \psi)$ :

$$\begin{aligned}
 f(x, y, \xi, \psi) &= f\left(x, y, \frac{x}{\varepsilon}, \frac{y}{\varepsilon}\right) \\
 \frac{\partial f}{\partial x} &= \frac{\partial f}{\partial x} + \frac{1}{\varepsilon} \frac{\partial f}{\partial \xi} \\
 \frac{\partial f}{\partial y} &= \frac{\partial f}{\partial y} + \frac{1}{\varepsilon} \frac{\partial f}{\partial \psi}
 \end{aligned}
 \tag{4.6}$$

The classical Reynolds' equation for incompressible and isoviscous fluid (4.2) then takes the following form:

$$\begin{aligned}
 \frac{\partial}{\partial x} \left[ h^3 \left( \frac{\partial p}{\partial x} + \frac{1}{\varepsilon} \frac{\partial p}{\partial \xi} \right) \right] + \frac{1}{\varepsilon} \frac{\partial}{\partial \xi} \left[ h^3 \left( \frac{\partial p}{\partial x} + \frac{1}{\varepsilon} \frac{\partial p}{\partial \xi} \right) \right] \\
 \frac{\partial}{\partial y} \left[ h^3 \left( \frac{\partial p}{\partial y} + \frac{1}{\varepsilon} \frac{\partial p}{\partial \psi} \right) \right] + \frac{1}{\varepsilon} \frac{\partial}{\partial \psi} \left[ h^3 \left( \frac{\partial p}{\partial y} + \frac{1}{\varepsilon} \frac{\partial p}{\partial \psi} \right) \right] = \lambda \frac{\partial h}{\partial x} + \lambda \frac{1}{\varepsilon} \frac{\partial h}{\partial \xi}
 \end{aligned}
 \tag{4.7}$$

where  $\lambda = 12\eta\bar{u}$ .

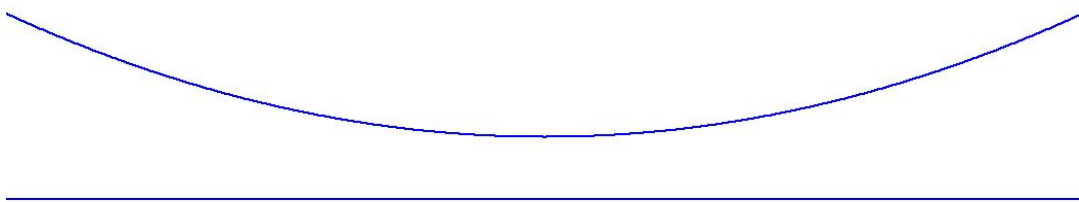


Figure 4.2 Global shape: smooth cylindrical roller

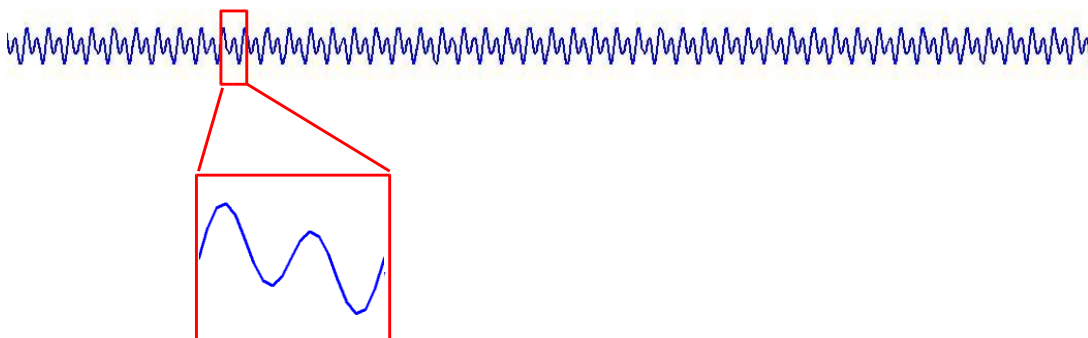


Figure 4.3 Local shape: repeated roughness profile and its period

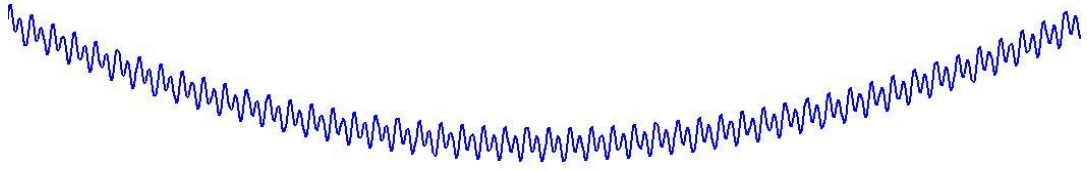


Figure 4.4 Total geometry: periodic roughness superimposed on a smooth global shape of a roller

This yields

$$\begin{aligned} & \frac{\partial}{\partial x} \left( h^3 \frac{\partial p}{\partial x} \right) + \frac{1}{\varepsilon} \frac{\partial}{\partial x} \left( h^3 \frac{\partial p}{\partial \xi} \right) + \frac{1}{\varepsilon} \frac{\partial}{\partial \xi} \left( h^3 \frac{\partial p}{\partial x} \right) + \frac{1}{\varepsilon^2} \frac{\partial}{\partial \xi} \left( h^3 \frac{\partial p}{\partial \xi} \right) + \\ & \frac{\partial}{\partial y} \left( h^3 \frac{\partial p}{\partial y} \right) + \frac{1}{\varepsilon} \frac{\partial}{\partial y} \left( h^3 \frac{\partial p}{\partial \psi} \right) + \frac{1}{\varepsilon} \frac{\partial}{\partial \psi} \left( h^3 \frac{\partial p}{\partial y} \right) + \frac{1}{\varepsilon^2} \frac{\partial}{\partial \psi} \left( h^3 \frac{\partial p}{\partial \psi} \right) = \lambda \frac{\partial h}{\partial x} + \lambda \frac{1}{\varepsilon} \frac{\partial h}{\partial \xi} \end{aligned}$$

In order to reduce the algebraic transforms the following auxiliary notation is adopted, similar to the one used by Bayada:

$$\begin{aligned} A_1[\cdot] &= \frac{\partial}{\partial \xi} \left( h^3 \frac{\partial[\cdot]}{\partial \xi} \right) + \frac{\partial}{\partial \psi} \left( h^3 \frac{\partial[\cdot]}{\partial \psi} \right) \\ A_2[\cdot] &= \frac{\partial}{\partial \xi} \left( h^3 \frac{\partial[\cdot]}{\partial x} \right) + \frac{\partial}{\partial \psi} \left( h^3 \frac{\partial[\cdot]}{\partial y} \right) + \frac{\partial}{\partial x} \left( h^3 \frac{\partial[\cdot]}{\partial \xi} \right) + \frac{\partial}{\partial y} \left( h^3 \frac{\partial[\cdot]}{\partial \psi} \right) \\ A_3[\cdot] &= \frac{\partial}{\partial x} \left( h^3 \frac{\partial[\cdot]}{\partial x} \right) + \frac{\partial}{\partial y} \left( h^3 \frac{\partial[\cdot]}{\partial y} \right) \\ B^\xi &= \lambda \frac{\partial[(\cdot)h]}{\partial \xi} \quad B^\psi = \lambda \frac{\partial[(\cdot)h]}{\partial \psi} \\ B^x &= \lambda \frac{\partial[(\cdot)h]}{\partial x} \quad B^y = \lambda \frac{\partial[(\cdot)h]}{\partial y} \end{aligned} \tag{4.8}$$

where  $(\cdot)$  denotes any function of  $(x, y, \xi, \psi)$ . With the notation of Equations (4.8), Equation (4.7) is equivalent to:

$$\frac{1}{\varepsilon^2} A_1[p] + \frac{1}{\varepsilon} A_2[p] + A_3[p] = \frac{1}{\varepsilon} B^\xi + B^x \tag{4.9}$$

Rough surface problems have two important directions, the direction of the entrainment velocity and the direction of the periodic roughness, and these do not necessarily coincide.

Now consider the case where the direction of motion does not coincide with the x-axis, in shown on the Figure 4.5. If the direction of the entrainment velocity  $\bar{u}$  is inclined at an angle  $\theta$  with respect to the axis of periodic expansion, then:

$$\bar{u} = \bar{i}|u|\cos\theta - \bar{j}|u|\sin\theta$$

where  $\bar{i}$  and  $\bar{j}$  are the basis vectors in the  $(x, y)$  coordinate system.

### Section 4.3 Periodic roughness and two-scale expansion

The right hand side of the Equation (4.2) therefore includes the term corresponding to the motion in  $Oy$  direction:

$$\frac{\partial}{\partial x} \left( h^3 \frac{\partial p}{\partial x} \right) + \frac{\partial}{\partial y} \left( h^3 \frac{\partial p}{\partial y} \right) = \lambda \frac{\partial h}{\partial x} \cos \theta - \lambda \frac{\partial h}{\partial y} \sin \theta$$

where  $\lambda = 12\eta\bar{u}$

(4.10)

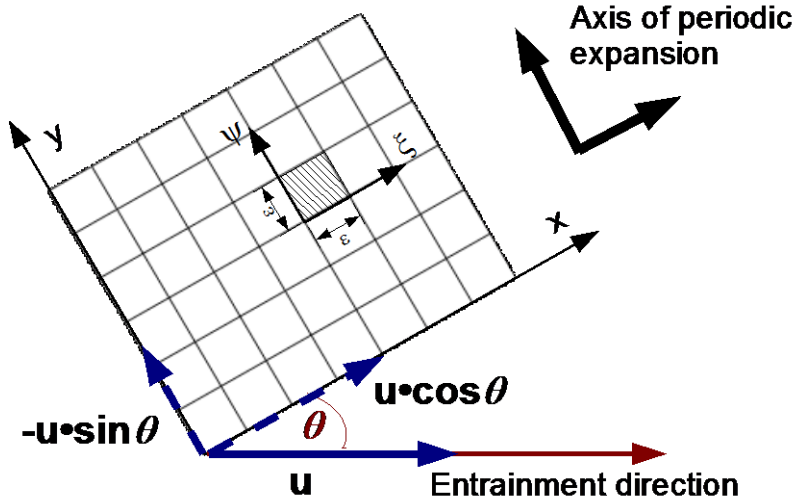


Figure 4.5 The case where the direction of motion of the surfaces does not coincide with the axes of periodic expansion .

Note, that  $\bar{u}$  is the velocity in the entrainment direction. Equation (4.9) then becomes

$$\frac{1}{\varepsilon^2} A_1[p] + \frac{1}{\varepsilon} A_2[p] + A_3[p] = \frac{1}{\varepsilon} B^\xi \cos \theta - \frac{1}{\varepsilon} B^\psi \sin \theta + B^x \cos \theta - B^y \sin \theta$$

(4.11)

Substituting the approximate solution (4.4) into Equation (4.11) above leads to

$$\frac{1}{\varepsilon^2} A_1[p_0 + \varepsilon p_1 + \varepsilon^2 p_2] + \frac{1}{\varepsilon} A_2[p_0 + \varepsilon p_1 + \varepsilon^2 p_2] + A_3[p_0 + \varepsilon p_1 + \varepsilon^2 p_2] = \frac{1}{\varepsilon} B^\xi \cos \theta - \frac{1}{\varepsilon} B^\psi \sin \theta + B^x \cos \theta - B^y \sin \theta$$

By equating the coefficients for the powers of  $\varepsilon^0, \varepsilon^{-1}, \varepsilon^{-2}$  terms the following system of equations is obtained:

$$\begin{cases} \varepsilon^0: A_1[p_2] + A_2[p_1] + A_3[p_0] = B^x \cos \theta - B^y \sin \theta \\ \frac{1}{\varepsilon}: A_1[p_1] + A_2[p_0] = B^\xi \cos \theta - B^\psi \sin \theta \\ \frac{1}{\varepsilon^2}: A_1[p_0] = 0 \end{cases}$$

which is equivalent to

$$\begin{cases} A_1[p_0] = 0 \\ A_1[p_1] = B^\xi \cos \theta - B^\psi \sin \theta - A_2[p_0] \\ A_1[p_2] = B^x \cos \theta - B^y \sin \theta - A_2[p_1] - A_3[p_0] \end{cases}$$

(4.12)

Note that the higher order terms  $\varepsilon^1, \varepsilon^2$  are omitted from the consideration for not contributing into the solution.

The equations in the system (4.12) are elliptic equations in the domain of local coordinates  $\Omega$  of the type  $A_1[q] = F$ . All the functions are assumed to be periodic in  $\Omega$ , as the local film thickness  $h_1$  is periodic. By integrating both sides of such equation and applying Green formula (Bayada, 1989) it is easy to show that the necessary condition for a periodic solution to exist is

$$A_1[q] = F \Rightarrow \int_{\Omega} F(\xi, \psi) d\xi d\psi = 0$$

$q, F - \text{periodic with period } |\Omega|$

(4.13)

From the Equation  $A_1[p_0] = 0$  in the system (4.12) it follows, that  $p_0$  must be constant, i.e.

$$p_0(x, y, \xi, \psi) = p_0(x, y)$$

$$\frac{\partial p_0}{\partial \xi} = \frac{\partial p_0}{\partial \psi} \equiv 0$$
(4.14)

In some papers, e.g. Kane and Bou-Said (2004) and Almqvist and Dasht (2006) this statement is taken as an assumption but it is actually a consequence of the first equation in the system (4.12).

According to (4.13) the necessary condition for the second equation in the system (4.12) to exist is that

$$\int_{\Omega} \{B^{\xi} \cos\theta - B^{\psi} \sin\theta - A_2[p_0]\} d\xi d\psi = 0$$
(4.15)

The condition for existence of the third equation in system (4.12) is considered later. Equation (4.15) is equivalent to:

$$\underbrace{\int_{\Omega} \left\{ \frac{\partial}{\partial \xi} \left( h^3 \frac{\partial p_0}{\partial x} \right) + \frac{\partial}{\partial \psi} \left( h^3 \frac{\partial p_0}{\partial y} \right) \right\} d\xi d\psi}_{=0} + \underbrace{\int_{\Omega} \left\{ -\lambda \frac{\partial(h)}{\partial \xi} \cos\theta + \lambda \frac{\partial(h)}{\partial \psi} \sin\theta \right\} d\xi d\psi}_{=0} +$$

$$\int_{\Omega} \underbrace{\left\{ \frac{\partial}{\partial x} \left( h^3 \frac{\partial p_0}{\partial \xi} \right) + \frac{\partial}{\partial y} \left( h^3 \frac{\partial p_0}{\partial \psi} \right) \right\} d\xi d\psi}_{=0} = 0$$

The last term is equal to zero because of (4.14) whereas the first two integrals are zero because of the periodicity of  $h$  in the coordinates  $(\xi, \psi)$ .

### Section 4.3 Periodic roughness and two-scale expansion

The second equation in system (4.12) has the following full form:

$$\begin{aligned} & \frac{\partial}{\partial \xi} \left( h^3 \frac{\partial p_1}{\partial \xi} \right) + \frac{\partial}{\partial \psi} \left( h^3 \frac{\partial p_1}{\partial \psi} \right) + \frac{\partial}{\partial \xi} \left( h^3 \frac{\partial p_0}{\partial x} \right) + \frac{\partial}{\partial \psi} \left( h^3 \frac{\partial p_0}{\partial y} \right) + \frac{\partial}{\partial x} \left( h^3 \frac{\partial p_0}{\partial \xi} \right) + \frac{\partial}{\partial y} \left( h^3 \frac{\partial p_0}{\partial \psi} \right) \\ & = \lambda \frac{\partial(h)}{\partial \xi} \cos\theta - \lambda \frac{\partial(h)}{\partial \psi} \sin\theta \end{aligned}$$

Bearing in mind Equation (4.14) and the fact that  $\frac{\partial}{\partial \xi} \left( \frac{\partial p_0}{\partial x} \right) \equiv \frac{\partial}{\partial x} \left( \frac{\partial p_0}{\partial \xi} \right) \equiv 0$  it yields

$$\frac{\partial}{\partial \xi} \left( h^3 \frac{\partial p_1}{\partial \xi} \right) + \frac{\partial}{\partial \psi} \left( h^3 \frac{\partial p_1}{\partial \psi} \right) + \frac{\partial h^3}{\partial \xi} \frac{\partial p_0}{\partial x} + \frac{\partial h^3}{\partial \psi} \frac{\partial p_0}{\partial y} = \lambda \frac{\partial(h)}{\partial \xi} \cos\theta - \lambda \frac{\partial(h)}{\partial \psi} \sin\theta \quad (4.16)$$

Equation (4.16) connects the local pressure  $p_1$  with the global pressure  $p_0$ . Note that  $p_1$  is presented in the frame of the local Reynolds equation  $A_1[p_1]$ . To be able to uncouple local and global pressures the following auxiliary functions  $\chi_1, \chi_2, \chi_3, \chi_4$  are introduced as the solutions of the local problem:

$$A_1[\chi_1] = -\frac{\partial h^3}{\partial \xi} \quad A_1[\chi_2] = -\frac{\partial h^3}{\partial \psi} \quad A_1[\chi_3] = \frac{\partial h}{\partial \xi} \quad A_1[\chi_4] = \frac{\partial h}{\partial \psi} \quad (4.17)$$

The functions  $\chi_1, \chi_2, \chi_3, \chi_4$  are assumed to be periodic.

The physical meaning of the solutions function  $\chi_1$  and  $\chi_2$  is the reduction of the gap between the global smooth surfaces due to presence of the roughness on the local scale. The reduced gap creates obstruction for the Poiseuille flow on the local scale. The values of  $\chi_1$  and  $\chi_2$  are measured in meters in SI units. The physical meaning of the auxiliary functions  $\chi_3$  and  $\chi_4$  is that they introduce the change in geometry due to presence of roughness in so far as it affects the Couette flow in the local representative cell caused by the motion of global surfaces.

Substituting (4.17) into (4.16) yields

$$A_1[p_1] - A_1[\chi_1] \frac{\partial p_0}{\partial x} - A_1[\chi_2] \frac{\partial p_0}{\partial y} = \lambda A_1[\chi_3] \cos\theta - \lambda A_1[\chi_4] \sin\theta$$

Bearing in mind that the operator  $A_1$  is linear, and also the fact that  $A_1$  is an operator in the local coordinates  $(\xi, \psi)$  only

$$A_1 \left[ p_1 - \chi_1 \frac{\partial p_0}{\partial x} - \chi_2 \frac{\partial p_0}{\partial y} - \lambda \chi_3 \cos\theta + \lambda \chi_4 \sin\theta \right] = 0$$

From this it follows that

$$\begin{aligned} p_1 - \chi_1 \frac{\partial p_0}{\partial x} - \chi_2 \frac{\partial p_0}{\partial y} - \lambda \chi_3 \cos\theta + \lambda \chi_4 \sin\theta &= C(x, y) \Leftrightarrow \\ p_1 &= \chi_1 \frac{\partial p_0}{\partial x} + \chi_2 \frac{\partial p_0}{\partial y} + \lambda \chi_3 \cos\theta - \lambda \chi_4 \sin\theta + C(x, y) \end{aligned} \quad (4.18)$$

This relation connects the local pressure  $p_1$  with the global pressure  $p_0$ . Note that in a number of papers e.g. Kane and Bou-Said (2004) the statement (4.18) is *postulated to exist*, and  $C(x,y)$  is assumed to be 0.

From (4.18) the partial derivatives can be calculated:

$$\begin{aligned}\frac{\partial p_1}{\partial \xi} &= \frac{\partial \chi_1}{\partial \xi} \frac{\partial p_0}{\partial x} + \frac{\partial \chi_2}{\partial \xi} \frac{\partial p_0}{\partial y} + \lambda \frac{\partial \chi_3}{\partial \xi} \cos\theta - \lambda \frac{\partial \chi_4}{\partial \xi} \sin\theta \\ \frac{\partial p_1}{\partial \psi} &= \frac{\partial \chi_1}{\partial \psi} \frac{\partial p_0}{\partial x} + \frac{\partial \chi_2}{\partial \psi} \frac{\partial p_0}{\partial y} + \lambda \frac{\partial \chi_3}{\partial \psi} \cos\theta - \lambda \frac{\partial \chi_4}{\partial \psi} \sin\theta\end{aligned}\tag{4.19}$$

Now returning to the third equation in the system (4.12), which is shown below for convenience:

$$A_1[p_2] = B^x \cos\theta - B^y \sin\theta - A_2[p_1] - A_3[p_0]\tag{4.20}$$

the necessary requirement for the solution of (4.20) to exist is similar to (4.15):

$$\int_{\Omega} \{B^x \cos\theta - B^y \sin\theta - A_2[p_1] - A_3[p_0]\} d\xi d\psi = 0\tag{4.21}$$

Substituting the expression for  $p_1$  of Equation (4.18) into Equation (4.21), with all terms multiplied by -1 for convenience, gives:

$$\int_{\Omega} \left( \underbrace{\frac{\partial}{\partial \xi} \left( h^3 \frac{\partial p_1}{\partial x} \right) + \frac{\partial}{\partial \psi} \left( h^3 \frac{\partial p_1}{\partial y} \right)}_{***} + \frac{\partial}{\partial x} \left( h^3 \frac{\partial p_1}{\partial \xi} \right) + \frac{\partial}{\partial y} \left( h^3 \frac{\partial p_1}{\partial \psi} \right) \right) d\xi d\psi = 0$$

$$\left( + \frac{\partial}{\partial x} \left( h^3 \frac{\partial p_0}{\partial x} \right) + \frac{\partial}{\partial y} \left( h^3 \frac{\partial p_0}{\partial y} \right) - \lambda \frac{\partial h}{\partial x} \cos\theta + \lambda \frac{\partial h}{\partial y} \sin\theta \right) d\xi d\psi = 0\tag{4.22}$$

Note that the term (\*\*\*) can be omitted as

$$\int_{\Omega} \left[ \frac{\partial}{\partial \xi} \left( h^3 \frac{\partial p_1}{\partial x} \right) + \frac{\partial}{\partial \psi} \left( h^3 \frac{\partial p_1}{\partial y} \right) \right] d\xi d\psi = 0$$

because of the periodicity of  $h$  and  $p_1$  in  $\Omega$ . Substituting (4.19) into (4.22) yields:

$$\int_{\Omega} \left\{ \begin{aligned} &\frac{\partial}{\partial x} \left[ h^3 \left( \frac{\partial \chi_1}{\partial \xi} \frac{\partial p_0}{\partial x} + \frac{\partial \chi_2}{\partial \xi} \frac{\partial p_0}{\partial y} + \lambda \frac{\partial \chi_3}{\partial \xi} \cos\theta - \lambda \frac{\partial \chi_4}{\partial \xi} \sin\theta \right) \right] \\ &+ \frac{\partial}{\partial y} \left[ h^3 \left( \frac{\partial \chi_1}{\partial \psi} \frac{\partial p_0}{\partial x} + \frac{\partial \chi_2}{\partial \psi} \frac{\partial p_0}{\partial y} + \lambda \frac{\partial \chi_3}{\partial \psi} \cos\theta - \lambda \frac{\partial \chi_4}{\partial \psi} \sin\theta \right) \right] \\ &+ \frac{\partial}{\partial x} \left( h^3 \frac{\partial p_0}{\partial x} \right) + \frac{\partial}{\partial y} \left( h^3 \frac{\partial p_0}{\partial y} \right) - \lambda \frac{\partial h}{\partial x} \cos\theta + \lambda \frac{\partial h}{\partial y} \sin\theta \end{aligned} \right\} d\xi d\psi = 0$$

Taking into account that the integration with respect to  $(\xi, \psi)$  is independent of differentiation with respect to  $(x,y)$  the order of integration and differentiation operations can be interchanged.

### Section 4.3 Periodic roughness and two-scale expansion

$$\begin{aligned}
& \frac{\partial}{\partial x} \left\{ \int_{\Omega} h^3 \left[ \frac{\partial p_0}{\partial x} \frac{\partial \chi_1}{\partial \xi} + \frac{\partial p_0}{\partial y} \frac{\partial \chi_2}{\partial \xi} + \lambda \frac{\partial \chi_3}{\partial \xi} \cos \theta - \lambda \frac{\partial \chi_4}{\partial \xi} \sin \theta \right] d\Omega \right\} \\
& + \frac{\partial}{\partial y} \left\{ \int_{\Omega} h^3 \left[ \frac{\partial p_0}{\partial x} \frac{\partial \chi_1}{\partial \psi} + \frac{\partial p_0}{\partial y} \frac{\partial \chi_2}{\partial \psi} + \lambda \frac{\partial \chi_3}{\partial \psi} \cos \theta - \lambda \frac{\partial \chi_4}{\partial \psi} \sin \theta \right] d\Omega \right\} \\
& + \frac{\partial}{\partial x} \left( \int_{\Omega} h^3 \frac{\partial p_0}{\partial x} d\Omega \right) + \frac{\partial}{\partial y} \left( \int_{\Omega} h^3 \frac{\partial p_0}{\partial y} d\Omega \right) = \lambda \int_{\Omega} \frac{\partial h}{\partial x} d\Omega \cos \theta - \lambda \int_{\Omega} \frac{\partial h}{\partial y} d\Omega \sin \theta
\end{aligned}$$

Rearranging the terms according to the differentiation involved:

$$\begin{aligned}
& \frac{\partial}{\partial x} \left( \int_{\Omega} h^3 \frac{\partial p_0}{\partial x} d\Omega \right) + \frac{\partial}{\partial x} \left\{ \int_{\Omega} h^3 \left[ \frac{\partial p_0}{\partial x} \frac{\partial \chi_1}{\partial \xi} + \frac{\partial p_0}{\partial y} \frac{\partial \chi_2}{\partial \xi} \right] d\Omega \right\} \\
& + \frac{\partial}{\partial y} \left( \int_{\Omega} h^3 \frac{\partial p_0}{\partial y} d\Omega \right) + \frac{\partial}{\partial y} \left\{ \int_{\Omega} h^3 \left[ \frac{\partial p_0}{\partial x} \frac{\partial \chi_1}{\partial \psi} + \frac{\partial p_0}{\partial y} \frac{\partial \chi_2}{\partial \psi} \right] d\Omega \right\} \\
& = \lambda \int_{\Omega} \frac{\partial h}{\partial x} d\Omega \cos \theta - \frac{\partial}{\partial x} \left\{ \int_{\Omega} h^3 \left[ \lambda \frac{\partial \chi_3}{\partial \xi} \cos \theta - \lambda \frac{\partial \chi_4}{\partial \xi} \sin \theta \right] d\Omega \right\} \\
& - \lambda \int_{\Omega} \frac{\partial h}{\partial y} d\Omega \sin \theta - \frac{\partial}{\partial y} \left\{ \int_{\Omega} h^3 \left[ \lambda \frac{\partial \chi_3}{\partial \psi} \cos \theta - \lambda \frac{\partial \chi_4}{\partial \psi} \sin \theta \right] d\Omega \right\}
\end{aligned}$$

Collecting the terms having the same derivatives of pressure:

$$\begin{aligned}
& \frac{\partial}{\partial x} \left\{ \int_{\Omega} h^3 \left[ \frac{\partial p_0}{\partial x} \left( 1 + \frac{\partial \chi_1}{\partial \xi} \right) \right] d\Omega \right\} + \frac{\partial}{\partial x} \left\{ \int_{\Omega} h^3 \left[ \frac{\partial p_0}{\partial y} \frac{\partial \chi_2}{\partial \xi} \right] d\Omega \right\} \\
& + \frac{\partial}{\partial y} \left\{ \int_{\Omega} h^3 \left[ \frac{\partial p_0}{\partial x} \frac{\partial \chi_1}{\partial \psi} \right] d\Omega \right\} + \frac{\partial}{\partial y} \left\{ \int_{\Omega} h^3 \left[ \left( \frac{\partial \chi_2}{\partial \psi} + 1 \right) \frac{\partial p_0}{\partial y} \right] d\Omega \right\} \\
& = \lambda \frac{\partial}{\partial x} \left\{ \int_{\Omega} h \cos \theta - h^3 \left[ \frac{\partial \chi_3}{\partial \xi} \cos \theta - \frac{\partial \chi_4}{\partial \xi} \sin \theta \right] d\Omega \right\} \\
& - \frac{\partial}{\lambda \partial y} \left\{ \int_{\Omega} h \sin \theta + h^3 \left[ \frac{\partial \chi_3}{\partial \psi} \cos \theta - \frac{\partial \chi_4}{\partial \psi} \sin \theta \right] d\Omega \right\}
\end{aligned}$$

Using the fact that  $p_0$  is a function of (x,y) only all  $p_0$  entries can be removed from being under the integration sign:

$$\begin{aligned}
& \frac{\partial}{\partial x} \left\{ \int_{\Omega} h^3 \left( 1 + \frac{\partial \chi_1}{\partial \xi} \right) d\Omega \frac{\partial p_0}{\partial x} \right\} + \frac{\partial}{\partial x} \left\{ \int_{\Omega} h^3 \frac{\partial \chi_2}{\partial \xi} d\Omega \frac{\partial p_0}{\partial y} \right\} \\
& + \frac{\partial}{\partial y} \left\{ \int_{\Omega} h^3 \frac{\partial \chi_1}{\partial \psi} d\Omega \frac{\partial p_0}{\partial x} \right\} + \frac{\partial}{\partial y} \left\{ \int_{\Omega} h^3 \left( \frac{\partial \chi_2}{\partial \psi} + 1 \right) d\Omega \frac{\partial p_0}{\partial y} \right\} \\
& = \lambda \frac{\partial}{\partial x} \left\{ \int_{\Omega} h \cos \theta - h^3 \left[ \frac{\partial \chi_3}{\partial \xi} \cos \theta - \frac{\partial \chi_4}{\partial \xi} \sin \theta \right] d\Omega \right\} \\
& - \frac{\partial}{\partial y} \left\{ \int_{\Omega} h \sin \theta + h^3 \left[ \lambda \frac{\partial \chi_3}{\partial \psi} \cos \theta - \lambda \frac{\partial \chi_4}{\partial \psi} \sin \theta \right] d\Omega \right\}
\end{aligned}$$

Scaling by the global part of the geometry  $h_0$  and separating the entries which represent the effect of local roughness:

$$\begin{aligned}
 & \frac{\partial}{\partial x} \left\{ h_0^3 \left[ \int_{\Omega} \frac{h^3}{h_0^3} \left( 1 + \frac{\partial \chi_1}{\partial \xi} \right) d\Omega \right] \frac{\partial p_0}{\partial x} \right\} + \frac{\partial}{\partial y} \left\{ h_0^3 \left[ \int_{\Omega} \frac{h^3}{h_0^3} \frac{\partial \chi_2}{\partial \xi} d\Omega \right] \frac{\partial p_0}{\partial y} \right\} \\
 & + \frac{\partial}{\partial y} \left\{ h_0^3 \left[ \int_{\Omega} \frac{h^3}{h_0^3} \frac{\partial \chi_1}{\partial \psi} d\Omega \right] \frac{\partial p_0}{\partial x} \right\} + \frac{\partial}{\partial x} \left\{ h_0^3 \left[ \int_{\Omega} \frac{h^3}{h_0^3} \left( \frac{\partial \chi_2}{\partial \psi} + 1 \right) d\Omega \right] \frac{\partial p_0}{\partial y} \right\} = \\
 & = \lambda \frac{\partial}{\partial x} \left\{ h_0 \left[ \int_{\Omega} \frac{h}{h_0} - \frac{h^3}{h_0} \frac{\partial \chi_3}{\partial \xi} d\Omega \right] \cos\theta + h_0 \left[ \int_{\Omega} \frac{h^3}{h_0} \frac{\partial \chi_4}{\partial \xi} d\Omega \right] \sin\theta \right\} \\
 & - \frac{\partial}{\partial y} \left\{ h_0 \left[ \int_{\Omega} \frac{h}{h_0} - \frac{h^3}{h_0} \frac{\partial \chi_4}{\partial \psi} d\Omega \right] \sin\theta + h_0 \left[ \int_{\Omega} \frac{h^3}{h_0} \frac{\partial \chi_3}{\partial \psi} d\Omega \right] \cos\theta \right\}
 \end{aligned} \tag{4.23}$$

#### 4.4 Flow factors

In this section eight scalar functions called flow factors are introduced as defined in Equations (4.24) and (4.25):

$$\begin{aligned}
 a_{11}(h_0) &= \int_{\Omega} \frac{h^3}{h_0^3} \left( 1 + \frac{\partial \chi_1}{\partial \xi} \right) d\Omega; & a_{12}(h_0) &= \int_{\Omega} \frac{h^3}{h_0^3} \frac{\partial \chi_2}{\partial \xi} d\Omega; \\
 a_{21}(h_0) &= \int_{\Omega} \frac{h^3}{h_0^3} \frac{\partial \chi_1}{\partial \psi} d\Omega; & a_{22}(h_0) &= \int_{\Omega} \frac{h^3}{h_0^3} \left( 1 + \frac{\partial \chi_2}{\partial \psi} \right) d\Omega
 \end{aligned} \tag{4.24}$$

$$\begin{aligned}
 b_{11}(h_0) &= \int_{\Omega} \left( \frac{h}{h_0} - \frac{h^3}{h_0} \frac{\partial \chi_3}{\partial \xi} \right) d\Omega; & b_{12}(h_0) &= \int_{\Omega} \frac{h^3}{h_0} \frac{\partial \chi_4}{\partial \xi} d\Omega; \\
 b_{21}(h_0) &= \int_{\Omega} \frac{h^3}{h_0} \frac{\partial \chi_3}{\partial \psi} d\Omega; & b_{22}(h_0) &= \int_{\Omega} \left( \frac{h}{h_0} - \frac{h^3}{h_0} \frac{\partial \chi_4}{\partial \psi} \right) d\Omega
 \end{aligned} \tag{4.25}$$

After substituting these functions Equation (4.23) takes the following form:

$$\begin{aligned}
 & \frac{\partial}{\partial x} \left\{ h_0^3 a_{11} \frac{\partial p_0}{\partial x} + h_0^3 a_{12} \frac{\partial p_0}{\partial y} \right\} + \frac{\partial}{\partial y} \left\{ h_0^3 a_{21} \frac{\partial p_0}{\partial x} + h_0^3 a_{22} \frac{\partial p_0}{\partial y} \right\} \\
 & = \lambda \frac{\partial}{\partial x} \{ h_0 b_{11} \cos\theta + h_0 b_{12} \sin\theta \} - \lambda \frac{\partial}{\partial y} \{ h_0 b_{21} \cos\theta + h_0 b_{22} \sin\theta \}
 \end{aligned} \tag{4.26}$$

which is called the *homogenised equation*.

From comparing the homogenised Equation (4.26) with the original one **Error! Reference source not found.** it becomes clear that the flow factors act as modifiers of the flow. The functions (4.24) modify the terms involved in the Poiseuille flow and are called *Poiseuille flow factors* whereas functions (4.25) modify the terms involved in the

## Section 4.5 Flow factors for oblique roughness

Couette flow and are called *Couette flow factors*. In other papers they are called pressure and shear flow factors respectively, e.g. Patir and Cheng (1979) Almquist and Dasht (2006).

In addition, the homogenised equation contains cross terms, i.e. the variation of the flow in X direction caused by the pressure gradient in Y direction and vice versa. The physical meaning of these terms is the additional flow created by the presence of the local asperities. This also applies to the Couette flow: additional flow caused by the motion of the surfaces can be diverted by the local asperities. These effects are qualified by  $a_{12}$  and  $a_{21}$ , and  $b_{12}$  and  $b_{21}$  respectively.

In order to maintain the flow factors non dimensional all the integrations can be replaced by averaging over the  $\Omega$  domain without violating the homogenised Equation (4.26):

$$\begin{aligned} a_{11}(h_0) &= \frac{1}{|\Omega|} \int_{\Omega} \frac{h^3}{h_0^3} \left(1 + \frac{\partial \chi_1}{\partial \xi}\right) d\Omega; & a_{12}(h_0) &= \frac{1}{|\Omega|} \int_{\Omega} \frac{h^3}{h_0^3} \frac{\partial \chi_2}{\partial \xi} d\Omega; \\ a_{21}(h_0) &= \frac{1}{|\Omega|} \int_{\Omega} \frac{h^3}{h_0^3} \frac{\partial \chi_1}{\partial \psi} d\Omega; & a_{22}(h_0) &= \frac{1}{|\Omega|} \int_{\Omega} \frac{h^3}{h_0^3} \left(1 + \frac{\partial \chi_2}{\partial \psi}\right) d\Omega \end{aligned} \quad (4.27)$$

$$\begin{aligned} b_{11}(h_0) &= \frac{1}{|\Omega|} \int_{\Omega} \left(\frac{h}{h_0} - \frac{h^3}{h_0} \frac{\partial \chi_3}{\partial \xi}\right) d\Omega; & b_{12}(h_0) &= \frac{1}{|\Omega|} \int_{\Omega} \frac{h^3}{h_0} \frac{\partial \chi_4}{\partial \xi} d\Omega; \\ b_{21}(h_0) &= \frac{1}{|\Omega|} \int_{\Omega} \frac{h^3}{h_0} \frac{\partial \chi_3}{\partial \psi} d\Omega; & b_{22}(h_0) &= \frac{1}{|\Omega|} \int_{\Omega} \left(\frac{h}{h_0} - \frac{h^3}{h_0} \frac{\partial \chi_4}{\partial \psi}\right) d\Omega \end{aligned} \quad (4.28)$$

## 4.5 Flow factors for oblique roughness

In the previous section the flow factors have been calculated for the system of coordinates coinciding with the axis of periodicity. The direction of motion of the surfaces was however not coincident with the axes of periodicity of the surface roughness. In this section the flow factors are calculated in the system of coordinates where the axes coincide with the entrainment and transverse directions. These flow factors are then calculated in the axis of periodicity and the direction of motion is defined by applying the rotational formulae to the flow factors. It can be used e.g. for

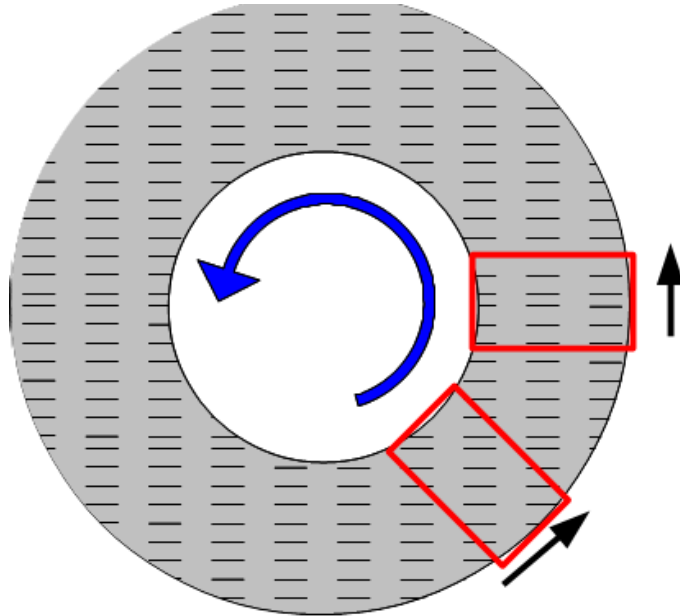


Figure 4.6 The rough surface of a thrust washer prepared by uni-directional grinding.. The counter surface is subjected to the counter clock wise circular motion. The 2 red squares represent the areas where the same roughness features are rotated at different angles relative to the motion direction

studying the effect of the oblique roughness with various angle of rotation on the pressure distribution in the system with the same direction of motion. The flow factors can also be applied to the systems where the roughness profile rotates with respect to the direction of motion, e.g. in the case of thrust washer (see Figure 4.6) with roughness created as a result of uni-directional grinding.

Consider the case of  $(X,Y)$  coordinates corresponding to the axis system which is aligned with the direction of periodicity, and  $(x,y)$  being those aligned with the entrainment and transverse directions as shown in Figure 4.7 .

If the angle between the axes of the systems  $(X,Y)$  and  $(x,y)$  is equal to  $\theta$ , then the homogenised equation defining the problem in  $(X,Y)$  is

$$\begin{aligned} & \frac{\partial}{\partial X} \left\{ h_0^3 a_{11} \frac{\partial p_0}{\partial X} + h_0^3 a_{12} \frac{\partial p_0}{\partial Y} \right\} + \frac{\partial}{\partial Y} \left\{ h_0^3 a_{21} \frac{\partial p_0}{\partial X} + h_0^3 a_{22} \frac{\partial p_0}{\partial Y} \right\} \\ & = \lambda \frac{\partial}{\partial X} \{ h_0 b_{11} \cos\theta + h_0 b_{12} \sin\theta \} - \lambda \frac{\partial}{\partial Y} \{ h_0 b_{21} \cos\theta + h_0 b_{22} \sin\theta \} \end{aligned} \quad (4.29)$$

which is identical to (4.26) with the only difference that it is solved in  $(X,Y)$  coordinates.

In order to get the solution in  $(x,y)$  coordinates, which are aligned with the entrainment and transverse directions then the rotational formulae are applied:

$$\begin{cases} X(x,y) = x \cos\theta + y \sin\theta \\ Y(x,y) = -x \sin\theta + y \cos\theta \end{cases} \Leftrightarrow \begin{cases} y = X \sin\theta + Y \cos\theta \\ x = X \cos\theta - Y \sin\theta \end{cases} \quad (4.30)$$

## Section 4.5 Flow factors for oblique roughness

The derivatives are then modified by the following rules:

$$\begin{aligned}\frac{\partial f(x(X,Y),y(X,Y))}{\partial X} &= \frac{\partial f}{\partial x} \frac{\partial x}{\partial X} + \frac{\partial f}{\partial y} \frac{\partial y}{\partial X} = \frac{\partial f}{\partial x} \cos\theta + \frac{\partial f}{\partial y} \sin\theta \\ \frac{\partial f(x(X,Y),y(X,Y))}{\partial Y} &= \frac{\partial f}{\partial x} \frac{\partial x}{\partial Y} + \frac{\partial f}{\partial y} \frac{\partial y}{\partial Y} = -\frac{\partial f}{\partial x} \sin\theta + \frac{\partial f}{\partial y} \cos\theta\end{aligned}\quad (4.31)$$

for every function  $f(X,Y)$ .

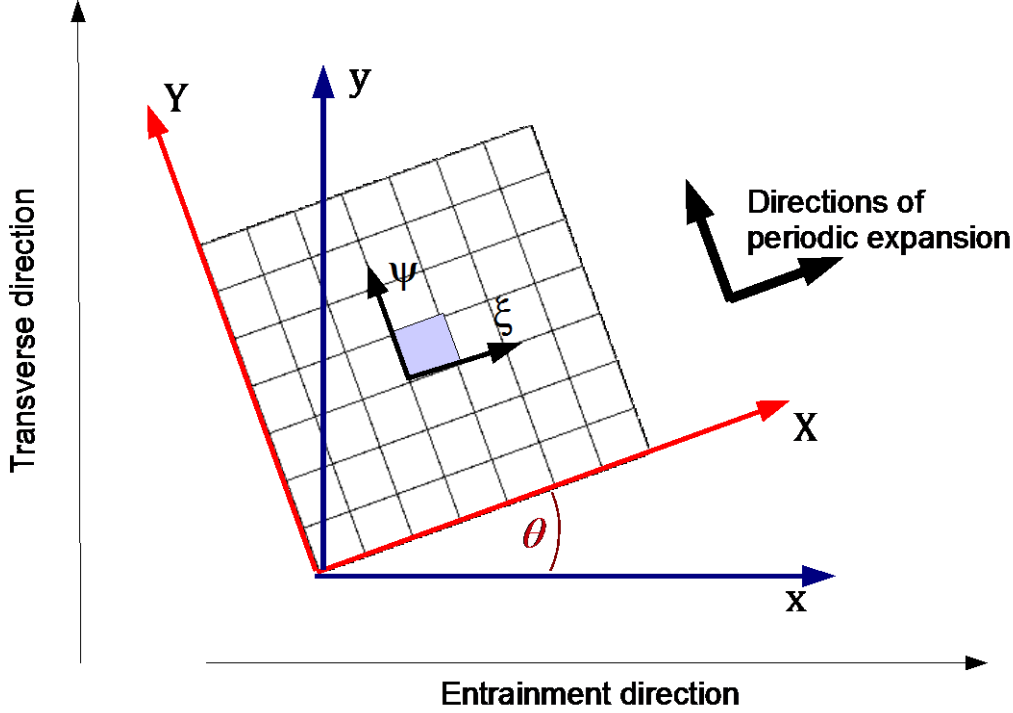


**Figure 4.7** Coordinates  $X,Y$  correspond to the system aligned with the directions of periodicity whereas  $x,y$  to the entrainment and transverse directions.

First consider modifying the derivatives in the Equation (4.29) according to the differentiation rules (4.31):

$$\begin{aligned}& \lambda \frac{\partial}{\partial x} \{h_0 [b_{11} \cos\theta + b_{12} \sin\theta]\} \cos\theta + \lambda \frac{\partial}{\partial y} \{h_0 [b_{11} \cos\theta + b_{12} \sin\theta]\} \sin\theta \\ & - \lambda \frac{\partial}{\partial y} \{h_0 [b_{22} \sin\theta + b_{21} \cos\theta]\} \cos\theta + \lambda \frac{\partial}{\partial x} \{h_0 [b_{22} \sin\theta + b_{21} \cos\theta]\} \sin\theta \\ & = \frac{\partial}{\partial x} \left\{ h_0^3 a_{11} \left[ \frac{\partial p_0}{\partial x} \cos\theta + \frac{\partial p_0}{\partial y} \sin\theta \right] + h_0^3 a_{12} \left[ -\frac{\partial p_0}{\partial x} \sin\theta + \frac{\partial p_0}{\partial y} \cos\theta \right] \right\} \cos\theta + \\ & \frac{\partial}{\partial y} \left\{ h_0^3 a_{11} \left[ \frac{\partial p_0}{\partial x} \cos\theta + \frac{\partial p_0}{\partial y} \sin\theta \right] + h_0^3 a_{12} \left[ -\frac{\partial p_0}{\partial x} \sin\theta + \frac{\partial p_0}{\partial y} \cos\theta \right] \right\} \sin\theta \\ & - \frac{\partial}{\partial x} \left\{ h_0^3 a_{22} \left[ -\frac{\partial p_0}{\partial x} \sin\theta + \frac{\partial p_0}{\partial y} \cos\theta \right] + h_0^3 a_{21} \left[ \frac{\partial p_0}{\partial x} \cos\theta + \frac{\partial p_0}{\partial y} \sin\theta \right] \right\} \sin\theta + \\ & \frac{\partial}{\partial y} \left\{ h_0^3 a_{22} \left[ -\frac{\partial p_0}{\partial x} \sin\theta + \frac{\partial p_0}{\partial y} \cos\theta \right] + h_0^3 a_{21} \left[ \frac{\partial p_0}{\partial x} \cos\theta + \frac{\partial p_0}{\partial y} \sin\theta \right] \right\} \cos\theta\end{aligned}$$

Arranging sine and cosine products it becomes:

$$\lambda \frac{\partial}{\partial x} \{h_0 [b_{11} \cos^2\theta + b_{12} \sin\theta \cos\theta]\} + \lambda \frac{\partial}{\partial y} \{h_0 [b_{11} \sin\theta \cos\theta + b_{12} \sin^2\theta]\}$$

$$\begin{aligned}
 & -\lambda \frac{\partial}{\partial y} \{h_0 [b_{22} \sin\theta \cos\theta + b_{21} \cos^2\theta]\} + \lambda \frac{\partial}{\partial x} \{h_0 [b_{22} \sin^2\theta + b_{21} \sin\theta \cos\theta]\} = \\
 & \frac{\partial}{\partial x} \left\{ h_0^3 a_{11} \left[ \frac{\partial p_0}{\partial x} \cos^2\theta + \frac{\partial p_0}{\partial y} \sin\theta \cos\theta \right] + h_0^3 a_{12} \left[ -\frac{\partial p_0}{\partial x} \sin\theta \cos\theta + \frac{\partial p_0}{\partial y} \cos^2\theta \right] \right\} \\
 & + \frac{\partial}{\partial y} \left\{ h_0^3 a_{11} \left[ \frac{\partial p_0}{\partial x} \sin\theta \cos\theta + \frac{\partial p_0}{\partial y} \sin^2\theta \right] + h_0^3 a_{12} \left[ -\frac{\partial p_0}{\partial x} \sin^2\theta + \frac{\partial p_0}{\partial y} \sin\theta \cos\theta \right] \right\} \\
 & - \frac{\partial}{\partial x} \left\{ h_0^3 a_{22} \left[ -\frac{\partial p_0}{\partial x} \sin^2\theta + \frac{\partial p_0}{\partial y} \sin\theta \cos\theta \right] + h_0^3 a_{21} \left[ \frac{\partial p_0}{\partial x} \sin\theta \cos\theta + \frac{\partial p_0}{\partial y} \sin^2\theta \right] \right\} \\
 & + \frac{\partial}{\partial y} \left\{ h_0^3 a_{22} \left[ -\frac{\partial p_0}{\partial x} \sin\theta \cos\theta + \frac{\partial p_0}{\partial y} \cos^2\theta \right] + h_0^3 a_{21} \left[ \frac{\partial p_0}{\partial x} \cos^2\theta + \frac{\partial p_0}{\partial y} \sin\theta \cos\theta \right] \right\}
 \end{aligned}$$

Collecting coefficients then gives:

$$\begin{aligned}
 & \lambda \frac{\partial}{\partial x} \left\{ h_0 \underbrace{[b_{11} \cos^2\theta + b_{12} \sin\theta \cos\theta + b_{22} \sin^2\theta + b_{21} \sin\theta \cos\theta]}_{B_1} \right\} \\
 & + \lambda \frac{\partial}{\partial y} \left\{ h_0 \underbrace{[b_{11} \sin\theta \cos\theta + b_{12} \sin^2\theta - b_{22} \sin\theta \cos\theta - b_{21} \cos^2\theta]}_{B_2} \right\} \\
 & = \frac{\partial}{\partial x} \left\{ \underbrace{h_0^3 [a_{11} \cos^2\theta - a_{12} \sin\theta \cos\theta - a_{21} \sin\theta \cos\theta + a_{22} \sin^2\theta]}_{A_{11}} \frac{\partial p_0}{\partial x} \right. \\
 & \quad \left. + \underbrace{h_0^3 [a_{11} \sin\theta \cos\theta + a_{12} \cos^2\theta - a_{21} \sin^2\theta - a_{22} \sin\theta \cos\theta]}_{A_{12}} \frac{\partial p_0}{\partial y} \right\} + \\
 & \quad + \frac{\partial}{\partial y} \left\{ \underbrace{h_0^3 [a_{11} \sin\theta \cos\theta - a_{12} \sin^2\theta - a_{22} \sin\theta \cos\theta + a_{21} \cos^2\theta]}_{A_{21}} \frac{\partial p_0}{\partial x} \right. \\
 & \quad \left. + \underbrace{h_0^3 [a_{11} \sin^2\theta + a_{12} \sin\theta \cos\theta + a_{21} \sin\theta \cos\theta + a_{22} \cos^2\theta]}_{A_{22}} \frac{\partial p_0}{\partial y} \right\}
 \end{aligned} \tag{4.32}$$

The square bracket terms (under braced) in Equation (4.32) are the oblique flow factors  $A_{11}$ ,  $A_{12}$ ,  $A_{21}$ ,  $A_{22}$ ,  $B_1$  and  $B_2$  which are defined as:

$$\begin{aligned}
 A_{11} &= a_{11} \cos^2\theta - (a_{12} + a_{21}) \sin\theta \cos\theta + a_{22} \sin^2\theta \\
 A_{12} &= a_{12} \cos^2\theta + (a_{11} - a_{22}) \sin\theta \cos\theta - a_{21} \sin^2\theta \\
 A_{21} &= a_{21} \cos^2\theta + (a_{11} - a_{22}) \sin\theta \cos\theta - a_{12} \sin^2\theta \\
 A_{22} &= a_{11} \sin^2\theta + (a_{12} + a_{21}) \sin\theta \cos\theta + a_{22} \cos^2\theta \\
 B_1 &= b_{11} \cos^2\theta + (b_{12} + b_{21}) \sin\theta \cos\theta + b_{22} \sin^2\theta \\
 B_2 &= b_{12} \sin^2\theta + (b_{11} - b_{22}) \sin\theta \cos\theta - b_{21} \cos^2\theta
 \end{aligned} \tag{4.33}$$

Flow factors  $a_{11}$ ,  $a_{12}$ ,  $a_{21}$ ,  $a_{22}$ ,  $b_{11}$ ,  $b_{12}$ ,  $b_{21}$ ,  $b_{22}$  are calculated in the axis of periodicity as specified by (4.27) and (4.28).

With the oblique flow factors the homogenised Reynolds Equation (4.26) becomes

### Section 4.5 Flow factors for oblique roughness

$$\begin{aligned} \frac{\partial}{\partial x} \left\{ h_0^3 A_{11} \frac{\partial p_0}{\partial x} + h_0^3 A_{12} \frac{\partial p_0}{\partial y} \right\} + \frac{\partial}{\partial y} \left\{ h_0^3 A_{21} \frac{\partial p_0}{\partial x} + h_0^3 A_{22} \frac{\partial p_0}{\partial y} \right\} \\ = \lambda \frac{\partial}{\partial x} \{ h_0 B_1 \} + \lambda \frac{\partial}{\partial y} \{ h_0 B_2 \} \end{aligned} \quad (4.34)$$

Note, that the Ox axis coincides with the direction of motion, therefore no velocity component in the transverse direction should be present. The last term in the Equation (4.34) represents the flow in the transverse direction diverted by the oblique roughness feature (as shown schematically on Figure 4.8).

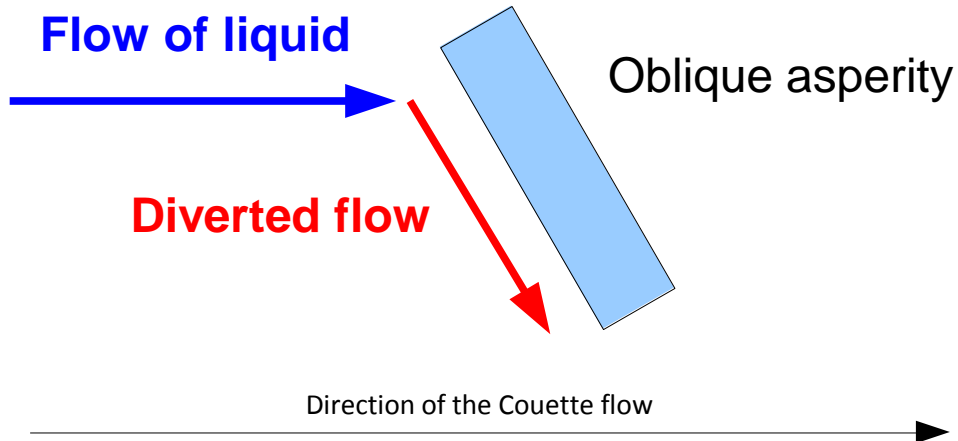


Figure 4.8 Diversion of the Couette flow by an oblique roughness feature

## 5 Evaluation of the flow factors

### 5.1 Solving the local problems

In order to calculate the flow factors the solutions of the local problems (4.17) are required. For convenience the full formulation of the local problems is provided below:

$$\begin{cases} \frac{\partial}{\partial \xi} \left\{ h^3 \frac{\partial \chi_1}{\partial \xi} \right\} + \frac{\partial}{\partial \psi} \left\{ h^3 \frac{\partial \chi_1}{\partial \psi} \right\} = - \frac{\partial (h^3)}{\partial \xi} \\ \frac{\partial}{\partial \xi} \left\{ h^3 \frac{\partial \chi_2}{\partial \xi} \right\} + \frac{\partial}{\partial \psi} \left\{ h^3 \frac{\partial \chi_2}{\partial \psi} \right\} = - \frac{\partial (h^3)}{\partial \psi} \\ \frac{\partial}{\partial \xi} \left\{ h^3 \frac{\partial \chi_3}{\partial \xi} \right\} + \frac{\partial}{\partial \psi} \left\{ h^3 \frac{\partial \chi_3}{\partial \psi} \right\} = \frac{\partial h}{\partial \xi} \\ \frac{\partial}{\partial \xi} \left\{ h^3 \frac{\partial \chi_4}{\partial \xi} \right\} + \frac{\partial}{\partial \psi} \left\{ h^3 \frac{\partial \chi_4}{\partial \psi} \right\} = \frac{\partial h}{\partial \psi} \end{cases} \quad (5.1)$$

The left hand side of all the equations for the local problem is exactly like Reynolds' equation defined on the local scale in the coordinates  $(\xi, \psi)$ . Note, that  $h$  is the total gap between the surfaces as defined by Equation (4.5). However, bearing in mind that the system is solved in local coordinates the only connection to the global coordinates  $(x, y)$  is the value of  $h_0(x, y)$ . Therefore the solutions obtained for  $\chi_1, \chi_2, \chi_3$ , and  $\chi_4$  can be considered as functions of  $(h_0, \xi, \psi)$ .

In the general case the analytic solution of Equations (5.1) is not available, however it is obtained in Sections 5.1.2 and 5.1.3 for  $\chi_1, \chi_3$  in the case of an extruded sinusoidal surface. In the following section the technique for solving the system (5.1) numerically is considered.

#### 5.1.1 Numerical solution

##### *Discretisation*

The left hand side of the equations from the system (5.1) is discretised using central differences. The second derivative terms are discretised using the values at the inter nodal points to maintain the conservation of flow. The sketch of the mesh points is shown in Figure 5.1.

For convenience the index of the local solution functions  $\chi_1, \chi_2, \chi_3, \chi_4$  is specified as the superscript:

$$\chi_1(i, j) \equiv \chi_{i,j}^{(1)}; \quad \chi_2(i, j) \equiv \chi_{i,j}^{(2)}; \quad \chi_3(i, j) \equiv \chi_{i,j}^{(3)}; \quad \chi_4(i, j) \equiv \chi_{i,j}^{(4)}$$

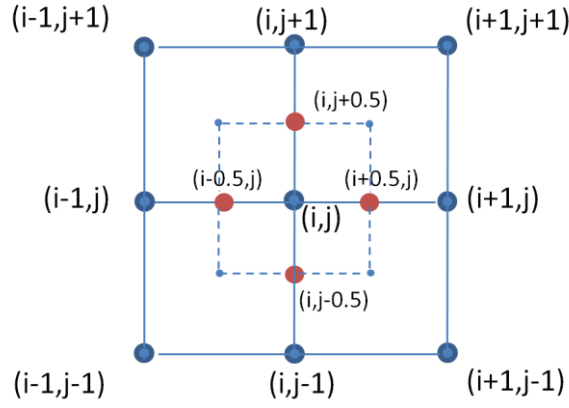


Figure 5.1 The nodes and inter nodal points used for the discretisation of the derivatives

The second derivative with respect to  $\xi$  is then discretised as follows:

$$\begin{aligned} \frac{\partial}{\partial \xi} \left( h^3 \frac{\partial \chi}{\partial \xi} \right) &= \frac{\left( h^3 \frac{\partial \chi}{\partial \xi} \right)_{i+0.5,j} - \left( h^3 \frac{\partial \chi}{\partial \xi} \right)_{i-0.5,j}}{\Delta \xi} \\ &= \frac{h_{i+0.5,j}^3 \frac{\chi_{i+1,j} - \chi_{i,j}}{\Delta \xi} - h_{i-0.5,j}^3 \frac{\chi_{i,j} - \chi_{i-1,j}}{\Delta \xi}}{\Delta \xi} \end{aligned} \quad (5.2)$$

The index of the  $\chi$  function is omitted as the same discretisation applies for all four functions. The value of a variable at the internodal point is assumed to be mean between the values of the two neighbouring nodes. In particular the values of  $h^3$  at the internodal points are:

$$h_{i+0.5}^3 = \frac{h_{i+1,j}^3 + h_{i,j}^3}{2}$$

The second derivative (5.2) then yields

$$\begin{aligned} \frac{\partial}{\partial \xi} \left( h^3 \frac{\partial \chi}{\partial \xi} \right) &= \frac{\frac{h_{i+1,j}^3 + h_{i,j}^3}{2} (\chi_{i+1,j} - \chi_{i,j}) - \frac{h_{i-1,j}^3 + h_{i,j}^3}{2} (\chi_{i,j} - \chi_{i-1,j})}{\Delta \xi^2} = \\ &= \frac{h_{i+1,j}^3 + h_{i,j}^3}{2\Delta \xi^2} \chi_{i+1,j} + \frac{h_{i-1,j}^3 + h_{i,j}^3}{2\Delta \xi^2} \chi_{i-1,j} - \frac{h_{i+1,j}^3 + 2h_{i,j}^3 + h_{i-1,j}^3}{2\Delta \xi^2} \chi_{i,j} \end{aligned}$$

Same applies to the second derivative with respect to  $\psi$ :

$$\frac{\partial}{\partial \psi} \left( h^3 \frac{\partial \chi}{\partial \psi} \right) = \frac{h_{i,j+1}^3 + h_{i,j}^3}{2\Delta \psi^2} \chi_{i,j+1} + \frac{h_{i,j-1}^3 + h_{i,j}^3}{2\Delta \psi^2} \chi_{i,j-1} - \frac{h_{i,j+1}^3 + 2h_{i,j}^3 + h_{i,j-1}^3}{2\Delta \psi^2} \chi_{i,j}$$

For the right hand sides the variation of the function between the two neighbouring inter nodal points is used as well, however, as the function is assumed to be linear between the nodes, it yields:

$$\frac{\partial h^3}{\partial \xi} = \frac{h_{i+0.5,j}^3 - h_{i-0.5,j}^3}{\Delta \xi} = \frac{h_{i+1,j}^3 - h_{i-1,j}^3}{2\Delta \xi}$$

The four equations of the system (5.1) are discretised in exactly the same way with the only difference being the right hand side (note that the multiplier 2 is cancelled everywhere):

$$\begin{aligned} & \frac{h_{i+1,j}^3 + h_{i,j}^3}{\Delta \xi^2} \chi_{i+1,j}^{(k)} + \frac{h_{i-1,j}^3 + h_{i,j}^3}{\Delta \xi^2} \chi_{i-1,j}^{(k)} + \frac{h_{i,j+1}^3 + h_{i,j}^3}{\Delta \psi^2} \chi_{i,j+1}^{(k)} + \frac{h_{i,j-1}^3 + h_{i,j}^3}{\Delta \psi^2} \chi_{i,j-1}^{(k)} \\ & - \left( \frac{h_{i+1,j}^3 + 2h_{i,j}^3 + h_{i-1,j}^3}{\Delta \xi^2} + \frac{h_{i,j+1}^3 + 2h_{i,j}^3 + h_{i,j-1}^3}{\Delta \psi^2} \right) \chi_{i,j}^{(k)} = E_{i,j}^{(k)} \end{aligned} \quad (5.3)$$

where  $k=1..4$  and the right hand sides corresponding to the functions  $\chi_1, \chi_2, \chi_3, \chi_4$  are

$$\begin{aligned} E_{i,j}^{(1)} &= -\frac{h_{i+1,j}^3 - h_{i-1,j}^3}{\Delta \xi}; \quad E_{i,j}^{(2)} = -\frac{h_{i,j+1}^3 - h_{i,j-1}^3}{\Delta \psi}; \\ E_{i,j}^{(3)} &= \frac{h_{i+1,j} - h_{i-1,j}}{\Delta \xi}; \quad E_{i,j}^{(4)} = \frac{h_{i,j+1} - h_{i,j-1}}{\Delta \psi} \end{aligned} \quad (5.4)$$

### *Gauss-Seidel iterative method*

Equations (5.3) can be treated as systems of linear equations with sparse matrix of coefficients. Indeed, the matrix would be 3-diagonal for a 1-dimensional case, and in a 2 dimensional case each row and each column have only 5 non zero components corresponding to the terms related to the neighbouring points. These systems can then be solved using the iterative Gauss-Seidel method.

The Gauss-Seidel method is based on presenting the value at the current node using the old values at the succeeding nodes and new values at the preceding nodes. The concept is schematically shown on Figure 5.2. The piece-wise algebraic formula for the new value at the point (i,j) is given below:

$$\chi_{i,j}^{new} = \frac{\frac{h_{i+1,j}^3 + h_{i,j}^3}{\Delta x^2} \chi_{i+1,j}^{old} + \frac{h_{i,j}^3 + h_{i-1,j}^3}{\Delta x^2} \chi_{i-1,j}^{new} + \frac{h_{i,j+1}^3 + h_{i,j}^3}{\Delta y^2} \chi_{i,j+1}^{old} + \frac{h_{i,j}^3 + h_{i,j-1}^3}{\Delta y^2} \chi_{i,j-1}^{new} - E_{i,j}^{(k)}}{\frac{h_{i+1,j}^3 + 2h_{i,j}^3 + h_{i-1,j}^3}{\Delta x^2} + \frac{h_{i,j+1}^3 + 2h_{i,j}^3 + h_{i,j-1}^3}{\Delta y^2}} \quad (5.5)$$

The Gauss Seidel method is faster than the traditional Jacobi iterative method in the case of sparse matrices, however, there is room for potential improvement of the algorithm for solving the local problems (5.1). The convergence of the numerical solution of the local problems is discussed in Section 5.1.1. The results obtained by

numerical technique are compared with the available analytical solutions obtained in Sections 5.1.2 and 5.1.3.

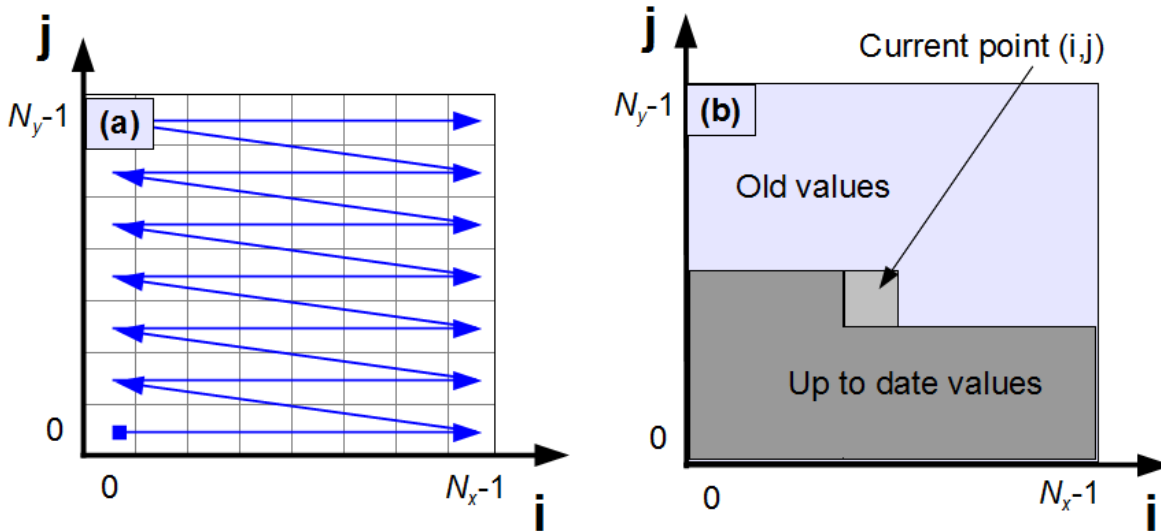


Figure 5.2 Schematic illustration of the Gauss-Seidel iterative method

### Boundary conditions

As described in Section 4.4, the solutions  $\chi^{(k)}$  of the local problems are assumed to be periodic in  $\Omega$ . Therefore the periodic boundary conditions can be applied provided that there is a point  $(\xi_0, \psi_0)$  in  $\Omega$  such that the value  $\chi^{(k)}(\xi_0, \psi_0)$  is known. Let  $\chi^{(k)}(\xi_0, \psi_0) = \chi_c$ , where  $\chi_c$  is a constant. Note however that the formulae for calculating the flow factors (4.27) and (4.28) use the derivatives of the  $\partial \chi^{(k)} / \partial \xi$  and  $\partial \chi^{(k)} / \partial \psi$  of the local solutions  $\chi^{(k)}$ . Therefore, the choice of the constant  $\chi_c$  does not affect the calculation of the flow factors in any way. Hence let  $\chi_c = 0$ .

Chapters 4 and 5 describe the general procedure for calculating the flow factors. As discussed the deflected shape of the rough surface obtained by means of the dry contact analysis may be used to take into account the effect of the deformed shape on the flow of lubricant. In such cases there is not flow in the areas of direct contact of the asperities. This adds a complication to the boundary conditions of the local problems. Indeed, the contact spots must be excluded from the solution and a no flow condition should be applied at the boundaries of the contact spots. In the current work, as well as in the works of Almqvist and Dasht (2006), Sahlin et al (2010a, 2010b) this issue is resolved by considering a small gap of  $10^{-9}$  m between the surfaces at the areas of direct contact. It is assumed that the flow through this gap is trivial and does not compromise the values of  $\chi_k$  in the area adjacent to the contacts.

### 5.1.2 Analytical solution for $\chi_1$ .

In this section the analytical solution is obtained for the first equation from system (5.1):

$$\frac{\partial}{\partial \xi} \left( h^3 \frac{\partial \chi_1}{\partial \xi} \right) + \frac{\partial}{\partial \psi} \left( h^3 \frac{\partial \chi_1}{\partial \psi} \right) = - \frac{\partial h^3}{\partial \xi} \quad (5.6)$$

First, let us define the surface as an extruded cosine wave:

$$h(x, y, \xi, \psi) = h_0(x, y) + h_r \cos \left( 2\pi \frac{\xi}{L} k \right) \quad (5.7)$$

where  $L$  is the length of the area of interest,  $h_r$  is the amplitude of the waviness and  $k$  is the number of waves across the area of interest.

Since extruded geometry is considered the solution is expected to be extruded as well. So there will be no variation with  $\psi$  and Equation (5.6) becomes:

$$\frac{\partial}{\partial \xi} \left( h^3 \frac{\partial \chi_1}{\partial \xi} \right) = - \frac{\partial h^3}{\partial \xi}$$

Integrating with respect to  $\xi$ :

$$h^3 \frac{\partial \chi_1}{\partial \xi} = -(h^3 - h_c^3)$$

where  $h_c^3$  is an integration constant and the cubed form is used for convenience. The equation can be written as

$$\frac{\partial \chi_1}{\partial \xi} = - \frac{(h^3 - h_c^3)}{h^3} \quad (5.8)$$

and finally integrated to give

$$\chi_1(\xi) = \chi_c - \int_0^\xi \frac{(h(s)^3 - h_c^3)}{h(s)^3} dt = \chi_c - \xi + h_c^3 \int_0^\xi \frac{ds}{h(s)^3} \quad (5.9)$$

where  $\chi_c$  is an additive integration constant and  $s$  is a dummy variable.

#### *Evaluating the integral*

The integral used in the equation can be transformed into the following form:

$$\int_0^{\xi} \frac{ds}{h^3} = \int_0^{\xi} \frac{ds}{\left[h_0 + h_r \cos\left(2\pi \frac{s}{L} k\right)\right]^3} = \left[t = 2\pi \frac{s}{L} k\right] = \frac{L}{2\pi k} \int_0^{2\pi \frac{\xi}{L} k} \frac{dt}{\left[h_0 + h_r \cos t\right]^3} =$$

$$\frac{L}{2\pi k h_r^3} \int_0^{2\pi \frac{\xi}{L} k} \left(\frac{h_0}{h_r} + \cos t\right)^{-3} dt = \left[\tau = \frac{h_0}{h_r}\right] = \frac{L}{2\pi k h_r^3} \int_0^{2\pi \frac{\xi}{L} k} \frac{dt}{(\tau + \cos t)^3}$$

The parameter  $\tau = h_0/h_r$  is introduced henceforth as the global film thickness relative to the amplitude of the local roughness. The square brackets “[ ]” in the sequence of equalities denote the condition used on which this sequence is continued.

The integral above is equivalent to the one calculated in Appendix A taking the dummy constant  $a = \tau$ . According to (A.12), this is equal to

$$\int_0^{\xi} \frac{ds}{h^3} = \frac{L}{2\pi k h_r^3} F\left(\tan\left(\pi \frac{\xi}{L} k\right)\right)$$

$$F(z) = (n+1)\pi F_1 + F_1 \arctan \frac{z}{m} + F_2 \frac{z}{[z^2 + m^2]} + F_3 \frac{z}{[z^2 + m^2]^2}$$
(5.10)

where

$$n = \left\lfloor \frac{\left(\frac{2\pi k \xi}{L} - \pi\right)}{2\pi} \right\rfloor; \quad m^2 = \left(\frac{\tau + 1}{\tau - 1}\right); \quad \tau = \frac{h_0}{h_r}$$

The brackets [ ] denote rounding down to the nearest interger value, which makes  $n$  the number of full periods within the current value of  $\xi$ : Note that for  $\xi=0$  the value of  $n = \lfloor -1/2 \rfloor = -1$  whereas for  $\xi=L$  the value of  $n = \lfloor k - 1/2 \rfloor = k - 1$ . The coefficients  $F_1, F_2, F_3$  are given by Equation (A.10) :

$$F_1 = \frac{2\tau^2 + 1}{(\tau - 1)^{2.5}(\tau + 1)^{2.5}}; \quad F_2 = -\frac{4\tau + 1}{(\tau - 1)^3(\tau + 1)^2}; \quad F_3 = \frac{2}{(\tau - 1)^4(\tau + 1)}$$
(5.11)

Equation (5.9) then yields:

$$\chi_1(\xi) = \chi_c - \xi + \frac{L h_c^3}{2\pi k h_r^3} F\left(\tan\left(\pi \frac{\xi}{L} k\right)\right)$$

where  $F(z) = (n+1)\pi F_1 + F_1 \arctan \frac{z}{m} + F_2 \frac{z}{[z^2 + m^2]} + F_3 \frac{z}{[z^2 + m^2]^2}$

(5.12)

*Boundary conditions*

The solution of the local problem  $\chi_1$  is assumed to be a periodic function. Therefore the periodic boundary conditions are applicable to the problem:

$$\chi_1(0) = \chi_1(L)$$

Substituting into (5.12)

$$\chi_1(0) = \chi_c + \frac{Lh_c^3}{2\pi kh_r^3}(n+1)\pi F_1 = \chi_c \quad (5.13)$$

The other terms are cancelled because for  $\xi=0$  the value of  $z=\tan(0)=0$  and  $n=\text{floor}(-1/2)=-1$ . Bearing in mind, that for  $\xi=L$  the value of  $z=\tan(\pi k)=0$  and  $n=\text{floor}(k-1/2)=k-1$ :

$$\chi_1(L) = \chi_c - L + \frac{Lh_c^3}{2h_r^3}F_1 \quad (5.14)$$

Equating (5.13) and (5.14) the periodic condition becomes:

$$\chi_c = \chi_c - L + \frac{Lh_c^3}{2h_r^3}F_1 \Leftrightarrow L = \frac{Lh_c^3}{2h_r^3}F_1 \Leftrightarrow h_c^3 = \frac{2h_r^3}{F_1}$$

Taking (5.11) into account:

$$h_c^3 = 2h_r^3 \frac{(\tau-1)^{2.5}(\tau+1)^{2.5}}{2\tau^2+1} \quad (5.15)$$

The second constant,  $\chi_c$  is not defined. As discussed in Section 5.1.1 defining of the additive constant is unnecessary because the derivatives of the local solutions are used for calculating the flow factors (4.19) and (4.24).

*Summary*

This section summarises the previous sections and gives the final formula for the  $\chi_1$  solution of the local problem (5.6) for the extruded cosine waviness defined by (5.7). Using the solution (5.12) and substituting the formulae (5.11) the analytical solution yields:

$$\chi_1(\xi) = \chi_c - \xi + \frac{L}{2\pi k} \frac{h_c^3}{h_r^3} \left\{ F_1 \left[ \pi(n+1) + \arctan \frac{z}{m} \right] + F_2 \frac{z}{[z^2+m^2]} + F_3 \frac{z}{[z^2+m^2]^2} \right\}$$

Where

$$z = \tan\left(\pi \frac{\xi}{L} k\right); \quad n = \left\lfloor \frac{k\xi}{L} - \frac{1}{2} \right\rfloor; \quad m^2 = \left(\frac{\tau + 1}{\tau - 1}\right); \quad h_c^3 = 2h_r^3 \frac{(\tau - 1)^{2.5} (\tau + 1)^{2.5}}{2\tau^2 + 1}$$

and the coefficients  $F_1$  to  $F_3$  are given by (5.11) Note that the brackets  $\lfloor \rfloor$  denote rounding down to the nearest integer value.

The expressions inside the curly brackets are non-dimensional and the solution  $\chi_1$  has the dimensions of metres.

### *Comparison of the analytical and numerical solutions*

The solution (5.17) allows a comparison to be made between the analytical solution and the solution obtained by numerical means as described in Section 5.1.1. The numerical solution was obtained on a square computational domain resolved in 64x64 mesh points. The analytical solution (5.17) was evaluated for 256 sampling points on the domain of the same size.

The surface geometry corresponds to the local roughness for the surface (5.7):

$$h(\xi, \psi) = h_0 + h_r \cos\left(2\pi \frac{\xi}{L} k\right)$$

and for the comparison the parameters given in Table 5.1 are used.

The geometry is shown in Figure 5.3, where the straight line illustrates the global film thickness  $h_0$  and the sinusoidal curve is the local roughness. Asperities are oriented upside down, so that the plane  $h(\xi, \psi)=0$  represents the smooth counterface.

The sequence of Figures 5.4-5.11 illustrates the comparison between the  $\chi_1$  obtained by analytical and numerical means for various global film thicknesses  $h_0$  given by Table 5.1. For convenience the total film thickness,  $h$ , is also plotted on every figure. The solution  $\chi_1$  starts from smooth sinusoidal function for high values of  $h_0$ . See e.g. the solution of  $\chi_1$  obtained for  $h_0=10\mu\text{m}$  which is plotted in Figure 5.4. As the value of the global film thickness  $h_0$  reduces the values of  $\chi_1$  cycles become progressively skewed in the direction opposite to the direction of motion as can be observed in Figures 5.4-5.9.

Table 5.1 Parameters used to formulate the local problems

Parameter	Description	Value	Units
$h_r$	Amplitude	1.0	$\mu\text{m}$
$h_0$	Global film thickness	10.0, 5.0; 2.0; 1.4;1.2; 1.1;1.0;0.9	$\mu\text{m}$
L	Length of the local domain ( $\Omega$ )	200	$\mu\text{m}$
W	Width of the local domain	200	$\mu\text{m}$
k	Number of waves per local cell	2	
N	Number of mesh points	64	
	Number of sampling points for analytical solution	256	

The solution of  $\chi_1$  systematically approaches the saw-toothed form corresponding to the limiting case of the analytic solution for  $h_0=1.001\mu\text{m}$  which is plotted on Figure 5.11. Note that the case of  $h_0=1.0\mu\text{m}$  corresponds to the contact of the surfaces. For an extruded surface this means the total blockage of the fluid flow which invalidates the formulation of the problem. The values of  $\chi_1$  obtained by analytical means are in perfect agreement with those obtained numerically for the whole range of  $h_0$  which is illustrated by the close fit of the markers on top of the analytical curves in Figures 5.4-5.11. The difference between the solutions is trivial and can be explained by the numerical inaccuracies.

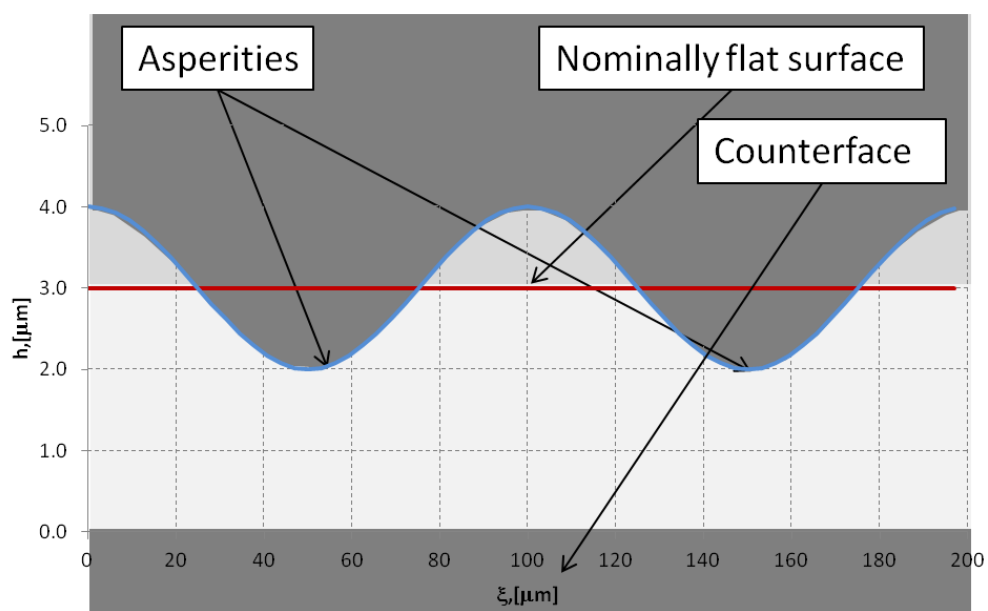


Figure 5.3 The local roughness (blue) and the mean line (red) of the extruded cosine surface with amplitude  $h_r=1.0\mu\text{m}$  and global film thickness  $h_0=3.0\mu\text{m}$

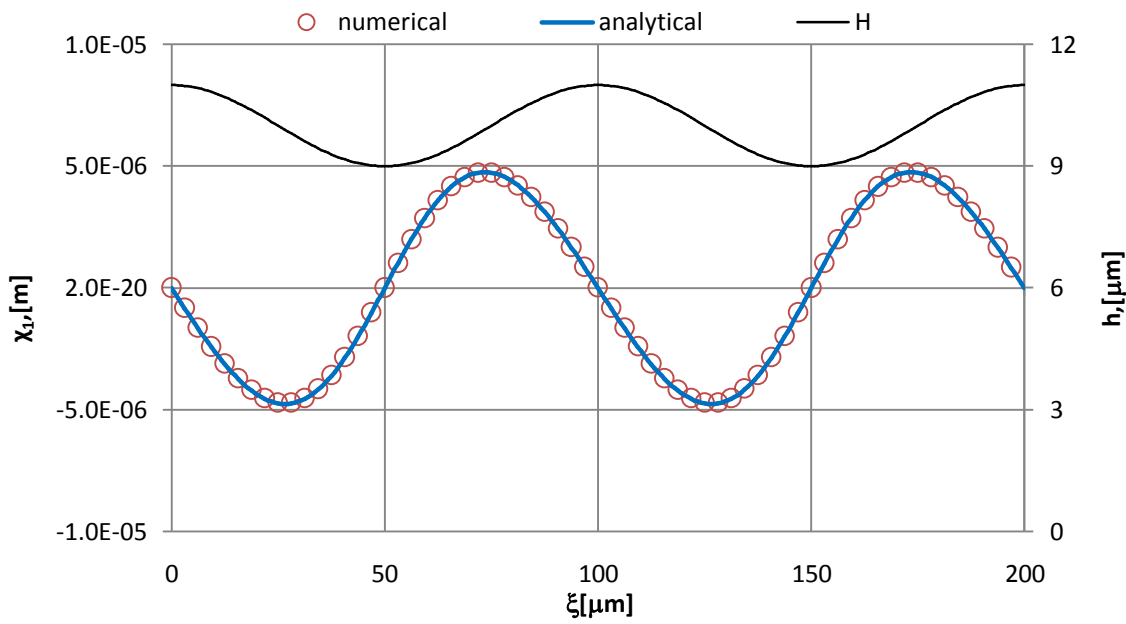


Figure 5.4 Primary axis: solutions for the local problem  $\chi_1$  obtained by analytical (solid line) and numerical (empty circles) means for the global film thickness  $h_0=10.0 \mu\text{m}$ . Secondary axis: total film thickness.

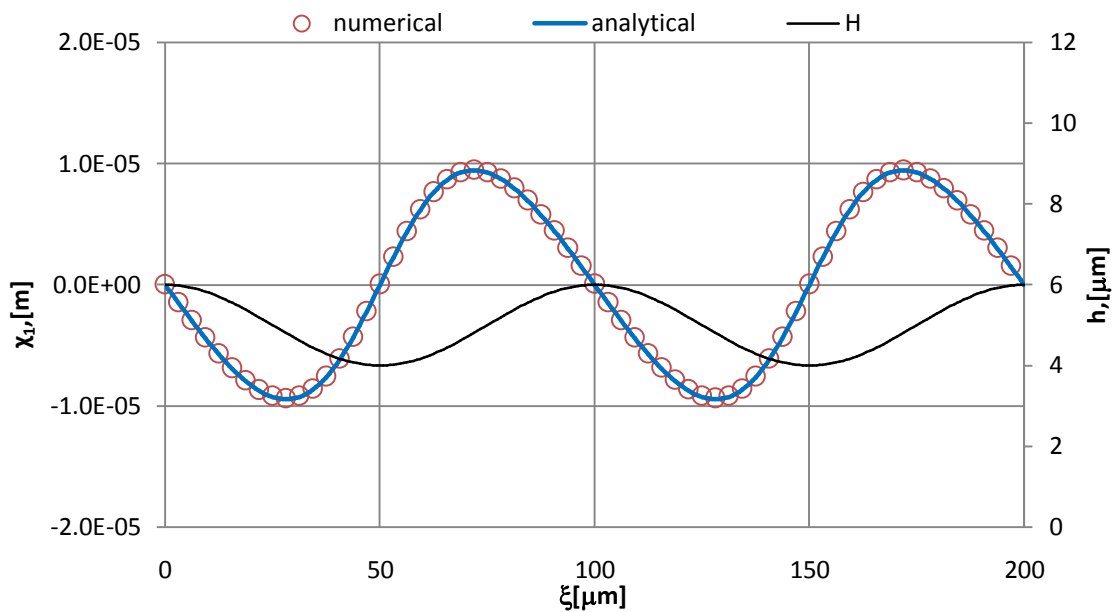


Figure 5.5 Primary axis: solutions for the local problem  $\chi_1$  obtained by analytical (solid line) and numerical (empty circles) means for the global film thickness  $h_0=5.0 \mu\text{m}$ . Secondary axis: total film thickness.

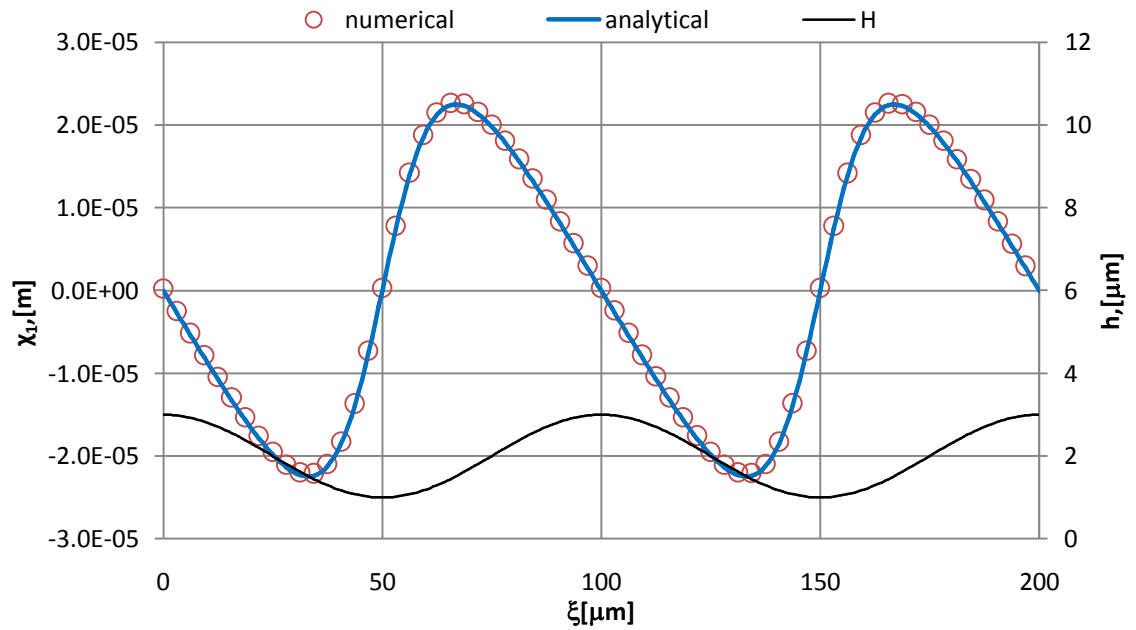


Figure 5.6 Primary axis: solutions for the local problem  $\chi_1$  obtained by analytical (solid line) and numerical (empty circles) means for the global film thickness  $h_0=2.0 \mu\text{m}$ . Secondary axis: total film thickness.

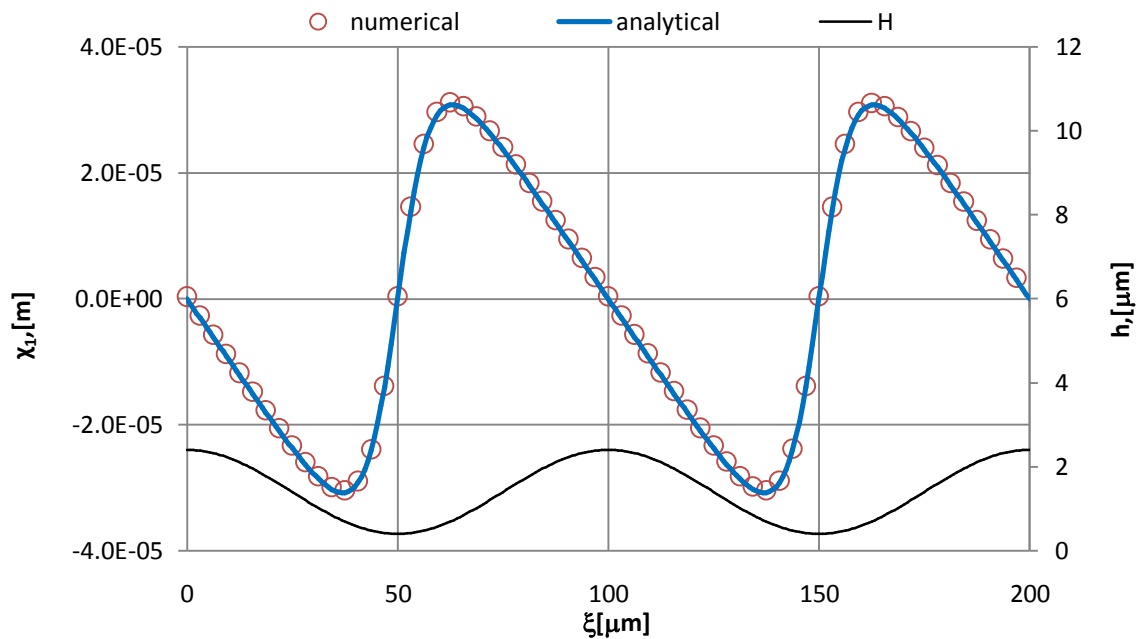


Figure 5.7 Primary axis: solutions for the local problem  $\chi_1$  obtained by analytical (solid blue) and numerical (empty circles) means for the global film thickness  $h_0=1.4 \mu\text{m}$ . Secondary axis: total film thickness.

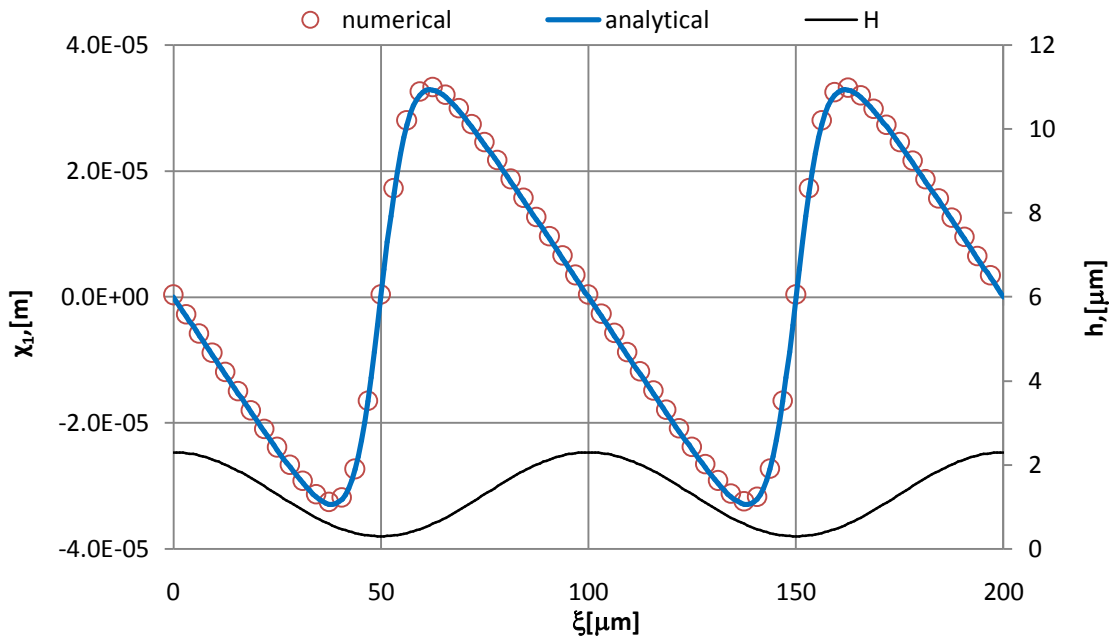


Figure 5.8 Primary axis: solutions for the local problem  $\chi_1$  obtained by analytical (solid line) and numerical (empty circles) means for the global film thickness  $h_0=1.3 \mu\text{m}$ . Secondary axis: total film thickness.

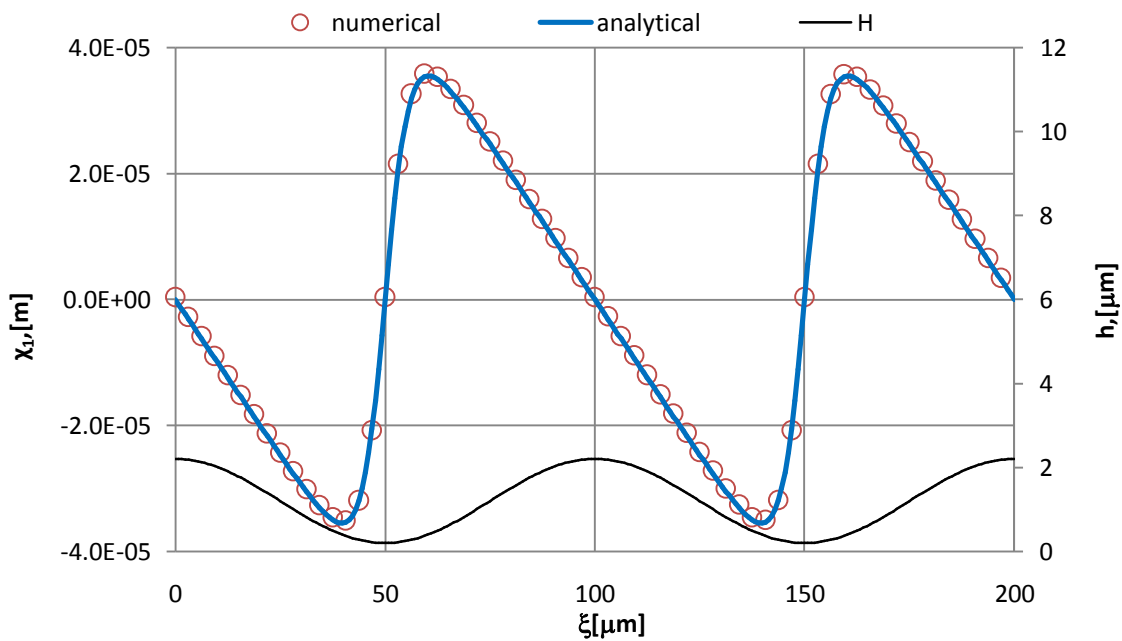


Figure 5.9 Primary axis: solutions for the local problem  $\chi_1$  obtained by analytical (solid line) and numerical (empty circles) means for the global film thickness  $h_0=1.2 \mu\text{m}$ . Secondary axis: total film thickness.

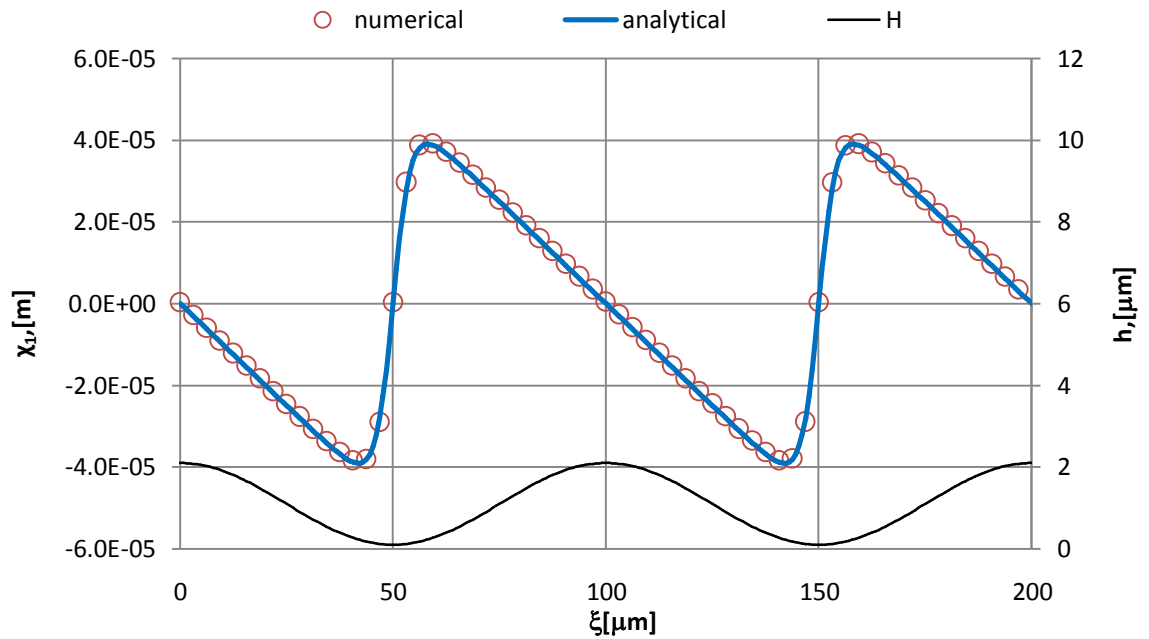


Figure 5.10 Primary axis: solutions for the local problem  $\chi_1$  obtained by analytical (solid line) and numerical (empty circles) means for the global film thickness  $h_0=1.1 \mu\text{m}$ . Secondary axis: total film thickness.

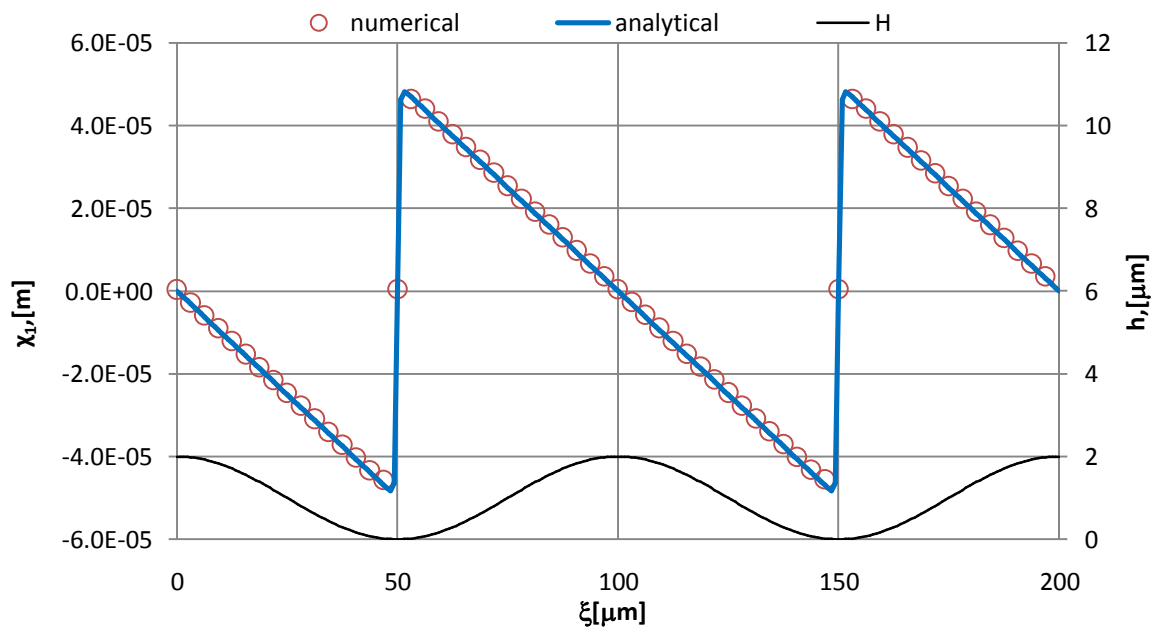
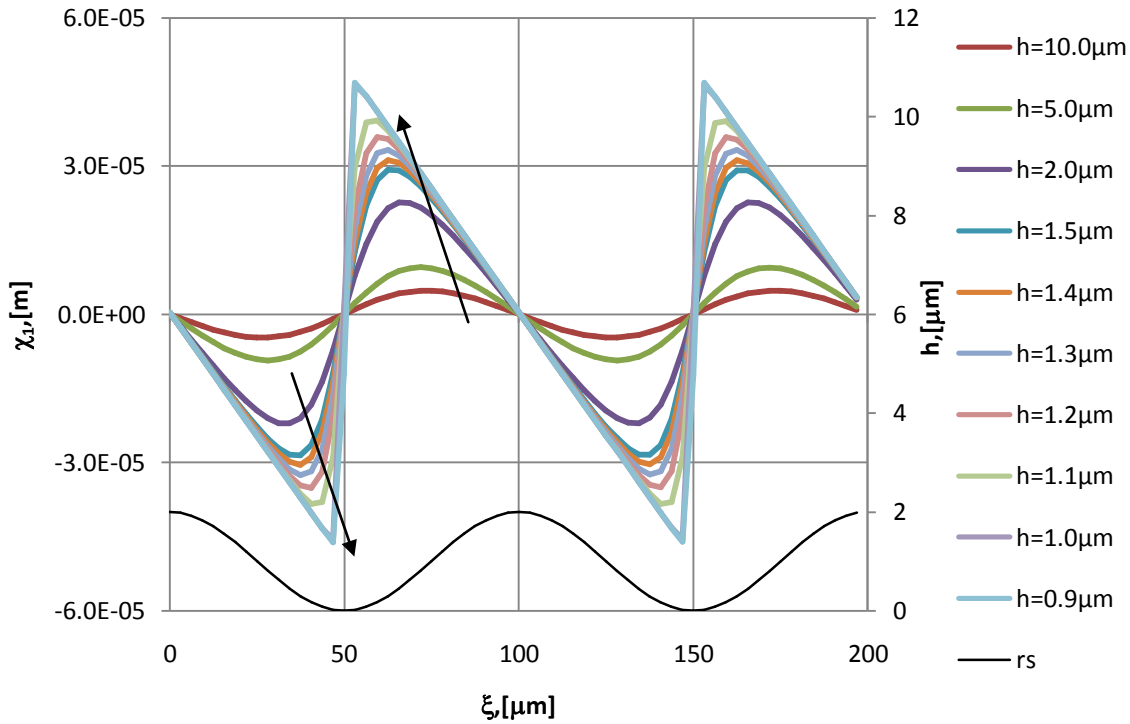


Figure 5.11 Primary axis: solutions for the local problem  $\chi_1$  obtained by analytical (solid line) and numerical (empty circles) means for the global film thickness  $h_0=1.001 \mu\text{m}$ . Secondary axis: total film thickness.

The sequence of the numerical solutions obtained for the whole range of global film thicknesses  $h_0=10.0-0.9 \mu\text{m}$  is plotted on Figure 5.12 where arrows indicate the sense of reducing  $h_0$ . The development of the solution from the smooth sinusoidal curve for large  $h_0$  values to the saw tooth shaped curves for the critical case of direct asperity contact can be observed on the graph. Note that the solutions are anti-symmetric with respect to the point of minimum film thickness and  $\chi_1$  reaches its maximum and

minimum values just before and immediately after the asperity tip. These positions correspond to the large fluid pressures generated before meeting the asperity followed by the pressure drop afterwards, where the fluid can potentially cavitate. The maximum and minimum values of  $\chi_1$  move towards the asperity tip as the gap decreases thus demonstrating the increased effect of roughness on the flow for smaller gaps. The numerical solution for the deflected surface roughness is also shown for  $h_0=0.9\mu\text{m}$  however it is equivalent to the case of  $h_0=1.0\mu\text{m}$ .



**Figure 5.12 Primary axis: The sequence of numerical solutions  $\chi_1$  for global film thickness value  $h_0$  in the range  $10.0\text{-}0.9\mu\text{m}$ . Secondary axis: the total film thickness for the value  $h_0=1.0\mu\text{m}$**

### 5.1.3 Analytical solution for $\chi_3$

Consider the third equation in the system (5.1)

$$\frac{\partial}{\partial \xi} \left( h^3 \frac{\partial \chi_3}{\partial \xi} \right) + \frac{\partial}{\partial \psi} \left( h^3 \frac{\partial \chi_3}{\partial \psi} \right) = \frac{\partial h}{\partial \xi} \quad (5.17)$$

An extruded cosine wave is used (5.7) as in the previous section, and as there is no variation of the equation coefficients in  $\psi$  direction the solution of  $\chi_3$  is assumed to be extruded as well. Then

$$\frac{\partial}{\partial \xi} \left( h^3 \frac{\partial \chi_3}{\partial \xi} \right) = \frac{\partial h}{\partial \xi} \Leftrightarrow h^3 \frac{\partial \chi_3}{\partial \xi} = h - h^*$$

where  $h^*$  is an integration constant. Furthermore,

$$\frac{\partial \chi_3}{\partial \xi} = \frac{h - h^*}{h^3} \Leftrightarrow \chi_3(\xi) = \chi^* + \int_0^{\xi} \frac{h - h^*}{h^3} ds \quad (5.18)$$

where  $\chi^*$  is an additive integration constant and  $s$  is a dummy integration constant. Therefore

$$\chi_3(\xi) = \chi^* + \int_0^{\xi} \frac{ds}{h^2} - h^* \int_0^{\xi} \frac{ds}{h^3} \quad (5.19)$$

### Indefinite integrals

Equation (5.19) contains two integrals. First,

$$\begin{aligned} \int_0^{\xi} \frac{ds}{h^2} &= \int_0^{\xi} \frac{ds}{\left[h_0 + h_r \cos\left(2\pi \frac{s}{L} k\right)\right]^2} = \left[t = 2\pi \frac{s}{L} k\right] = \frac{L}{2\pi k} \int_0^{2\pi \frac{\xi}{L} k} \frac{dt}{\left[h_0 + h_r \cos t\right]^2} \\ &= \frac{L}{2\pi k h_r^2} \int_0^{2\pi k \frac{\xi}{L}} \left(\frac{h_0}{h_r} + \cos t\right)^{-2} dt = \left[\tau = \frac{h_0}{h_r}\right] = \frac{L}{2\pi k h_r^2} \int_0^{2\pi k \frac{\xi}{L}} \frac{dt}{(\tau + \cos t)^2} \end{aligned}$$

where  $\tau = h_0/h_r$  is a non dimensional ratio of the global film thickness to the roughness amplitude. Taking the dummy constant  $\alpha = \tau$  this integral is equivalent to the one calculated analytically in Appendix B. Substituting (B.8):

$$\begin{aligned} \int_0^{\xi} \frac{ds}{h^2} &= \frac{L}{2\pi k h_r^2} G\left(\tan\left(\pi \frac{\xi}{L} k\right)\right) \\ G(z) &= (n+1)\pi G_1 + G_1 \arctan \frac{z}{m} + G_2 \frac{z}{[z^2 + m^2]} \end{aligned} \quad (5.20)$$

where

$$n = \left\lfloor \frac{(2\pi k \xi / L - \pi)}{2\pi} \right\rfloor; \quad m^2 = \left(\frac{\tau + 1}{\tau - 1}\right); \quad \tau = \frac{h_0}{h_r}$$

The brackets  $\lfloor \rfloor$  denote the rounding down to the nearest integer. The coefficients  $G_1$  and  $G_2$  are given by (B.6):

$$G_1 = \frac{2\tau}{(\tau - 1)^{2.5}(\tau + 1)^{2.5}}; \quad G_2 = \frac{2}{(\tau - 1)^2(\tau + 1)} \quad (5.21)$$

The second integral is exactly the same as given in Section 5.1.2, see (5.10) and (5.11).

Equation (5.19) then becomes:

$$\chi_3(\xi) = \chi^* + \frac{L}{2\pi kh_r^2} G\left(\tan\left(\pi \frac{\xi}{L} k\right)\right) - h^* \frac{L}{2\pi kh_r^3} F\left(\tan\left(\pi \frac{\xi}{L} k\right)\right) \quad (5.22)$$

The two constants  $h^*$  and  $\chi^*$  should be defined from the boundary conditions.

### *Boundary conditions*

Periodic boundary conditions are applied, meaning that

$$\chi_3(0) = \chi_3(L)$$

Substituting into (5.22)

$$\chi_3(0) = \chi^* + \frac{L}{2\pi kh_r^2} G(\tan 0) - h^* \frac{L}{2\pi kh_r^3} F(\tan 0) = \chi^* \quad (5.23)$$

The other terms are cancelled because for  $\xi=0$  the value of  $n=-1$ . Bearing in mind, that for  $\xi=L$  the value of  $n=k-1$ <sup>1</sup>:

$$\begin{aligned} \chi_3(L) &= \chi^* + \frac{L}{2\pi kh_r^2} G(\tan \pi k) - h^* \frac{L}{2\pi kh_r^3} F(\tan \pi k) = \\ \chi^* + \frac{L}{2\pi kh_r^2} (n+1)\pi G_1 - \frac{L}{2\pi kh_r^3} h^* (n+1)\pi F_1 &= \chi^* + \frac{L}{2h_r^2} G_1 - \frac{L}{2h_r^3} h^* F_1 \end{aligned} \quad (5.24)$$

Equating (5.23) and (5.24),

$$\chi^* = \chi^* + \frac{L}{2h_r^2} G_1 - \frac{L}{2h_r^3} h^* F_1 \Leftrightarrow \frac{L}{2h_r^2} G_1 = \frac{L}{2h_r^3} h^* F_1 \Leftrightarrow h^* = h_r \frac{G_1}{F_1}$$

Taking into account (5.11) and (5.21):

$$h^* = h_r \frac{2\tau}{(\tau-1)^{1.5}(\tau+1)^{1.5}} \frac{(\tau-1)^{2.5}(\tau+1)^{2.5}}{2\tau^2+1} = h_r \frac{2\tau(\tau^2-1)}{2\tau^2+1} \quad (5.25)$$

As before the additive constant  $\chi_0$  is not defined, since the local solutions enter the formulae for calculating the flow factors (4.19) and (4.25) in a form of derivatives.

<sup>1</sup> For  $\xi=0$  the value of  $n = \lfloor -1/2 \rfloor = -1$ , whereas for  $\xi=L$  the value of  $n = \lfloor k - 1/2 \rfloor = k - 1$

### Summary

This section summarises the previous sections and give the final formula for the  $\chi_3$  solution of the local problem (5.17) for the extruded cosine waviness defined by (5.7). Using the solution (5.22) and substituting the formulae (5.10) and (5.20) the analytical solution yields:

$$\chi_3(\xi) = \chi^* + \frac{L}{2\pi k h_r^2} \left\{ \left( G_2 - F_2 \frac{h^*}{h_r} \right) \frac{z}{[z^2 + m^2]} - F_3 \frac{h^*}{h_r} \frac{z}{[z^2 + m^2]^2} \right\} \quad (5.26)$$

Where

$$z = \tan\left(\pi \frac{\xi}{L} k\right); \quad m^2 = \left(\frac{\tau + 1}{\tau - 1}\right); \quad h^* = h_r \frac{2\tau(\tau^2 - 1)}{2\tau^2 + 1}$$

and the coefficients  $F_2, F_3$  and  $G_2$  are given by (5.11) and (5.21) Note, that the terms multiplied by the coefficients  $G_1$  and  $F_1$  were cancelled, as:

$$\frac{L}{2\pi k h_r^2} G_1 = \frac{h^* L}{2\pi k h_r^3} F_1$$

The functions  $G(z)$  and  $F(z)$  are non-dimensional, therefore the units of the solution are defined by the multipliers  $\frac{L}{2\pi k h_r^2}$  and  $\frac{h^* L}{2\pi k h_r^3}$  which have units [ $m^{-1}$ ].

### Comparison of the analytical and numerical solutions

In this section the obtained analytical solution (5.26) is compared to the  $\chi_3$  values obtained by numerical means (see Section 5.1).

Again this is made for surface geometry corresponding to the local roughness for the surface given in Equation (5.7):

$$h(\xi, \psi) = h_0 + h_r \cos\left(2\pi \frac{\xi}{L} k\right) \quad (5.27)$$

with the parameters given by Table 5.1. The geometry is shown on Figure 5.3 and sequence of Figures 5.13-5.20 illustrate the comparison between the  $\chi_3$  obtained by analytical and numerical means for the global film thickness  $h_0$  given by Table 5.1.

Equation (5.17) is in essence the isoviscous incompressible Reynolds' equation on the scale of local roughness. Indeed, the right hand side of the equation represents the variation of the Couette flow with respect to the local coordinate  $\xi$ . The term  $\lambda = 6\mu\eta$  [Pa·m] is removed which makes the units of  $\chi_3$  to be [ $m^{-1}$ ] The physical meaning of  $\chi_3$  is then the perturbation of pressure caused by the presence of the local roughness.

## Section 5.1 Solving the local problems

Solutions for the function  $\chi_3$  start from smooth waves slightly skewed in the direction of entrainment, with largest values being generated just before the fluid meets the asperity feature and the lowest values occurring immediately after it. This skewness is explained by the fluid motion being restricted by the surface asperities thus reflecting the effect of roughness on the Couette flow, see for example Figures 5.13 and 5.14. Bringing the rough surface closer to its counterface increases the effect of the asperities interacting with the flow. Indeed, Figures 5.14 and 5.15 show higher peak values in the position before the asperities and lower minimum values after it.

The last figure of the series (Figure 5.20) shows the solutions for the global film thickness  $h_0=1.001 \mu\text{m}$ , where the cosine surface is 1.0 nm away from contacting the counterface. As the surface is extruded, the contact would mean complete blockage of the flow, which invalidates the formulation of the problem. The apparent tendency is that the values of  $\chi_3$  in the positions before and after the asperity yield to plus and minus infinity as the surface approaches to the contact condition. Note that the necessary requirement for the analytical solutions to exist is that  $a=h_0/h_r>1$ , otherwise the integrals (A.8) and (B.4) are invalid.

The difference for the analytical and numerical solutions remains trivial for the most of the range of the global film thickness values ( $h_0=10.0-1.2\mu\text{m}$ ) and becomes apparent for the lowest global film thickness values  $h_0=1.1-1.001\mu\text{m}$  as shown in Figures 5.19 and 5.20. This is considered to be due to discretisation inaccuracy.

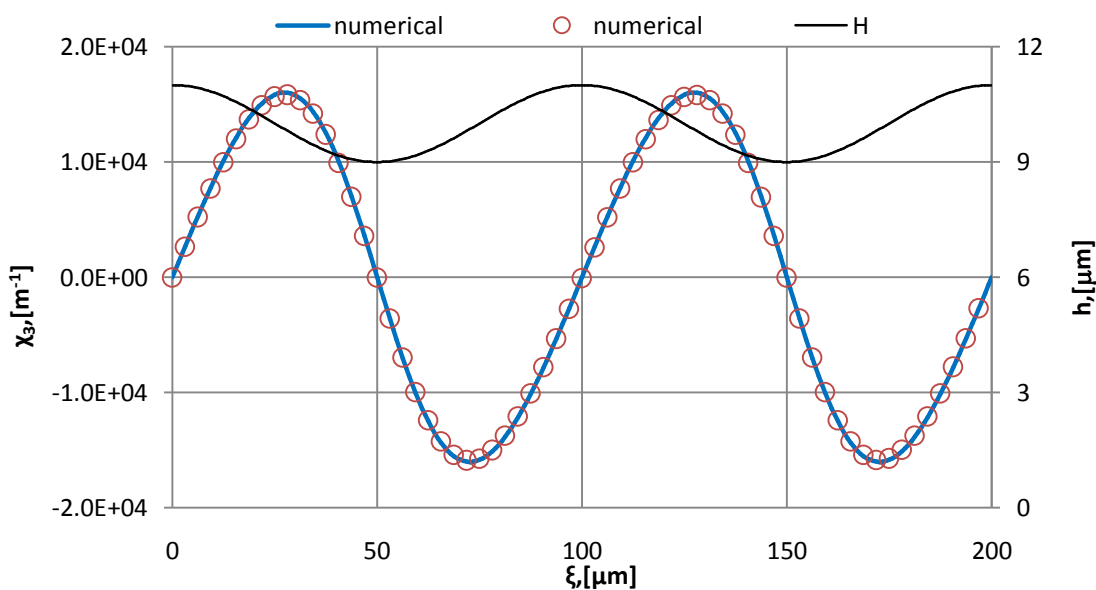


**Figure 5.13** Primary axis: solutions for the local problem  $\chi_3$  obtained by analytical (solid line) and numerical (empty circles) means for the global film thickness  $h_0=10.0 \mu\text{m}$ . Secondary axis: total film thickness.

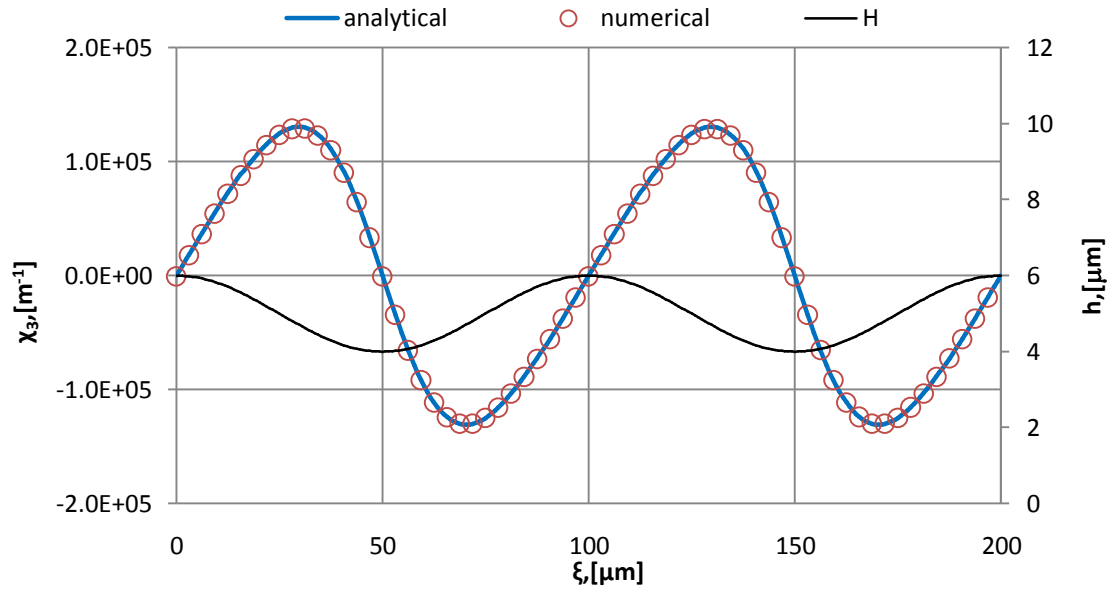


Figure 5.14 Primary axis: solutions for the local problem  $\chi_3$  obtained by analytical (solid line) and numerical (empty circles) means for the global film thickness  $h_0=5.0 \mu\text{m}$ . Secondary axis: total film thickness.

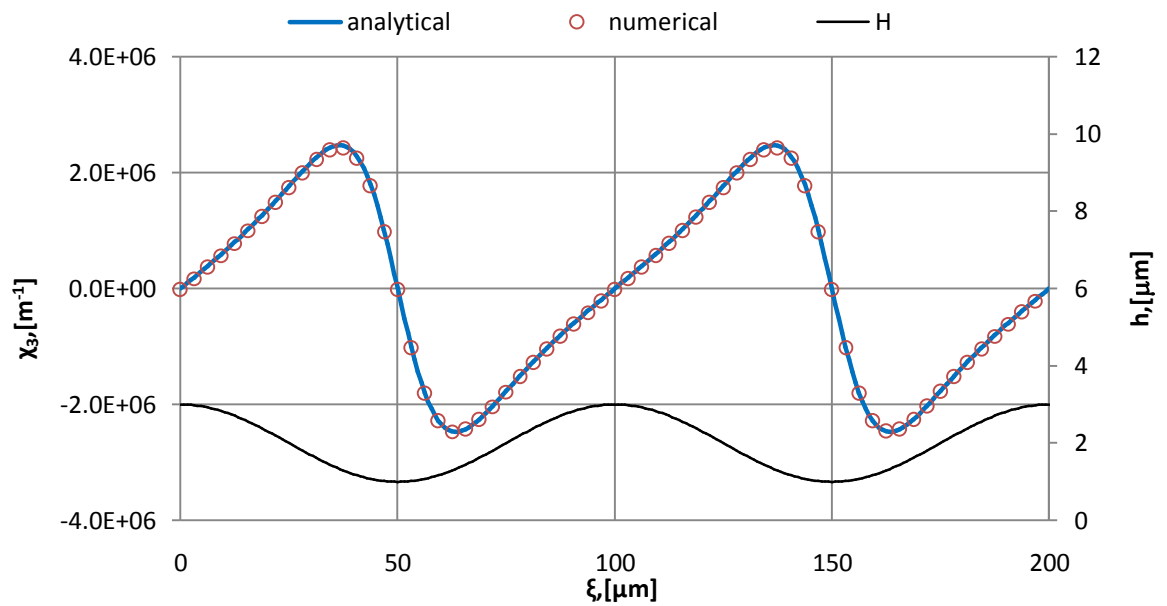


Figure 5.15 Primary axis: solutions for the local problem  $\chi_3$  obtained by analytical (solid line) and numerical (empty circles) means for the global film thickness  $h_0=2.0 \mu\text{m}$ . Secondary axis: total film thickness.

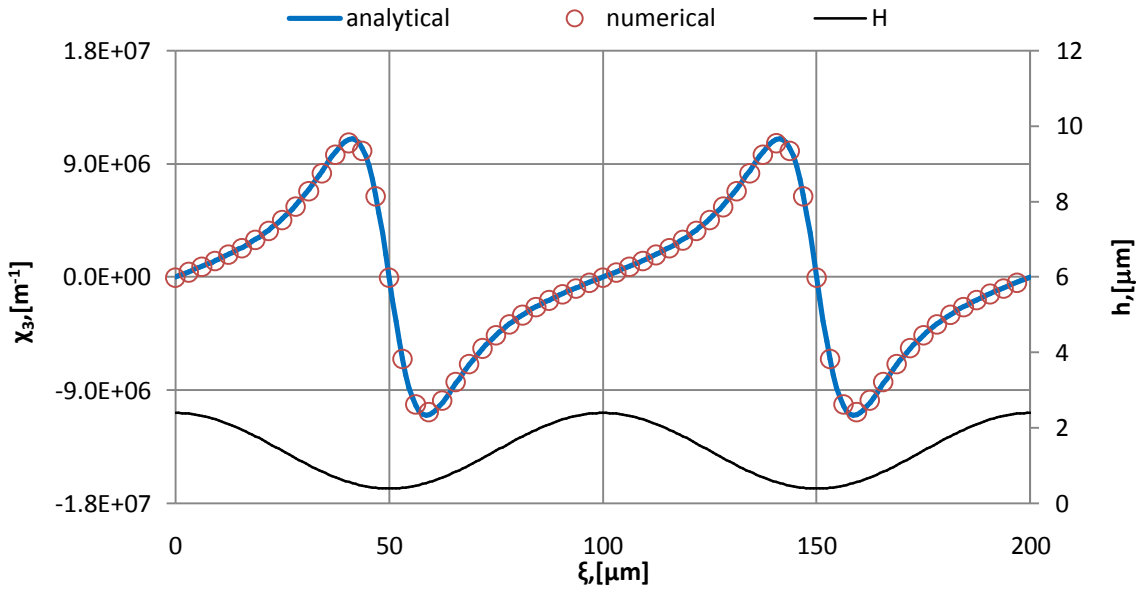


Figure 5.16 Primary axis: solutions for the local problem  $\chi_3$  obtained by analytical (solid line) and numerical (empty circles) means for the global film thickness  $h_0=1.4 \mu\text{m}$ . Secondary axis: total film thickness.

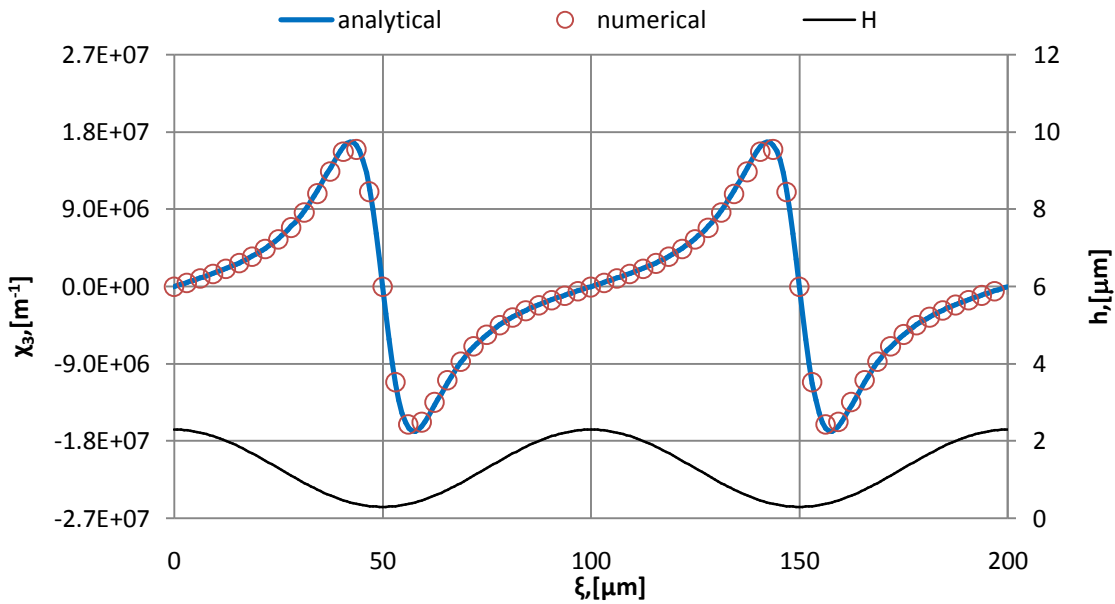


Figure 5.17 Primary axis: solutions for the local problem  $\chi_3$  obtained by analytical (solid line) and numerical (empty circles) means for the global film thickness  $h_0=1.3 \mu\text{m}$ . Secondary axis: total film thickness.

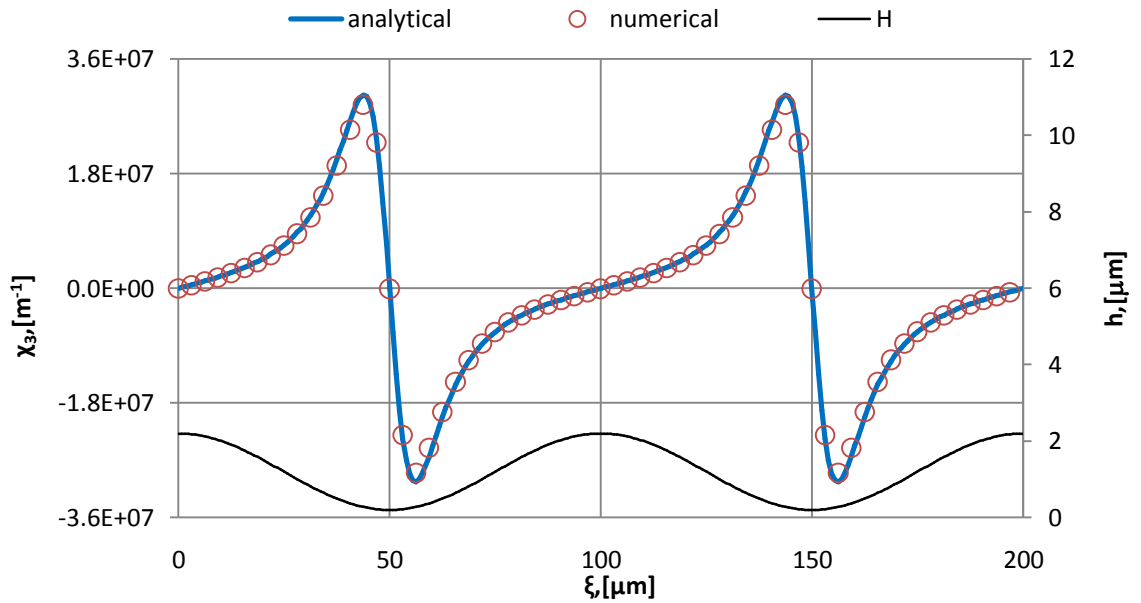


Figure 5.18 Primary axis: solutions for the local problem  $\chi_3$  obtained by analytical (solid line) and numerical (empty circles) means for the global film thickness  $h_0=1.2 \mu\text{m}$ . Secondary axis: total film thickness.

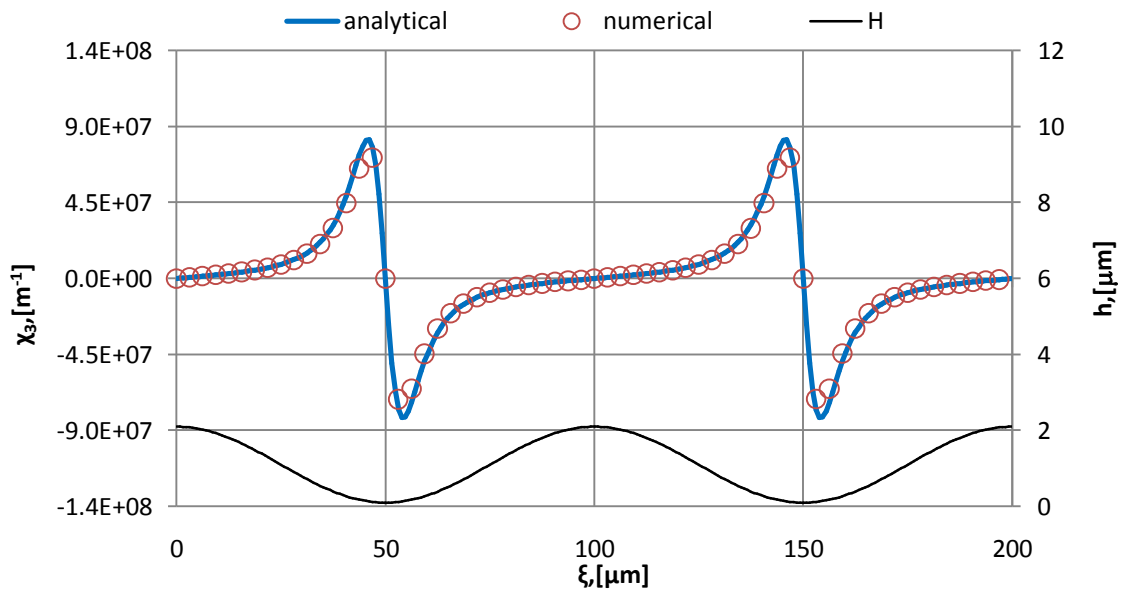
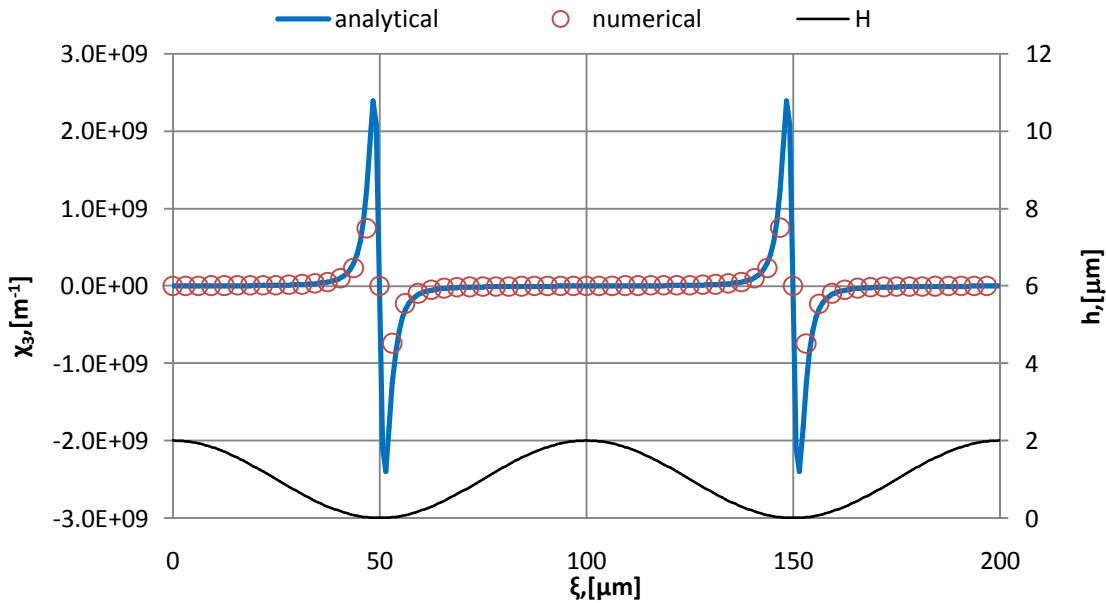


Figure 5.19 Primary axis: solutions for the local problem  $\chi_3$  obtained by analytical (solid line) and numerical (empty circles) means for the global film thickness  $h_0=1.1 \mu\text{m}$ . Secondary axis: total film thickness.



**Figure 5.20 Primary axis: solutions for the local problem  $\chi_3$  obtained by analytical (solid line) and numerical (empty circles) means for the global film thickness  $h_0=1.001 \mu\text{m}$ . Secondary axis: total film thickness.**

The effect of the proximity of the surface roughness to the counterface on the local solution  $\chi_3$  is summarised in Figure 5.21 where the solutions are shown for the whole sequence of global film thicknesses given by Table 5.1. All curves plotted on the same scale which makes apparent the negligible effect of roughness on the local solution for the large global film thickness values ( $h_0=10.0-2.0 \mu\text{m}$ ) and the developing effect as the asperity clearance approaches contact. For convenience the roughness profile is plotted on the same graph using the secondary Y axis. The arrows indicate sense of reducing  $h_0$ .

Bearing in mind that the local solution enters the homogenised Equation (4.23) in a form of derivative it is reasonable to consider the derivative  $\partial\chi_3/\partial\xi$  which is plotted against  $\xi$  in Figure 5.22. Note that the dimensions of the derivative are  $\text{m}^{-2}$  which multiplied by  $h^3/h_0$  makes it non dimensional (see Equation (4.23)). The physical meaning of this value is the modification of the Couette flow term in Reynolds' equation due to obstructions caused by the presence of roughness. The arrows plotted on the graph illustrate how the effect of roughness increases as the contact case is approached. This effect reaches its maximum just before the fluid meets the asperity tip and immediately after it.

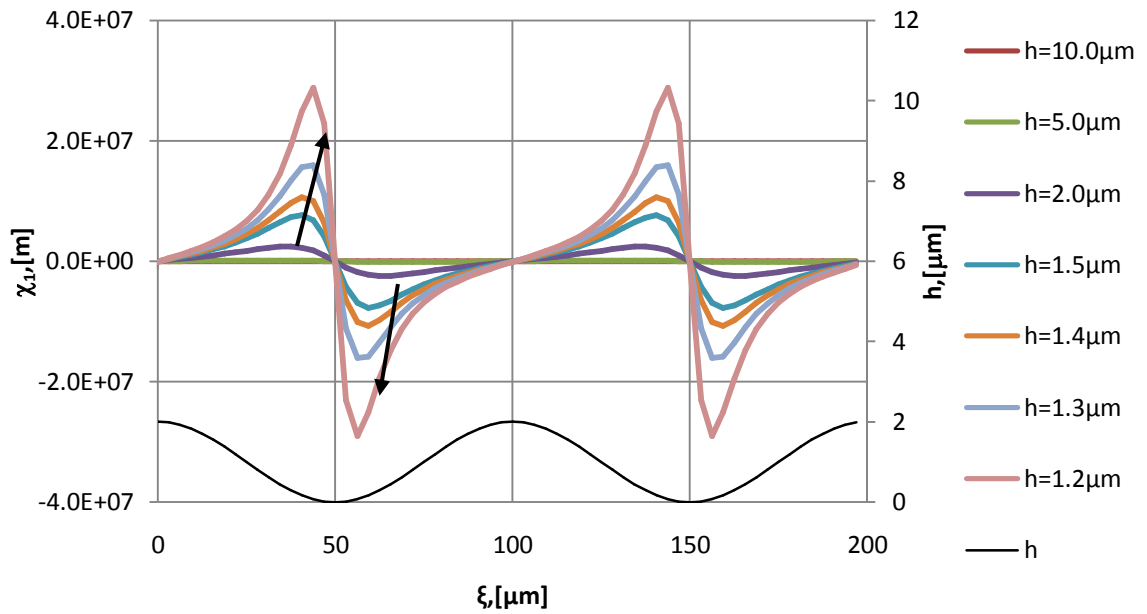


Figure 5.21 The effect of the proximity of the rough surface to the counterface on the solution for the local problem  $\chi_3$  for varying  $h_0$ . The total film thickness  $h$  is plotted on the secondary Y axis.

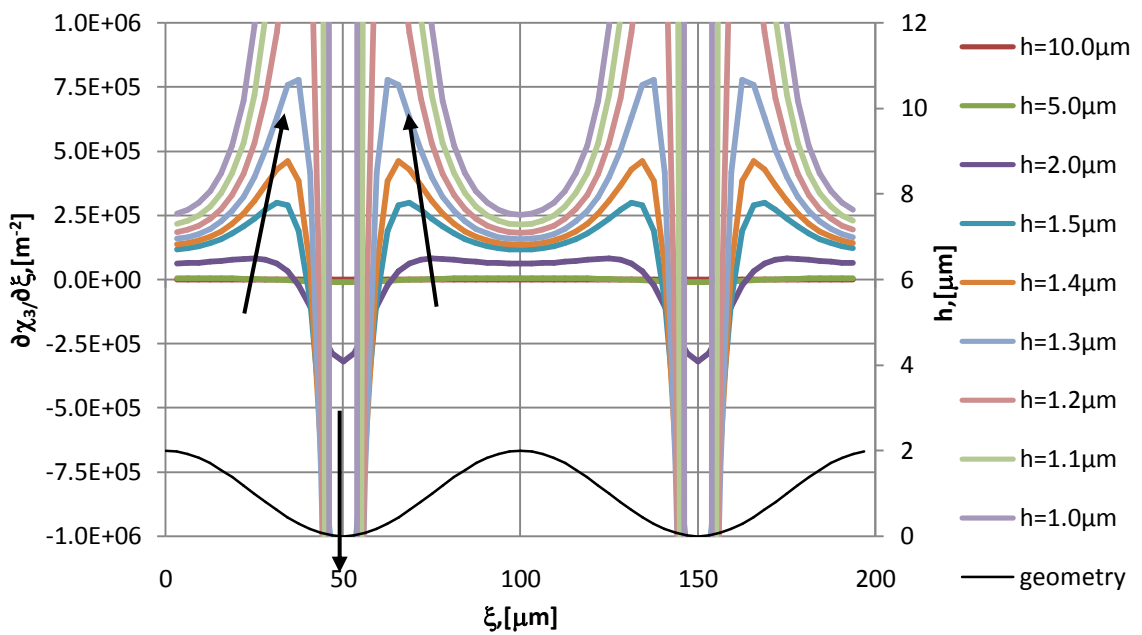


Figure 5.22 The effect of the proximity of the rough surface to the counterface on the derivative of solution for the local problem  $\partial\chi_3/\partial\xi$  with varying  $h_0$ .

## 5.2 Calculating of the flow factors

After the solution of the local problems (5.1) has been obtained the flow factors must be calculated according to the integrals (4.27) and (4.28). In general case the integrals are calculated numerically for which the algorithm is described in Section 5.2.1. For a case of an extruded cosine roughness function the flow factors are expressed as analytical functions of the ratio  $\tau$  of the global film thickness and roughness amplitude

in Section 5.2.2. These analytical expressions are compared with the numerical solutions in Section 5.2.3.

The flow factors for an oblique cosine roughness are calculated using the formulae (4.33) and the effect of obliqueness is discussed in Section 5.2.4. In addition, the flow factors for double sinusoidal surfaces with transverse and oblique roughness are presented in that section.

### 5.2.1 Numerical evaluation of the flow factors

As stated previously converging the local problems can be time consuming. However, the errors in the approximation for the local solution will be smoothed when calculating the integrals (4.27) and (4.28). Therefore, an iterative algorithm has been implemented to ensure that converging of the local solutions continues only while the new approximation affects the values of the flow factors. The routine then have an outer loop where the flow factors are calculated based on the current approximations for the local solutions. The convergence of the flow factors is then checked and if they are not converged then a (small) number of relaxation sweeps is performed to improve the approximated solution of the appropriate local problem. Note that the solution for each local problem is required for calculating a pair of flow factors and these calculations are independent of other local solutions. The algorithm for solving the local problems is discussed in the Section 5.1, whereas that for calculating the flow factors is schematically shown in the flowchart of Figure 5.23. The convergence of the flow factors is checked on the basis of trivial changes. In addition to that the relative changes to the solutions of the local problems are checked and the residual error of the local solutions.

### 5.2.2 Analytical calculation of flow factors

For an extruded cosine surface (5.7) the flow factors can be calculated analytically using the solution (5.16) and (5.26). Note in the case of an extruded surface the cross-flow factors  $a_{12}$ ,  $b_{12}$ ,  $a_{21}$  and  $b_{21}$  are equal to zero. Indeed, the right hand sides of the second and fourth equations in (5.1) are zero, which makes the solutions for  $\chi_2=0$  and  $\chi_4=0$ . In addition, the derivatives  $\partial \chi_1 / \partial \psi = 0$ , and  $\partial \chi_3 / \partial \psi = 0$  due to the extruded nature of the solutions for  $\chi_1, \chi_3$ .

$$a_{12}(h_0) = \int_{\Omega} \frac{h^3}{h_0^3} \frac{\partial \chi_2}{\partial \xi} d\Omega = 0; \quad a_{21}(h_0) = \int_{\Omega} \frac{h^3}{h_0^3} \frac{\partial \chi_1}{\partial \psi} d\Omega = 0;$$

$$b_{12}(h_0) = \int_{\Omega} \frac{h^3}{h_0} \frac{\partial \chi_4}{\partial \xi} d\Omega = 0; \quad b_{21}(h_0) = \int_{\Omega} \frac{h^3}{h_0} \frac{\partial \chi_3}{\partial \psi} d\Omega = 0;$$

The remaining flow factors  $a_{11}$ ,  $a_{22}$ ,  $b_{11}$ , and  $b_{22}$  are calculated in the sections below.

### *Calculating the flow factor $a_{11}$*

Considering the extruded solution of  $\chi_1$  Equation (5.6) takes form (5.8), which is given below for convenience:

$$\frac{\partial \chi_1}{\partial \xi} = -\frac{(h^3 - h_c^3)}{h^3}$$

Using this expression the formula (4.24) for the flow factor  $a_{11}$  becomes:

$$a_{11}(h_0) = \frac{1}{|\Omega|} \int_{\Omega} \frac{h^3}{h_0^3} \left(1 - \frac{h^3 - h_c^3}{h^3}\right) d\Omega = \frac{1}{|\Omega|} \frac{1}{h_0^3} \int_{\Omega} h_c^3 d\Omega = \frac{h_c^3}{h_0^3}$$

. where  $h_0(x,y)$  is the global film thickness and  $h_c^3$  is the integration constant which is calculated in 5.1.2 using the periodic the boundary conditions for  $\chi_1$ .

Substituting (5.15) gives:

$$a_{11}(\tau) = 2 \frac{(\tau - 1)^{2.5} (\tau + 1)^{2.5}}{2\tau^2 + 1} \tag{5.28}$$

where  $\tau=h_0/h_r$  is the parameter introduced in 5.1.2 as the global film thickness value relative to the amplitude of the cosine wave.

The expression for flow factor  $a_{11}$  given by (5.28) is in agreement with the flow factors obtained by Bayada (2005) with the only difference being that the flow factors in the current work are divided by the global film thickness  $h_0^3(x,y)$  to maintain non-dimensionality. Note, that the flow factor  $a_{11}$  does not directly depend on either  $h_0$  or  $h_r$ , being a function of their ratio only.

### *Calculating the flow factor $a_{22}$*

In order to calculate the transverse flow factor  $a_{22}$  Equation (4.24) is modified taking into account the fact that  $\chi_2=0$ :

$$a_{22}(h_0) = \frac{1}{|\Omega|} \int_{\Omega} \frac{h^3}{h_0^3} \left(1 + \frac{\partial \chi_2}{\partial \psi}\right) d\Omega = \frac{1}{|\Omega|} \int_{\Omega} \frac{h^3}{h_0^3} d\Omega$$

## Section 5.2 Calculating of the flow factors

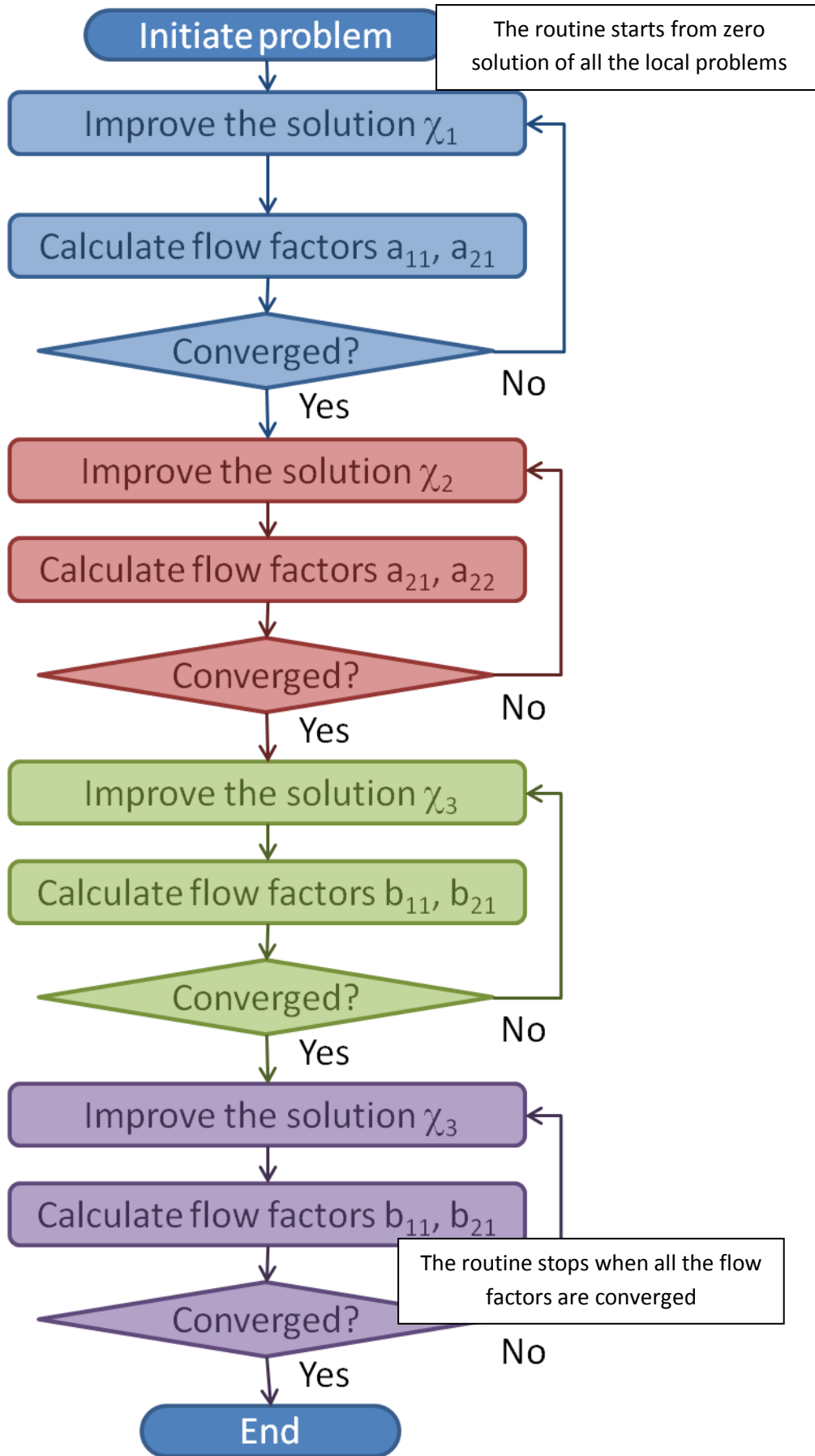


Figure 5.23 Flowchart of the algorithm for solving the local problems and calculating the flow factors.

After substituting the roughness function (5.7) and the dimensions of the local domain  $\Omega = [0, L] \times [0, W]$  this integral becomes:

$$a_{22}(h_0) = \frac{1}{|\Omega|h_0^3} \int_{\Omega} \left[ h_0 + h_r \cos\left(2\pi \frac{k\xi}{L}\right) \right]^3 d\Omega = \frac{1}{LW} \frac{1}{\tau^3} \int_0^L \int_0^W \left[ \tau + \cos 2\pi \frac{k\xi}{L} \right]^3 d\xi d\psi$$

Note that the amplitude of the cosine waves and the denominator  $h_0^3$  are replaced by  $1/\tau^3$ . Bearing in mind that the sub integral function does not depend on  $\psi$ :

$$a_{22}(h_0) = \frac{1}{L} \frac{1}{\tau^3} \int_0^L \left[ \tau + \cos\left(2\pi \frac{k\xi}{L}\right) \right]^3 d\xi$$

For convenience the substitution  $t=2\pi k\xi/L$  is used:

$$\begin{aligned} a_{22}(h_0) &= \frac{1}{L} \frac{1}{\tau^3} \int_0^L \left[ \tau + \cos\left(2\pi \frac{k\xi}{L}\right) \right]^3 d\xi = \left[ \begin{array}{l} t = 2\pi \frac{k\xi}{L} \\ d\xi = \frac{L}{2\pi k} dt \end{array} \right] \\ &= \frac{1}{2\pi k} \frac{1}{\tau^3} \int_0^{2\pi k} [\tau + \cos t]^3 dt \end{aligned}$$

Taking into account the periodicity of the integrand, the integral over the range  $[0, 2\pi k]$  is equal to summation of  $k$  integrals over the period  $2\pi$  :

$$a_{22}(h_0) = \frac{1}{2\pi k} k \frac{1}{\tau^3} \int_0^{2\pi} [\tau + \cos t]^3 dt = \frac{1}{2\pi} \frac{1}{\tau^3} \int_0^{2\pi} [\tau + \cos t]^3 dt$$

Expanding the integrand, the integral becomes the summation of the following integrals:

$$\begin{aligned} a_{22}(h_0) &= \frac{1}{2\pi} \frac{1}{\tau^3} \int_0^{2\pi} [\tau + \cos t]^3 dt = \\ &= \frac{1}{2\pi} \frac{1}{\tau^3} \int_0^{2\pi} \tau^3 dt + \frac{1}{2\pi} \frac{1}{\tau^3} \int_0^{2\pi} 3\tau^2 \cos t dt + \frac{1}{2\pi} \frac{1}{\tau^3} \int_0^{2\pi} 3\tau \cos^2 t dt + \frac{1}{2\pi} \frac{1}{\tau^3} \int_0^{2\pi} \cos^3 t dt = \\ &= 1 + \underbrace{\frac{3}{2\pi} \frac{1}{\tau} \sin t \Big|_0^{2\pi}}_{=0} + \frac{3}{2\pi} \frac{1}{\tau^2} \frac{1}{2} (t + \sin t \cos t) \Big|_0^{2\pi} + \frac{1}{\tau^3} \underbrace{\left[ \frac{\cos t \sin t}{3} + \frac{2}{3} \sin t \right]_0^{2\pi}}_{=0} \end{aligned}$$

Collecting all the terms gives:

$$a_{22}(\tau) = 1 + \frac{3}{2} \frac{1}{\tau^2} \tag{5.29}$$

As well as the flow factor  $a_{11}$  the formula (5.29) is not directly dependent on either  $h_0$  or on  $h_r$  and differs from the transverse flow factor  $a_{22}$  obtained by Bayada (2005) by the multiplier  $h_0^3(x, y)$ .

*Calculating the flow factor  $b_{11}$*

Considering the extruded solution of  $\chi_3$ , Equation (5.17) takes form (5.18), which is given below for convenience:

$$\frac{\partial \chi_3}{\partial \xi} = \frac{h - h^*}{h^3}$$

Substituting into the formula for the flow factor  $b_{11}$  (4.25) gives:

$$b_{11}(h_0) = \frac{1}{|\Omega|} \int_{\Omega} \left( \frac{h}{h_0} - \frac{h^3}{h_0} \frac{h - h^*}{h^3} \right) d\Omega = \frac{1}{|\Omega|} \int_{\Omega} \frac{h^*}{h_0} d\Omega = \frac{h^*}{h_0}$$

where  $h_0(x,y)$  is the global film thickness and  $h^*$  is the integration constant calculated in 5.1.3 using the periodic boundary conditions for  $\chi_3$ . Substituting expression (5.25) for  $h^*$  gives:

$$b_{11}(\tau) = \frac{h^*}{h_0} = \frac{2(\tau^2 - 1)}{2\tau^2 + 1} \tag{5.30}$$

which is equal to the non-dimensional modification of this factor calculated by Bayada (2005) and is dependent on the ratio of  $h_0$  and  $h_r$  only..

*Calculating the flow factor  $b_{22}$*

In order to calculate the flow factor  $b_{22}$  expression (4.25) is used. Bearing in mind that  $\chi_4=0$  it yields:

$$b_{22}(h_0) = \frac{1}{|\Omega|} \int_{\Omega} \frac{h}{h_0} d\Omega = \frac{1}{h_0} \frac{1}{|\Omega|} \int_{\Omega} \left[ h_0 + h_r \cos\left(2\pi \frac{k\xi}{L}\right) \right] d\Omega$$

Using the rectangular dimensions of the local domain  $\Omega = [0, L] \times [0, W]$ :

$$b_{22}(h_0) = \frac{1}{h_0} \frac{1}{LW} \int_0^L \int_0^W \left[ h_0 + h_r \cos\left(2\pi \frac{k\xi}{L}\right) \right] d\xi d\psi = \frac{1}{h_0} \frac{1}{L} \int_0^L \left[ h_0 + h_r \cos\left(2\pi \frac{k\xi}{L}\right) \right] d\xi$$

Integrating by substitution of the function  $t=2\pi k\xi/L$ :

$$\begin{aligned} b_{22}(h_0) &= \frac{1}{h_0} \frac{1}{L} \int_0^L \left[ h_0 + h_r \cos\left(2\pi \frac{k\xi}{L}\right) \right] d\xi = \left[ \begin{array}{l} t = 2\pi \frac{k\xi}{L} \\ d\xi = \frac{L}{2\pi k} dt \end{array} \right] \\ &= \frac{1}{h_0} \frac{1}{2\pi k} \int_0^{2\pi k} [h_0 + h_r \cos t] dt \end{aligned}$$

Bearing in mind the periodicity of the sub integral function:

$$b_{22}(h_0) = \frac{1}{h_0} \frac{1}{2\pi} \int_0^{2\pi} [h_0 + h_r \cos t] dt = 1 + \underbrace{\frac{1}{h_0} \frac{1}{2\pi} h_r \cos t}_=0 \Big|_0^{2\pi}$$

The value of the Couette flow factor  $b_{22}=1$  is explained by the fact that the surface is extruded and there is no modification of the flow in the direction of extrusion. Note that the Couette flow in Y direction can be non zero if the direction of motion does not coincide with the directions of periodicity.

### 5.2.3 Comparison of the analytical and numerical flow factors

In this section the flow factors evaluated analytically are compared with those calculated numerically. In a general case the analytic evaluation of the flow factors is not possible. In the current work the flow factors have been evaluated analytically for an extruded cosine surface only. However, as shown in Section 5.2.2, the mixed flow factors  $a_{12}, a_{21}, b_{12}$  and  $b_{21}$  are equal to zero for an extruded surface. The surface geometry corresponds to the local roughness for the surface (5.7):

$$h(\xi, \psi) = h_0 + h_r \cos\left(2\pi \frac{\xi}{L} k\right)$$

and for the comparison the parameters given in Table 5.2 are used.

**Table 5.2 Parameters of the surface used to calculate the flow factors**

Parameter	Description	Value	Units
<b>Geometry</b>			
hr	Amplitude	1.0	$\mu\text{m}$
h0	Global film thickness	6.0-0.05	$\mu\text{m}$
L	Length of the local domain ( $\square$ )	200	$\mu\text{m}$
W	Width of the local domain	200	$\mu\text{m}$
k	Number of waves per local cell	2	
N	Number of mesh points	64	
$\theta$	Orientation of roughness	0, 15, 30, 45, 60, 90	$^\circ$ (degrees)
<b>Material properties</b>			
$E$	Elastic modulus	200	GPa
$\nu$	Poisson's ratio	0.32	
$P_{\max}$	Maximum pressure	4.3	GPa

Note that the analytical solution is not available for the case of direct contact asperities. The numerical solution can use the deflected shape of the surface obtained

## Section 5.2 Calculating of the flow factors

by means of the dry contact analysis. For this analysis the elastic properties of the material are given in Table 5.2.

Figures 5.24 to 5.27 show the Poiseuille ( $a_{11}, a_{22}$ ) and Couette ( $b_{11}, b_{22}$ ) flow factors calculated for an extruded cosine roughness given by Equation (5.7). The solid curves on both figures represent the analytical solutions (5.28)-(5.30) whereas the open squares and circles show the flow factors calculated numerically. The dashed solid black lines are given by equations  $x=1$  and  $y=1$ . As the ratio  $\tau=h_0/h_r$  is the x coordinate, the line  $x=1$  represents the case of  $h_0=h_r$  which means direct contact of the tips of the surface asperities with the counterface. The line  $y=1$  means that the flow factors are equal to unity, i.e. according to the homogenised Equation (4.34) the roughness has trivial effect on the flow of the lubricant and the homogenised equation is identical to the commonly used isoviscous incompressible Reynolds Equation (4.2). Note that the analytical solution is available only for  $\tau > 1.0$  i.e. for no contact cases.

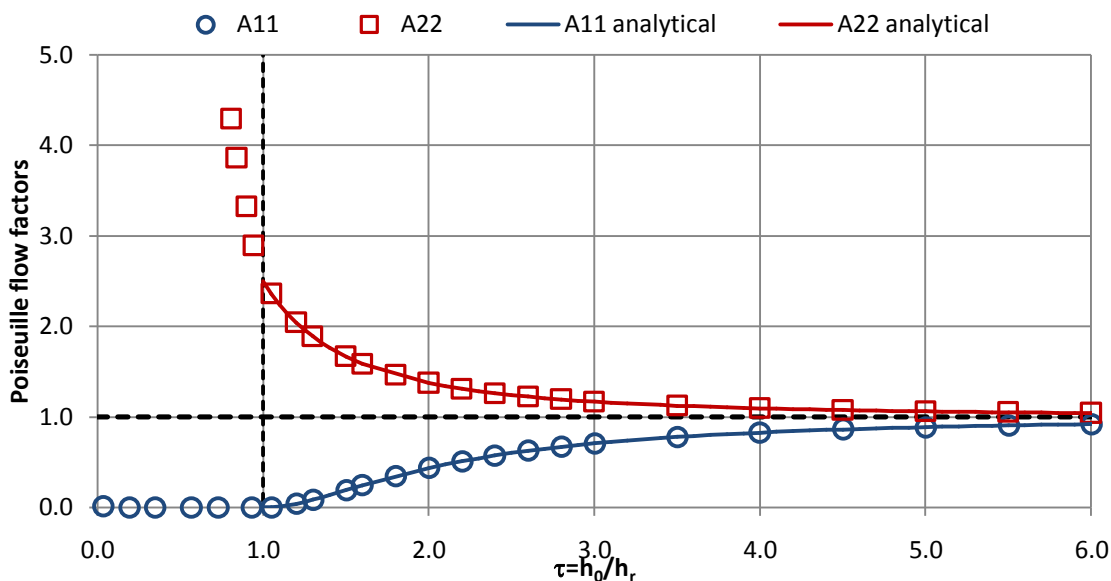


Figure 5.24 Poiseuille flow factors calculated by numerical (empty circles and squares) and analytical (solid lines) means.

Figure 5.24 shows a perfect match between the flow factors obtained by analytical and numerical methods until the direct contact of the surface asperities occurs. The values of both flow factors  $a_{11}$  and  $a_{22}$  for  $\tau > 5$  are very close to unity which means that roughness has no effect on the lubrication analysis when the global film thickness is more than four times greater than the amplitude of the surface asperities.

The physical meaning of the Poiseuille flow factors can be clarified by considering the reduced volume terms  $a_{11}h^3$  and  $a_{22}h^3$ . It is clear from the homogenised Equation (4.34) that the values of  $a_{11}$  and  $a_{22}$  can be considered as a reduction of fluid volume

transferred by the pressure gradients across and along the roughness features respectively. Note that the values of  $a_{11}$  (blue curve, blue empty circles) are always less than unity. This means that less volume can be moved in the entrainment direction due to the presence of roughness. This results in higher pressures being generated as the lubricant encounters the roughness features. The values of  $a_{22}$  (red curve, empty squares) on the other hand are always above unity. The reason for this is the additional flow created in the transverse direction due to the lubricant being trapped between the asperities, which enhances the flow along the extruded roughness features. This effect is summarised in Figure 5.25 where the effective fluid volume values  $a_{11}h^3$ ,  $a_{22}h^3$  and nominal volume  $h^3$  are plotted representing the volume of fluid that is able to flow across and along the roughness features for a rough surface and in both directions for a smooth case.

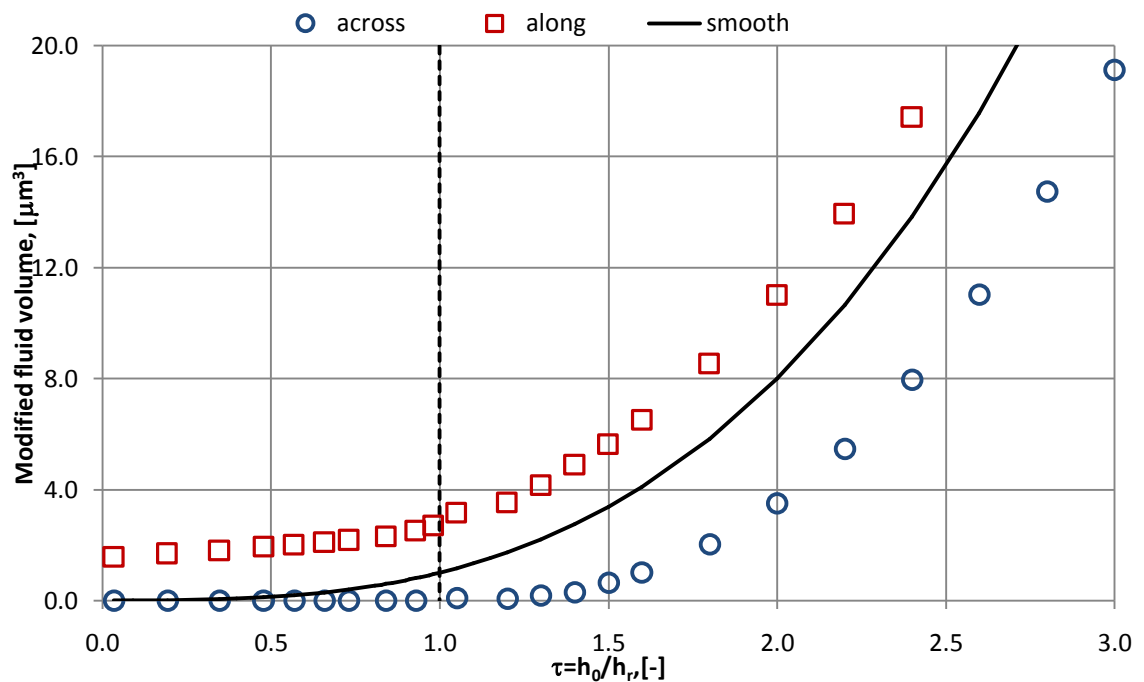


Figure 5.25 Effective volume of fluid  $a_{11}h^3$  (blue circles),  $a_{22}h^3$  (red squares) and nominal volume  $h^3$  (solid black line)

Note that the values of  $\tau < 1$  correspond to direct contact which means total blockage of the flow across the extruded roughness features. This can be illustrated by both zero values of the flow factor  $a_{11}$  in Figure 5.24 and zero effective volume in Figure 5.25.

The increasing value of  $a_{22}$  tends to infinity as  $\tau$  approaches zero. This is explained by the fact that as the global film thickness approaches zero the rough surface deforms and keeps the roughness features which can store fluid whereas the nominal volume becomes zero. Indeed, the red squares in Figure 5.25 show a slight decrease of the

## Section 5.2 Calculating of the flow factors

volume that can be transferred in the direction along the roughness features. This decrease corresponds to flattening of the asperities and thus a reduction in the depth of the valleys caused by contact pressures. The lowest value of the modified volume  $a_{22}h^3$  is non zero as it would be zero when the asperities are completely flattened, which is far beyond the consideration of the mixed lubrication analysis. The schematic sketch of the fluid trapped between the deformed asperities is shown in Figure 5.26, where the nominal gap is the global film thickness  $h_0$ , the actual gap is the total film thickness which takes the roughness into account and solid and dashed curves represent the deformed and undeformed shape of the asperities.

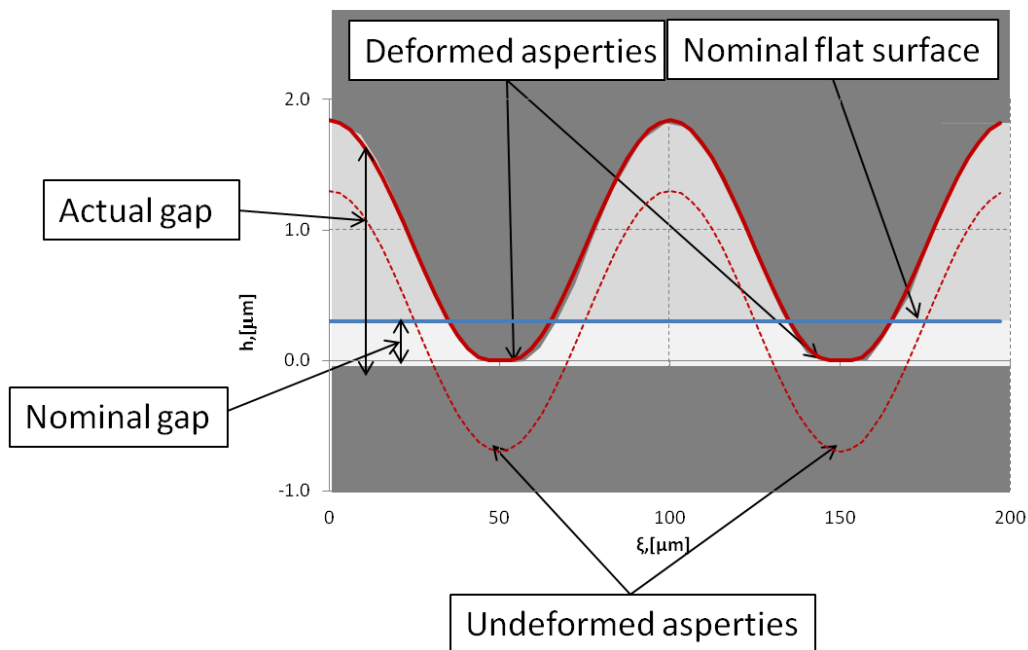


**Figure 5.26 Fluid trapped between the deformed asperities in direct contact**

Figure 5.27 shows the Couette flow factors  $b_{11}$  (blue circles, blue line) and  $b_{22}$  (red squares, red line). As the Couette flow depends on the gap between the surfaces the Couette flow factors can be considered as an effective film thickness, modified due to presence of the roughness in comparison with the global film thickness.

The values of  $b_{22}$  are equal to unity until the contact occurs as the extruded roughness features do not cause any obstruction to the Couette flow in the direction of extrusion. As with the Poiseuille flow factor  $a_{22}$ , after the contact occurs the  $b_{22}$  value tends to infinity as  $\tau$  approaches to zero. The reason for this is that the deformed surface preserves the valleys which makes the effective gap greater than a nominal gap corresponding to the film thickness of a smooth case as shown in Figure 5.26. The effective gap is shown in Figure 5.28 where the solid black line corresponds to the nominal gap ( $h_0$ ), whereas red squares and blue circles denote the effective gap in the

directions along and across the roughness features of the surface  $b_{22}h$  and  $b_{11}h$ . As with the Poiseuille flow factors, the  $b_{11}$  term is equal to zero after the contact occurs as the Couette flow is completely blocked by the asperities, whereas the  $b_{22}$  term decays slowly due to deflection of the roughness features. Note that the effective gap becomes equal to zero only when the asperities are completely flattened.

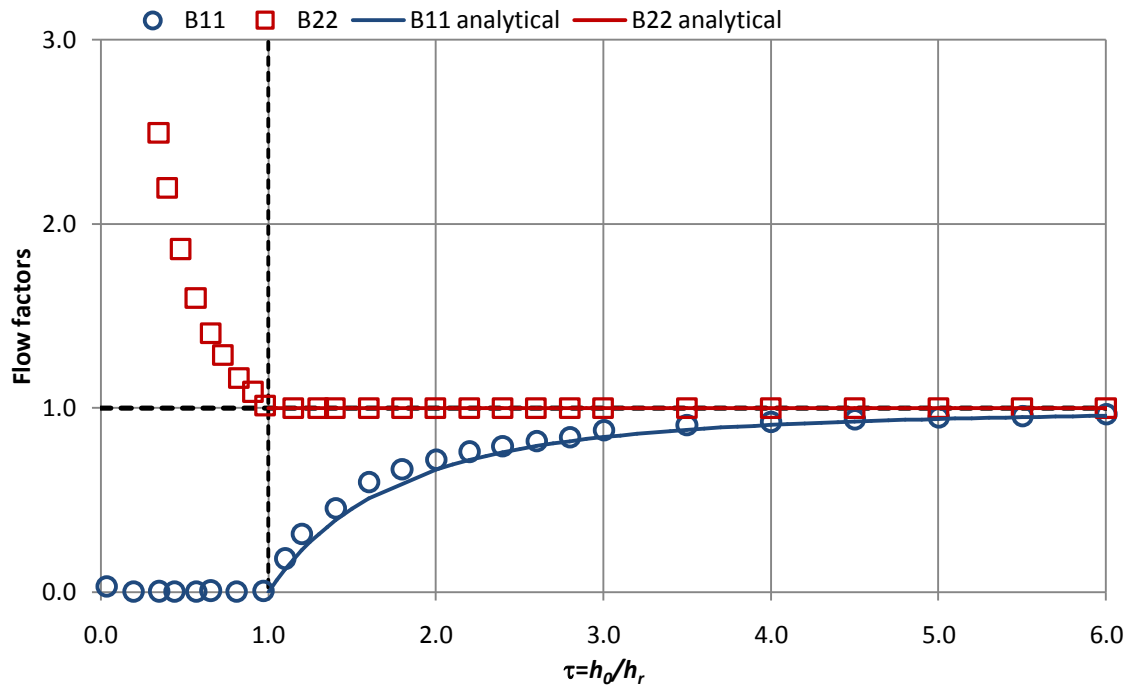


Figure 5.27 Couette flow factors calculated by numerical (empty circles and squares) and analytical (solid lines) means.

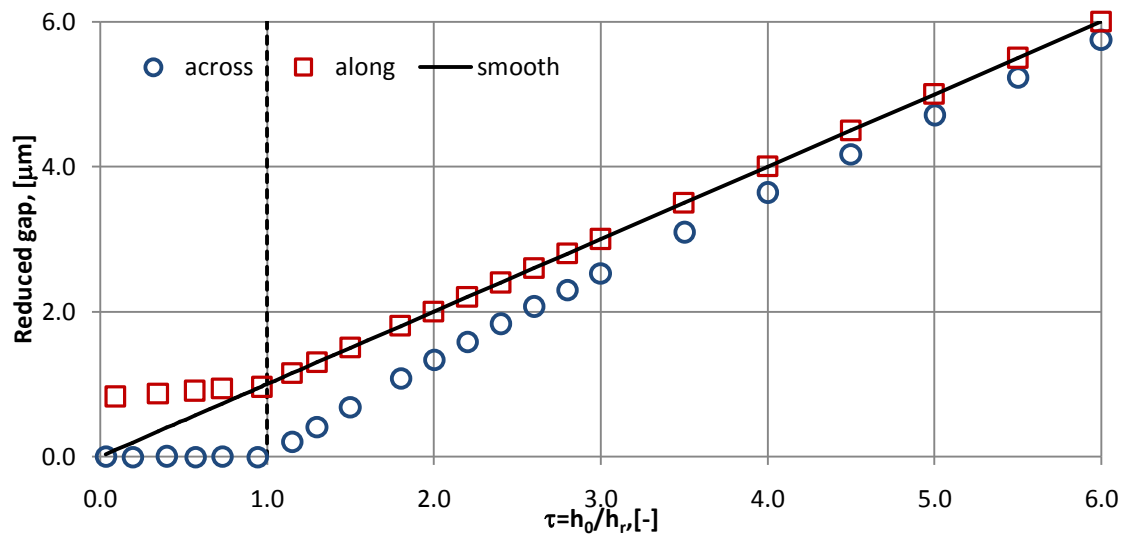


Figure 5.28 Effective film thickness due to the presence of roughness: along the roughness features (red squares), across the roughness features (blue circles), smooth case (solid black line).

### 5.2.4 The effect of the roughness orientation

The effect of oblique roughness is of interest when the rough surface has directions of periodicity not coinciding with the direction of motion as shown schematically in Figure 4.7. The flow factors calculated using Equations (4.27) and (4.28) are properties of the surface roughness and global film thickness only. The flow factors for oblique roughness are calculated by applying the formulae given by Equation (4.33) to these flow factors. This allows the effect of orientation of the characteristic roughness features with respect to the direction of motion on the flow of lubricant to be clearly illustrated.

In this section an extruded cosine roughness function given by Equation (5.7) is considered. The parameters given by Table 5.2 are used. Note that the flow factors  $a_{12} = a_{21} = b_{12} = b_{21} = 0$  for an extruded surface, therefore Equation (4.3) becomes:

$$\begin{aligned}
 A_{11} &= a_{11} \cos^2 \theta + a_{22} \sin^2 \theta \\
 A_{12} = A_{21} &= (a_{11} - a_{22}) \sin \theta \cos \theta \\
 A_{22} &= a_{11} \sin^2 \theta + a_{22} \cos^2 \theta \\
 B_1 &= b_{11} \cos^2 \theta + b_{22} \sin^2 \theta \\
 B_2 &= (b_{11} - b_{22}) \sin \theta \cos \theta
 \end{aligned}
 \tag{5.31}$$

If the direction of entrainment coincides with the direction of motion then  $\theta=0$  and Equation (5.31) yields:

$$A_{11} = a_{11}; \quad A_{22} = a_{22}; \quad B_1 = b_{11}; \quad A_{12} = A_{21} = B_2 = 0$$

These flow factors have been considered in the previous section. Here the oblique flow factors are calculated for  $\theta=0^\circ, 15^\circ, 45^\circ, 60^\circ, 75^\circ$  and  $90^\circ$ . The case of  $\theta=0^\circ$  is a case of pure transverse roughness, i.e. the direction of extrusion coincides with the transverse direction, whereas  $\theta=90^\circ$  corresponds to the pure longitudinal roughness, i.e. the asperities are extruded in the entrainment direction. The contour plots of the surfaces with oblique roughness are shown in Figures 5.29-5.35 where the number of waves  $k=16$  for demonstration purposes. In all of the cases it is assumed that the entrainment and transverse directions are aligned with  $x$  and  $y$  axes respectively.

Figure 5.36 illustrates the development of the flow factor  $A_{11}$  as the orientation angle increases from 0 up to 90 degrees. This flow factor reflects the effect of roughness on the Poiseuille flow in  $x$  direction. As in the previous section the dashed black line  $x=1$  indicates the case when the direct contact of the asperities occurs, whereas  $y=1$  means no effect of roughness.

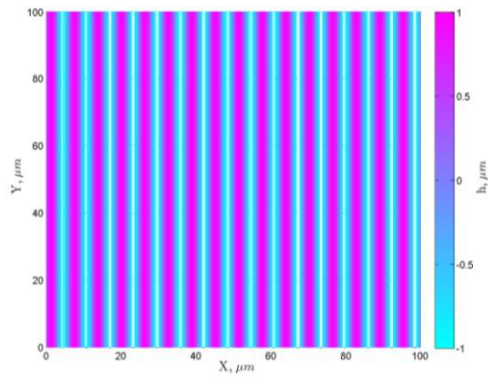


Figure 5.29 Oblique extruded cosine surface  $\theta = 0^\circ$

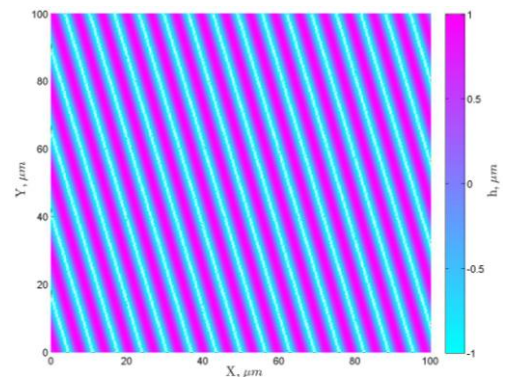


Figure 5.30 Oblique extruded cosine surface  $\theta = 15^\circ$

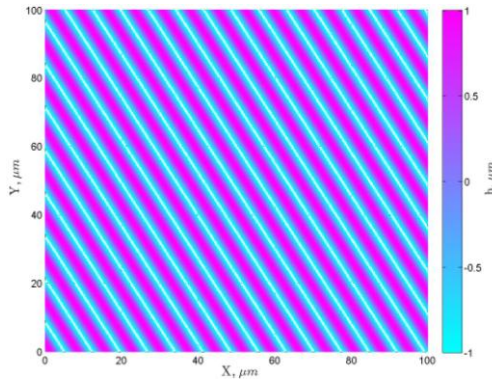


Figure 5.31 Oblique extruded cosine surface  $\theta = 30^\circ$



Figure 5.32 Oblique extruded cosine surface  $\theta = 45^\circ$



Figure 5.33 Oblique extruded cosine surface  $\theta = 60^\circ$

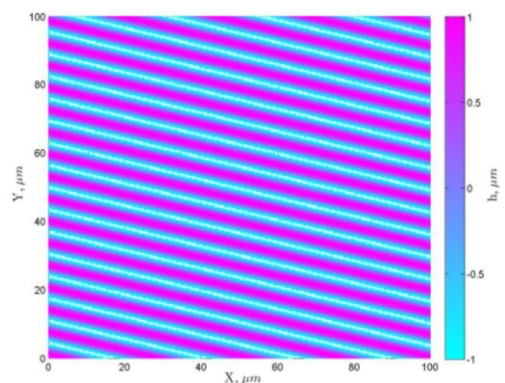


Figure 5.34 Oblique extruded cosine surface  $\theta = 75^\circ$

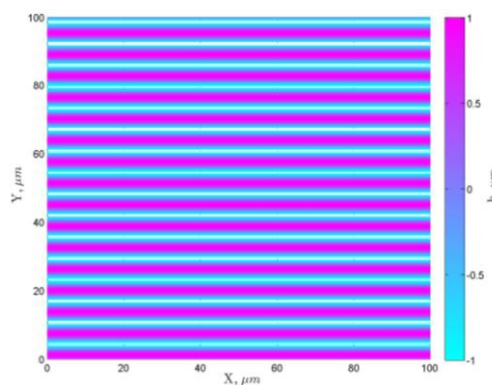


Figure 5.35 Oblique extruded cosine surface  $\theta = 90^\circ$

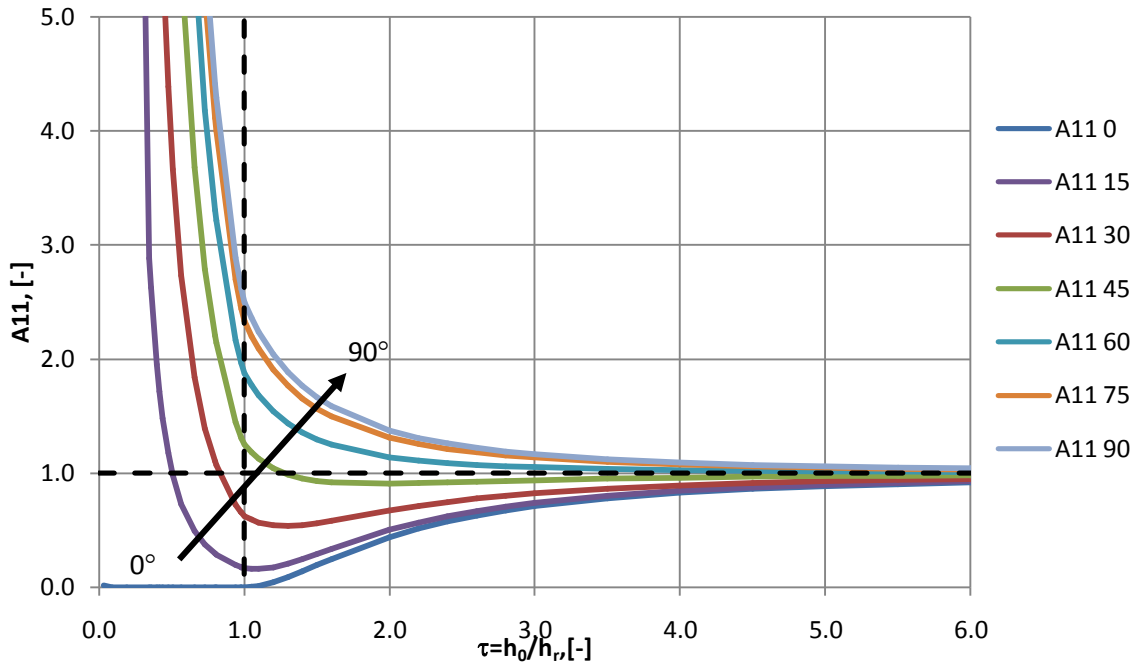


Figure 5.36 Oblique flow factor  $A_{11}$  for a range of roughness orientations from pure transverse to pure longitudinal roughnesses. Arrow indicates the sense of increasing the orientation angle from  $0^\circ$  to  $90^\circ$  degrees.

Note that the values of  $A_{11}$  for transverse roughness only ( $\theta=0^\circ$ ) become zero after the contact occurs. This is explained by the flow in  $x$  direction being blocked by the contacting asperities as discussed in Section 5.2.3. On the other hand the flow factors with non transverse orientation tend to infinity as the nominal film thickness approaches to zero, which means that the asperities are being deformed. As well as the flow factor  $a_{22}$  in Figure 5.24 the infinite values of  $A_{11}$  for oblique roughness mean that as the nominal film thickness decreases the fluid flow becomes blocked by the contacting asperities. However, the trapped fluid may flow along the oblique asperities as shown in Figure 5.37 which results in non zero flow in both  $x$  and  $y$  directions. Note also that the values of  $A_{11}$  for the orientation angle  $\theta > 45^\circ$  are above the  $y=1$  line. This is explained by the fact that as the lubricant is partially constricted between the extruded asperities from both sides in  $y$  direction the average fluid flow in the  $x$  direction is increased.

Figure 5.38 shows the sequence of flow factors  $A_{22}$  for a range of roughness orientations from  $\theta=0^\circ$  to  $\theta=90^\circ$ . Comparing this chart to the one in Figure 5.36 makes it clear, that they are identical if the order of the data series is reversed, i.e. the value of  $A_{11}$  for  $\theta=\theta_1$  is equal to the value of  $A_{22}$  for  $\theta=90^\circ-\theta_1$ . This follows from the expressions for  $A_{11}$  and  $A_{22}$  given in Equation (5.31).

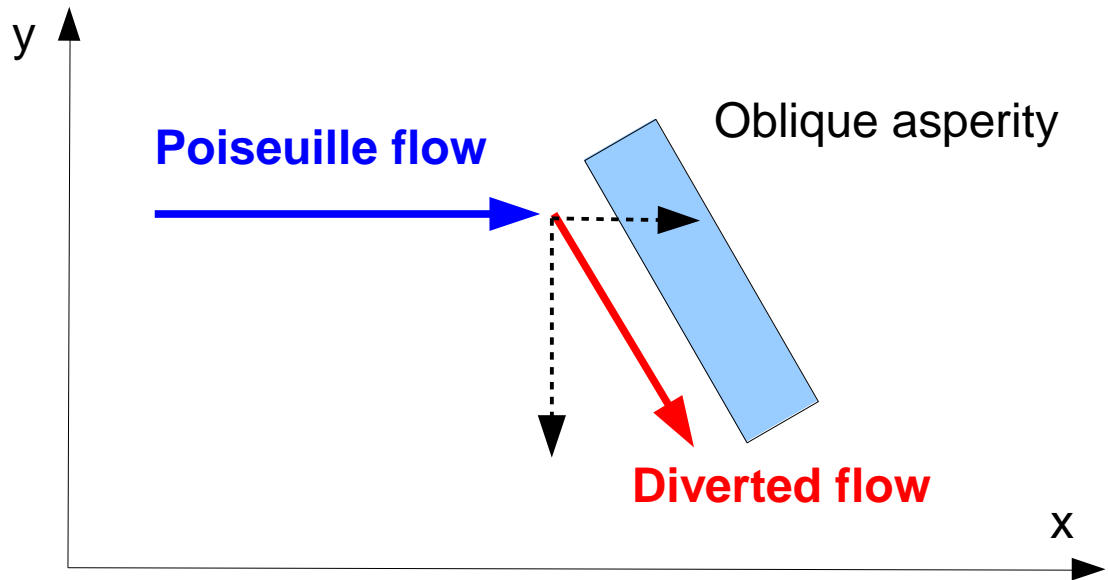


Figure 5.37 The x and y components of the Poiseuille flow diverted in front of the asperity

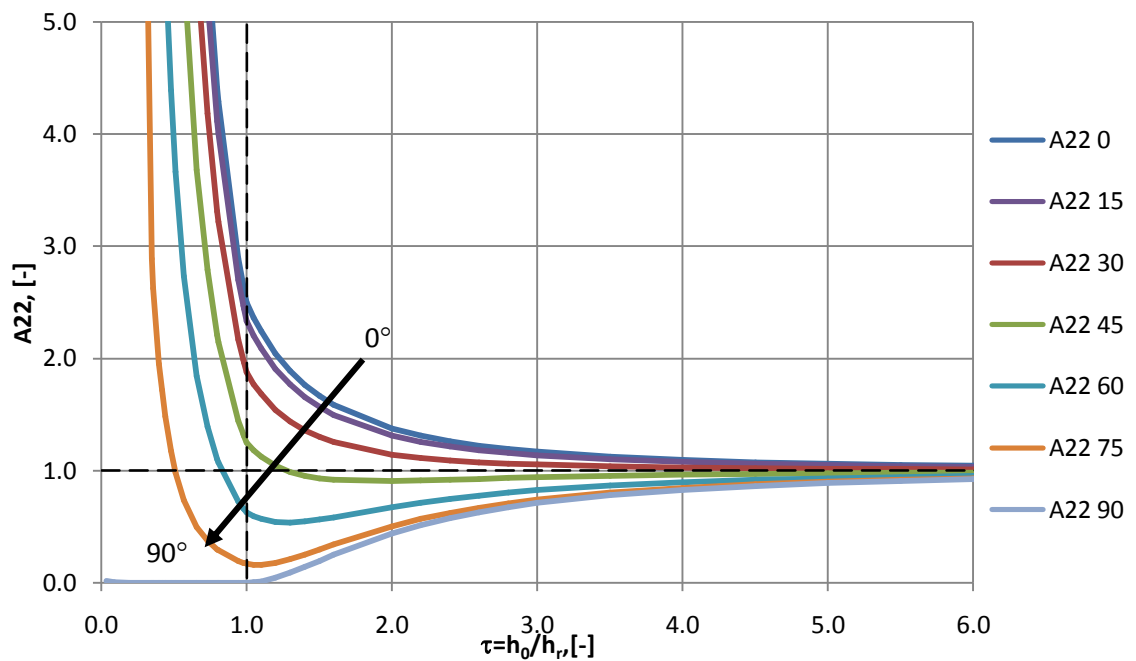


Figure 5.38 Oblique flow factor  $A_{22}$  for a range of roughness orientations from pure transverse to pure longitudinal roughnesses. Arrow indicates the sense of increasing the orientation angle from 0 to 90 degrees.

Figure 5.39 below shows the flow factor  $A_{12}(=A_{21})$  for the range of roughness orientations from  $0^\circ$  to  $90^\circ$  degrees. As seen from the homogenised Equation (4.34) the cross flow factor  $A_{12}$  reflects the additional flow in x direction caused by the pressure gradient in y direction in the presence of an oblique asperity. Note that  $A_{12}=0$  for  $\theta=0^\circ$  and  $\theta=90^\circ$  which makes the cross term  $\frac{\partial}{\partial x}\left(A_{12}h^3\frac{\partial p}{\partial y}\right)$  equal to zero. It is clear from Figure 5.39 that the contribution of the cross terms to the Poiseuille flow reaches its maximum value for the orientation angle  $\theta=45^\circ$ . Also the value of  $A_{12}$  calculated for the orientation  $\theta=\theta_1$  is equal to the one calculated for  $\theta=90^\circ-\theta_1$ .

## Section 5.2 Calculating of the flow factors

The next Figures 5.40 and 5.41 illustrate the Couette flow factors  $B_1$  and  $B_2$  for the range of roughness orientation angles from  $0^\circ$  to  $90^\circ$  degrees. As seen for  $A_{11}$  and  $A_{22}$ , the family of  $B_1$  curves lies between the  $B_1$  values calculated for the transverse and the longitudinal roughnesses. Again, if the roughness is oblique, the flow in the direction of entrainment is not completely blocked as soon as the contact of the surfaces occurs.

The behaviour of the cross term  $B_2$  is similarly to that of the term  $A_{12}$  in the sense that it is most pronounced for the orientation  $\theta=45^\circ$ . The similarity of behaviour between the Poiseuille and Couette factors as the orientation changes is not surprising as the oblique roughness features divert the Couette and Poiseuille flows in the same way.

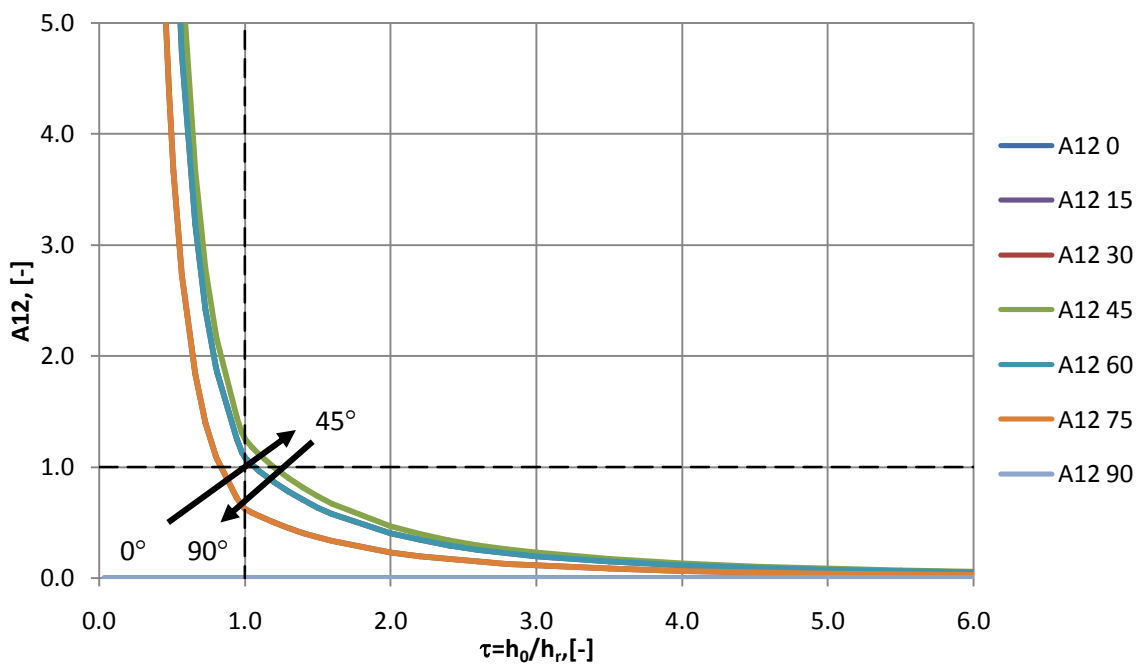


Figure 5.39 Oblique flow factor  $A_{12}$  for a range of roughness orientations from pure transverse to pure longitudinal roughnesses. Arrows indicate the sense of increasing the orientation angle from  $0^\circ$  to  $45^\circ$  and from  $45^\circ$  to  $90^\circ$  degrees.

### 5.2.5 Double cosine roughness

In this section the flow factors for the double sinusoidal (cosine) surface are considered. These factors are of interest as the average flow is not blocked by the asperities as they come into contact.

The double cosine roughness is defined as follows:

$$h(x, y, \xi, \psi) = h_0(x, y) + h_r \cos\left(2\pi \frac{k_1 \xi}{L}\right) \cos\left(2\pi \frac{k_2 \psi}{W}\right) \quad (5.32)$$

where  $L$  and  $W$  are the dimensions of a rectangular representative area,  $\Omega$ ,  $k_1$  and  $k_2$  define the number of waves in  $x$  and  $y$  directions respectively and  $h_r$  is the amplitude.

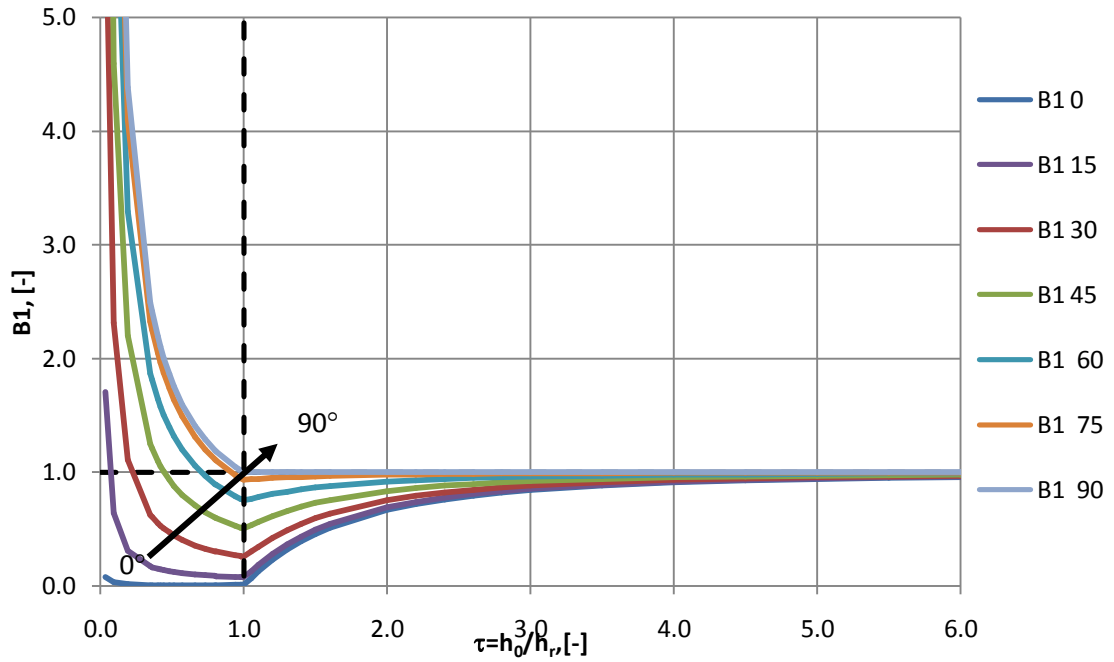


Figure 5.40 Oblique flow factor  $B_1$  for a range of roughness orientations from pure transverse to pure longitudinal roughnesses. Arrow indicates the sense of increasing the orientation angle from  $0^\circ$  to  $90^\circ$  degrees.

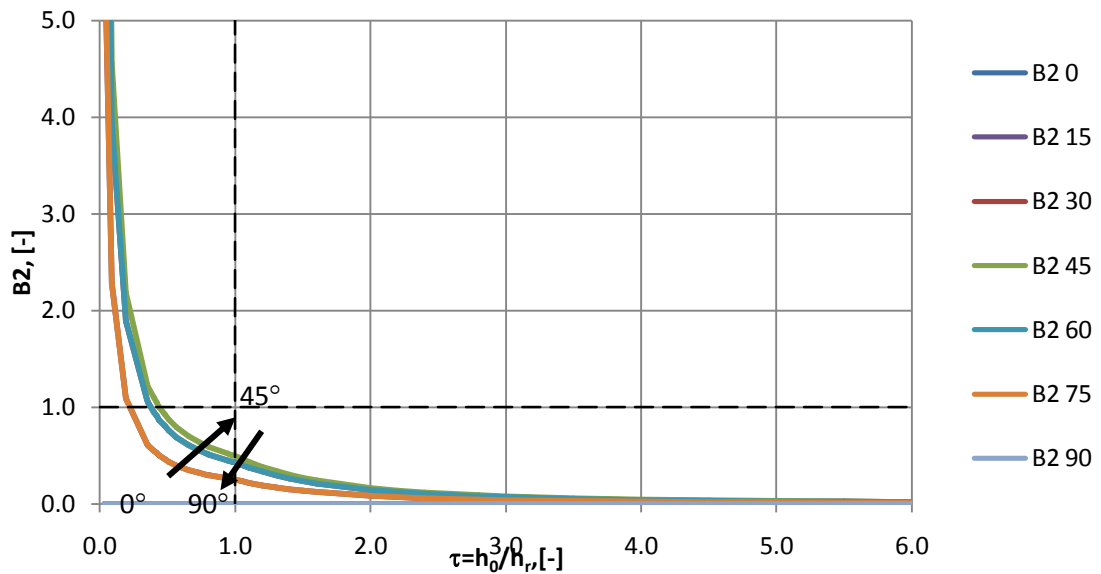


Figure 5.41 Oblique flow factor  $B_2$  for a range of roughness orientations from pure transverse to pure longitudinal roughnesses. Arrows indicate the sense of increasing the orientation angle from  $0^\circ$  to  $45^\circ$  and from  $45^\circ$  to  $90^\circ$  degrees.

Three types of surfaces are considered: with equal wavelengths of asperities in both directions i.e.  $k_1/k_2=1$ , with  $k_1/k_2=2$  and  $k_1/k_2=4$ . The parameters used are summarised in Table 5.3.

Again, in case of contact the deformed shape obtained by means of the dry contact analysis is used for calculating the flow factors. The orientation of the surface roughness has been considered for the whole range of  $\theta$  from  $0^\circ$  to  $90^\circ$  degrees.

## Section 5.2 Calculating of the flow factors

Examples of the surfaces are shown in Figures 5.42-5.44 where arrows indicate the orientation of the axis of periodicity with respect to the entrainment direction. For demonstration purposes the number of waves per period is selected as  $k_1=16$  and  $k_2=8$  for each of these figures. Figure 5.44 shows an isotropic double cosine surface with  $k_1=k_2=16$ .

**Table 5.3 Parameters of the surface used to calculate the flow factors**

Parameter	Description	Value	Units
<b>Geometry</b>			
hr	Amplitude	1.0	$\mu\text{m}$
h0	Global film thickness	6.0-0.05	$\mu\text{m}$
L	Length of the local domain ( $\Omega$ )	200	$\mu\text{m}$
W	Width of the local domain	200	$\mu\text{m}$
$k_1$	Number of waves in x direction	2, 2, 4	
$k_2$	Number of waves in y direction	2, 1, 1	
$N_x$	Number of mesh points in x direction	64	
$N_y$	Number of mesh points in y direction	64	
$\theta$	Orientation of roughness	0, 15, 30, 45, 60, 90	$^\circ$ (degrees)
<b>Material properties</b>			
$E$	Elastic modulus	200	GPa
$\nu$	Poisson's ratio	0.32	
$P_{\text{max}}$	Maximum pressure	4.3	GPa

The Poiseuille flow factor  $A_{11}$  for the surfaces with local roughness defined by (5.32), and the parameters given in Table 5.3 are shown in Figures 5.45-5.47. Wavelength ratios  $k_1/k_2$  are equal to 4 and 2.

The general behaviour of the flow factors when the values  $\tau=h_0/h_r$  are high is similar to that of the flow factor for the extruded surface shown in Figure 5.36 in the sense that  $A_{11}\approx 1$  meaning no effect of roughness. When  $\tau$  approaches 0 the values of  $A_{11}$  tend to infinity for the reasons explained in Section 5.2.3. However, the values of  $A_{11}$  are non zero for the transverse roughness ( $\theta=0^\circ$ ), meaning that the flow of lubricant is not blocked when surface is in direct contact with the counterface.

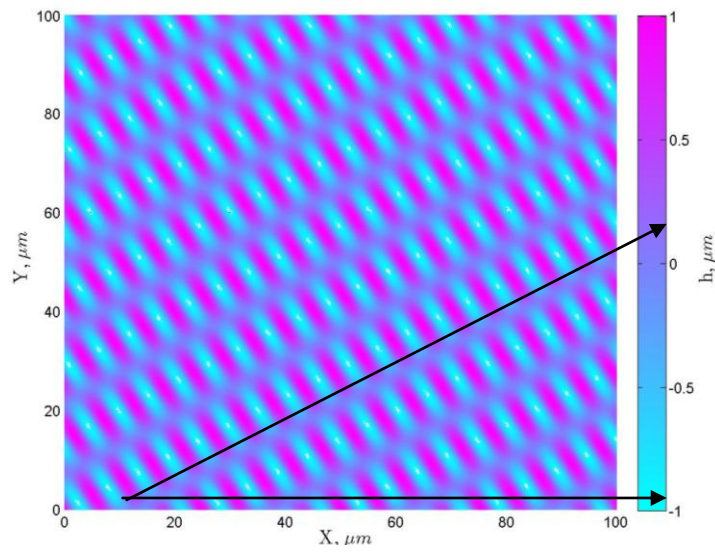


Figure 5.42 Double cosine surface,  $k_1/k_2=4$ ,  $\theta=30^\circ$

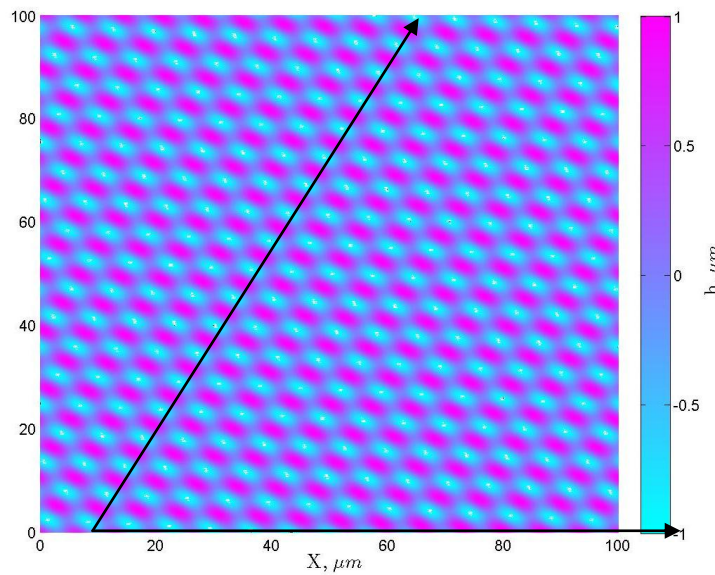


Figure 5.43 Double cosine surface  $k_1/k_2=2$ ,  $\theta=60^\circ$

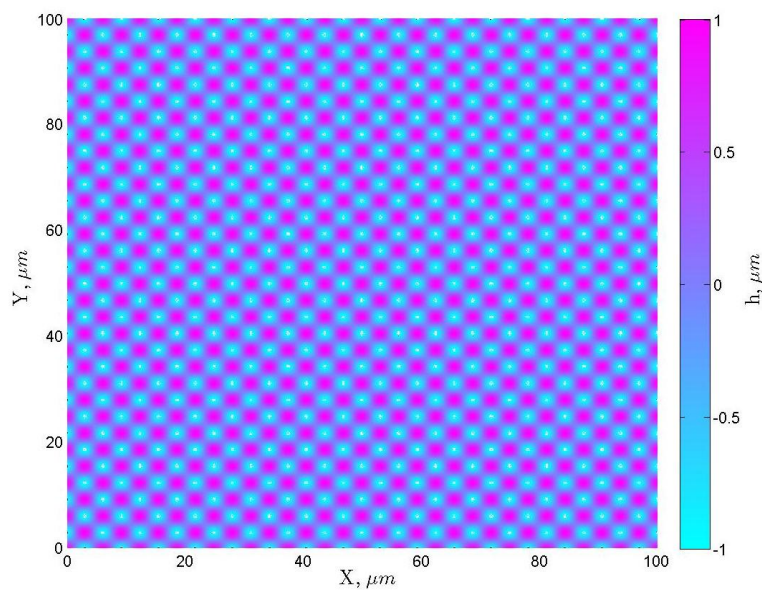


Figure 5.44 Isotropic double cosine surface,  $k_1/k_2=1$

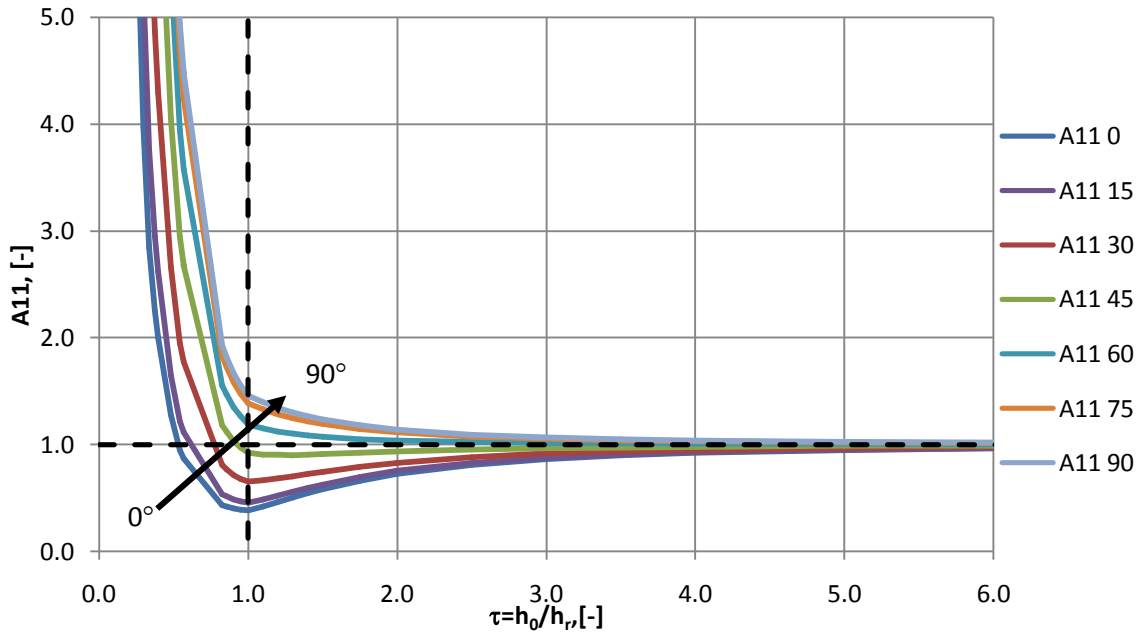


Figure 5.45 Flow factor  $A_{11}$  for double cosine surface, wavelength ratio  $k_1/k_2=4$ ; arrow indicates the sense of increasing the orientation angle from  $0^\circ$  to  $90^\circ$  degrees.

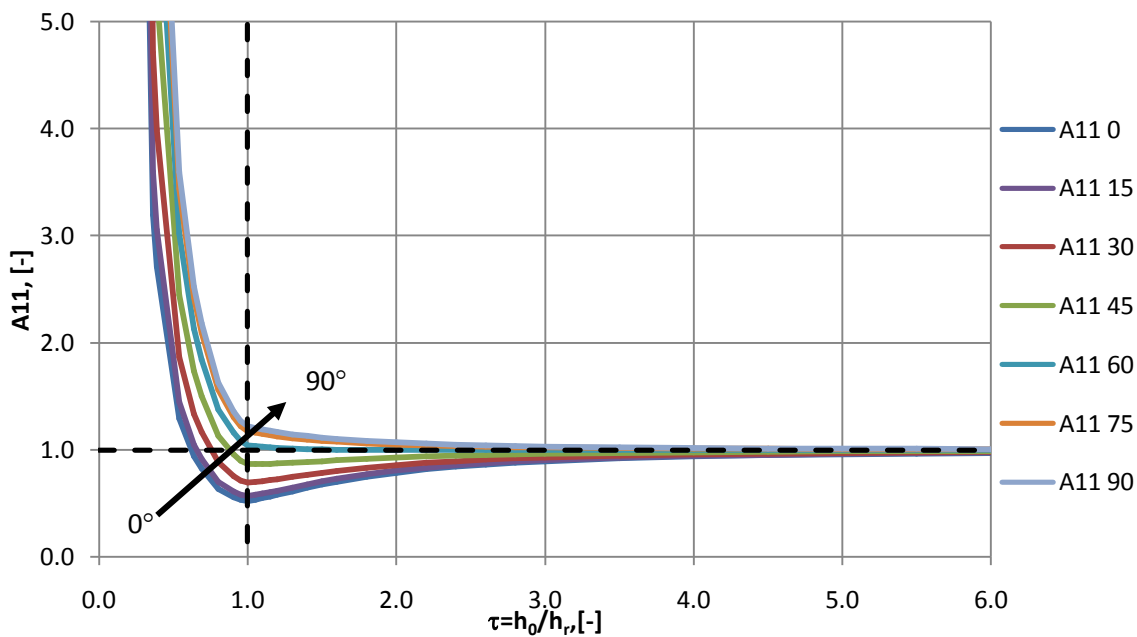


Figure 5.46 Flow factor  $A_{11}$  for double cosine surface, wavelength ratio  $k_1/k_2=2$ ; arrow indicates the sense of increasing the orientation angle from  $0^\circ$  to  $90^\circ$  degrees.

Another effect observed from comparing Figures 5.36, 5.45 and 5.46 is that the family of curves plotted for various roughness orientations  $\theta$  is more narrow for the double cosine surface than for the extruded one shown in Figure 5.36. This is explained by a less significant effect of the roughness orientation for the double cosine surface. The width of the band occupied by the family of curves plotted for various orientation angles progressively reduces when the ratio  $k_1/k_2$  becomes smaller, indicating a decrease in the effect of roughness orientation on the flow. For the wavelength ratio

$k_1/k_2=1$  the flow factor  $A_{11}$  is independent of the orientation angle  $\theta$ , which is illustrated by overlapped curves in Figure 5.47.

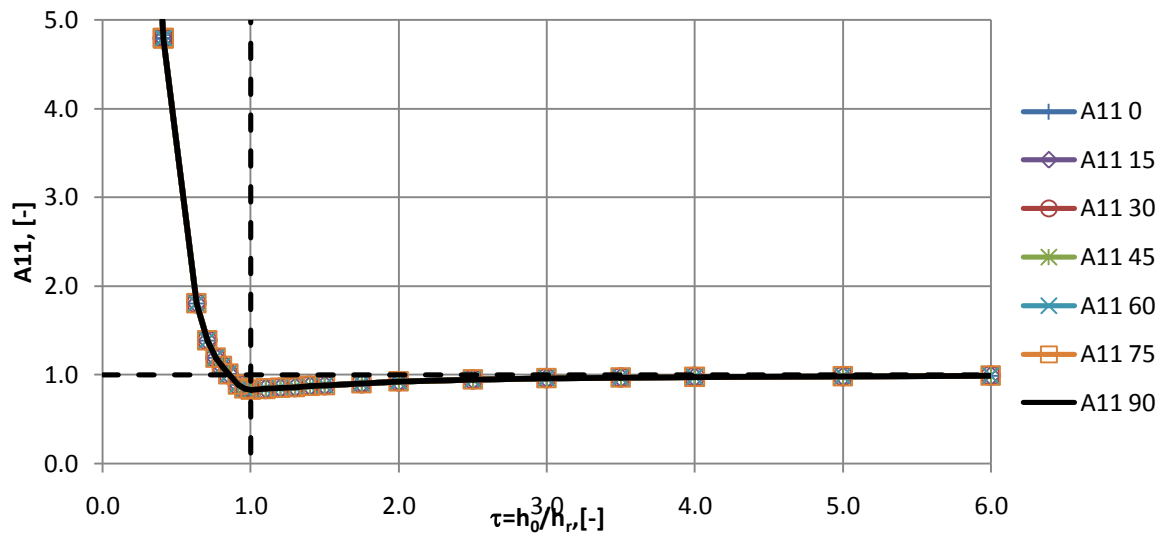


Figure 5.47 Flow factor  $A_{11}$  for double cosine surface, wavelength ratio  $k_1/k_2=1$ , roughness orientation  $\theta$  from 0 to 90 degrees.

The same effects, i.e. non-zero flow factors for the contact case and the reduction of the influence of roughness orientation on the flow can be observed from comparing the flow factor  $A_{22}$  or  $B_1$ . The values of  $A_{22}$  are not plotted, as they are the same as in Figures 5.45 and 5.46 with reversed order of the data series. The values of  $B_1$  are plotted in Figures 5.48- 5.50.

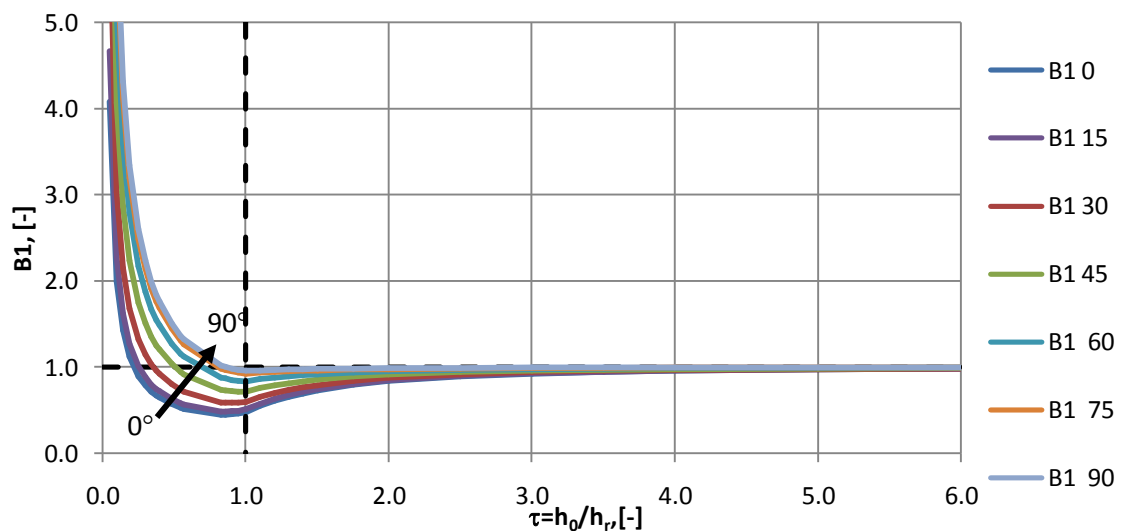


Figure 5.48 Flow factor  $B_1$  for double cosine surface, wavelength ratio  $k_1/k_2=4$ ; arrow indicates the sense of increasing the orientation angle from 0° to 90° degrees.

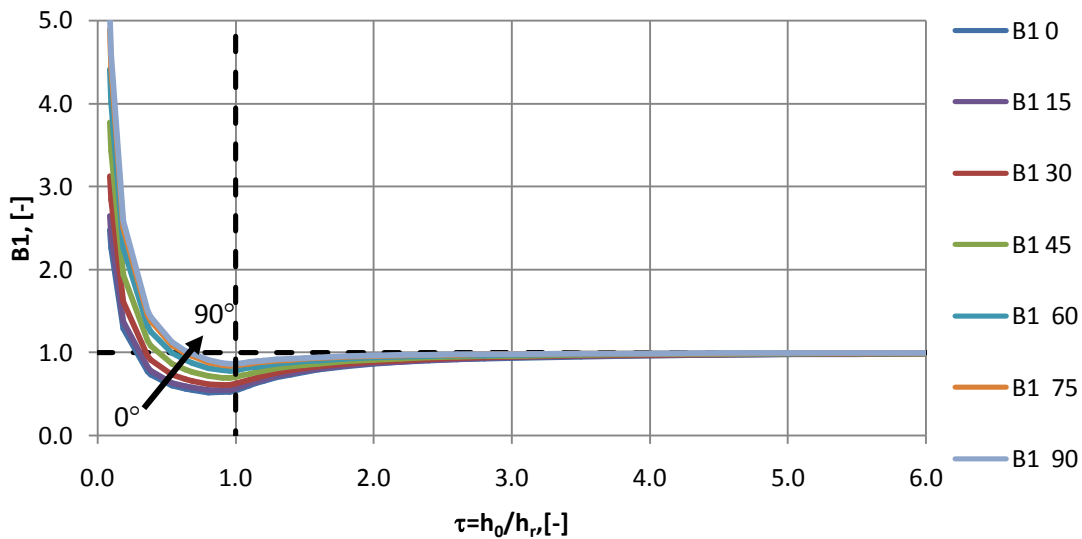


Figure 5.49 Flow factor  $B_1$  for double cosine surface, wavelength ratio  $k_1/k_2=2$ , roughness orientation  $\theta$  from 0 to 90 degrees.

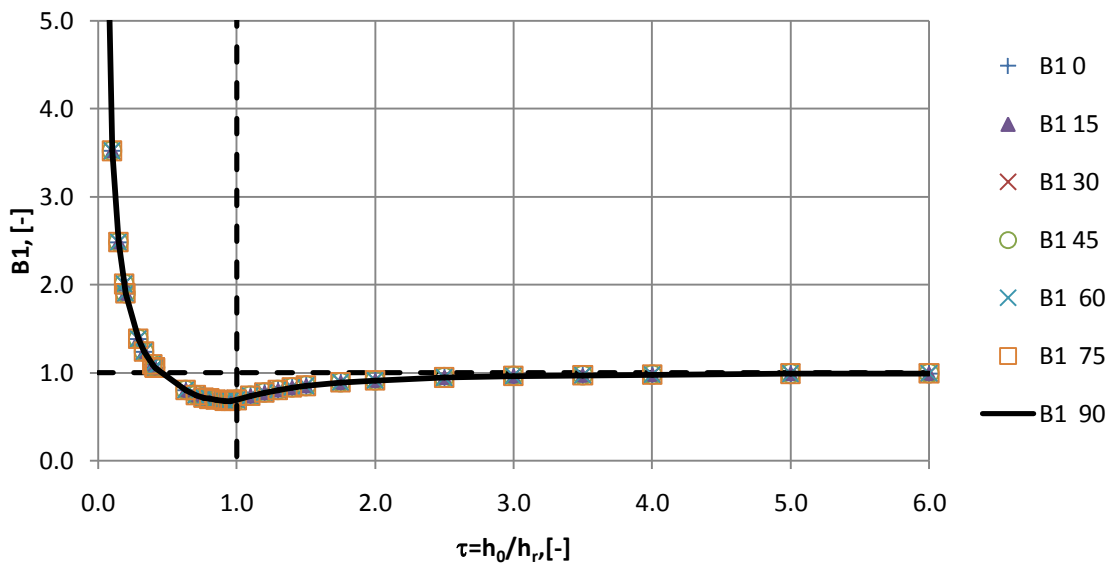


Figure 5.50 Flow factor  $B_1$  for double cosine surface, wavelength ratio  $k_1/k_2=1$ , roughness orientation  $\theta$  from 0 to 90 degrees.

### 5.2.6 The effect of the local cell dimensions on the flow factors

In the previous section the same dimensions were used for the local domain  $\Omega$ : it was considered to be a rectangular with sides  $L=W=200\mu\text{m}$ . In this section the effect of the dimensions of the local domain on the flow factors is investigated.

Consider stretching the roughness, i.e. increasing its wavelength, by a factor  $\kappa$  and denote the new roughness profile  $h^*$ . Figures 5.51a and 5.51b show the sinusoidal roughness profiles with 4 waves per period defined on a 0.2 mm and 0.4 mm representative areas. Coordinates  $\xi_2, \psi_2$  and  $\xi, \psi$  are related by:

$$\xi_2 = \kappa \xi, \psi_2 = \kappa \psi, \tag{5.33}$$

The stretched roughness have the property

$$h^*(\xi_2, \psi_2) = h(\xi, \psi). \quad (5.34)$$

To evaluate the flow factors in the plane  $\xi_2, \psi_2$  requires the solutions  $\chi_1^*$  of the equation

$$\frac{\partial}{\partial \xi_2} \left\{ h^{*3} \frac{\partial \chi_1^*}{\partial \xi_2} \right\} + \frac{\partial}{\partial \psi_2} \left\{ h^{*3} \frac{\partial \chi_1^*}{\partial \psi_2} \right\} = - \frac{\partial (h^{*3})}{\partial \xi_2} \quad (5.35)$$

The chain rule yields:

$$\frac{\partial}{\partial \xi_2} = \frac{\partial \xi}{\partial \xi_2} \frac{\partial}{\partial \xi} = \frac{1}{\kappa} \frac{\partial}{\partial \xi}; \quad \frac{\partial}{\partial \psi_2} = \frac{\partial \psi}{\partial \psi_2} \frac{\partial}{\partial \psi} = \frac{1}{\kappa} \frac{\partial}{\partial \psi}$$

So (5.35) becomes

$$\frac{1}{\kappa^2} \frac{\partial}{\partial \xi} \left\{ h^{*3} \frac{\partial \chi_1^*}{\partial \xi} \right\} + \frac{1}{\kappa^2} \frac{\partial}{\partial \psi} \left\{ h^{*3} \frac{\partial \chi_1^*}{\partial \psi} \right\} = - \frac{1}{\kappa} \frac{\partial (h^{*3})}{\partial \xi}$$

Using (5.34) this can be written as

$$\frac{1}{\kappa} \frac{\partial}{\partial \xi} \left\{ h^3 \frac{\partial \chi_1^*}{\partial \xi} \right\} + \frac{1}{\kappa} \frac{\partial}{\partial \psi} \left\{ h^3 \frac{\partial \chi_1^*}{\partial \psi} \right\} = - \frac{\partial (h^3)}{\partial \xi} \quad (5.36)$$

For the unstretched profile  $\chi_1$  is the solution to

$$\frac{\partial}{\partial \xi} \left\{ h^3 \frac{\partial \chi_1}{\partial \xi} \right\} + \frac{\partial}{\partial \psi} \left\{ h^3 \frac{\partial \chi_1}{\partial \psi} \right\} = - \frac{\partial (h^3)}{\partial \xi} \quad (5.37)$$

So comparing Equations (5.36) and (5.37) it is apparent that

$$\frac{1}{\kappa} \chi_1^* = \chi_1, \quad \chi_1^* = \kappa \chi_1$$

To complete the calculation of  $a_{11}$  requires evaluation of the integral

$$a_{11}(h_0) = \frac{1}{|\Omega_2|} \int_{\Omega_2} \frac{h^{*3}}{h_0^3} \left( 1 + \frac{\partial \chi_1^*}{\partial \xi_2} \right) d\Omega_2$$

i.e.

$$a_{11} h_0 = \frac{1}{\kappa^2 L W} \int_0^{\kappa L} \int_0^{\kappa W} \frac{h^{*3}}{h_0^3} \left( 1 + \frac{\partial \chi_1^*}{\partial \xi_2} \right) d\xi_2 d\psi_2$$

Since  $\chi_1^* = \kappa \chi_1$  and  $h^*(\xi_2, \psi_2) = h(\xi, \psi)$ . the substitution  $\xi_2 = \kappa \xi, \psi_2 = \kappa \psi$  gives

$$a_{11} h_0 = \frac{1}{\kappa^2 L W} \int_0^L \int_0^W \frac{h^3}{h_0^3} \left( 1 + \frac{1}{\kappa} \frac{\partial \kappa \chi_1}{\partial \xi_2} \right) \kappa^2 d\xi d\psi$$

i.e.

$$a_{11} h_0 = \frac{1}{\kappa^2 L W} \int_0^L \int_0^W \frac{h^3}{h_0^3} \left( 1 + \frac{1}{\kappa} \frac{\partial \kappa \chi_1}{\partial \xi_2} \right) d\xi d\psi \quad (5.38)$$

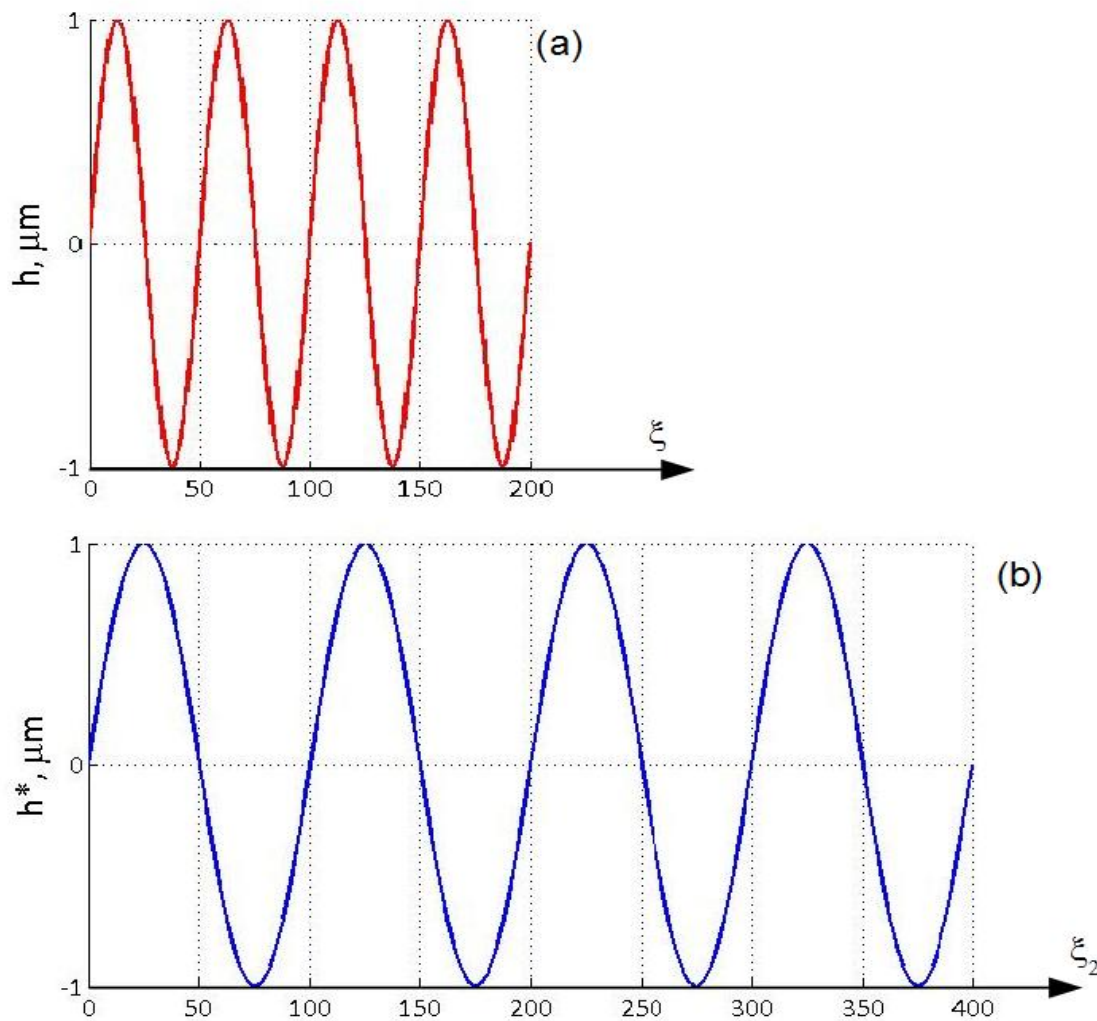


**Figure 5.51 Sinusoidal roughness in the original and stretched coordinates  $\xi, \psi$  and  $\xi_2, \psi_2$  respectively**

Equation (5.38) is identical to the definition of  $a_{11}(h_0)$  in terms of  $h(\xi, \psi)$  and so it can be concluded that stretching the roughness profile by the same factors in both directions leads to no changes in the flow factors  $a_{11}$ . The same procedure can be applied to other flow factors and thus all the flow factors  $a_{ij}$  and  $b_{ij}$  for  $i, j=1,2$  are independent of stretching.

Note also that the analytical expressions for an extruded cosine surface (5.28)-(5.30) are not dependent on the dimensions of the area in any way. For a double cosine surface this effect can be observed in Figures 5.52 and 5.53 where the flow factors were calculated for a surface defined by the formula (5.32) with  $k_1=4$ ,  $k_2=1$ . The dimensions of the area of interest are  $200 \times 200 \mu\text{m}$  (solid curve, crosses) and  $2 \times 2 \text{ mm}$  (dashed curve, circles).

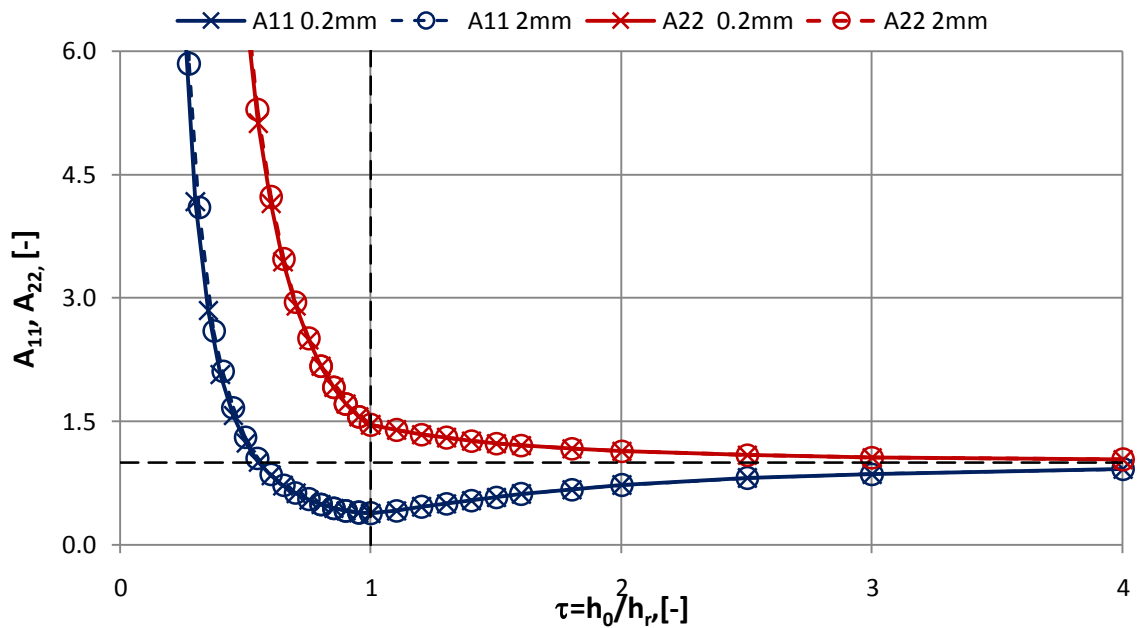


Figure 5.52 Poiseuille flow factors  $A_{11}$  and  $A_{22}$  for a double cosine surface with number of waves  $k_1=4$ ,  $k_2=1$  and representative areas  $0.2 \times 0.2$  mm and  $2 \times 2$  mm.

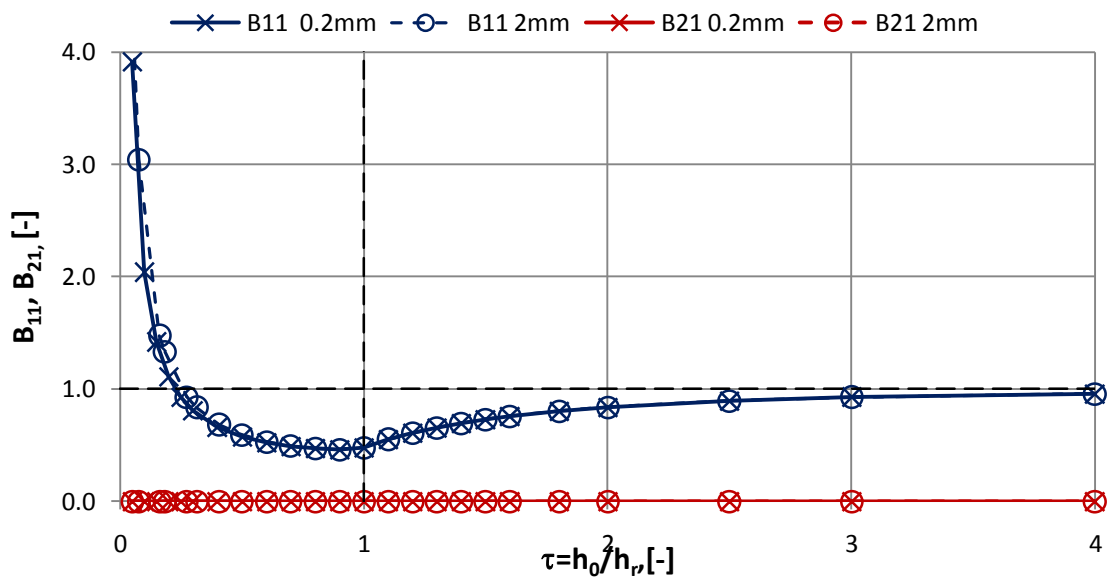


Figure 5.53 Couette flow factors  $B_{11}$  and  $B_{21}$  for a double cosine surface with number of waves  $k_1=4$ ,  $k_2=1$  and representative areas  $0.2 \times 0.2$  mm and  $2 \times 2$  mm.

The data series are in perfect agreement for the values of  $\tau > 1$  with minor deviations for  $\tau < 0.6$ . The case of direct contact of the surface asperities ( $\tau < 1$ ) deserves special attention. The surface with smaller representative area has smaller wavelength of the roughness features for the same roughness function. Therefore the radius of curvature of the asperity tips is smaller which according to the Hertzian contact theory results in higher pressures. However, as the flow factors are calculated for a specified gap, the elastic displacement for both cases is the same. This means that the flow factors are independent of the dimensions of the representative area even for the case of contact

## Section 5.2 Calculating of the flow factors

as long as the pressures are within the elastic limit. This is illustrated in Figures 5.52 and 5.53 by the coinciding points for the values of  $0.6 < \tau < 1$ . The pressures for the case of smaller dimensions are higher, therefore contact points may exhibit plastic deflection while in the larger area all the points are still elastic. This effect can be observed in Figures 5.54 and 5.55 where the mean pressure and contact area are plotted for both cases. Contact area here is defined as the number of nodes which are in contact multiplied by the mesh cell area and mean pressure is defined as the total load carried by the asperities divided by the nominal area. It can be observed that both the mean pressure and contact area for original roughness remain proportional to the case of stretched roughness for the values of  $\tau$  down to 0.6. The coefficient of proportionality is  $\kappa$  for the mean pressure and  $1/\kappa^2$  for the contact area. In the example shown  $\kappa = 2.0/0.2 \text{ mm} = 10$ , i.e. mean pressure for the stretched roughness multiplied by 10 is compared with the mean pressure for the original roughness and the contact area for the original roughness is multiplied by 100. For the values of  $\tau < 0.6$  the difference between the mean pressure and contact area for the dimensions of  $0.2 \times 0.2 \text{ mm}$  and  $2 \times 2 \text{ mm}$  becomes apparent. The reason for this is that the roughness features with smaller tangential dimensions are stiffer and they start experiencing plastic deflection when  $\tau < 0.6$  whereas the asperities in the  $2 \times 2 \text{ mm}$  case remain elastic throughout the whole range of  $\tau$ .

### 5.2.7 Flow factors for measured surfaces

In this section the flow factors are calculated for measured surfaces. Surface roughness was measured using a Taylor-Hobson form profilometer in the traverse ( $x$ ) direction with spacing of  $0.5 \mu\text{m}$ . The 2 dimensional roughness function was obtained by taking a series of such profiles with the sample moved in the transverse ( $y$ ) direction by a step of  $0.5 \mu\text{m}$  between each profile. The samples used for measurements were machined in different ways producing different surface roughness which is summarised in Table 5.4. The profiles of the surfaces considered are plotted at the same scale in Figure 5.72 for comparison, and the machining process of each surface is explained in more details in the appropriate section. The shape of the measured surfaces and potential waviness was removed using high-pass Gaussian filter with a cut off wavelength of  $0.25 \text{ mm}$ .

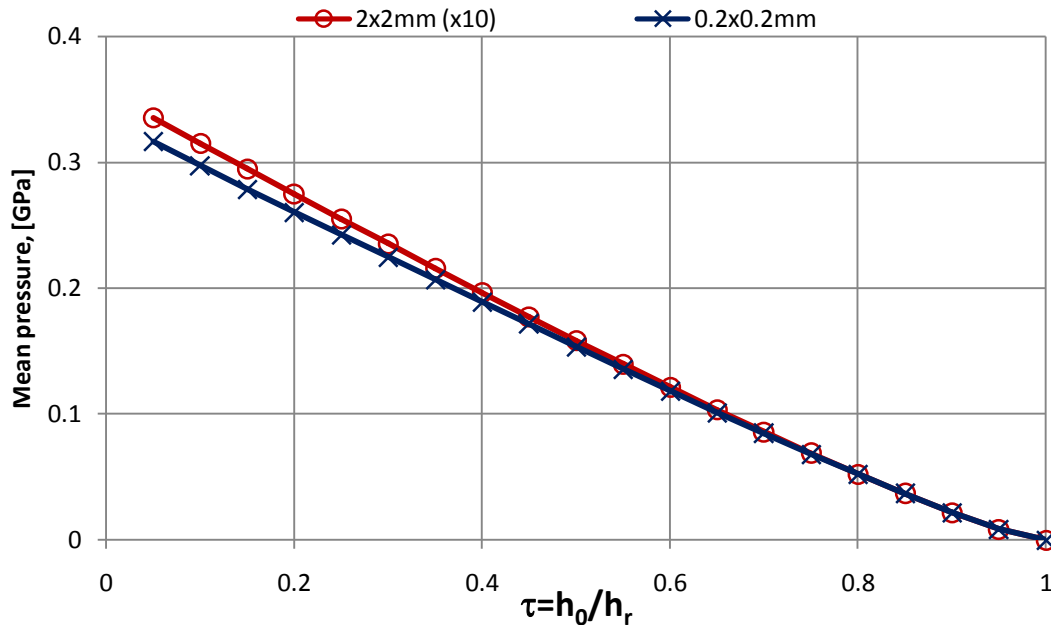


Figure 5.54 Mean pressure for a double cosine surface with number of waves  $k_1=4$ ,  $k_2=1$  and representative area  $0.2 \times 0.2$  mm and  $2 \times 2$  mm. Mean pressure for a  $2 \times 2$  mm representative area is multiplied by 10.

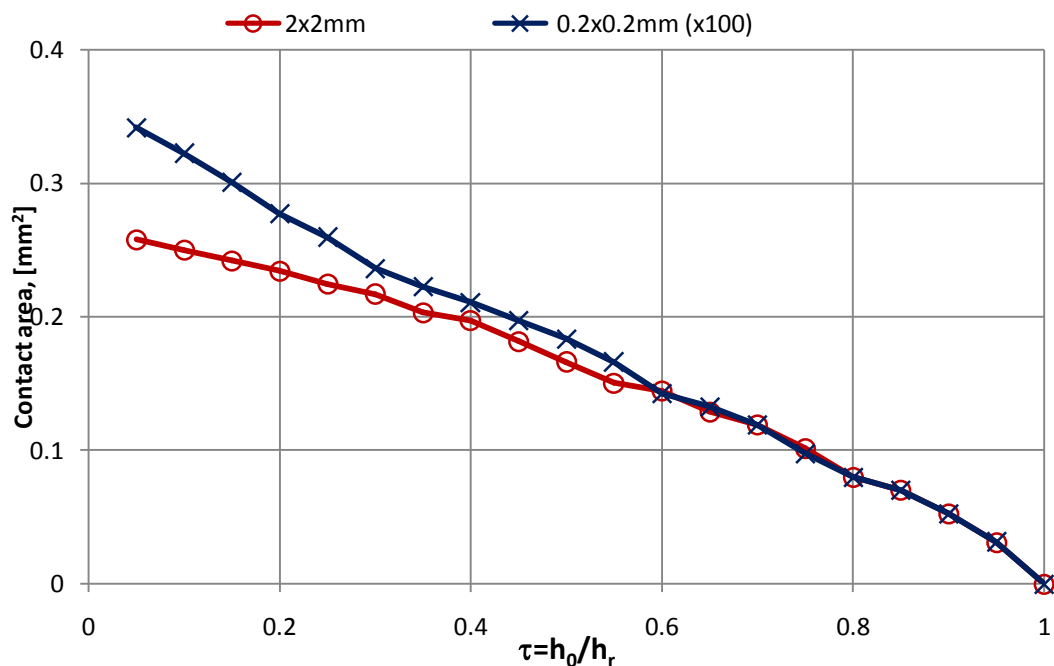


Figure 5.55 Contact area for a double cosine surface with number of waves  $k_1=4$ ,  $k_2=1$  representative area  $0.2 \times 0.2$  mm and  $2 \times 2$  mm. Contact area for a  $0.2 \times 0.2$  mm representative area is multiplied by 100.

#### *Axially ground disc*

The first measured surface considered was that of a hardened steel disc, *disk A*. The disk was machined by a coned abrasive wheel which created a crowning and (approximately) axial finishing. The principle of axial grinding is illustrated in Figure 5.56 in plan (A) and side (B) views.

## Section 5.2 Calculating of the flow factors

Table 5.4 Roughness characteristics for measured surfaces

Roughness characteristic		Ground surface (Disk A)	Super finished (Disk B)	EDM
Highest peak	$S_p$	$0.8 \mu\text{m}$	$0.27 \mu\text{m}$	$13.81 \mu\text{m}$
Deepest valley	$S_v$	$-1.14 \mu\text{m}$	$-0.3 \mu\text{m}$	$-11.7 \mu\text{m}$
Mean roughness	$S_a$	$0.25 \mu\text{m}$	$0.042 \mu\text{m}$	$3.02 \mu\text{m}$
Standard deviation	$S_q$	$0.32 \mu\text{m}$	$0.056 \mu\text{m}$	$3.72 \mu\text{m}$
Skewness	$S_{sk}$	-0.4	-0.17	0.034
Kurtosis	$S_{ku}$	2.87	4.4	2.67

The roughness function obtained for disk A is shown in Figure 5.57. The form of the disk (radius and crowning) disk were filtered out from the profile measurements in both directions. The surface in Figure 5.57 has an aggressive roughness profile in X direction with amplitude of the roughness features of up to  $1\mu\text{m}$  corresponding to the marks left by the abrasive wheel. In the Y direction the deviations are of the order of  $0.1\mu\text{m}$  along the motion path of abrasive features of a grinding wheel. The resulting surface is equivalent to a uni-directionally ground surface and is almost extruded in nature. The statistical roughness characteristics of this surface are given in Table 5.4 and profiles of the cross Sections parallel to x and y axes are given in Figures 5.58 and 5.59 respectively.

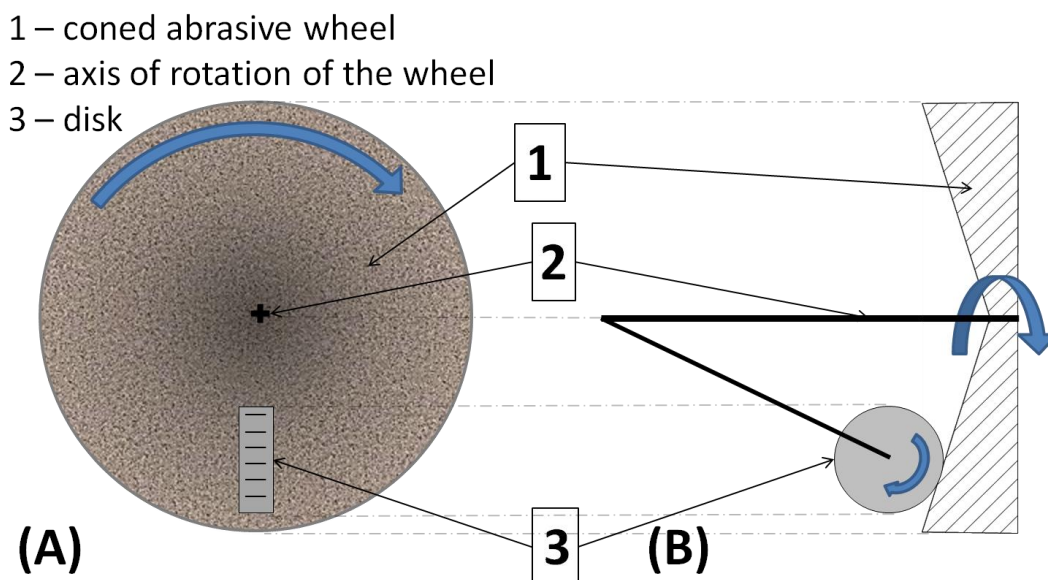


Figure 5.56 Axial grinding using a cone shaped abrasive wheel: plan view(A), side view (B)

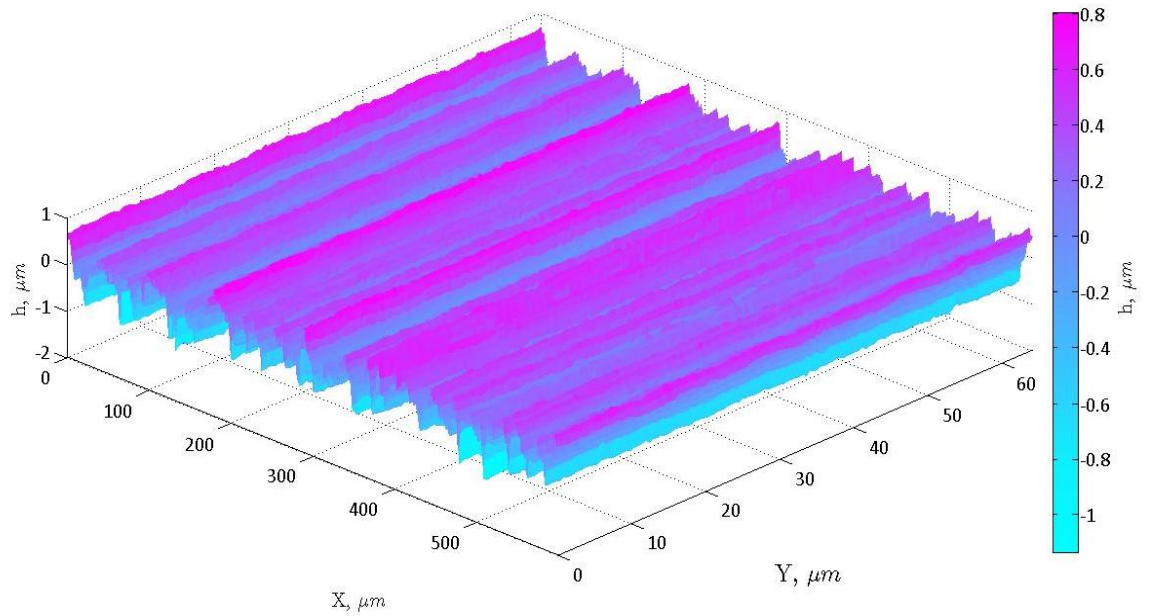


Figure 5.57 Uni directionally ground surface, isometric view

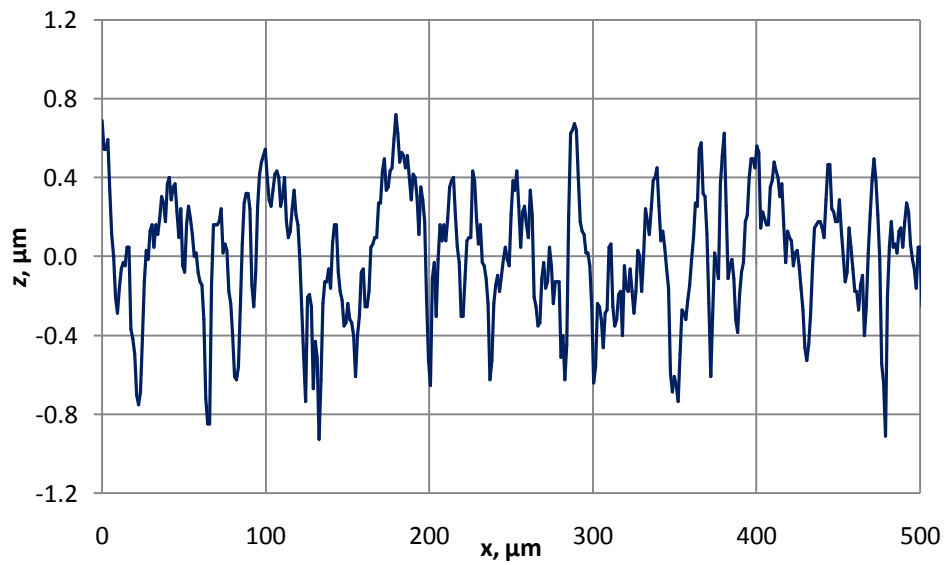


Figure 5.58 Uni directionally ground surface: profile of a cross section parallel to  $x$  axis

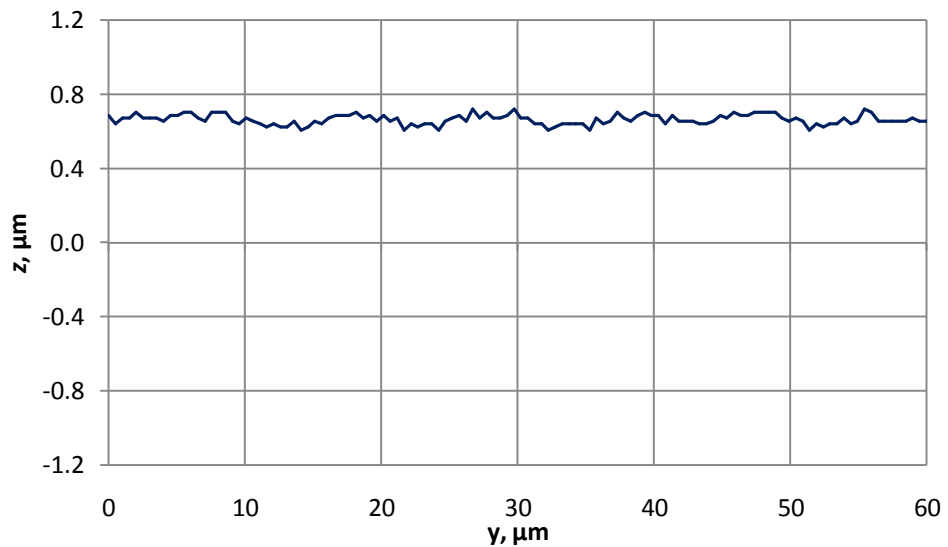


Figure 5.59 Uni directionally ground surface: profile of a cross section parallel to  $y$  axis

## Section 5.2 Calculating of the flow factors

The flow factors for the surface of disk A are plotted in Figures 5.60 and 5.61. Note that these flow factors are plotted against the ratio  $\tau=h_0/S_p$ . As for the sinusoidal roughness the ratio  $\tau$  denotes the distance between the mean planes of the surfaces relative to the surface highest peak. Therefore  $\tau=1$  (denoted by a vertical dashed line) means that the first contact occurs at the highest asperity peak, however the behaviour of the flow factors is not significantly affected until more asperities come into contact.

The first observation that can be made is that the values of the Poiseuille flow factor  $A_{11}$  are below the unity value line (shown dashed). The values are also quite low and keep decreasing after the contact occurs. This behaviour is similar to the one observed for the flow factors calculated for an extruded surface, see e.g. Figure 5.24, as opposed to the one which the double cosine surface shows in Figure 5.45. This can be explained by the fact that a ground surface is almost extruded in the direction of the grinding lay. However, after the contact occurs the small deviations of asperity heights in the  $y$  direction prevent the roughness features away from making total contact thus preventing the complete blockage of flow. This effect is illustrated by non zero values of  $A_{11}$  in case of a contact ( $\tau < 1$ ) in Figure 5.60.

The Couette flow factors plotted in Figure 5.61 also behave in a similar way to the extruded surface (see e.g. Figure 5.27) before the contact occurs, while showing non zero values after the contact which means that the flow is never completely blocked. Note also that both cross terms  $A_{12}$  and  $B_2$  are always zero as there is no significant side flow caused by the presence of the roughness.

### *Super finished surface*

The second surface was measured on a reground crowned disk. The disk was reground in circumferential direction and after that was super finished. The roughness function was obtained by filtering out both the radius and circular crowning of the disk from the measured data. The roughness function is shown in Figure 5.62 in isometric view and profiles of the cross Sections parallel to  $x$  and  $y$  axes are shown in Figures 5.63 and 5.64 respectively.

This surface has a much lower roughness amplitude than the ground one: the maximum value does not exceed  $0.3\mu\text{m}$ . The more detailed roughness characteristics are given in Table 5.4.

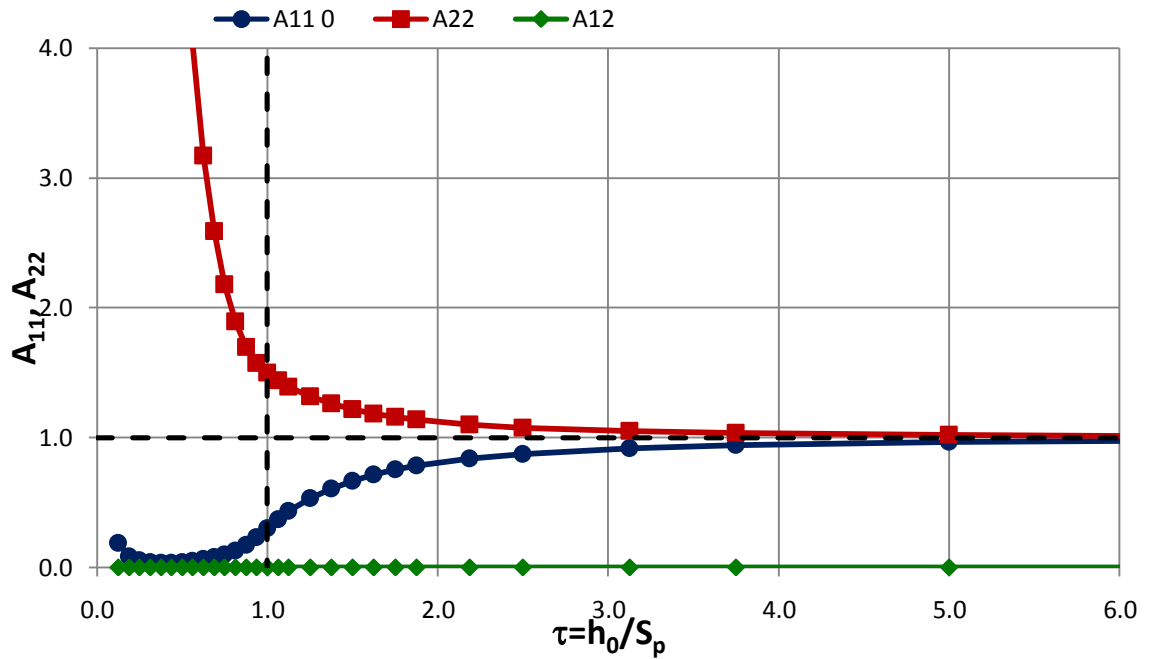


Figure 5.60 Poiseuille flow factors calculated for the uni directionally ground surface

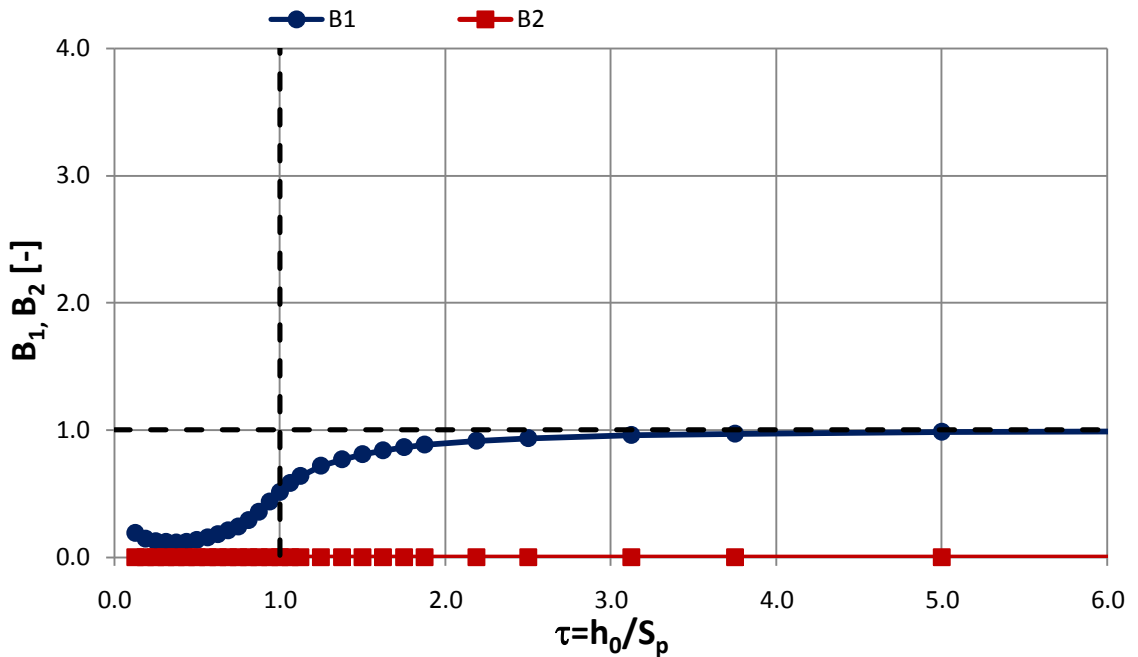


Figure 5.61 Couette flow factors calculated for the uni directionally ground surface

The low  $S_p$  and  $S_a$  values are explained by the super finishing of a disk. However the regrinding process left circumferential marks visible even after super finishing, as can be seen in Figure 5.64. As opposed to the ground surface these roughness features have a longitudinal orientation and the deviations of roughness in the direction of entrainment ( $x$ ) are much smaller than in the transverse direction due to the super finishing. Note that the Z axis in Figures 5.58-5.59 and 5.63-5.64 has the same scale.

## Section 5.2 Calculating of the flow factors

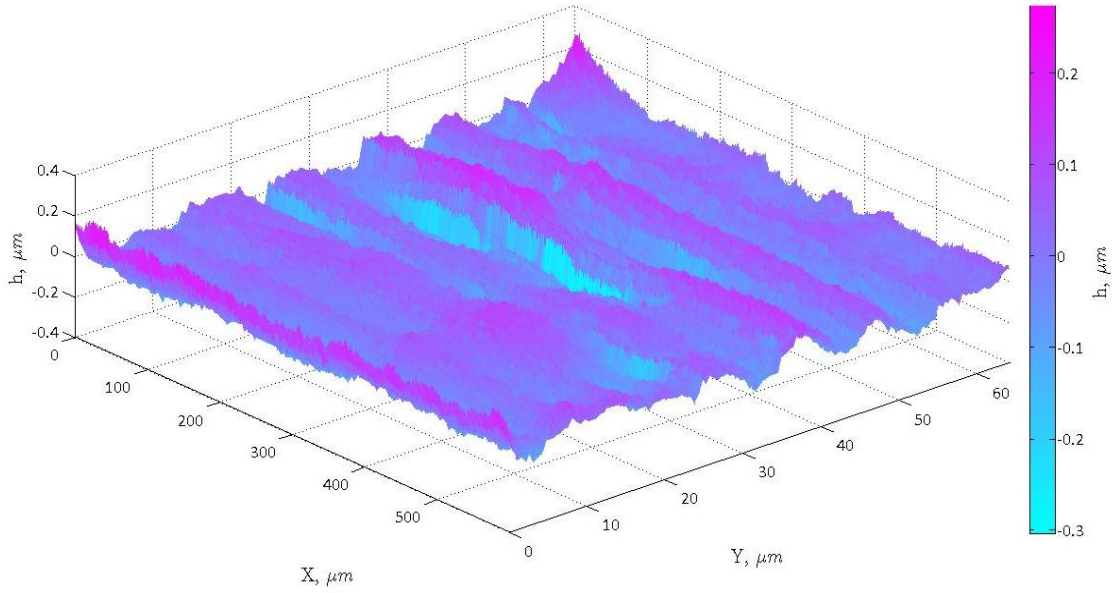


Figure 5.62 Super finished surface: isometric view

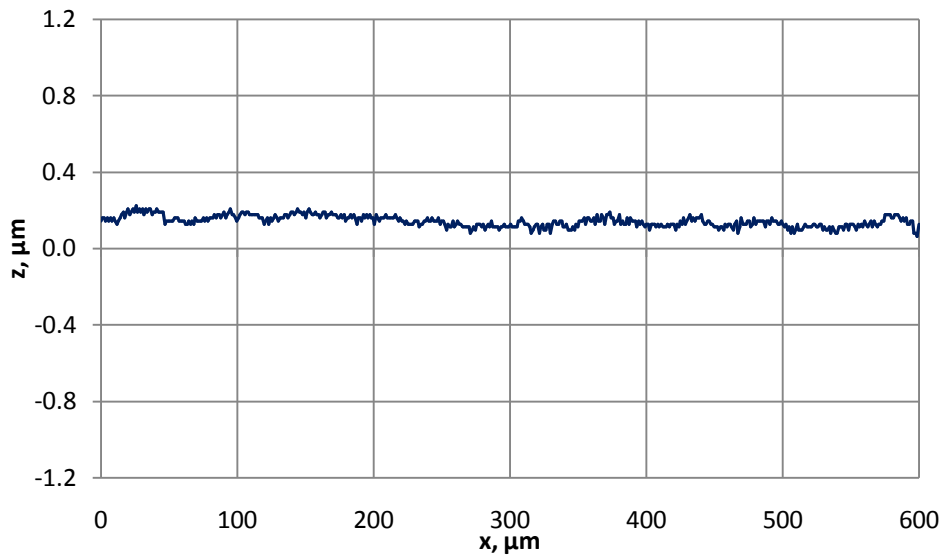


Figure 5.63 Super finished surface: profile of a cross section parallel to  $x$  axis.

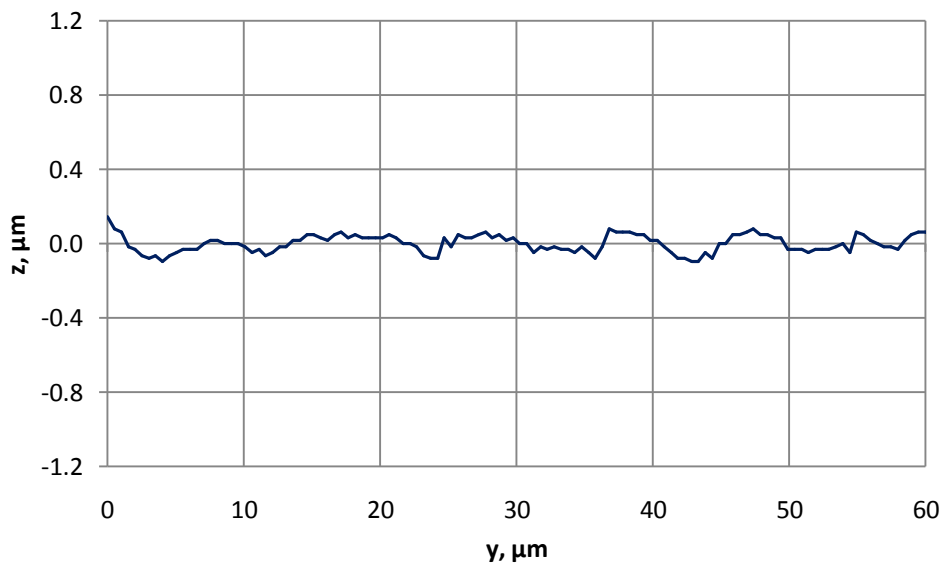


Figure 5.64 Super finished surface: profile of a cross section parallel to  $y$  axis.

First observation that can be made from the flow factors plotted in Figures 5.65-5.66 is that the deviations of  $A_{11}$ ,  $A_{22}$  and  $B_1$  from the unity line are much smaller than that for the ground surface (Figures 5.60-5.61). This means that the effect of roughness on the flow is much less significant than that for the ground surface. Note also that the flow factors are plotted against a non dimensional parameter  $\tau=h_0/S_p$  i.e.  $\tau=1$  for a ground surface is equivalent to  $\tau=3$  for the super finished one in terms of the global film thickness.

Second, the values of the flow factor  $A_{11}$  are above zero, as seen for the surfaces with longitudinal roughness (see e.g. Figure 5.36, curve corresponding to  $\theta=90$ ). Also, it is apparent from Figures 5.62 and 5.63 that the cross terms  $A_{12}$  and  $B_2$  become non-zero when surfaces are in contact which means that the fluid flow diverted by the roughness features is non-zero as  $\tau$  approaches 0.

#### *Surface prepared by electrical discharge machining*

The third measured roughness was obtained from a surface prepared by electrical discharge machining (EDM). During this process the material is removed from the work piece by a series of rapidly recurring current discharges between two electrodes, separated by a dielectric liquid and subject to an electric voltage. This process creates a surface with random two dimensional roughness with no characteristic orientation of the asperities. The two dimensional roughness function for this surface is shown in Figure 5.67 in isometric view and profiles of cross sections parallel to  $x$  and  $y$  axes are shown in Figures 5.68-5.69 respectively. The highest asperity on this surface reaches  $S_p=13.8\mu\text{m}$  while the  $S_a$  value is  $\sim 3.0\mu\text{m}$ . This means that the first direct contact occurs when  $h_0=13.8\mu\text{m}$  for a single asperity; however the flow will not be significantly reduced until more asperities come into contact.

The flow factors for this surface are plotted in Figures 5.70 and 5.71. The first striking observation that can be made is that the values of  $A_{11}$  are very close to those of  $A_{22}$ . This effect is observed in its strongest form for pure isotropic surfaces such as double cosine surface (see e.g. Figure 5.44) for which the flow factors are plotted in Figures 5.47 and 5.50. This is explained by the random nature of the roughness features of the surface.

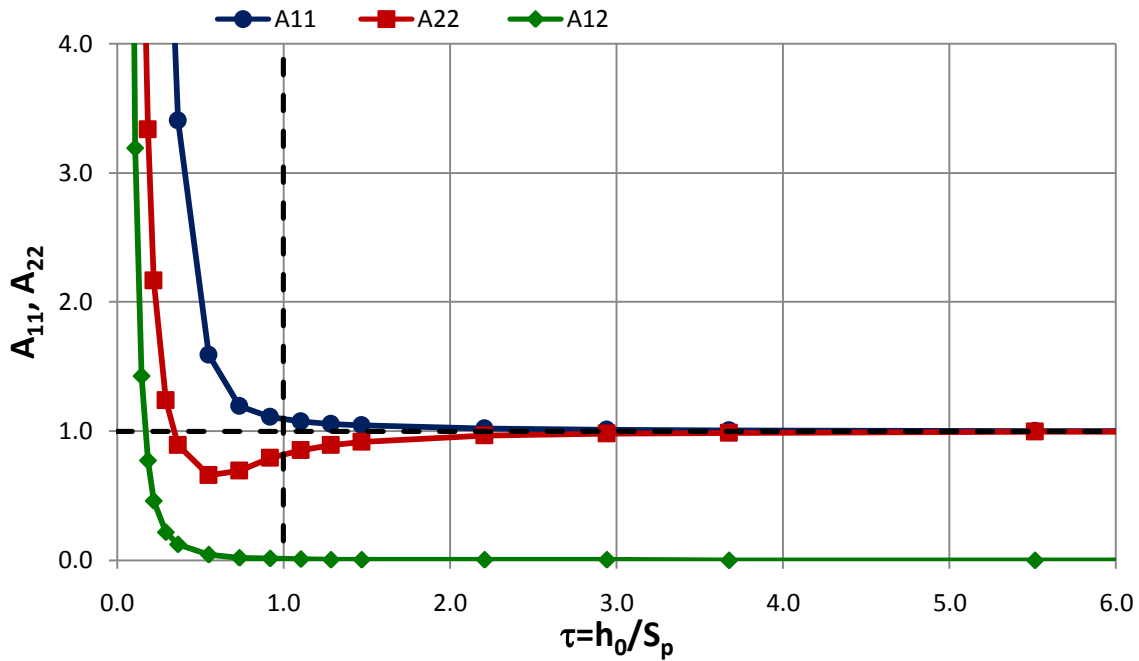


Figure 5.65 Poiseuille flow factors for the super finished surface

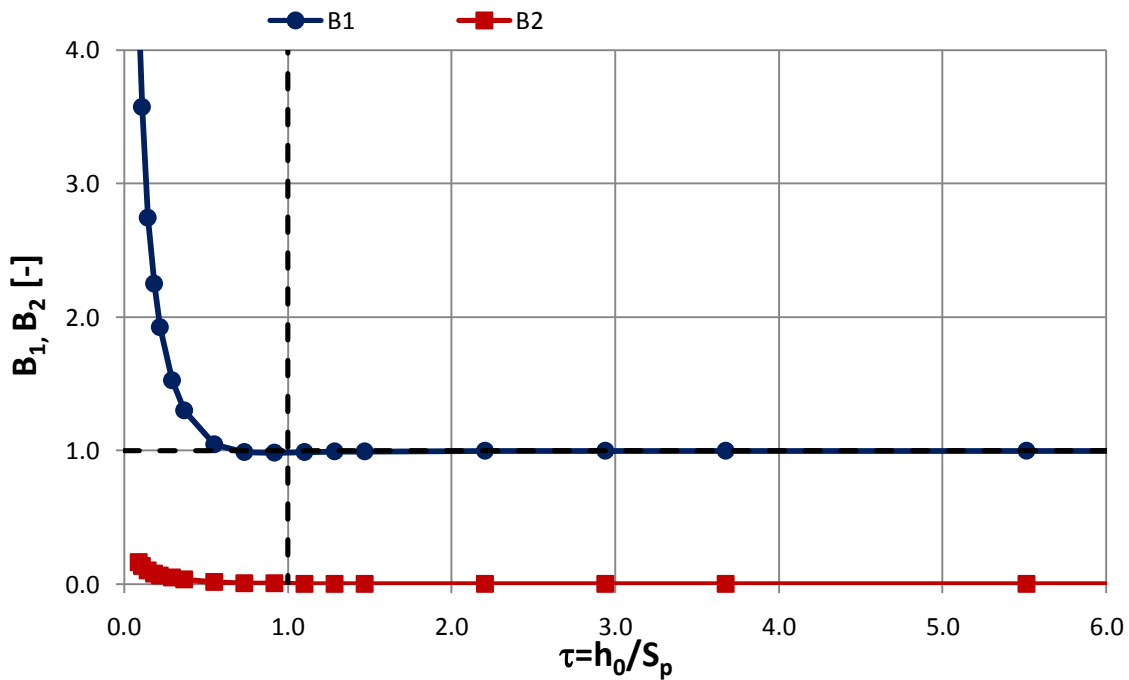


Figure 5.66 Couette flow factors for the finished surface

Second observation is that both  $A_{11}$  and  $A_{22}$  values approach infinity as  $\tau$  approaches 0. This is caused by the direct contact of the roughness features keeping the surfaces apart and thus allowing the fluid flow equally in both directions. Also the flow factor being above unity line means that there is more flow of lubricant in the presence of roughness than in the case of smooth surfaces. This effect was explained in Section 5.2.3 and illustrated in Figure 5.26.

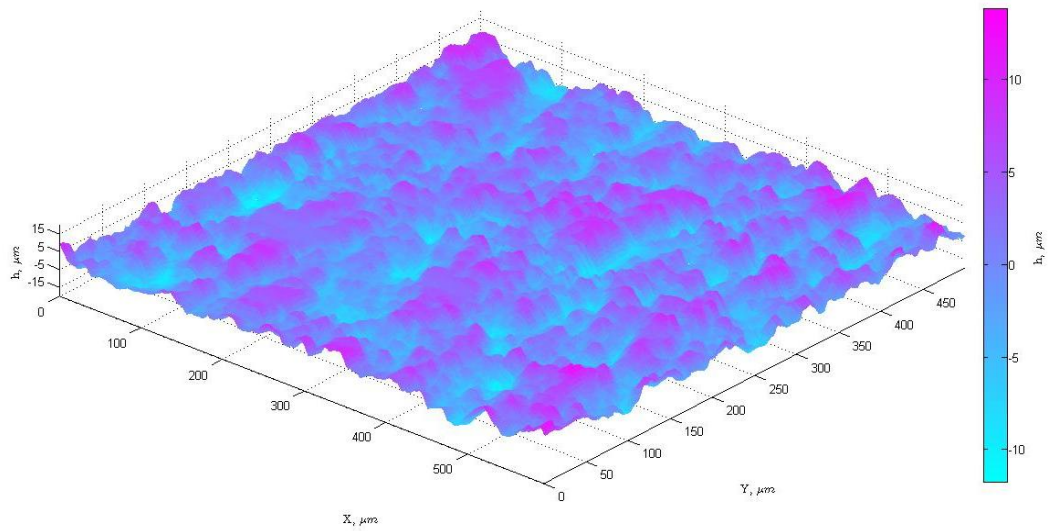


Figure 5.67 Surface prepared by electrical discharge machining: isometric view

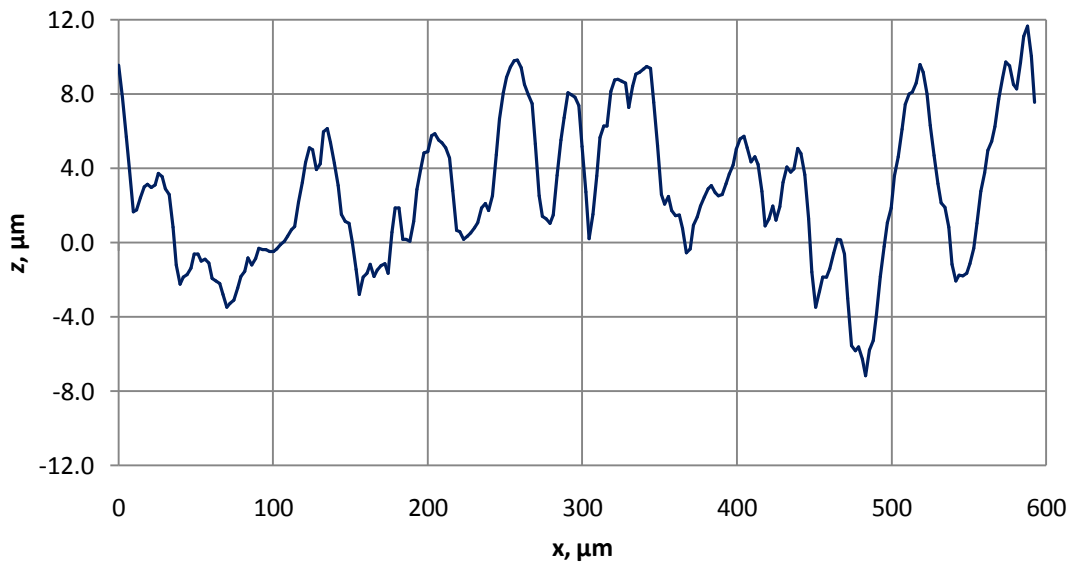


Figure 5.68 Surface prepared by electrical discharge machining: profile of a cross section parallel to x axis

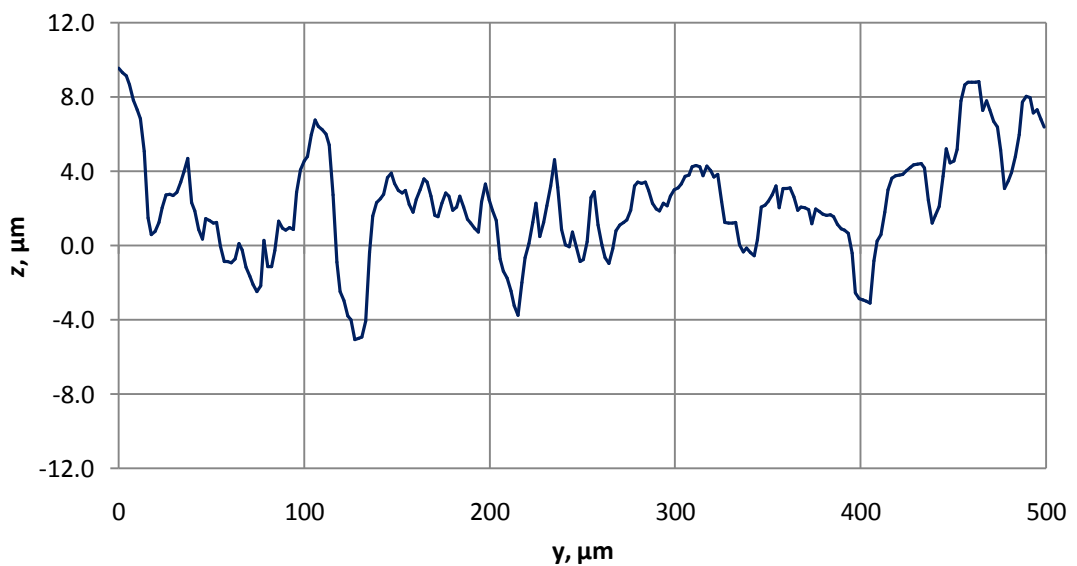


Figure 5.69 Surface prepared by electrical discharge machining: : profile of a cross section parallel to y axis

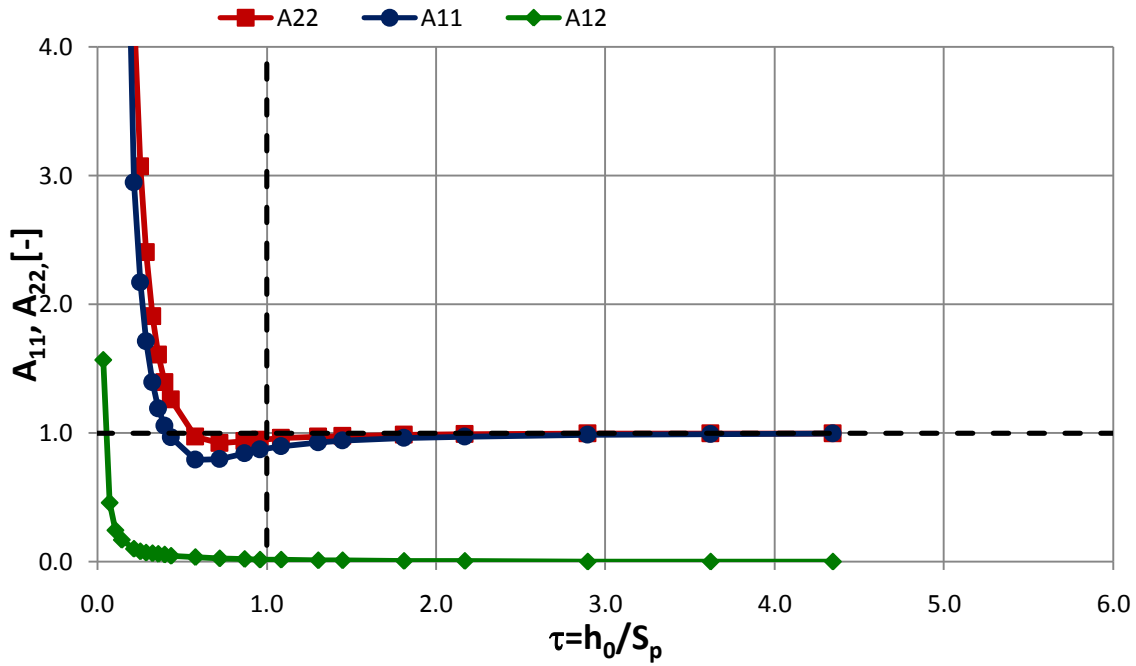


Figure 5.70 Poiseuille flow factors for the surface prepared by electrical discharge machining

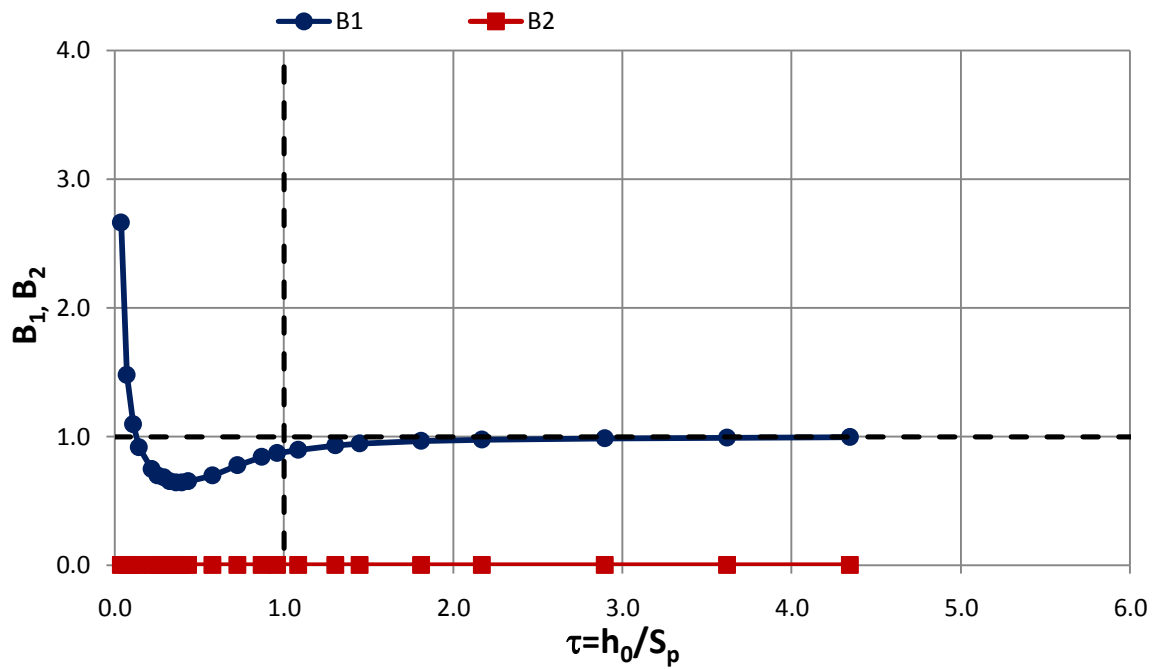


Figure 5.71 Couette flow factors for the surface prepared by electrical discharge machining

Figure 5.72 shows profiles of all three surfaces brought at the same scale which makes it easier to compare the roughness obtained by different treatment of the surfaces. Mean lines are shifted in z direction in order to accommodate all profiles on one chart.

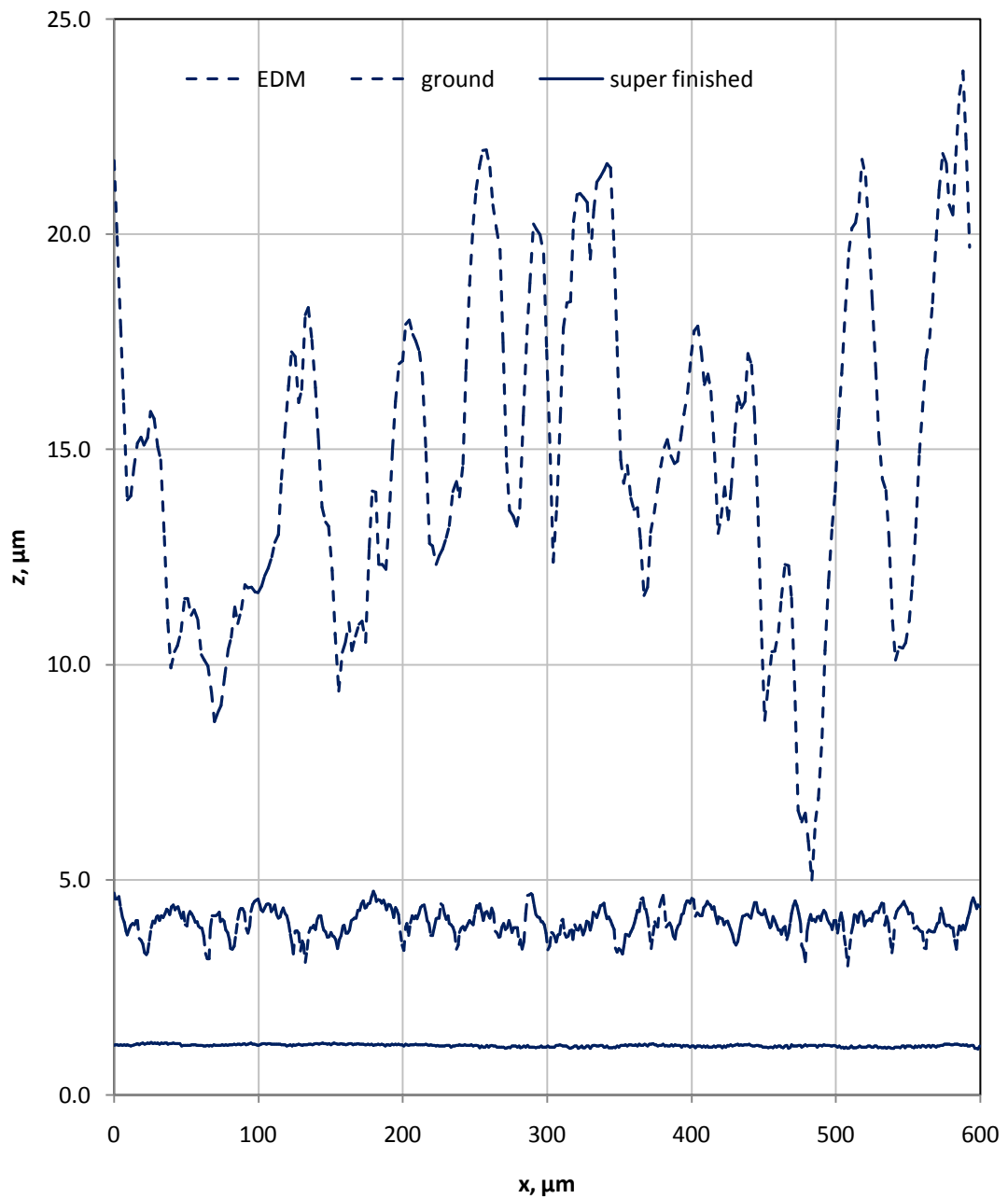


Figure 5.72 Profiles parallel to  $x$  axis of three surfaces used: ground, super finished and prepared by EDM.

(intentionally blank)

## 6 Mixed lubrication in plain bearings

### 6.1 Introduction

In this chapter the problem of mixed lubrication in plain bearings is formulated and then a solution method is presented based on the homogenised Reynolds equation approach. The homogenised Reynolds equation approach is described in Chapter 4 and allows the effect of roughness on the flow of liquid lubricant to be taken into account in an averaged way. This method is proposed instead of a deterministic one which considers the contributions of the individual asperities. The deterministic approach requires a very fine resolution and consequently is very demanding computationally. In case of the direct contact of surface asperities the solution method based on the homogenised approach allows the elastic and plastic deflection of the surface asperities obtained by means of the dry contact analysis which is described in Chapter 3 to be taken into account.

The method starts from selecting a (small) representative area which captures the characteristic roughness features of the surface. The roughness is assumed to be a periodic repetition of this representative area. The effect of roughness is included into the consideration in the form of flow factors which are functions of the surface roughness and the global smooth surface film thickness. If the values of the global film thickness are not high enough to prevent the surfaces from making contact, then the deflected shape is used to calculate the flow factors. In addition the load carried by the contacting asperities is calculated as a function of the global film thickness so that it can be taken into account in determining the load to be carried by the lubricant pressure in the smooth surface homogenised solution.

In this work the mixed lubrication problem in tilted pad bearings is considered. The reason for this choice is convenience in that the formulation of this problem does not consider zones of cavitation of the fluid. Cavitation problems have been addressed by e.g. Bayada (2005) and Kane and Bou-Said (2004) in application of the homogenised Reynolds equation to the lubrication in journal bearings.

A photograph and a schematic representation of a tilted pad thrust bearings are shown in Figures 6.1 and 6.2. Tilted pad thrust bearings were first introduced and patented by Australian engineer George Michell (1905). Michell bearings contain a number of

## Section 6.2 Formulation of a tilted pad problem

sector-shaped pads, arranged in a circle around the shaft, and which are free to pivot. These create regions of pressurised oil between the pads and rotating disc which support the applied thrust and eliminate metal-on-metal contact. The tilting angle of the pads seriously affects the load carrying capacity of a bearing. Pivoting allows the pads to self align for the best performance.



Figure 6.1 A photo of a tilted pad thrust bearing (source: <http://basicsofmarineengineering.blogspot.co.uk/>)

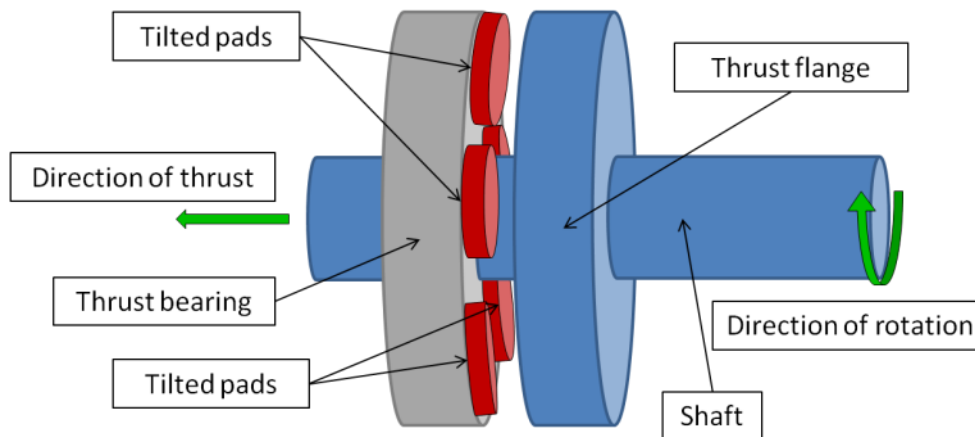


Figure 6.2 A schematic representation of a tilted pad thrust bearing

### 6.2 Formulation of a tilted pad problem

The lubrication of a single tilted pad is considered. A single tilted pad is a sector shaped pad placed on a thrust bearing facing the rotating disk. The geometry of a tilted pad is shown in Figure 6.3. In the current work the problem is simplified by assuming that a tilted pad is a stationary rectangular plate of length  $L$  and width  $W$  separated from a counterface by a minimum distance of  $h_{min}$  and tilted with respect to it at the angle  $\alpha$ . The counterface is assumed to be an area on the flange of the rotating shaft. For simplicity the motion of the counterface is considered to be rectilinear rather than circumferential. It is clear from the drawing of Figure 6.3 that for a given angular speed

of the shaft the linear velocity of a point on the flange depends on the radial position of the point, having its minimum value at the position denoted by “c” and maximum at “a”. The velocity at the point “b” is used in the formulation of the current problem.

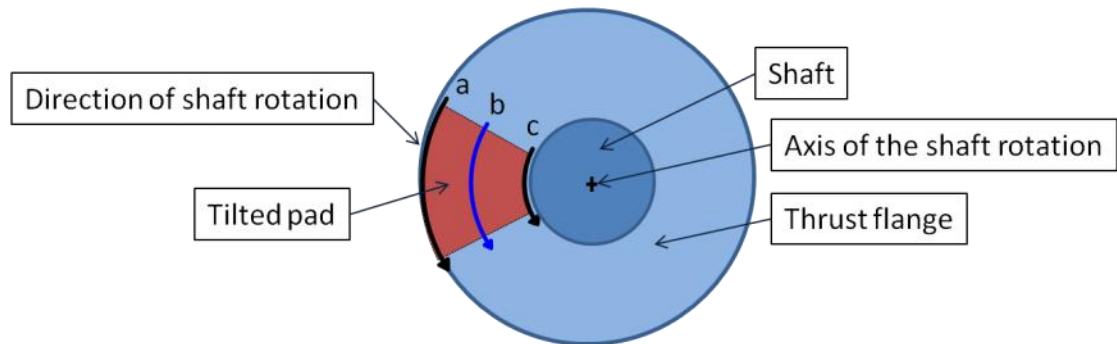


Figure 6.3 Geometry of a tilted pad

The problem of a single tilted pad in the formulation considered in this thesis is shown schematically in Figure 6.4. Note that the configuration of a tilted pad can be defined by two variables connecting the gap at the position of the pivot and the angle of tilting  $\alpha$ . In the work of Almqvist and Dasht (2006) the geometry is defined by the film thickness values at the entrance and the exit of the lubrication zone. However, in the current work the minimum gap  $h_{min}$  and tilting angle  $\alpha$  are used.

The system of Cartesian coordinates is introduced so that the x axis is directed along the direction of motion of the counterface. The origin is placed at the point of maximum clearance with respect to x axis and in the centre of the counterface with respect to y axis. Note that the geometry of the problem is extruded in the transverse (y) direction. The system of coordinates is shown in Figure 6.5.

The gap between the tilted pad and the counterface is then defined as follows:

$$h_0(x, y) = h_{min} \left[ \gamma + \frac{x}{L} (1 - \gamma) \right] \quad (6.1)$$

where  $\gamma = \tan \alpha = h_{max}/L$  defines the tilting angle of the pad. As explained earlier the geometry is constant in the y direction. The solutions given in this chapter are for a fixed position of the tilting pad.

The surface of a tilted pad is assumed to be rough and stationary while the counterface is smooth and subjected to linear motion. This choice of configuration makes the film thickness (or gap) function  $h(x, y)$  independent of the time variable. Also, the origin of the coordinates is fixed at the point of maximum film thickness.

## Section 6.2 Formulation of a tilted pad problem

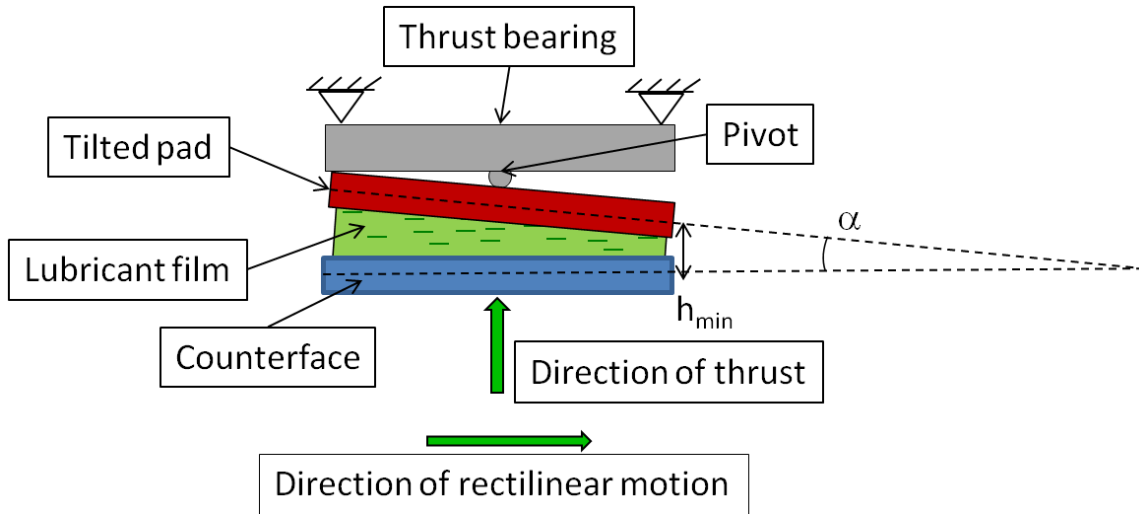


Figure 6.4 Lubrication of a single tilted pad

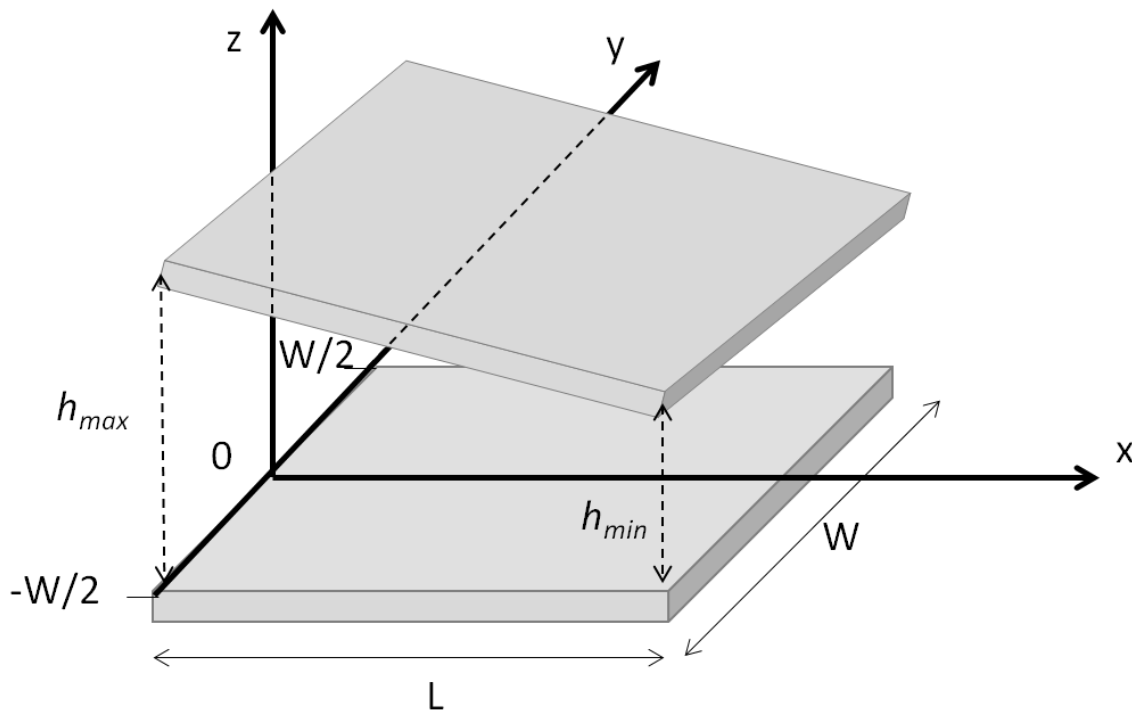


Figure 6.5 System of coordinates for the tilted pad problem

Taking into account roughness of the tilted pad the film thickness function becomes:

$$h(x, y) = h_0(x, y) + R(x, y) \quad (6.2)$$

where  $h_0(x, y)$  is called the *global film thickness* and is defined by the geometry of a problem, whereas  $R(x, y)$  is the roughness function. In the current case of tilted pad bearing the global film thickness is given by Equation (6.1). The problem can then be formulated as follows:

- Find the load (in a form of pressure distribution) for a specified clearance  $h_{min}$ , tilting  $\alpha$ , and roughness  $R(x, y)$
- Find the clearance  $h_{min}$  for a specified load, tilting  $\alpha$ , and roughness  $R(x, y)$
- Find the tilting angle for a specified load, clearance  $h_{min}$  and  $R(x, y)$

In this thesis the problem formulation (a) is considered.

Assuming that the conditions given in Section 4.3 are satisfied, the Reynolds equation can be used to solve the problem in formulation (a).

In this chapter three variations of the problem are considered: the smooth case, the rough surface case and the homogenised roughness case. For the smooth and rough surface cases the Reynolds Equation (4.1) is solved, or if the lubricant can be assumed incompressible and isoviscous the equation can be simplified to the form (4.2). The homogenised case is an attempt to solve the problem of mixed lubrication without considering the individual effect of the roughness features as described in Chapters 4 and 5. The homogenised Equation (4.34) is then solved, which is given below for convenience:

$$\frac{\partial}{\partial x} \left\{ h_0^3 A_{11} \frac{\partial p}{\partial x} + h_0^3 A_{12} \frac{\partial p}{\partial y} \right\} + \frac{\partial}{\partial y} \left\{ h_0^3 A_{21} \frac{\partial p}{\partial x} + h_0^3 A_{22} \frac{\partial p}{\partial y} \right\} = \lambda \frac{\partial}{\partial x} \{ h_0 B_1 \} + \lambda \frac{\partial}{\partial y} \{ h_0 B_2 \} \quad (6.3)$$

The six oblique flow factors  $A_{ij}$ , and  $B_i$  ( $i,j=1,2$ ) are evaluated as defined by Equation (4.33) using the eight flow factors  $a_{ij}$ ,  $b_{ij}$  ( $i,j=1,2$ ) calculated in the axis of the roughness periodicity according to the formulae (4.27) and (4.28).

Note that the homogenised Reynolds Equation (6.3) also defines the mixed lubrication problem for the smooth case if the values of the flow factors are set as  $A_{11}=A_{22}=B_1=1$  and  $A_{12}=A_{21}=B_2=0$ . In addition, replacing the global film thickness function  $h_0(x,y)$  defined by (6.1) with the total film thickness function  $h(x,y)$  defined by (6.2) gives the equation for the rough surface case.

Homogenised Equation (6.3) is an elliptical second order partial differential equation. It is proposed in the next section to solve this equation numerically using the Gauss-Seidel method.

### 6.3 Solving the Reynolds equation using the Gauss-Seidel method

The Gauss-Seidel method is described in Section 5.1.1 where it is applied for solving the local problems.

#### 6.3.1 Discretisation

Equation (6.3) is discretised on a  $[0..N_x] \times [-N_y/2..N_y/2]$  mesh grid using central differences. As in Section 5.1.1 the internodal points are used in discretisation of the

### Section 6.3 Solving the Reynolds equation using the Gauss-Seidel method

second derivative terms in order to maintain the conservation of flow. The sketch of the mesh points is shown in Figure 6.6 which is equivalent to Figure 5.1.

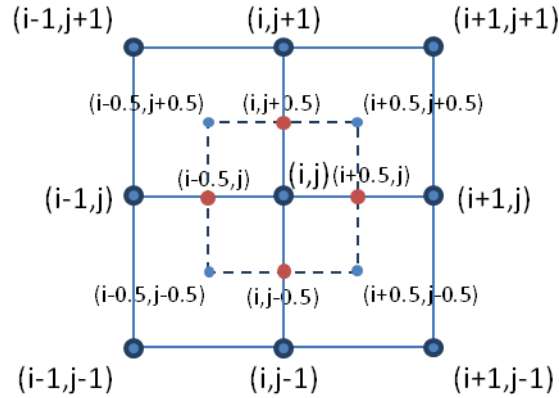


Figure 6.6 The nodes and inter nodal points used for the Discretisation of the derivatives

As the flow factors are functions of  $h_0$  the following notations are introduced for convenience:

$$\begin{aligned}
 \Phi_{ij}^{(1)} &= A_{11}(h_{i,j})h_{i,j}^3 & \Phi_{ij}^{(2)} &= A_{12}(h_{i,j})h_{i,j}^3 \\
 \Phi_{ij}^{(3)} &= A_{21}(h_{i,j})h_{i,j}^3 & \Phi_{ij}^{(4)} &= A_{22}(h_{i,j})h_{i,j}^3 \\
 \Phi_{ij}^{(5)} &= B_1(h_{i,j})h_{i,j} & \Phi_{ij}^{(6)} &= B_2(h_{i,j})h_{i,j}
 \end{aligned}
 \tag{6.4}$$

Note that the super scripts 1 to 6 denote the six different  $\Phi$  functions and are not operations on a single function  $\Phi$ . Equation (6.3) then becomes:

$$\frac{\partial}{\partial x} \left\{ \Phi^{(1)} \frac{\partial p}{\partial x} + \Phi^{(2)} \frac{\partial p}{\partial y} \right\} + \frac{\partial}{\partial y} \left\{ \Phi^{(3)} \frac{\partial p}{\partial x} + \Phi^{(4)} \frac{\partial p}{\partial y} \right\} = \lambda \frac{\partial}{\partial x} \{ \Phi^{(5)} \} + \lambda \frac{\partial}{\partial y} \{ \Phi^{(6)} \}
 \tag{6.5}$$

Using the internodal point the second derivative is discretised as follows:

$$\begin{aligned}
 \frac{\partial}{\partial x} \left( \Phi^{(1)} \frac{\partial p}{\partial x} \right) \Big|_{i,j} &= \frac{\left( \Phi^{(1)} \frac{\partial p}{\partial x} \right)_{i+0.5,j} - \left( \Phi^{(1)} \frac{\partial p}{\partial x} \right)_{i-0.5,j}}{\Delta x} \\
 &= \frac{\Phi_{i+0.5,j}^{(1)} p_{i+1,j} + \Phi_{i-0.5,j}^{(1)} p_{i-1,j} - \left( \Phi_{i+0.5,j}^{(1)} + \Phi_{i-0.5,j}^{(1)} \right) p_{i,j}}{\Delta x^2}
 \end{aligned}
 \tag{6.6}$$

Similarly,

$$\begin{aligned}
 \frac{\partial}{\partial y} \left( \Phi^{(4)} \frac{\partial p}{\partial y} \right) \Big|_{i,j} &= \frac{\left( \Phi^{(4)} \frac{\partial p}{\partial y} \right)_{i,j+0.5} - \left( \Phi^{(4)} \frac{\partial p}{\partial y} \right)_{i,j-0.5}}{\Delta y} \\
 &= \frac{\Phi_{i,j+0.5}^{(4)} p_{i,j+1} + \Phi_{i,j-0.5}^{(4)} p_{i,j-1} - \left( \Phi_{i,j+0.5}^{(4)} + \Phi_{i,j-0.5}^{(4)} \right) p_{i,j}}{\Delta y^2}
 \end{aligned}
 \tag{6.7}$$

Cross derivatives are discretised using the internodal points in a similar manner:

$$\begin{aligned} \left. \frac{\partial}{\partial x} \left( \Phi^{(2)} \frac{\partial p}{\partial y} \right) \right|_{i,j} &= \frac{\left( \Phi^{(2)} \frac{\partial p}{\partial y} \right)_{i+0.5,j} - \left( \Phi^{(2)} \frac{\partial p}{\partial y} \right)_{i-0.5,j}}{\Delta x} = \\ &= \frac{\Phi_{i+0.5,j}^{(2)} (p_{i+0.5,j+0.5} - p_{i+0.5,j-0.5}) - \Phi_{i-0.5,j}^{(2)} (p_{i-0.5,j+0.5} - p_{i-0.5,j-0.5})}{\Delta x \Delta y} \end{aligned} \quad (6.8)$$

The second cross term:

$$\begin{aligned} \left. \frac{\partial}{\partial y} \left( \Phi^{(3)} \frac{\partial p}{\partial x} \right) \right|_{i,j} &= \frac{\left( \Phi^{(3)} \frac{\partial p}{\partial x} \right)_{i,j+0.5} - \left( \Phi^{(3)} \frac{\partial p}{\partial x} \right)_{i,j-0.5}}{\Delta y} = \\ &= \frac{\Phi_{i,j+0.5}^{(3)} (p_{i+0.5,j+0.5} - p_{i-0.5,j+0.5}) - \Phi_{i,j-0.5}^{(3)} (p_{i+0.5,j-0.5} - p_{i-0.5,j-0.5})}{\Delta x \Delta y} \end{aligned} \quad (6.9)$$

The right hand side terms are discretised in the same way:

$$\lambda \left. \frac{\partial \Phi^{(5)}}{\partial x} \right|_{i,j} = \lambda \frac{\Phi_{i+0.5,j}^{(5)} - \Phi_{i-0.5,j}^{(5)}}{\Delta x}; \quad \lambda \left. \frac{\partial \Phi^{(6)}}{\partial y} \right|_{i,j} = \lambda \frac{\Phi_{i,j+0.5}^{(6)} - \Phi_{i,j-0.5}^{(6)}}{\Delta y} \quad (6.10)$$

Note that in the current problem the second right hand side term is always zero. If homogenised or smooth problem is considered then  $h(x,y)$  is defined by Equation (6.1) which is extruded in  $y$  direction. Therefore, as  $\Phi^{(6)}$  is a function of  $h$  and its derivative the  $\frac{\partial}{\partial y}$  operation results in zero values for these cases. If the rough case is considered then  $h(x,y)$  is defined by Equation (6.2) and the derivative  $\frac{\partial}{\partial y}$  is non zero, however the flow factor  $B_2$  is zero for this case.

The value of a variable at the inter nodal point is assumed to be the mean of the values of the two or four neighbouring nodes. In particular the values of  $p$  at the internodal points are:

$$p_{i+0.5,j} = \frac{p_{i+1,j} + p_{i,j}}{2}; \quad p_{i+0.5,j+0.5} = \frac{p_{i+1,j} + p_{i,j} + p_{i+1,j+1} + p_{i,j+1}}{4} \quad (6.11)$$

taking into account the discretised derivatives (6.6)-(6.10) and the rule for inter nodal points (6.11) Equation (6.5) becomes:

### Section 6.3 Solving the Reynolds equation using the Gauss-Seidel method

$$\begin{aligned} & \frac{\Phi_{i+0.5,j}^{(1)} p_{i+1,j} + \Phi_{i-0.5,j}^{(1)} p_{i-1,j} - (\Phi_{i+0.5,j}^{(1)} + \Phi_{i-0.5,j}^{(1)}) p_{i,j}}{\Delta x^2} + \\ & \frac{\Phi_{i+0.5,j}^{(2)} (p_{i+1,j+1} + p_{i,j+1} - p_{i+1,j-1} - p_{i,j-1}) - \Phi_{i-0.5,j}^{(2)} (p_{i,j+1} + p_{i-1,j+1} - p_{i,j-1} - p_{i-1,j-1})}{4\Delta x\Delta y} + \\ & \frac{\Phi_{i,j+0.5}^{(3)} (p_{i+1,j+1} + p_{i+1,j} - p_{i-1,j+1} - p_{i-1,j}) - \Phi_{i,j-0.5}^{(3)} (p_{i+1,j} + p_{i+1,j-1} - p_{i-1,j} - p_{i-1,j-1})}{4\Delta x\Delta y} + \\ & \frac{\Phi_{i,j+0.5}^{(4)} p_{i,j+1} + \Phi_{i,j-0.5}^{(4)} p_{i,j-1} - (\Phi_{i,j+0.5}^{(4)} + \Phi_{i,j-0.5}^{(4)}) p_{i,j}}{\Delta y^2} = \lambda \frac{\Phi_{i+0.5,j}^{(5)} - \Phi_{i-0.5,j}^{(5)}}{\Delta x} \end{aligned}$$

Grouping together the coefficients for pressures at the 9 mesh points gives:

$$\begin{aligned} & p_{i,j} \left[ -\frac{(\Phi_{i+0.5,j}^{(1)} + \Phi_{i-0.5,j}^{(1)})}{\Delta x^2} - \frac{(\Phi_{i,j+0.5}^{(4)} + \Phi_{i,j-0.5}^{(4)})}{\Delta y^2} \right] + \\ & p_{i+1,j} \left[ \frac{\Phi_{i+0.5,j}^{(1)}}{\Delta x^2} + \frac{\Phi_{i,j+0.5}^{(3)} - \Phi_{i,j-0.5}^{(3)}}{4\Delta x\Delta y} \right] + p_{i-1,j} \left[ \frac{\Phi_{i-0.5,j}^{(1)}}{\Delta x^2} - \frac{\Phi_{i,j+0.5}^{(3)} - \Phi_{i,j-0.5}^{(3)}}{4\Delta x\Delta y} \right] + \\ & p_{i,j+1} \left[ \frac{\Phi_{i,j+0.5}^{(4)}}{\Delta y^2} + \frac{\Phi_{i+0.5,j}^{(2)} - \Phi_{i-0.5,j}^{(2)}}{4\Delta x\Delta y} \right] + p_{i,j-1} \left[ \frac{\Phi_{i,j-0.5}^{(4)}}{\Delta y^2} - \frac{\Phi_{i+0.5,j}^{(2)} - \Phi_{i-0.5,j}^{(2)}}{4\Delta x\Delta y} \right] + \\ & p_{i+1,j+1} \left[ \frac{\Phi_{i+0.5,j}^{(2)}}{4\Delta x\Delta y} + \frac{\Phi_{i,j+0.5}^{(3)}}{4\Delta x\Delta y} \right] + p_{i-1,j+1} \left[ -\frac{\Phi_{i-0.5,j}^{(2)}}{4\Delta x\Delta y} - \frac{\Phi_{i,j+0.5}^{(3)}}{4\Delta x\Delta y} \right] + \\ & p_{i+1,j-1} \left[ -\frac{\Phi_{i+0.5,j}^{(2)}}{4\Delta x\Delta y} - \frac{-\Phi_{i,j-0.5}^{(3)}}{4\Delta x\Delta y} \right] + p_{i-1,j-1} \left[ \frac{\Phi_{i-0.5,j}^{(2)}}{4\Delta x\Delta y} + \frac{\Phi_{i,j-0.5}^{(3)}}{4\Delta x\Delta y} \right] = \lambda \frac{\Phi_{i+0.5,j}^{(5)} - \Phi_{i-0.5,j}^{(5)}}{\Delta x} \end{aligned} \quad (6.12)$$

Adopting the notation  $C_0, C_1, C_2, \dots, C_8$  for the 9 pressure coefficients and  $E_{ij}$  for the right hand side Equation (6.12) can be written as:

$$\begin{aligned} & -C_0 p_{i,j} + C_1 p_{i+1,j} + C_2 p_{i-1,j} + C_3 p_{i,j+1} + C_4 p_{i,j-1} + \\ & C_5 p_{i+1,j+1} + C_6 p_{i-1,j+1} + C_7 p_{i+1,j-1} + C_8 p_{i-1,j-1} = E_{i,j} \end{aligned} \quad (6.13)$$

The coefficients  $C_0..C_8$  and  $E_{ij}$  are defined as follows:

$$\begin{aligned} C_0 &= \frac{(\Phi_{i+0.5,j}^{(1)} + \Phi_{i-0.5,j}^{(1)})}{\Delta x^2} + \frac{(\Phi_{i,j+0.5}^{(4)} + \Phi_{i,j-0.5}^{(4)})}{\Delta y^2} \\ C_1 &= \frac{\Phi_{i+0.5,j}^{(1)}}{\Delta x^2} + \frac{\Phi_{i,j+0.5}^{(3)} - \Phi_{i,j-0.5}^{(3)}}{4\Delta x\Delta y}; \quad C_2 = \frac{\Phi_{i-0.5,j}^{(1)}}{\Delta x^2} - \frac{\Phi_{i,j+0.5}^{(3)} - \Phi_{i,j-0.5}^{(3)}}{4\Delta x\Delta y} \\ C_3 &= \frac{\Phi_{i,j+0.5}^{(4)}}{\Delta y^2} + \frac{\Phi_{i+0.5,j}^{(2)} - \Phi_{i-0.5,j}^{(2)}}{4\Delta x\Delta y}; \quad C_4 = \frac{\Phi_{i,j-0.5}^{(4)}}{\Delta y^2} - \frac{\Phi_{i+0.5,j}^{(2)} - \Phi_{i-0.5,j}^{(2)}}{4\Delta x\Delta y} \\ C_5 &= \frac{\Phi_{i+0.5,j}^{(2)}}{4\Delta x\Delta y} + \frac{\Phi_{i,j+0.5}^{(3)}}{4\Delta x\Delta y}; \quad C_6 = -\frac{\Phi_{i-0.5,j}^{(2)}}{4\Delta x\Delta y} - \frac{\Phi_{i,j+0.5}^{(3)}}{4\Delta x\Delta y} \\ C_7 &= -\frac{\Phi_{i+0.5,j}^{(2)}}{4\Delta x\Delta y} - \frac{\Phi_{i,j-0.5}^{(3)}}{4\Delta x\Delta y}; \quad C_8 = \frac{\Phi_{i-0.5,j}^{(2)}}{4\Delta x\Delta y} + \frac{\Phi_{i,j-0.5}^{(3)}}{4\Delta x\Delta y} \\ E_{i,j} &= \lambda \frac{\Phi_{i+0.5,j}^{(5)} - \Phi_{i-0.5,j}^{(5)}}{\Delta x} \end{aligned}$$

For the inter nodal values of  $\Phi^{(1)}, \dots, \Phi^{(6)}$  the same formulae (6.11) are used:

$$\Phi_{i-0.5,j}^{(k)} = \frac{\Phi_{i-1,j}^{(k)} + \Phi_{i,j}^{(k)}}{2}; \quad \Phi_{i-0.5,j-0.5}^{(k)} = \frac{\Phi_{i-1,j}^{(k)} + \Phi_{i-1,j-1}^{(k)} + \Phi_{i,j-1}^{(k)} + \Phi_{i,j}^{(k)}}{4}$$

The coefficients  $C_0..C_8$  and  $E_{i,j}$  then become:

$$\begin{aligned} C_0 &= \frac{(\Phi_{i+1,j}^{(1)} + 2\Phi_{i,j}^{(1)} + \Phi_{i-1,j}^{(1)})}{2\Delta x^2} + \frac{(\Phi_{i,j+1}^{(4)} + 2\Phi_{i,j}^{(4)} + \Phi_{i,j-1}^{(4)})}{2\Delta y^2} \\ C_1 &= \frac{\Phi_{i+1,j}^{(1)} + \Phi_{i,j}^{(1)}}{2\Delta x^2} + \frac{\Phi_{i,j+1}^{(3)} - \Phi_{i,j-1}^{(3)}}{8\Delta x\Delta y}; \quad C_2 = \frac{\Phi_{i,j}^{(1)} + \Phi_{i-1,j}^{(1)}}{2\Delta x^2} - \frac{\Phi_{i,j+1}^{(3)} - \Phi_{i,j-1}^{(3)}}{8\Delta x\Delta y} \\ C_3 &= \frac{\Phi_{i,j+1}^{(4)} + \Phi_{i,j}^{(4)}}{2\Delta y^2} + \frac{\Phi_{i+1,j}^{(2)} - \Phi_{i-1,j}^{(2)}}{8\Delta x\Delta y}; \quad C_4 = \frac{\Phi_{i,j}^{(4)} + \Phi_{i,j-1}^{(4)}}{2\Delta y^2} - \frac{\Phi_{i+1,j}^{(2)} - \Phi_{i-1,j}^{(2)}}{8\Delta x\Delta y} \\ C_5 &= \frac{\Phi_{i+1,j}^{(2)} + \Phi_{i,j}^{(2)}}{8\Delta x\Delta y} + \frac{\Phi_{i,j+1}^{(3)} + \Phi_{i,j}^{(3)}}{8\Delta x\Delta y}; \quad C_6 = -\frac{\Phi_{i,j}^{(2)} + \Phi_{i-1,j}^{(2)}}{8\Delta x\Delta y} - \frac{\Phi_{i,j+1}^{(3)} + \Phi_{i,j}^{(3)}}{8\Delta x\Delta y} \\ C_7 &= -\frac{\Phi_{i+1,j}^{(2)} + \Phi_{i,j}^{(2)}}{8\Delta x\Delta y} - \frac{\Phi_{i,j}^{(3)} + \Phi_{i,j-1}^{(3)}}{8\Delta x\Delta y}; \quad C_8 = \frac{\Phi_{i,j}^{(2)} + \Phi_{i-1,j}^{(2)}}{8\Delta x\Delta y} + \frac{\Phi_{i,j-1}^{(3)} + \Phi_{i,j}^{(3)}}{8\Delta x\Delta y} \\ E_{i,j} &= \lambda \frac{\Phi_{i+1,j}^{(5)} - \Phi_{i-1,j}^{(5)}}{2\Delta x} \end{aligned} \tag{6.14}$$

Repeating discretised Equation (6.12) for each  $i=1..N_x-1$  and  $j=-N_y/2+1..N_y/2-1$  gives a system of  $(N_x-1)*(N_y-1)$  linear equations with a sparse matrix of coefficients as there are only 9 nonzero entries in each row and each column of the matrix. The system can be written as follows:

$$Cp = E \tag{6.15}$$

where C is a  $(N_x - 1)^2 \times (N_y - 1)^2$  matrix of coefficients and E is a vector of right hand sides of length  $(N_x - 1) \times (N_y - 1)$ . The values of  $p_{i,j}$  for  $i=0..N_x, j=0, N_y$  or  $i=0, N_x, j=-N_y/2..N_y/2$  are assumed to be known from the boundary conditions. Introducing the matrix notations here is convenient, as they can then be used in describing the multigrid routines.

The system (6.15) is then solved using the Gauss-Seidel method which is described in application to solving the local problems in Section 5.1.1. Point-wise one iteration for a point with coordinates (i,j) takes the form:

$$p_{i,j} = \frac{C_1 p_{i+1,j}^{old} + C_2 p_{i-1,j}^{new} + C_3 p_{i,j+1}^{old} + C_4 p_{i,j-1}^{new} + C_5 p_{i+1,j+1}^{old} + C_6 p_{i-1,j+1}^{old} + C_7 p_{i+1,j-1}^{new} + C_8 p_{i-1,j-1}^{new} - E_{i,j}}{C_0}$$

## Section 6.3 Solving the Reynolds equation using the Gauss-Seidel method

where the superscript “old” denotes the approximated value available from the previous iteration whereas “new” stands for a value previously updated in the current sweep. The illustration given in Figure 5.2 shows the schematic representation of the method.

### 6.3.2 Boundary conditions

The Dirichlet boundary conditions were applied by means of specifying the pressure value on the boundary to be equal to the atmospheric pressure  $\sim 10^5$ Pa. All pressure values are assumed to be greater or equal than  $\sim 10^5$ Pa, i.e. the cavitation effects are not considered in this thesis. The geometry of the tilted pad does not presume presence of the cavitation zones, which therefore can occur only as a result of surface roughness. In this case pressure value is forced to be equal to  $\sim 10^5$ Pa.

### 6.3.3 Convergence

#### *Effect of the asperity wavelength on the convergence speed*

Convergence of the solution is assessed based on the relative differences between an approximated solution obtained at the previous iteration and the current one. The Gauss-Seidel method has proven to reduce efficiently the approximate solution error of the wavelength of a few mesh points. When solving Reynolds equation for the rough surface this means that the efficiency of Gauss-Seidel method decays as the wavelength of the roughness features increases. To illustrate this effect a series of numerical analyses has been conducted for the same total number of mesh points and double sinusoidal roughness with various wavelengths. Note that when numerical analysis is concerned the wavelength is considered to be the number of mesh points of a feature rather than physical dimensions. The global shape was considered flat ( $\gamma=1$ ) in order to isolate the effect of roughness wavelength from that of the global shape.

The total number of mesh elements used was 512x512 and the wavelength of the roughness was 8, 16, 32, 64, 128 and 512 mesh points which means from 2 up to 64 waves per total area. The analysis was conducted on Intel i3 32bit processor with 2Gb RAM. The solution assumed to be converged when the average relative changes to pressure values  $|p^{new}-p^{old}|/p^{old}$  were less than  $10^{-6}$ . The bar chart of Figure 6.7 shows the convergence time in minutes against the wavelength of the asperities in number of mesh points. It is apparent from the chart that if the asperities are less than 32 mesh points in wavelength, then solving the Reynolds equation for nominally flat surface

using the Gauss-Seidel method can be considered efficient, i.e. less than 2 minutes for an area of 512x512 mesh points. That is why the Gauss-Seidel method was used in Section 5.1.1 to obtain the solutions of the local problems.

However, introducing the tilting angle creates a perturbation to the solution of a much larger wavelength: of the scale of the total area. Therefore the Gauss-Seidel method is expected to be inefficient for solving the problem of a tilted pad bearing and this was found to be the case.

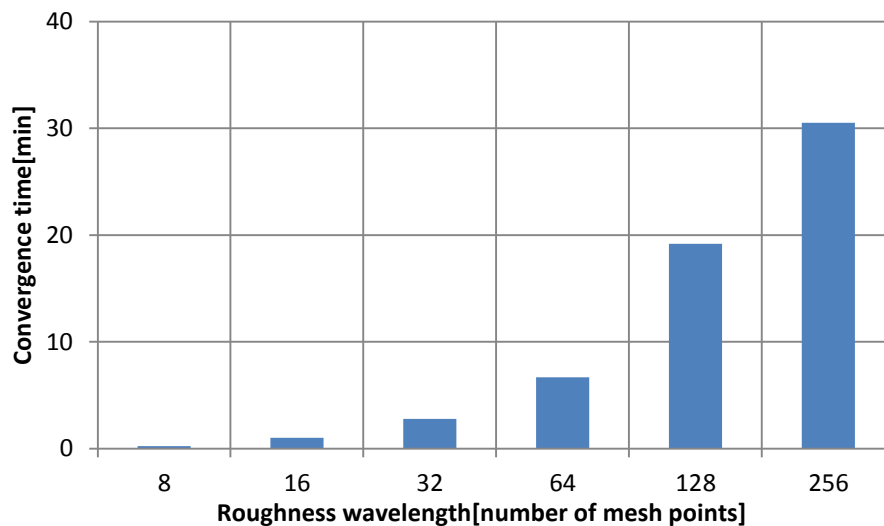


Figure 6.7 Convergence time for nominally flat sinusoidal surface with various wavelength of roughness features.

#### *Convergence of a tilted pad bearing problem using the Gauss-Seidel iterative method*

The tilted pad bearing problem with a tilting ratio  $\gamma=1.25$  and  $h_{min}=2.0\mu m$  was considered. The mesh grids used were 64x64, 128x128, 256x256 and 512x512 mesh elements. The roughness used is sinusoidal with the wavelength of 8 mesh points for each case which makes it 8, 16, 32 and 64 waves in total. Convergence time for the tilted pad bearing problem considered is shown in Figure 6.8 against the number of mesh points. As before the solution is assumed converged if the average relative change to the pressure values is below  $10^{-6}$ .—

Two main observations can be brought forward from the convergence time chart of Figure 6.8. First, using the Gauss-Seidel method for a tilted pad bearing problem with a number of mesh elements more than 256x256 takes an unreasonably long time. The problem with 1024x1024 mesh elements takes more than 12 hours to converge up to the accuracy of  $10^{-6}$ . Second, it is clear from comparing the convergence time of a

## Section 6.4 The multigrid method

smooth problem with that of the rough one that the presence of roughness does not significantly increase the convergence time. From this it can be concluded that the Gauss-Seidel method resolves the effect of the global shape very slowly. For this reason, the multigrid technique is applied to the tilted pad bearing problem. The multigrid technique is discussed in the subsequent sections.

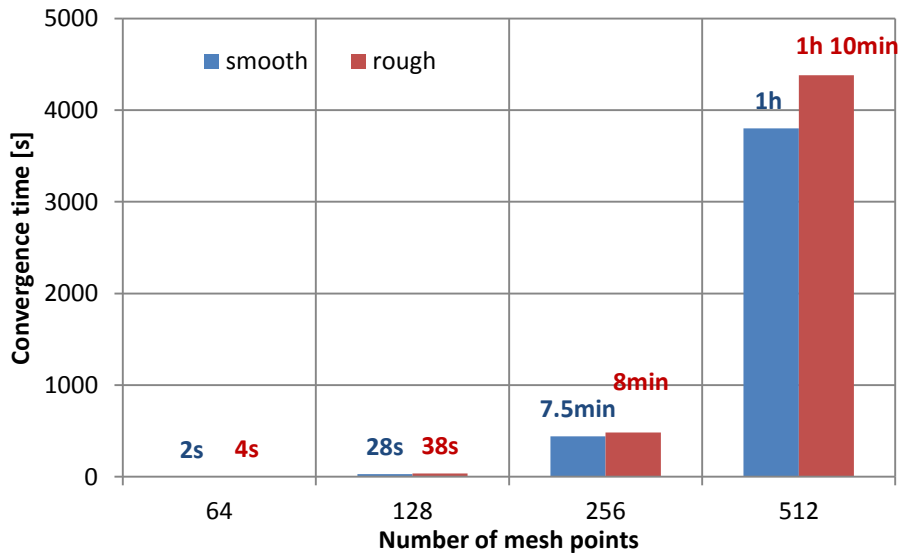


Figure 6.8 Convergence time for a tilted pad bearing problem: smooth and sinusoidal roughness

## 6.4 The multigrid method

### 6.4.1 Introduction

In order to approximate better the continuous solution of a problem a fine discretisation is often used which results in a large number of unknown variables. Especially when the rough surface problems are considered the resolution plays vital role in taking into account the effect of the individual asperities on the lubrication. This one of the reasons to use the homogenised approach based on the flow factors rather than deterministic. As shown in the previous section convergence of the solution of a rough surface problem can be time consuming. Also in most of the iterative solution techniques (such as e.g. Gauss-Seidel iterative method) the error occurred as a result of approximation is reduced fast on the scale of few mesh points whereas it takes significantly longer to eliminate the error on larger scales. It is proposed in this section to use the multigrid method in order to accelerate the convergence of the solutions.

The multigrid method was first introduced by Brandt (1977) as a general algorithm for solving the partial differential equations quickly. This method was subsequently applied by a number of researchers to various problems including solving the Reynolds

equation in fluid dynamics. Venner and Lubrecht thoroughly described its application to the problems of dry contact, hydrodynamic lubrication and elasto-hydrodynamic lubrication in their book (2000).

The main idea behind the method is to introduce a series of mesh grids of different resolutions, where the finest resolution is the target grid. Using the restriction and interpolation operators to transfer the approximated solution from one grid to another a number of relaxation sweeps are performed at each level. This allows errors of different wavelengths to be eliminated at the appropriate mesh level, where eliminating the error of such wavelength takes the least time.

In this thesis the multigrid method is used as described by Venner and Lubrecht (2000) with minor modifications.

#### 6.4.2 Fine and coarse grids

Consider a tilted pad bearing problem discretised on the uniform mesh grid of  $N_x$  by  $N_y$  nodes. This grid is referred to as the *target grid*, or *level 0*. Assume that as observed in Section 6.3.2 the high frequency components of the error (caused by roughness) are reduced efficiently whereas the low frequency components (caused by waviness, global shape) converge significantly more slowly. This means that after a small number of relaxations the approximation of the effect of roughness cannot improve any more without better approximation of the large wavelength components which improve only very slowly. It is then suggested that a coarser grid is introduced where convergence of the larger wavelength components is more efficient. The improved approximation of the larger wavelength components of the solution is then used to update the fine grid approximation.

In the general case a sequence of  $m$  mesh grids is introduced, which is shown schematically in Figures 6.9 and 6.10. Figure 6.9 shows 3 levels of mesh grids starting from the level 0, i.e. the target grid. The spacing  $\Delta x$ ,  $\Delta y$  of each subsequent grid is twice the spacing of the current grid so that:

$$\left\{ \begin{array}{l} \Delta_1 x = 2\Delta_0 x; \quad \Delta_1 y = 2\Delta_0 y; \\ \Delta_2 x = 2\Delta_1 x = 4\Delta_0 x; \quad \Delta_2 y = 2\Delta_1 y = 4\Delta_0 y; \\ \dots \\ \Delta_m x = 2^m \Delta_0 x; \quad \Delta_m y = 2^m \Delta_0 y \end{array} \right. \quad (6.16)$$

## Section 6.4 The multigrid method

where  $\Delta_0x$ ,  $\Delta_0y$  is the spacing of the target grid in x and y directions respectively. Note, that as oppose to the notation used in [Venner and Lubrecht] the target grid has level 0 and the level increases for coarser grids.

The number of mesh cells at each level is half the number of mesh cells at the current level, so that:

$$\begin{cases} N_x^1 = \frac{1}{2} N_x; & N_y^1 = \frac{1}{2} N_y \\ N_x^2 = \frac{1}{4} N_x; & N_y^2 = \frac{1}{4} N_y \\ \dots \\ N_x^m = \frac{1}{2^m} N_x; & N_y^m = \frac{1}{2^m} N_y \end{cases} \quad (6.17)$$

where  $N_x$  and  $N_y$  is the number of elements in x and y directions respectively. For this reason it is convenient to use powers of 2 as the number of mesh elements.

The total number of grids depends on the complexity of the input geometry. For example for a nominally flat surface with roughness it is sufficient to have 1 or 2 levels corresponding to the different frequencies of the roughness features, whereas if the geometry consists of the global shape, waviness and short wavelength roughness then more levels are required.

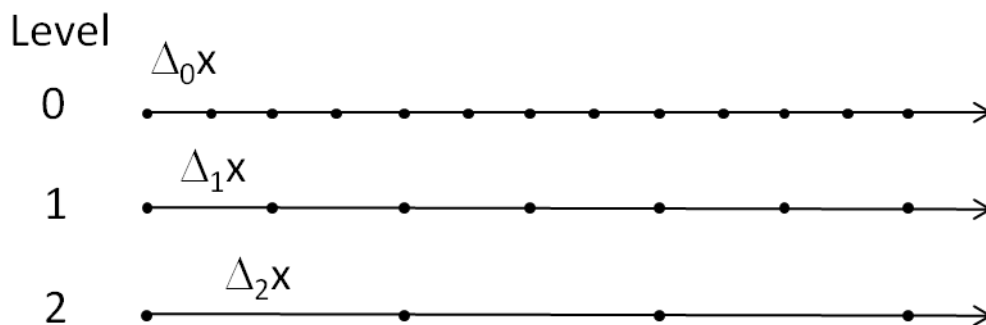


Figure 6.9 Mesh grids of levels 0, 1 and 2 and corresponding grid sizes in one dimension

In this thesis a modification has been proposed where the number of refinement levels is different in x and y direction. This modification implies amendments of the intergrid routines, however it allows faster error reduction in case if the number of elements in x direction  $N_x$  is different to that in y direction  $N_y$ .

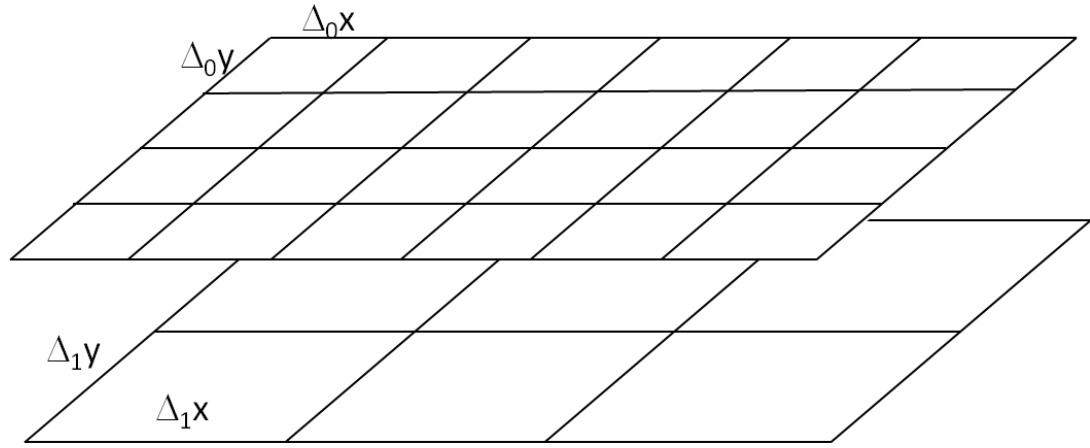


Figure 6.10 Fine and coarse mesh grids (levels 0 and 1) and corresponding grid sizes in two dimensions

### 6.4.3 Intergrid transfers

#### *Restriction operator*

The restriction operator is introduced to obtain a coarser grid approximation  $r^{k+1}$  of a function  $r^k$  defined on a finer grid of level  $k$ . Function  $r$  can be e.g. the pressure function  $p$ , film thickness function  $h$  or the function that defines the boundary conditions. The restriction operation is denoted  $I_k^{k+1}$ , where the subscript  $k$  denotes the finer level and  $k+1$  the coarser level:

$$r^{k+1} = I_k^{k+1} r^k \quad (6.18)$$

The restriction therefore transforms a function defined on  $(N_x^k + 1) \times (N_y^k + 1)$  mesh points (i.e.  $N_x^k \times N_y^k$  mesh elements) to the function defined on  $(N_x^k/2 + 1) \times (N_y^k/2 + 1)$  mesh points.

The simplest way to obtain a coarser grid representation of a function  $r^k$  is a direct injection of the fine grid values into the coinciding nodes of the coarser grid as follows:

$$r_{I,J}^{k+1} \leftarrow r_{2I,2J}^k \quad (6.19)$$

where  $I, J$  are dummy indexes on the coarser grid. The simple injection is schematically shown in Figures 6.11 and 6.12 for one and two dimensional cases respectively.

Another way to obtain a coarse representation of a function defined on the fine grid is the so-called *full weighting* operator. As follows from the name it uses the weighted average value at the nodes neighbouring to the coinciding one:

## Section 6.4 The multigrid method

$$r_{l,j}^{k+1} \leftarrow \frac{1}{16} \left[ \begin{array}{l} 4r_{2l,2j}^k + \\ 2(r_{2l-1,2j}^k + r_{2l+1,2j}^k + r_{2l,2j-1}^k + r_{2l,2j+1}^k) + \\ (r_{2l-1,2j+1}^k + r_{2l+1,2j+1}^k + r_{2l+1,2j-1}^k + r_{2l-1,2j-1}^k) \end{array} \right] \quad (6.20)$$

In a one dimensional case it is reduced to

$$r_l^{k+1} \leftarrow \frac{1}{4} [r_{2l-1}^k + 2r_{2l}^k + r_{2l+1}^k] \quad (6.21)$$

The restriction by weighted averaging is schematically shown in Figures 6.13 and 6.14.

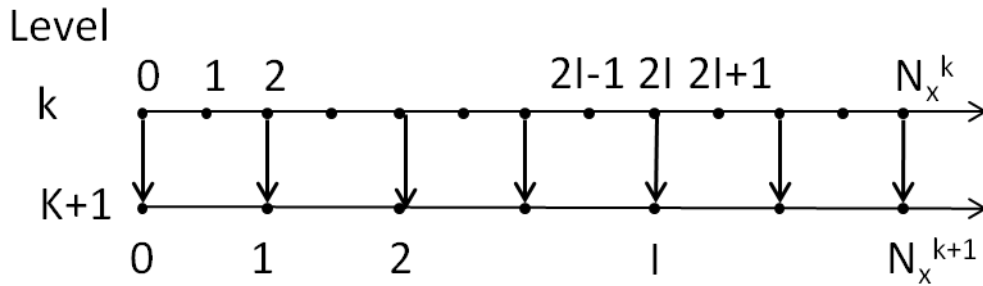


Figure 6.11 Restriction by simple injection in one dimensional case

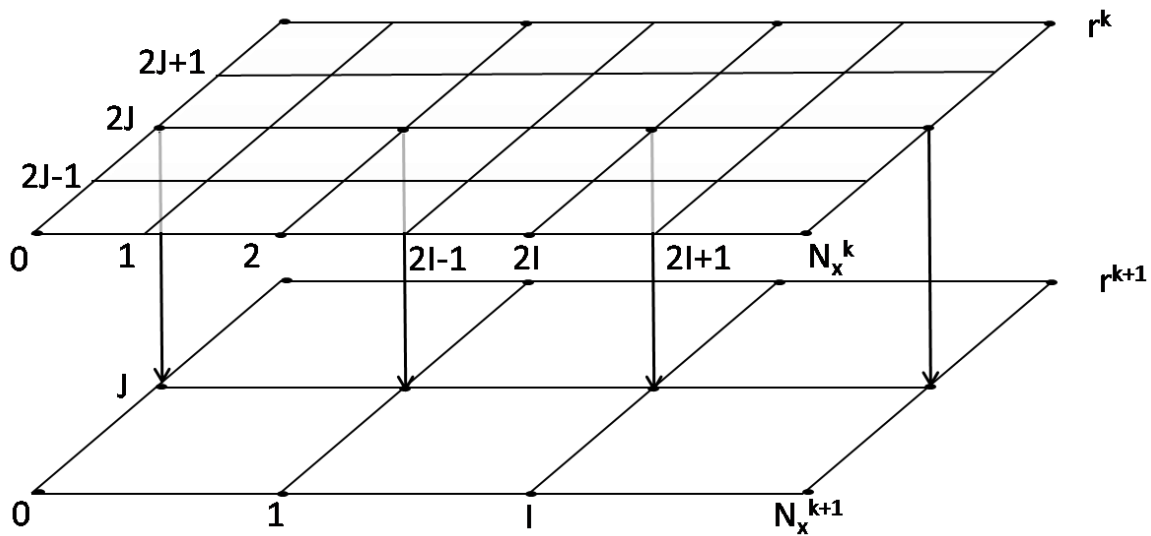


Figure 6.12 Restriction by simple injection in two dimensional cases

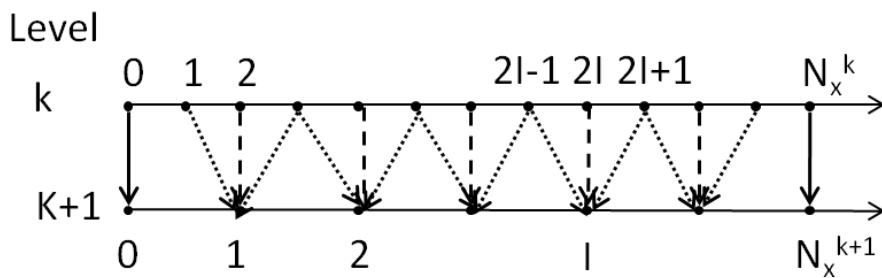


Figure 6.13 Restriction by fully weighted averaging in a one dimensional case

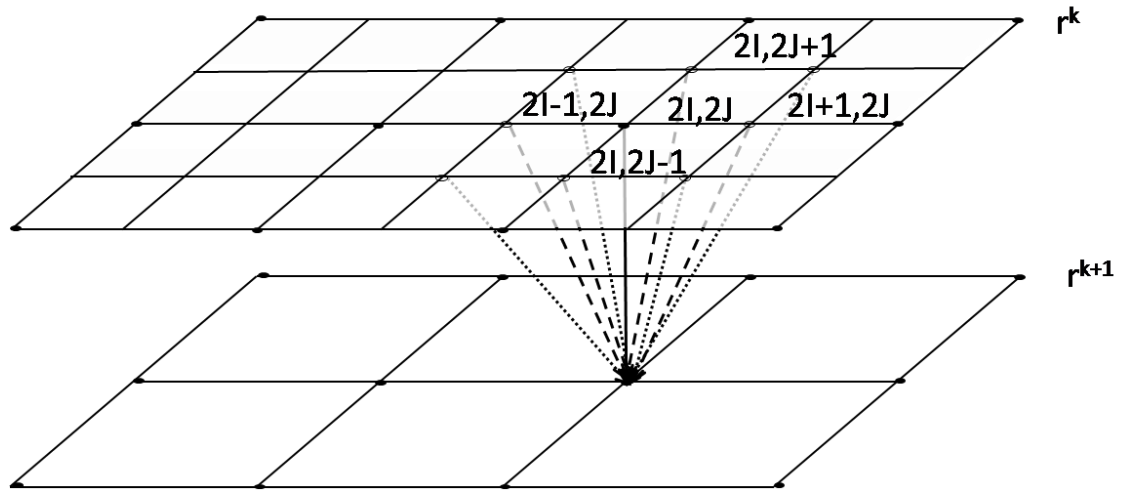


Figure 6.14 Restriction by fully weighted averaging in a two dimensional case

### Interpolation operator

The second intergrid operator used in the interpolation operator denoted  $I_{k+1}^k$ . It is used to transfer a function  $r^{k+1}$  defined on a coarser  $(N_x^k + 1) \times (N_y^k + 1)$  grid to the finer grid  $(2N_x^k + 1) \times (2N_y^k + 1)$  so that:

$$r^k = I_{k+1}^k r^{k+1} \quad (6.22)$$

The simplest form of the interpolation operator used is based on only the values at the nearest nodes:

$$\begin{cases} r_{2l,2j}^k = r_{l,j}^{k+1}; & 0 \leq l \leq N_x^{k+1}, & 0 \leq j \leq N_y^{k+1} \\ r_{2l+1,2j}^k = \frac{1}{2}(r_{l,j}^{k+1} + r_{l+1,j}^{k+1}); & 0 \leq l < N_x^{k+1}, & 0 \leq j \leq N_y^{k+1} \\ r_{2l,2j+1}^k = \frac{1}{2}(r_{l,j}^{k+1} + r_{l,j+1}^{k+1}); & 0 \leq l \leq N_x^{k+1}, & 0 \leq j < N_y^{k+1} \\ r_{2l+1,2j+1}^k = \frac{1}{4}(r_{l,j}^{k+1} + r_{l,j+1}^{k+1} + r_{l+1,j}^{k+1} + r_{l+1,j+1}^{k+1}); & 0 \leq l < N_x^{k+1}, & 0 \leq j < N_y^{k+1} \end{cases} \quad (6.23)$$

The interpolation formulae (6.23) is schematically illustrated in Figure 6.15.

In the one dimensional case the interpolation operator takes the following simplified form:

$$\begin{cases} r_{2l}^k = r_l^{k+1}; & 0 \leq l \leq N_x^{k+1} \\ r_{2l+1}^k = \frac{1}{2}(r_l^{k+1} + r_{l+1}^{k+1}); & 0 \leq l < N_x^{k+1} \end{cases} \quad (6.24)$$

The schematic illustration of the one dimensional interpolation operator is given in Figure 6.16.

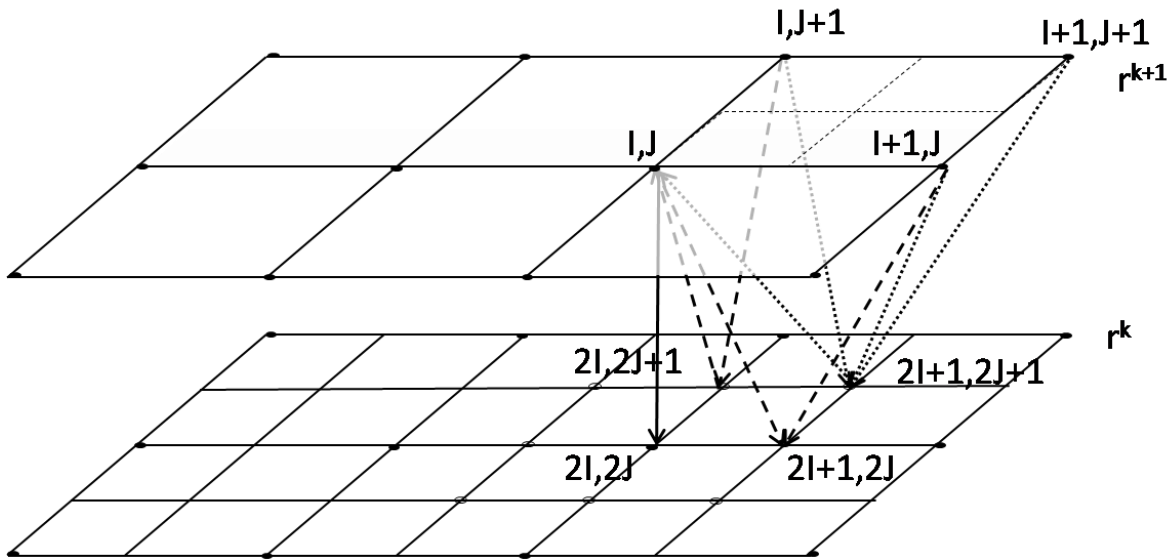


Figure 6.15 Linear Interpolation operator in a two dimensional case

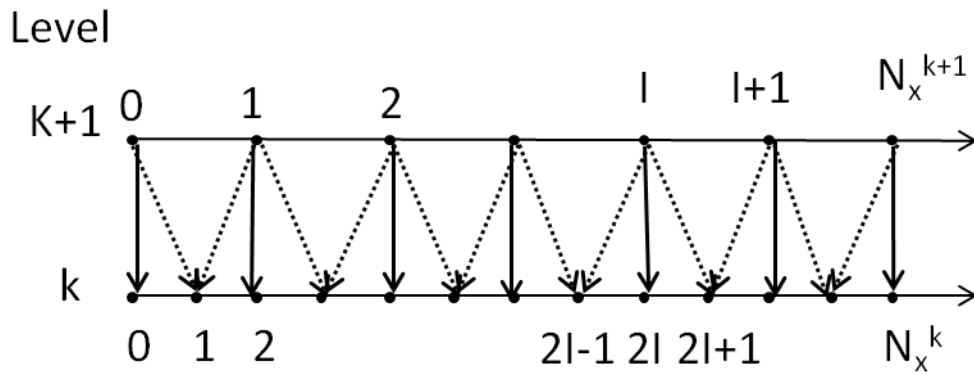


Figure 6.16 Linear interpolation operator in a one dimensional case

The interpolation operator given by formulae (6.23) and (6.24) uses only values at the nearest two nodes. For more accurate results higher order interpolation operators are possible which use more nodes. In the one dimensional case the influence coefficients for the nearest points can be calculated using the Lagrange interpolation formula which is given below for convenience:

$$f(x) = \sum_{i=1}^n f(x_i) l_i \tag{6.25}$$

where  $f(x)$  is the interpolated function,  $x_i$  are the sampling points for which the values of  $f$  are known and the coefficients  $l_i$  are as follows:

$$l_i = \prod_{\substack{1 \leq j \leq n \\ j \neq i}} \frac{x - x_j}{x_i - x_j} \tag{6.26}$$

Note that  $n$  here is the number of nodes on the coarse grid used to obtain the interpolated value for a point on the fine grid. If  $n=2$  then the interpolation coefficients

from Equation (6.26) are linear, whereas if  $n=4$  then Equation (6.26) becomes a 3<sup>rd</sup> order polynomial. Thus for  $n=2$  the interpolation is referred to as linear, whereas in case of  $n=4$  the interpolation is referred to as cubic.

If a value of the function  $r^k$  at the node on the finer grid is obtained as a result of cubic interpolation using four values of  $r^{k+1}$  then formula (6.25) becomes:

$$\begin{cases} r_{2I}^k = r_I^{k+1} \\ r_{2I+1}^k = r_{I-1}^{k+1}l_{I-1} + r_I^{k+1}l_I + r_{I+1}^{k+1}l_{I+1} + r_{I+2}^{k+1}l_{I+2} \end{cases} \quad (6.27)$$

where  $I$  is the dummy index on the coarse grid. The use of cubic interpolation for the finer grid values is schematically illustrated in Figure 6.17 and the influence coefficients for the coarser grid values are then as follows:

$$\begin{aligned} l_{I-1} &= \frac{x_{2I+1}^k - x_I^{k+1}}{x_{I-1}^{k+1} - x_I^{k+1}} \cdot \frac{x_{2I+1}^k - x_{I+1}^{k+1}}{x_{I-1}^{k+1} - x_{I+1}^{k+1}} \cdot \frac{x_{2I+1}^k - x_{I+2}^{k+1}}{x_{I-1}^{k+1} - x_{I+2}^{k+1}} = \frac{\Delta^k x}{-\Delta^{k+1} x} \cdot \frac{-\Delta^k x}{-2\Delta^{k+1} x} \cdot \frac{-3\Delta^k x}{-3\Delta^{k+1} x} \\ &= \frac{1}{2} \cdot \frac{1}{4} \cdot \frac{1}{2} = -\frac{1}{16} \\ l_I &= \frac{x_{2I+1}^k - x_{I-1}^{k+1}}{x_I^{k+1} - x_{I-1}^{k+1}} \cdot \frac{x_{2I+1}^k - x_{I+1}^{k+1}}{x_I^{k+1} - x_{I+1}^{k+1}} \cdot \frac{x_{2I+1}^k - x_{I+2}^{k+1}}{x_I^{k+1} - x_{I+2}^{k+1}} = \frac{3\Delta^k x}{\Delta^{k+1} x} \cdot \frac{-\Delta^k x}{-\Delta^{k+1} x} \cdot \frac{-3\Delta^k x}{-2\Delta^{k+1} x} = \frac{3}{2} \cdot \frac{1}{2} \cdot \frac{3}{4} \\ &= \frac{9}{16} \\ l_{I+1} &= \frac{x_{2I+1}^k - x_{I-1}^{k+1}}{x_{I+1}^{k+1} - x_{I-1}^{k+1}} \cdot \frac{x_{2I+1}^k - x_{I+1}^{k+1}}{x_{I+1}^{k+1} - x_{I+1}^{k+1}} \cdot \frac{x_{2I+1}^k - x_{I+2}^{k+1}}{x_{I+1}^{k+1} - x_{I+2}^{k+1}} = \frac{3\Delta^k x}{2\Delta^{k+1} x} \cdot \frac{\Delta^k x}{\Delta^{k+1} x} \cdot \frac{-3\Delta^k x}{-2\Delta^{k+1} x} = \frac{3}{4} \cdot \frac{1}{2} \cdot \frac{3}{4} \\ &= \frac{9}{16} \\ l_{I+2} &= \frac{x_{2I+1}^k - x_{I-1}^{k+1}}{x_{I+2}^{k+1} - x_{I-1}^{k+1}} \cdot \frac{x_{2I+1}^k - x_I^{k+1}}{x_{I+2}^{k+1} - x_I^{k+1}} \cdot \frac{x_{2I+1}^k - x_{I+1}^{k+1}}{x_{I+2}^{k+1} - x_{I+1}^{k+1}} = \frac{3\Delta^k x}{3\Delta^{k+1} x} \cdot \frac{\Delta^k x}{2\Delta^{k+1} x} \cdot \frac{-\Delta^k x}{\Delta^{k+1} x} = \frac{1}{2} \cdot \frac{1}{4} \cdot \frac{1}{2} \\ &= -\frac{1}{16} \end{aligned}$$

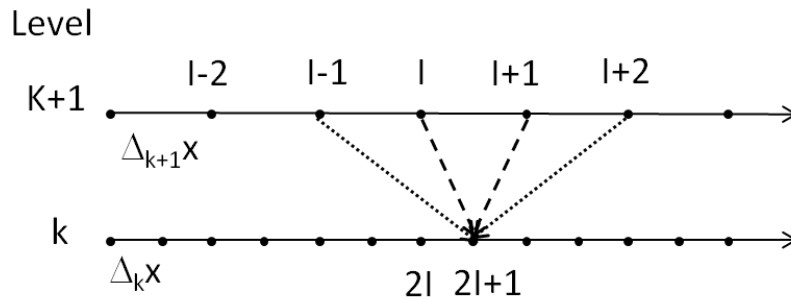


Figure 6.17 Cubic interpolation operator in one dimensional case

Using cubic interpolation to obtain the finer grid values implies the modification of the formulae (6.27) for the nodes close to the boundary:

$$r_1^k = r_0^{k+1}l_0 + r_1^{k+1}l_1 + r_2^{k+1}l_2 + r_3^{k+1}l_3$$

## Section 6.4 The multigrid method

where the coefficients calculated according to (6.26) are:

$$l_0 = \frac{5}{16}; \quad l_1 = \frac{15}{16}; \quad l_2 = -\frac{5}{16}; \quad l_3 = \frac{1}{16}$$

The schematic illustration of the cubic interpolation close to the border is shown in Figure 6.18.

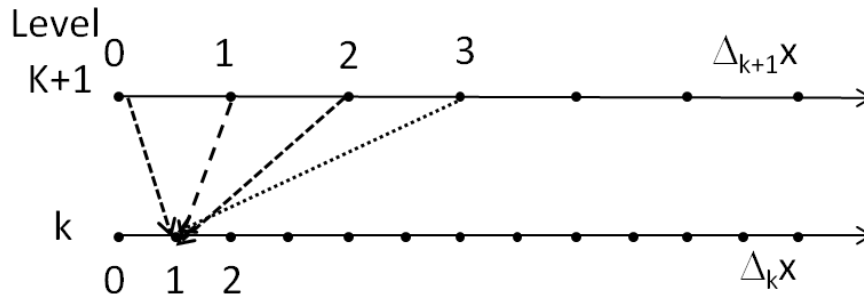


**Figure 6.18** Cubic interpolation operator in one dimensional case for the nodes close to the boundary

The same applies to other nodes which are next to the boundary.

In the case of two dimensions first the values at the coinciding nodes are directly injected from the coarser grid to the finer one. Then one dimensional cubic interpolation is applied in  $y$  direction to the coarse grid nodes producing the values for the finer grid nodes which have the  $x$  coordinate coinciding with the coarse grid node. Then the interpolation is applied in  $x$  direction using the values obtained at the previous step as shown schematically in Figure 6.19.

### 6.4.4 Correction scheme

This section describes the coarse grid correction scheme used by Venner and Lubrecht. Consider the problem discretised on a finer grid of level  $k$ . The problem is linearised to give the system of linear equations similar to the one given by Equation (6.15). For convenience the notations for the Reynolds equation in tilted pad bearing problem is used, although the system can represent another linearised problem:

$$C^k p^k = E^k \tag{6.28}$$

where  $p$  is the vector of the solution (pressure distribution in case of the Reynolds equation).  $C$  is the matrix of coefficients and  $E$  is the vector of right hand sides. The superscript  $k$  denotes that the quantities are attributed to the grid of level  $k$ .

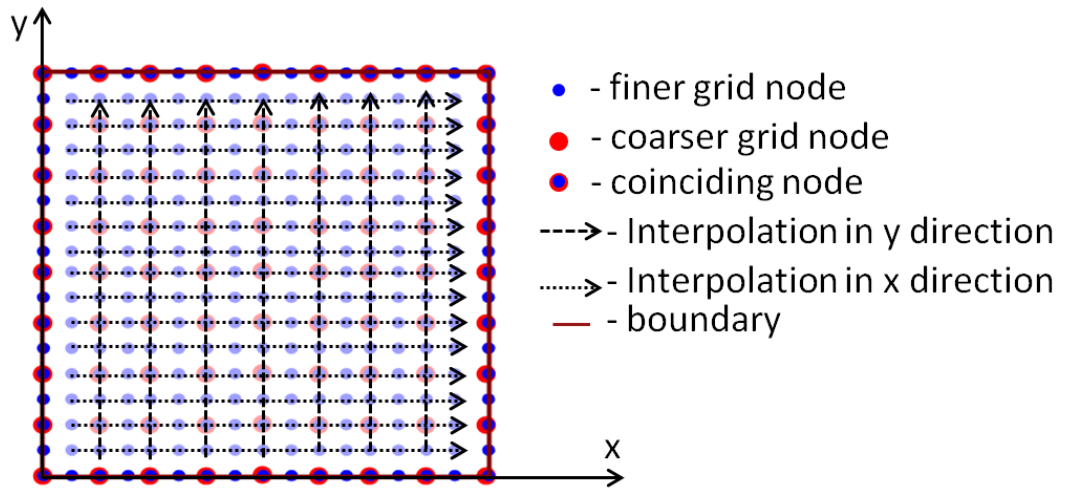


Figure 6.19 Two dimensional interpolation carried out by subsequent cubic interpolations in the y direction using the coinciding nodes and then in the x direction for the remaining nodes.

A small number of relaxations on the grid of level  $k$  results in an approximate solution  $\tilde{p}^k$ . In the current work the relaxations are performed using the Gauss-Seidel iterative method, although the multigrid technique does not limit the choice of iterative method adopted. A vector of residuals is then introduced as the difference between the right hand side  $E$  and the result of a linear operator applied to the approximate solution:

$$r^k = E^k - C^k \tilde{p}^k \quad (6.29)$$

If the vector of residuals  $r^k=0$  then the approximate solution  $\tilde{p}^k = p^k$  and the problem is solved. Substituting (6.28) yields:

$$r^k = C^k p^k - C^k \tilde{p}^k = C^k (p^k - \tilde{p}^k) \quad (6.30)$$

The error vector  $v^k$  is then introduced as difference between the approximation  $\tilde{p}^k$  and actual solution  $p^k$ . System (6.30) is then equivalent to the equation connecting the error with residuals:

$$C^k v^k = r^k \quad (6.31)$$

As mentioned earlier the Gauss-Seidel method (as well as many other iterative methods) require a small number of iterations to reduce the localised error, i.e. the component of the error which has a wavelength of a few mesh elements. After a small number of relaxations the error on grid  $k$  then becomes “smooth” so that it can be represented on the coarser grid (level  $k+1$ ) without a significant loss of accuracy. The coarse grid error denoted by  $v^{k+1}$  is then a solution of the following equation:

## Section 6.4 The multigrid method

$$C^{k+1}v^{k+1} = I_k^{k+1}r^k \quad (6.32)$$

where the restriction operator is used to translate the finer grid vector of residuals onto the coarser grid. The operator  $C^{k+1}$  is a coarser grid version of the operator  $C^k$ . Note that use of the multigrid method implies evaluating the coefficients of the matrix  $C^k$  for every level  $k$  using formulae (6.14) or in a different way. The coarse grid operator is discussed in Section 6.4.5 in more detail.

System (6.32) is then solved using the Gauss-Seidel iterative method. After that the approximated solution  $\tilde{p}^k$  is improved by adding the solution of Equation (6.32),  $v^{k+1}$ , interpolated, onto the finer grid:

$$\bar{p}^k = \tilde{p}^k + I_{k+1}^k v^{k+1} \quad (6.33)$$

The procedure described is referred to as *one level coarse grid correction* as it uses only one coarser grid.

### 6.4.5 Multi level coarse grid correction scheme

In most of the cases multiple grids are used are used, therefore the coarse grid correction scheme is applied recursively starting from the current grid and down to the coarsest one. The flow of the multi-level cycle is shown below.

1. Consider a problem defined on the level  $k$ . A small number of prerelaxations sweeps are performed on the level  $k$  Equation

$$C^k p^k = E^k$$

resulting in the approximate solution  $\tilde{p}^k$ . If the current level  $k$  is the coarsest then the number of relaxations is  $v_0$  and the correction cycle is finished, otherwise  $v_1$  relaxations are performed and the following steps are implemented.

2. Vector of residuals  $r^k$  is then evaluated as

$$r^k = E^k - C^k \tilde{p}^k$$

3. Introduce a coarse grid problem on level  $k+1$ :

$$C^{k+1}v^{k+1} = I_k^{k+1}r^k \quad (6.34)$$

where  $C^{k+1}$  is a coarse grid modification of the operator  $C^k$  and the right hand side is obtained by restricting the level  $k$  residuals. Note that the solution of (6.34) is not

the pressure that satisfies the Reynolds equation but the components of pressure required to reduce the error of level  $k$  solution.

4. Perform  $\omega$  correction cycles for the level  $k+1$  resulting in approximated solution  $\tilde{p}^{k+1}$

5. Improve the level  $k$  solution using the interpolated values of  $\tilde{p}^{k+1}$ :

$$p^k = \tilde{p}^k + I_{k+1}^k \tilde{p}^{k+1}$$

6. Perform  $v_2$  post-relaxations on level  $k$ .

The flow diagrams of the multi level coarse grid correction cycle for  $\omega=1$  and  $\omega=2$  are shown in Figures 6.21 and 6.22. Note that the general structure consists of  $v_1$  pre-relaxations, coarser  $(k+1)$  level correction cycle which is highlighted by red circle and  $v_2$  post-relaxations.

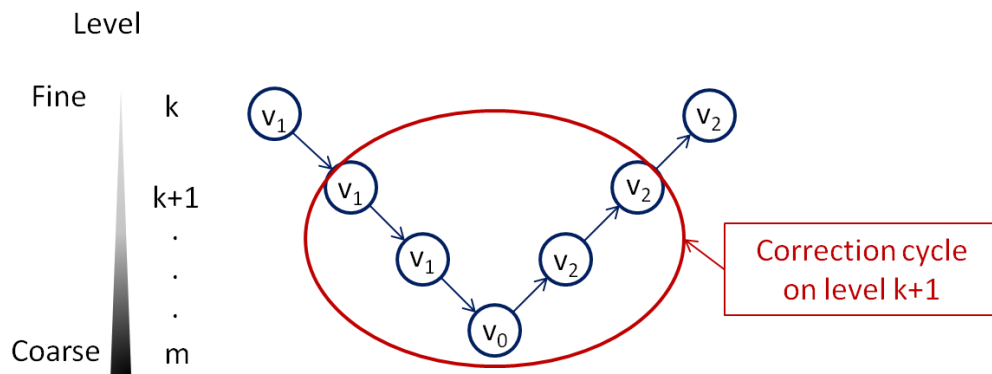


Figure 6.20 The flow diagram of the multi level correction cycle at level  $k$  with  $\omega=1$

If  $\omega = 2$  then two coarser level  $(k+1)$  correction cycles are performed. Due to the shape of the flow diagram illustrated in Figure 6.21 for the case of  $\omega = 1$ , this is called *V-cycle* whereas the case of  $\omega = 2$  illustrated in Figure 6.22 is called the *W-cycle* (see Venner and Lubrecht, 2000). According to Venner and Lubrecht (2000) the *W-cycle* proves to be more efficient for non-linear problems however the detailed study of how the number  $\omega$  affects the convergence speed is not considered in the current work.

The total number  $T_k$  of relaxations performed during the multi level correction cycle on level  $k$  can be calculated using the recursive formula:

$$T_k = v_1 + \frac{\omega}{2^d} T_{k+1} + v_2$$

where  $d=1,2$  stands for one and two dimensional problem.

## Section 6.4 The multigrid method

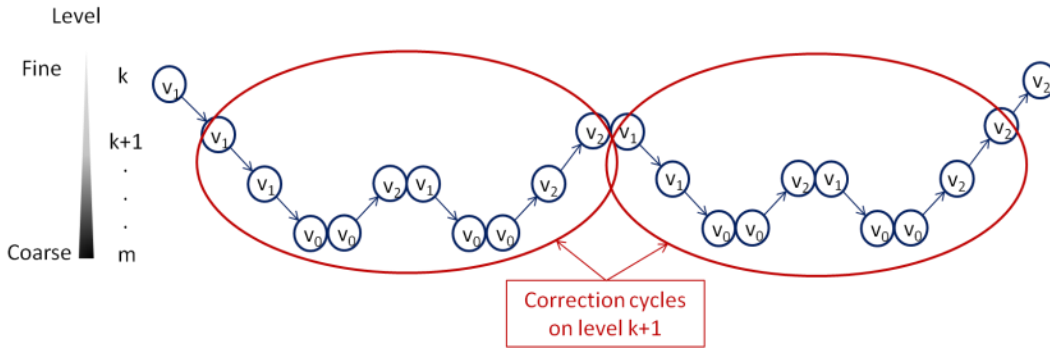


Figure 6.21 The flow diagram of the multi level correction cycle at level  $k$  with  $\omega = 2$

Note that the term  $T_{k+1}$  is divided by  $2^d$  as each relaxation sweep on the finer grid ( $k$ ) is equivalent to  $2^d$  relaxation sweeps on the coarser level  $k+1$ . Substituting the total number of relaxation sweeps caused by the level  $k+1$  correction cycle gives:

$$T_k = v_1 + \frac{\omega}{2^d} \left( v_1 + \frac{\omega}{2^d} T_{k+2} + v_2 \right) + v_2 = v_1 \left( 1 + \frac{\omega}{2^d} \right) + \frac{\omega^3}{2^{3d}} T_{k+2} + v_2 \left( 1 + \frac{\omega}{2^d} \right)$$

This process can be repeated recursively until the coarsest level  $m$ :

$$T_{m-1} = v_1 + \frac{\omega}{2^d} T_m + v_2 = v_1 + \frac{\omega}{2^d} v_0 + v_2$$

Substituting all the terms gives:

$$T_k = (v_1 + v_2) \left( 1 + \frac{\omega}{2^d} + \frac{\omega^2}{2^{2d}} + \dots + \frac{\omega^{m-k}}{2^{(m-k)d}} \right) + \frac{\omega^{m-k}}{2^{(m-k)d}} v_0$$

The formula for the geometric series gives

$$T_k = (v_1 + v_2) \frac{1 - (\omega/2^d)^{m-k}}{1 - \omega/2^d} + (\omega/2^d)^{m-k} v_0 \quad (6.35)$$

This value does not reflect the number of operations required for the intergrid transfers. Assume that every sequence of  $v_1$  relaxations is followed by a restriction operator, whereas every sequence of  $v_2$  relaxations is preceded by an interpolation operator (see Figures 6.21 or 6.22). Also assume that interpolation from level  $k+1$  to  $k$  is equivalent to one relaxation sweep on  $k$  level, whereas a restriction operator from level  $k$  down to level  $k+1$  is equivalent to one sweep on level  $k+1$ . Equation (6.35) then becomes:

$$T_k = (v_1 + v_2 + 1 + 1/2^d) \frac{1 - (\omega/2^d)^{m-k}}{1 - \omega/2^d} + (\omega/2^d)^{m-k} v_0 \quad (6.36)$$

### 6.4.6 Full multigrid

The multi level coarse grid correction cycle described in Section 6.4.5 is dedicated to improve the initial approximation of the finest grid solution. However, if the initial approximation is not known the convergence may still be quite time consuming. Having the infrastructure for working with the multiple grids implemented for the correction cycle makes it convenient to apply it also for evaluating the initial approximation of the solution on every grid by interpolating the coarser grid solution. The full multi-grid routine can then be described by the following recursive rules:

0. If the current level  $k$  is the coarsest one then perform  $v_0$  relaxations on the coarsest level
1. If the current level  $k < m$  then perform the multigrid routine on the coarser grid (level  $k+1$ ) resulting in a solution  $\bar{u}^{k+1}$ ;
2. Obtain an approximated  $k$  level solution  $\tilde{u}^k$  using the cubic interpolation (6.27) of the coarser grid solution  $\bar{u}^{k+1}$ :

$$\tilde{u}^k = I_{k+1}^k \bar{u}^{k+1}$$

The solution  $\tilde{u}^k$  serves as an initial approximation of the solution on level  $k$ .

3. Perform  $n_c$  coarse grid correction cycles on level  $k$ .

The flow diagram of the full multigrid method is shown in Figure 6.23 for 3 grids, level 0 being the finest (target) grid and level 2 being the coarsest level. Note that the V type correction cycle is used, i.e.  $\omega=1$ . The variable in the circle denotes the number of relaxations on the current level whereas arrows indicate intergrid transfers of the solution from the level where the arrow begins to the level where arrow ends. Note also that cubic interpolation is used to obtain the initial approximation of the solution while linear interpolation is used within the coarse grid correction cycle.

The total number of relaxations sweeps performed during the execution of the full multigrid method on level  $k$  is then a sum of relaxations per  $n_c$  correction cycles and of relaxations required for the full multigrid routine on level  $k+1$ . For the target grid (level 0) the total number of relaxations is then equivalent to:

$$T_0^{FMG} = \sum_{k=0}^{m-1} \frac{n_c}{2^{kd}} \left[ \left( v_1 + v_2 + 1^* + \frac{1}{2^d} \right) \frac{1 - (\omega/2^d)^{m-k}}{1 - \omega/2^d} + (\omega/2^d)^{m-k} v_0 + 1^* \right] + \frac{v_0}{2^{kd}}$$

## Section 6.5 Solving the tilted pad bearing problem using the multigrid method

(6.37)

Terms corresponding to the intergrid transfers are marked with asterisk (\*) sign. Note that the relaxations on the coarsest grid are treated separately as there are no correction cycles at this level.

Consider the example illustrated in Figure 6.23, where the coarsest level is  $m=2$ , number of correction cycles  $n_c=2$  and the type of cycle is "V" i.e.  $\omega=1$ . As the two dimensional problem is considered then  $d=2$ . If  $v_0=v_1=v_2=1$  then  $T_0^{FMG}=6.3125$  excluding the intergrid transfers which can be easily checked using the diagram in Figure 6.23 and  $T_0^{FMG}=10.0625$  including the intergrid transfers.

### 6.4.7 Multigrid boundary conditions

In case of using the multi grid method for solving the system of PDE the boundary condition defined on the target grid (see e.g. Section 6.3.2) should be adapted on all the grids. This can be done by simply injecting the nodes on the boundary of the finer grid coinciding with the coarser grid. Alternatively, the pressure values on the boundary of the coarse grid can be evaluated as fully weighted average of the finer grid boundary values using formula (6.21).

## 6.5 Solving the tilted pad bearing problem using the multigrid method

In this section the homogenised Reynolds equation approach is applied for solving the tilted pad bearing problem. The problem is solved for the given entrance and exit gap values and unknown load. Firstly, the guidelines on using the homogenised roughness approach are presented. Then the efficiency of the multigrid technique in solving the homogenised Reynolds equation is investigated. A modification to the method described by V&L is proposed which has shown to improve the convergence speed. Also the problems emerging from applying the multigrid technique to the deterministic rough problem are addressed in sub Section 6.5.2. After that a series of cases of the cosine and sinusoidal waviness are investigated. In these cases the comparison is made between the homogenised solution and the deterministic solution. Finally tilted pad bearing problem with measured surface roughness is considered. As opposed to the sinusoidal and cosine roughness the deterministic solution for these cases is not available due to very high computational resources required.

### 6.5.1 The convergence speed

The Reynolds Equation (6.5) is solved using the multi grid method. The solutions of the smooth, rough and homogenised problems are considered in order to compare the convergence time. Note that when using a conventional Gauss-Seidel iterative method the solution is considered converged if the average relative changes to the pressure are less than a specified value ( $10^{-6}$ ). Until that point is reached the further relaxations are performed on the same grid. In case of the multigrid method the majority of relaxation sweeps are not made on the target grid. If the convergence criteria based on the relative pressure changes are met on a coarser grid of level  $k > 0$  it does not necessarily imply that the solution has converged enough on the target grid (level 0). This creates difficulties in continuing the execution of the algorithm until the required accuracy has been achieved and terminating the execution once it is achieved. Therefore, the configuration parameters ( $v_0$ - $v_2$ ,  $n_c$ ,  $\omega$ ) should be defined to give enough relaxations to achieve the necessary convergence level.

A modification to the multigrid method described by Venner and Lubrecht (2000) is proposed where the particular block of relaxation sweeps on the grid of level  $k$  is terminated if the convergence criteria based on the relative pressure changes are met before the number of relaxations reached the defined maximum values of  $v_0$ ,  $v_1$  or  $v_2$ . The execution of the main algorithm is then continued. The positive effect of this modification is illustrated later in this section.

The problem of a tilted pad was considered. The geometry is defined by the dimensions of the area  $L=W=0.04\text{m}$ , tilting ratio  $\gamma=1.25$  and  $h_{min}=1.0\mu\text{m}$ . The surface used was either smooth or having sinusoidal roughness with 8, 16, 32, 64 and 128 waves of the amplitude  $h_r=0.5\mu\text{m}$  in both  $x$  and  $y$  directions. The sinusoidal waves were discretised using 8 mesh points per wave in both directions. The configuration parameters of the multigrid algorithm is provided in Table 6.1. In comparison to the method described in Section 6.4.6 an additional modification to the method has been made in which  $v_3$  relaxations are performed on the target grid after the multigrid routine has been executed. This was found especially efficient for the rough surface cases, as the coarse grid representation of the roughness features affect the resulting pressure differently to the target grid roughness features. The number of grid levels  $m$  was specified according to following rule:

$$m = \min(\log_2 N_x - 4, \log_2 N_y - 4)$$

Levels of refinement

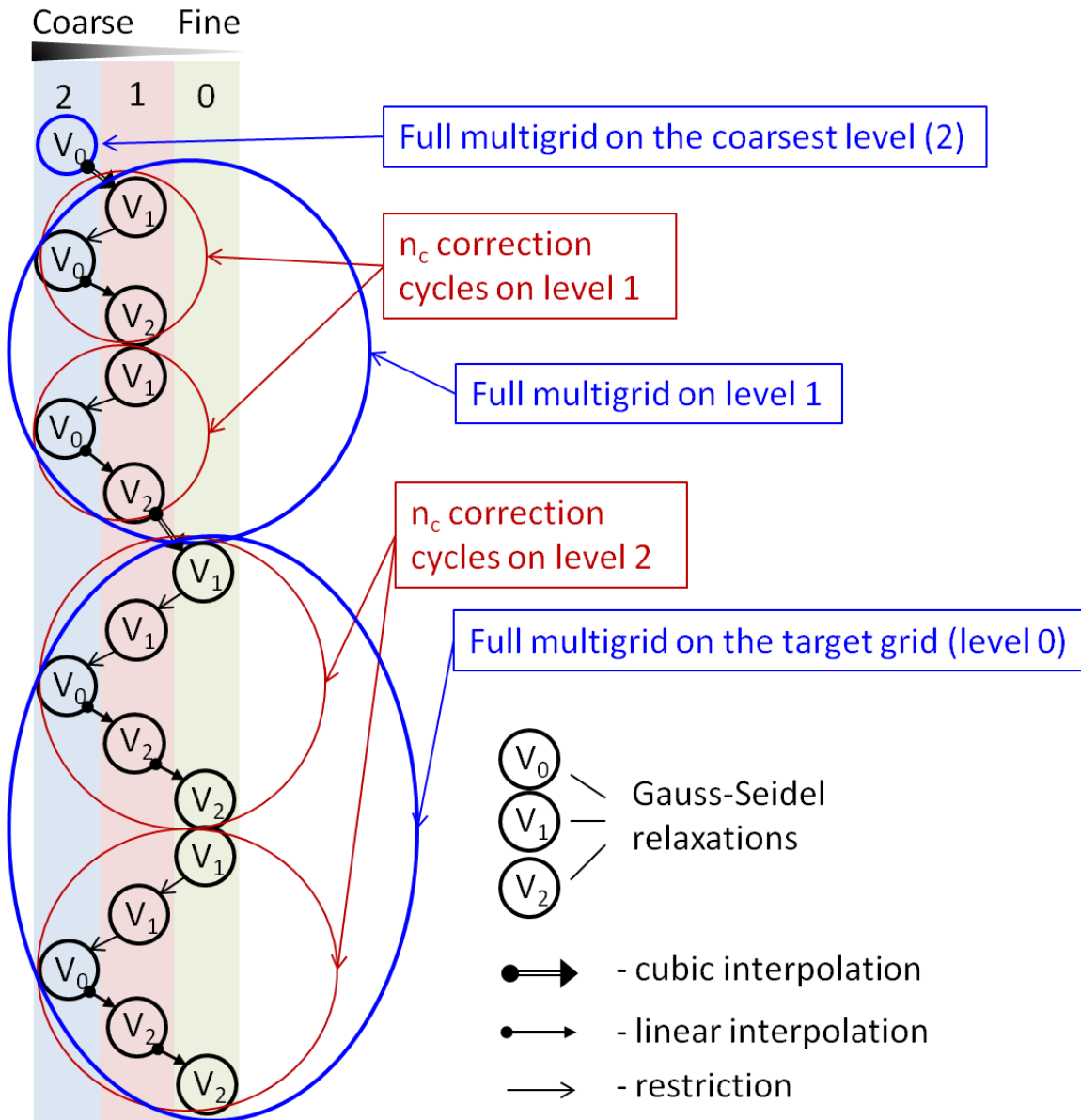


Figure 6.22 Flow diagram of the full multi grid method

The coarsest grid then have 16x16 elements if number of mesh elements on the target grid is the same in both directions, i.e.  $N_x=N_y$ . If this is not the case then the intergrid transfer operators need to be modified in order to consider coarsening and refinement with respect to one direction only.

The efficiency of the multigrid method time is summarised in three charts in Figures 6.23-6.25 showing the execution time, the accuracy and the effective number of relaxation sweeps plotted for smooth, rough and homogenised cases for the target grids of 64x64, 128x128, 256x256, 512x512 and 1024x1024 mesh elements. The execution time for the homogenised problem does not include time required for the evaluation of the flow factors which is carried out once covering the whole range of

$h_{min}$  from 0 to  $5\mu\text{m}$ . Note that the actual execution time depends on the current CPU usage i.e. the same number of operations can take different time. For this reason an average execution time of three identical cases is shown in Figure 6.23.

**Table 6.1 Parameters of the multigrid routine**

Parameter	Description	Value
$v_0$	Number of relaxations on the coarsest grid	10
$v_1$	Number of prerelaxations	20
$v_2$	Number of post relaxations	60
$v_3$	Target grid relaxations after the multigrid routine	150
$\omega$	Type of the correction cycle	2
$n_c$	Number of correction cycles	2
$m$	Number of refinement levels	2,3,4,5,6
$N_x, N_y$	Number of elements in the target grid	64,128,256,512,1024
$\varepsilon$	The target accuracy	$10^{-6}$

The first observation that can be made from comparing the execution time for the rough smooth and homogenised cases in Figure 6.23 is that the homogenised case takes approximately the same time as the smooth one whereas the rough case takes at least twice as long. This is the consequence of the homogenised equation being in essence a solution of the smooth geometry problem with the flow modifying coefficients, i.e. flow factors.

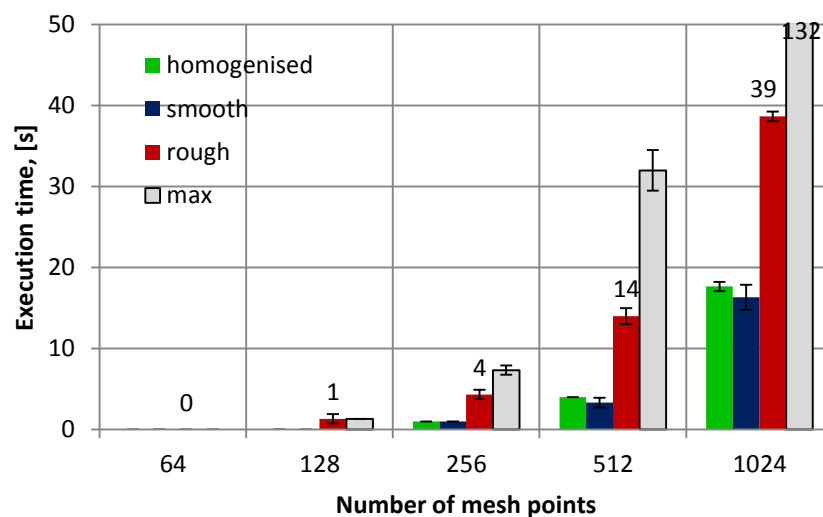


**Figure 6.23 Execution time of the modified multigrid algorithm for the homogenised smooth and rough cases and execution time of the multigrid algorithm with defined maximum number of cycles.**

Second, in comparison to the solver based on the conventional Gauss-Seidel iterative method (see Figure 6.8) the multigrid method is  $\sim 40$  times faster for the mesh grid of

## Section 6.5 Solving the tilted pad bearing problem using the multigrid method

256x256 elements and the difference increases up to ~250 times faster for 512x512 grid and more than 1000 times faster for the 1024x1024 grid. The explanation for this is that the Gauss-Seidel method is incapable of handling the perturbations of large wavelength (i.e. larger than few mesh points).

Third is that the execution time of the original multigrid algorithm as given by Venner and Lubrecht is longer than that of the modified algorithm. Note, that the execution time of the original algorithm is a result of the choice of the algorithm parameters given in Table 6.1, i.e. each particular block of the algorithm execution has the defined maximum number of cycles. With the appropriate choice of these parameters the execution time of the original algorithm can be improved. However if the optimal set of parameters is not known (from e.g. previous experiments) it is more convenient to perform a larger number of relaxations ( $v_0$ ,  $v_1$ , and  $v_2$ ) at any level with the possibility to terminate the execution once the required convergence level is achieved.

Figure 6.24 shows the average relative changes to the pressure value on the target grid obtained by means of the multigrid method for rough smooth and homogenised cases for the mesh grids with  $N_x=64, 128, 256, 512$  and 1024 elements.

The y axis is logarithmic with base 10, the positive y direction indicates the sense of improving the accuracy, and the target accuracy of  $10^{-6}$  is shown dashed. It is clear from the chart that the convergence improves with increasing the number of mesh points. This can possibly be explained by the fact that more nodes allow more refinement levels to be used. It can also be observed that smooth and homogenised problems converge better than a rough one for the same configuration of the multigrid method.

The rough problem for 64 and 128 elements has not been converged to the target accuracy level. The reason for this as mentioned earlier is that the coarse grid representation of the roughness features may not reflect the behaviour in the same way as on the fine grid.

The maximum number of relaxation sweeps can be calculated using the formula (6.37). It is clear from the chart that the more nodes are used the less relaxation sweeps are needed to achieve the required convergence level. The chart with the number of relaxations also confirms that for the grids of 64 and 128 elements the rough problem

does not give an accurate enough result. Also the convergence of the smooth and homogenised cases is equally efficient and better than that of the rough case.

Figure 6.25 shows the *actual* effective number of relaxation sweeps for smooth rough and homogenised problems discretised using 64, 128, 256, 512 and 1024 elements. It is called *actual* as opposed to the maximum possible number of relaxation sweeps defined by the parameters given in Table 6.1.

### 6.5.2 Coarse grid roughness problem

The coarse grid correction scheme described in Section 6.4.4 uses the coarse grid operator which is a representation of the linear operator on the grid of the coarser level  $k+1$ . The matrix of coefficients  $C^{k+1}$  can then be evaluated by discretising the Reynolds equation on the coarser grid. This can be implemented simply by applying the formulae (6.14) on the coarser grid of level  $k+1$ . The evaluation of coefficients  $C^{k+1}$  requires the total clearance function  $h(x,y)$  which in the case of the rough surface problem includes the roughness function  $R(x,y)$ . It has been found by the author that for some types of roughness (e.g. cosine waves, or double cosine waves) coarsening of the operator results in the incorrect representation of the roughness features on the coarser grids. This creates instabilities in the course of the algorithm, increases the execution time and may produce incorrect results. The general observation is that the coarse grid correction fails if the coarse grid representation of the roughness has a mean line that is different to that of the finer grid roughness.

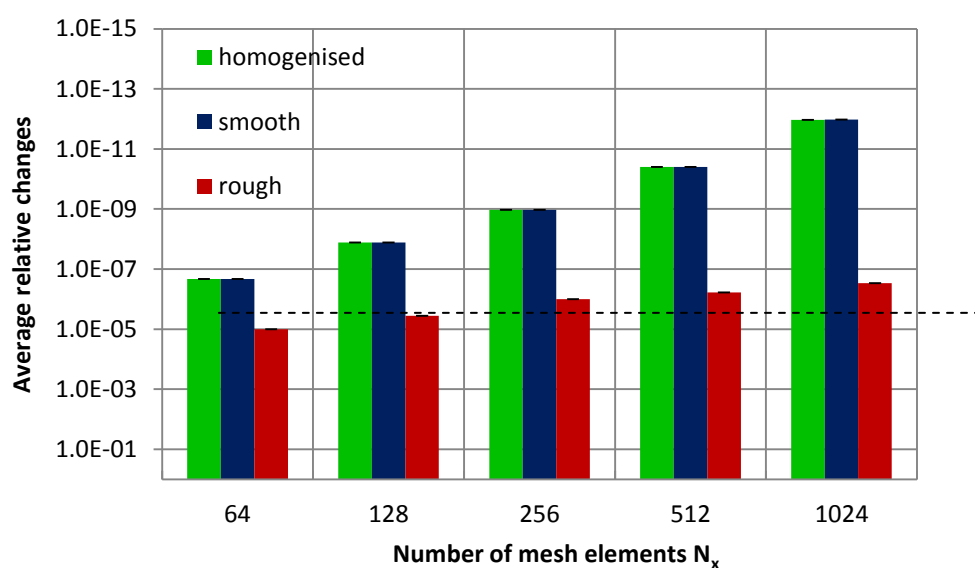


Figure 6.24 Average relative changes to the pressures obtained by the multigrid method and the target accuracy of  $10^{-6}$  (dashed line)

## Section 6.5 Solving the tilted pad bearing problem using the multigrid method

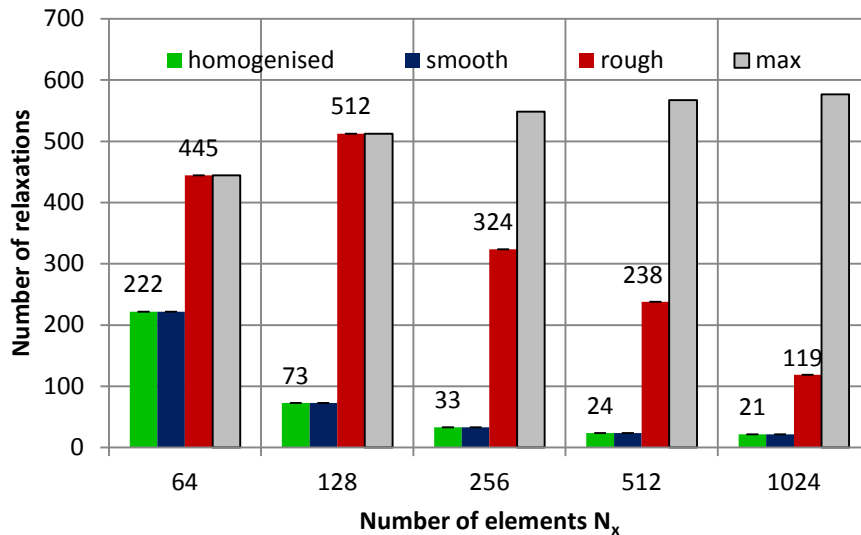


Figure 6.25 Actual effective number of relaxations using multigrid method for smooth rough and homogenised cases and the maximum effective number of relaxations defined by the multigrid routine parameters given in Table 6.1.

Figure 6.26 shows cross sections of the surface with extruded cosine waviness for the whole range of grid levels from the target grid (level 0) to the coarsest grid which has level 6. Starting from the level 0 the surface representation becomes coarser as the level increases. Until level 4 surface the roughness features demonstrate the same behaviour, i.e. both valleys and peaks coincide.

The level 4 representation shown by dotted line fails to capture the first peak however the remaining features are still correct.. Level 5 and 6 representations demonstrate completely different behaviour as shown by dashed and dashed-and-dotted lines. If the global film thickness is comparable to the roughness amplitude then these incorrect representations result in much higher pressures being generated at the coarser levels which leads to instabilities of the method.

Venner and Lubrecht (2000) addressed this problem in applications of the multi grid method to the dry contact analysis. They suggested decreasing the number of coarsenings, which however reduces the positive effect of using multiple grids and significantly slows down the total convergence time, especially if the roughness features are resolved in a few mesh points.

It was found by the author that treating the surface as smooth on coarser grids results in a better stability than incorrect coarse grid representation of the roughness. For this reason in this thesis the author suggests truncation of the roughness on the grids which are incapable of capturing the peaks and valleys of the rough surface. The ability of the grid to resolve the roughness features is judged upon the difference between

the mean lines of the roughness function sampled at the current grid and the target grid. In the example above the, surface is assumed smooth on levels 5 and above.

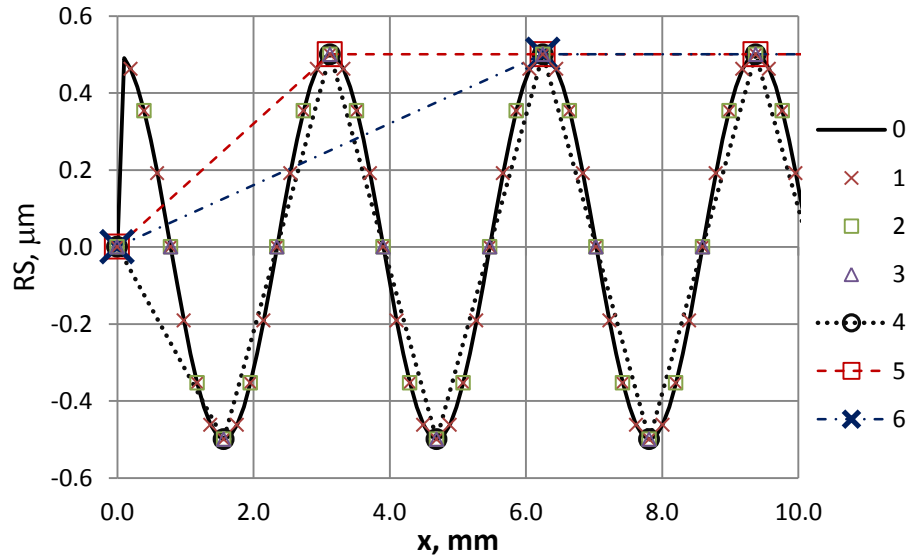


Figure 6.26 Representation of the cosine roughness on the grid of levels 0 to 6

Venner and Lubrecht also suggested an alternative way of evaluating the coarse grid operator in the general case (with no relation to the rough problem in particular). This way considers applying a restriction operator to both sides of Equation (6.31), which results in:

$$I_k^{k+1} (C^k v^k) = I_k^{k+1} r^k$$

where  $v^k$  and  $r^k$  are the vector of solution and the vector of residuals at the level  $k$ . Representing the solution  $v^k$  vector as the interpolation of  $v^{k+1}$  gives:

$$I_k^{k+1} \left\{ C^k \left[ I_{k+1}^k (v^k) \right] \right\} = I_k^{k+1} r^k \quad (6.38)$$

The right hand side of Equation (6.38) gives  $r^{k+1}$  which is the right hand side of the coarse grid operator as defined by the coarse grid correction scheme, whereas the coarse grid operator itself can be defined as follows:

$$C^{k+1} (\cdot) = I_k^{k+1} C^k I_{k+1}^k (\cdot) \quad (6.39)$$

where " $\cdot$ " denotes a vector on the coarser grid of level  $k+1$ .

Defining the coarse grid operator as in Equation (6.39) allows the evaluation of the coarse grid coefficients to disregard the incorrect representation of roughness on the coarse grid. Such method is an alternative to directly discretising the matrix coefficients on the coarser grid using formulae (6.14). However, it was found by author that the direct discretisation results in a faster convergence of the solution.

## Section 6.5 Solving the tilted pad bearing problem using the multigrid method

### 6.5.3 Extruded cosine roughness

In this section the tilted pad bearing problem was formulated and solved for a sequence of the minimum clearance values. Problem was considered for the smooth, rough, and homogenised rough cases. A comparison has been made between the solution of the homogenised equation for tilted pad bearing problem developed by author and the solution of the identical problem given by Almqvist and Dasht (2006) where the latter is available.

The roughness  $R(x,y)$  was assumed to be a cosine wave in  $x$  direction and extruded in  $y$  direction, i.e.

$$R(x,y) = R_{max} \cos\left(2\pi k \frac{x}{L}\right) \quad (6.40)$$

The total gap between the rough surface and the smooth counterface is a combination of the linear global shape (6.1) and the roughness function (6.40):

$$h(x,y) = h_{min} \left[ \gamma + \frac{x}{L} (1 - \gamma) \right] + R_{max} \cos\left(2\pi k \frac{x}{L}\right) \quad (6.41)$$

The geometry of the tilted pad and the roughness parameters are provided in Table 6.2. The problem was discretised on a grid mesh of 1024x1024 elements. The number of refinement levels used is  $m=6$ , i.e. the coarsest grid consists of 16x16 elements.

The geometry of the rough problem is defined by Equation (6.41), where the number of extruded cosine waves was 16, 32, 64 and 128. This makes the resolution of roughness features 64, 32, 16 and 8 elements per wave.

The geometry and physical quantities given in Table 6.2 are identical to those for the similar problem considered by Almqvist and Dasht (2006). The minimum clearance used is  $h_{min}=4.0\mu m$ . Figure 6.27 shows solutions of the smooth, rough and homogenised rough tilted pad bearing problems.

First, Figure 6.27 is in excellent agreement with the one given in the paper of Almqvist and Dasht (2006). Second, the sequence of rough surface solutions shown by thin solid lines approaches the homogenised solution which is shown by thick solid line as the number of waves increases. This effect is an illustration of the statement (4.4) given in Chapter 4 that the homogenised solution is an asymptotic limit of the rough solution when the size of the representative roughness area  $\varepsilon$  approaches zero. It was shown in Section 5.2.6 that mathematically the flow factors are robust to the proportional

stretching as long as no direct contact occurs. This means that the flow factors for 16, 32, 64 or 128 cosine waves should be the same. However, this statement is true only if the same resolution of the roughness is used. In fact, cosine roughness resolved in different number of points results in different flow factors.

Table 6.2 Parameters of the tilted pad bearing problem (Almqvist and Dasht configuration)

Parameter	Value	Units	Description
$h_{min}$	4.0	$\mu\text{m}$	Minimum clearance
$\gamma$	1.25		Tilting ratio
$R_{max}$	0.5	$\mu\text{m}$	Roughness amplitude
$k_1$	16		Number of sinusoidal waves 1
$k_2$	32		Number of sinusoidal waves 2
$k_3$	64		Number of sinusoidal waves 3
$k_4$	128		Number of sinusoidal waves 4
$L$	10	cm	Length
$W$	10	cm	Width
$u$	0.5	m/s	Linear velocity of the counterface
$\eta$	0.14	Pa·s	Viscosity of the fluid
$P_0$	$10^5$	Pa	Atmospheric pressure
$N_x N_y$	1024,1024		Number of mesh elements in x and y directions

The effect of the resolution of the local problem diminishes as the resolution improves: for example the flow factors evaluated for the resolution of 64 and 32 elements per wave produce identical homogenised solutions, whereas the flow factors that use 8 elements per wave result in a solution which is slightly different. In Figure 6.27 all four homogenised solutions coincide, therefore only one solution is shown. This effect is more apparent in the sequence of Figures 6.29-6.35 where both deterministic and homogenised rough solutions are shown for extruded cosine waviness with 16, 32, 64 and 128 waves. The corresponding flow factors are calculated individually for a single cosine wave resolved in 64, 32, 16 and 8 elements respectively to maintain the same resolution of roughness on the local scale as on the global scale. In Section 5.2.3 of Chapter 5 it was also shown that the flow factors calculated analytically for the extruded cosine roughness are in an agreement with the flow factors calculated numerically using 32 elements per wave.

## Section 6.5 Solving the tilted pad bearing problem using the multigrid method

The difference between the smooth and homogenised rough solutions observed in Figure 6.27 is not significant, as can be seen by comparing the solid thick line and dashed line. Indeed, the amplitude of roughness  $R_{max}=0.5 \mu\text{m}$  makes the ratio  $\tau = h_{min}/R_{max}=8$  for the case shown in Figure 6.27. The flow factors for the extruded sine wave were calculated in Chapter 5, see Figure 5.24. For the highest value of  $\tau=6$  available in Figure 5.24 the flow factors are very close to unity, i.e. roughness has almost no effect. It is assumed here that the flow factors for the sine waves are identical to those for the cosine waves.

In order to enrich the comparison of the smooth, rough and homogenized rough solutions, a sequence of tilted pad bearing problems has been considered, where the minimum clearance values used were  $h_{min}=3.0, 2.0, 1.5, 1.0, 0.8, 0.6, 0.55$  and  $0.5 \mu\text{m}$ .

The ratio  $\tau = h_{min}/R_{max}$  is then 6, 4, 3, 2, 1.6, 1.2, 1.1 and 1.

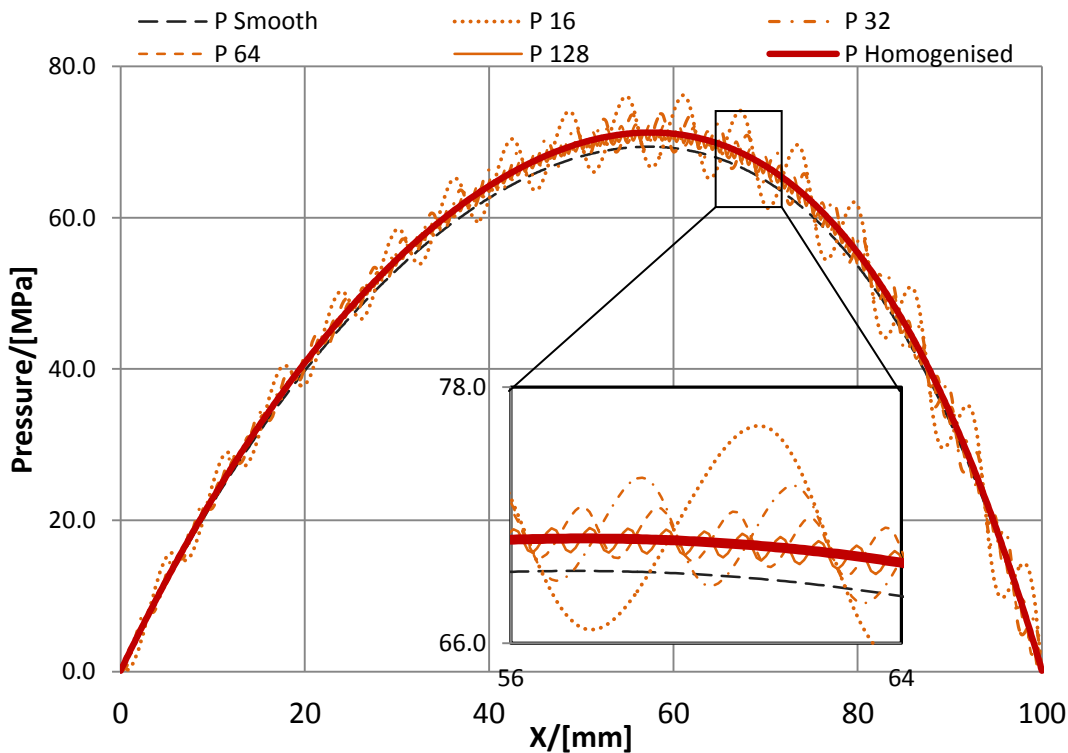


Figure 6.27 Solutions of the tilted pad bearing problem with extruded cosine roughness with 16, 32, 64 and 128 waves (thin solid lines), homogenized solution (thick solid line), smooth solution (dashed black). The minimum clearance  $h_{min}=4.0 \mu\text{m}$ .

The lower values of  $h_{min}$  result in a stronger effect of roughness than observed in Figure 6.27. Other configuration parameters of the problem are given in Table 6.3. The multigrid configuration remains the same throughout the rest of the test cases. Note that the dimensions of the area are  $1 \times 1 \text{cm}$ , as opposed to  $10 \times 10 \text{cm}$  in Table 6.2.

Figure 6.28 shows the load evaluated in terms of the mean pressure for the tilted pad bearing problem for the smooth, rough and homogenised rough surfaces for the

specified sequence of minimum clearance values  $h_{min}$ . Four solutions of the rough problem are shown corresponding to the extruded cosine roughness with 128, 64, 32 and 16 waves. Two solutions of the homogenised problem are also shown which are based on the flow factors calculated for cosine roughness resolved in 8 and 32 elements. These resolutions correspond to 128 and 32 waves respectively. The other two homogenised solutions are not present as they were found to be identical to the one for 32 waves.

**Table 6.3 Configuration parameters of the tilted pad problem for extruded cosine roughness**

Parameter	Value	Units	Description
$h_{min}$	3.0-0.5	$\mu\text{m}$	Minimum clearance range
$\gamma$	1.25		Tilting ratio
$R_{max}$	0.5	$\mu\text{m}$	Roughness amplitude
$k$	64		Number of sinusoidal waves
L	1.0	cm	Length
W	1.0	cm	Width
$u$	0.5	m/s	Linear velocity of the counterface
$\eta$	0.14	Pa·s	Viscosity of the fluid
$N_x, N_y$	1024		Number of mesh elements

It can be seen from the figure that load for the smooth case is lower than for both rough and homogenised rough problems. Also, the load for the rough case is different for the cases of different number of cosine waves, i.e. roughness with larger wavelength results in a higher load. The load for the homogenised case based on the resolution of 8 elements is very close to the load for the rough solution for 128 waves, whereas load for other rough solutions differs increasingly from the corresponding homogenised load the more so as the wavelength increases. This can be explained by the fact that, as described in Chapter 4, mathematically the homogenised solution is an asymptotic limit of the rough solution when the roughness wavelength approaches zero, i.e. the case of 128 waves is supposed to give the best fit to the homogenised solution. However, in case of 128 cosine waves each feature is resolved in 8 elements, which is a very poor representation of the cosine function. This explains the fact that homogenised solutions that use 16 and more elements per wave are identical, as they are a good enough approximation of a cosine function, whereas using 8 elements per wave gives a different solution.

## Section 6.5 Solving the tilted pad bearing problem using the multigrid method

The sequence of Figures 6.29-6.35 show the smooth, rough and homogenised rough solutions of the tilted pad bearing problem with various values of minimum clearance. Four rough and four homogenised rough solutions are shown corresponding to the resolutions of roughness using 8, 16, 32 and 64 elements, i.e. 128, 32, 64 and 16 waves respectively. In the cases of higher minimum film thickness the latter three homogenised solutions are indistinguishable.

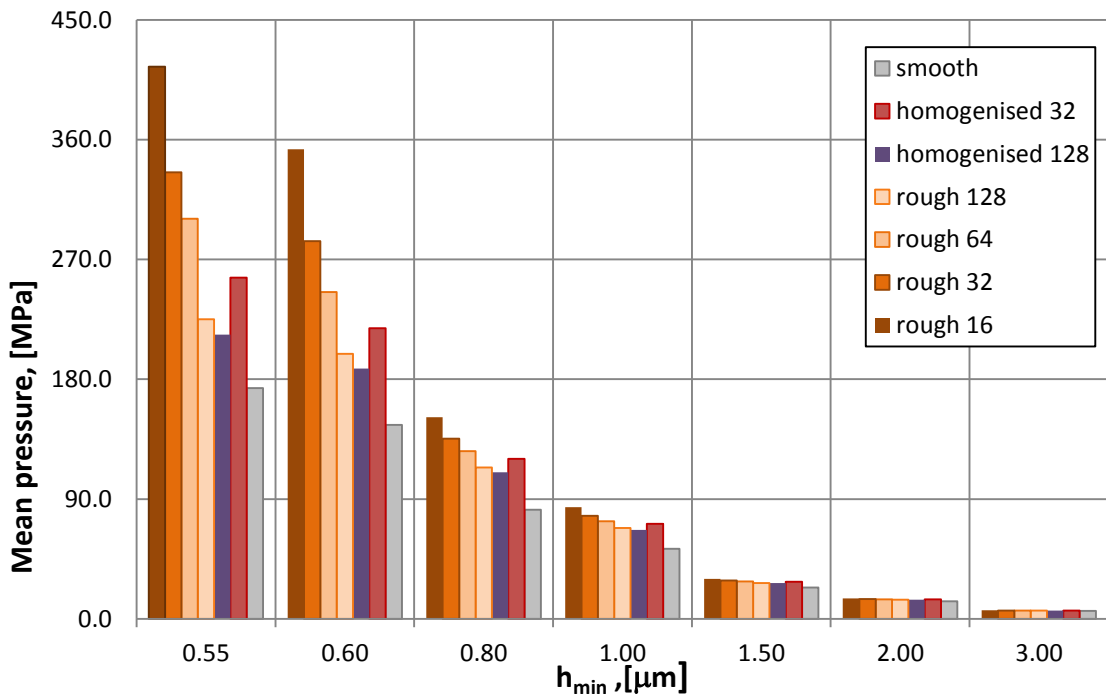


Figure 6.28 Hydrodynamic load carried by the tilted pad for a sequence of minimum clearances for the smooth, rough and homogenized rough problems.

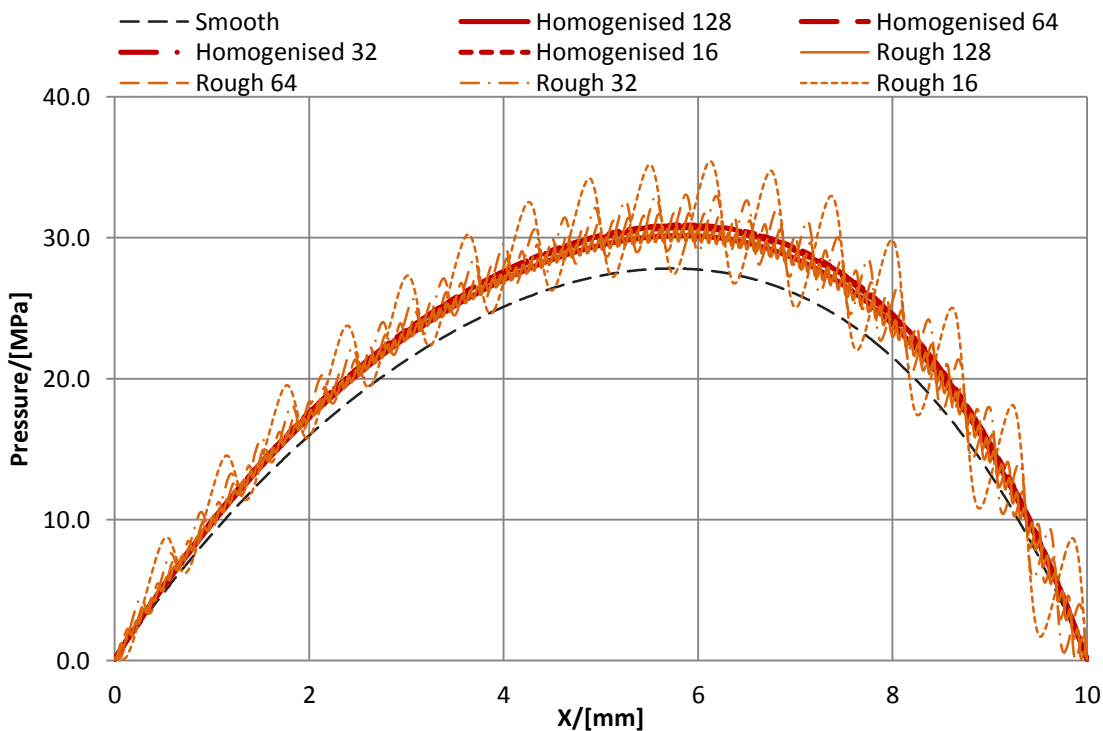


Figure 6.29 Solution for the tilted pad bearing problem with the smooth, rough and homogenized rough surfaces with 16, 32, 64 and 128 waves. Minimum clearance value  $h_{\min}=2.0\mu\text{m}$

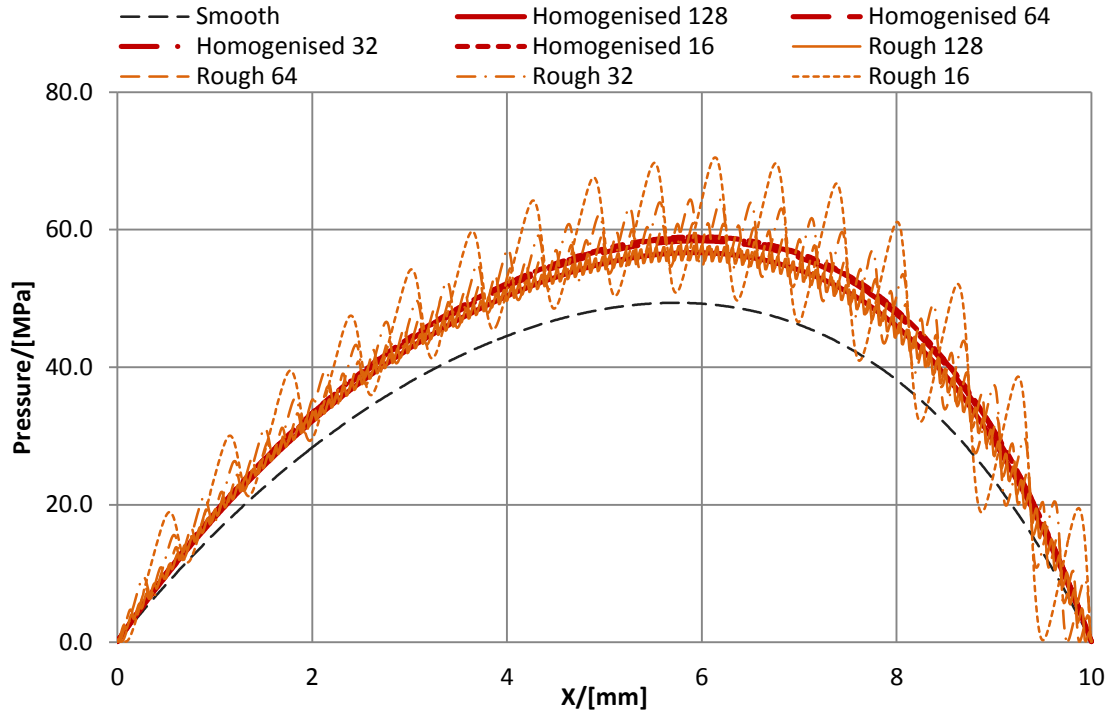


Figure 6.30 Solution for the tilted pad bearing problem with the smooth, rough and homogenised rough surfaces with 16, 32, 64 and 128 waves. Minimum clearance value  $h_{min}=1.5\mu m$

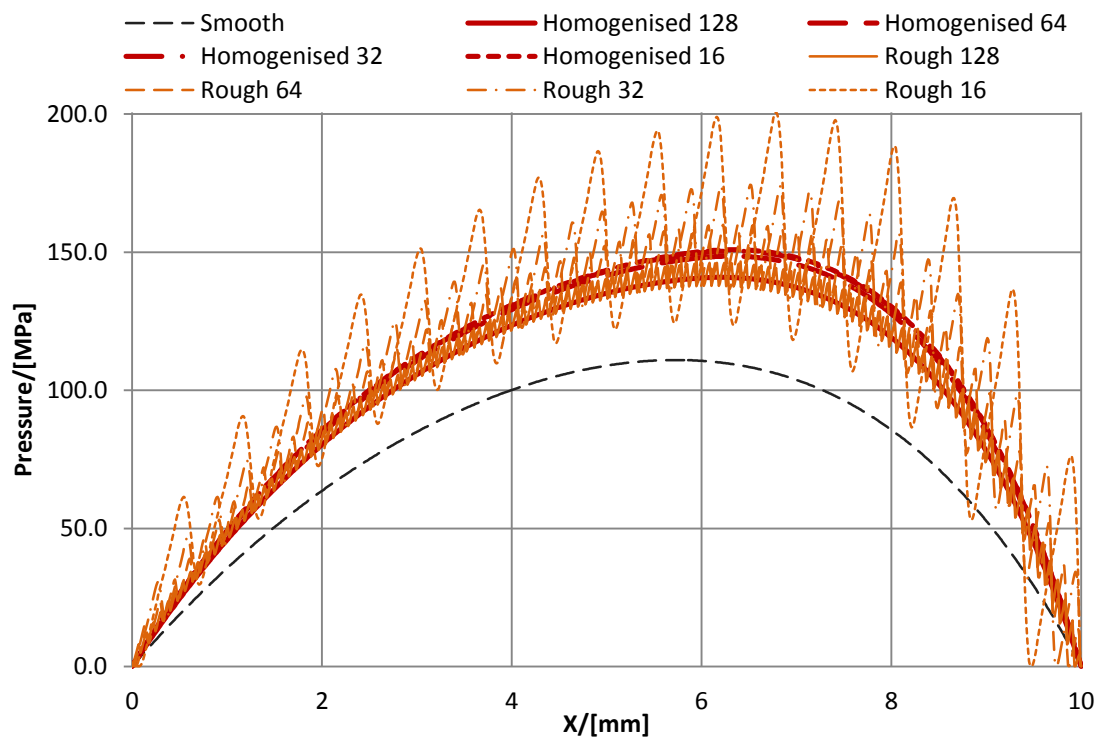


Figure 6.31 Solution for the tilted pad bearing problem with the smooth, rough and homogenised rough surfaces with 16, 32, 64 and 128 waves. Minimum clearance value  $h_{min}=1.0\mu m$

## Section 6.5 Solving the tilted pad bearing problem using the multigrid method

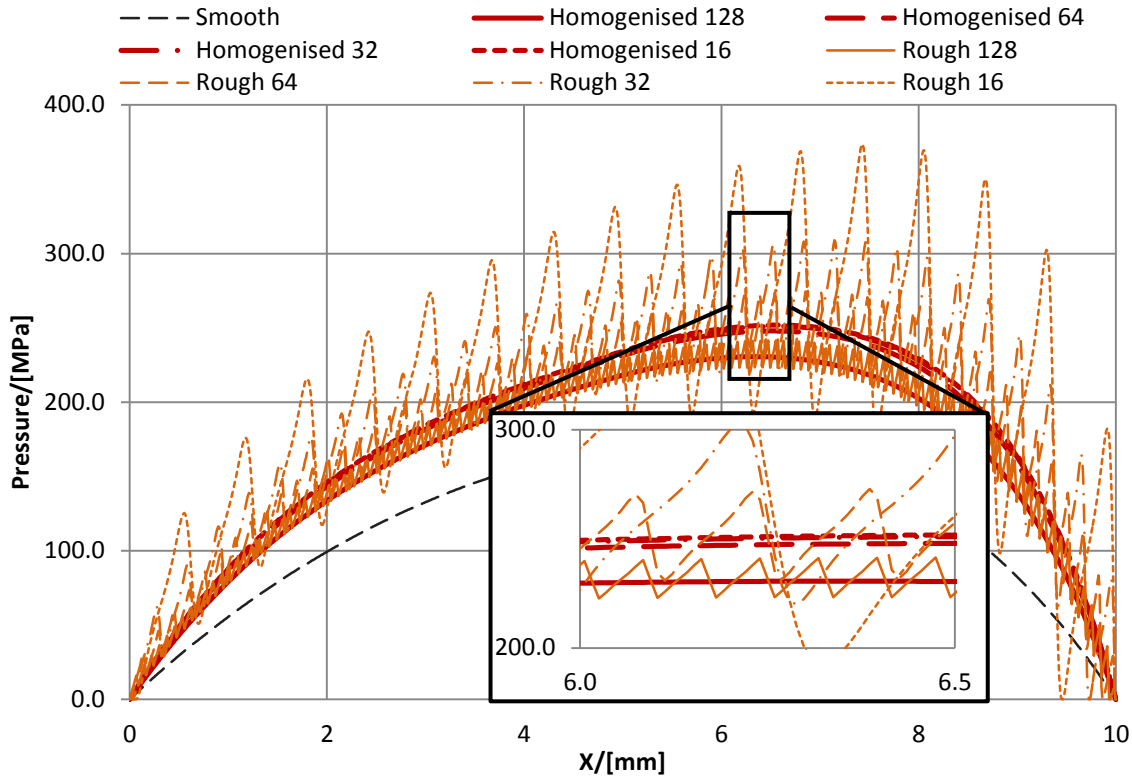


Figure 6.32 Solution for the tilted pad bearing problem with the smooth, rough and homogenized rough surfaces with 16, 32, 64 and 128 waves. Minimum clearance value  $h_{min}=0.8\mu\text{m}$

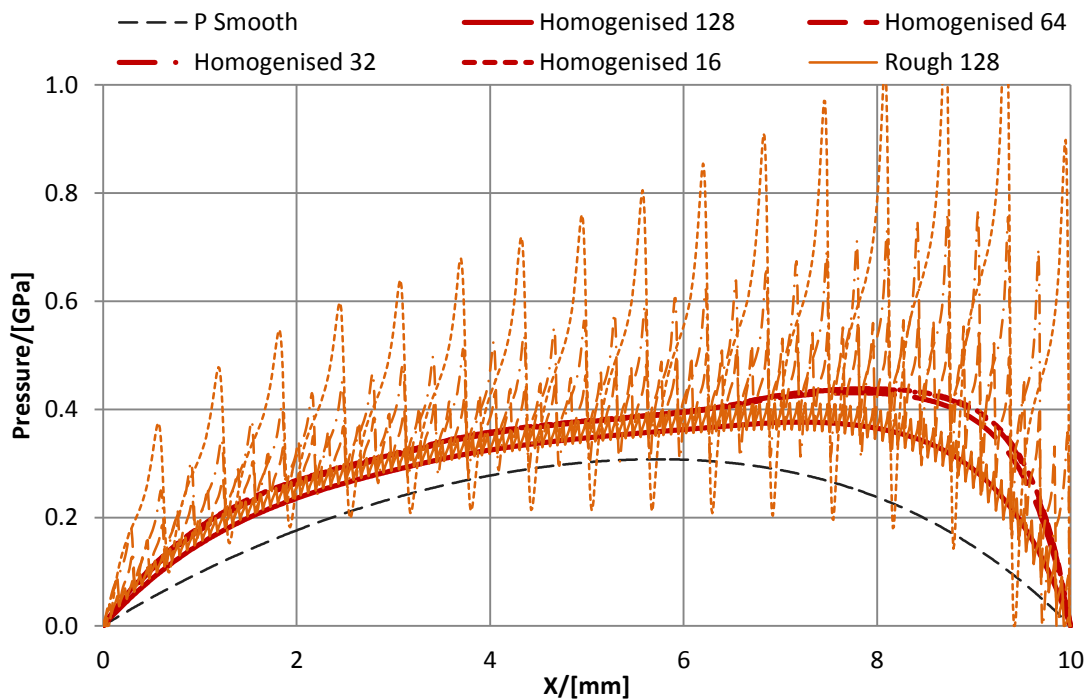


Figure 6.33 Solution for the tilted pad bearing problem with the smooth, rough and homogenized rough surfaces with 16, 32, 64 and 128 waves. Minimum clearance value  $h_{min}=0.6\mu\text{m}$

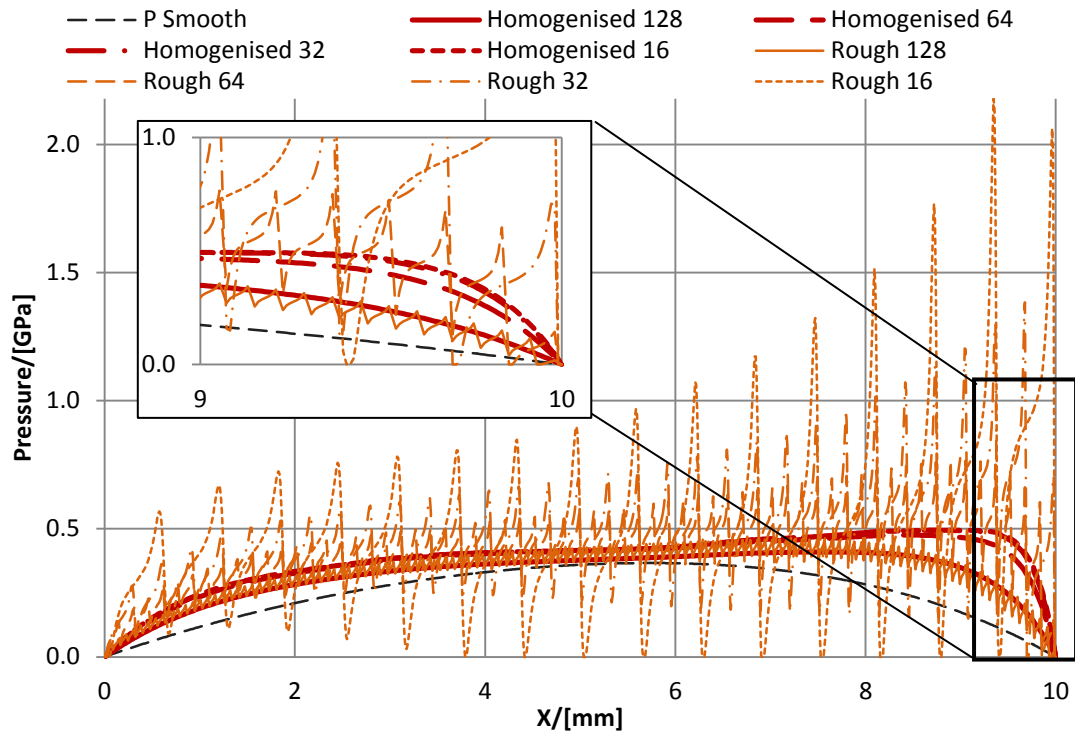


Figure 6.34 Solution for the tilted pad bearing problem with the smooth, rough and homogenized rough surfaces with 16, 32, 64 and 128 waves. Minimum clearance value  $h_{min}=0.55\mu m$

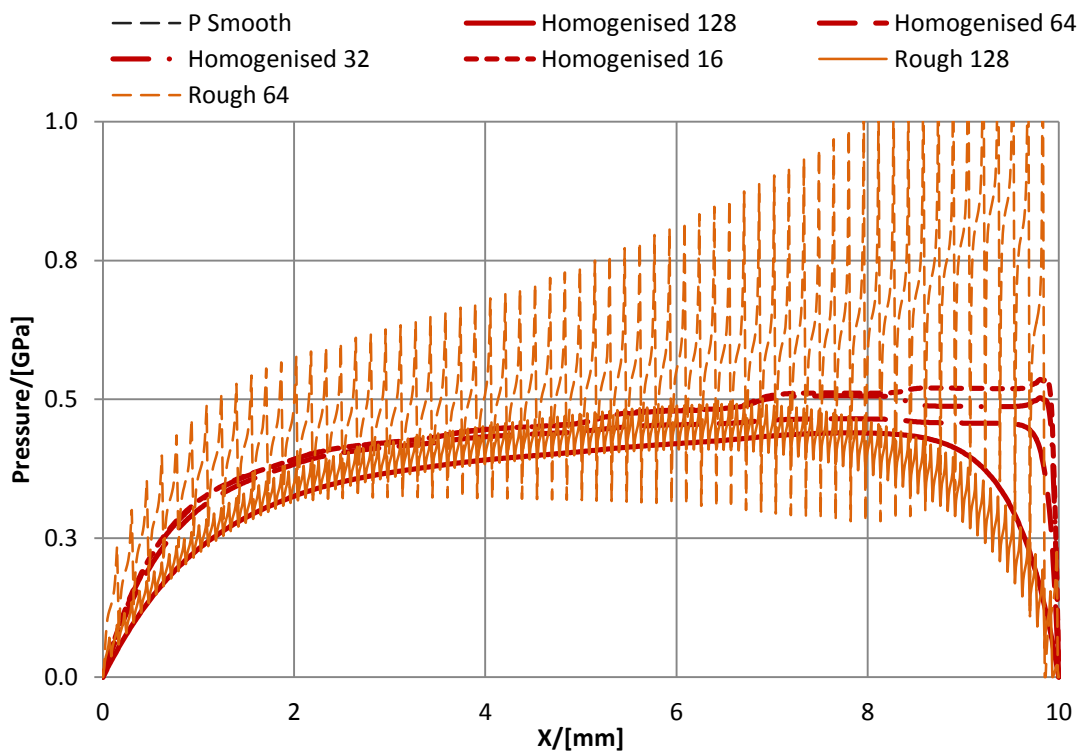


Figure 6.35 Solution for the tilted pad bearing problem with the smooth, rough and homogenized rough surfaces with 16, 32, 64 and 128 waves. Minimum clearance value  $h_{min}=0.50\mu m$

The sequence of figures illustrates the evolution of the solution starting from smooth shape of the pressure distribution having its maximum at approximately  $x=5.7mm$ . As

## Section 6.5 Solving the tilted pad bearing problem using the multigrid method

the minimum clearance decreases the point of maximum pressure moves in the positive  $x$  direction towards the exit of the bearing. The first observation that can be brought forward from Figures 6.29-6.35 is that the difference between smooth solution and rough and homogenised solutions increases as the  $h_{min}$  value decreases, which illustrates the increasing effect of the roughness on the lubrication. The second observation is that all the rough solutions have the basic shape coincident with the corresponding homogenised solution. The perturbations of the rough surface pressure depend on the wavelength of the roughness, i.e. longer wavelength generates higher pressures. These perturbations are caused by the effects of the individual asperities, which is thus not predicted by the homogenised solution. Note also, that the difference between the homogenised solutions based on different resolutions of roughness becomes more apparent for lower clearance values which can be seen in e.g. Figure 6.32 when comparing the homogenised solutions based on 128 waves with other homogenised solutions. The baselines of the pressure distributions for different wavelengths of roughness start to deviate for the values of  $h_{min} < 2\mu\text{m}$ . The corresponding homogenised solutions however remain coincident with those baselines, until the value of  $h_{min}$  become equal to  $0.55\mu\text{m}$  as observed in Figure 6.35. Note, that in Figure 6.34 the homogenised solution predicts the average pressure for the cases of 128 and 64 waves quite accurately, whereas the higher pressure peaks corresponding to the solutions of 32 and 16 waves remain uncaptured by the homogenisation process. From this it can be concluded that in case of very thin gaps ( $h_{min} - R_{max} < 0.05\mu\text{m}$ ) the effect of the individual large wavelength components on the pressure overwhelms the global effect of the roughness which therefore cannot be predicted by the homogenisation treating the roughness features in an average way only. Also, thin gaps result in very high pressure values which create instabilities when solving the deterministic rough problem and result in slow convergence of the numerical methods. The process of solving the homogenised problem remains stable and well converged.

Figure 6.36 shows the homogenised and rough solutions of the problems with minimum clearance  $h_{min} = 0.45\mu\text{m}$ . The only deterministic rough solution shown is the one for 128 waves. Other rough solutions have been found unstable and result in unrealistic pressure values. The reason for this is that value of  $h_{min} = 0.45\mu\text{m}$  is lower than the amplitude of the roughness  $R_{max} = 0.5\mu\text{m}$  which means that the part of the tilted pad starting from the point  $x = 5.6\text{mm}$  is brought into (partial) contact. In the case

of the extruded roughness this results in the total blockage of flow. The non zero values of pressure beyond the point  $x=5.6\text{mm}$  are then the numerical artefacts caused by the program trying to solve the problem where the flow is blocked. Note also that the zero values of the gap  $h$  were replaced by the value of  $10^{-9}$  for numerical reasons.

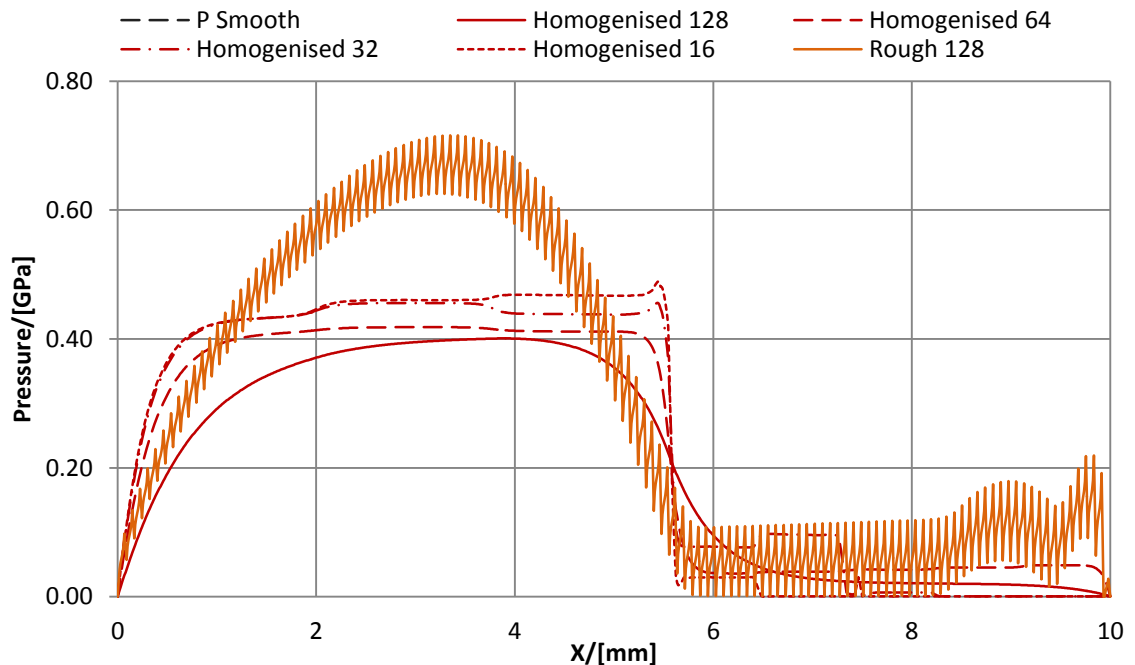


**Figure 6.36** Solution for the tilted pad bearing problem with the smooth, rough and homogenized rough surfaces with 16, 32, 64 and 128 waves. Minimum clearance value  $h_{\min}=0.45\mu\text{m}$

The elastic load carried by asperities was calculated at the stage of evaluating the flow factors and added to the hydrodynamic load in the case of the homogenised solution. However in Figure 6.35 the elastic part of the load is not visible as it is too small in comparison to the hydrodynamic load. For this reason in Section 6.5.4 the solution of the problem is shown where the hydrodynamic load is of the same magnitude as the one carried by the contacting asperities.

#### 6.5.4 Extruded cosine roughness: contact case

The tilted pad bearing problem with extruded cosine roughness is considered where the specific configuration parameters of the problem are given in Table 6.4.

Note that the viscosity-velocity product was reduced 10 times in comparison to that given in Table 6.3. This reduction allows the hydrodynamic load to be of the same magnitude as the elastic load carried by asperities in case of the extruded roughness. The roughness function is considered extruded in  $y$  direction and having 128 cosine waves in  $x$  direction.

## Section 6.5 Solving the tilted pad bearing problem using the multigrid method

Table 6.4 Configuration of the tilted pad bearing problem for the case of contact

Parameter	Value	Units	Description
$h_{min}$	0.5-0.42	$\mu\text{m}$	Minimum clearance range1
$\gamma$	1.25		Titling ratio
$R_{max}$	0.5	$\mu\text{m}$	Roughness amplitude
$k$	128		Number of sinusoidal waves
$L$	1.0	cm	Length
$W$	1.0	cm	Width
$u$	0.1	m/s	Linear velocity of the counterface
$\eta$	0.7	Pa·s	Viscosity of the fluid

Figure 6.37 shows the homogenised solutions of the tilted pad bearing problem for the minimum clearance values  $h_{min}=0.5, 0.48, 0.46, 0.44$  and  $0.42 \mu\text{m}$ , where the arrow indicates the sense of reducing the  $h_{min}$  value from  $0.5\mu\text{m}$  down to  $0.42\mu\text{m}$ . The elastic load supported by the asperities was obtained at the stage of evaluation of the flow factors. The load is then divided by the area of the local domain to give mean elastic contact pressure as a function of global film thickness. The value of the mean elastic contact pressure corresponding to the global film thickness value is subsequently added to the hydrodynamic pressure after the homogenised Reynolds equation has been solved.

The solution corresponding to  $h_{min}=0.5\mu\text{m}$  (solid line) has no elastic component of the pressure in it as the contact occurs only at the exit boundary, i.e.  $x=1\text{cm}$ . The rest of the solutions have a hump in the pressure distribution corresponding to the hydrodynamic pressure followed by a drop where the flow of fluid is completely blocked by the contacting asperities. The pressure after that drop is the elastic pressure generated at the direct asperity contacts. The case of homogenised solution for a mixed lubrication problem is also considered in Section 6.5.6 for the two dimensional cosine roughness. The two dimensional roughness allows the hydrodynamic pressure coexist with the one generated at the asperity contacts.

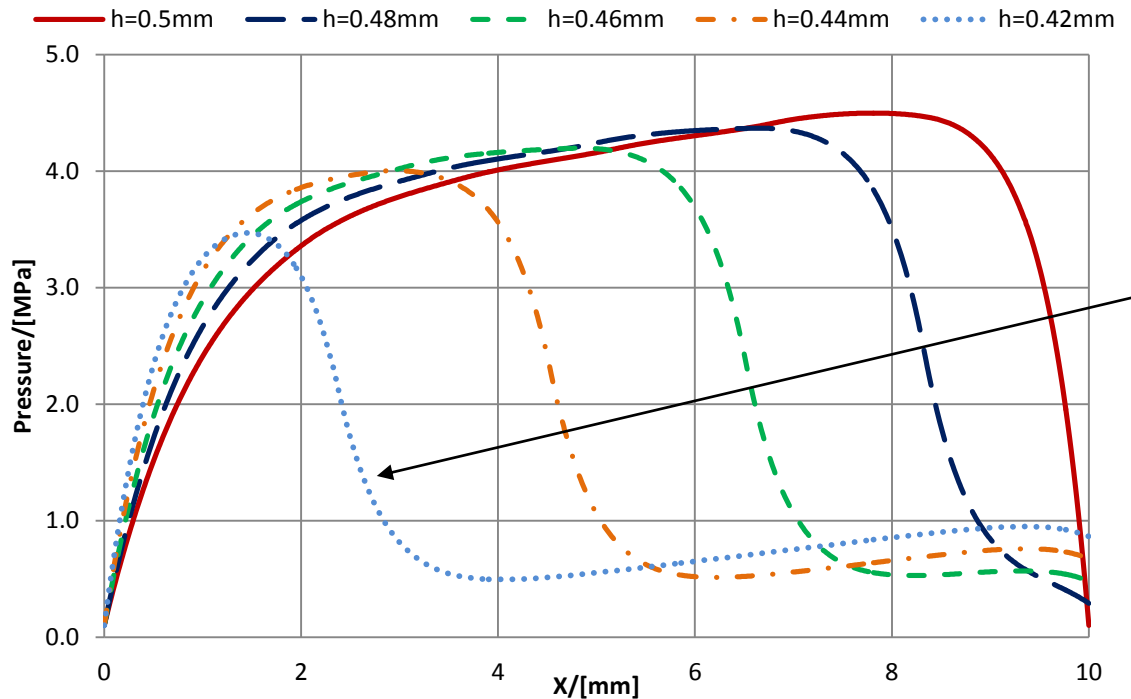


Figure 6.37 Homogenised solution of the tilted pad bearing problem in case of the direct contact of the surfaces. Minimum clearance values  $h_{min}=0.5, 0.48, 0.46, 0.44$  and  $0.42 \mu\text{m}$ . Arrow indicates sense of decreasing the minimum clearance starting from the case where contact first occurs at the exit of the bearing and progressively increasing the area of direct contact.

### 6.5.5 The oblique roughness effect

In this section the effect of the oblique roughness on the pressure distribution within the tilted pad bearing problem was studied. For this purpose the extruded cosine roughness function was considered as given by Equation (6.40). The geometry and configuration of the tilted pad problem are given in Table 6.5. The resolution used was 16 elements per wave i.e. 64 waves in total. The roughness function was rotated at  $30^\circ$  angle clockwise and the contours of a  $2 \times 2 \text{mm}$  portion of the rough surface are shown in Figure 6.38.

At the stage of evaluating the flow factors the oblique flow factors formulae (4.33) were applied to the flow factors calculated for an extruded cosine surface in Section 6.5.3. A sequence of Figures (6.39-6.46) show the comparison of the deterministic and homogenised rough solutions for the values of minimum clearance  $h_{min}=1.5, 0.8, 0.6$  and  $0.55 \mu\text{m}$ . These figures present the central cross section of the pressure distribution parallel to the x axis as well as the contour plot.

## Section 6.5 Solving the tilted pad bearing problem using the multigrid method

Table 6.5 Configuration of the tilted pad bearing problem for the case of oblique roughness

Parameter	Value	Units	Description
$h_{min}$	1.5-0.55	$\mu\text{m}$	Minimum clearance range1
$\gamma$	1.25		Tilting ratio
$R_{max}$	0.5	$\mu\text{m}$	Roughness amplitude
$k$	128		Number of sinusoidal waves
$\theta$	$30^\circ$		Orientation of the roughness features
$L$	1.0	cm	Length
$W$	1.0	cm	Width
$u$	0.1	m/s	Linear velocity of the counterface
$\eta$	0.7	Pa·s	Viscosity of the fluid

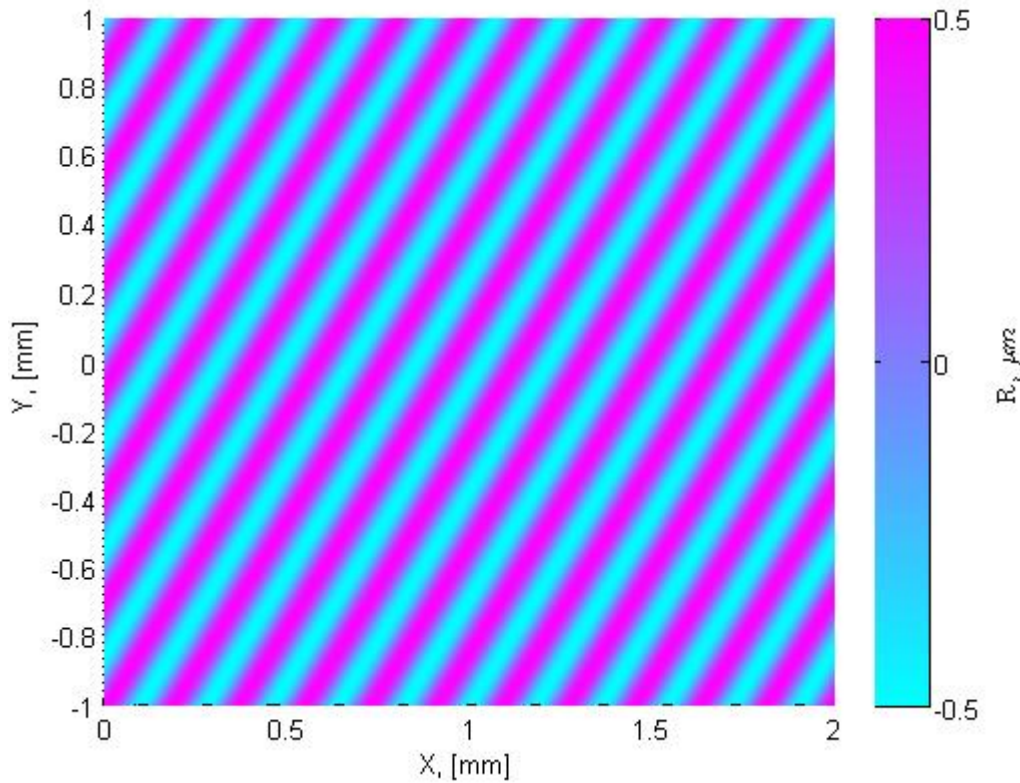


Figure 6.38 Extruded cosine roughness function rotated at  $30^\circ$  clockwise.

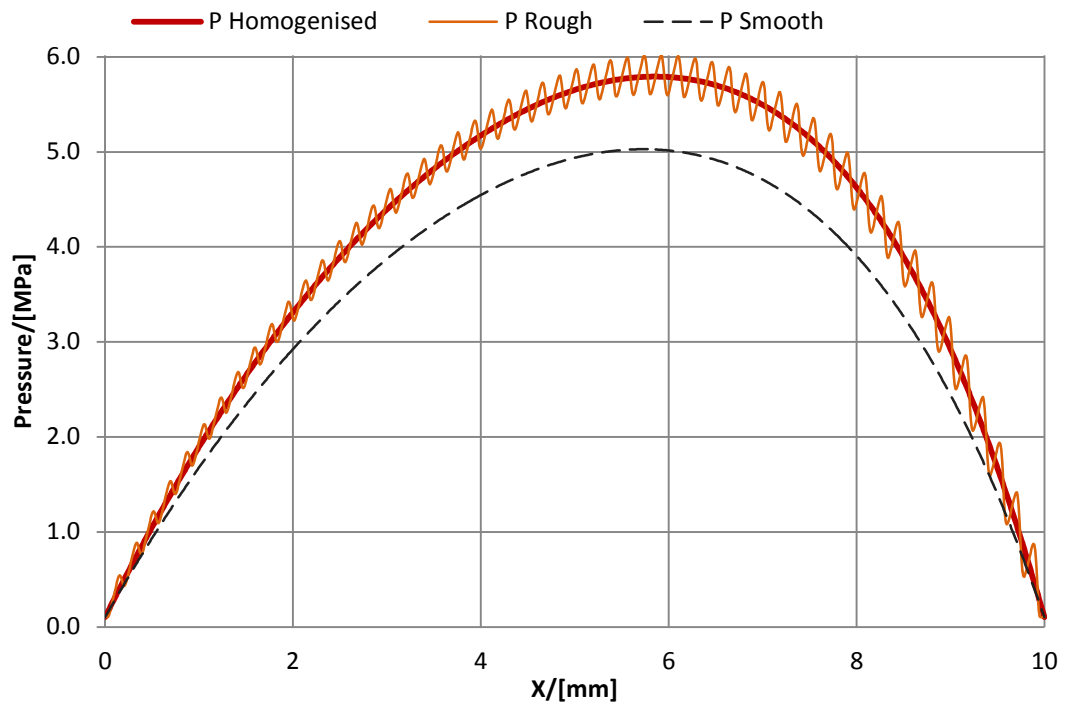


Figure 6.39 Central cross section of the pressure distribution parallel to the  $x$  axis for deterministic rough, homogenized and smooth solutions. Minimum clearance  $h_{min}=1.5\mu m$

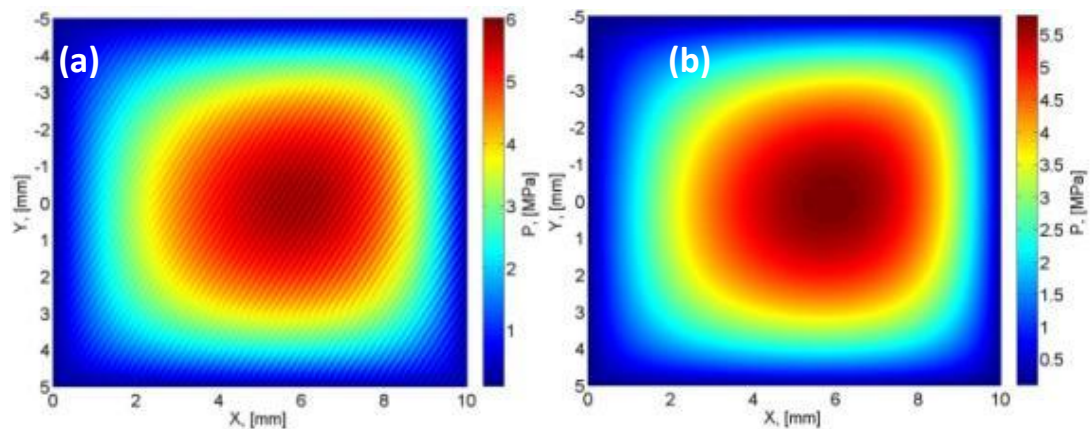


Figure 6.40 Contour plot of the pressure distribution for (a) the deterministic, and (b) the homogenised rough solutions. Minimum clearance  $h_{min}=1.5\mu m$

The first set of Figures 6.39 and 6.40 correspond to the minimum clearance value  $h_{min}=1.5\mu m$ . Firstly, it can be seen that the homogenised solution coincides with the base line of the pressure distribution obtained for the deterministic rough case. Secondly, although it is clear that both deterministic and homogenised rough cases produce results that are different from the smooth one, the shapes of the pressure distribution for all three cases do not show any apparent effect of oblique roughness as shown on contour plots of Figures 6.40a and 6.40b. This means that on the global scale the rough solution behaves in the same way as the smooth one except for the ridges corresponding to the effect of the individual roughness features.

## Section 6.5 Solving the tilted pad bearing problem using the multigrid method

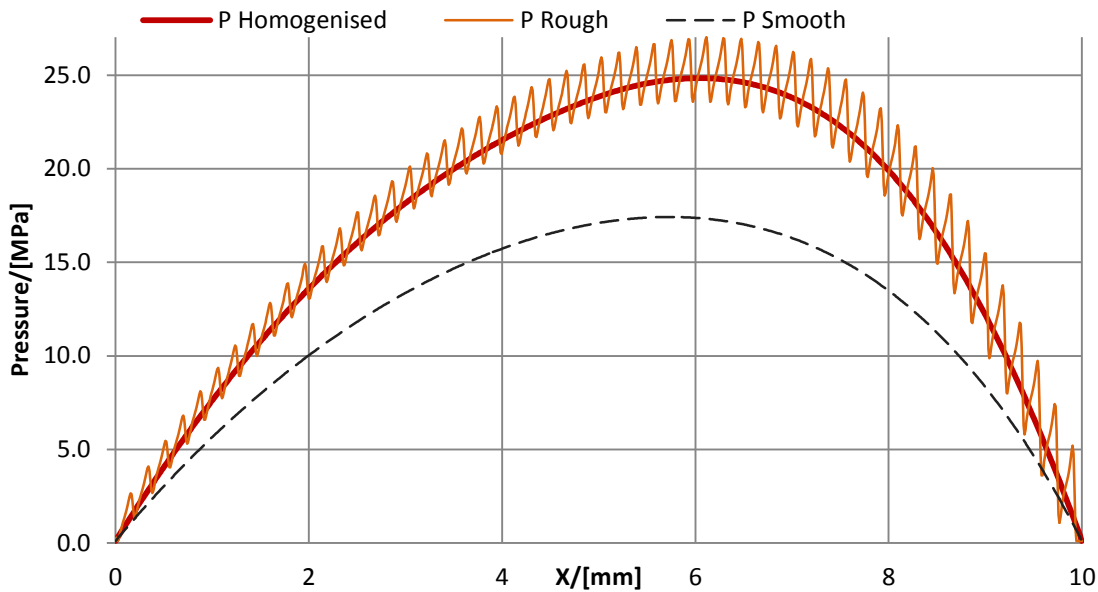


Figure 6.41 Central cross section of the pressure distribution parallel to the  $x$  axis for deterministic rough, homogenized and smooth solutions. Minimum clearance  $h_{min}=0.8\mu m$

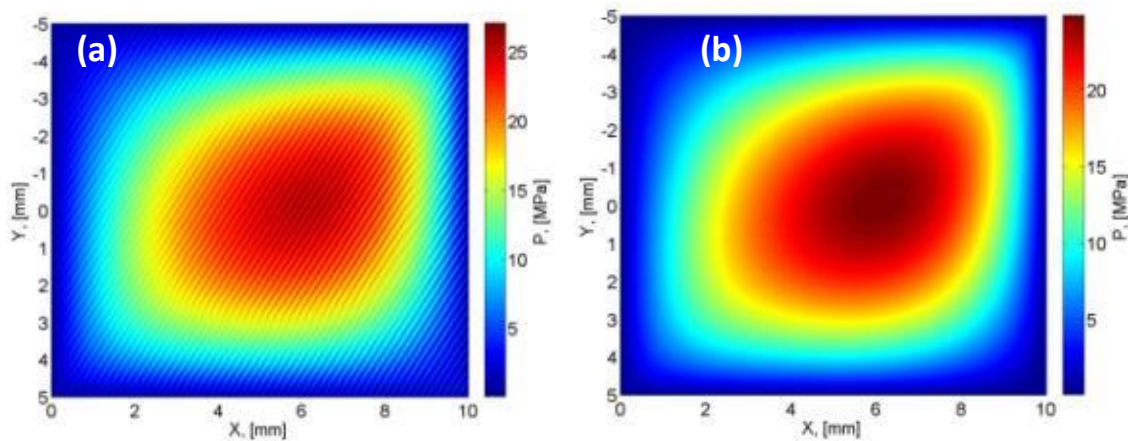


Figure 6.42 Contour plot of the pressure distribution for (a) the deterministic and (b) the homogenised rough solutions. Minimum clearance  $h_{min}=0.8\mu m$

The second set of Figures 6.41 and 6.42 are for the minimum clearance value  $h_{min}=0.8\mu m$ . The solution for the deterministic rough case shown in Figure 6.42a illustrates the distinctive behaviour of the pressure distribution caused by the oblique roughness. The homogenised solution in Figure 6.42b is capable of predicting the same distortion of the pressure distribution caused by rotating of the roughness features through an angle of  $30^\circ$ . The remaining Figures 6.43-6.46 demonstrate the evolution of the effect of the oblique roughness as the minimum clearance value  $h_{min}$  decreases down to the value of  $0.55\mu m$ .

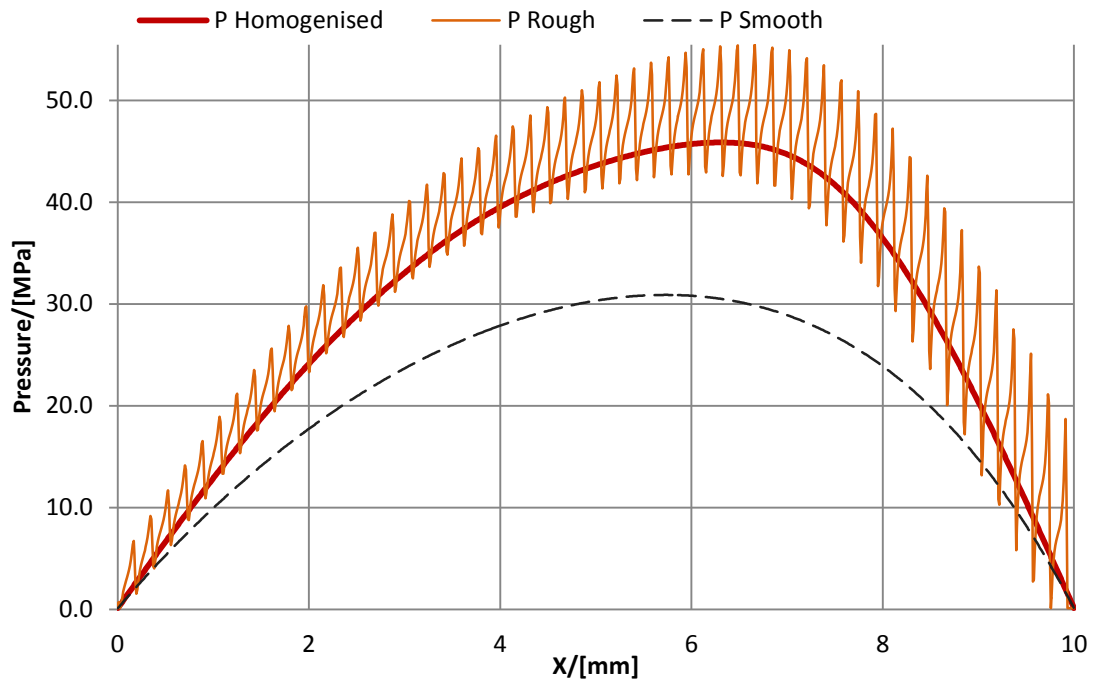


Figure 6.43 Central cross section of the pressure distribution parallel to the x axis for deterministic rough, homogenized and smooth solutions. Minimum clearance  $h_{min}=0.6\mu m$

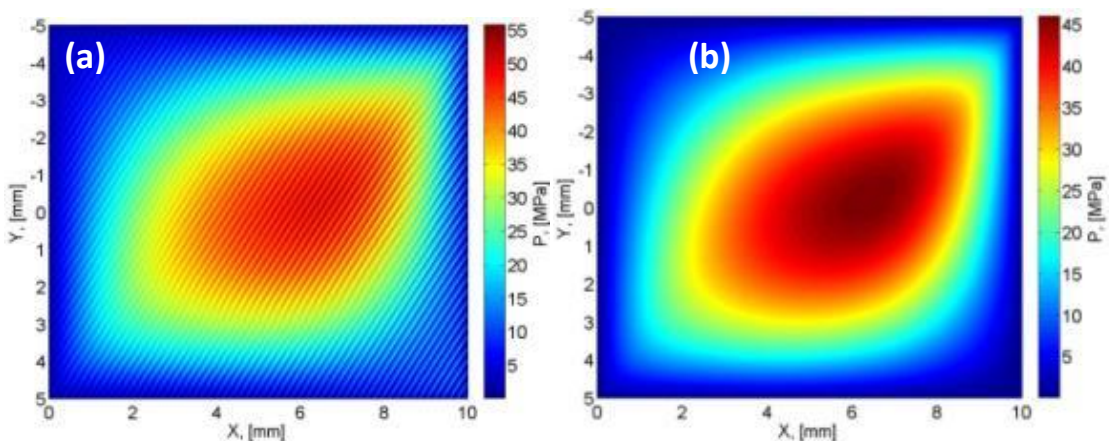


Figure 6.44 Contour plot of the pressure distribution for (a) the deterministic and (b) the homogenised rough solutions. Minimum clearance  $h_{min}=0.6\mu m$

The oblique roughness features create a pressure gradient along the oblique direction which results in the distortion of the pressure distribution. It is clear from the figures that the effect of oblique roughness on the pressure distribution is captured by the homogenised method quite well. It can also be observed, that for the higher values of  $h_{min}>0.6\mu m$  the relative difference between the homogenised and the smooth solution cross sections increases as  $h_{min}$  decreases, whereas for the values  $h_{min}=0.6\mu m$  this difference becomes smaller. This can be explained by the fact the maximum pressure value moves in the oblique direction.

## Section 6.5 Solving the tilted pad bearing problem using the multigrid method

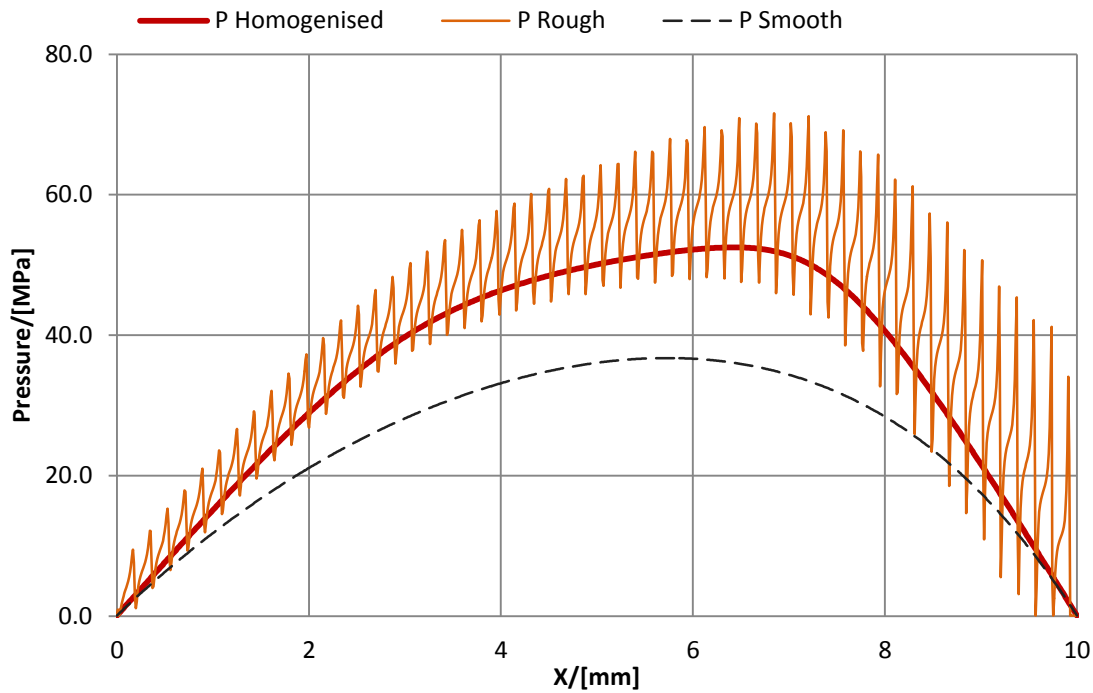


Figure 6.45 Central cross section of the pressure distribution parallel to the x axis for deterministic rough, homogenised and smooth solutions. Minimum clearance  $h_{min}=0.55\mu\text{m}$

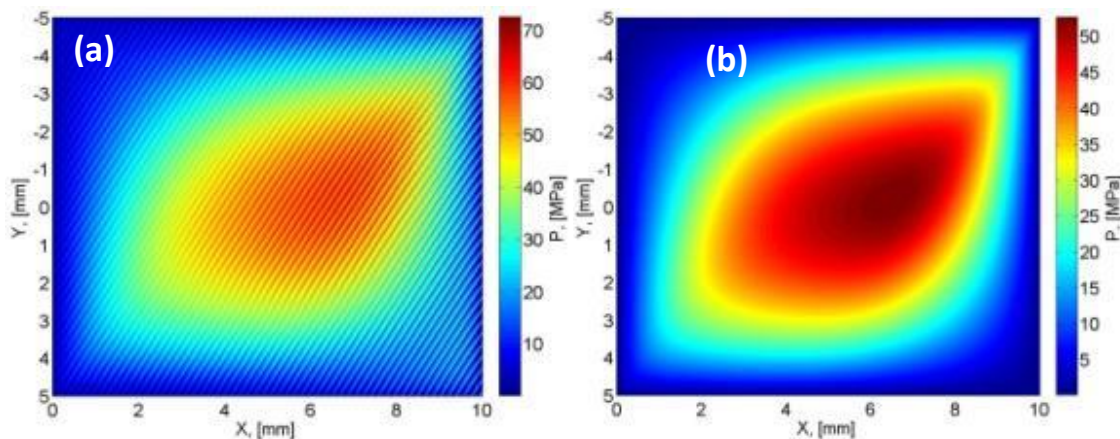


Figure 6.46 Contour plot of the pressure distribution for (a) the deterministic and (b) the homogenised rough solutions. Minimum clearance  $h_{min}=0.55\mu\text{m}$

### 6.5.6 The two dimensional roughness problems

The extruded roughness used in Sections 6.5.3-6.5.5 creates significant obstruction to the flow across the roughness features. The extruded surface roughness may represent the characteristic roughness features of the surface prepared by grinding (see Section 5.2.7) and is well suited for illustrating certain effects of roughness. Real surfaces however may well not be extruded, which creates the possibility for the lubricant to flow around the asperity features even if the asperities are in direct contact. In this section surfaces with a double sinusoidal roughness function have been considered on a bearing of 1x1cm area. The reason for selecting the sine function as

opposed to the cosine one is the more accurate coarse grid representation of the  $\sin(x)$  function rather than the  $\cos(x)$  one without any phase shift.

The double sinusoidal roughness can be defined by an equation similar to (5.32) with the cosine function replaced by sine:

$$h(x, y) = h_0(x, y) + R_{max} \sin\left(2\pi \frac{k_1 x}{L}\right) \sin\left(2\pi \frac{k_2 y}{W}\right) \tag{6.42}$$

where  $L$  and  $W$  are the dimensions of the total area,  $k_1$  and  $k_2$  define the number of waves in  $x$  and  $y$  directions respectively and  $R_{max}$  is the amplitude. The configuration parameters of the problem are given in Table 6.6. Note the low velocity  $u=1\text{cm/s}$  of the counterface which is selected to decrease the values of the hydrodynamic pressure in order to make them comparable to the contact pressure.

Table 6.6 Configuration of the tilted pad bearing problem for the double sine surface

Parameter	Value	Units	Description
$h_{min}$	1.5-0.3	$\mu\text{m}$	Minimum clearance values range
$\gamma$	1.25		Tilting ratio
$R_{max}$	0.5	$\mu\text{m}$	Roughness amplitude
$k_1$	64		Number of sinusoidal waves in entrainment ( $x$ ) direction
$k_2$	16		Number of sinusoidal waves in transverse( $y$ ) direction
$\theta$	$30^\circ$	$^\circ$	Rotation of the roughness features (clock wise)
$L$	1	cm	Length
$W$	1	cm	Width
$u$	1	cm/s	Linear velocity of the counterface
$\eta$	0.14	Pa·s	Viscosity of the fluid
$P_0$	$10^5$	Pa	Atmospheric pressure

The double sinusoidal roughness function is plotted in Figure 6.48. Note that only a 2x2mm portion is shown on in this contour plot. For the example chosen for analysis the roughness features are extended in  $y$  direction (before rotation) by a factor of  $k_1/k_2=4$ .

## Section 6.5 Solving the tilted pad bearing problem using the multigrid method

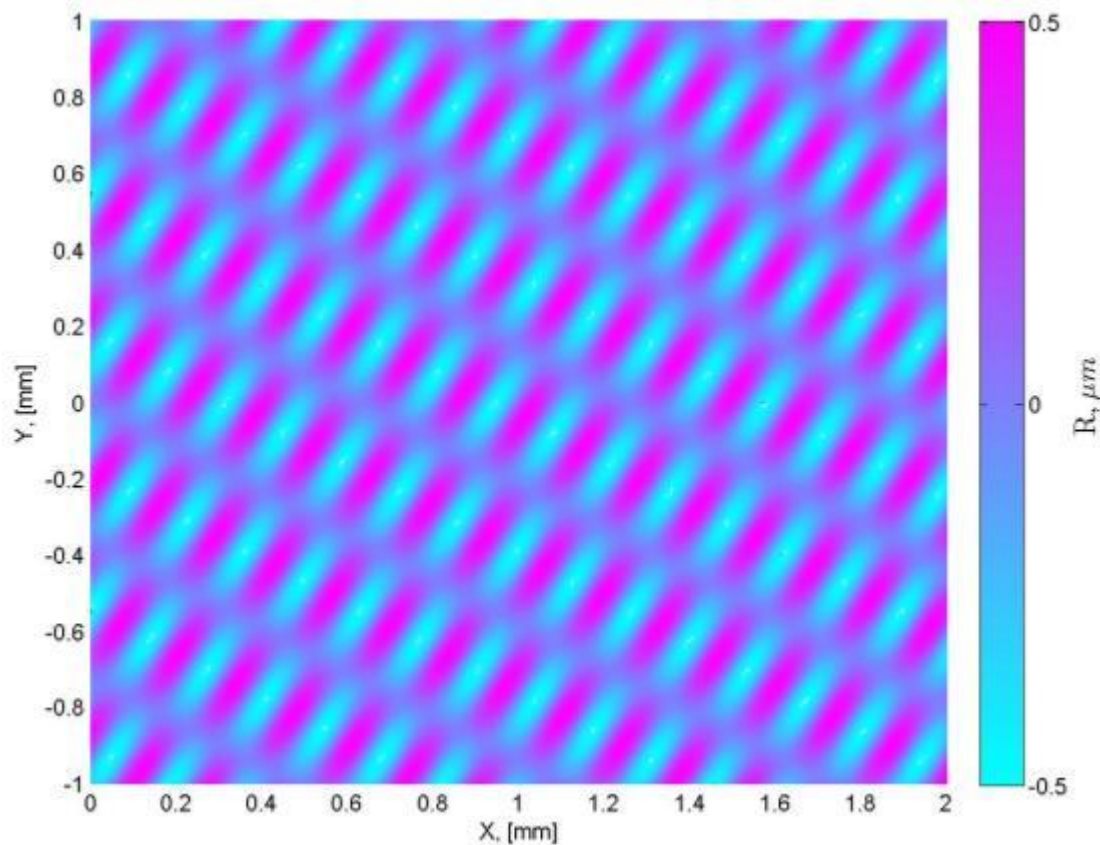


Figure 6.47 Double sine surface with 64 and 16 waves in x and y directions respectively.

Figure 6.48 shows the load-clearance behaviour for the smooth, deterministic and homogenised cases. The hydrodynamic and elastic contact components of the homogenised load are also shown separately. The deterministic solution is not available for the cases of direct contact, i.e.  $h_{min} < 0.5\mu m$ , as the elastic deflection is not considered in the method of solving the Reynolds equation for the tilted pad bearing formulation. In case of the homogenised solution the elastic and plastic deflection of the surface are taken into account at the stage of calculating the flow factors, which is explained in Chapters 3-5. Note that the elastic contact load carried by the asperities is calculated as a function of the global film thickness. The mean contact pressure corresponding to the film thickness at each mesh point on the global grid mesh is added to the hydrodynamic pressure calculated at that point.

A clear increase in the total homogenised load can be observed in Figure 6.48 as the minimum clearance value  $h_{min}$  is getting smaller. This can be explained by the progressively significant obstruction of the flow due to the roughness, which causes higher pressures to be generated. The maximum value of the homogenised load is reached where  $h_{min} = 0.5\mu m$ , i.e. the direct contact of the surface and the counterface occurs. The maximum value is followed by a drop which means that the hydrodynamic

lubrication mechanism starts to fail. This is confirmed by the drop in the hydrodynamic load value when  $h_{min} < 0.5 \mu\text{m}$ .

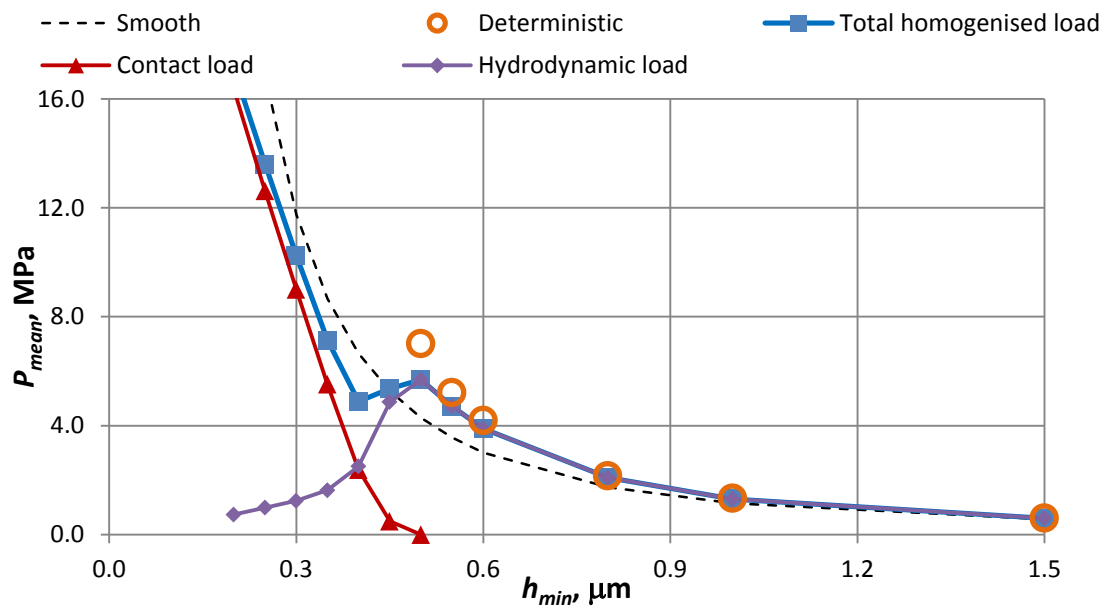


Figure 6.48 Load-clearance curves obtained for smooth deterministic and homogenised solutions. The hydrodynamic and contact parts of the homogenised load are also shown separately.

As the clearance value decreases more and more load is carried by the contacting asperities which is illustrated by the contact load curve, shown red with triangular markers. The majority of the total homogenised load is then due to the elastic contact load.

Note that the homogenised load (blue line, square markers) agrees quite well with the deterministic one (orange circles) until the direct contact occurs, i.e. when  $h_{min} = 0.5 \mu\text{m}$ . As before, in case of the low clearance the effect of the individual asperities is much higher than the average effect of roughness and therefore it is poorly reflected in the homogenised analysis. This inconsistency is expected to vanish for the case of measured rough surfaces, where the representative area contains multiple asperity features rather than a single sine wave. The detailed comparison of the pressure distribution for the deterministic and homogenised solutions is given in Figures 6.49-6.59.

The sequence of Figures 6.48-6.58 illustrate the smooth, deterministic and homogenised rough solutions for the tilted pad bearing problem with minimum clearance values  $h_{min} = 1.0, 0.6, 0.5, 0.45, 0.4$  and  $0.3 \mu\text{m}$ . In the case of  $h_{min} < 0.5 \mu\text{m}$  surface asperities undergo a direct contact with the counterface.

## Section 6.5 Solving the tilted pad bearing problem using the multigrid method

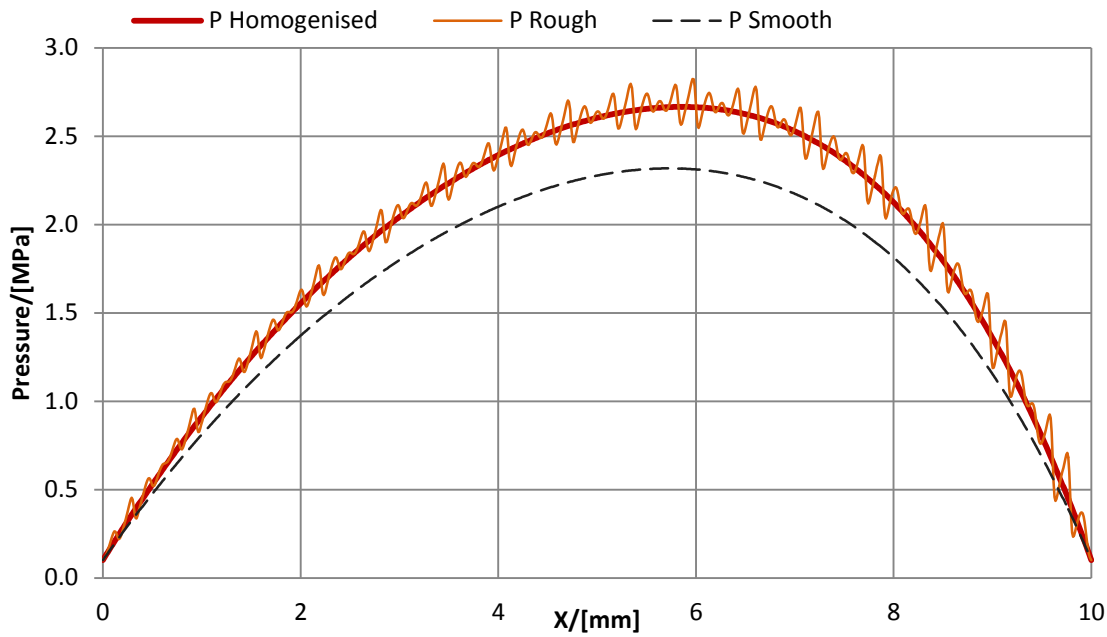


Figure 6.49 Central cross section of the pressure distribution parallel to the x axis for deterministic rough, homogenised and smooth solutions. Minimum clearance  $h_{min}=1.0\mu\text{m}$

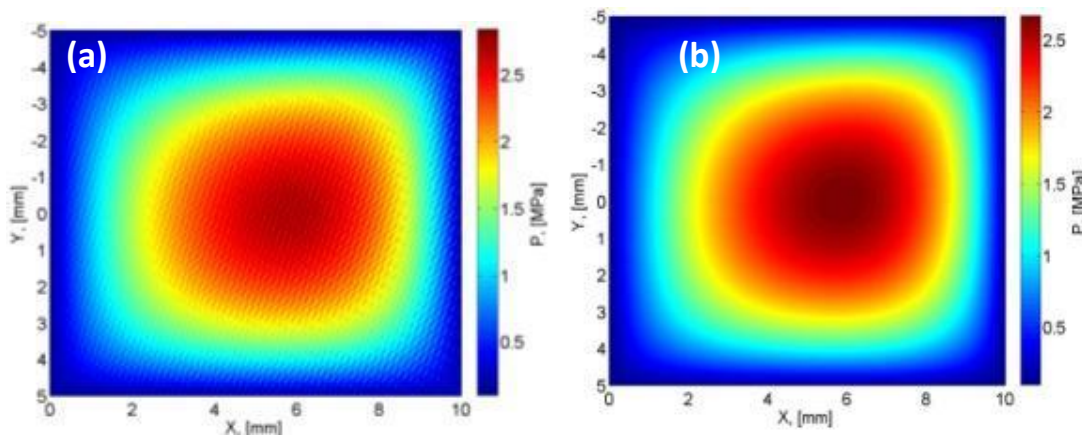


Figure 6.50 Contour plot of the pressure distribution for (a) the deterministic and (b) the homogenised rough solutions. Minimum clearance  $h_{min}=1.0\mu\text{m}$

Figures 6.49-6.52 correspond to the minimum film thickness value of  $h_{min}=1.0$  and  $0.6\mu\text{m}$ , i.e. the cases of pure hydrodynamic lubrication. Note that the pressure values in this example are much lower (up to 12MPa) than in the previous cases considered. This is the result of (i) smaller dimensions, 1x1cm as opposed to 10x10cm in Section 6.5.4 and (ii) lower velocity of 1cm/s as opposed to that used in the previous sections. These parameters were selected in order to make the hydrodynamic pressure comparable to the contact pressure.

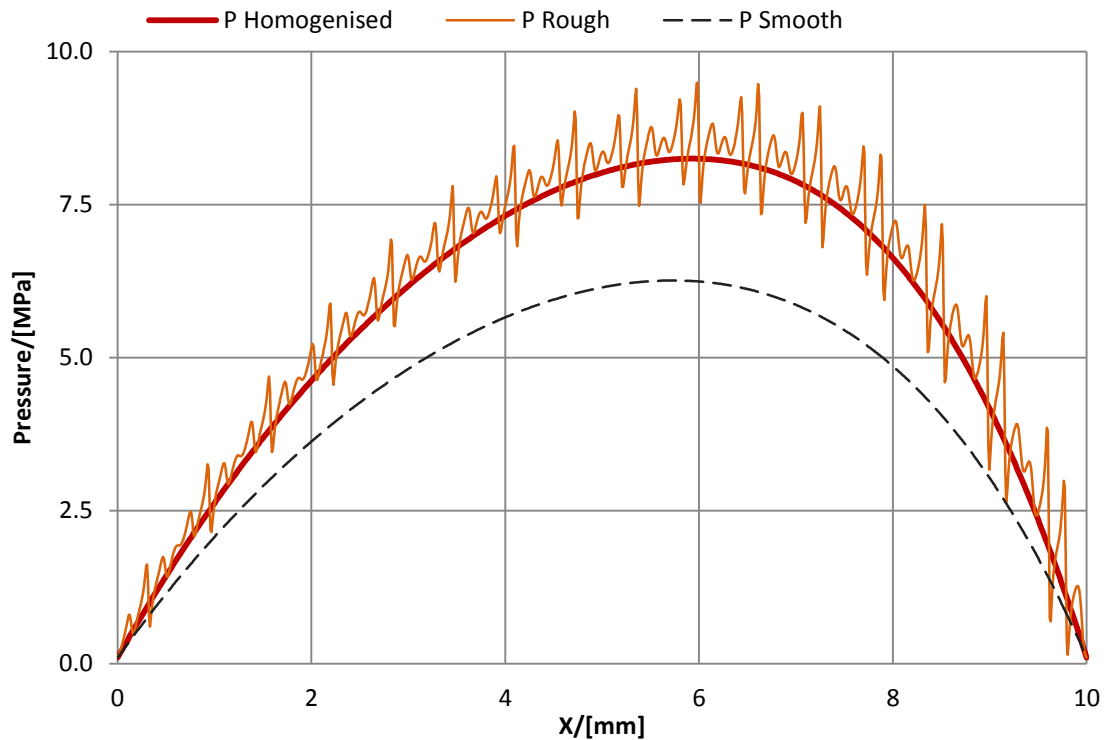


Figure 6.51 Central cross section of the pressure distribution parallel to the  $x$  axis for deterministic rough, homogenised and smooth solutions. Minimum clearance  $h_{min}=0.6\mu\text{m}$

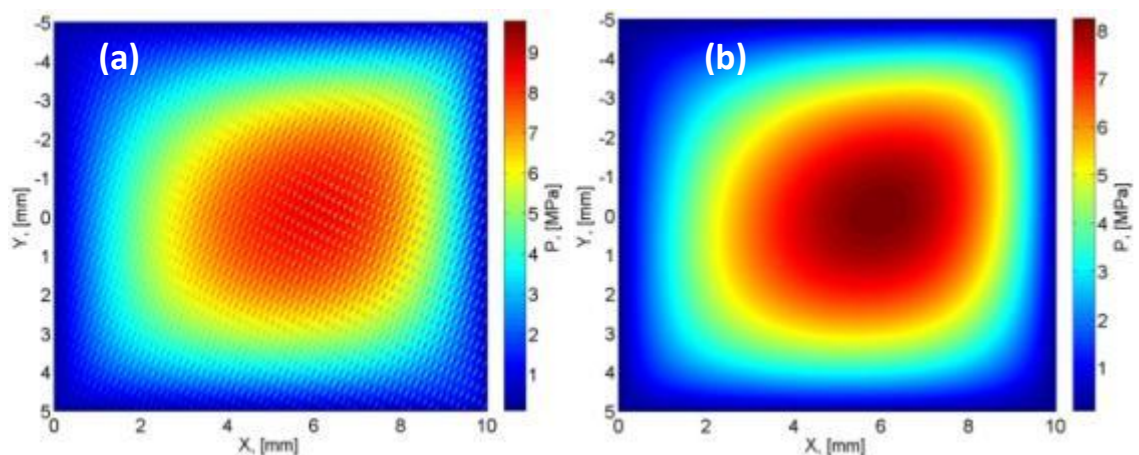


Figure 6.52 Contour plot of the pressure distribution for (a) the deterministic and (b) the homogenised rough solutions. Minimum clearance  $h_{min}=0.6\mu\text{m}$

The following observations can be brought forward from Figures 6.49-6.52. First, the effect of the oblique roughness ( $30^\circ$  clockwise rotation) is much smaller than observed for the extruded oblique roughness, compare e.g. Figures 6.52 and 6.44 for the same  $h_{min}$  value. Since the flow factors are independent of the velocity and viscosity values, the less significant effect of the oblique roughness in this section is explained only by the roughness being two dimensional, i.e. the lubricant is not forced to flow along the roughness features in such a strong way. The second effect that can be observed in Figures 6.49-6.52 is that, as before, the homogenised solution follows the shape of the

## Section 6.5 Solving the tilted pad bearing problem using the multigrid method

deterministic solution thus predicting the average effect of the roughness on lubrication.

Figure 6.53 shows the case of the minimum clearance value  $h_{min}=0.5\mu\text{m}$ . The difference between the homogenised and deterministic solutions becomes apparent. It was shown in Section 6.5.3 that the smaller is the characteristic wavelength of the roughness features the more accurate is the homogenised. In the case considered the wavelength of the features is 1/64 of the total length in x direction and 1/16 of the total width in y direction.

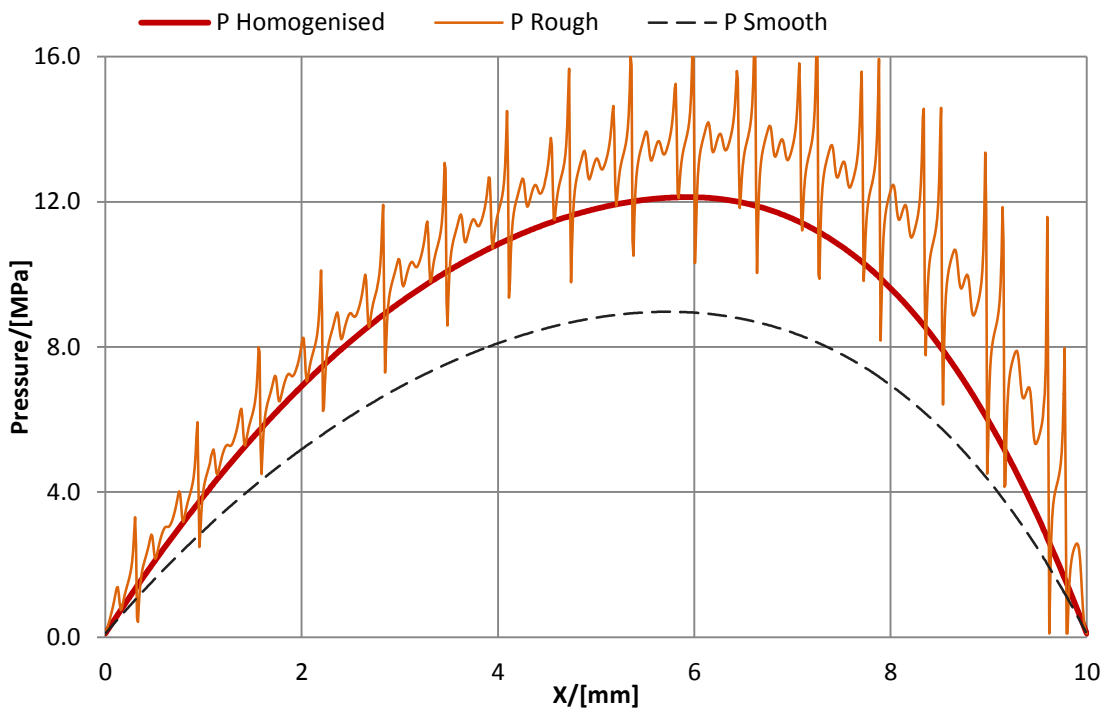


**Figure 6.53 Central cross section of the pressure distribution parallel to the x axis for deterministic rough, homogenised and smooth solutions. Minimum clearance  $h_{min}=0.5\mu\text{m}$**

In the next series of Figures 6.54-6.60 the central cross section and contour plots of the homogenised solution are shown for the cases where direct contact of the asperities occurs. The homogenised pressure shown by red thick line on the cross section charts is the sum of the hydrodynamic and elastic contact pressures, which are also shown separately by purple dotted and orange dashed curves.

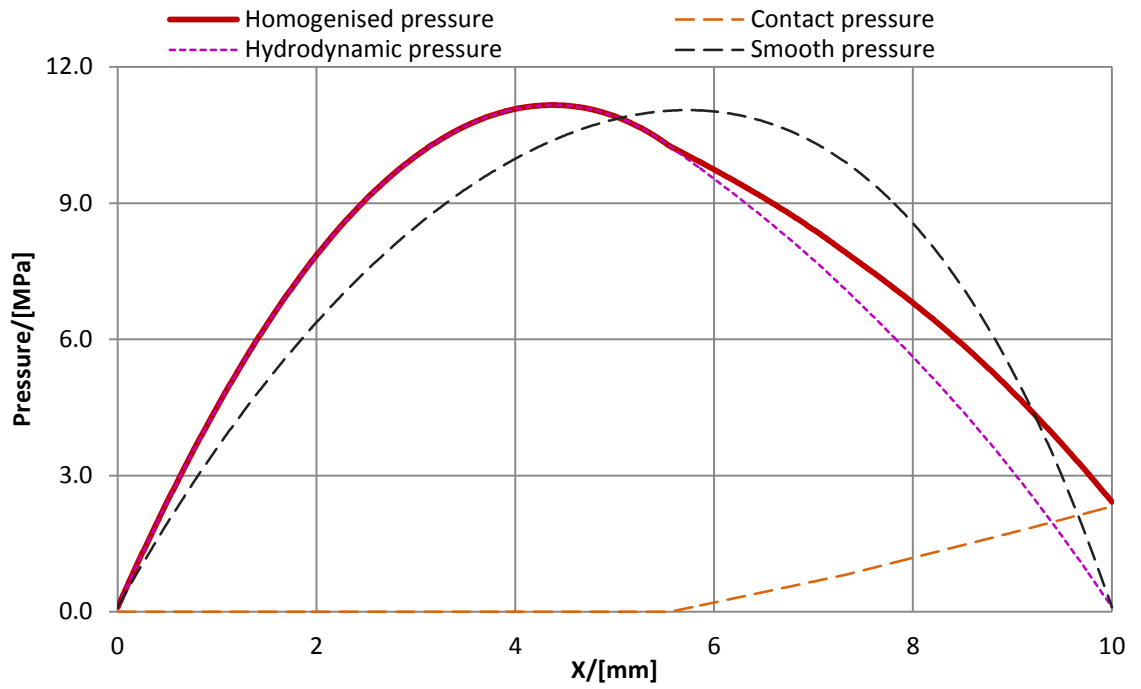


Figure 6.54 Central cross section of the pressure distribution parallel to the x axis for the homogenised and smooth solutions. Minimum clearance  $h_{min}=0.45\mu\text{m}$

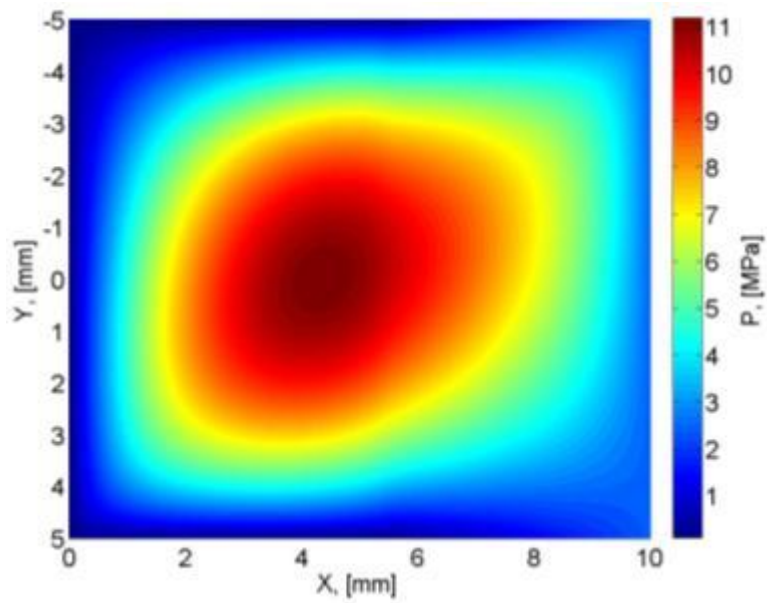


Figure 6.55 Contour plot of the pressure distribution for homogenised rough solution. Minimum clearance  $h_{min}=0.45\mu\text{m}$

Section 6.5 Solving the tilted pad bearing problem using the multigrid method

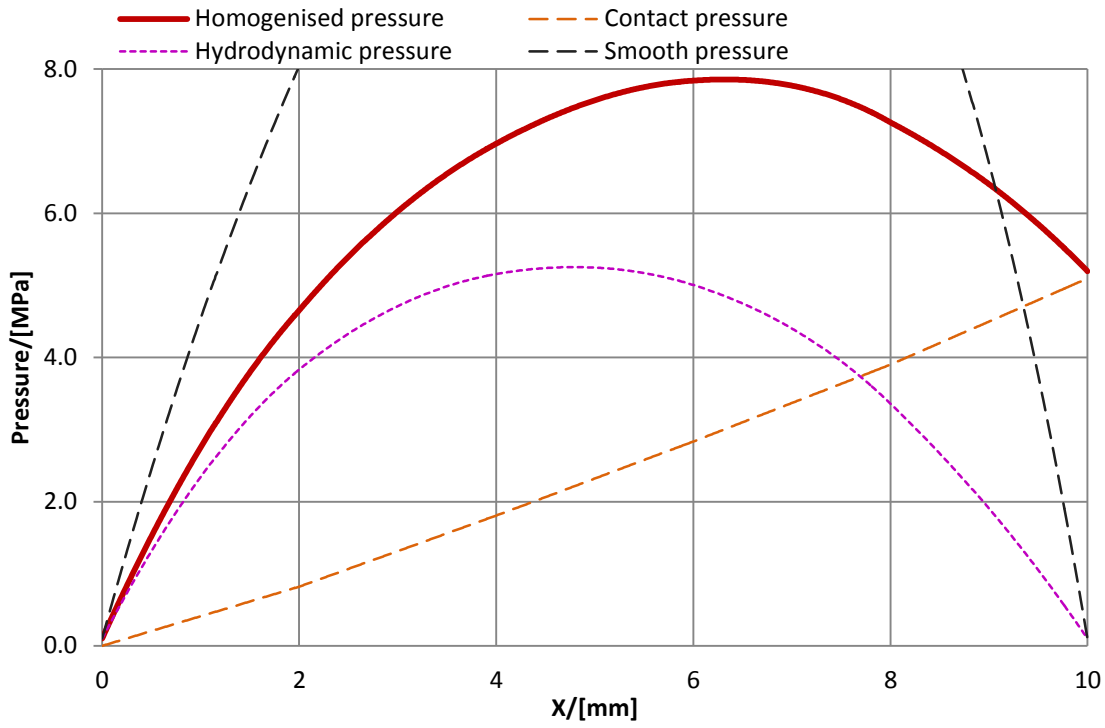


Figure 6.56 Central cross section of the pressure distribution parallel to the x axis for the homogenised and smooth solutions. Minimum clearance  $h_{min}=0.4\mu\text{m}$ . Maximum smooth surface pressure  $p_{smooth}=14\text{MPa}$

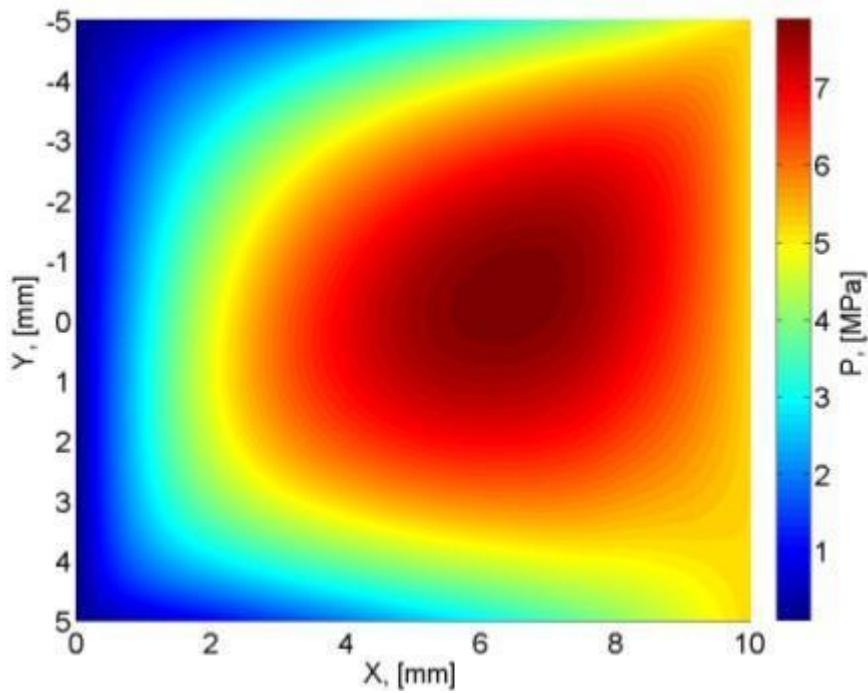


Figure 6.57 Contour plot of the pressure distribution for homogenised rough solution. Minimum clearance  $h_{min}=0.4\mu\text{m}$

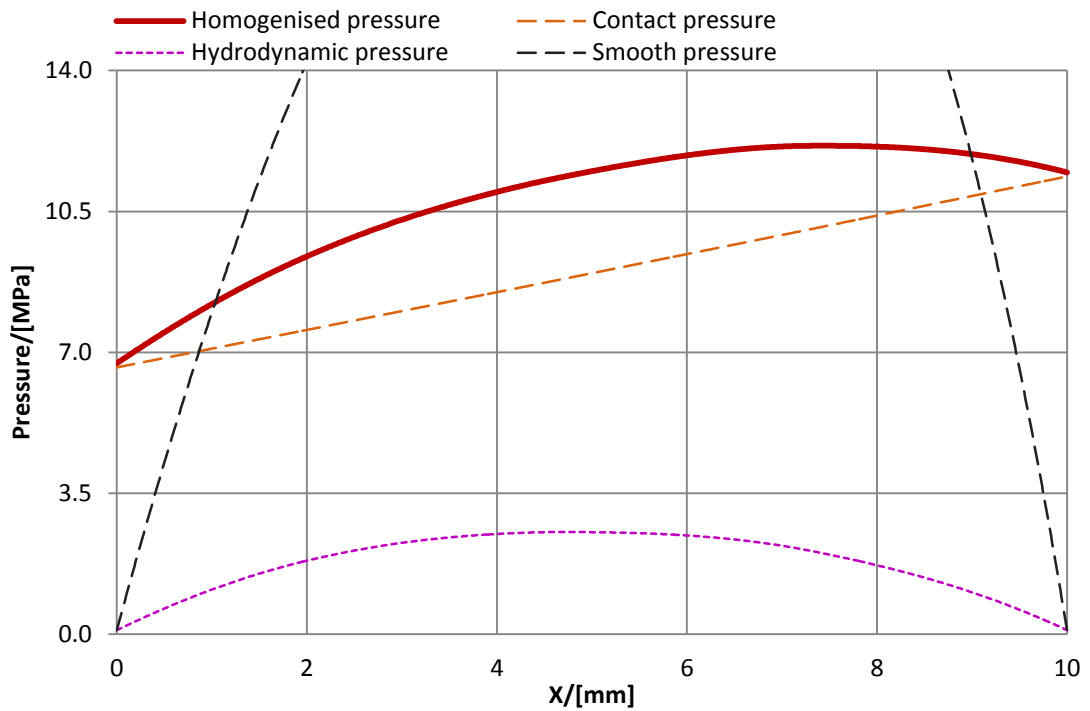


Figure 6.58 Central cross Section of the pressure distribution parallel to the x axis for the homogenised and smooth solutions. Minimum clearance  $h_{min}=0.3\mu\text{m}$ . Maximum smooth surface pressure  $p_{smooth}=25\text{MPa}$

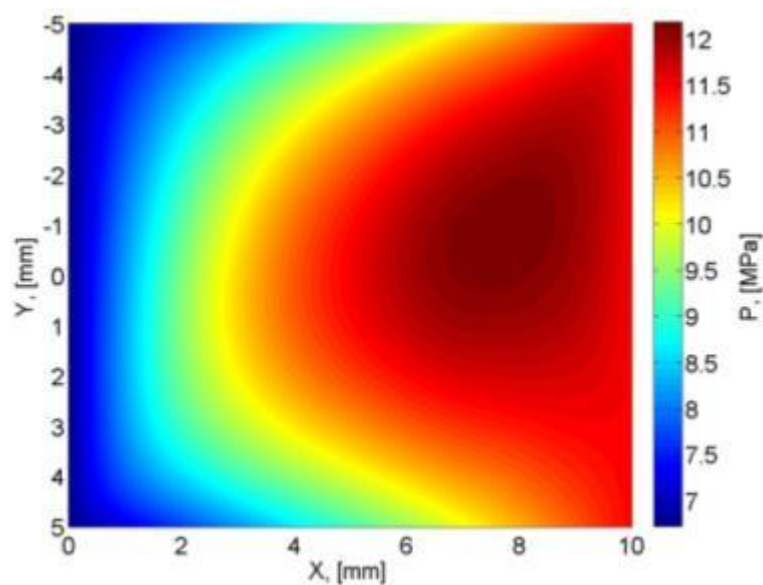


Figure 6.59 Contour plot of the pressure distribution for homogenised rough solution. Minimum clearance  $h_{min}=0.3\mu\text{m}$

It can be seen from the sequence of Figures 6.54-6.59 that the hydrodynamic component becomes progressively less significant. The maximum hydrodynamic pressure moves towards the entrance zone of the bearing, i.e. where the clearance value is higher and therefore the lubrication is less affected by the roughness. In Figure 6.59 the major part of the load is carried by the contacting asperities.

## Section 6.5 Solving the tilted pad bearing problem using the multigrid method

### 6.5.7 Measured roughness cases

In Sections 6.5.1-6.5.6 the roughness function was considered as cosine, sine or a 2D product of the sine functions. For the surface with 16 up to 128 sine waves it was possible to solve the deterministic problem for the grid mesh of 1024x1024 elements thus resolving each wave in from 64 down to 8 sampling points. It is convenient to have the deterministic solution in order to validate the results of the homogenised method. However, solving the deterministic rough problem for the real rough surface requires a very high resolution which results in high demand of the computational time and resources. The main aim of the homogenised method developed is that the roughness can be resolved using fine grid mesh on the local scale. The global problem then incorporates the average effect of the local scale roughness by means of the factors which are functions of the global film thickness.

In this section the homogenised solution of the tilted pad bearing problem has been considered for three real surfaces measured using a Taylor-Hobson profilometer. The characteristics of these surfaces and the details of the manufacturing method are given in Chapter 5, Section 5.2.7. The surfaces used are: a disk circumferential surface prepared by axial grinding (AG), a disk circumferential surface produced by superfinishing a reground disk (SF), and a surface prepared by the electric discharge machining (EDM). The roughness characteristics for each of the surfaces is given in Table 6.7.

**Table 6.7 Roughness characteristics for measured surfaces**

Roughness characteristic		AG	SF	EDM
Highest peak	$S_p$	0.8 $\mu\text{m}$	0.27 $\mu\text{m}$	13.81 $\mu\text{m}$
Deepest valley	$S_v$	-1.14 $\mu\text{m}$	-0.3 $\mu\text{m}$	-11.7 $\mu\text{m}$
Mean roughness	$S_a$	0.25 $\mu\text{m}$	0.042 $\mu\text{m}$	3.02 $\mu\text{m}$
Standard deviation	$S_q$	0.32 $\mu\text{m}$	0.056 $\mu\text{m}$	3.72 $\mu\text{m}$
Skewness	$S_{sk}$	-0.4	-0.17	0.034
Kurtosis	$S_{ku}$	2.87	4.4	2.67

Note that due to different roughness amplitudes of the measured surfaces, different configurations of the tilted pad bearing problem were considered. All three surfaces were rotated by 30° clockwise in order to consider the effect of orientation of surface lay with the sliding direction for the different roughness types.

*Ground surface*

The surface prepared by axial grinding is shown in Figures 5.57-5.59. The machining process created the grinding marks parallel to the  $y$  axis which makes the surface roughness almost extruded. The details of the machining process of this surface are explained in Chapter 5, Section 5.2.7.1. The configuration parameters of the tilted pad bearing problem are given in Table 6.8.

**Table 6.8 Configuration of the tilted pad bearing problem for the AG surface**

Parameter	Value	Units	Description
$h_{min}$	1.5-0.3	$\mu\text{m}$	Minimum clearances range
$\gamma$	1.25		Tilting ratio
$L$	6.0	cm	Length
$W$	5.0	cm	Width
$\theta$	$30^\circ$		Orientation of the roughness features
$u$	0.1	m/s	Linear velocity of the counterface
$\eta$	0.07	Pa·s	Viscosity of the fluid
$P_0$	$10^5$	Pa	Atmospheric pressure

Figure 6.60 shows the total and contact load for the tilted pad bearing problem with ground surface roughness. The load is presented in terms of the mean pressure for the smooth and homogenised rough cases. The homogenised pressure is a sum of two components: the hydrodynamic pressure and the elastic contact pressure which are shown by separate curves.

In the sections related to the measured roughness problems it is convenient to introduce the value  $\Lambda$  of the average clearance value relative to the standard deviation of the roughness. This value helps to indicate the condition where most of the surface asperities are in contact as opposed to the contact at the highest peak. The value of  $\Lambda$  is calculated as follows:

$$\Lambda = \frac{h_{min} + h_{max}}{2S_q} = \frac{h_{min}(1 + \gamma)}{2S_q} \quad (6.43)$$

where  $h_{min}$  and  $h_{max}$  are the clearance values at the exit and entrance zone of the tilted pad bearing respectively.

## Section 6.5 Solving the tilted pad bearing problem using the multigrid method

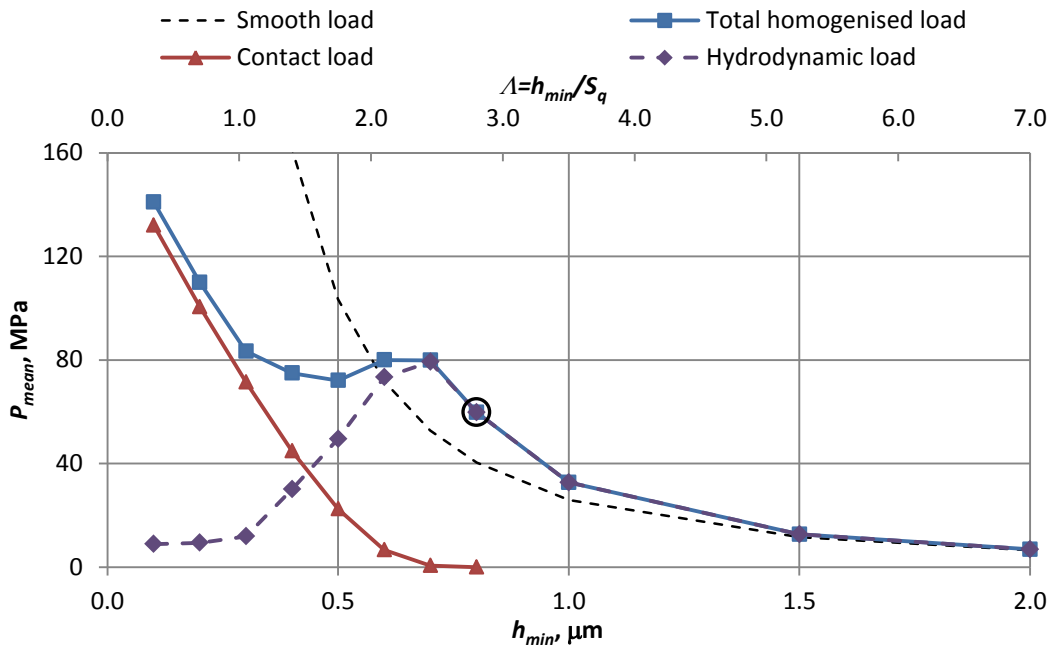


Figure 6.60 Total and contact load for the homogenised solution and load for the smooth solution of the tilted pad bearing problem with ground surface roughness. The empty black circle denotes the configuration where the first direct asperity contact occurs.

The behaviour of the load-clearance curves shown in Figure 6.60 is similar to that observed in Figure 6.48 for the two dimensional roughness. As before, the total homogenised load is equal to the smooth one until the value of  $h_{min}=1.5\mu\text{m}$  and the total homogenised load increases which illustrates the effect of roughness on the lubrication. The local maximum value of the total load is reached for  $h_{min}=0.7\mu\text{m}$  ( $\Lambda=2.5$ ), which is beyond the point when the first contact occurs. This means that the tilted pad bearing operates in the mixed lubrication regime, i.e. the majority of the load is carried by the pressurised lubricant, however part of the load is carried by the contacting asperities (shown red, triangles). The condition when the first contact occurs is marked by an empty circle on the graph.

As the value of  $h_{min}$  decreases further, more load is carried by the direct contact, while the hydrodynamic load decreases (dashed purple, diamonds). This can be explained by the fact, that the roughness features create significant obstruction to the lubricant flow which make the lubricant less capable of supporting the load. The increase in the total load for the value of the minimum clearance  $h_{min}<0.3\mu\text{m}$  can be explained by the fact that the lower values of the hydrodynamic load are compensated by the higher load carried by the contacting asperities. The  $\Lambda$  value for these cases is 1.5 and less.

The more detailed comparison of the homogenised and smooth solutions is given in Figures 6.61-6.72 which show the central cross section values and the contour plots for the pressure distribution obtained as a solution of a tilted pad bearing problem with

smooth and homogenised rough problem. Solution of the smooth problem is shown dashed black, whereas the homogenised solution is shown by solid red line. In the case of direct contact, additional orange dashed line represent the load carried by the contacting asperities.

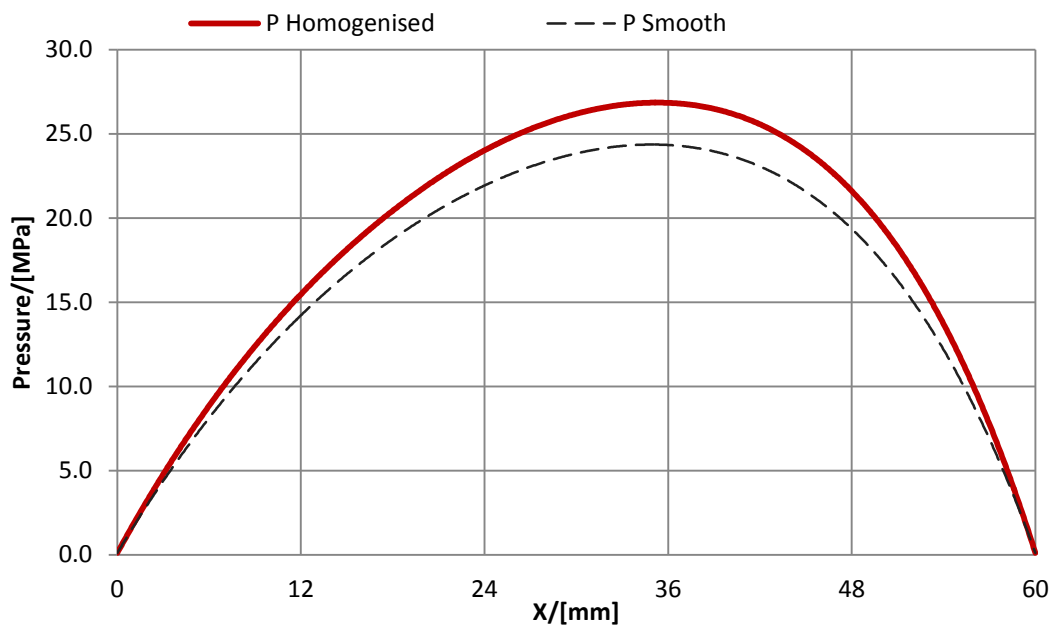


Figure 6.61 Central cross section of the pressure distribution parallel to the x axis for the homogenised and smooth solutions. Minimum clearance  $h_{min}=1.5\mu m$

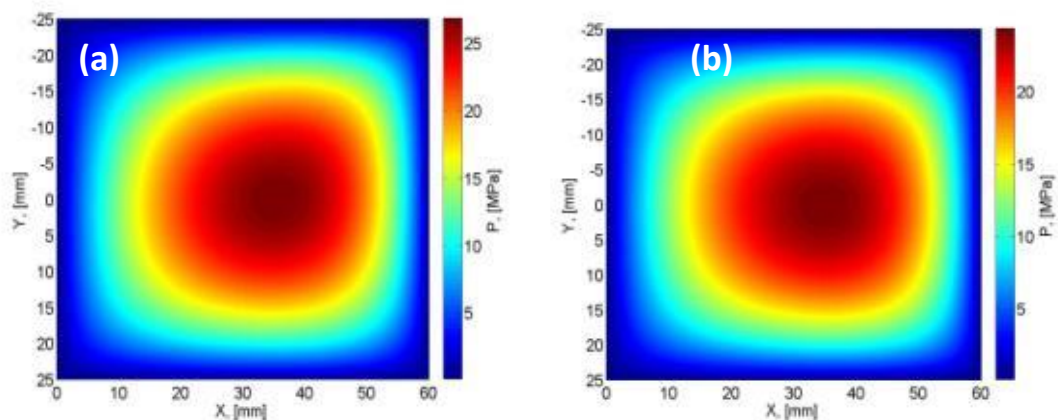


Figure 6.62 Contour plot of the pressure distribution for (a) the smooth and (b) the homogenised rough solutions. Minimum clearance  $h_{min}=1.5\mu m$

Figure 6.61 show the comparison of the solution for the value of the minimum clearance  $h_{min}=1.5\mu m$ . It can be observed that the homogenised solution results in slightly higher values of the pressure, however the general shape of the pressure distribution is not much different from the smooth one, as can be appreciated from Figures 6.61a and 6.61b. Note that no effect of the oblique nature of roughness is apparent in Figures 6.61a and 6.61b.

## Section 6.5 Solving the tilted pad bearing problem using the multigrid method

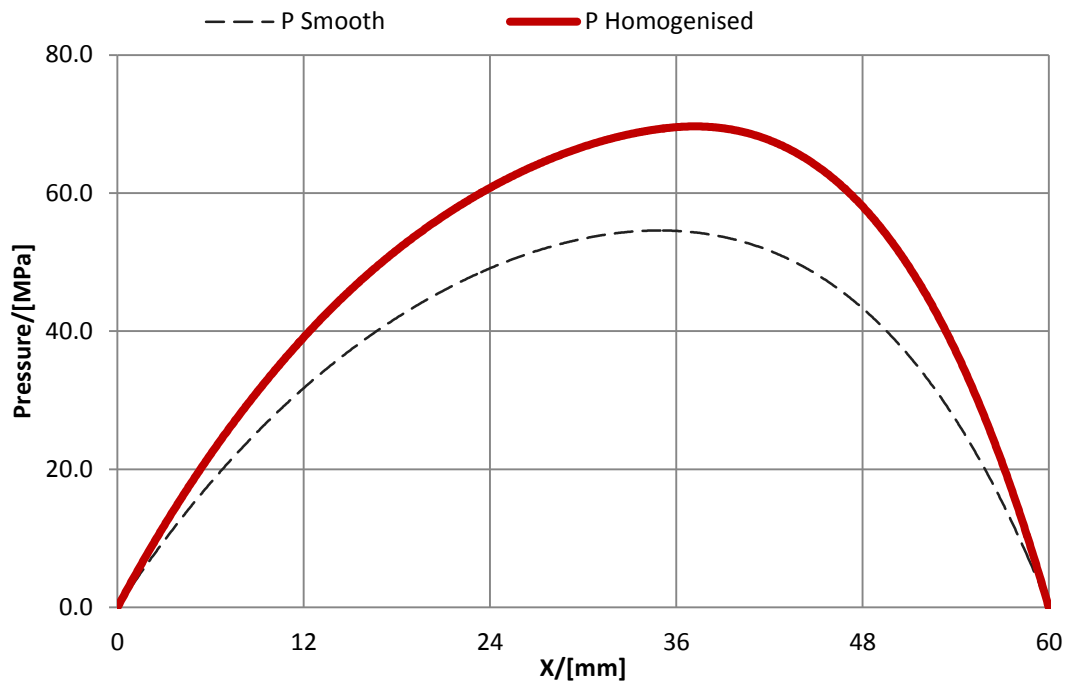


Figure 6.63 Central cross section of the pressure distribution parallel to the  $x$  axis for the homogenised and smooth solutions. Minimum clearance  $h_{min}=1.0\mu\text{m}$

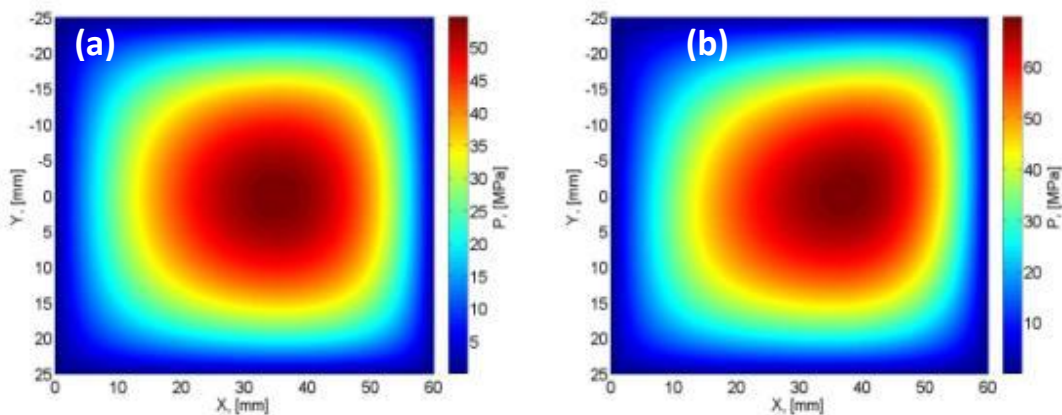


Figure 6.64 Contour plot of the pressure distribution for (a) the smooth and (b) the homogenised rough solutions. Minimum clearance  $h_{min}=1.0\mu\text{m}$

Figures 6.63-6.66 correspond to the minimum clearance values  $h_{min}=1.0$  and  $0.8\mu\text{m}$ . The effect of the oblique roughness can now be clearly seen in Figures 6.64b and 6.66b. The pressure values increase as the minimum clearance values  $h_{min}$  decreases, however the maximum pressure remains closer to the exit zone of the bearing.

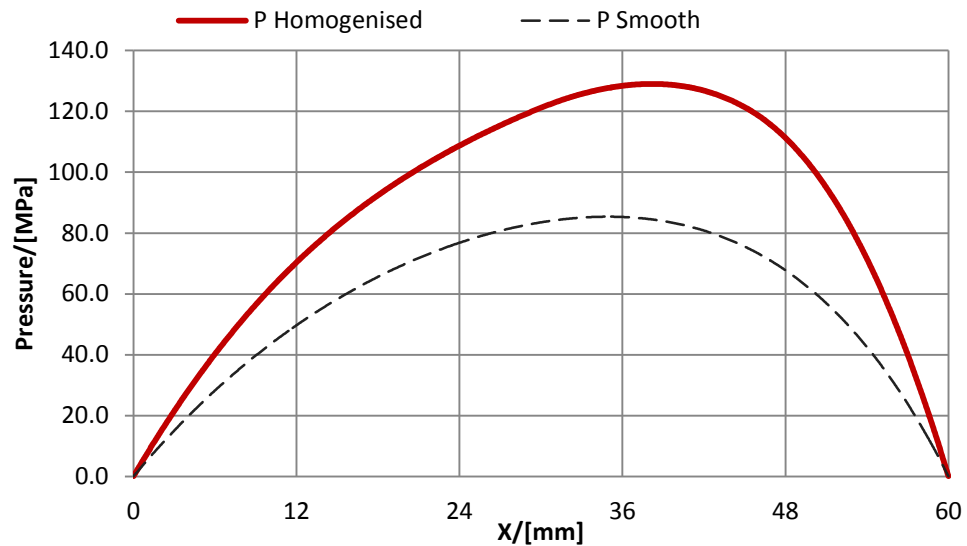


Figure 6.65 Central cross section of the pressure distribution parallel to the x axis for the homogenised and smooth solutions. Minimum clearance  $h_{min}=0.8\mu\text{m}$

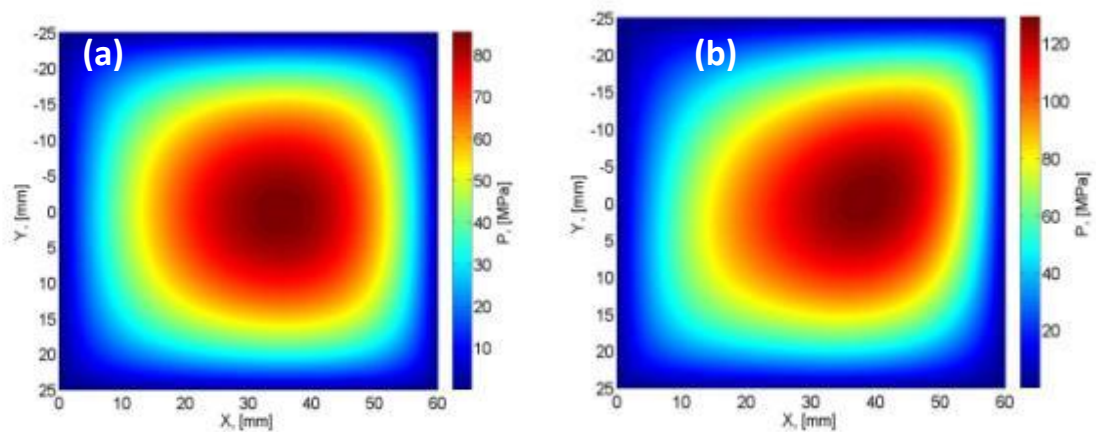


Figure 6.66 Contour plot of the pressure distribution for (a) the smooth and (b) the homogenised rough solutions. Minimum clearance  $h_{min}=0.8\mu\text{m}$

In Figures 6.67-6.68 where the solution is given for  $h_{min}=0.6\mu\text{m}$ , the point of the maximum pressure value has moved towards the inlet zone of the bearing. This can be explained by the fact, that the clearance value reduces as x coordinate approaches the exit zone ( $x=L$ ). For smaller clearance values the lubricant flow is obstructed more significantly by the roughness features. Also, in case of the minimum clearance  $h_{min}=0.6\mu\text{m}$  the direct contact of the asperities occurs over the whole surface of the tilted pad.

## Section 6.5 Solving the tilted pad bearing problem using the multigrid method

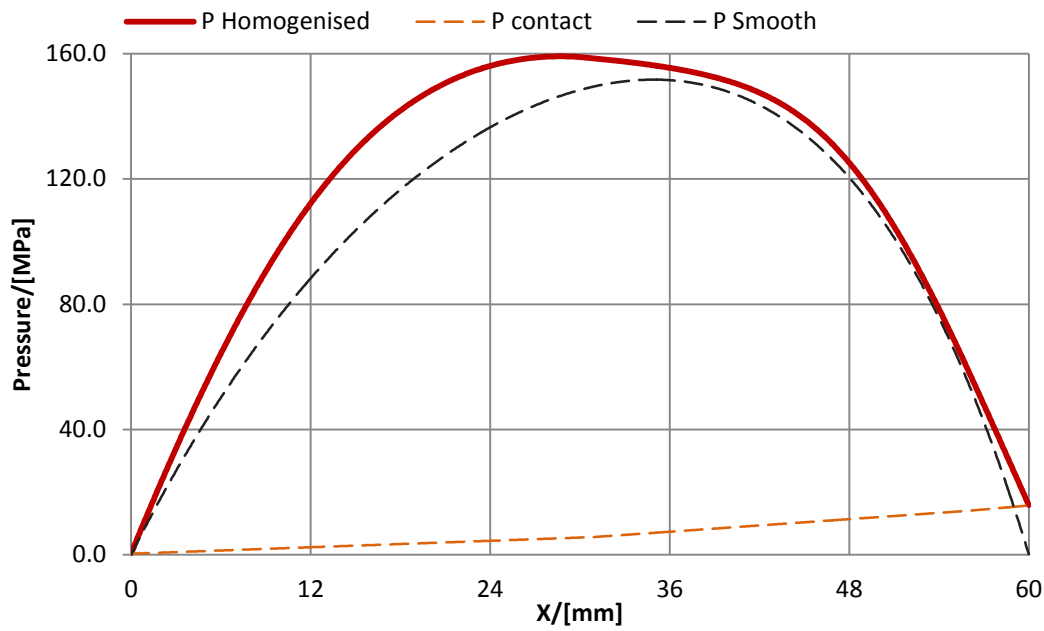


Figure 6.67 Central cross section of the pressure distribution parallel to the  $x$  axis for the homogenised and smooth solutions. Minimum clearance  $h_{min}=0.6\mu\text{m}$

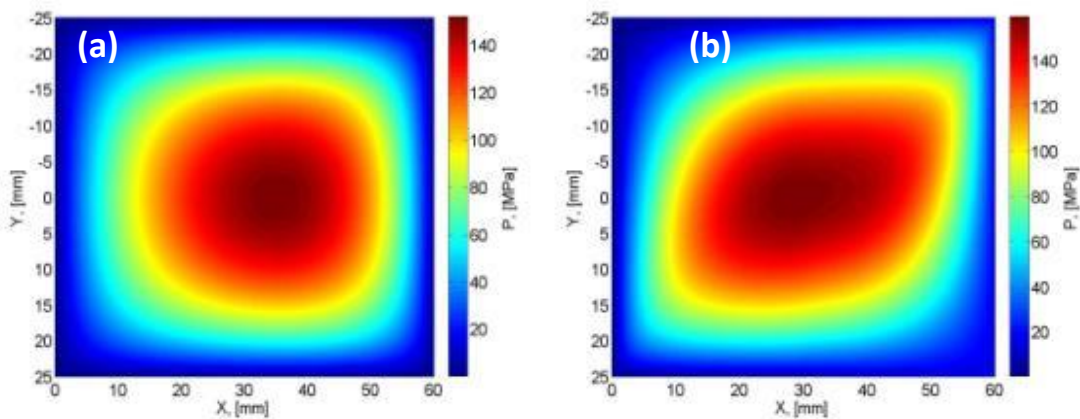


Figure 6.68 Contour plot of the pressure distribution for (a) the smooth and (b) the homogenised rough solutions. Minimum clearance  $h_{min}=0.6\mu\text{m}$

Figure 6.69 shows the homogenised rough and smooth solutions for  $h_{min}=0.5$ . In this figure the ability of the rough surface to support the load hydrodynamically is significantly reduced in comparison to the smooth surface. The contact load is however not high enough to contribute to the total load carrying capacity.

Finally, Figures 6.71-6.72 correspond to the minimum clearance value  $h_{min}=0.3$ . The smooth solution is not shown in 6.71 as it is  $\sim 20$  times greater than the homogenised one. The contribution of the contact pressure is the most significant however the total load is quite low.

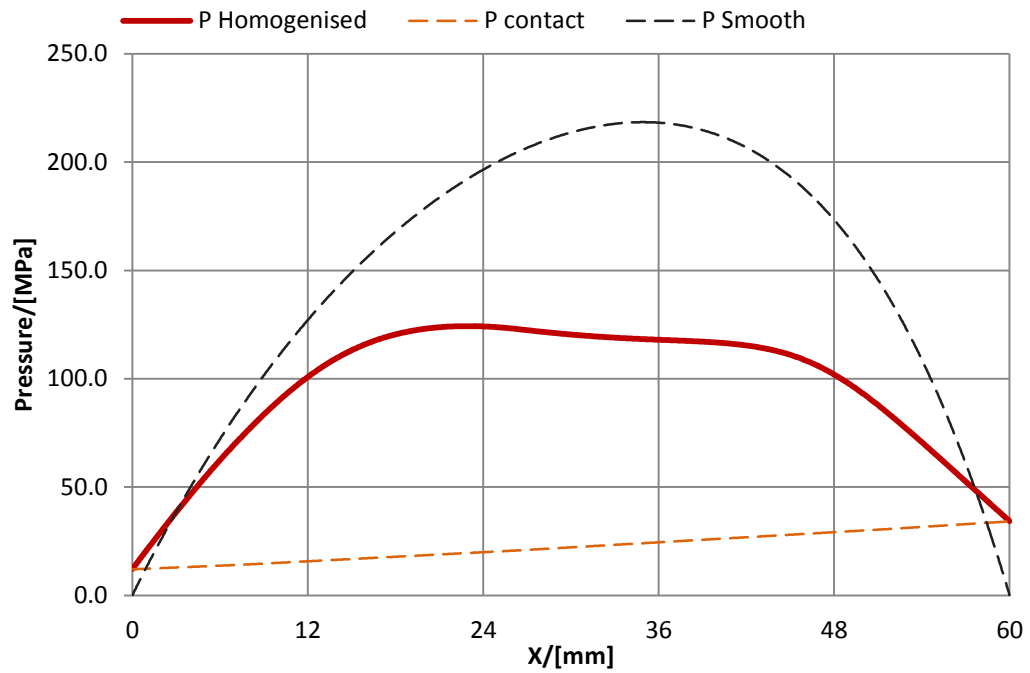


Figure 6.69 Central cross section of the pressure distribution parallel to the x axis for the homogenised and smooth solutions. Minimum clearance  $h_{min}=0.5\mu\text{m}$

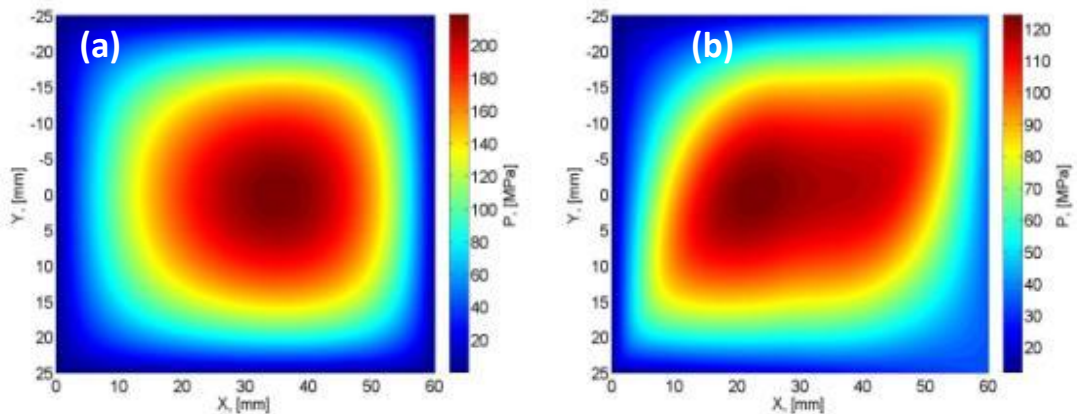


Figure 6.70 Contour plot of the pressure distribution for (a) the smooth and (b) the homogenised rough solutions. Minimum clearance  $h_{min}=0.5\mu\text{m}$

The analysis of the tilted pad bearing problem with the surface prepared by axial grinding can be concluded by stating that the peak load for the homogenised solution in comparison with the smooth tilted pad bearing in terms of the load carried is achieved when the minimum clearance value  $h_{min}=0.7\mu\text{m}$ .

## Section 6.5 Solving the tilted pad bearing problem using the multigrid method

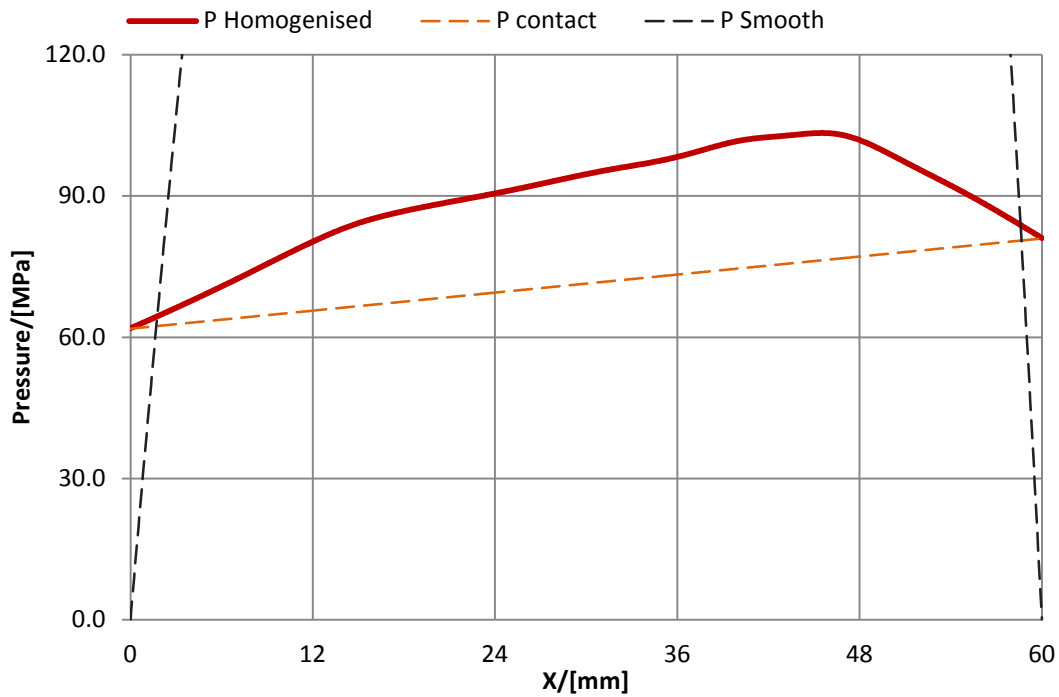


Figure 6.71 Central cross section of the pressure distribution parallel to the x axis for the homogenised solution. Minimum clearance  $h_{min}=0.3\mu\text{m}$ . The maximum smooth pressure value  $p_{smooth}=0.6\text{GPa}$ .

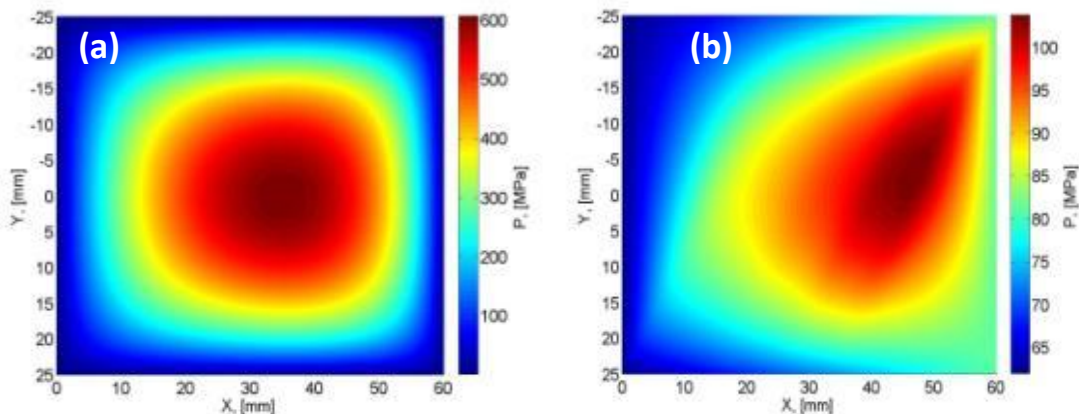


Figure 6.72 Contour plot of the pressure distribution for (a) the smooth and (b) the homogenised rough solutions. Minimum clearance  $h_{min}=0.3\mu\text{m}$

### *Super finished surface*

In this section the surface prepared by superfinishing is considered. The details of the manufacturing process are given in Chapter 5, Section 5.2.7.2. Note that surface was measured on the surface of a crowned disk that had been used in a scuffing experiment. The surface was re-ground with the grinding lay in the circumferential direction and the disk was then superfinished. Both the disk and the crowning shapes were then removed from the measurement by filtering. The roughness parameters of the surface are shown in Table 6.7 and the resulting surface is shown in Figures

5.62-5.64. It has the longitudinal marks caused by the regrinding which results in the highest peak being  $S_p=0.27\mu\text{m}$ , however the average roughness is quite low:  $S_a=0.042\mu\text{m}$ . The configuration of the tilted pad bearing problem with superfinished surface is given in Table 6.9.

Table 6.9 Configuration of the tilted pad bearing problem for the SF surface

Parameter	Value	Units	Description
$h_{min}$	1.5-0.3	$\mu\text{m}$	Minimum clearances range
$\gamma$	1.25		Tilting ratio
$\theta$	$30^\circ$	$^\circ$	Rotation of the roughness features (clock wise)
$L$	6.0	cm	Length
$W$	5.0	cm	Width
$\theta$	$30^\circ$		Orientation of the roughness features
$u$	0.05	m/s	Linear velocity of the counterface
$\eta$	0.005	Pa·s	Viscosity of the fluid
$P_0$	$10^5$	Pa	Atmospheric pressure

Figure 6.71 shows load for the tilted pad bearing problem with smooth and superfinished surface roughness. The load is presented in terms of the mean pressure. The average film thickness value  $\lambda$  is calculated at the middle of the tilted pad using formula (6.43). The value of  $\lambda$  is shown in Figure 6.73 as a secondary horizontal axis. As before, the point of the first direct contact is marked by black empty circle.

In case of the homogenised solution the total load as well as the hydrodynamic and elastic contact components are shown in Figure 6.73. It is clear from the figure that the curve corresponding to the homogenised solution coincides perfectly with the one for the smooth solution for the values of  $h_{min}>0.3\mu\text{m}$ . This can be explained by the very low average roughness  $S_a=0.027\mu\text{m}$  as a result of the superfinishing process. For the clearance values between  $0.4\mu\text{m}$  and  $0.16\mu\text{m}$  the load for the homogenised case is slightly higher than the smooth one as the roughness features result in the higher pressure values. Also the total homogenised load is equal to its hydrodynamic component until the value of minimum clearance becomes  $h_{min}=0.16\mu\text{m}$ , which corresponds to the average  $\lambda\approx 3$ .

## Section 6.5 Solving the tilted pad bearing problem using the multigrid method

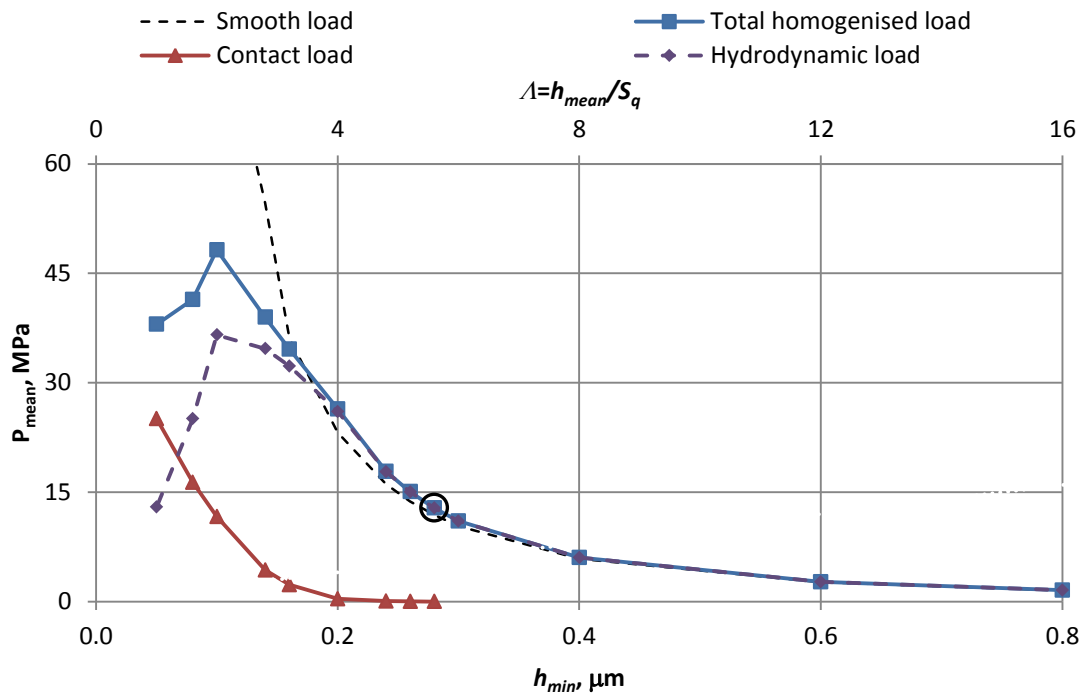


Figure 6.73 Total and contact load for the homogenised solution and load for the smooth solution of the tilted pad bearing problem with super finished surface roughness. The empty black circle denotes the configuration where the first direct asperity contact occurs.

For the values of the minimum clearance  $h_{min} < 0.16 \mu m$  a change in the slope of the hydrodynamic load/clearance curve can be observed followed by a drop. The reason for this change is that the most prominent surface asperities are flattened bringing more asperities into contact and thus increasing the total area of contact. This results in significant obstruction of the lubricant flow, therefore the hydrodynamic lubrication starts to fail and the hydrodynamic part of the load drops. The increasing contact load compensates for the drop in the hydrodynamic component, although the total homogenised load is still lower than the smooth one..

Sequence of Figures 6.74-6.81 show the central cross section values and the contour plots for the pressure distribution obtained as a solution of a tilted pad bearing problem with smooth and homogenised rough problem. The clearance values considered are  $h_{min} = 0.4, 0.2, 0.16$  and  $0.1 \mu m$ . The solution of the smooth problem is shown dashed black, whereas the homogenised solution is shown by solid red line. The load carried by the contacting asperities is shown by orange dashed line.

Figures 6.74 and 6.81 show no apparent difference between the smooth and homogenised rough solutions for the clearance value  $h_{min} = 4.0 \mu m$ . As mentioned earlier this can be explained by the very low average roughness which has negligible effect on the pressure distribution.

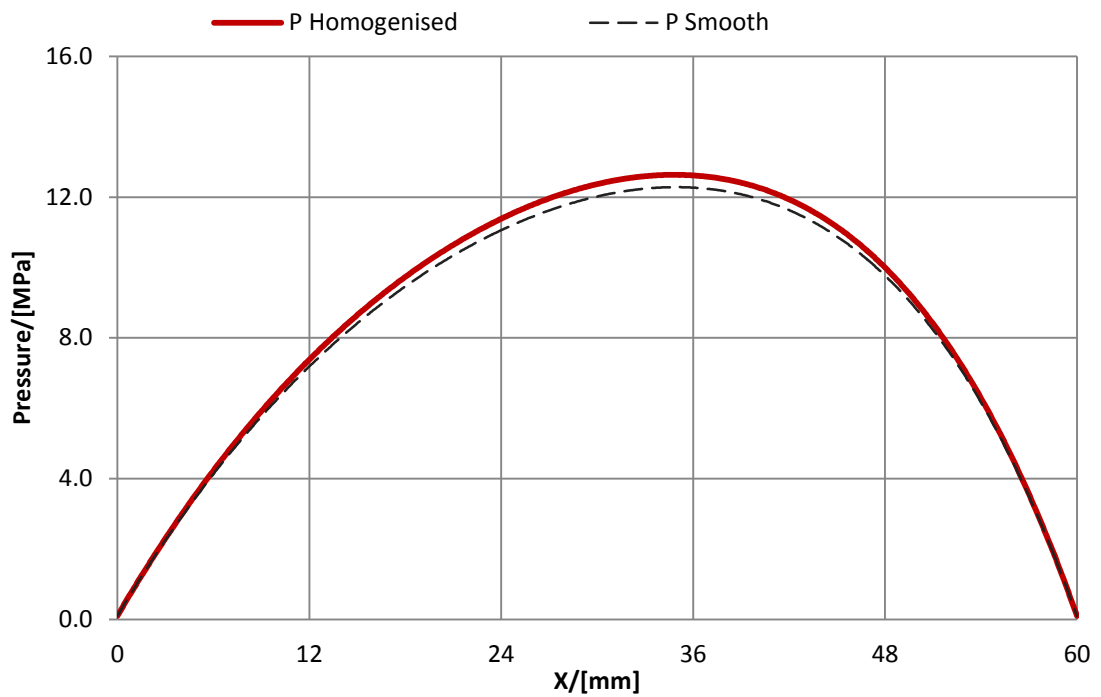


Figure 6.74 Central cross section of the pressure distribution parallel to the x axis for the homogenised solution. Minimum clearance  $h_{min}=0.4\mu\text{m}$

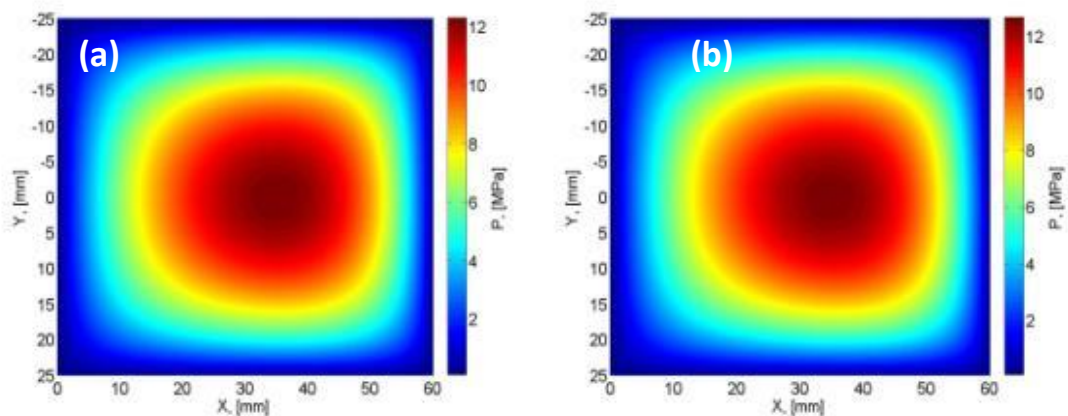


Figure 6.75 Contour plot of the pressure distribution for (a) the smooth and (b) homogenised rough solutions. Minimum clearance  $h_{min}=0.4\mu\text{m}$

For the clearance value  $h_{min}=2.0\mu\text{m}$  the solutions are given in Figures 6.76 and 6.77. Note a slight distortion of the homogenised rough solution caused by rotation of the longitudinal roughness features by an angle of  $30^\circ$  clockwise. The load for the homogenised rough solution is higher than for the smooth one in this case.

## Section 6.5 Solving the tilted pad bearing problem using the multigrid method

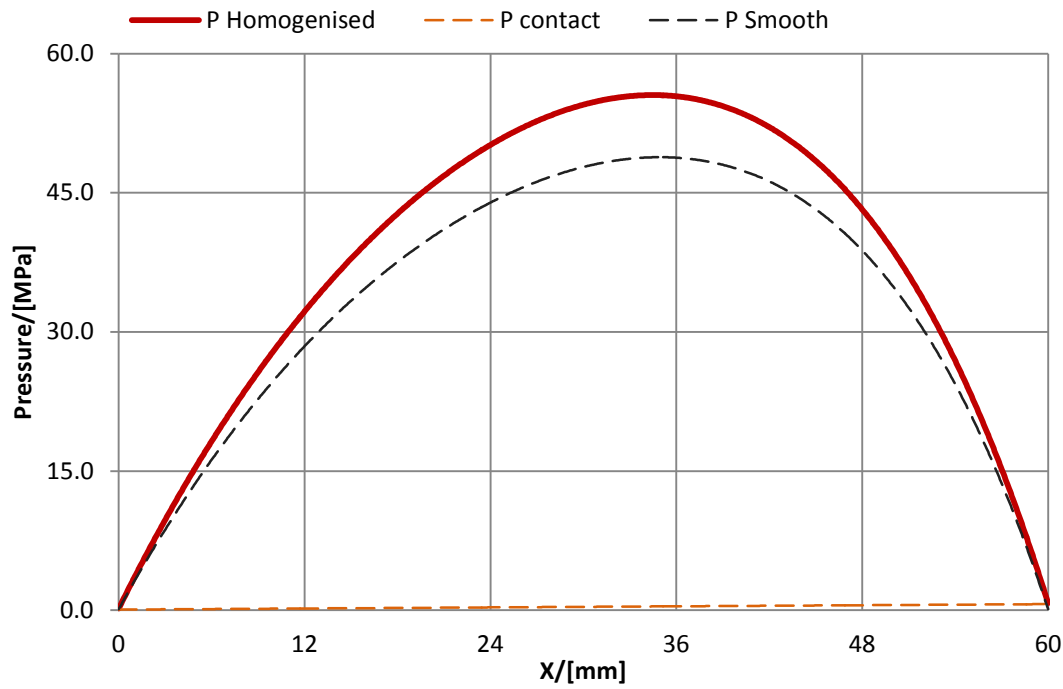


Figure 6.76 Central cross section of the pressure distribution parallel to the x axis for the homogenised solution. Minimum clearance  $h_{min}=0.2\mu\text{m}$

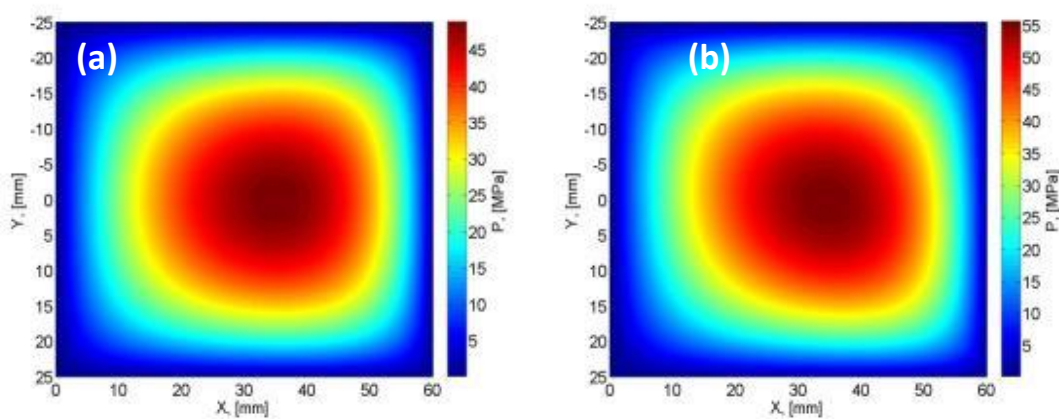


Figure 6.77 Contour plot of the pressure distribution for (a) the smooth and (b) the homogenised rough solutions. Minimum clearance  $h_{min}=0.2\mu\text{m}$

From Figures 6.78-6.81 representing solutions for the minimum clearance  $h_{min}=0.16$  and  $0.1\mu\text{m}$  it is clear that the effect of the orientation of the longitudinal features created by a faceting tool becomes more significant. The homogenised pressure grows due to increased elastic contact pressure.

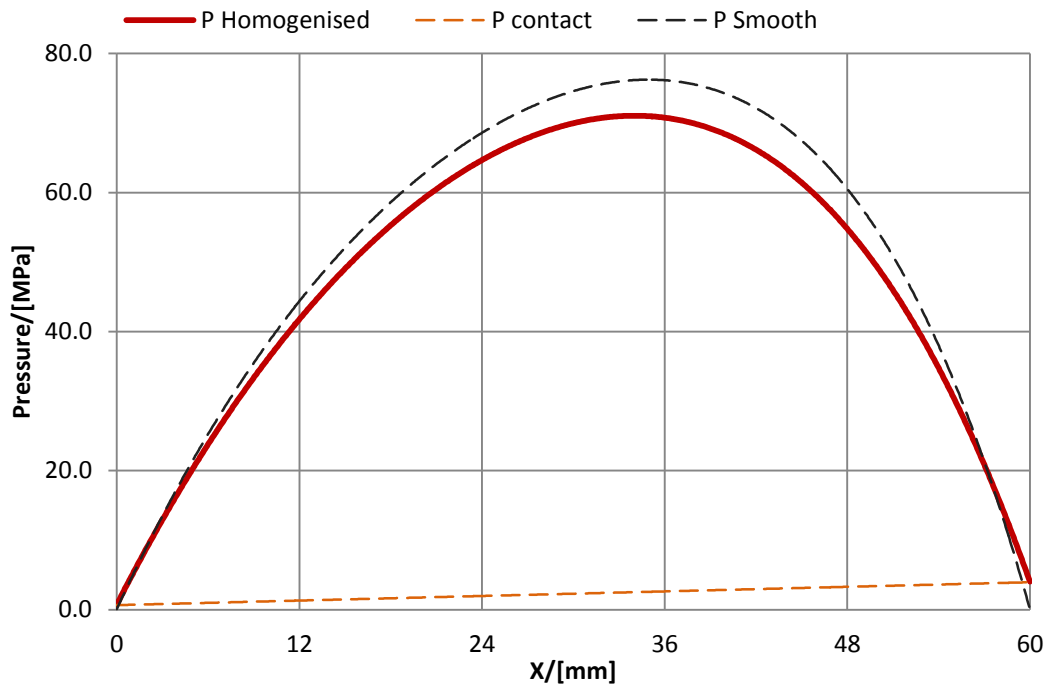


Figure 6.78 Central cross section of the pressure distribution parallel to the x axis for the homogenised solution. Minimum clearance  $h_{min}=0.16\mu\text{m}$

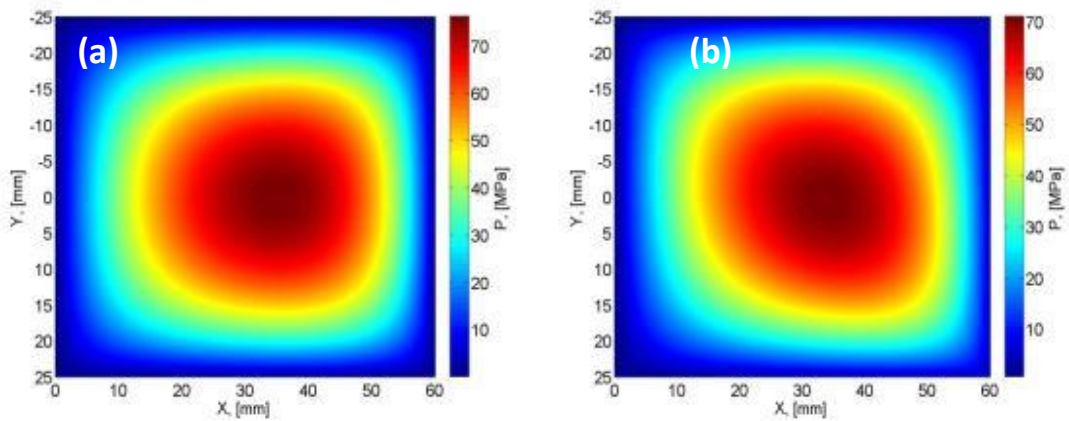


Figure 6.79 Contour plot of the pressure distribution for (a) the smooth and (b) the homogenised rough solutions. Minimum clearance  $h_{min}=0.16\mu\text{m}$

## Section 6.5 Solving the tilted pad bearing problem using the multigrid method

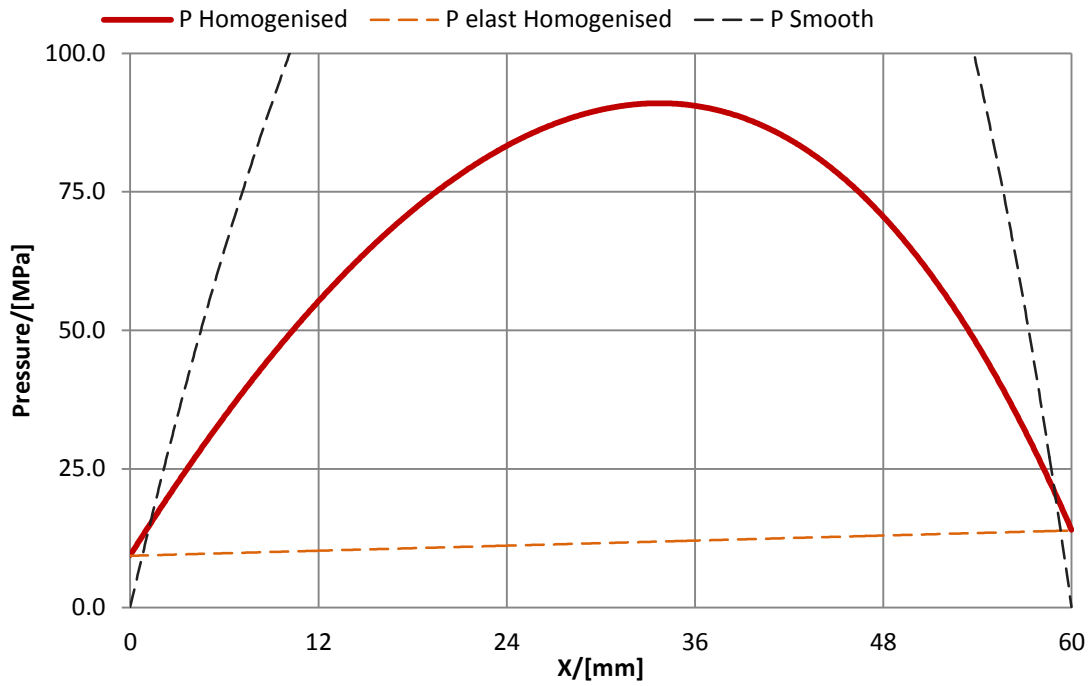


Figure 6.80 Central cross section of the pressure distribution parallel to the x axis for the homogenised solution. Minimum clearance  $h_{min}=0.1\mu\text{m}$ . Maximum smooth pressure value  $p_{smooth}=200\text{MPa}$ .

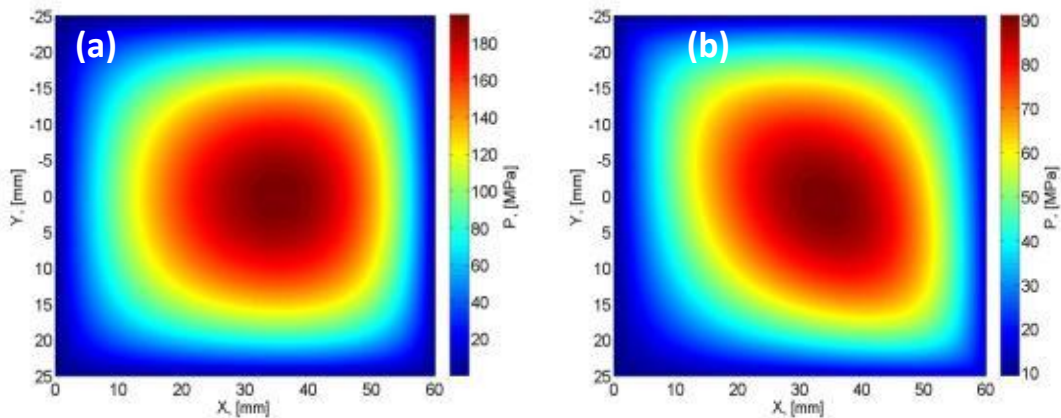


Figure 6.81 Contour plot of the pressure distribution for (a) the smooth and (b) the homogenised rough solutions. Minimum clearance  $h_{min}=0.1\mu\text{m}$

*EDM surface*

The surface prepared by the electrical discharge machining is considered in this section. The roughness parameters and the details of the manufacturing process of such surface are explained in Chapter 5, Section 5.2.7.3. Surface roughness parameters are given in Table 6.7 and the surface is shown in Figures 5.67-5.69. Due to the nature of the manufacturing process this surface does not have a characteristic orientation of the roughness features. In this section it is demonstrated that rotating the surface which is naturally isotropic does not show any effect.

**Table 6.10 Configuration of the tilted pad bearing problem for the EDM surface**

Parameter	Value	Units	Description
$h_{min}$	20.0-1.0	$\mu\text{m}$	Minimum clearances range
$\gamma$	1.25		Tilting ratio
$\theta$	30°	°	Rotation of the roughness features (clock wise)
$L$	6.0	cm	Length
$W$	5.0	cm	Width
$\theta$	30°		Orientation of the roughness features
$u$	0.1	m/s	Linear velocity of the counterface
$\eta$	0.8	Pa·s	Viscosity of the fluid
$P_0$	10 <sup>5</sup>	Pa	Atmospheric pressure

As can be seen from Table 6.7 the roughness of the surface prepared by EDM is significantly higher than that of the other surfaces considered. Indeed, the highest peak value  $S_p=13.8\mu\text{m}$  and the average roughness  $S_a=3.0\mu\text{m}$ . For this reason higher minimum clearance values have been considered in order to illustrate the whole range of cases from the case of no effect of roughness to the configuration where the hydrodynamic lubrication fails. Also, due to the surface roughness, direct contact occurs for quite high clearance values. As a result it can be expected that the hydrodynamic part of the load would be dominated by the elastic contact part. In order to make a more realistic comparison the value of viscosity has been increased up to  $\eta=0.8$  Pa·s which corresponds to a high viscosity oil. The surface with such roughness would not normally be used in bearings, however it gives a good example of the naturally isotropic surface.

## Section 6.5 Solving the tilted pad bearing problem using the multigrid method

The load in terms of the mean pressure is plotted against the minimum clearance value  $h_{min}$  in Figure 6.82. The load is shown for the smooth and homogenised cases. In the homogenised case the hydrodynamic and elastic contact components of the load are also shown by separate curves.

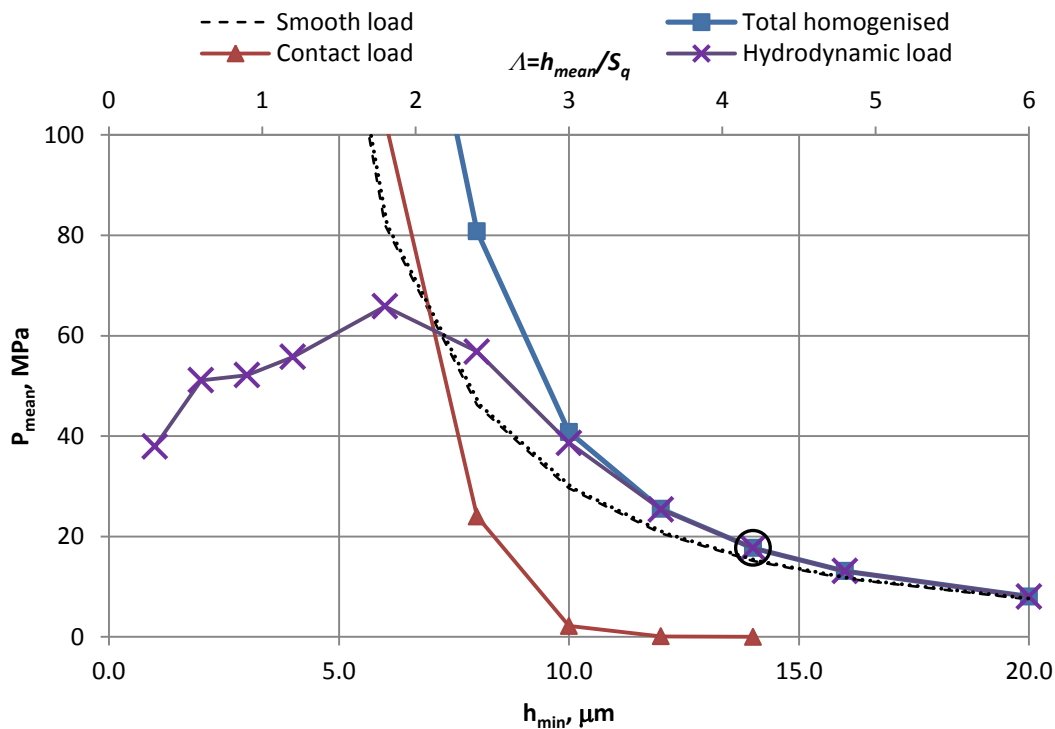


Figure 6.82 Total and contact load for the homogenised solution and load for the smooth solution of the tilted pad bearing problem with the surface manufactured using the EDM. The empty black circle denotes the configuration where the first direct asperity contact occurs.

The configuration where the direct contact of the asperities occurs first is marked by black empty circle on the graph. The first observation that can be made concerning Figure 6.82 is that although first direct contact occurs for  $h_{min}=13.8 \mu m$ , the majority of the homogenised load is hydrodynamic until the minimum clearance becomes  $h_{min}=10 \mu m$ , which corresponds to the value of  $\Lambda=3$ . Indeed, the total homogenised load curve (blue squares) overlaps the curve corresponding to the hydrodynamic load (purple crosses). The reason for this is that only few peaks are in contact and the majority of the roughness features are separated by the fluid film.. Indeed, the highest peak of the EDM surface is  $S_p=13.8 \mu m$  whereas the average roughness is  $S_q=3.0 \mu m$ .

Secondly, it can be observed from Figure 6.82 that as the minimum clearance value decreases beyond the value  $h_{min}=10 \mu m$ , the total homogenised load increases due to the contact load component. The hydrodynamic part grows up slowly up to the maximum value of 65MPa for  $h_{min}=6 \mu m$ . For the lower values of  $h_{min}$  the

hydrodynamic component of the load drops as the contacting roughness features significantly obstruct the flow.

The sequence of Figures 6.83-6.90 shows the central cross section of the pressure distribution obtained for smooth and homogenised solutions of the tilted pad bearing problem with minimum clearance values  $h_{min}=20, 14, 10$  and  $6\mu\text{m}$ .

The first case of the sequence shows the case of  $h_{min}=20\mu\text{m}$ . There is no apparent effect of roughness in Figures 6.83 and 6.84.

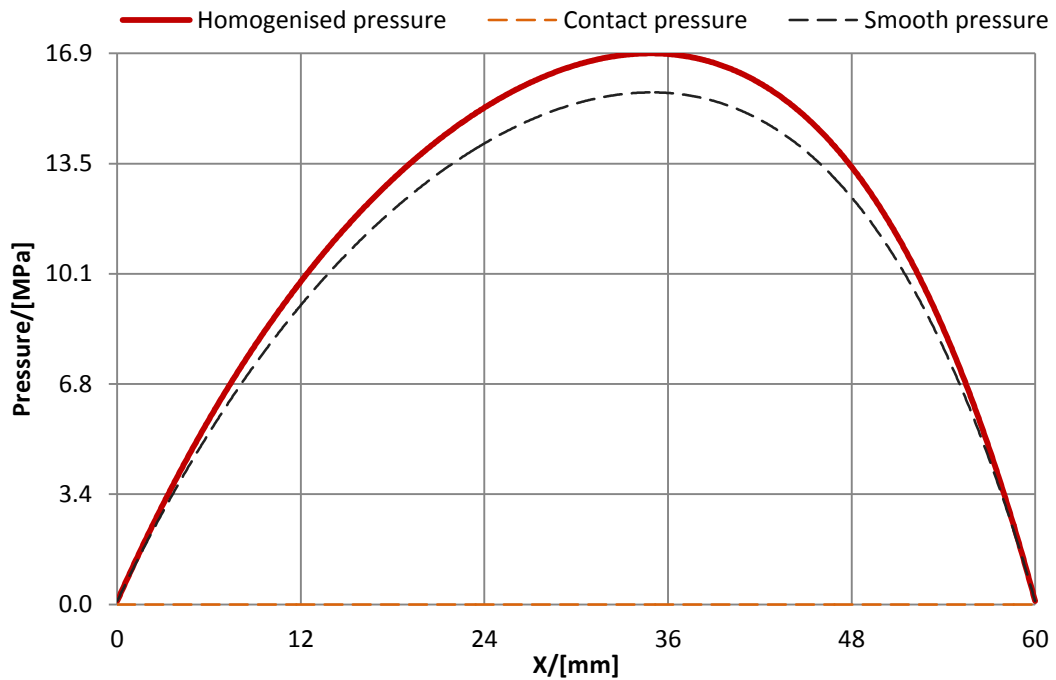


Figure 6.83 Central cross section of the pressure distribution parallel to the x axis for the homogenised solution. Minimum clearance  $h_{min}=20\mu\text{m}$

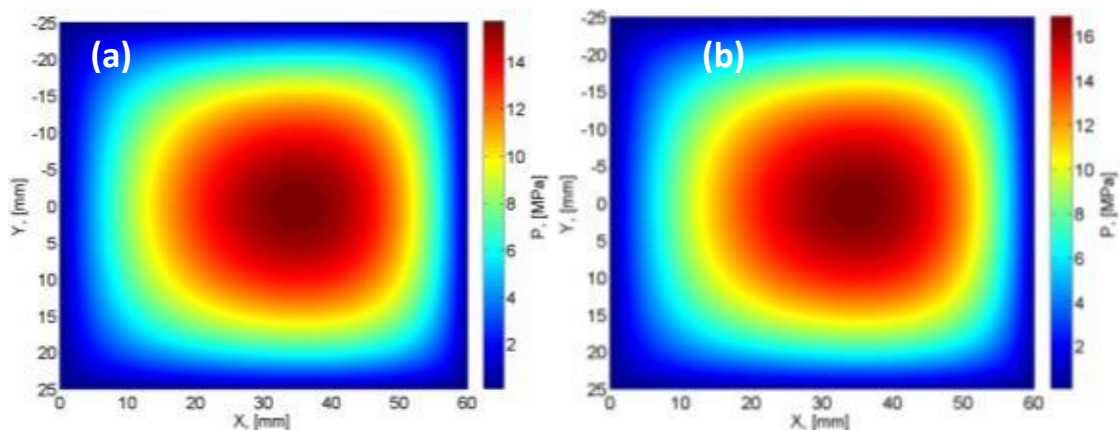


Figure 6.84 Contour plot of the pressure distribution for (a) the smooth and (b) the homogenised rough solutions. Minimum clearance  $h_{min}=20\mu\text{m}$

The second case shown in Figures 6.84-6.85 represents the smooth and homogenised rough solutions for the minimum clearance value  $h_{min}=14\mu\text{m}$ . The homogenised rough solution results in higher pressures caused by presence of the roughness, however the

## Section 6.5 Solving the tilted pad bearing problem using the multigrid method

shape of the pressure distribution does not differ much from the smooth solution. This means that even though  $h_{min}$  is less than the higher peak value  $S_p=13.8\mu m$ , the elastic load is still negligible in comparison to the hydrodynamic one. This can be explained by the fact that majority of the roughness features are not yet in contact.

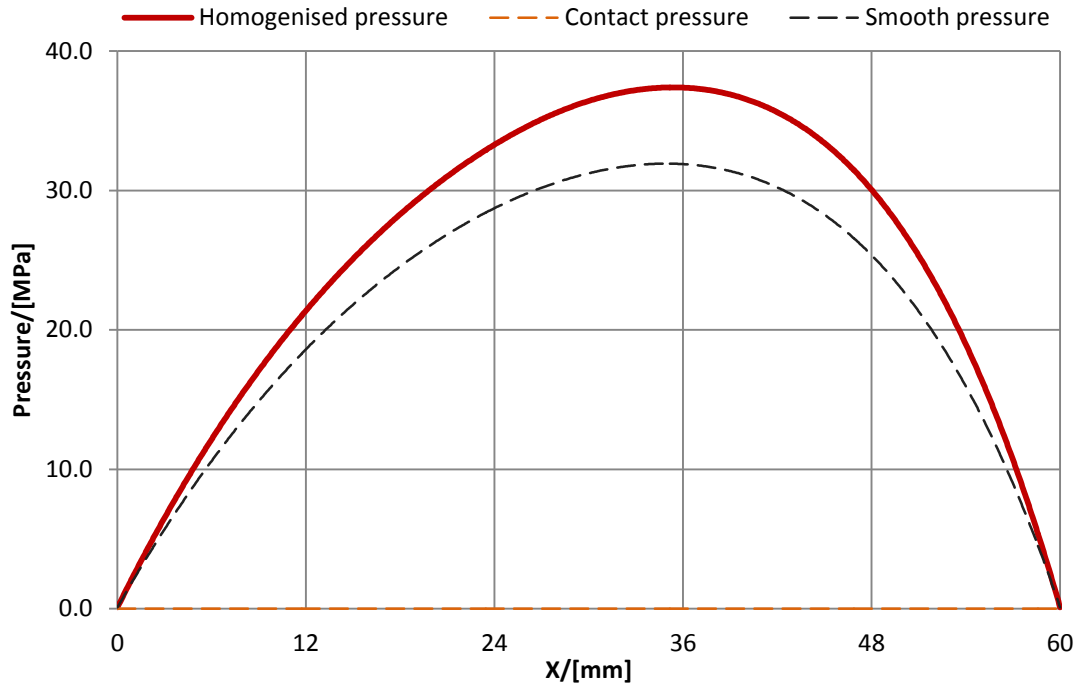


Figure 6.85 Central cross Section of the pressure distribution parallel to the x axis for the homogenised solution. Minimum clearance  $h_{min}=14\mu m$

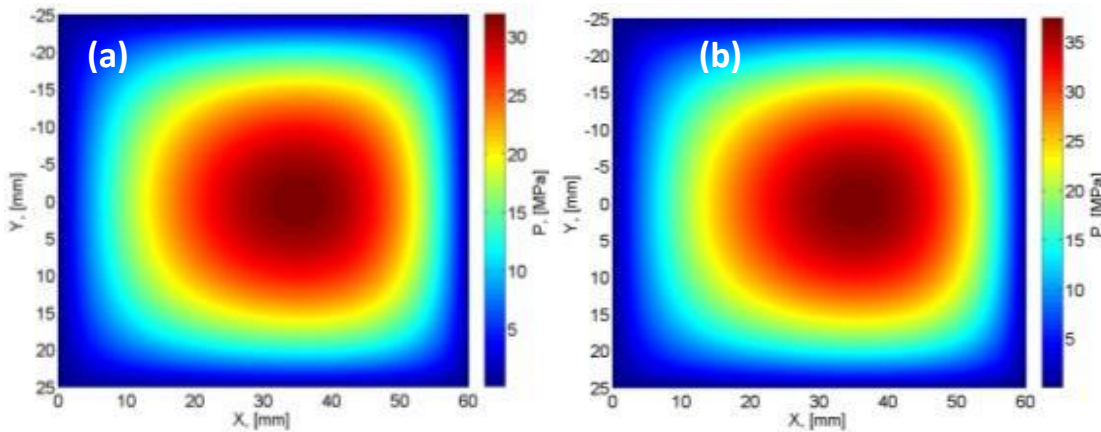


Figure 6.86 Contour plot of the pressure distribution for (a) the smooth and (b) the homogenised rough solutions. Minimum clearance  $h_{min}=14\mu m$

In Figures 6.87-6.88 the solutions are shown for  $h_{min}=10\mu m$ . In this case the load carried by the contacting asperities has become higher and is shown by orange dashed line. It can be seen in Figure 6.87 that the elastic contact pressure is presented by a piece-wise linear function. This is due to linear interpolation of the mean contact pressure values between the values of the film thickness for which the mean contact pressure has been evaluated. Minor distortion of the pressure distribution shape can

also be seen in Figure 6.88. The reason for such distortion is that being obstructed more significantly in the direction to the exit of the bearing (positive x direction) the fluid flow is enhanced in sideways directions.

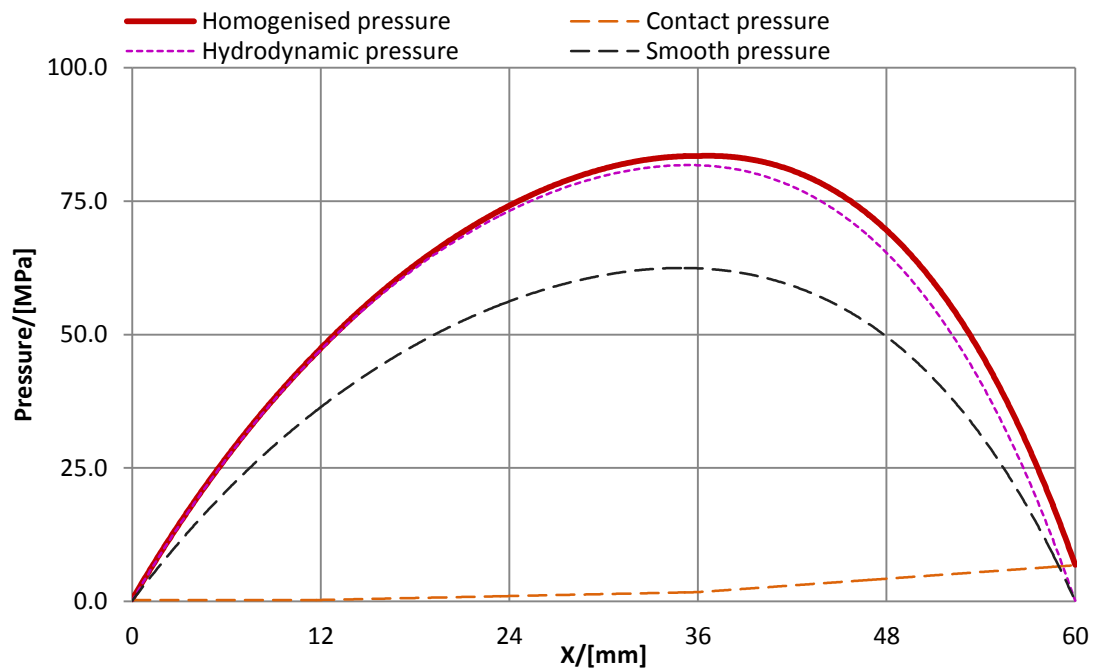


Figure 6.87 Central cross Section of the pressure distribution parallel to the x axis for the homogenised solution. Minimum clearance  $h_{min}=10\mu\text{m}$

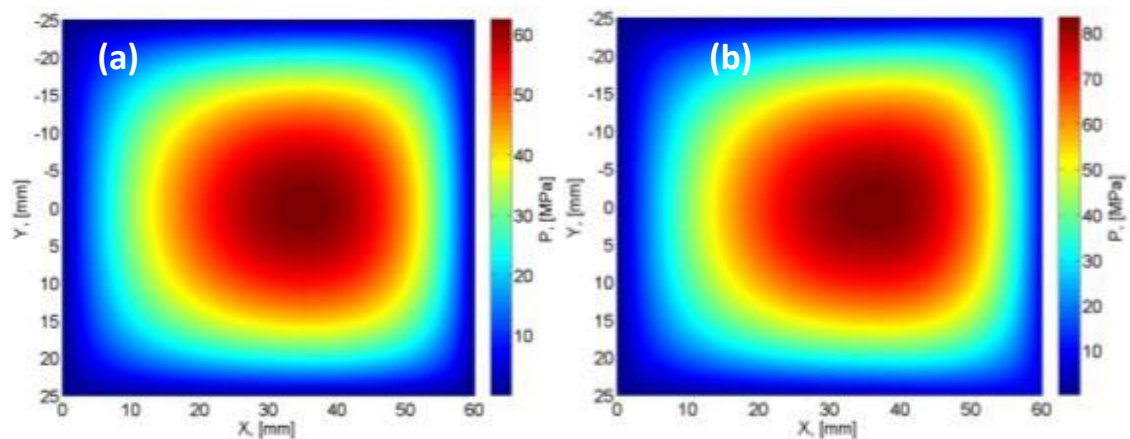


Figure 6.88 Contour plot of the pressure distribution for (a) the smooth and (b) the homogenised rough solutions. Minimum clearance  $h_{min}=10\mu\text{m}$

In case of the minimum clearance value  $h_{min}=6\mu\text{m}$  which is shown in Figures 6.89-6.90 the contact part of the load becomes a significant part of the total load. Further decreasing the minimum clearance value down to  $h_{min}=6\mu\text{m}$  results in the majority of the load being carried by the contacting asperities as can be observed in Figure 6.89. In this case the hydrodynamic component of the pressure is lower than the smooth case pressure. This value of the minimum clearance  $h_{min}=6\mu\text{m}$  corresponds to the maximum load supported hydrodynamically. As the clearance decreases further, the obstruction of flow overwhelms the increase of the pressure caused by the presence of roughness.

## Section 6.5 Solving the tilted pad bearing problem using the multigrid method

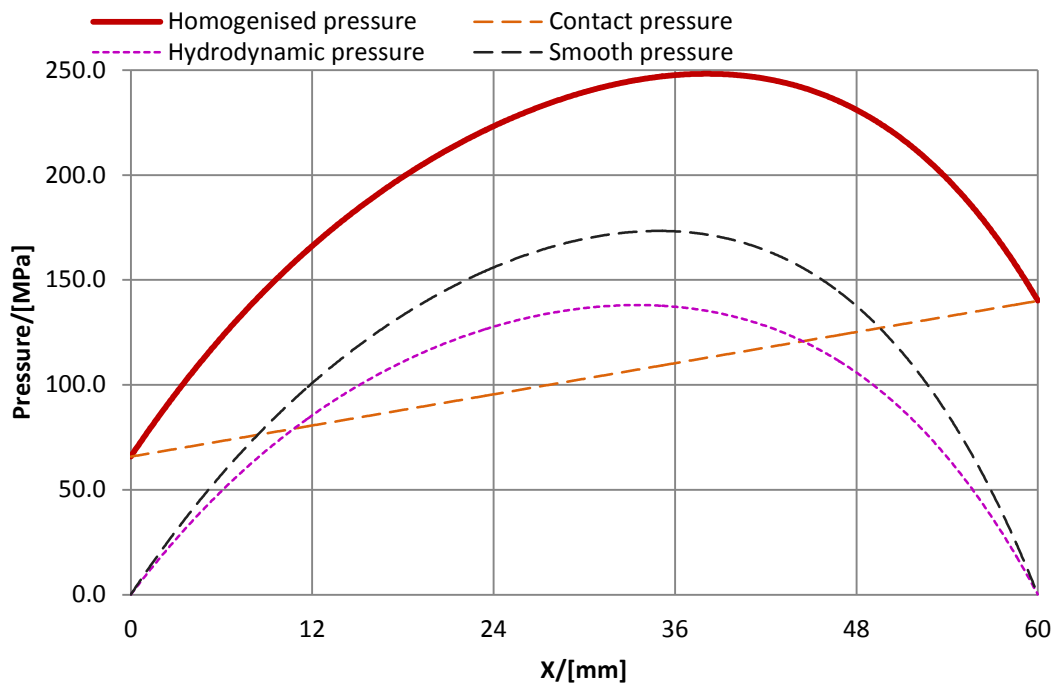


Figure 6.89 Central cross Section of the pressure distribution parallel to the x axis for the homogenised solution. Minimum clearance  $h_{min}=6\mu\text{m}$

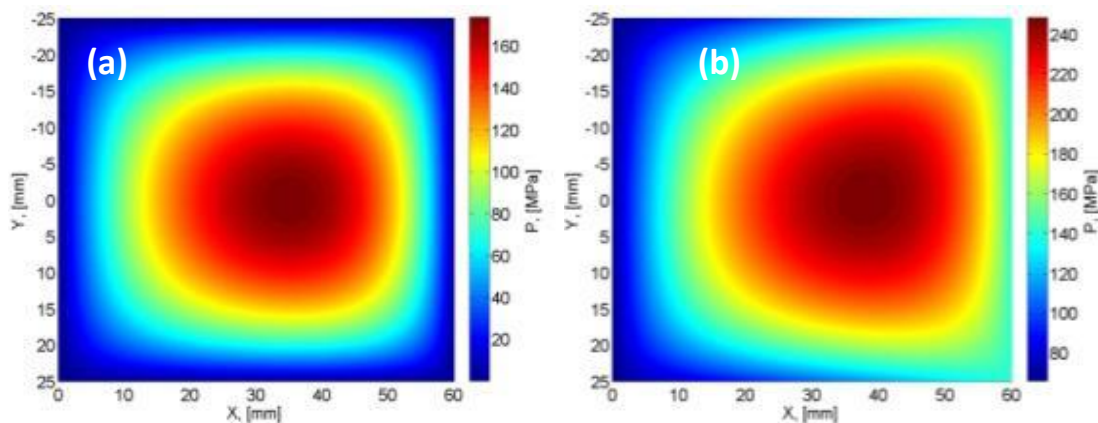


Figure 6.90 Contour plot of the pressure distribution for (a) the smooth and (b) the homogenised rough solutions. Minimum clearance  $h_{min}=6\mu\text{m}$

Note also that none of the Figures 6.83-6.90 show any effect of the oblique roughness. This is the result of the rough surface being naturally isotropic. Even in the case of contact, where the most prominent roughness features are flattened, no oblique effect can be observed.

Further decrease of the clearance would result in higher total load carried mostly by the contacting asperities. These cases are not considered in the thesis because the micro-EHL effects at the individual asperities scale become more significant than the global effect of roughness. This means that the roughness cannot be treated in a homogenised way.

## 6.6 Practical guidelines on using the flow factors approach

The homogenised Reynolds Equation approach can be applied to the plain bearing problem in order to take into account the average effect of roughness. The homogenisation of the Reynolds Equation is described in detail in Chapter 4 of this thesis. The necessary steps for applying of the homogenised approach to the plain bearing problem are summarised in the list below.

1. Select the representative area of the working surface.

This area must be sufficiently large to cover the characteristic roughness pattern of the surface while being smaller than the total area by a factor  $1/\varepsilon > 100$  in both  $x$  and  $y$  directions<sup>1</sup>. In the examples considered in this thesis it is shown that the agreement between the homogenised and deterministic solutions is progressively better for  $\varepsilon = 1/16, 1/32, 1/64,$  and  $1/128$ . In cases of cosine and sine waviness the representative area should include at least a single cosine or sine wave. For cases of measured surface roughness the dimensions of the measured area should be 100 times smaller than each of the dimensions of the total area of the tilted pad. It was shown that for the lower values of the minimum clearance the effect of individual asperities becomes overwhelming and this is not captured by the homogenised solution particularly well. However, in case of the measured surfaces, the representative area has multiple asperities, and therefore the homogenised solution can be expected to give accurate results for the whole range of applicability.

2. Formulate the local problems for an appropriate sequence of the global film thickness values as described in Chapters 4 and 5.

The local problems consider a nominally flat surface with periodic roughness which is separated from the counterface by a distance equal to the current global film thickness value. The range of the global film thickness values needs to be wide enough to cover possible global geometries. The resolution used in the formulation of the local problem should be sufficient to represent the roughness features well. It was shown that resolving the sinusoidal wave in 8 or 16 mesh elements gives different results. However, resolutions of 32 or 64 mesh elements per wave result in identical solutions.

3. Perform the dry contact analysis

---

<sup>1</sup>  $\varepsilon$  is a scaling factor of the local coordinates to the global coordinates. The homogenised solution is an asymptotic limit of the deterministic solution when  $\varepsilon$  approaches to zero. See Chapter 4 for more details.

## Section 6.6 Practical guidelines on using the flow factors approach

The formulated local problem considers the representative roughness function and the mean separation of the nominally flat surface from the counterface. The difference between the mean separation and the highest asperity peak of the representative roughness then gives the value of the elastic approach. The dry contact analysis presented in Chapter 3 aims to evaluate the contact pressure distribution and the deflected shape of the rough surface for a given elastic approach distance.

### 4. Calculate the flow factors

The procedure of calculating the flow factors is described in detail in Chapter 5. The local problems are solved based on the local film thickness function. In the case of contact the local film thickness is equal to the gap between the deflected rough surface and the flat rigid counterface. As a result of this procedure eight flow factors ( $a_{ij}, b_{ij}, i,j=1,2$ ) and the elastic load carried by the contacting asperities are generated as functions of the global film thickness value. The number of the global film thickness values defined at step 2 must be sufficient for the flow factors functions to be smooth and differentiable. As a result of this step a table of flow factors and mean elastic contact pressure values for the specified sequence of the global film thickness values defined at step 2 is created which determines the effect of the surface asperities on the lubrication and contact load for a particular surface roughness.

### 5. Take into account the roughness orientation

The flow factors calculated at the step 4 consider the axes of periodicity of the roughness to be coincident with the direction of entrainment and direction normal to entrainment. The set of flow factors are modified taking into account the roughness orientation, which results in six flow factors  $A_{ij}, B_i, i,j=1,2$ .

### 6. Create a map of flow factors

For the given global geometry each point  $(x,y)$  on the global mesh grid is associated with the flow factors values and the mean elastic contact pressure corresponding to the global film thickness  $h(x,y)$  at this point. Note that resolution of the global problem does not depend on the resolution of the local problems and needs to be sufficient to represent the global geometry only. As a result a map of flow factors as functions of the global coordinates  $(x,y)$  is created. If the value  $h(x,y)$  does not coincide with any of the sequence of  $h$  values specified at the step 2, then the flow factors and the mean elastic contact pressure at the point  $(x,y)$  are obtained using linear interpolation or cubic splines with respect to the sequence of  $h$  values.

### 7. Solve the homogenised Reynolds Equation

The Reynolds Equation modified with flow factors is solved using the multigrid method resulting in a hydrodynamic pressure distribution. The elastic contact pressure obtained by means of the local dry contact analysis is added to the hydrodynamic one at the points, where the lubricant film is not sufficiently thick to prevent direct contact.

### 6.7 Discussion

This section concludes the results of solving the tilted pad bearing problem using homogenised roughness approach. First, it was found that the Gauss-Seidel iterative method is very inefficient in solving the Reynolds Equation for the tilted pad bearing problem. This was explained by the fact that the Gauss-Seidel method can quickly reduce the error with the wavelength of a few mesh points but requires a large number of iterations to reduce errors that occur at longer wavelengths. The multigrid method was introduced which allowed the Gauss-Seidel method to be used in order to reduce the error in the most efficient way by using a hierarchy of grids with different resolution. As a result convergence of the solution to the required accuracy was then achieved very quickly. It was however found that due to the complex nature of the method it was not possible to terminate the execution as soon as the necessary level of convergence has been achieved. As a result the defined number of iterations and correction cycles is either excessive or not sufficient. A modification of the method in comparison with the version given by Venner and Lubrecht was proposed in which the execution of the method is stopped at a certain level of refinement whereas the iterations at the other levels continued. This allowed the total number of cycles and the total execution time to be significantly reduced.

Second, using the extruded cosine roughness of various wavelengths it was shown that the homogenised rough solution is an asymptotic limit of the rough solution as the size of the cell with representative roughness decreases. In the case of cosine or sine roughness a single cosine or sine wave could be used in the representative cell. The case of direct contact of the asperities was also considered, however the extruded roughness features completely block the flow of lubricant as soon as the first such contact occurs. The case of direct contact is therefore more relevant when the roughness is two dimensional. Consideration of two-dimensional sinusoidal roughness shows that both the hydrodynamic load and the one carried by the contacting asperities can then coexist.

## Section 6.7 Discussion

Third, the effect of the oblique roughness on the lubrication has been studied. It was shown that the homogenised solution captures the distortion of the shape of pressure distribution caused by rotating of the roughness by  $30^\circ$  clockwise quite well. The effect of oblique roughness was also demonstrated for the case of two-dimensional sinusoidal waves. As the two dimensional roughness allows the lubricant to flow around the oblique roughness features, the effect of oblique roughness is reduced for this case in comparison to the extruded oblique roughness. The homogenised solution was also shown to be capable of capturing this effect. The formulae for the oblique flow factors were obtained by Bayada (2005) , however no published records were found where these formulae were applied to the measured surfaces.

Another effect that the homogenised solution is able to predict is the ability of the lubricant to flow around the two dimensional roughness features. This feature was shown in the case of the two-dimensional sinusoidal surface and the measured surfaces rotated through an angle of  $30^\circ$ . This aspect of the homogenised solution is driven by so called cross terms of the homogenised Reynolds Equation and the cross flow factors  $a_{12}$ ,  $a_{21}$ , and  $b_2$ . Note that Patir and Cheng (1978, 1979) being the first significant contributors to the theory of flow factors did not consider the diagonal terms in the Reynolds Equation. Their method therefore was limited to isotropic, pure transverse or pure longitudinal roughness. The importance of the cross terms in the homogenised Reynolds equation is widely discussed by Almqvist et al (2011).

The deterministic solution used e.g. for validation of the homogenised method in case of sine or cosine roughness functions is not available for the measured surface cases due to a very high resolution required. Therefore it was not possible to validate the homogenised solution by comparison with a deterministic solution in these cases. However, it was shown that the homogenised solution captures any global effect of the roughness quite well as long as the individual effects of the asperities do not dominate.

Finally three surfaces measured using a Taylor-Hobson profilometer were considered. The results of the analysis conducted for the range of are summarised in Figures 6.91-6.93 where total load and contributions of hydrodynamic pressure and contact pressure are plotted against the value of relative gap,  $\Lambda$ , for all three surfaces considered. Scaling the minimum gap  $h_{min}$  with respect to the roughness of the surface allows the effect of different types of roughness profiles on the mixed lubrication to be

compared on the same chart. It can be seen from Figure 6.91 that in all three cases the total load behaves in the same way for the values of  $\Lambda > 3$ . In the case of  $\Lambda < 3$  the differences between the three surfaces considered become apparent. The values of  $\Lambda < 3$  correspond to the condition where the contribution of the load carried by the contacting asperities becomes comparable to the total load. This fact can be confirmed by the contact pressure contribution shown in Figure 6.92. The hydrodynamic pressure contribution is shown in Figure 6.93. It can be seen that the hydrodynamic load first increases in the presence of roughness and then decreases for the lower minimum clearance values. The maximum value of the hydrodynamic load is reached when some of the asperities are in direct contact while the major part of the surface is still separated from the counterface. This means that the highest load is carried by the bearing operating in a mixed lubrication regime.

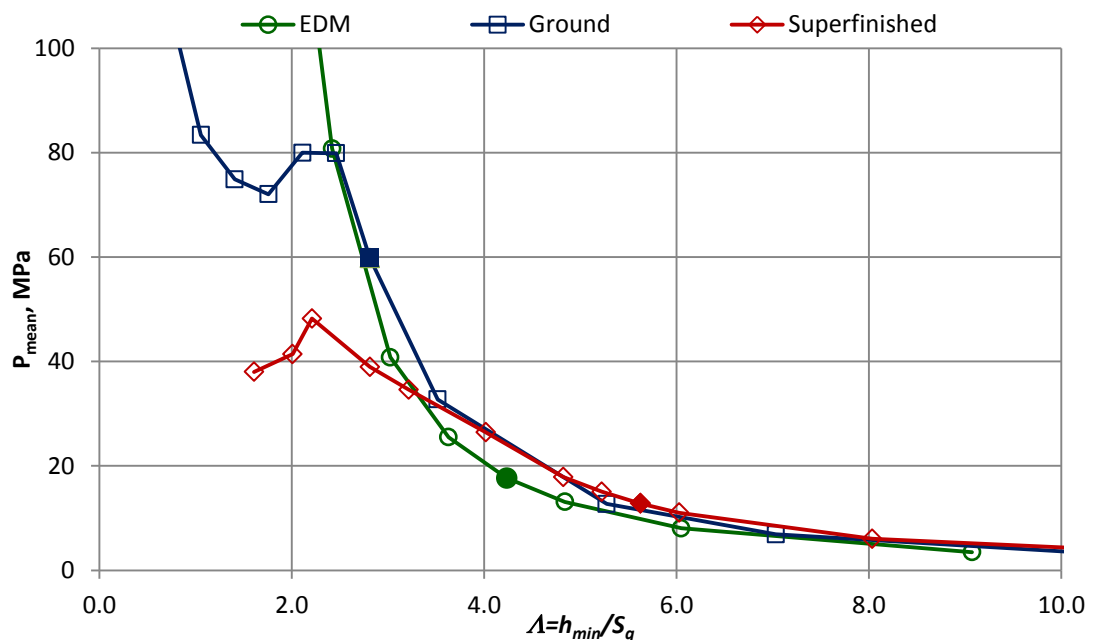


Figure 6.91 Total load expressed by means of average pressure plotted against the relative gap,  $\Lambda$ , for all three surfaces considered: Axially ground (square markers), Superfinished reground (diamond markers), prepared by EDM (circular markers). The case of first direct contact is denoted by corresponding solid markers.

The elastic and perfectly plastic deflection obtained by means of the dry contact analysis is taken into account at the stage of evaluation of the flow factors. The dry contact analysis is based on the assumption of periodic roughness and differential formulation of the deflection. It was shown in Chapter 3 that the predictions of the analysis method developed are quite accurate as long as the contact is mostly elastic and the zones of plastic deflection are isolated. Therefore the applicability of the homogenised method is limited to the cases of mixed lubrication, where the majority of the load is hydrodynamic with occasional contacts of the most prominent surface

## Section 6.7 Discussion

asperities. Bobach et al (2012) presented a model for the EHL contact incorporating the roughness effects by means of flow factors. It can be seen that their results do not reflect the micro-EHL effects observed by e.g. Evans et al (2012), who presented a deterministic solution to the problem. From this it can be concluded that the homogenised method is inefficient in the cases where the micro-EHL effects are dominant.

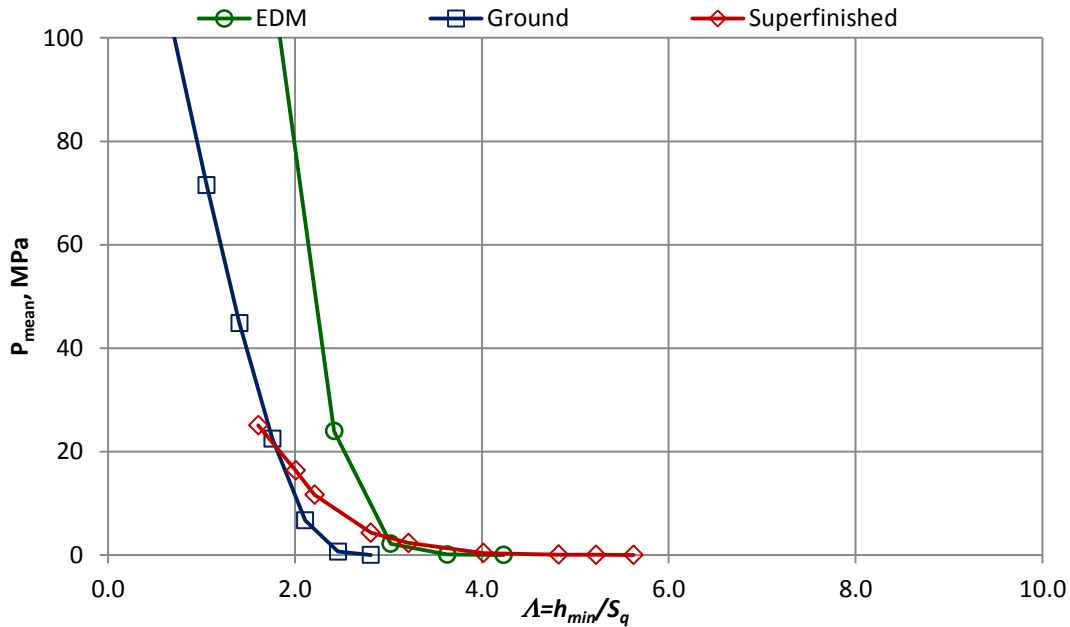


Figure 6.92 Contact pressure contribution to the total load plotted against the relative gap,  $\Lambda$ , for all three surfaces considered: Axially ground (square markers), Superfinished reground (diamond markers), prepared by EDM (circular markers).

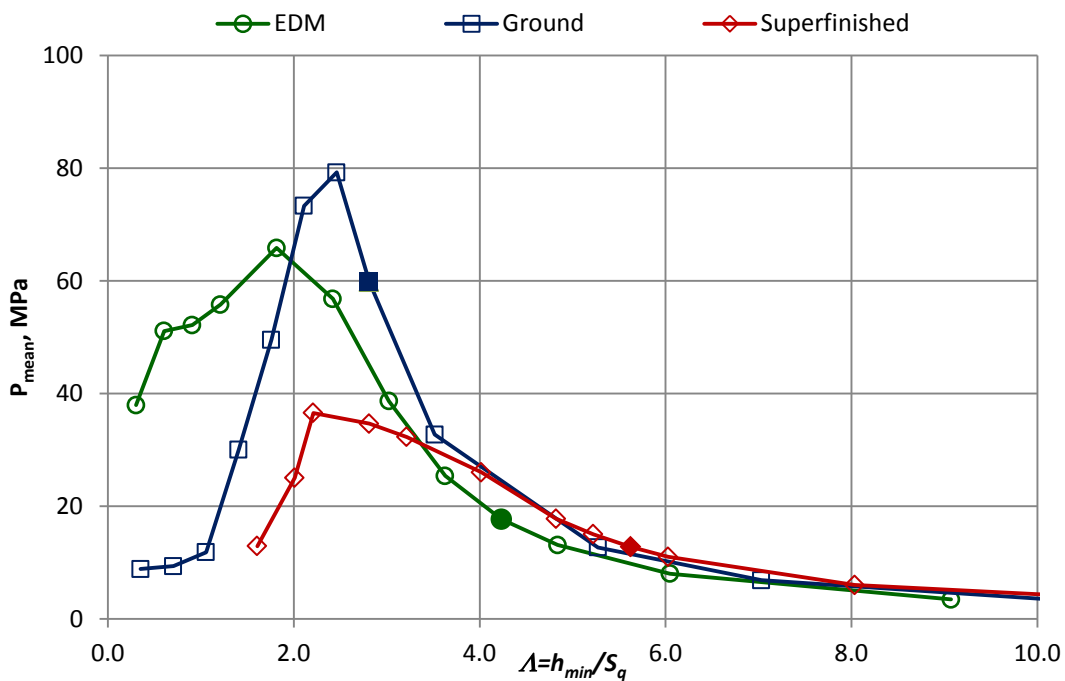


Figure 6.93 Hydrodynamic contribution to the total load plotted against the relative gap,  $\Lambda$ , for all three surfaces considered: Axially ground (square markers), Superfinished reground (diamond markers), prepared by EDM (circular markers). The case of first direct contact is denoted by corresponding solid markers.

## 7. Conclusions and potential developments

### 7.1. Elastic properties of the porous materials

1. In approximating pores in the material as isolated spheres, it was shown that the total volume of pores is the governing parameter for evaluating the effective elastic properties, while the statistical distribution of pores by size has only a second order effect.
2. The model based on isolated spherical pores shows quite accurate results for a number of porous materials, such as titanium foam, porous glass and sandstone. The model does not require significant improvements as long as it is applied to materials such as these, where pores can be considered isolated and roughly spherical, as can be seen, for example, in the cross section of titanium foam material in Figure 2.5.
3. The elastic properties of porous materials prepared by sintering have been shown to disagree with predictions given by the model based on isolated spherical pores. This is explained by the fact that such materials have much more complex structure of pores as can be appreciated from Figure 2.9, for example.
4. A better fit of the predictions to the data on sintered material has been achieved by considering randomly oriented elliptical pores. The amount of elliptical pores and their sizes were evaluated using the probability that two spherical pores merge. This model can be potentially developed further by assuming agglomerates of three or more merged pores. This development however requires a complicated analysis of the merging probabilities and further knowledge regarding the effect of various spatial configurations of merged pores on the elastic properties of the porous material.
5. A concept of damaged material has been introduced into the model for predicting the effective elastic properties. It was assumed that complex interconnected structures of pores, also called open pores, do not carry any load. Firstly, the effective characteristics of the material with isolated spherical and elliptical pores were evaluated as described earlier. The obtained values were then multiplied by an integrity factor which is the volume fraction of the material capable of carrying the load, i.e. excluding the volume occupied by open pores.

## Section 7.2 Dry contact analysis

6. The value of the integrity factor has been established using a curve fitting function based on the available open porosity data from the literature and from the manufacturer of porous bearings.
7. A model combining the effect of elliptical pores as well as the reduction of load carrying capacity caused by open pores was presented in Section 2.8. It was shown that with the appropriate choice of the integrity factor function the combined model agrees well with the available experimental data on sintered materials.
8. The elastic properties of porous materials are highly dependent on the type of pores that they contain, and thus on the manufacturing process. A detailed analysis of the material's porous microstructure is therefore required for selecting the appropriate model and establishing the integrity factor function.
9. Another potential development of the model would be to consider constructing a porous material by adding spherical grains of the host material of decreasing size into a fictitious medium. The fictitious medium would then be removed from the material and pores would be modelled as the resulting voids between the grains. This might be regarded as a more natural approximation of a material prepared by sintering.

### 7.2.Dry contact analysis

A method of dry contact analysis based on the differential deflection originally developed by Evans and Hughes (2000) is developed. The differential formulation of the deflection allows the effect of pressure to be more localised which results in a faster and more stable convergence of the problem.

Plasticity is incorporated into the model by limiting the maximum value of the elastic pressure to a value  $P_{max}$  nominally equal to the hardness value of the material. Once the maximum value is reached the further deformation is assumed to be plastic. This simple plastic model does not take the subsurface plasticity into account and therefore the change of surface height due to plastic deflection can only occur at the points where the pressure values are equal to  $P_{max}$ .

Convolution integrals involved in calculating the deflection and differential deflection are evaluated using the Fourier convolution theorem. Aliasing occurring as a result of using the circular convolution is exploited to represent a contact problem of a periodically repeated rough surface. Periodic boundary conditions are set.

1. In the case of pure elastic deformations the developed method was found to be in excellent agreement with the closed form solution developed by Westergaard (1937) for extruded sinusoidal waviness, as shown in Figure 3.9.
2. The results of the method developed are compared with those obtained using two-dimensional FE plane strain analysis of the dry contact of extruded rough surface. Comparison was based on load, contact area and free surface volume values evaluated by both methods for five load cases as well as pressure, gap and residual deflection distributions for high and low load cases. Perfect plasticity was considered in the FE analysis and von Mises criterion was used. In the case of lower loads a good agreement of the pressure, gap and residual deflection distributions can be observed in Figures 3.20 and 3.22. For the higher load case a minor discrepancy of the deformed gap can be observed in Figure 3.21. This is explained by the fact that higher loads result in upwelling of the material surrounding the high pressure zones which is not accounted for in the simple plasticity model incorporated in the developed dry contact analysis method. This can be confirmed by Figure 3.23 where the residual deflection is shown obtained by the developed method and by FEA. It can be seen in Figure 3.23 that the relative plastic deformation at the points of high pressures is captured quite well by the method developed, however the negative values of the plastic deformation corresponding to the upwelling of the material are not captured.
3. The method developed was also compared with the results of a full three dimensional FEA conducted by Yastrebov et al (2011). The comparison was based on the load, contact area and free surface volume values obtained for a sequence of penetration distances. The contours of the contact zones were also compared. Comparison showed that with the appropriate choice of the limiting pressure value  $P_{max}=2.6$  GPa the agreement of the load to contact area relationship is achieved (see Figure 3.28). The contours of the contact zones also agree very well as can be seen in Figure 3.30. This value of  $P_{max}$  however results in the free surface volume being underestimated by 10%. This disagreement can be explained by the fact that as the penetration increases, the subsurface plastic flow and corresponding upwelling of the material allow the contact area required for supporting the load to be achieved without further reduction of the depth of the valleys. This explanation can also be supported by Figure 3.21, where contact zones evaluated by both methods are the same, whereas the depth of the valleys is lower when evaluated using the method developed.

### **Section 7.3 Evaluation of the flow factors**

4. The inaccuracy of the deformed gap obtained by the method developed is considered acceptable in application to the mixed lubrication analysis. The method benefits significantly in terms of time and the computational resources required. In the case of extruded roughness the developed method is approximately 60-80 times faster than line contact FEA conducted on Intel i3 32bit 2GB RAM machine. Note that method was developed for analysis of two dimensional roughness problems. In the case of extruded roughness it can be easily modified to solve the one-dimensional roughness problem even faster. In the case of two-dimensional roughness (three dimensional contact problem) the time difference for one load case is 10 minutes on Intel i3 laptop against one hour on a high performance parallel computing unit (8 bi-core processors Intel Xeon X5550 2.67 GHz, 160Gb RAM).

5. Potential developments of the model include evaluating the plastic deformation in the zones adjacent to the high pressure points as a function which has positive values at the high pressure points and negative at the neighbouring points corresponding to the upwelling of the material.

### **7.3.Evaluation of the flow factors**

Chapters 4 and 5 present a theory and method for incorporating the effect of surface roughness in mixed lubrication problems into the classical isoviscous Reynolds' equation for smooth surfaces. This is achieved by means of flow factors, which modify both Poiseuille and Couette flow terms. Also, cross derivative terms are added into the Reynolds' equation to account for additional flow caused by the presence of roughness features. Flow factors are functions of the surface roughness and the nominal surface separation corresponding to the geometry of the problem. Flow factors are obtained as the solutions of local problems, assuming parallel nominally flat rough surfaces with periodic roughness.

1. An algorithm for solving the local problems numerically was developed and validated using the closed form analytical solution obtained by the author for the case of extruded sinusoidal waviness.
2. Flow factors evaluated numerically for the extruded sinusoidal waviness were validated using the analytical expressions for such flow factors obtained by Bayada (2005), see Figures 5.24 and 5.27.

3. The case of extruded sinusoidal waviness in contact was considered. It was shown that the flow factors reflect the complete blockage of flow in the direction across the extruded features and the enhancement of flow of the trapped fluid along the extruded features, see Figures 5.24-5.28.
4. The effect of oblique roughness was studied using the formulae obtained by Bayada (2005). The evolution of the flow factors values for extruded sinusoidal roughness was shown as the rotation of the extrusion direction relative to the entrainment direction varies from  $0^\circ$  to  $90^\circ$ , as shown in Figures 5.36-5.41.
5. Flow factors for two-dimensional sinusoidal waviness were evaluated. It was shown that the effect of the oblique features gradually decreases in progressing from the case of extruded roughness features down to isotropic features such as double sinusoidal waviness with equal wavelength in both  $x$  and  $y$  directions, as shown in Figures 5.45-5.50.
6. In the case of two dimensional sinusoidal roughness it was also shown that the flow is not completely blocked as a result of the direct asperity contact.
7. The effect of uniform stretching of the representative roughness area on the flow factors was studied. It was shown that as long as the original surface asperities do not experience plastic contact, stretching of the surface equally in both directions does not affect the calculation of the flow factors. For the case of no contact this was also confirmed analytically. In case of elastic contact the deformed shape of the stretched surface can be obtained by stretching the deformed original surface equally in both  $x$  and  $y$  directions. The original asperities have lower radii of curvature than the stretched ones therefore the original surface experiences higher contact pressures for the same penetration distance. The mean pressure experienced by the original surface is then higher by a factor of stretching. However, if the asperities of the original surface experience plastic pressures, and the stretched ones do not, then the flow factors are different. This can be observed in Figures 5.52-5.55.
8. Flow factors for three rough surfaces measured by a profilometer were evaluated. The surfaces considered were those of an axially ground disk (AG), superfinished circumferentially ground disk (SF), and a surface prepared by the electrical discharge machining (EDM) method. The flow factors of the AG surface illustrate behaviour similar to those of a surface with roughness extruded across the direction of

## Section 7.4 Mixed lubrication analysis based on the theory of flow factors

entrainment. This is explained by the extruded marks left by an abrasive wheel during the grinding process across the direction of entrainment. The flow factors calculated for the SF surface reflect the effect of superfinishing as well as the effect of circumferential marks occurred as a result of regrinding. Finally, the flow factors for EDM surface demonstrate behaviour similar to that of an isotropic surface roughness. This is due to the random nature of the roughness features created by the EDM process.

### 7.4.Mixed lubrication analysis based on the theory of flow factors

1. In Chapter 6 a problem of the lubrication of a single inclined pad is formulated and solved using the Gauss-Seidel iterative method. It was shown that the Gauss-Seidel method converges quickly if the error is of a low wavelength such as occurs in the presence of the roughness features, for example. At the same time the Gauss-Seidel method is very slow in resolving the error corresponding to the waviness features and to the global geometry of the problem. For this reason a multigrid method was used to solve the problem of mixed lubrication of an inclined pad with a rough surface.
2. The multigrid method was shown to be effective in solving the problem of lubrication of inclined pad with smooth, deterministic rough surface and roughness incorporated by means of the flow factors. A modification to the multigrid method described by Venner and Lubrecht (2000) was introduced which improved the convergence speed of the method as shown in Figures 6.23-6.25.
3. The problem of representing the roughness on the coarser grids was discussed. It was found that starting from a certain level the resolution of the coarse grids is not high enough to represent the roughness correctly. This significantly reduces the stability of the convergence process and may cause incorrect results. It was proposed to consider only the global geometry of the problem at the coarse grids which are incapable of representing the roughness correctly.
4. Using extruded cosine waviness it was shown that the deterministic roughness solution approaches the homogenised solution as the wavelength of the individual roughness features decreases. It can be concluded that the method based on the flow factors is accurate as long as contribution of individual asperities does not overwhelm the global effect of roughness on the flow of lubricant. This can be achieved by ensuring that the tangential dimensions of the individual roughness features are at

least 100 times smaller than the dimensions of the global problem, which is easily realised when solving real roughness problems.

5. The mixed lubrication modelling method based on the theory of flow factors is capable of capturing the effect of the roughness orientation, as shown in figures 6.39-6.47.

6. The effect of non isotropic roughness features on the flow of lubricant was studied in Section 5.2.5 by means of the flow factors. Non isotropic features increase the flow of lubricant in the direction of their longer side. This behaviour was also observed in Section 6.5.6, where the effect of oblique roughness on the flow was significantly reduced for two dimensional features in comparison to extruded ones.

7. Three measured rough surfaces were considered and it was shown that all three surfaces have the maximum value of the load carried hydrodynamically when operating in mixed lubrication regime.

8. Considering the fact that direct asperity contact was incorporated into the lubrication model by means of the dry contact analysis for the specified nominal gap, it can be concluded that the model developed is applicable to the mixed lubrication analysis, where the majority of the load is carried by the lubricant with only occasional direct asperity contacts occurring.

9. The method based on the flow factors is significantly faster than those based on deterministic roughness due to a very high computational resources required for the latter.

10. A potential improvement of the method would be to introduce the dependence of the density and the viscosity of the lubricant on the pressure. This can be achieved by considering the incompressible isoviscous problem at the local scale when calculating the flow factors, while varying the viscosity and density values according to the pressures when solving the global homogenised problem.

**Section 7.4 Mixed lubrication analysis based on the theory of flow factors**

(intentionally blank)

## Appendices

### Appendix A Evaluating the integral of $(a+\cos t)^{-3}$

In this appendix the integral of a function  $f(t) = [a + \cos t]^{-3}$  is evaluated analytically. The analytical expression for this function is used in solving the local problems and calculating the flow factors for a surface with extruded cosine roughness profile.

The function  $h$  is equal to:

$$h(t) = a + \cos t$$

which corresponds to the extruded cosine wave with the mean line  $a$  and amplitude equal to 1. Mathematically  $a$  is an arbitrary constant, however the physical implication dictates it to be greater or equal than the amplitude so that the total gap remains positive.

The aim of this section is to calculate the integral

$$F(x) = \int_0^x \frac{dt}{[a + \cos t]^3} \tag{A.1}$$

#### A.1 The integration by substitution

First the integration by substitution rule is used<sup>1</sup>:

$$\begin{aligned} \int_0^x \frac{dt}{(a + \cos t)^3} &= \left[ \begin{array}{l} z = \tan \frac{t}{2} \\ dt = 2 \cos^2 \frac{t}{2} dz \end{array} \right] = \int_0^x \frac{2 \cos^2 \frac{t}{2} dz}{(a + \cos t)^3} = \left[ \begin{array}{l} \cos 2t = \frac{1 - \tan^2 t}{1 + \tan^2 t} \\ \cos^2 t = \frac{1}{1 + \tan^2 t} \end{array} \right] = \\ \int_0^{\tan \frac{x}{2}} \frac{2 \frac{1}{1+z^2} dz}{\left(a + \frac{1-z^2}{1+z^2}\right)^3} &= \int_0^{\tan \frac{x}{2}} \frac{2(1+z^2)^2 dz}{(1+z^2)^3 \left(a + \frac{1-z^2}{1+z^2}\right)^3} = \int_0^{\tan \frac{x}{2}} \frac{2(1+z^2)^2 dz}{(a(1+z^2) + 1 - z^2)^3} \end{aligned} \tag{A.2}$$

Note, that the integration by substitution is applicable only where the substitution function is continuous and has a continuous derivative. Function  $z = \tan \frac{t}{2}$  satisfies this condition only piece-wise. Indeed,

$$z = \tan \frac{t}{2} = \pm \infty \Leftrightarrow \frac{t}{2} = \frac{\pi}{2} + \pi k \Leftrightarrow t = \pi(2k + 1), \quad k \in \mathbb{Z}$$

<sup>1</sup> The expressions in square brackets denote the conditions used in the sequence of equalities

### Appendix A: Evaluating the integral of $(a+\cos t)^{-3}$

Therefore, the substitution is applicable on the set of subintervals where the function  $z = \tan \frac{t}{2}$  is continuous and differentiable:

$$t \in [0, x] = \underbrace{[0, \pi)}_{\pi} \cup \underbrace{(\pi, 3\pi) \cup (3\pi, 5\pi) \cup \dots \cup ((2n-1)\pi, (2n+1)\pi)}_{2n\pi} \cup ((2n+1)\pi, x] \quad (\text{A.3})$$

The interval (A.3) is illustrated in Figure A.1. The value of  $n$  is a number of full periods of the tangential function in the interval  $[0, x]$ . If the value of  $x$  corresponds to the position  $x_0$  in Figure A.1 then  $n=-1$ , otherwise  $n \geq 0$  and is defined as<sup>22</sup>:

$$n = \left\lfloor \frac{(x - \pi)}{2\pi} \right\rfloor \quad (\text{A.4})$$

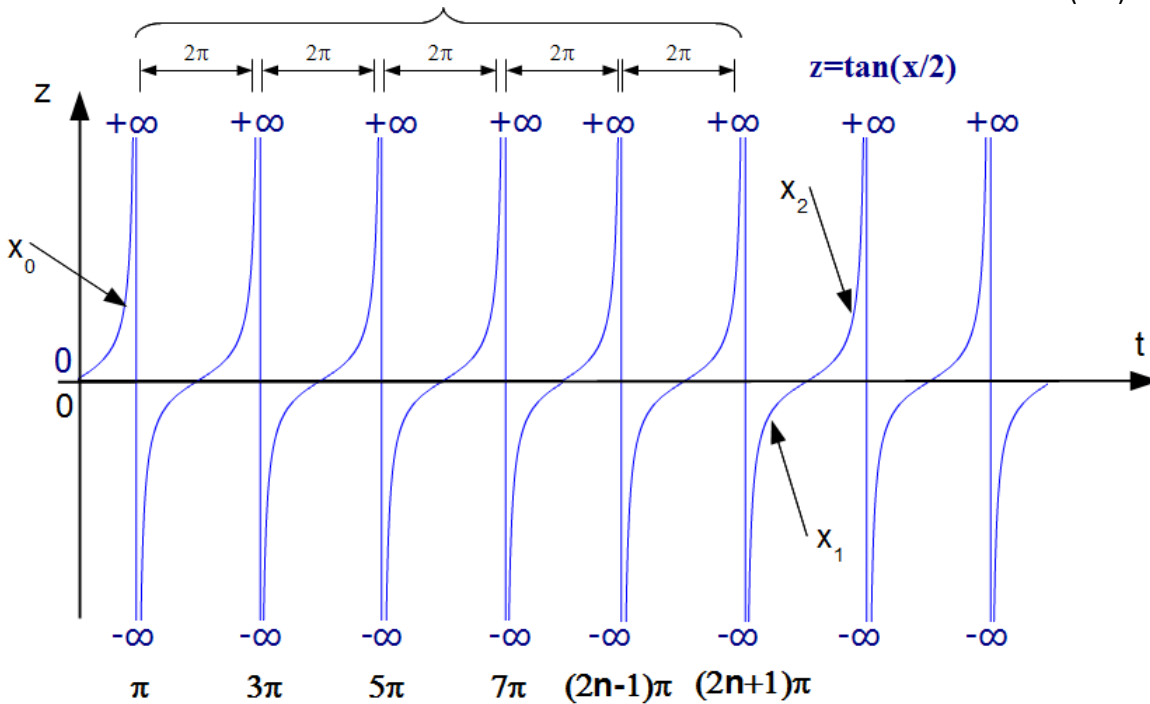


**Fig. A.1** The substitution function  $z = \tan \frac{t}{2}$  and sub intervals of the interval  $[0, x]$  where it is continuous and differentiable

The integral (A.1) is then equal to a summation of integrals defined on the sequence of sub intervals where the integration by substitution is applicable:

$$\int_0^x \frac{dt}{(a + \cos t)^3} = \int_0^{\pi-\varepsilon} \frac{dt}{(a + \cos t)^3} + \int_{\pi+\varepsilon}^{3\pi-\varepsilon} \frac{dt}{(a + \cos t)^3} + \dots + \int_{(2n-1)\pi+\varepsilon}^{(2n+1)\pi-\varepsilon} \frac{dt}{(a + \cos t)^3} + \int_{(2n+1)\pi+\varepsilon}^x \frac{dt}{(a + \cos t)^3} \quad (\text{A.5})$$

with  $\varepsilon$  being sufficiently small this equality is correct.

<sup>22</sup> The operation  $\lfloor x \rfloor$  denotes rounding real number  $x$  down to the nearest integer

From now on when mentioning the integral (A.1) the definition (A.5) is actually used.

### A.2 Integral of the rational functions

The integral (A.2) can be presented as a combination of integrals of rational functions:

$$\frac{2(1+z^2)^2}{[(a-1)z^2+a+1]^3} = \frac{Az+B}{[(a-1)z^2+a+1]^3} + \frac{Cz+D}{[(a-1)z^2+a+1]^2} + \frac{Ez+F}{[(a-1)z^2+a+1]}$$

Bringing the terms to the common denominator:

$$2(1+z^2)^2 = Az+B+(Cz+D)[(a-1)z^2+a+1] + (Ez+F)[(a-1)z^2+a+1]^2$$

Equating the coefficients for the powers of  $z$  lead to the following system:

$$\begin{cases} 1: 2 = B + D(a+1) + F(a+1)^2 \\ z: 0 = A + C(a+1) + E(a+1)^2 \\ z^2: 4 = D(a-1) + 2F(a^2-1) \\ z^3: 0 = C(a-1) + 2E(a^2-1) \\ z^4: 2 = F(a-1)^2 \\ z^5: 0 = E(a-1)^2 \end{cases}$$

by solving the system we obtain:

$$\begin{aligned} \frac{2(1+z^2)^2}{[(a-1)z^2+a+1]^3} &= \frac{\left\{\frac{8}{(a-1)^2}\right\}}{[(a-1)z^2+a+1]^3} + \frac{\left\{\frac{-8}{(a-1)^2}\right\}}{[(a-1)z^2+a+1]^2} + \frac{\frac{2}{(a-1)^2}}{[(a-1)z^2+a+1]} = \\ &\left\{\frac{8}{(a-1)^5}\right\} \frac{1}{\left[z^2 + \frac{(a+1)}{(a-1)}\right]^3} + \left\{\frac{-8}{(a-1)^4}\right\} \frac{1}{\left[z^2 + \frac{(a+1)}{(a-1)}\right]^2} + \frac{2}{(a-1)^3} \frac{1}{\left[z^2 + \frac{(a+1)}{(a-1)}\right]} \end{aligned}$$

Let us adopt the following notations:

$$P = \frac{8}{(a-1)^5} \quad Q = \frac{-8}{(a-1)^4} \quad R = \frac{2}{(a-1)^3} \quad m^2 = \left(\frac{a+1}{a-1}\right) \tag{A.6}$$

With this notations the integral (A.1) yields:

$$F(z) = \int \frac{2(1+z^2)^2 dz}{[(a-1)z^2+a+1]^3} = \int \frac{Pdz}{[z^2+m^2]^3} + \int \frac{Qdz}{[z^2+m^2]^2} + \int \frac{Rdz}{[z^2+m^2]} \tag{A.7}$$

## Appendix A: Evaluating the integral of (a+cost)-3

The integrals of the rational functions above are calculated using the following formulae:

$$\int \frac{Rdz}{[z^2 + m^2]} = R \frac{1}{m} \arctan \frac{z}{m}$$

$$\int \frac{Qdz}{[z^2 + m^2]^2} = Q \frac{z}{2m^2(z^2 + m^2)} + Q \frac{1}{2m^2} \frac{1}{m} \arctan \frac{z}{m}$$

$$\int \frac{Pdz}{[z^2 + m^2]^3} = P \frac{z}{4m^2(z^2 + m^2)^2} + P \frac{3}{4m^2} \left[ \frac{z}{2m^2(z^2 + m^2)} + \frac{1}{2m^3} \arctan \frac{z}{m} \right]$$
(A.8)

Note that these solutions are applicable for  $\left(\frac{a+1}{a-1}\right) > 0$  which creates a restriction on  $a$  to be strictly greater than 1 or lower than -1. The values  $a > 1$  only will be considered, as the physical meaning of such choice is that the gap between the surfaces is positive and no contact occurs.

The integral (A.7),(A.1) is then

$$F(z) = \left\{ \begin{array}{l} R \frac{1}{m} \arctan \frac{z}{m} + Q \frac{z}{2m^2(z^2 + m^2)} + Q \frac{1}{2m^2} \frac{1}{m} \arctan \frac{z}{m} + \\ P \frac{z}{4m^2(z^2 + m^2)^2} + P \frac{3}{4m^2} \left[ \frac{z}{2m^2(z^2 + m^2)} + \frac{1}{2m^3} \arctan \frac{z}{m} \right] \end{array} \right\}$$

Rearranging the terms in the right hand side:

$$F(z) = \underbrace{\left[ \frac{R}{m} + \frac{1}{2m^2} \frac{Q}{m} + \frac{3}{4m^2} \frac{P}{2m^3} \right]}_{F_1} \arctan \frac{z}{m} + \underbrace{\left[ Q + \frac{3P}{4m^2} \right]}_{F_2} \frac{1}{2m^2} \frac{z}{(z^2 + m^2)} +$$

$$\underbrace{\frac{P}{4m^2}}_{F_3} \frac{z}{(z^2 + m^2)^2} = F_1 \arctan \frac{z}{m} + F_2 \frac{z}{(z^2 + m^2)} + F_3 \frac{z}{(z^2 + m^2)^2}$$
(A.9)

The coefficients  $F_1, F_2, F_3$  identified in equation (A.9) are calculated as follows:

$$F_1 = \frac{2}{(a-1)^3} \sqrt{\frac{a-1}{a+1}} - \frac{8}{2(a-1)^4} \sqrt{\left(\frac{a-1}{a+1}\right)^3} + \frac{8}{(a-1)^5} \frac{3}{8} \sqrt{\left(\frac{a-1}{a+1}\right)^5} =$$

$$\frac{2}{(a-1)^{2.5}(a+1)^{0.5}} - \frac{4}{(a-1)^{2.5}(a+1)^{1.5}} + \frac{3}{(a-1)^{2.5}(a+1)^{2.5}} =$$

$$\frac{2(a+1)^2 - 4(a+1) + 3}{(a-1)^{2.5}(a+1)^{2.5}} = \frac{2a^2 + 4a + 2 - 4a - 4 + 3}{(a-1)^{2.5}(a+1)^{2.5}} = \frac{2a^2 + 1}{(a-1)^{2.5}(a+1)^{2.5}}$$

$$F_2 = -\frac{8}{2(a-1)^4} \left(\frac{a-1}{a+1}\right) + \frac{8}{(a-1)^5} \frac{3}{8} \left(\frac{a-1}{a+1}\right)^2 =$$

$$-\frac{4}{(a-1)^3(a+1)} + \frac{3}{(a-1)^3(a+1)^2} = \frac{-4(a+1) + 3}{(a-1)^3(a+1)^2} = \frac{-4a-1}{(a-1)^3(a+1)^2}$$

$$F_3 = \frac{8}{4(a-1)^5} \left( \frac{a-1}{a+1} \right) = \frac{2}{(a-1)^4(a+1)} \tag{A.10}$$

### A.3 Calculating the definite integral on the interval [0,x]

Using the indefinite integral  $F(z)$  obtained in the previous section the expression for the definite integral (A.1) on the interval  $[0,x]$  can be written as:

$$\int_0^x \frac{dt}{(a + \text{cost})^3} = F(z) = \left[ F_1 \arctan \frac{z}{m} + F_2 \frac{z}{(z^2 + m^2)} + F_3 \frac{z}{(z^2 + m^2)^2} \right]_0^{\tan \frac{x}{2}}$$

However, bearing in mind the modification (A.5) which is a necessary condition for the integration by substitution to be valid

$$\begin{aligned} \int_0^x \frac{dt}{(a + \text{cost})^3} &= \\ \int_0^{\pi-\varepsilon} \frac{dt}{(a + \text{cost})^3} + \int_{\pi+\varepsilon}^{3\pi-\varepsilon} \frac{dt}{(a + \text{cost})^3} + \dots + \int_{(2n-1)\pi+\varepsilon}^{(2n+1)\pi-\varepsilon} \frac{dt}{(a + \text{cost})^3} + \int_{(2n+1)\pi+\varepsilon}^x \frac{dt}{(a + \text{cost})^3} &= \\ = F(z)|_0^{+\infty} + nF(z)|_{-\infty}^{+\infty} + F(z)|_{-\infty}^{\tan \frac{x}{2}} = (n+1)F(z)|_{-\infty}^{+\infty} + F(z)|_0^{\tan \frac{x}{2}} \end{aligned} \tag{A.11}$$

Now calculate the values of  $F(z)$  for  $z=\pm\infty$  and  $z=0$ :

$$\begin{aligned} F(+\infty) &= \lim_{z \rightarrow +\infty} \left[ F_1 \arctan \frac{z}{m} + F_2 \frac{1}{\left(z + \frac{m^2}{z}\right)} + F_3 \frac{1}{\left(z^3 + 2zm^2 + \frac{m^4}{z}\right)} \right] = F_1 \frac{\pi}{2} \\ F(-\infty) &= \lim_{z \rightarrow -\infty} \left[ F_1 \arctan \frac{z}{m} + F_2 \frac{1}{\left(z + \frac{m^2}{z}\right)} + F_3 \frac{1}{\left(z^3 + 2zm^2 + \frac{m^4}{z}\right)} \right] = -F_1 \frac{\pi}{2} \end{aligned}$$

The values for  $\arctan(z)$  at  $z=\pm\infty$  are selected so that  $F(z)|_{\pm\infty}^{+\infty}$  covers the whole period of  $z = \tan \frac{t}{2}$  function.

$$F(0) = \left[ F_1 \arctan \frac{z}{m} + F_2 \frac{z}{(z^2 + m^2)} + F_3 \frac{z}{(z^2 + m^2)^2} \right] = 0$$

Therefore, the final formula for the integral (A.1) is:

$$\begin{aligned} \int_0^x \frac{dt}{(a + \text{cost})^3} &= (n+1)F(z)|_{-\infty}^{+\infty} + F(z)|_0^{\tan \frac{x}{2}} = \\ (n+1)\pi F_1 + F_1 \arctan \frac{\tan x/2}{m} + F_2 \frac{\tan x/2}{(\tan^2 x/2 + m^2)} + F_3 \frac{\tan x/2}{(\tan^2 x/2 + m^2)^2} \end{aligned} \tag{A.12}$$

where  $F_1, F_2, F_3$  are defined by (A.10) and  $m^2 = \left(\frac{a+1}{a-1}\right)$ .

## Appendix B: Evaluating the integral of $(a+\cos t)^{-2}$

### Appendix B Evaluating the integral of $(a+\cos t)^{-2}$

In this appendix the integral of a function  $f(t) = [a + \cos t]^{-2}$  is evaluated analytically. The same approach is used as in Appendix A therefore some of the calculations are omitted.

The function  $h$  equal to:

$$h(t) = a + \cos t$$

corresponds to the extruded cosine wave with the mean line  $a$  and amplitude equal to

1. The aim of this section is to calculate the integral

$$G(x) = \int_0^x \frac{dt}{[a + \cos t]^2} \quad (\text{B.1})$$

#### B.1 The integration by substitution

Same substitution function  $z = \tan \frac{t}{2}$  is used as in Appendix A:

$$\begin{aligned} \int_0^x \frac{dt}{(a + \cos t)^2} &= \left[ \begin{array}{l} z = \tan \frac{t}{2} \\ dt = 2 \cos^2 \frac{t}{2} dz \end{array} \right] = \int_0^x \frac{2 \cos^2 \frac{t}{2} dz}{(a + \cos t)^2} = \left[ \begin{array}{l} \cos 2t = \frac{1 - \tan^2 t}{1 + \tan^2 t} \\ \cos^2 t = \frac{1}{1 + \tan^2 t} \end{array} \right] = \\ \int_0^{\tan \frac{x}{2}} \frac{2 \frac{1}{1+z^2} dz}{\left(a + \frac{1-z^2}{1+z^2}\right)^2} &= \int_0^{\tan \frac{x}{2}} \frac{2(1+z^2) dz}{(1+z^2)^2 \left(a + \frac{1-z^2}{1+z^2}\right)^2} = \int_0^{\tan \frac{x}{2}} \frac{2(1+z^2) dz}{(a(1+z^2) + 1 - z^2)^2} \end{aligned} \quad (\text{B.2})$$

The similar piece-wise integration technique is applied, using the sequence of sub intervals where the function  $z = \tan \frac{t}{2}$  is continuous and differentiable:

$$t \in [0, x] = \underbrace{[0, \pi]}_{\pi} \cup \underbrace{(\pi, 3\pi) \cup (3\pi, 5\pi) \cup \dots \cup ((2n-1)\pi, (2n+1)\pi)}_{2n\pi} \cup [(2n+1)\pi, x] \quad (\text{B.3})$$

The interval (B.3) is illustrated on the Fig. A.1 and the value of  $n$  is given by (A.4).

#### B.2 Integral of the rational functions

The integral (B.2) can be presented as a combination of integrals of rational functions:

$$\frac{2(1+z^2)}{[(a-1)z^2 + a + 1]^2} = \frac{Az + B}{[(a-1)z^2 + a + 1]^2} + \frac{Cz + D}{[(a-1)z^2 + a + 1]}$$

Bringing the terms to the common denominator:

$$2(1+z^2) = (Az + B) + (Cz + D)[(a-1)z^2 + a + 1]$$

Equating the coefficients for the powers of  $z$  lead to the following system:

$$\begin{cases} 1: 2 = B + D(a + 1) \\ z: 0 = A + C(a + 1) \\ z^2: 2 = D(a - 1) \\ z^3: 0 = C(a - 1) \end{cases} \Leftrightarrow \begin{cases} C = 0 \\ D = \frac{2}{(a - 1)} \\ A = 0 \\ B = 2 - \frac{2(a + 1)}{(a - 1)} = \frac{2(a - 1) - 2(a + 1)}{(a - 1)} = \frac{-4}{(a - 1)} \end{cases}$$

Therefore,

$$\frac{2(1 + z^2)}{[(a - 1)z^2 + a + 1]^2} = \frac{-4}{(a - 1)} \frac{1}{[(a - 1)z^2 + a + 1]^2} + \frac{2}{(a - 1)} \frac{1}{[(a - 1)z^2 + a + 1]} = \frac{-4}{(a - 1)^3} \frac{1}{\left[z^2 + \left(\frac{a+1}{a-1}\right)\right]^2} + \frac{2}{(a - 1)^2} \frac{1}{\left[z^2 + \left(\frac{a+1}{a-1}\right)\right]}$$

The integral (B.1) then yields:

$$G(z) = \int \frac{2(1 + z^2)dz}{[(a - 1)z^2 + a + 1]^2} = \frac{-4}{(a - 1)^3} \int \frac{dz}{[z^2 + m^2]^2} + \frac{2}{(a - 1)^2} \int \frac{dz}{[z^2 + m^2]} \tag{B.4}$$

where  $m^2 = \left(\frac{a+1}{a-1}\right)$  as in Appendix A and again the restriction of  $a > 1$  applies.

Using the formulae for the anti-derivatives of the rational functions (A.8) the integral (B.4) and is then

$$G(z) = \left\{ \frac{2}{(a - 1)^2} \frac{1}{m} \arctan \frac{z}{m} - \frac{4}{(a - 1)^3} \frac{z}{2m^2(z^2 + m^2)} - \frac{4}{(a - 1)^3} \frac{1}{2m^2} \frac{1}{m} \arctan \frac{z}{m} \right\}$$

Substituting the expression for  $m$ :

$$\begin{aligned} G(z) &= \left\{ \frac{2}{(a - 1)^2} \sqrt{\frac{a - 1}{a + 1}} - \frac{4}{(a - 1)^3} \frac{1}{2} \sqrt{\frac{a - 1}{a + 1}} \frac{(a - 1)}{(a + 1)} \right\} \arctan \frac{z}{m} - \frac{4}{(a - 1)^3} \frac{(a - 1)}{(a + 1)} \frac{z}{2(z^2 + m^2)} = \\ &= \left\{ \frac{2}{(a - 1)^{1.5}(a + 1)^{0.5}} - \frac{2}{(a - 1)^{1.5}(a + 1)^{1.5}} \right\} \arctan \frac{z}{m} - \frac{2}{(a - 1)^2(a + 1)} \frac{z}{(z^2 + m^2)} = \\ &= \underbrace{\frac{2a}{(a - 1)^{1.5}(a + 1)^{1.5}}}_{G_1} \arctan \frac{z}{m} - \underbrace{\frac{2}{(a - 1)^2(a + 1)}}_{G_2} \frac{z}{(z^2 + m^2)} = G_1 \arctan \frac{z}{m} - G_2 \frac{z}{(z^2 + m^2)} \end{aligned} \tag{B.5}$$

The coefficients  $G_1, G_2$  identified in equation (B.5) are then:

$$G_1 = \frac{2a}{(a - 1)^{1.5}(a + 1)^{1.5}}; \quad G_2 = \frac{2}{(a - 1)^2(a + 1)} \tag{B.6}$$

## Appendix B: Evaluating the integral of (a+cost)-2

### B.3 Calculating the definite integral on the interval [0,x]

Using the indefinite integral  $G(z)$  obtained in the previous section the expression for the definite integral (B.1) on the interval  $[0,x]$  can be written as:

$$\int_0^x \frac{dt}{(a + \cos t)^2} = G(z) = \left[ G_1 \arctan \frac{z}{m} - G_2 \frac{z}{(z^2 + m^2)} \right]_{0}^{\tan \frac{x}{2}}$$

However, bearing in mind the modification (A.5) which is a necessary condition for the integration by substitution to be valid

$$\begin{aligned} \int_0^x \frac{dt}{(a + \cos t)^2} &= \\ \int_0^{\pi-\varepsilon} \frac{dt}{(a + \cos t)^2} &+ \int_{\pi+\varepsilon}^{3\pi-\varepsilon} \frac{dt}{(a + \cos t)^2} + \dots + \int_{(2n-1)\pi+\varepsilon}^{(2n+1)\pi-\varepsilon} \frac{dt}{(a + \cos t)^2} + \int_{(2n+1)\pi+\varepsilon}^x \frac{dt}{(a + \cos t)^2} = \\ &= G(z)|_0^{+\infty} + nG(z)|_{-\infty}^{+\infty} + G(z)|_{-\infty}^{\tan \frac{x}{2}} = (n+1)G(z)|_{-\infty}^{+\infty} + G(z)|_0^{\tan \frac{x}{2}} \end{aligned} \quad (\text{B.7})$$

Now calculate the values of  $G(z)$  for  $z=\pm\infty$  and  $z=0$ :

$$\begin{aligned} G(+\infty) &= \lim_{z \rightarrow +\infty} \left[ G_1 \arctan \frac{z}{m} - G_2 \frac{1}{\left(z + \frac{m^2}{z}\right)} \right] = G_1 \frac{\pi}{2} \\ G(-\infty) &= \lim_{z \rightarrow -\infty} \left[ G_1 \arctan \frac{z}{m} + G_2 \frac{1}{\left(z + \frac{m^2}{z}\right)} \right] = -G_1 \frac{\pi}{2} \end{aligned}$$

The values for  $\arctan(z)$  at  $z=\pm\infty$  are selected so that  $G(z)|_{-\infty}^{+\infty}$  covers the whole period of  $z = \tan \frac{t}{2}$  function.

$$G(0) = \left[ G_1 \arctan \frac{z}{m} + G_2 \frac{z}{(z^2 + m^2)} \right] = 0$$

Therefore, the final formula for the integral (B.1) is:

$$\begin{aligned} \int_0^x \frac{dt}{(a + \cos t)^2} &= (n+1)G(z)|_{-\infty}^{+\infty} + G(z)|_0^{\tan \frac{x}{2}} = \\ &(n+1)\pi G_1 + G_1 \arctan \frac{\tan x/2}{m} + G_2 \frac{\tan x/2}{(\tan^2 x/2 + m^2)} \end{aligned} \quad (\text{B.8})$$

where  $G_1, G_2$  are defined by (B.6) and  $m^2 = \left(\frac{a+1}{a-1}\right)$ .

## References

1. Almqvist, A. and Dasht, J. "The homogenization process of the Reynolds equation describing compressible liquid flow", *Tribology International* (2006), 39, 994-1002, doi: 10.1016/j.triboint.2005.09.036
2. Almqvist, A., Fabricius, J., Spencer, A., and Wall, P. "Similarities and differences between the flow factor method by Patir and Cheng and Homogenization" *Journal of Tribology-Transactions of the ASME* (2001), 133, 031702.1-5, doi: 10.1115/1.4004078
3. Altman, A., Valakina, V., Karpova, V., Memelov, V., Sorokina, V. "Relationship between the total and open porosity of sintered Cu–Sn–C materials". *Soviet Powder Metallurgy* [Translated from Russian] (1966), 5, 33–36.
4. Appleby, D., Hussey, C. L., Seddon, K. R. and Turp, J. E. "Room temperature ionic liquids as solvents for electronic absorption spectroscopy of halide complexes", *Nature* (1986), 323, 614-616.
5. Archard, J. F. "Elastic deformation and the laws of friction", *Proceedings of the Royal Society of London Series a-Mathematical and Physical Sciences* (1957), 243, 190-205.
6. Armitage, P. "An overlap problem arising in particle counting", *Biometrika* (1949), 36, 257-266, doi: 10.2307/2332666.
7. Avellaneda, M. "Iterated homogenization, differential effective medium theory and applications", *Commun. Pure Appl. Math.* (1987), 40, 527–554, doi:10.1002/cpa.3160400502
8. Bakhvalov, N. S. "Averaged characteristics of bodies with periodic structure", *Doklady Akademii Nauk SSSR* (1974), 218, 1046–1048.
9. Bayada, G. and Chambat, M. "New models in the theory of the hydrodynamic lubrication of rough surfaces", *Journal of Tribology-Transactions of the ASME* (1988), 110, 402-407.

10. Bayada, G. and Faure, J. B. "A double scale analysis approach of the Reynolds roughness comments and application to the journal bearing", *Journal of Tribology-Transactions of the ASME* (1989), 111, 323-330.
11. Bayada, G., Martin, S., Vazquez, C. "An Average Flow Model of the Reynolds Roughness Including a Mass-Flow Preserving Cavitation Model", *Journal of Tribology* (2005), 127(4), 793-802, doi:10.1115/1.2005307.
12. Berge, P. A., Bonner, B. P., Berryman, J. G. "Ultrasonic velocity porosity relationships for sandstone analogues made from fused glass-beads", *Geophysics* (1995), 60, 108–119, doi:10.1190/1.1443738.
13. Berryman, J. G. "Long-wavelength propagation in composite elastic media I. spherical inclusions", *J. Acoust. Soc. Am.* (1980), 68, 1809–1819, doi:10.1121/1.385171
14. Berryman, J. G. "Effective medium theories for multicomponent poroelastic composites", *J. Eng. Mech. ASCE* (2006), 132, 519–531, doi:10.1061/(ASCE)0733-9399(2006)132:5(519)
15. Bobach, L., Beilicke, R., Bartel, D. et al "Thermal elastohydrodynamic simulation of involute spur gears incorporating mixed friction", *Tribology International* (2012), 48, 191-206, doi:10.1016/j.triboint.2011.11.025.
16. Borodich, F. M. and Galanov, B. A. "Non-direct estimations of adhesive and elastic properties of materials by depth-sensing indentation", *Proceedings of the Royal Society a-Mathematical Physical and Engineering Sciences* (2008), 464, 2759-2776, doi:10.1098/rspa.2008.0044.
17. F. M. Borodich, Comment, *Phys. Rev. Lett.* (2002), 88, 069601.
18. Borodich, F. M., Galanov, B. A., Gorb, S. N., Prostov, M. Y., Prostov, Y. I. and Suarez-Alvarez, M. M "Evaluation of adhesive and elastic properties of materials by depth-sensing indentation of spheres", *Applied Physics a-Materials Science & Processing* (2012), 108, 13-18, doi:10.1007/s00339-012-6982-7.

19. Borodich, F. M., Galanov, B. A., Gorb, S. N., Prostov, M. Y., Prostov, Y. I. and Suarez-Alvarez, M. M "Evaluation of adhesive and elastic properties of polymers by BG method", *Macromol. React. Eng.* (2013), 7, 555-563, doi:10.1002/mren.201300107.
20. Borodich, F. M. "Modelling for elastic deformation of multilayer plates with small initial imperfections in the layers", Ph.D. thesis, Moscow State University (1984).
21. Borodich, F. M. "Deformation properties of multilayer metallic stack", *Mech. of Solids* (1987), 22, 103-110.
22. Bowden, F. P. and Tabor, D. "The area of contact between stationary and between moving surfaces", *Proceedings of the Royal Society of London Series a-Mathematical and Physical Sciences* (1939), 169, 391-413.
23. Bowden, F. P., Gregory, J. N. and Tabor, D. "Lubrication of metal surfaces by fatty acids", *Nature* (1945), 156, 97-101.
24. Bradley, R. S. "The cohesive force between solid surfaces and the surface energy of solids", *Philosophical Magazine* (1932), 13, 853-862.
25. Brandt, A. "Multi-level adaptive solutions to boundary value problems", *Mathematics of Computation* (1977), 138, 333-390.
26. Bruggeman, D. A. G. "Calculation of various physics constants in heterogeneous substances I Dielectricity constants and conductivity of mixed bodies from isotropic substances", *Annalen Der Physik* (1935), 24, 636-670.
27. Bryant, M. J., Evans, H. P., and Snidle, R. W. "Plastic deformation in rough surface line contacts-a finite element study", *Tribology International* (2012), 46, 269-278.
28. Bush, A. W., Gibson, R. D., and Thomas, T. R. "Elastic contact of a rough surface", *Wear* (1975), 35, 87-111.
29. Chapman A. M., Higdon J. J. L. "Effective elastic properties for a periodic bicontinuous porous-medium", *J. Mech. Phys. Solids* (1994), 42 , 283–305, doi:10.1016/0022-5096(94)90011-6.

30. Chen W. W., Liu S., Wang Q.J. "*Fast Fourier transform based numerical methods for elasto-plastic contacts of nominally flat surfaces*", Journal of Applied Mechanics-Transactions of the ASME (2008), 75, 0110221–01102211
31. Chilamakuri S. K., Bhushan B. "*Contact analysis of non-Gaussian random surfaces*", Proceedings of the Institution of Mechanical Engineers Part J-Journal of Engineering Tribology (1998), 212, 19–32.
32. Christensen, H. and Tonder, K. "*Hydrodynamic lubrication of rough bearing surface of finite width*", Journal of Lubrication Technology (1971), 93, 324-329.
33. Christensen, H. and Tonder, K. "*Hydrodynamic lubrication of rough journal bearings*," Mechanical Engineering (1972), 94, 166-172.
34. Derjaguin, B. "*Molecular theory of outer friction*", Zeitschrift Fur Physik (1934), 88, 661-675, 1934.
35. Derjaguin, B. "*Analysis of friction and adhesion IV The theory of the adhesion of small particles*" Kolloid-Zeitschrift (1934), 69, 155-164.
36. Derjaguin, B. V., Muller, V. M. and Toporov, Y. P. "*Effect of contact deformations on adhesion of particles*", Journal of Colloid and Interface Science (1975), 53, 314-326.
37. Dowson, D. and Hamrock, B. J. "*Numerical evaluation of surface deformation of elastic solids subjected to a Hertzian contact stress*" ASLE Transactions (1976), 19, 279-286.
38. Earle, M. J. and Seddon, K. R. "*Ionic liquids. Green solvents for the future*", Pure and Applied Chemistry (2000), 72, 1391-1398.
39. Elias, H. and Hyde, D. M. "*Introduction to stereology (quantitative microscopy)*", American Journal of Anatomy (1980), 159.
40. Elsharkawy A. A., Holmes M. J. A., Evans H. P., Snidle R. W. "*Micro-elastohydrodynamic lubrication of coated cylinders using coupled differential deflection method*", Proceedings of the Institution of Mechanical Engineers Part J- Journal of Engineering Tribology (2006), 220, 29–41.

41. Eshelby J. D. "*The determination of the elastic field of an ellipsoidal inclusion, and related problems*", Proc. R. Soc. Lond. A (1957), 241, 376-396, doi:10.1098/rspa.1957.0133
42. Eshelby J. D. "*The elastic field outside an ellipsoidal inclusion*", Proc. R. Soc. Lond. A, 1959, 252,561–569, doi:10.1098/rspa.1959.0173
43. Evans H. P., Hughes G., "*Evaluation of deflection in semi-infinite bodies by a differential method*", Proceedings of the Institution of Mechanical Engineers Part C- Journal of Mechanical Engineering Science (2000), 214, 563-584.
44. Evans H. P., Snidle R. W., Sharif K. J., Bryant M. J. "*Predictive modelling of failure in concentrated lubricated contacts*", Faraday Discussions (2012), 156, 105–21.
45. Freemantle, M. "*Designer solvents - Ionic liquids may boost clean technology development*" Chemical & Engineering News (1998), 76, 32-37.
46. Garboczi, E. J. and Berryman, J. G. "*Elastic moduli of a material containing composite inclusions: effective medium theory and finite element computations*", Mechanics of Materials (2001), 33.
47. GKN Sinter Metals "*Materials and Processes*" Brochure (2012)  
<http://www.gkn.com/sintermetals/media/Pages/Brochures.aspx>
48. GKN Sinter Metals "*Bearing Technologies*" Brochure (2008)  
<http://www.gkn.com/sintermetals/media/Pages/Brochures.aspx>
49. Goryacheva I.G. "*Contact mechanics in tribology*", Springer, 1998
50. Greenwood J.A., Tripp J.H. "*The contact of two nominally flat rough surfaces*", Proceedings of the Institution of Mechanical Engineers (1971), 187,625–33.
51. Greenwood, J. A. and Williamson, J. B. "*Contact of nominally flat surfaces*", Proceedings of the Royal Society of London Series a-Mathematical and Physical Sciences (1966), 295, 300-323.

52. Hamrock, B. J. and Dowson, D. "*Isothermal elastohydrodynamic lubrication of point contacts. 1. Theoretical formulation*", Journal of Lubrication Technology-Transactions of the ASME (1976), 98, 223-229.
53. Harp S. R., Salant R. F. "*An average flow model of rough surface lubrication with inter asperity cavitation*", Journal of Tribology-Transactions of the ASME (2001), 123, 134-43.
54. Hertz, H. "*Ueber die Beruehrung elastischer Koerper*", Journal fur die Reine und angewandte Mathematic (1881), 92, 156-171 (English translation by Jones, D. E. and Schott, G. A., Aberystwyth, 1896).
55. Holmes M. J. A, Evans H. P., Snidle R. W. "*Analysis of mixed lubrication effects in simulated gear tooth contacts*", Journal of Tribology - Transactions of the ASME (2005), 127,61-69.
56. Hooke, C. J. and Venner, C. H. "*Surface roughness attenuation in line and point contacts*", Proceedings of the Institution of Mechanical Engineers Part J-Journal of Engineering Tribology (2000), 214, 439-444.
57. Jacq, C., Nelias, D., Lormand, G. and Girodin, D. "*Development of a three-dimensional semi-analytical elastic-plastic contact code*", Journal of Tribology-Transactions of the ASME (2002), 124, 653-667.
58. Jai, M. "*Homogenisation and 2-scale convergence of the compressible Reynolds lubrication equation modelling the flying characteristics of a rough magnetic head over a rough rigid disk surface*" Rairo-Mathematical Modelling and Numerical Analysis-Modelisation Mathematique Et Analyse Numerique (1995), 29, 199-233.
59. Ji, S. C., Gu, Q. and Xia, B. "*Porosity dependence of mechanical properties of solid materials*", Journal of Materials Science (2006), 41.
60. Johnson, K. L. "*A note on the adhesion of elastic solids*", British Journal of Applied Physics (1958), 9, 199-200.

61. Johnson, K. L., Greenwood, J. A. and Higginson, J. G. "*The contact of elastic regular wavy surfaces*", International Journal of Mechanical Sciences (1985), 27, 383-398.
62. Johnson, K. L., Greenwood, J. A. and Poon, S. Y. "*Simple theory of asperity contact in elastohydrodynamic lubrication*" Wear (1972), 19, 91-104.
63. Johnson, K. L., Kendall, K. and Roberts, A. D. "*Surface energy and contact of elastic solids*", Proceedings of the Royal Society of London Series a-Mathematical and Physical Sciences (1971), 324, 301-317.
64. Ju Y, Farris T.N. "*Spectral analysis of two-dimensional contact problems*", Journal of Tribology-Transactions of the ASME (1996), 118, 320–28.
65. Kachanov, L. "*Basics of fracture mechanics*", Moscow: Nauka, 1974
66. Kalker, J. J. "*Variational principles of contact elastostatics*", Journal of the Institute of Mathematics and Its Applications (1977), 20, 199-219.
67. Kane, M. and Bou-Said, B. "*Comparison of homogenization and direct techniques for the treatment of roughness in incompressible lubrication*" Journal of Tribology-Transactions of the ASME (2004), 126, 733-737.
68. Kendall M., Moran P. "*Geometrical probabilities*", New York, NY: Hafner, 1963.
69. Knudsen, F. P. "*Effect of porosity on Young's modulus of alumina*", J. Am. Ceram. Soc. 45, 94–95, doi:10.1111/j.1151-2916.1962.tb11089.x.
70. Krivoglaz, M. A. and Cherevko, A. "*On the elastic moduli of a solid mixture*", Fiz. Met. Metalloved. (1959), 8, 161-164.
71. Kronberger, M., Pejakovic, V., Gabler, C., and Kalin, M. "*How anion and cation species influence the tribology of a green lubricant based on ionic liquids*", Proceedings of the Institution of Mechanical Engineers Part J-Journal of Engineering Tribology (2012), 226, 933-951.

72. Kusoglu, A., Santare, M. H. and Karlsson, A. M. "*Mechanics-based model for non-affine swelling in perfluorosulfonic acid (PFSA) membranes*", *Polymer* (2009), 50, 2481-2491.
73. Kusoglu, A., Santare, M. H., Karlsson, A. M., Cleghorn, S. and Johnson, W. B. "*Micromechanics Model Based on the Nanostructure of PFSA Membranes*", *Journal of Polymer Science Part B-Polymer Physics* (2008), 46, 2404-2417.
74. Liu S. B., Wang Q., Liu G. "*A versatile method of discrete convolution and FFT (DC-FFT) for contact analyses*", *Wear* (2000), 243:101–11.
75. Liu, W. M., Ye, C. F., Gong, Q. Y., Wang, H. Z. and Wang, P. "*Tribological performance of room-temperature ionic liquids as lubricant*", *Tribology Letters* (2002), 13, 81-85
76. Liu, X., Zhou, F., Liang, Y., and Liu, W. "*Benzotriazole as the additive for ionic liquid lubricant: one pathway towards actual application of ionic liquids*", *Tribology Letters* (2006), 23, 191-196.
77. Love, A.E.H. "*A Treatise on the Mathematical Theory of Elasticity*", Cambridge University Press, Cambridge, 1952.
78. Luo, J. and Stevens, R. "*Micromechanics of randomly oriented ellipsoidal inclusion composites .2. Elastic moduli*", *Journal of Applied Physics* (1996), 79, 9057-9063.
79. Mahrova, M., Vilas, M., Dominguez, A., Gomez, E., Calvar, N., and Tojo, E. "*Physicochemical Characterization of New Sulfonate and Sulfate Ammonium Ionic Liquids*", *Journal of Chemical and Engineering Data* (2012), 57, 241-248.
80. Manners W. and Greenwood J.A., "*Some observations on Persson's diffusion theory of elastic contact*", *Wear* (2006), 261, 600–610,
81. Manoylov, A. V., Borodich, F. M., and Evans, H. P., "*Modelling of elastic properties of sintered porous materials*", *Proceedings of the Royal Society a-Mathematical Physical and Engineering Sciences* (2013), 469, doi:10.1098/rspa.2012.0689.

82. Manoylov, A. V., Bryant, M. J., and Evans, H. P., "*Dry elasto-plastic contact of nominally flat surfaces*", Tribology International (2013), 65, 248-258, doi:10.1016/j.triboint.2013.02.029.
83. Martini, A., Escoffier, B., Wang, Q., Liu, S. B., Keer, L. M., Zhu, D., et al., "*Prediction of subsurface stress in elastic perfectly plastic rough components*", Tribology Letters (2006), 23, 243-251.
84. Mason M. "*The doubly periodic solutions of Poisson's equation in two independent variables*", Transactions of the American Mathematical Society (1905), 6, 159–64.
85. Matikas, T. E., Karpur, P., and Shamasundar, S., "*Measurement of the dynamic elastic moduli of porous titanium aluminide compacts*", Journal of Materials Science (1997), 32, 1099-1103.
86. Maugis, D., "*Adhesion of Spheres – the JKR-DMT Transition using a Dugdale Model*", Journal of Colloid and Interface Science (1992), 150, 243-269.
87. Maugis, D, "*Contact, Adhesion and Rupture of Elastic Solids*", Springer, Berlin, 2000
88. Mendonca-Fernandes, A.C., Dorr, N., and Padua, A. "*Predicting thermophysical properties of ionic liquids as a function of temperature and pressure*", Proceedings of the Institution of Mechanical Engineers Part J-Journal of Engineering Tribology (2012), 226, 965-976.
89. MICHELL, A. G. M. "*Improvements in Thrust and like Bearings*" British Patent GB190500875, 1905
90. Milton, G. W., "*Concerning Bounds on the Transport and Mechanical Properties of Multicomponent Composite Materials*", Applied Physics a-Materials Science & Processing (1981), 26, 125-130.
91. Milton, G. W., "*Correlation of the Electromagnetic and Elastic Properties of Composites and Micro geometries Corresponding with Effective Medium Approxiamtions*" AIP Conference Proceedings (1984), 66-77.

92. Minami, I., "*Ionic Liquids in Tribology*", *Molecules* (2009), 14, 2286-2305.
93. Mukerji, T., Berryman, J., Mavko, G., and Berge, P., "*Differential Effective Medium Modeling of Rock Elastic Moduli with Critical Porosity Constraints*" *Geophysical Research Letters* (1995), 22, 555-558.
94. Nayfeh A. H. "*Perturbation Methods*" WILEY-VCH Verlag GmbH & Co., 2004 ISBN: 9780471399179 DOI: 10.1002/9783527617609
95. Neal, M. J., "*The Tribology Handbook*", 2nd Edition, Butterworth-Heinemann, Oxford, 1995
96. Nelias, D., Antaluca, E., Boucly, V., and Cretu, S., "*A three-dimensional semianalytical model for elastic-plastic sliding-contacts*", *Journal of Tribology-Transactions of the ASME* (2007), 129, 761-771.
97. Norris, A. N. , "*A Differential Scheme for the Effective Moduli of Composites*" *Mechanics of Materials* (1985), 4, 1-16.
98. Norris, A. N., Callegari, A. J., and Sheng, P., "*A generalized Differential Effective Medium Theory*", *Journal of the Mechanics and Physics of Solids* (1985), 33, 525-543.
99. Oh, I. H., Nomura, N., Masahashi, N., and Hanada, S., "*Mechanical properties of porous titanium compacts prepared by powder sintering*", *Scripta Materialia* (2003), 49, 1197-1202.
100. Oppenheim, Alan V.; Schafer, Ronald W.; Buck, John A. "*Discrete-time signal processing*", Upper Saddle River, N.J.: Prentice Hall, 1999, ISBN 0137549202.
101. Pagano, F., Gabler, C., Zare, P., Mahrova, M., Dorr, N., Bayon, R., et al., "*Dicationic ionic liquids as lubricants*", *Proceedings of the Institution of Mechanical Engineers Part J-Journal of Engineering Tribology* (2012), 226, 952-964.
102. Patir, N., Cheng, H, "*Average Flow Model for Determining Effects of Three-Dimensional Roughness on Partial Hydrodynamics Lubrication*" *Journal of Lubrication Technology-Transactions of the ASME* (1978), 100, 12-17.

103. Patir, N., Cheng, H, "*Application of Average Flow Model to Lubrication Between Rough Sliding Surfaces*" *Journal of Lubrication Technology-Transactions of the ASME* (1979), 101, 220-230.
104. Pejakovic, V., Kronberger, M., Mahrova, M., Vilas, M., Tojo, E., and Kalin, M., "*Pyrrrolidinium sulfate and ammonium sulfate ionic liquids as lubricant additives for steel/steel contact lubrication*", *Proceedings of the Institution of Mechanical Engineers Part J-Journal of Engineering Tribology* (2012), 226, 923-932.
105. Pensado, A. S., Comunas M. J., and J. Fernandez, "*The pressure-viscosity coefficient of several ionic liquids*", *Tribology Letters* (2008), 31, 107-118.
106. Pensado, A. S., Padua, A.A., P, Comunas, M. J. and Fernandez, J., "*Relationship between viscosity coefficients and volumetric properties using a scaling concept for molecular and ionic liquids*", *Journal of Physical Chemistry B* (2008), 112, 5563-5574.
107. Persson B N J. "*Elastoplastic contact between randomly rough surfaces*", *Physical Review Letters* (2001), 87.
108. Pindera, M. J., Khatam, H., Drago, A. S., and Bansal, Y., "*Micromechanics of spatially uniform heterogeneous media: A critical review and emerging approaches*", *Composites Part B-Engineering* (2009), 40, 349-378.
109. Pisarova, L., Steudte, S., Dorr, N., Pittenauer, E., Allmaier, G., Stepnowski, P. et al., "*Ionic liquid long-term stability assessment and its contribution to toxicity and biodegradation study of untreated and altered ionic liquids*" *Proceedings of the Institution of Mechanical Engineers Part J-Journal of Engineering Tribology* (2012), 226, 903-922.
110. Polder, D. and Vansanten, J. H., "*The Effective Permeability of Mixtures of Solids*", *Physica* (1946), 12, 257-271.
111. Polonsky, I. A. and Keer, L. M., "*A fast and accurate method for numerical analysis of elastic layered contacts*", *Journal of Tribology-Transactions of the ASME* (2000), 122, 30-35.

112. Polonsky, I. A. and Keer, L. M., "*A numerical method for solving rough contact problems based on the multi-level multi-summation and conjugate gradient techniques*", *Wear* (1999), 231, 206-219.
113. Porter, D. F., Reed, J. S. and Lewis, D., "*Elastic Moduli of Refractory Spinel*", *Journal of the American Ceramic Society* (1977), 60, 345–349,.
114. Poutet, J., Manzoni, D., Hagechade, F., Jacquin, J. C. ., Bouteica, M. J., Thovert, J. F., et al., "*The effective mechanical properties of random porous media*", *Journal of the Mechanics and Physics of Solids* (1996), 44, 1587-1620.
115. Rabotnov, Y. "*Mechanics of solids*", Moscow: Nauka, 1979
116. Rayleigh, "*Notes on the theory of lubrication*" *Philosophical Magazine*, 1918, 35, 1-12.
117. Reynaud, C., Thevenot, F., Chartier, T., and Besson, J. L., "*Mechanical properties and mechanical behaviour of SiC dense-porous laminates*", *Journal of the European Ceramic Society* (2005), 25, 589–597.
118. Roberts, A. P. and Garboczi, E. J., "*Computation of the linear elastic properties of random porous materials with a wide variety of microstructure*", *Proceedings of the Royal Society of London Series a-Mathematical Physical and Engineering Sciences* (2002), 458, 1033-1054.
119. Sahlin, F., Larsson, R., Almqvist, A., Lugt, P. M., and Marklund, P., "*A mixed lubrication model incorporating measured surface topography. Part 1: theory of flow factors*", *Proceedings of the Institution of Mechanical Engineers Part J-Journal of Engineering Tribology* (2010), 224, 335-351.
120. Sahlin, F., Larsson, R., Marklund, P., Almqvist, A., and Lugt, P. M., "*A mixed lubrication model incorporating measured surface topography. Part 2: roughness treatment, model validation, and simulation*", *Proceedings of the Institution of Mechanical Engineers Part J-Journal of Engineering Tribology* (2010), 224, 353-365, 2010.

121. Salganik R.L., Fedotov A.A. , "Evaluation of concentration of cracks in porous material using its overall deformability and their influence on its strength" Proc. 19th European Conf. on Fracture, Kazan, Russia, 26–31 August 2012.
122. Salganik, R. L. and Gotlib, V. A., "Continuum versus discontinuum damage mechanics of creep caused by microcracking", International Journal of Fracture (2000), 101, 181-201.
123. Salganik, R. L. "Mechanics of bodies with many cracks", Mech. of Solids (1973), 8,135-143.
124. Scaraggi M, Carbone G, Persson B N J, Dini D. "Lubrication in soft rough contacts: a novel homogenised approach. Part I—theory", Soft Matter (2011), 7:10395–406.
125. Scaraggi M, Carbone G, Dini D. "Lubrication in soft rough contacts: a novel homogenised approach. Part II—discussion", Soft Matter (2011), 7:10407–16.
126. Sevostianov, I. and Kachanov, M., "Effective properties of heterogeneous materials: Proper application of the non-interaction and the "dilute limit" approximations", International Journal of Engineering Science (2012), 58, 124-128.
127. Shen, H., Oppenheimer, S. M., Dunand, D. C., and Brinson, L. C., "Numerical modeling of pore size and distribution in foamed titanium", Mechanics of Materials (2006), 38, 933-944.
128. Spriggs, R. M., "Effect of Open and Closed Pores on elastic Moduli of Polycrystalline Alumina", Journal of the American Ceramic Society (1962), 45, 454-454.
129. Spriggs, R. M., "Expression for Effect of Porosity on Elastic Modulus of Polycrystalline Refractory Materials, Particularly Aluminum Oxide" Journal of the American Ceramic Society (1961), 44, 628–629, 1961.
130. Stanley H M, Kato T. "An FFT-based method for rough surface contact", Journal of Tribology-Transactions of the ASME (1997), 119, 481–5.
131. Stolte, S., Steudte, S., Areitioaurtena, O., Pagano, F., Thoming, J., Stepnowski, P. et al., "Ionic liquids as lubricants or lubrication additives: An ecotoxicity and biodegradability assessment", Chemosphere (2012), 89, 1135-1141.

132. Talbot D. R. and Willis, J. R., "*Bounds and Self Consistent Estimates for the Overall Properties of Nonlinear Composites*", Journal of Applied Mathematics (1987), 39, 215-240.
133. Timoshenko S. P., Goodier J. N. "*Theory of elasticity*", New York: McGraw-Hill, 1970.
134. Totolin, V., Ranetcaia, N., Hamciuc, V., Shore, N., Dorr, N., Lbanescu, C., et al., "*Influence of ionic Structure on tribological properties of poly(dimethylsiloxane-alkylene oxide) graft copolymers*" Tribology International (2013), 67, 1-10.
135. Tripp J.H. "*Surface roughness effects in hydrodynamic lubrication: the flow factor method*", .ASME Transactions Journal of Lubrication Technology (1983), 105,458–65.
136. Tzeng, S. T. and Saibel, E., "*Surface Roughness Effects on Slider Bearing Lubrication*", ASLE Transactions (1967), 10, 334-343.
137. Vallet, C., Lasseux, D., Sainsot, P., Zahouani, H. "*Real versus synthesized fractal surfaces: Contact mechanics and transport properties*", TRIBOLOGY INTERNATIONAL (2009), 42(2), pp. 250-259, doi: 10.1016/j.triboint.2008.06.005.
138. Vavakin, A. S. and Salganik, R. L. "*Effective characteristics of non-homogeneous media with isolated non homogeneities*", Mech. of Solids (1975), 10, 65-75.
139. Vavakin, A. S. and Salganik, R. L. "*Effective elastic characteristics of bodies with isolated cracks, cavities, and rigid non-homogeneities*", Mech. of Solids (1978), 13,87-97.
140. Venner, C.H. and Lubrecht, A.A. "*Multilevel Methods in Lubrication*" Hardcover, 400 Pages, Published 2000 by Elsevier Science ISBN-13: 978-0-444-50503-3, ISBN: 0-444-50503-2
141. Walsh, J. B., Brace, W. F., and England, A. W., "*Effect of Porosity on Compressibility of Glass*" Journal of the American Ceramic Society (1965), 48, 605–608.
142. Wang, F. and Keer, L. M., "*Numerical simulation for three dimensional elastic-plastic contact with hardening behavior*", Journal of Tribology-Transactions of the ASME (2005), 127, 494-502.

143. Wang, F. S., Block, J. M., Chen, W. W., Martini, A., Zhou, K., Keer, L. M., et al., "A Multilevel Model for Elastic-Plastic Contact Between a Sphere and a Flat Rough Surface", *Journal of Tribology-Transactions of the ASME* (2006), 131, 6.
144. Wang, J. C., "Young Modulus of Porous Materials. 1. Theoretical Derivation of Modulus Porosity Correlation" *Journal of Materials Science* (1984), 19, 801-808.
145. Wang, J. C., "Young Modulus of Porous Materials. 2. Young Modulus of Porous Alumina with Changing Pore Structure" *Journal of Materials Science* (1984), 19, 809-814.
146. Welton, T., "Room-temperature ionic liquids. Solvents for synthesis and catalysis", *Chemical Reviews* (1999), 99, 2071-2083.
147. Westergaard, H. M. "Bearing pressures and cracks", *Journal of Applied Mechanics* (1939), 6, pp. 49–53.
148. Williamson J. B. P. and Hunt, R. T. "Asperity Persistence and the Real Area of Contact Between Rough Surfaces", *Proc. R. Soc. Lond. A* (1972), 327(1569), pp. 147-157, doi: 10.1098/rspa.1972.0037.
149. Willis, J. R., " Bounds and Self Consistent Estimates for the Overall Properties of Anisotropic Composites", *Journal of the Mechanics and Physics of Solids* (1977), 25, 185-202.
150. Yastrebov, V. A., Durand, J., Proudhon, H., Cailletaud, G. "Rough surface contact analysis by means of the Finite Element Method and of a new reduced model", *COMPTEs RENDUS MECANIQUE* (2011), 339 (7-8), pp. 473-490, doi: 10.1016/j.crme.2011.05.006
151. Ye, C. F., Liu, W. M., Chen, Y. X., and Yu, L. G., "Room-temperature ionic liquids: a novel versatile lubricant", *Chemical Communications* (2001), 2244-2245.
152. Zare, P., Mahrova, M., Tojo, E., Stojanovic, A., and Binder, W. H., "Ethylene glycol-based ionic liquids via azide/alkyne click chemistry", *Journal of Polymer Science Part a-Polymer Chemistry* (2013), 51, 190-202.

153. Zhuravlev, V. A. *“On question of theoretical justification of the Amontons–Coulomb law for friction of unlubricated surfaces”*, Zh. Tekh. Fiz., (1940), 10(17), 1447–1452.

154. Zhuravlev, V. A. *“On question of theoretical justification of the Amontons–Coulomb law for friction of unlubricated surfaces”*, Translation and introduction by Borodich, F. M. in Proceedings of the Institution of Mechanical Engineers Part J-Journal of Engineering Tribology (2007), 221, 893-895.